[redacted]

NASA-CR-112087

X72-10685

Classification changed to Unclassified per authority of H.G. Maines.

DOWNGRADED AT 3 YEAR INTERVALS;
DECLASSIFIED AFTER 12 YEARS
DOD DIR 5200.10

OCT 1975
RECEIVED
NASA STI FACILITY
INPUT BRANCH

(NASA-CR-112087) HYPERSONIC RESEARCH ENGINE PROJECT. PHASE 2: STRUCTURES AND COOLING DEVELOPMENT, DATA ITEM NO. 55-7.18 Final Technical Data Report, 3 Feb. 1967 - 31 May 1971 (AiResearch Mfg. Co., Los Angeles, 00/98

N76-70980

Unclas
42354

GARRETT

AIRESEARCH MANUFACTURING COMPANY
A DIVISION OF THE GARRETT CORPORATION
9851-9951 SEPULVEDA BLVD. • LOS ANGELES, CALIFORNIA 90009
TELEPHONE: SPRING 6-1010, ORCHARD 0-0131 • CABLE: GARRETTAIR LOS ANGELES

C O N [redacted]

"This material co[redacted] within the meaning of [redacted] U.S.C. Sec. 793 and 794 [redacted] in any manner to an unauthorized person is prohibited by law."

CONFIDENTIAL
PAGE IS UNCLASSIFIED

Classification changed to Unclassified
per authority of HG Maine

GARRETT

AIRESEARCH MANUFACTURING COMPANY
Los Angeles, California

HYPERSONIC RESEARCH ENGINE PROJECT - PHASE II
STRUCTURES AND COOLING DEVELOPMENT
FINAL TECHNICAL DATA REPORT(U)
DATA ITEM NO. 55-7.18
3 FEBRUARY 1967 THROUGH 31 MAY 1971
NASA CONTRACT NO. NAS1-6666

Document No. AP-72-8237

Group 4

Downgraded at 3 year intervals;
declassified after 12 years
DOD DIR 5200.10

This material contains information affecting the national defense of the United States within the meaning of the espionage laws, Title 18, U.S.C., Sections 793 and 794, the transmission or revelation of which in any manner to an unauthorized person is prohibited by law.

Number of pages 474

Original date 18 May 1972

Prepared by Engineering Staff

Edited by L. F. Jilly

Approved by E N Harris
Edward N. Harris
HRE Program Manager

Revision	Date	Pages Affected (Revised, Added, Eliminated)

CONFIDENTIAL
PAGE IS UNCLASSIFIED

FOREWORD

This final technical data report is submitted to the NASA Langley Research Center by the AiResearch Manufacturing Company, Los Angeles, California. The document was prepared in accordance with the guidelines established by paragraph 5.7.3.2.2 of NASA Statement of Work L-4947-B (Revised).

The document in hand presents a detailed technical discussion of the Structures and Cooling development for the period of 3 February 1967 through 31 May 1971, and represents a summation of the work previously reported in the quarterly interim technical data reports for the Cooling and Structures Development generated under the Hypersonic Research Engine Project.

ACKNOWLEDGEMENTS

Acknowledgements for the completion of this document are herewith extended to the following contributors:

Design and Development:	O. A. Buchmann C. M. Lee
Heat Transfer Analyses:	A. A. Vuigner C. F. Young
Stress Analyses:	W. G. Flieder E. Katinszky
Technical Supervision:	O. A. Buchmann
Development:	C. M. Lee

CONTENTS

Section		Page
1.	SUMMARY AND CONCLUSIONS	1-1
	1.1 Program Summary	1-1
	1.2 Conclusions	1-3
2.	PROBLEM STATEMENT	2-1
3.	TOPICAL BACKBROUND	3-1
	3.1 General Design Guidelines	3-1
	3.2 Operational Boundaries	3-4
4.	OVERALL APPROACH	4-1
	4.1 Thermal Design	4-1
	4.2 Structural Design	4-2
	4.3 Mechanical Design	4-3
	4.4 Manufacturing	4-3
5.	ANALYTICAL DESIGN	5-1
	5.1 System Thermal Analysis (Flight)	5-1
	5.2 System Structural Analysis (Flight)	5-26
	5.3 Engine Structural Dynamics	5-66
	5.4 Vibration Fixture	5-73
	5.5 Engine Components	5-79
	5.6 Shell Assembly Flow Test Adapters	5-133
	5.7 System Wind Tunnel Analysis	5-141
	5.8 Water-Cooled Wind Tunnel Adapters	5-150
	5.9 Temperature and Pressure Control Systems	5-161
6.	DESIGN FEATURES	6-1
	6.1 Inlet Spike	6-1
	6.2 Inner Shell	6-4
	6.3 Nozzle	6-6
	6.4 Leading Edge	6-7
	6.5 Outer Shell	6-10
	6.6 Support Struts	6-15
	6.7 Engine Assemblies	6-18

CONTENTS (Cont)

Section		Page
	6.8 SAM Fuel/Coolant Systems	6-23
	6.9 Wind Tunnel Test Adapters	6-26
	6.10 Inlet Spike Actuation System	6-30
	6.11 Temperature and Pressure Control System	6-32
	6.12 Vibration Model	6-39
7.	MANUFACTURING	7-1
	7.1 Flightweight Shells	7-1
	7.2 Flightweight Components	7-5
	7.3 Inlet Spike Actuator	7-26
	7.4 Engine Suspension Frame	7-29
	7.5 Water-Cooled Wind Tunnel Adapters	7-34
	7.6 SAM Assembly	7-42
	7.7 Vibration Model	7-54
	7.8 Shell Assembly Flow Test Adapters	7-58
	7.9 Temperature Control System	7-58
8.	TESTING	8-1
	8.1 Struts	8-1
	8.2 Leading Edge Straight Section	8-20
	8.3 Flat Panels	8-35
	8.4 Inlet Spike Actuation System	8-63
	8.5 Coolant Bellows	8-72
	8.6 Component Pressure Drop and Flow Distribution	8-73
	8.7 SAM Flow Calibration	8-81
	8.8 SAM Wind Tunnel Testing	8-90

CONTENTS (Cont)

Section	Page
REFERENCES	R-1

Drawings attached at end of report

L980604	L980617
L980609	L980618
L980610	L980619, Sheets 1 and 2
L980611	L980622, Sheets 1 and 2
L980612	980800, Sheets 1 and 2
980614	980801, Sheets 1 and 2
L980615, Sheets 1 and 2	981189, Sheets 1, 2 and 3

ILLUSTRATIONS

Figure		Page
3.-1	Cooled Structures Nomenclature	3-2
3.2-1	Typical Engine Operating Cycles	3-6
5.1-1	Aerodynamic Parameters and Heat Flux Distribution at Mach 8, Freestream and Local, 88,000 Ft Altitude	5-4
5.1-2	Aerodynamic Parameters and Heat Flux Distribution at Mach 8, Freestream, and Mach 6.5, Local - 88,000 Ft Altitude	5-5
5.1-3	Coolant Flow Routing Design	5-6
5.1-4	Steady-State Thermal Performance at Mach 8, Freestream and Local, 88,000 Ft Altitude	5-9
5.1-5	Steady-State Thermal Performance at Mach 8, Freestream,and Mach 6.5, Local - 85,000 Ft Altitude	5-10
5.1-6	HRE Hydrogen System Schematic	5-14
5.1-7	Cooling Hydrogen System Details, First Flightweight Engine	5-15
5.1-8	HRE Cooling System Flow Distribution	5-18
5.1-9	Temperature Histories at Innerbody Subsonic Injector Manifold from Mach 6.5L to Shutdown	5-20
5.1-10	Temperature Histories at Innerbody Subsonic Manifold During Mach 4 Combustion	5-21
5.1-11	Outerbody Outlet Manifold Thermal Transient	5-21
5.1-12	Proposed X-15A-2 Trajectory for HRE Mission to Mach 8	5-24
5.2-1	HRE Coordinate System and Sign Convention	5-27
5.2-2	HRE Center-of-Gravity and Center-of-Pressure Locations	5-28
5.2-3	X-15A Engine-Lit Mission Envelope	5-31

ILLUSTRATIONS (Continued)

Figure		Page
5.2-4	HRE Pressure Distribution at $M_\infty = 8.0$	5-32
5.2-5	Estimated Axial Load Profile on Spike During a Typical Symmetrical Inlet Unstart Sequence (Shock Expelled)	5-36
5.2-6	Estimated Load Profiles on Spike During a Typical Asymmetric Inlet Unstart Sequence (Shock Expelled)	5-38
5.2-7	Strut Design Loads	5-41
5.2-8	Innerbody-Outerbody Aerodynamic Parameters	5-42
5.2-9	Outerbody Aerodynamic Parameters	5-43
5.2-10	HRE Cowl Aerodynamic Loads	5-44
5.2-11	Engine-Mount Manifolds Stress Analysis	5-47
5.2-12	HRE Fuel Control Valve Manifold System	5-50
5.2-13	HRE Manifold Locations	5-57
5.2-14	Manifold Cross Sections	5-58
5.2-15	Typical Hot-Skin Plastic Strain Loop	5-61
5.2-16	Hastelloy X Plate-Fin Low-Cycle Fatigue Test Results	5-64
5.2-17	Effects of Elevated Temperature Fatigue Life	5-65
5.3-1	Schematic of Vibration Analysis Model	5-69
5.3-2	Vibration Analysis Model	5-70
5.3-3	HRE Vibration Test Unit	5-74
5.4-1	Shaker, Fixture, and Specimen Schematic - Team Bearing Support or Oil Film With Flexures	5-76

ILLUSTRATIONS (Continued)

Figure		Page
5.4-2	Dynamic Structural Model With Oil-Film Support and Without Flexures	5-76
5.4-3	Extensional-Mode Lumped-Parameter Model	5-77
5.4-4	Lateral Bending Mode Shapes	5-78
5.5-1	Spike Tip Coolant Conditions (Mach 8, 88,000 Ft)	5-80
5.5-2	Spike Folded-Flow Section Thermal Performance	5-82
5.5-3	Spike Analytical Model	5-83
5.5-4	Summary of Design Changes on Inner Shell	5-85
5.5-5	Cross Section of Nozzle Cap	5-90
5.5-6	Cowl Leading Edge Tip Configurations and Coolant Flow Paths	5-93
5.5-7	Leading Edge Design Thermal Performance	5-95
5.5-8	Leading Edge Test Section	5-97
5.5-9	Schematic of Test Apparatus	5-98
5.5-10	Outerbody Leading Edge Test Section	5-100
5.5-11	Summary of HRE Strut Cooling Design	5-103
5.5-12	HRE Struts Thermal Performance	5-105
5.5-13	HRE Struts Thermal Performance	5-106
5.5-14	HRE Strut Leading Edge Fin Geometry	5-107
5.5-15	Strut Test Section Instrumentation	5-109
5.5-16	Strut Support Panels Hot Gas Heat Flux Distribution	5-110
5.5-17	Reactions to Unsymmetrical Unstart Loads (Radius) 10.4 in., Station 65.05	5-112
5.5-18	Design Loads - Actuator Support Structure	5-113

ILLUSTRATIONS (Continued)

Figure		Page
5.5-19	Inlet Spike Actuation System - Nitrogen Blowdown System	5-116
5.5-20	Actuator Loading With Unsymmetric Unstart	5-118
5.5-21	Actuator Loading With Symmetric Unstart	5-118
5.5-22	Actuator Load Flow Due to 1000-lb Unit Load	5-119
5.5-23	Actuator Load Flow Due to 1000 lb-in. Unit Moment	5-120
5.5-24	Diagram of Inlet Spike Actuator System	5-122
5.5-25	Transient Response to a Step Command Signal of +0.2 in. From the Initial Position of 0.45 in.	5-124
5.5-26	Diagram of Inlet Spike Actuation System Transient Response to a Step Command Signal of +0.2 in. From the Initial Position of 1.45 in.	5-125
5.5-27	Transient Response During Retraction of Spike	5-126
5.5-28	Transient Response During Extension of Spike	5-128
5.5-29	HRE Suspension Frame	5-129
5.5-30	Ablative Cowl Heat Loads at Mach 8	5-131
5.6-1	Outer Shell Test Fixture Configuration and Loads	5-139
5.7-1	Aerodynamic Parameters and Heat Flux Distribution for SAM Wind Tunnel Conditions	5-142
5.7-2	SAM Weight Distribution, Spike Retracted	5-144
5.7-3	SAM Aerodynamic Loads	5-144
5.7-4	SAM Centerbody Thermal Performance	5-145

ILLUSTRATIONS (Continued)

Figure		Page
5.7-5	SAM Outerbody Thermal Performance	5-147
5.8-1	SAM Water-Cooled Wind Tunnel Adapters	5-151
5.8-2	Support Wedge (Route 5) - Cooling of Mating Surface With Pylon, Leading Edge, and Part of Sides (Reference Figure 5.8-3)	5-154
5.8-3	Support Wedge (Route 5) - Cooling of Remaining Part of Sides (Reference Figure 5.8-2)	5-155
5.8-4	SAM Cowl/Pylon Stress Analysis	5-157
5.8-5	SAM Cowl/Pylon Aerodynamic, Thermal, and Coolant-Pressure Load Summary	5-158
5.8-6	SAM Support Structure	5-160
5.9-1	Functional Diagram of Temperature Control System	5-163
5.9-2	Logic Diagram for SAM Temperature Control System	5-166
6.4-1	Outerbody Leading Edge Straight Section	6-11
6.4-2	Leading Edge Straight Section With Separate Tip Cooling Circuit	6-12
6.6-1	Innerbody-Outerbody Strut--Separate Inlets to Flow Routes	6-16
6.8-1	HRE/SAM Hydrogen System	6-25
6.8-2	HRE/SAM Water Systems	6-27
6.11-1	HRE Temperature Control	6-35
6.11-2	Startup and Shutdown Circuit	6-37
6.11-3	Pressure-Control Valve Drive Assembly	6-40
6.11-4	HRE/SAM Pressure-Control System	6-41

ILLUSTRATIONS (Continued)

Figure		Date
7.1-1	HRE Shell Assembly Shells	7-2
7.1-2	Outer Shell "Electroshape" Forming Die - Die Halves Separated to Show Machined Inside Contour	7-4
7.1-3	Outer Shell "Electroshape" Forming Die Ready for Firing	7-4
7.1-4	Inner Shell Assembly	7-6
7.2-1	Major Components of Inlet Spike Brazed Assembly	7-8
7.2-2	SAM Inlet Spike	7-10
7.2-3	Inner Shell Assembly - Detail Components	7-11
7.2-4	Inner Shell Final Assembly - Braze Joint Arrangement and Flow Paths	7-11
7.2-5	Inner Shell Assembly - View Into Aft End Showing Actuator Mounting Pads, Strut, Mounting Pads, and Nozzle Mounting Flange	7-12
7.2-6	Nozzle Assembly Details	7-15
7.2-7	SAM Nozzle Assembly	7-16
7.2-8	Leading Edge Assembly	7-18
7.2-9	Leading Edge Shell Assemblies	7-19
7.2-10	Leading Edge Assembly	7-21
7.2-11	SAM Outer Shell Assembly	7-23
7.2-12	Struts Internal Details	7-25
7.2-13	Flightweight Engine Mockup	7-28
7.3-1	SAM Inlet Spike Actuator	7-30
7.3-2	Support Structure	7-31
7.3-3	Hydraulic Actuator	7-32

ILLUSTRATIONS (Continued)

Figure		Page
7.4-1	SAM Suspension Frame	7-33
7.5-1	Cowl/Pylon Subassemblies	7-35
7.5-2	SAM Cowl/Pylon Assembly Ready for Proof-Pressure Test	7-36
7.5-3	Rear Pylon Cover Assembly	7-38
7.5-4	Water-Cooled Rear Seal Ring	7-39
7.5-5	Water-Cooled Forward Cowl	7-40
7.5-6	Water-Cooled Support Wedge	7-41
7.6-1	SAM Components	7-43
7.6-2	Experimental Assemblies	7-44
7.6-3	HRE SAM Outer Shell Assembly Mounted on Holding/Positioning Fixture	7-46
7.6-4	SAM Structural Assembly Ready for Start of Plumbing Fitup, Showing Fuel Plenum and its Locating Fixture	7-46
7.6-5	SAM Structural Assembly After Completion	7-48
7.6-6	SAM Structural Assembly - View Looking Into Front End	7-48
7.6-7	SAM Engine Assembly - Setup for Installation of Spike and Actuator	7-49
7.6-8	Nozzle Assembly Showing Pressure Transducer Housing	7-51
7.6-9	SAM Engine Assembly - Nozzle in Place for Connection of Cable Assemblies	7-51
7.6-10	SAM Engine Assembly - Installation of Cap on Nozzle	7-51
7.6-11	Base Plate Mounted on the Plywood Elevator Carriage Mockup	7-53

ILLUSTRATIONS (Continued)

Figure		Page
7.6-12	Completed Manifold/Valve Assembly on Mockup of Elevator Carriage	7-53
7.6-13	SAM Engine Final Assembly Operations	7-55
7.6-14	SAM Engine and Water-Cooled Structures Mounted on Manifold/Valve Assembly	7-56
7.6-15	SAM Handling Cart	7-57
7.7-1	Vibration Model Components	7-59
7.8-1	Innerbody (Spike) Flow Test Adapter Subassemblies	7-60
7.8-2	Innerbody (Spike) Flow Test Adapter, Tack-Welded Assembly - Left Side View	7-60
7.8-3	Details for Outer Shroud and Plug Assembly, Leading Edge Flow Test Adapter	7-61
7.9-1	Temperature Control System Control Panel	7-62
7.9-2	Temperature Control Chassis, Front View	7-63
7.9-3	Temperature Control Chassis, Front Panel Open to Expose Circuit Boards	7-63
7.9-4	Printed Circuit Board Types in Temperature Control Chassis	7-64
7.9-5	Flow Calculator Chassis, Front View	7-65
7.9-6	Flow Calculator Chassis, Front Panel Open to Expose Circuit Boards	7-65
7.9-7	Printed Circuit Board Types in Flow Calculator Chassis	7-66
8.1-1	Strut Test Specimens	8-3
8.1-2	Strut Leading Edge Heat Transfer Results	8-7
8.1-3	Strut Assembly After Rupture Test	8-11

ILLUSTRATIONS (Continued)

Figure		Page
8.1-4	Strut Thermal Fatigue Temperatures	8-12
8.2-1	Leading Edge Straight Section, Radiant Heating Test Fixture Schematic	8-22
8.2-2	Cowl Leading Edge Internal Cooling Nusselt Number	8-25
8.2-3	Cooling of Leading Edge With Parallel Flow	8-27
8.2-4	Leading Edge Thermal Cycles	8-28
8.2-5	Leading Edge Straight Section Flow Ratio	8-34
8.3-1	Detail Components of Basic Static Test Flat Panel	8-36
8.3-2	Basic Flat Panel Configuration	8-36
8.3-3	Static Test Local Joint Flat Panel	8-38
8.3-4	Coolant Exhaust Continuous-Gap Flat Panel	8-38
8.3-5	Regenerative-Cooled Panels High Temperature Test Facility	8-39
8.3-6	Inner Shell-Nozzle Joint Flat Panels	8-43
8.3-7	Flat Plate Collector Manifold Pull Test	8-45
8.3-8	Flat Panel Thermal Fatigue Test Specimen	8-47
8.3-9	Flat Panel Thermal Cycle Test Setup	8-49
8.3-10	Thermal Fatigue Test Results	8-54
8.3-11	Flow Distribution Test Specimens	8-55
8.3-12	Insert Flow Test Panel Schematic	8-57
8.3-13	Temperature-Indicating Paint for First and Second Insert Panels After Run A	8-58
8.3-14	X-rays of Plate-Fin Braze Void Panels, Nondestructive Testing Techniques	8-61

ILLUSTRATIONS (Continued)

Figure		Page
8.3-15	Nondestructive Testing Evaluation - Braze Void Panels (Void Side) "StressCoat" Coated	8-62
8.4-1	Spike Actuation System Test Schematic	8-64
8.4-2	Functional Block Daigram of ISACS Test Setup	8-65
8.4-3	ISACS Installed in Test Fixture	8-66
8.4-4	Schematic of ISACS Test Setup	8-68
8.5-1	SAM Bellows Details	8-72
8.5-2	Coolant Inlet Bellows Assembly Installed in Cycle Test Fixture	8-74
8.5-3	Nitrogen Source and Hydraulic Pump Shown Outside of Burst Chamber Used For Bellows Cycle Testing	8-74
8.6-1	SAM Spike Air-Pressure-Drop Test Results	8-76
8.6-2	Nozzle, Innerbody, and Inner Shell Air-Pressure-Drop Test Results	8-77
8.6-3	Leading Edge Air-Pressure-Drop Test Results	8-78
8.6-4	Outer Shell Air-Pressure-Drop Test Results	8-80
8.6-5	Strut-Sides Air-Pressure-Drop Test Results	8-82
8.7-1	SAM Spike Air-Pressure-Drop Test Results	8-84
8.7-2	Coolant Route Flow Rate Percentages	8-86
8.8-1	HRE/SAM Hydrogen System	8-92
8.8-2	NASA-Langley 8-Foot High Temperature Structures Tunnel - SAM Tests	8-96
8.8-3	SAM at Wind Tunnel, on Mockup of Elevator Carriage	8-96
8.8-4	SAM Installed in Wind Tunnel Test Section - Side View	8-98

ILLUSTRATIONS (Continued)

Figure		Page
8.8-5	SAM Installed in Wind Tunnel Test Section - Front View	8-98
8.8-6	Wind Tunnel Test Cycle	8-101
8.8-7	Test Hydrogen Heat Loads	8-107
8.8-8	Enthalpy of Normal Hydrogen	8-109
8.8-9	Aerodynamic Static Pressure Distributions	8-112
8.8-10	Trailing Edge Average Structure Temperature and Hydrogen Heat Load	8-114
8.8-11	Thermal Fatigue Critical Areas	8-119
8.8-12	Outerbody Outlet Manifold Cross Section	8-120
8.8-13	Typical Cycle Metal-Temperature History	8-124
8.8-14	Strain Gage and Accelerometer Locations	8-126
8.8-15	SAM External Reactions	8-128
8.8-16	Mounting Frame and Measured Maximum Reactions	8-129
8.8-17	Inlet Spike Actuator	8-131
8.8-18	Force at Aft End of Actuator	8-133
8.8-19	Actuator Loads vs Spike Movement	8-137
8.8-20	SAM Test 42, Run 19 A4X Accelerometer Data	8-141
8.8-21	Instantaneous Acceleration, X-Direction	8-144

TABLES

Table		Page
5.1-1	HRE Coolant Passage Fin Configurations	5-8
5.1-2	Hydrogen Flow Requirements at Mach 8 Local and Mach 6.5 Local	5-11
5.1-3	Summary of Ascent and Descent Coolant Requirements	5-23
5.2-1	Flight Conditions Affecting Structural Design of HRE	5-29
5.2-2	HRE Freebody Aerodynamic Loads	5-33
5.2-3	Summary of Engine-Mount Manifolds Stress Analysis	5-48
5.2-4	Bellows Stress Analysis Summary	5-52
5.2-5	Fin-Containment Data	5-54
5.2-6	Shell Proof-Pressure Targets	5-55
5.2-7	HRE Manifolds Stresses and Sectional Properties	5-59
5.3-1	Output for Spike-Mounting Cone Assembly	5-72
5.5-1	Comparisons of Inlet Spike Actuation Systems	5-115
5.5-2	Ablatively Cooled Cowl Aerodynamic Heating Summary	5-132
5.6-1	Full-Scale Component Test Conditions	5-134
5.7-1	Summary of SAM Transient Structural Temperature Differences	5-149
5.8-1	SAM Coolant Water Requirements for SAM Adapters	5-153
7.2-1	Component Test Summary	7-27
8.1-1	Strut Test Conditions	8-6

TABLES (Continued)

Table		Page
8.2-1	Configuration No. 2, SN 5 Data Reduction	8-30
8.3-1	HRE Flat Panels Test Summary	8-40
8.3-2	Local Joint Flat Panel Test Results	8-42
8.3-3	Thermal Fatigue Test Specimen Particulars	8-48
8.3-4	Thermal Cycle Test Results	8-52
8.7-1	Water Test Results and Modified Conditions for SAM Testing	8-89
8.8-1	SAM Test Instrumentation Summary	8-94
8.8-2	Summary of HRE SAM Structural and Cooling Tests	8-103
8.8-3	Hydrogen Heat Load Distribution for Test 41, Run 39	8-110
8.8-4	Trailing Edge Flow Route Heat Loads (Test 42)	8-115
8.8-5	Thermal Fatigue Summary	8-121
8.8-6	SAM External Reactions	8-130
8.8-7	Force at Aft End of Actuator	8-135
8.8-8	Variation of Actuator Loads During Spike Movements	8-136
8.8-9	Maximum Stresses	8-138
8.8-10	Maximum Instantaneous Accelerations	8-139
8.8-11	SAM Test Standard Deviations of Nine Runs	8-143

1. SUMMARY AND CONCLUSIONS

This report summarizes the structures and cooling development effort on the Hypersonic Research Engine Project. The objective of this development was the design and fabrication of a research-scale, regeneratively cooled engine structural system to provide the geometric and surface controls required for the aerothermochemical processes involved in supersonic combustion. The structure had to withstand the environment of Mach 8 flight for 100 missions. A combination of (1) the reliability required for flight on a manned carrier aircraft, (2) the environmental conditions, (3) weight limitations, and (4) cycle life required, all contributed to make the structural and thermal control design of this engine a very challenging task. Considerable extensions in technology in the areas of materials application, structural design, and fabrication were required. Where these special extensions arose, tests were conducted to provide the needed data. Techniques were then developed to satisfy design requirements and improve design capability. This report describes this experience and discusses the specific design problems in detail.

1.1 PROGRAM SUMMARY

The original project plan for the overall program comprises three principal phases.

(1) In Phase I, work was undertaken to create a concept, develop a preliminary design, and plan the follow-on development of the actual hypersonic research engine hardware.

(2) Phase II, as originally planned, was to cover the research and development for the engine concept, fabrication, testing, and qualification for flight use in the manned carrying vehicle. The work described in this report was performed as part of this phase.

(3) Phase III was planned as a flight experimentation program in which the engine, airborne on the X-15A-2 research airplane, would be tested in actual flight at Mach 8.

Contract work on Phase II began in February 1967. A year later the X-15 program was phased out, necessitating adjustments to the project plan and scope. These adjustments were effected without detriment to achievement of the basic project objectives. In terms of the structures and cooling development, the structural evaluation was redirected toward Mach 7 true-temperature testing in the Langley Research Center's High Temperature Structures Tunnel. An assembly of the structural components (the Structures Assembly Model, SAM), as the final act in structural development, reflects the design concepts evolved for the flight engine.

The configuration used in the SAM is a plate-fin monocoque structure with local stiffening as required to resist buckling. The stiffening rings double as fuel injection manifolds. The SAM is hydrogen cooled except for a water-cooled cowling outer surface which is part of the wind tunnel installation. A hydraulic actuator was incorporated in the design to provide for positioning of the variable geometry inlet. Since the vitiation heated SAM test facility lacked the oxygen replenishment for testing with combustion, the model was fitted with only the first of the several rows of fuel injectors which would be fitted to an operational engine.

The SAM was successfully tested at a nominal Mach 7 true temperature and altitude at Langley Research Center's 8-ft High Temperature Structures Tunnel. As far as is known, the SAM tests were conducted at the highest temperature and pressure of any engine structural test to date. In the SAM, as a complete engine, are reproduced the aerodynamic interferences which cause uneven heating and thermal expansions which give rise to structural interactions. During the tests, metal temperature differences up to 1300°F were obtained. The metal temperatures ranged to 1400°F. A total of 30 minutes of operation and 60 operating cycles was imposed on the SAM at tunnel total conditions up to 3400°R and 3300 psia.

The operating conditions and design requirements used in structures and cooling development make reference to operation at both Mach 8 freestream and local, and to Mach 8 freestream, Mach 6.5 local. The Mach 8 freestream, Mach 6.5 local condition is associated with operation of the HRE on the X-15 airplane. As part of the program restructuring, following retirement of the flight test vehicle, operating peculiarities associated with the vehicle were generally deleted from the program. Since extensive analyses had been performed prior to this, some of the results are included in the following discussions. In addition, analyses related to operation of the SAM in the wind tunnel are presented.

Investigations in certain areas specifically associated with development of a flight engine for use on the X-15 test vehicle were stopped following retirement of the vehicle. In particular, efforts aimed at qualification for flight of components and assemblies were discontinued. Specific areas of investigation affected are component flow tests; vibration testing; ablatively cooled cowl design, fabrication, and testing; and inlet spike actuator development as a self-contained engine subsystem. The design and fabrication of flow test adapters for use in the component flow tests is described in the report. Analyses in support of engine vibration performance and testing are also reported, as is the design of a vibration test fixture and engine vibration model. Only preliminary analyses of the ablatively cooled cowl were performed when efforts were discontinued. The actuator system was completed as a flight system, development tested, and used in the SAM. Those features of the actuator which made it a self-contained subsystem were not evaluated; rather, the actuator was developed and used with external hydraulic power. Reference to both actuator systems will be found in this report.

This report describes in considerable detail various development tests performed in support of flightweight engine and SAM design and fabrication. The plate-fin structures were tested on a sub-element basis to evaluate pressure containment strength and thermal fatigue performance at the high design operating temperatures. Support struts and models of the outer body leading edge were tested for thermal performance, flow distribution, and thermal fatigue to verify the design. Finally, a series of pressure drop and flow distribution tests were run on the full-scale shell components.

1.2 CONCLUSIONS

The tests of the SAM in the NASA Langley 8-ft High Temperature Structures Tunnel were the culmination of the cooling and structures development effort on the program. Features previously investigated on a detail basis were assessed in an integrated system. The overall conclusion of this assessment is that the capability exists, by appropriate design, to cope with non-linearities and other peculiarities inherent in a total engine structure. The basic design concepts and approaches used in the HRE were found to be valid. The cooled structure proved to be rugged and capable of sustaining considerable abuse without degradation of performance.

1.2.1 Analysis and Design

The cooling and structures development effort described in this report shows contributions in the area of transient response analyses of cooled structures, low cycle fatigue analysis and test, and the approach to thermal simulation of the complex aerothermodynamics that occur in the engine. The problem of low cycle fatigue in intensely heated structures is critical in any cooled hypersonic structure and the basic determinant in establishing operating life. Analytical techniques were modified by empirical data and found to be valid as applied to the engine structure. Since no thermal fatigue failures were encountered in the SAM tests and only a single engine was tested, verification of the analysis approach is limited to the extent of the test cycle imposed and to the conclusions drawn from the subelement tests reported here.

1.2.2 Manufacture

In the area of manufacturing, the fabrication of the cooled sandwich shells was a basic requirement. It has been shown by the program and by the test results that the manufacture of the plate-fin sandwich structure for use under conditions of high pressure, high temperature, and high applied loads is feasible. The shells can be sized to precise dimensions and brazed with high reliability. Testing methods were developed which permitted non-destructive testing of the brazed shells and a simple evaluation of the results. Specifically, brittle lacquer techniques were used to indicate braze voids for highly stressed areas. The specific geometry of the engine, whether axisymmetric or two-dimensional, is not basic to the applicability of the manufacture and test techniques used with this structure. Rather, the experience gained in this area is broadly applicable to future development of hypersonic structures. Specific areas within this broad category are applicable to other types of structures as well. In particular, results for brazing as they relate to the capabilities of as-fabricated structures are extendible.

1.2.3 Special Features

Once the basic structural problems have been solved in terms of analyses, design, and manufacture, any ramjet structure will involve a number of specific features which require special treatment. Clearly, fuel injection is basic to an engine. The design and installation of the fuel injectors used in the SAM are specific to the plate-fin type of structure. When the general problem of fuel injection is considered, the use of nozzles in a plate-fin structure may be considered as applicable to other basic structural concepts, as a local solution. Support struts are required in most engine configurations. The struts are highly loaded structural components and are subjected to severe thermal loads if located downstream of the fuel injectors. Conditions here can range to gas temperatures of 5800°R and provide heat fluxes on the strut leading edges of 1800 Btu/sec-ft^2. The successful solution to the problem that was developed as part of this program is certainly applicable to any ramjet engine and adaptable to a considerable range of strut configurations.

The cowl leading edge evaluated on a model basis and used in the SAM proved rugged and exhibited entirely satisfactory performance in the tests. It has a regeneratively cooled tip of 0.030-inch radius. The design capability extends to shock-on-lip operation at Mach 8 and a freestream dynamic of 1800 psf. Heat fluxes of 1200 Btu/sec-ft^2 and localized fluxes of 10,000 Btu/sec-ft^2 are predicted for these conditions. The capability of this design provides the potential in any future application for achieving good aerodynamic performance and extended life for the cowl leading edge. It has successfully absorbed foreign object damage, including perforations, without impairment of operation.

Other areas of design and fabrication of particular interest include the following:

(1) A working design for joining shells that avoids discontinuities in the aerodynamic surface. This is important not only for aerodynamic performance but also for temperature control of the structure.

(2) A working design for a panel which can handle nonuniform heating, accidental obstructions, and yield stable operation of parallel cooling circuits.

(3) The ability to introduce inserts into the cooling flow passages without degradation of the cooling. This is a consideration for both fuel injection and for the use of static pressure and temperature instrumentation in the engine.

(4) The design of struts and the installation of the struts in a manner that avoids large thermal gradients which could lead to unacceptable structural degradation.

(5) Integral design for manifold and stiffeners which reduces thermal stress and weight. This is also a necessary consideration in the design of shell joints to avoid discontinuities in the surface.

2. PROBLEM STATEMENT

The objective of the structures and cooling development program was to analyze, design, and fabricate the regeneratively cooled surfaces and their associated structures and to verify the performance of these surfaces and structures at conditions that simulate the operating conditions expected in a flight test engine.

The Hypersonic Research Engine requires regenerative cooling on all surfaces that contact the engine airstream. The use of ablative coating on the engine aerodynamic surfaces was barred by the Statement of Work to minimize extraneous effects on engine performance. No such restriction was imposed on the engine cowl; therefore, ablative protection was planned for this component.

The characteristic design problem in regeneratively cooled structures for this type of application is associated with the large heat fluxes encountered over major portions of the engine surfaces. These heat fluxes range from values of approximately 10 Btu/sec-ft^2 to 1800 Btu/sec-ft^2 on the stagnation line of the support strut leading edge. The conservation of fuel requires that these heat fluxes be accommodated at temperature differences across the regeneratively cooled surfaces which range up to approximately 800°F in flat surfaces and 1200°F in leading-edge areas. These temperature differences, in turn, result in strains that cause plastic deformation of the hot surfaces. Design, therefore, is governed by low-cycle fatigue conditions. Uncertainties associated with the prediction of low-cycle fatigue performance have led to emphasis on its evaluation in the experimental portions of the program.

The general performance objectives that were set for the cooled structures are as follows:

> Design life - 10 hr of hot operation, of which 3 hr are at Mach 7 to 8 flight conditions
>
> Cycle life - 100 cycles, at conditions which produce the highest plastic strain

3. TOPICAL BACKGROUND

The cooled structures, which were designed, fabricated, and tested as part of this task, and the associated connecting structures constitute the basic structural elements of the engine. The cooled surfaces of these structures also form the aerodynamic surfaces of the engine, as shown in Figure 3.-1. The design of the cooled structures required the consideration of all aspects of the HRE design and its subsystems, as well as the interfaces with the aircraft to which it would be attached. These constraints were generally retained even though the flight test portion of the program was deleted. Many of the design features had been established at that time, while others were basic to the engine design. Some of the more important design constraints are presented below.

3.1 GENERAL DESIGN GUIDELINES

The following guidelines reflect the broad interactions involved in design of the cooled structures.

1. The regeneratively cooled surfaces must be designed and fabricated to minimize engine performance losses. In addition to providing the basic contours, the cooled surfaces must be fabricated and assembled in a way that avoids discontinuities; leading edges must use the minimum radius compatible with reliable structural design.

2. Because of the research nature of the HRE program, temperatures and pressures must be measured throughout the engine. Consequently, the engine structures must accommodate static pressure taps and metal temperature thermocouples.

3. The total amount of fuel available to the engine in flight and for cooling of its structure must be limited to the storage capabilities of the aircraft to which it is attached. Consequently, in cooling the structure, fuel usage in excess of combustion requirements must be minimized. To accomplish this goal, the cooled surfaces must function at maximum metal temperatures and temperature differences compatible with sound structural design.

4. Engine internal structures and plumbing must be designed to allow space for installing fuel system components, engine controls, instrumentation transducers, and signal conditioning equipment. Because of operating limitations, electronic equipment must be installed in locations having the least severe

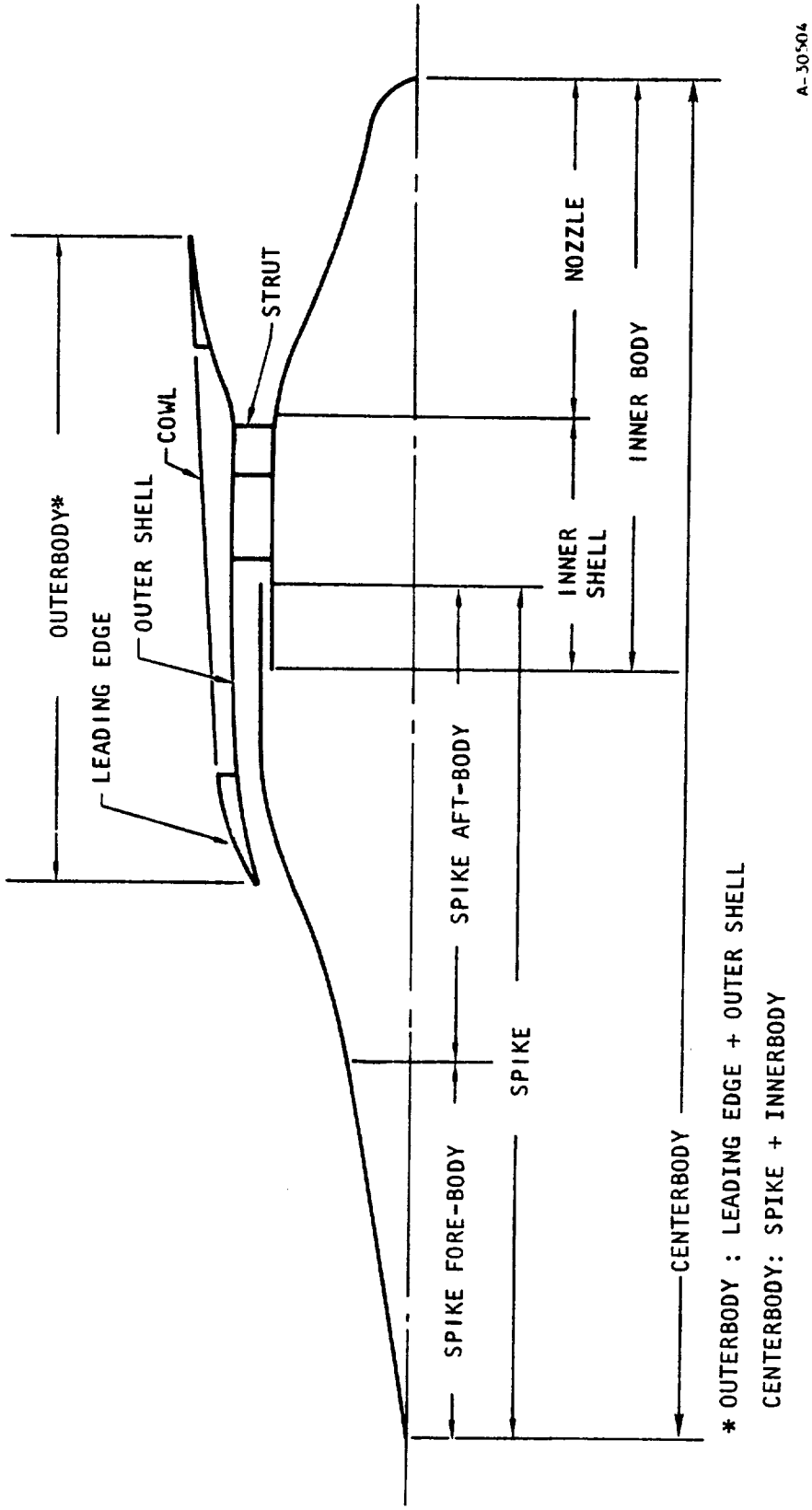

Figure 3-1. Cooled Structures Nomenclature

environment. In addition, the instrumentation, controls, and fuel subsystems contained in the engine cavity will require servicing prior to and after each test. Consequently, the mechanical assembly of the engine cooled-structure components must provide easy access to subsystem components for replacement in the field.

5. To permit the engine to operate over the flight Mach number range from 3 to 8, the inlet spike must be translated to various positions. To conserve coolant prior to and after engine operation, the inlet spike must be translated to a position nearly in contact with the outerbody leading edge. Consequently, it is necessary to have a spike actuation system capable of the desired positioning accuracy, with control provided by the control system computer.

6. Engine fuel pressurization is provided by a hydrogen turbopump. Therefore, the total pressure drop in the regeneratively cooled surfaces, manifolds, and associated plumbing must be compatible with the pressure output of the turbopump.

7. In addition to control of temperatures and temperature differences, the integrity of the cooled structures requires that the flow routes within the engine be matched in such a way as to minimize temperature differences at axial stations for innerbody and outerbody surfaces. This will minimize distortion of the engine internal passages. Axial temperature discontinuities in a single surface as produced, for example, by the termination of two flow routes that differ greatly in temperature at the same station, are objectionable because of the severe thermal strains that result.

8. Engine internal thrust must be measured during operation. Consequently, external loads (drag and lift) that are transmitted directly to the thrust-measuring device must be minimized. Specifically, the engine cowl has drag loads that are of the same order of magnitude as the engine thrust. Mounting of the cowl in such a way as to minimize this external drag load and, thus, the uncertainties in calculation of thrust is, therefore, required.

9. A basic engine design requirement is that malfunction of the engine in flight will not endanger the safety of the aircraft to which it is attached or the life of its pilot. Therefore, provision must be made to jettison the engine. Because of probable hydrogen leakage to the engine cavities, the innerbody engine cavity must either be inerted or must be capable of containing an explosive mixture of hot hydrogen and air.

10. The weight of cooled structures, inlet spike actuation system internal supporting structures, and plumbing is most of the

total engine weight. Although optimization of the structures and structural components for minimum weight was not an objective, the specified weight limitation requires careful consideration of structural weight.

3.2 OPERATIONAL BOUNDARIES

Operational boundaries were established on the basis of specific flight test requirements. These requirements were used to design the cooled structures.

3.2.1 General Design Ground Rules

The maximum dynamic pressure specified for this phase (IIA) of the program was 2000 psf. This compares with the specified dynamic pressure of 2500 psf for the HRE Phase I program. Consequently, the minimum altitude at Mach 8, during which cooling must be provided, is 85,000 ft, as compared to the Phase I minimum altitude of 81,000 ft. The minimum design altitude for the current program is 88,000 ft. The increased altitude results in a reduction of heat flux throughout the engine, but this reduction is offset in part by an increase in engine contraction ratio from 10 in Phase I to 14.6 in Phase IIA. In summary, the operating envelope for the engine is as follows:

Engine Structural Design - With engine either lit or not lit, dynamic pressure q_∞ = 2000 psf and q_L = 3600 psf (M_∞ = 8, M_L = 6.5)

Engine Cooling Design -

Normal design, engine lit: $q_\infty = q_L$ = 1800 psf ($M_\infty = M_L$ = 8),

h = 88,000 ft minimum

Emergency design, engine lit: q_∞ = 2000 psf and q_L = 3240 psf

(M_∞ = 8, M_L = 6.5), h = 85,000 ft minimum

For the emergency-design, engine-lit conditions, all of the pump output pressure is available for coolant pressure drop. The dump valve opens and fuel injection valves close as the aircraft approaches these conditions from the normal operating line.

3.2.2 Engine Operating Cycles

A qualitative definition of the engine operating cycles was used to provide a basis for analyzing heat transfer transients, evaluating the structural effect of transient temperature differences, establishing general control requirements and typical environmental conditions, and for defining acceptable operating cycles. The types of missions or conditions the engine was to survive are as follows:

Case I - Constant M, with aircraft power on, at a constant high q

Case II - Constant M, with aircraft power off, aircraft diving

Case III - Variable M, expected to involve a change in M of 0.5 during 20-sec engine operating cycle

Case IV - Subsonic-supersonic combustion transition at M = 6

Case V - Inlet unstart, with shock expelled

Figure 3.2-1 is a qualitative representation of the critical cases. The common features, typical for all simulated missions, are numbered on the figure and are as follows:

1. Launch to M = 3+, during which the engine structure is assumed to go from a soak at -65°F to a soak at 1140°F. No cooling is required. At the end of this period, the helium purge is performed and coolant flow started through all portions of the cooled structure.

2. Approach to test Mach number, inlet closed (leakage flow only), during which coolant flow is increased to maintain maximum structure temperature (cold surface) at 1140°F.

3. Time for retraction of inlet spike to desired position. The solid lines assume programmed cooling flow; the dashed line assumes controlled cooling flow based on temperature sensing. The approach selected will be a function of control system response and actuating system response. Controlled cooling is preferred.

4. Inlet spike in starting position, full airflow through the engine, no combustion.

5. Programmed increase in cooling flow to starting combustion equivalence ratio (ϕ). This ϕ will be less than the test ϕ. Combustion ϕ will ramp to test ϕ (not shown).

6. Combustion terminated and inlet spike being extended to closed position.

7. Inlet closed (leakage flow only), deceleration to M = 4+, with coolant flow decreased to maintain maximum structure temperature at 1140°F. Helium purge.

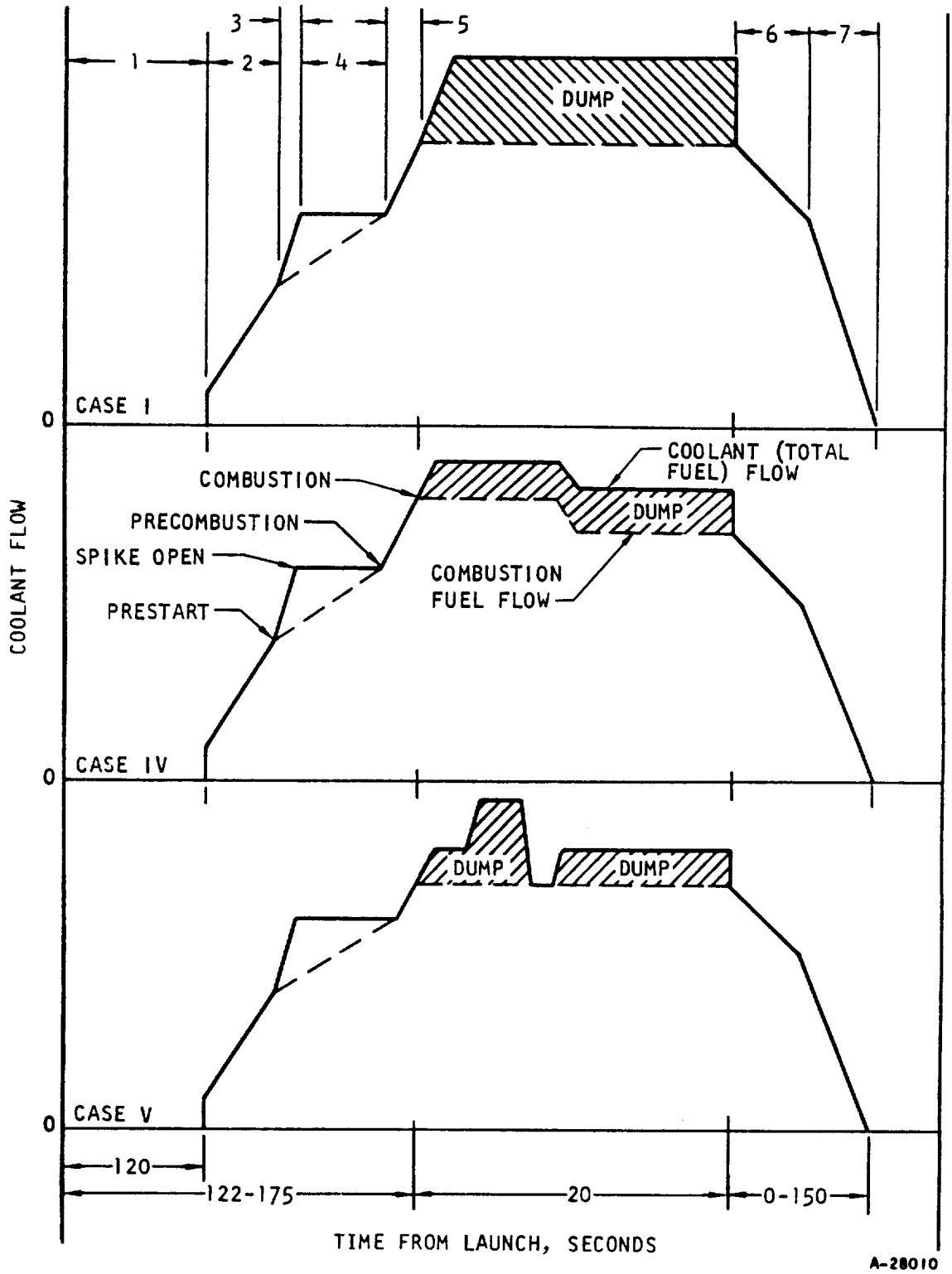

Figure 3.2-1. **Typical Engine Operating Cycles**

As combustion starts, the cooling ϕ must be controlled to accommodate increasing heat fluxes. The variations among missions occurring during the combustion phase are as follows:

Case I - Shown in Figure 3.2-1. Cooling ϕ is in excess of combustion ϕ. Combustion ϕ will ramp at beginning and end of test. Ramps of 5-sec duration to and from $\phi = 1$ may be assumed at beginning and end of test.

Case II - Not shown. Represents a gradual change in conditions shown for Case I and will involve less severe transients. Not considered a design point.

Case III - Same comments as Case II, but may become a design point at lower Mach numbers because of potential for increased test time and wider Mach number range.

Case IV - Shown in Figure 3.2-1. Involves a near-step change in gas-side engine conditions during test run.

Case V - Shown in Figure 3.2-1. The general rise in pressure would be expected to cause a step-change type increase in heat flux. Spike will extend and close, then retract to operating position for second attempt at starting. At this point, either normal operation or a second unstart is possible.

4. OVERALL APPROACH

The diverse requirements imposed on the cooled structures required iteration of the cooled structural design with (1) the engine aerodynamic design, (2) the instrumentation, control, and fuel subsystems designs, and (3) the airplane interface design. Internal constraints on cooled structural design are imposed by the close coordination required in thermal design, mechanical design, and manufacturing. It is generally not possible to treat any one of these areas independently of the others. During Phase I of the program, the basic design concepts for the engine were defined. These concepts and the design data generated during Phase I were used as the starting point for design of the Phase IIA cooled structures. Component layout drawings of acceptable mechanical design and with acceptable manufacturing features formed the initial step in the iteration. These layout drawings were evaluated to establish the required thermal and structural design features and revised to incorporate the required features.

The general approach to cooled structures development placed heavy emphasis on fabrication and testing of the full-scale components. A limited number of types of cooled structural elements and models was fabricated and tested to evaluate the problems which are basic to the overall engine design, or which are sufficiently localized in nature to permit use of subscale evaluation. All significant manufacturing development and evaluation was accomplished using the full-scale components. The nature of the required manufacturing operations for the components is such that use of subscale components would lead to only limited information on the adequacy of manufacturing techniques and processes.

4.1 THERMAL DESIGN

The overall thermal design approach used analyses based on experimental data obtained from tests on similar geometric configurations and heat transfer situations. These experiment-based analyses, in turn, were verified by experiments where the geometry or fluid conditions, or both, were like those existing for the flight engine.

The basic goals of all thermal analyses and designs were (1) limiting temperature and temperature differences to structurally acceptable values, while keeping hydrogen cooling flow equal to or less than hydrogen flow required for combustion, and (2) at the same time maintaining hydrogen pressure drop compatible with cooling jacket pressure containment and pump outlet pressure capabilities. The limiting values that were used were (1) a maximum gas-side metal temperature of 1700°F (2160°R), (2) a maximum primary structure temperature of 1140°F (1600°R), and (3) a hydrogen pump outlet pressure of 1100 psia.

The thermal design procedure involved separate calculation of aerodynamic heating and cooling jacket performance. The aerodynamic heating conditions were calculated (as during Phase I) primarily by use of the computer program H1940. Special aerodynamic heating conditions, such as shock wave/boundary layer interaction, were computed separately. Cooling jacket fin performance was calculated (as in Phase I) by use of computer program H1930. Special conditions, such as pressure and flow distributions for inlet, outlets, and bolted flange/manifolds, required separate calculations. Verification of aerodynamic and cooling jacket heat transfer and pressure drop calculations was accomplished by actual tests of selected components. Flow distribution and associated temperature distribution and its effects on structural performance were an important consideration and separately evaluated.

4.2 STRUCTURAL DESIGN

The structural design approach utilized a combination of analytical and experimental methods. Experimental verification of detailed parts, such as short-term burst, creep-rupture, and thermal fatigue tests on sandwich plate-fin elements, were employed wherever necessary.

The bulk of the HRE structures consists of ring-stiffened orthotropic shell structures of variable thicknesses and contours. The ring stiffeners are also used for coolant flow manifolding and fuel injection rings for the engine combustor section. The structural loadings produce axisymmetric and asymmetric forces and moments due to static normal pressures, acceleration, vibrational inputs, and aerodynamic flutter and buffeting effects.

Fully operational computer solutions are available to analyze axisymmetric isotropic thin shells of variable thicknesses and contours for stresses due to axisymmetric loads and temperature profiles. In addition, the isotropic shell analysis has been extended to treat orthotropic cylindrical shells with axisymmetric loads. Two MIT finite difference nodal circle solutions (SABOR III and DASHER I), which have been adapted for use on the AiResearch computer system (IBM-360/50), were available for use.

The SABOR III program is applicable for axisymmetric isotropic shells (local departures from ideal isotropy can be treated) that may be subjected to nonsymmetrical static forces. It may also be used to obtain the stiffness and mass matrixes for direct input into the DASHER I program to obtain dynamic response.

It would have required an extensive programming effort to modify the SABOR III and DASHER I programs to treat accurately many of the problems that were encountered in the HRE. Rather than attempt this approach, a further survey of existing shell programs determined that an applicable program had been developed under the auspices of the Analysis Group of the Theoretical Mechanics Branch, Structures Division, Wright-Patterson Air Force Base, Dayton, Ohio. This program is based upon the improvement in matrix shell solutions generated by A.Kalnins (Department of Mechanics, Lehigh University). It solves the general axisymmetric orthotropic thin shell problem for symmetric and nonsymmetric loads due to static as well as dynamic inputs. The program has been adapted for use on the AiResearch computer system.

The objective of the test program was to verify the actual performance capabilities of the structures as fabricated. Although it was not possible to predict analytically the influence of realistic fabrication restrictions and limitations on the end product, the initial analysis served to identify the serious design problem areas. Results of the test program were then used to assess the extent of the changes required to achieve the structural integrity goals.

4.3 MECHANICAL DESIGN

The guidelines used in mechanical design of the cooled structures components and assembly of the components into the engine required the use of known materials and joining techniques. Standard fasteners and seals were used to the greatest extent possible. Design for brazing was aimed at minimizing the total number of braze cycles to which a given part must be subjected. In some cases, this was done by redesigning the parts to allow use of prebrazed subassemblies, substitution of machined or welded subassemblies, or substitution of bolted interfaces. Also, as a general rule, all welding into, or close to,braze joints was avoided.

The mechanical design effort was supported by experimental verification in selected areas. In particular, selected configurations that presented analytical problems and raised questions as to manufacturing feasibility were fabricated and tested on a subscale basis. The purpose of such tests was to provide design data and guidance for possible design revision. Tests which were in support of mechanical design, rather than thermal or structural design, included the following:

1. Evaluation of the feasibility of bolting the nozzle flange manifold to the inner shell through the removable nozzle cap, using a mockup of the parts.

2. Fabrication of a section of the inlet spike near the spike tip to help resolve questions regarding the best manufacturing approach, and hence, the best design for this portion of the inlet spike.

3. Fabrication of a straight section of the bolted nozzle manifold to verify both the manufacturing aspects and structural integrity of the design solution.

4. Fabrication and evaluation of the various mechanical seals used in the components to verify the adequacy of the design solution.

5. Fabrication of flat panels using the various instrumentation and fuel injector fittings that penetrate the regeneratively cooled surfaces to verify manufacturing feasibility and structural integrity of the design.

4.4 MANUFACTURING

The manufacturing effort for this program had two aspects: (1) that

dealing with the approach to development of manufacturing techniques and processes, and (2) that dealing with the specific manufacturing processes planned for use.

4.4.1 Development Approach

The development of the manufacturing techniques and processes relied primarily on full-scale components. Except where isolated problems or basic data were to be obtained, the use of subscale components would have represented a duplication of development effort. The compound forming of the shell-face sheets in half-scale, for example, results in working with radii of curvature which are half those encountered in the full-scale part. Use of lighter-gauge material to facilitate forming, on the other hand, is impractical. In addition, the size of the full-scale tooling, the machines required to use this tooling, and the unique problems associated with the forming of large thin wall shells cannot be duplicated in half-scale. As a result, a half-scale compound-curved model of the isentropic surface of the inlet spike was the only subscale component on which fabrication development work was done. This part was used to establish forming characteristics, evaluate electrohydraulic forming parameters, and investigate brazing problems.

4.4.2 Fabrication Approach

The most critical area of cooled structures fabrication is in the cooled surface shell-face sheets. The starting point for these shells can either be rolled-and-welded-cone sections or flat sheets. The rolled-and-welded cones are bulge-formed, then final-sized, using electrohydraulic forming. Using flat sheets as a starting point, the shells must be deep drawn in about three stages. Final sizing of the shells occurs as for the welded cones. Of the two approaches, the one using the seam-welded cone was selected. The weld seam is not considered structurally objectionable and the approach involved fewer steps than are required for deep drawing.

To ensure adequate braze fitup, forming accuracy for the shells must be high. In addition, to ensure sound braze joints, pressure must be exerted on the shells in such a way during brazing as to provide a crushing load on the fins. The methods available for providing this braze fixturing load include the following, as a function of the component being brazed:

1. Graphite fixtures, with an external piece containing the assembly and an internal piece using expanding segments to exert pressure.

2. Steel bags placed inside the shell and pressurized to a level sufficient to deform the shell with which the bag is in contact.

3. Application of gas pressure directly on the internal shell, by making that shell a part of a pressure vessel.

4. Evacuation and backfilling of the space between the two shell-face sheets, using atmospheric pressure to provide the load.

Methods 1 and 3 were used during the program. Integrity of the shell joining was experimentally evaluated and adjustments in shell forming tools and brazing procedures and fixtures were made to correct problems that appeared.

4.4.3 Nondestructive Testing

The critical area in fabrication of the full-scale components involves the shells themselves, as discussed in the two previous paragraphs. For structural integrity of the shells, only very limited areas of unbrazed joint areas are tolerable. These joints are detectable by proof-pressure testing at sufficiently high pressure levels. Only in exceptional cases, however, will a defect that is revealed by proof-pressure test be repairable. In general, a nondestructive test capable of revealing braze voids is preferable and offers better opportunity for subsequent repair. The technique developed for this purpose during the program used pressure testing of shells that had been coated with brittle lacquer.

The repair techniques available for unbonded joints in the shells would generally be the following:

Recycling of the complete shell to a slightly higher temperature than used during the first braze cycle. In this way, remelt and flow of the braze alloy is obtained with the objective of filling the void. Orientation of the shell in the brazing furnace can be used to assist the process.

Removal of a portion of the face sheet in the unbrazed area, addition of filler alloy and closeout using a patch, with the entire shell recycled in the brazing furnace. The applicability of this repair procedure is a function of the location of the affected shell area in the engine gas stream.

5. ANALYTICAL DESIGN

5.1 SYSTEM THERMAL ANALYSIS (FLIGHT)

The hypersonic research engine requires thermal protection on all surfaces that are exposed to the hot gas stream. Surfaces wetted by the engine propulsive stream are regeneratively cooled with gaseous hydrogen flowing through passages beneath the surfaces. The use of ablative coating on these surfaces is barred by the Statement of Work to minimize the extraneous effects on flight performance. No such restriction was imposed on the engine cowl; therefore, ablative protection is used for this component.

The overall thermal design approach was by analyses based on correlated experimental data from tests on similar geometric configurations and heat transfer situations. These experiment-based analyses, in turn, were verified by experiments where the geometry, or fluid conditions, or both, were similar to those existing for the flight engine.

The basic objectives of all thermal analyses and designs was to fulfill the following engine structural design goals.

(a) Maintain hot-gas-side metal temperatures at, or below, 2060°R (1600°F)

(b) Maintain primary structural temperatures at, or below, 1600°R (1140°F)

(c) Maintain cross sectional temperature differences to values at, or compatible with, the desired fatigue life of the structure

(d) Minimize the coolant hydrogen usage in excess of combustion requirements

(e) Maintain hydrogen pressure drop compatible with plate-fin panel pressure containment, pump outlet pressure capabilities (1100 psia), and fuel plenum pressure requirements (525 psia)

(f) Minimize structural temperature differences from innerbody to outerbody at the same axial station in order to minimize distortion and thermal strain of the hot gas annular passage.

The thermal design point for all of the above objectives is the "B-B" line flight condition of Mach 8 (freestream and local) at 88,000 ft altitude.

This corresponds to a dynamic pressure of 1800 psf and compares with a specified dynamic pressure of 2500 psf for the HRE Phase I program (Mach 8, 81,000 ft altitude). The Phase II A Statement of Work indicates a maximum dynamic pressure of 2000 psf for engine-lit and non-lit conditions (Mach 8, 85,000 ft altitude). However, this is considered an emergency case and the objective (d) above need not be fulfilled. For this case, with engine lit, all of the pump output pressure is available for coolant pressure drop over the requirements for "B-B" line operation. The dump valve opens and the fuel injection valves close as the aircraft approaches these conditions from the "B-B" line operating point.

The most severe operating condition for the HRE occurs at Mach 8 free-stream, 85,000 ft altitude (2000 psf freestream dynamic pressure) with a positive 4-deg angle-of-attack. For this condition the HRE is in the X-15A-2 flow field. This produces a local approaching Mach number of 6.5 and a dynamic pressure of 3600 psf. Though the HRE thermal design was based on normal "B-B" line operation, thermal analyses were performed at this most severe condition. This engine-lit condition was considered an off-design condition and the thermal design objectives (c), (d), and (f) above were waived in preference to engine survivability, i.e., objectives (a) and (b).

5.1.1 Aerodynamic Heating

The aerodynamic heating analysis provided the basis for the cooling design and the hydrogen coolant requirements for the operating engine. Axial profiles of the aerodynamic parameters (static pressure, velocity, fuel-fraction burned) were used with Eckert's reference enthalpy in flat-plate aerodynamic heat transfer calculations to determine hot gas convective heat transfer coefficients and adiabatic wall temperatures along the cooled panel surfaces of the engine. The vertical origins of the centerbody were at the spike tip and cowl lip, respectively. Hot gas heat transfer coefficients on the spike surface were multiplied by the cone-rule factor ($3^{0.5}$ for laminar flow and $2^{0.2}$ for turbulent flow) from the spike tip to the axial location of the cowl leading edge. The cone-rule factor was not used on other engine surfaces. Laminar-to-turbulent flow transition Reynolds numbers of 10^7 and 10^5 were selected on the spike and inside leading edge surfaces, respectively. The aerodynamic flow was considered laminar on the outside of the leading edge and turbulent on the outside surface of the trailing edge.

Several alternate heat transfer calculation methods were considered in the design analysis. Thus, methods included the use of a reference enthalpy (for hot gas property evaluation) other than Eckert's reference enthalpy, a hydraulic diameter as the characteristic length in the annular combustor section, and the simultaneous solution of the momentum and moment-of-momentum integral equations of the boundary layer. However, two factors led to the retention of the flat-plate equation with Eckert's reference temperature: (1) limited data are available in the wall-to-total temperature ratio range of greatest interest for the flight engine (0.3 to 0.4), and (2) convergence of the above alternate correlations with Eckert's flat plate reference enthalpy method is toward 1.0 for the available data at higher wall-to-total temperature ratios.

The two flight conditions of interest were the (1) Mach 8 freestream and local, 88,000-ft altitude ("B-B" line) condition with freestream and local dynamic pressure of 1800 psf; and (2) Mach 8 freestream, Mach 6.5 (4-deg angle-of-attack), 85,000 ft altitude condition with freestream and local dynamic pressures of 2000 and 3600 psf, respectively. The engine was lit for both conditions and the fuel fraction burned was equal to 1.0. The "B-B"-line condition provided the basis for the cooled structures design while the angle-of-attack condition represented the most severe thermal and structural off-design case.

The axial profiles of aerodynamic data (static pressure, velocity, fuel fraction burned) and surface heat flux are shown in Figure 5.1-1 for the "B-B"-line design condition and in Figure 5.1-2 for the angle-of-attack condition. The angle-of-attack condition produces the higher heat fluxes and heat loads. The maximum heat flux for the angle-of-attack conditions is 870 Btu/sec-ft^2 compared with 700 Btu/sec-ft^2 for "B-B" line operation. Similarly, the total angle-of-attack heat load is 13,800 Btu/sec while the "B-B" line heat load is 10,800 Btu/sec. The increased heating is primarily caused by higher captured air flow rate at the angle-of-attack condition (53 lb/sec vs 26 lb/sec for for "B-B" line operation).

The local peak in centerbody heat flux (to 400 Btu/sec ft^2) in Figure 5.1-1 ("B-B" line operation) is caused by shock impingement resulting from the rearward facing step at the end of the spike (Station XX = 55.76). A heat flux increase of twice the local flat plate calculation was estimated from Reference 5.1-1 for this shock impingement. Localized heat fluxes due to high shock impingement were calculated at other locations along the engine surfaces but are not shown in Figure 5.1-1. These hydrogen fuel entering the hot gas stream through the injectors at Station XX = 43 on the spike and at Station XX = 47 on the outer shell will cause a shock system with reattachment of separated flow on surfaces just upstream of the injectors. The local heat flux is increased from 255 Btu/sec-ft^2 shown in Figure 5.1-1 for the spike, to 280 Btu/sec-ft^2. The local heat flux at Station XX = 47 on the outer shell increases from 600 Btu/sec-ft^2 shown in Figure 5.1-1 to 865 Btu/sec-ft^2. Localized high heat fluxes occur on the inner and outer shells just upstream of the strut leading edge (Station XX = 59.6). These heat fluxes are caused by reattachment of separated flow associated with the strut bow-shock waves. The hot gas heat flux is locally increased from 200 Btu/sec-ft^2 to 600 Btu/sec-ft^2.

5.1.2 Cooling Design and Analysis

5.1.2.1 Flow Routing

The coolant flow routing was revised from the Phase I design reported in Reference 5.1-2 to the configuration shown in Figure 5.1-3. To provide acceptable strut leading edge temperatures with a heat flux of 1400 Btu/sec-ft^2 on a 80-mil radius leading edge, the flow to the innerbody was routed through the strut leading edge rather than through a tube passing through the interior

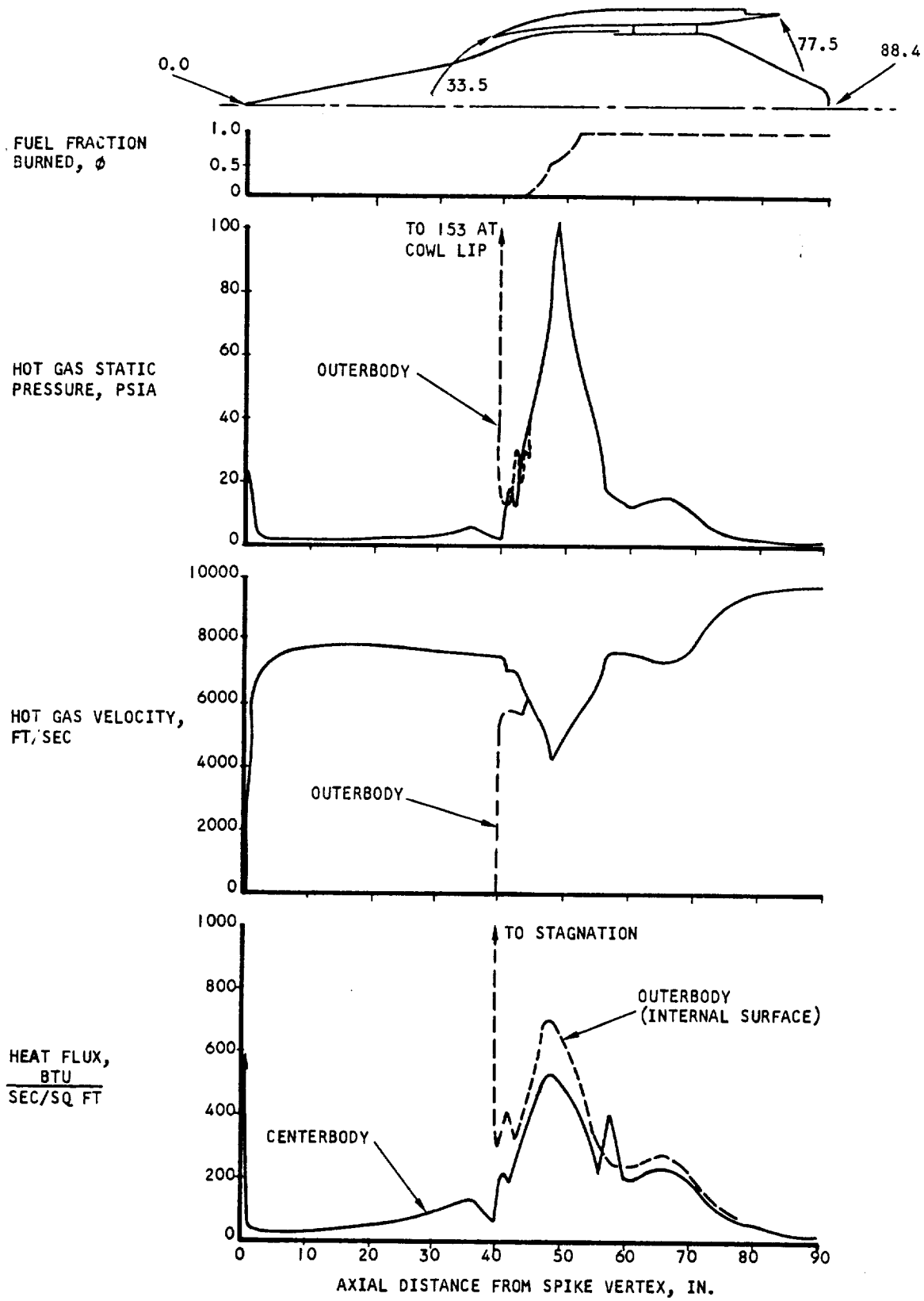

S-72709

Figure 5.1-1. Aerodynamic Parameters and Heat Flux Distribution at Mach 8, Freestream and Local, 88,000 Ft Altitude

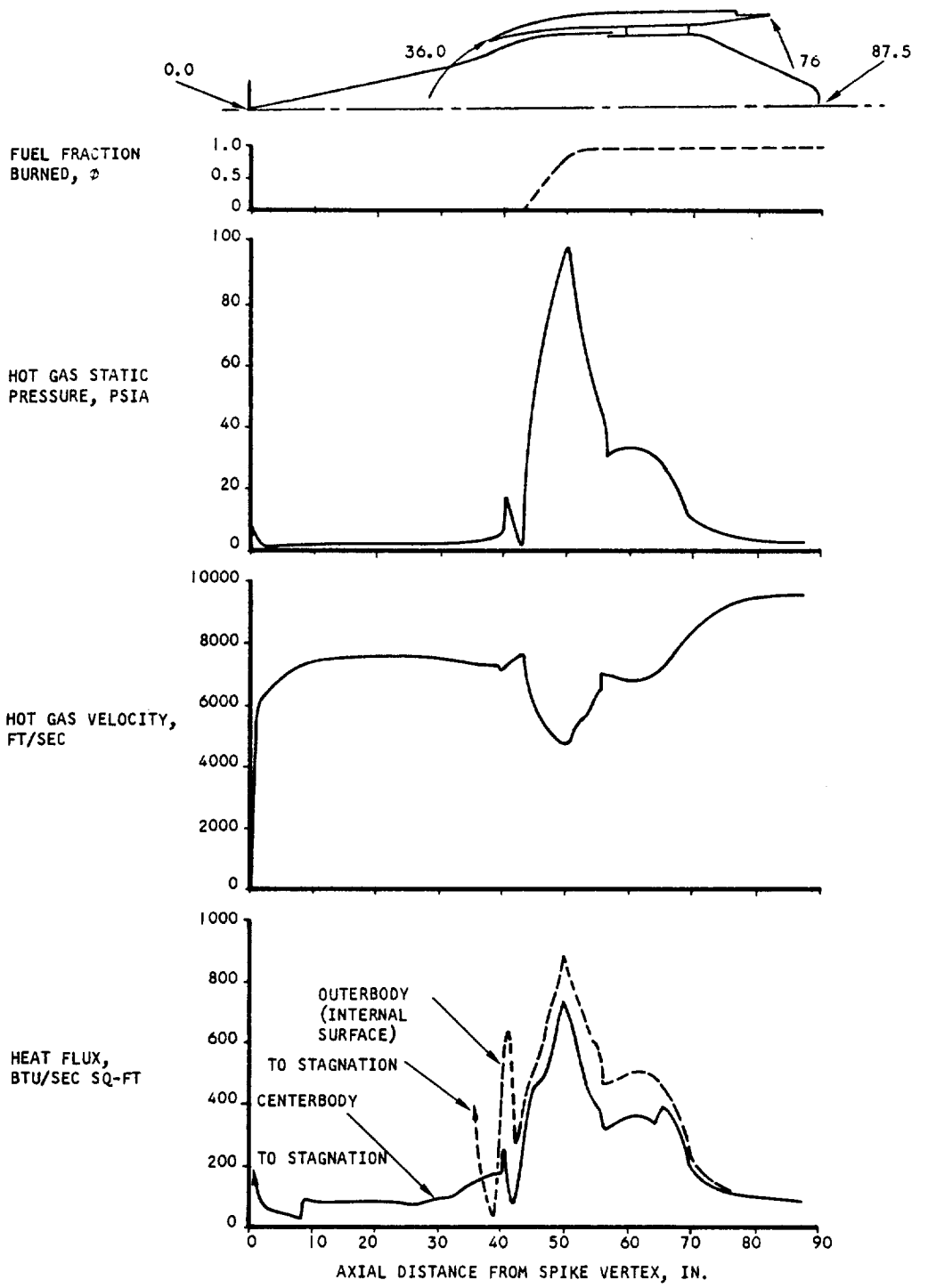

Figure 5.1-2. Aerodynamic Parameters and Heat Flux Distribution at Mach 8, Freestream, and Mach 6.5, Local - 88,000 Ft Altitude

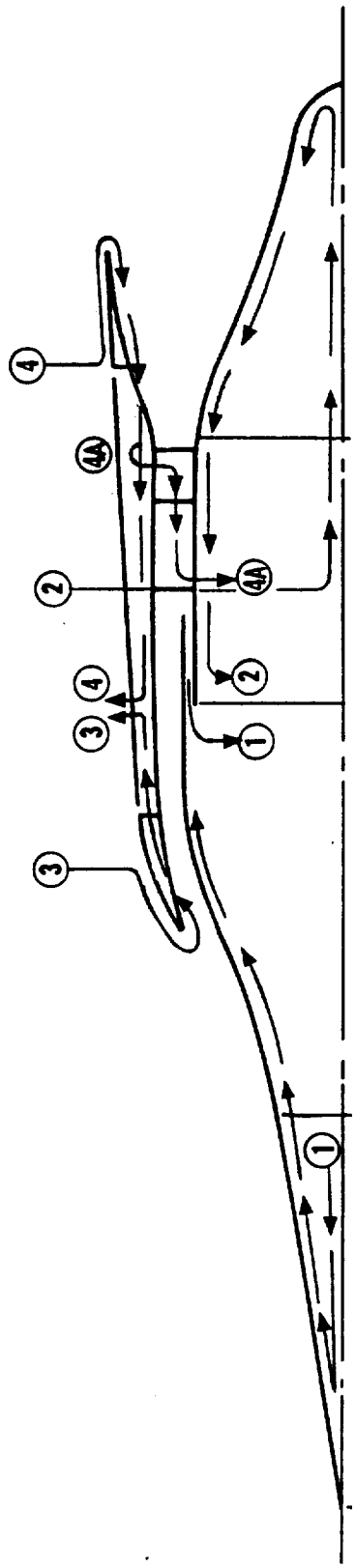

S-72563

① SPIKE FLOW ROUTE

② STRUT LEADING EDGES AND INNERBODY FLOW ROUTE

③ LEADING EDGE FLOW ROUTE

④ TRAILING EDGE FLOW ROUTE

④A STRUT SIDES FLOW ROUTE

Figure 5.1-3. Coolant Flow Routing Design

of the strut. This is discussed in detail in Section 5.5.6. Coolant from the aft outer shell is used to cool the strut sides. The strut-sides coolant is routed directly to the fuel plenum in the centerbody cavity. The coolant from the strut sides is approximately 1400°R rather than 1600°R, but the strut hydrogen flow is very small.

5.1.2.2 Selection of Plate-Fin Panels Configuration

The selection of the fin geometry for the engine coolant routes was based on five conditions; (1) the outer skin temperature was not to exceed 2060°R, (2) the hydrogen outlet temperature was not to exceed approximately 1600°R, (3) overall ΔT (fin ΔT + 0.015-in.-thick wall ΔT) was not to exceed 1000°R (with 800°R as a design goal), (4) the pressure drop in each individual fin jacket was not to exceed 100 psi (ultimately increased to 163 psi in the spike), and (5) manufacturing limitations. The candidate fin sizes selected during Phase I (Table A-36, page 229 of Reference 5.1-2) were reduced to a total of three on the basis of the above criteria, the aerodynamic heating profile shown in Figure 5.1-1 and the flow routing shown in Figure 5.1-3. These fin sizes are 16R-.153-.143(0)-.006 (16 rectangular (R) fins per in. of passage width, 0.153 in. height, 0.143 in. offset length, and 0.006 in. thickness), 20R-.020-plain-.006, and approximately 20R-.050-.083(0)-.006. The 16R-.153-.143(0)-.006 fins were retained (from the Phase I design) on the forward part of the inlet spike to axial Station XX = 35.7 in. The 0.50 in. length of cowl leading edge inner and outer surfaces and adjacent to the cowl lip was covered by a 20R-.020-.006 plain fin as well as the entire side surfaces of the struts. Passages of 0.006-in. height, as indicated in Table A-36 of Reference 5.1-2 for the strut leading edges were eliminated because the small passages are both difficult to fabricate and difficult to maintain open for flow. The strut leading edge will be cooled by hydrogen flow in a tube that is parallel to the strut leading edge and has an inside diameter of 0.13 in. Details of the strut flow routing and passage geometry are discussed in Section 5.5.6. Based on preliminary coolant passage heat transfer analyses, a 20R-.050-.083(0)-.006 offset fin was tentatively selected for the remainder of the engine surfaces. Detailed design analyses were performed to determine the precise number, thickness, and height of these fins with the number of fins ranging from 20 to 40 fins per in., fin heights ranging ±0.010 in. about the 0.050 in. fin height, and fin thicknesses ranging downward from 0.006 in. to 0.003 in. The final selection of the offset fins and their location on the engine is presented in Table 5.1-1.

5.1.2.3 Plate-Fin Panel Thermal Performance

The steady state thermal performance (hot surface and structural temperatures, and temperature difference) of the selected plate-fin surfaces are presented in Figure 5.1-4 for the Mach 8 freestream and local, 88,000-ft altitude ("B-B" line) condition with freestream and local dynamic pressure of

1800 psf; and in Figure 5.1-5 for the Mach 8 freestream, Mach 6.5 local (4-deg angle-of-attack), 85,000 ft altitude condition with freestream and local dynamic pressures of 2000 and 3600 psf, respectively. These performance curves are based on the heat flux distributions presented in Figures 5.1-1 and 5.1-2 and the hydrogen coolant flow rates presented in Table 5.1-2.

The Mach 8 local thermal performance curves (Figure 5.1-4) indicate that the plate-fin panel cross-sectional temperature differences can be maintained below 800°R except on the leading edge and forward outer shell. A cross-section ΔT of 950°R was predicted across the 20R-0.050-0.100(0)-0.006 offset fins and 0.015-in.-thick hot sheet on the leading edge at the leading edge/forward outer shell interface (axial Station XX = 46 in.). On the forward outer shell, a ΔT of 930°R is predicted across the 28R-0.050-0.100(0)-0.006 offset fins and hot sheet at Station XX = 48.0 in. In addition, the selected hydrogen coolant rates allow the structure to reach the maximum allowable value of 1600°R (near the flow route outlets) while maintaining hot surface temperatures at or below the design objective of 2060°R (1600°F).

TABLE 5.1-1

HRE COOLANT PASSAGE FIN CONFIGURATIONS

Fin Designation		Location
16R-0.153-0.143(0)-0.006	(1)	Forward spike to Station XX = 35 in.
20R-0.050-0.100(0)-0.006	(1)	Inner side of spike folded-flow section (Station XX = 46 to 55.76 in.)
	(2)	Nozzle
	(3)	Inner and outer surfaces of leading edge component starting at 0.5 in. in back of tip.
	(4)	Outer surface of trailing edge.
28R-0.050-0.100(0)-0.005	(1)	Aft spike (from Station XX = 35 in.) and including the outer side of spike folded-flow section.
	(2)	Inner shell
	(3)	Forward and aft outer shell
20R-0.020-plain-0.004	(1)	Strut sides
	(2)	Inner and outer surfaces of leading edge component (0.5 in. length) in back of tip.

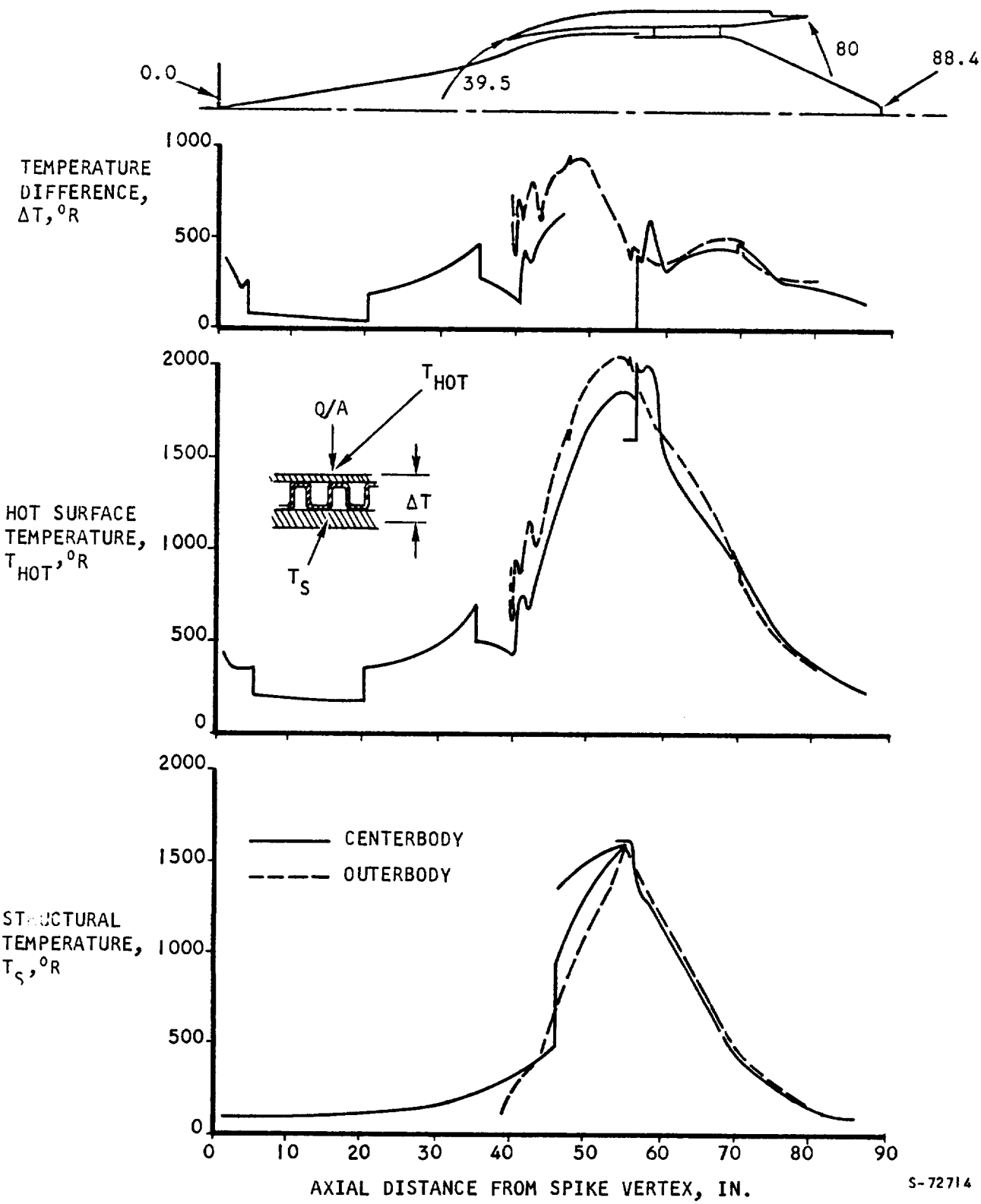

Figure 5.1-4. Steady-State Thermal Performance at Mach 8, Freestream and Local, 88,000 Ft Altitude

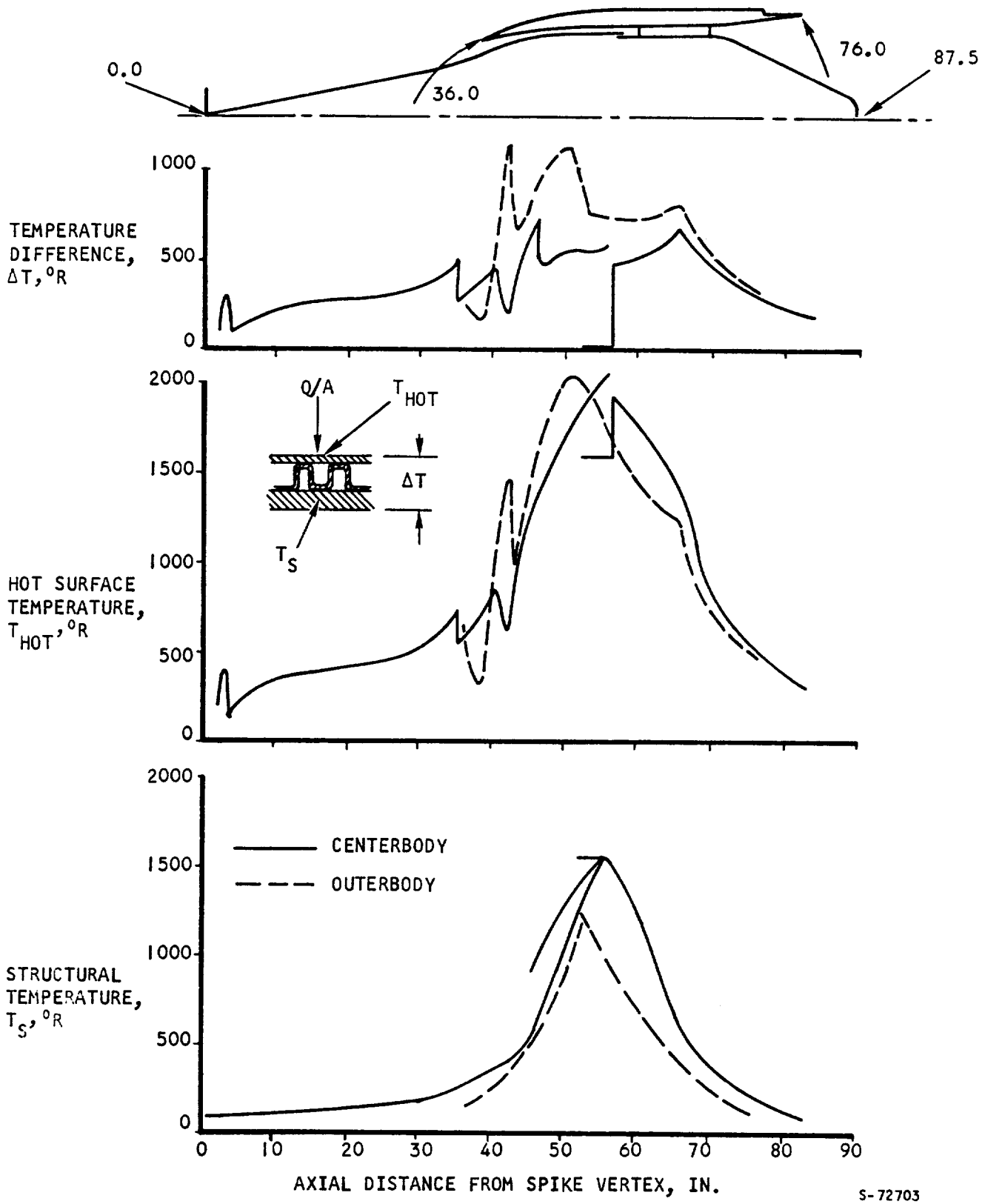

Figure 5.1-5. Steady-State Thermal Performance at Mach 8, Freestream, and Mach 6.5, Local - 85,000 Ft Altitude

TABLE 5.1-2

HYDROGEN FLOW REQUIREMENTS AT MACH 8 LOCAL AND MACH 6.5 LOCAL

Flow Route	Mach 8 Local		Mach 6.5 Local	
	Hydrogen Flow, lb/sec	Hydrogen Outlet, ^{0}R	Hydrogen Flow, lb/sec	Hydrogen Outlet, ^{0}R
Spike	0.655	1300	0.82	1300
Innerbody	0.340	1600	0.42	1580
Leading edge	0.655	1600	0.92	1150
Trailing edge	0.540	1600	1.10	1260
Total	2.19	1470	3.26	1280

Hydrogen inlet temperature = $100^{0}R$.

At the Mach 6.5 local conditions, the higher panel heat fluxes (870 Btu/sec-ft^2 maximum vs 700 Btu/sec-ft^2 maximum at Mach 8 local) and higher total heat load (13,800 Btu/sec vs 10,800 Btu/sec at Mach 8 local) produce cross-section ΔT's as high as 1150°R (Station XX = 42 on the leading edge) and a total hydrogen coolant requirement of 3.26 lb/sec (versus 2.19 lb/sec at Mach 8 local). This Mach 6.5 local flow requirement is 49 percent higher than the Mach 8 local requirement, even though the total heat load is 28 percent higher and was selected to maintain hot surface temperatures at or below 2060°R. A total flow rate of 1.28-times the 2.19 lb/sec Mach 8 local flow requirement (2.80 lb/sec) could not maintain hot surface temperatures below 2060°R. As a result, the increased flow requirement (above 2.80 lb/sec) produced maximum structural temperatures and hydrogen outlet temperatures less than 1600°R on the outerbody as indicated in Figure 5.1-5 and Table 5.1-2. The lower outerbody structural temperatures produced centerbody-to-structural temperature differences of up to 600°R at about Station XX = 60 in.

5.1.3 Coolant Pressure Drop and Flow Distribution

The engine coolant system was analyzed to estimate the coolant (gaseous hydrogen) conditions at various locations in the flow routes. The case of Mach 6.5 local was chosen because it requires the maximum pump flow rate and the highest pump outlet pressure. The results are shown in Figures 5.1-6 and 5.1-7. Figure 5.1-6 is a pictorial presentation of the four principal flow routes for the spike, strut leading edge and innerbody, outerbody leading edge, and outerbody trailing edge and strut sides, with hydrogen conditions indicated at selected locations. Figure 5.1-7 gives detailed information on the coolant pressure and temperature at intermediate locations. The results indicate that the maximum pump design pressure of 1100 psia is high enough to permit the maximum flow rate of 3 lb/sec through the flow routes. The largest pressure drop occurs in the spike which consumes almost all of the available pressure difference of 575 psi between the pump outlet plenum at 1100 psia and the fuel plenum at 525 psia. The pressure drops in the other three flow routes are about 300 psi less than the maximum available.

The coolant flow rates used in the pressure drop analysis (3.0 lb/sec total as shown in Figure 5.1-7) are smaller than the required flow rates for Mach 6.5 local at 88,000 ft and combustion $\phi = 1$, as listed in Table 5.1-2. The flow rate values in Figure 5.1-7 were also used for value design. The variations of the coolant temperature along the flow routes, but before the fuel plenum or the outerbody outlet manifold, where flow routes merge together, were taken from the Mach 6.5 local analysis in Section 5.1.2.3. The coolant temperature in and downstream of the outerbody outlet manifold and the fuel plenum was taken equal to 1600°R, the maximum design temperature of the hydrogen. This temperature will produce the maximum possible pressure drop and was used for conservatism.

The increase in pressure drop due to blockage of the cooling jacket passages by the fuel injectors was found to be negligible. The flow rate from the dump valve plenum to the turbine control valve at 0.2 lb/sec was considered as the maximum turbine flow rate.

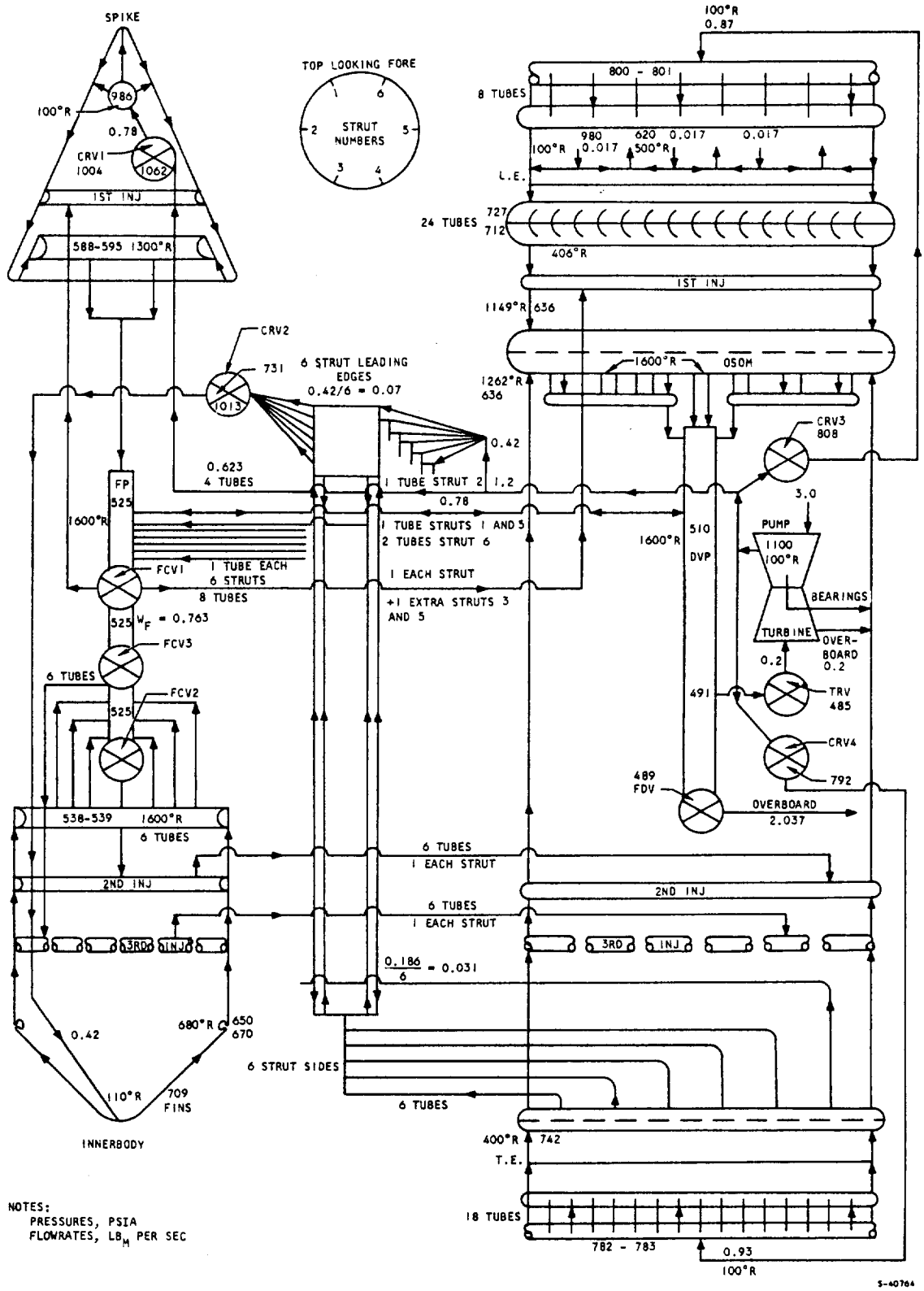

Figure 5.1-6. Hydrogen System Schematic

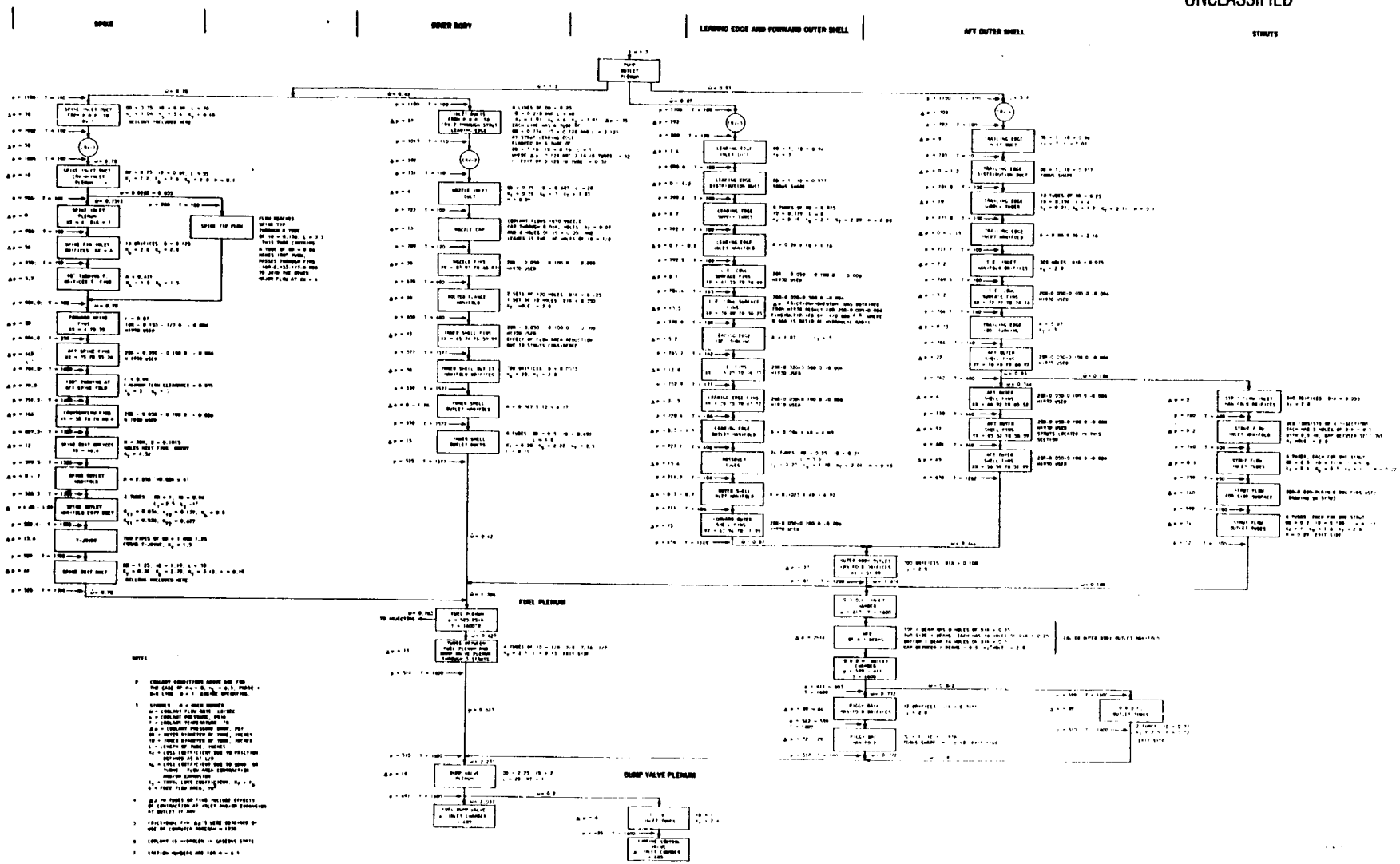

Figure 5.1-7. Cooling Hydrogen System Details, First Flight-weight Engine

In two locations, the design tube sizes were different from the ones used in the analysis to permit tube size adjustments after flow test pressure drop results became available for the various components. In the analysis, tubes were sized to provide correct flow distribution and equality of coolant pressures from different flow routes at junction points.

The six tubes connecting the strut sides to the fuel plenum were assumed as 0.312 in. ID for layout design purposes, although the analysis indicates a 0.188-in. ID is adequate. The six tubes connecting the strut-flow inlet manifold on the outer shell and the strut sides are indicated as being 0.5 in. OD in Figure 5.1-7 but were reduced to 0.375 in. OD on the layout design because of the almost negligible effect on overall pressure drop. This type of change was made to other details in the system without significant effect on the validity of the current analysis.

The two tubes which directly connect the outer shell outlet manifold to the dump valve plenum were sized to 0.81 in. ID on the layout, while this analysis indicates a 0.73-in. ID. Flow split between the piggyback manifold and these two tubes is controlled by the relative resistance of these parallel flow paths. Flow distribution around the outer shell was adjusted somewhat by varying the diameter of these two tubes after test flow distribution data became available.

The flow distribution in the coolant flow routes was determined from the ratio of cooling jacket pressure drop to overall flow route pressure drop. By definition, when this ratio is unity, the flow is uniform. The cooling jacket pressure drop includes that resulting from friction and flow acceleration in the fins as well as any resistance uniformly distributed at the inlet or outlet of the fin jackets. In addition to these cooling jacket pressure drops, the pressure drop associated with circumferential flow in the manifolds is added to make up the overall ΔP. All the flow routes, which are separately manifolded, have pressure-drop ratios from 0.885 to 1.0 as shown in Figure 5.1-8. The resulting percentage-flow increase above that required for each flow route is less than 5 percent and the overall flow increase is less than 2 percent. The flow increase of 1.3 percent for the forward outer shell is sufficient to provide the flow increase of 0.8 percent required for the cowl leading edge. The two flow increases are in series and would not be additive.

5.1.4 Transient Analysis

Transient thermal analyses were performed on several engine components to determine if the design objectives for steady-state operation were violated during the transient startup and shutdown phases of a total engine mission. The basic areas of interest investigated were the engine manifolds where large transient temperature differences were produced from fast thermally responding hot skins adjacent to slow-responding manifold structures during startup and shutdown. Results of two such areas (subsonic fuel injector manifold and outerbody coolant outlet manifold) where transient temperature differences exceeded steady-state values are presented in this section. Transient thermal results for other engine components are presented in Section 5.5.

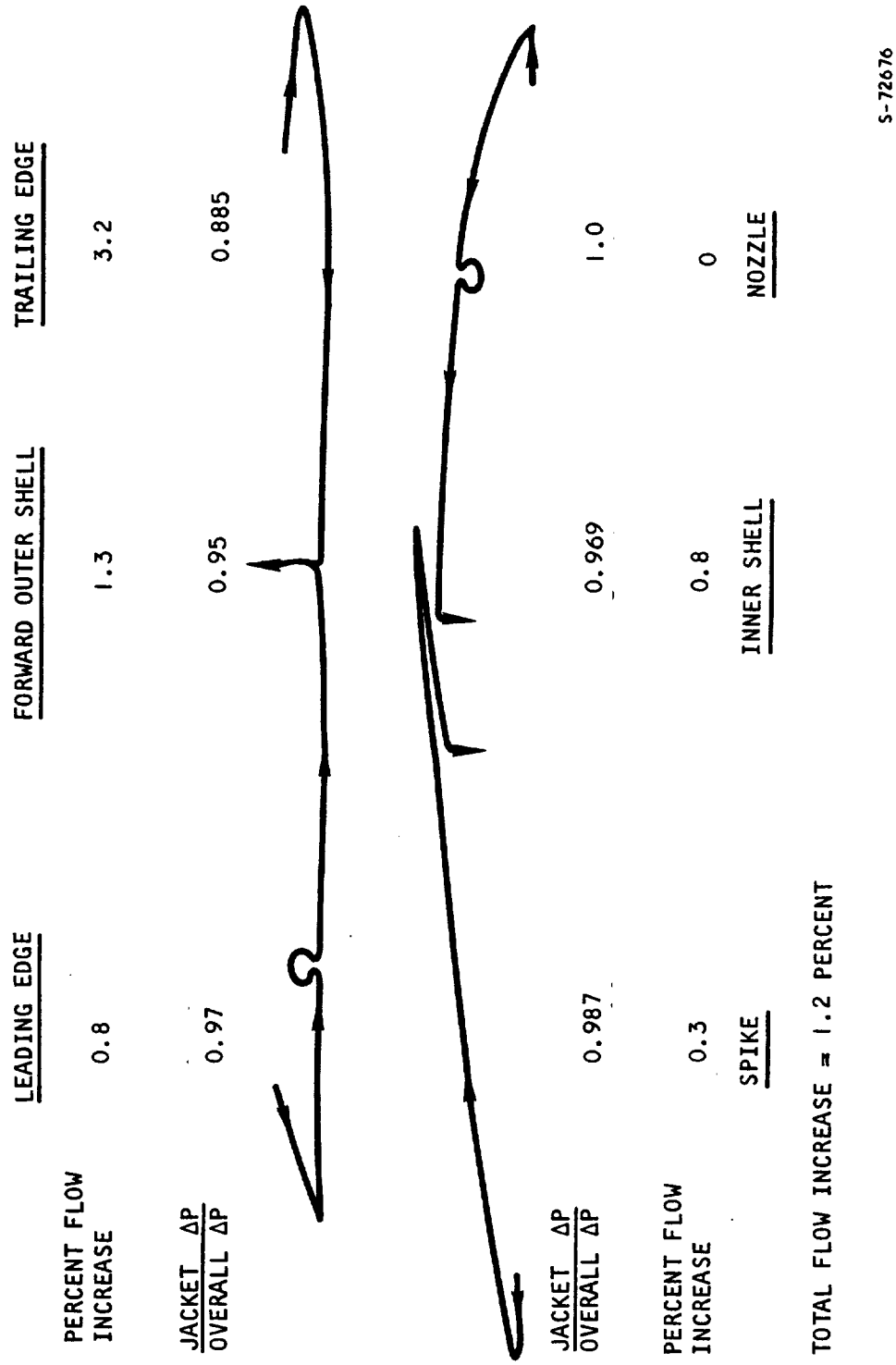

Figure 5.1-8. HRE Cooling System Flow Distribution

5.1.4.1 Fuel Injection Manifold

The response of the subsonic injector manifolds at Station XX = 55.67 was investigated, based on coolant outlet temperature control. The resulting temperature differences were larger than designed, however, so the feasibility of using electrical heaters as a means of eliminating excessive metal ΔT's (1000°R or greater) during engine operation was explored. Heaters could preheat the manifolds to 1160°R from B-52 takeoff to X-15A-2 dropoff at 45,000 ft altitude (75 min total). The wattage requirements to these heaters is estimated at 500 watts total for two manifolds. The 146-watts minimum required to heat each 11-lb manifold from -65°F to 700°F (1160°R) has been increased to 250 watts to allow for heat losses. The heaters will be inoperative during the entire period of X-15A-2 flight.

Two cases were considered critical for design: (1) shutdown of Mach 8 (Mach 6.5L) combustion condition, and (2) combustion at Mach 4. Transient temperature responses for these conditions on the innerbody are shown in Figures 5.1-9 and 5.1-10, respectively, and include the use of heaters on the manifolds. For these two cases, the maximum ΔT across the manifold at any time during the two considered flight profiles (from hot wall surface to manifold farthest from cold wall) is estimated at 800°R. The range of Mach 4 combustion manifold response in Figure 5.1-10 represents more extreme cooling than expected. The high fuel heat transfer, that will occur at the injectors only, was used on all fuel-wetted surfaces of the manifold. Also, the heating effect of 1200°R coolant hydrogen in the fin jackets, which was not considered in the analysis, will retard cooling of the manifold to the fuel temperature at 740°R. Flight profiles to Mach 6 (both supersonic and subsonic combustion) were not considered critical for design.

5.1.4.2 Outerbody Outlet Manifold

Transient thermal analysis was performed on the outerbody outlet manifold for ascent to, and for design point operation at Mach 8 (6.5 local), 88,000 ft altitude. The object was to determine the maximum cross-section ΔT between the outer surface of the 0.015-in.-thick hot wall and the 0.187-in.-thick manifold wall.

Results in Figure 5.1-11 indicate a maximum cross-section ΔT of 1160°R that will occur just after start of combustion when the outer wall maximum temperature increases from the local coolant hydrogen temperature of 1200° to 2000°R. This maximum cross-section ΔT is located near bottom dead center of the manifold. Circumferential flow of hydrogen in the manifold at bottom dead center is almost nil because this location is on the line of symmetry between manifold outlet tubes. The small hydrogen flow and the associated small convective heat transfer coefficient at bottom dead center in the manifold results in a slow manifold heatup (such as T_2 in Figure 5.1-11). The temperature T_W (outer) will be uniform around the outerbody circumference because it will be dependent only on hot-gas heating and fin-hydrogen cooling. If needed, electrical heaters attached to the manifold can preheat the manifolds and reduce ΔT's, as discussed for the subsonic injector manifolds in Section 5.1.4.1.

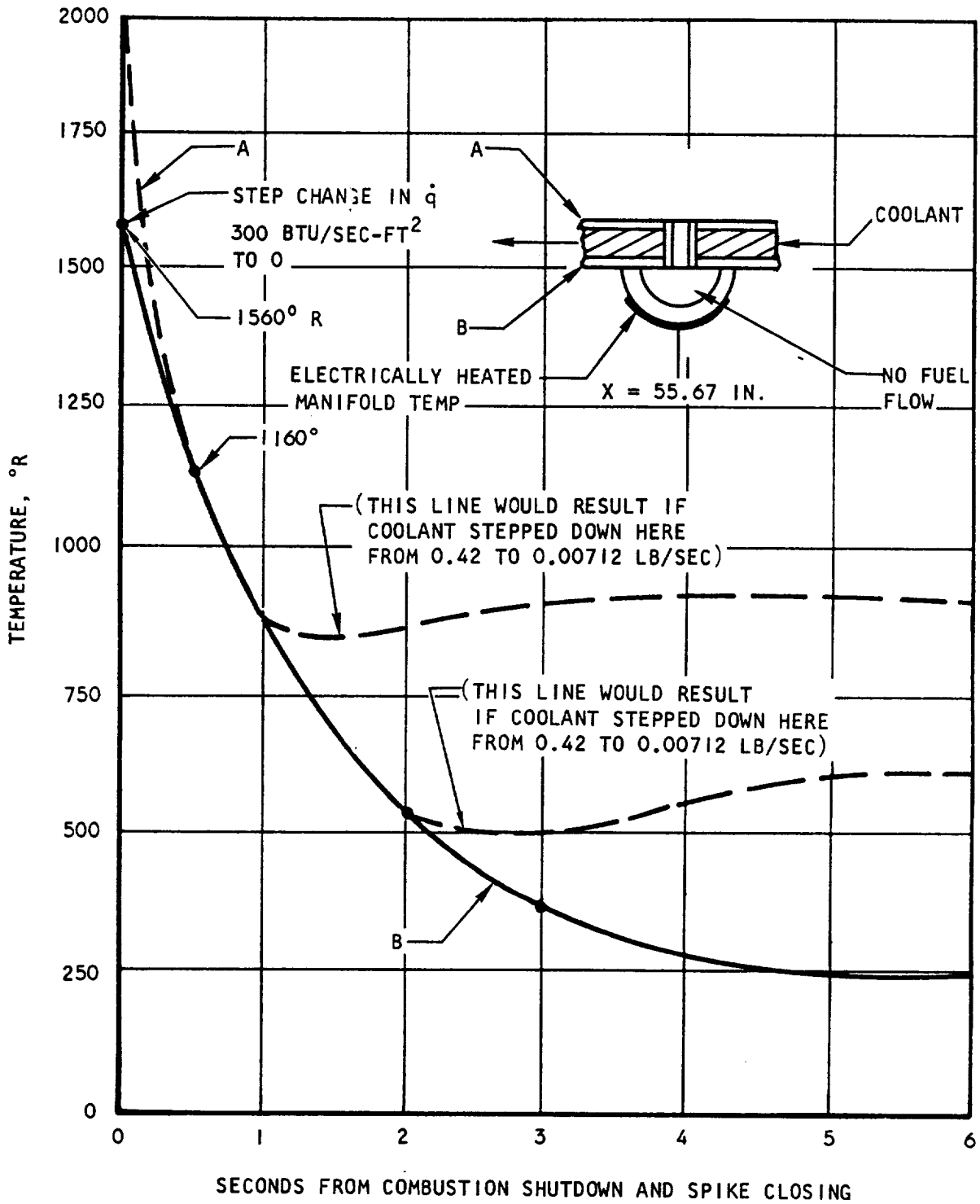

Figure 5.1-9. Temperature Histories at Innerbody Subsonic Injector Manifold from Mach 6.5L to Shutdown

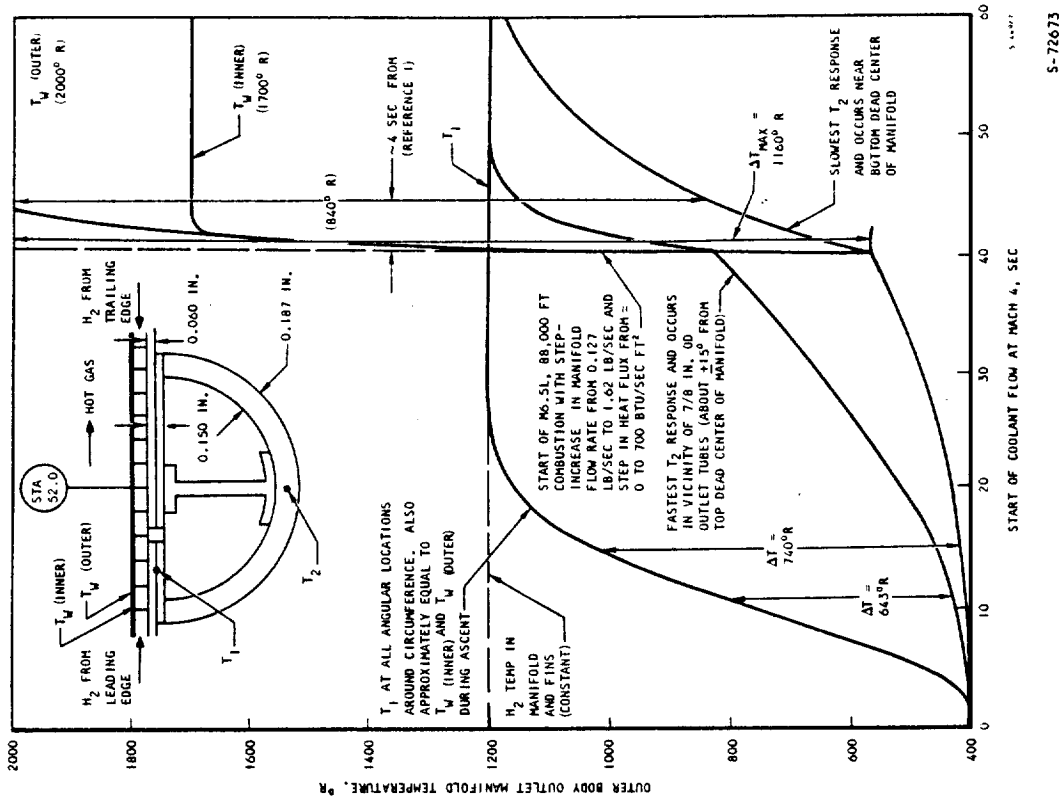

Figure 5.1-11. Outerbody Outlet Manifold Thermal Transient

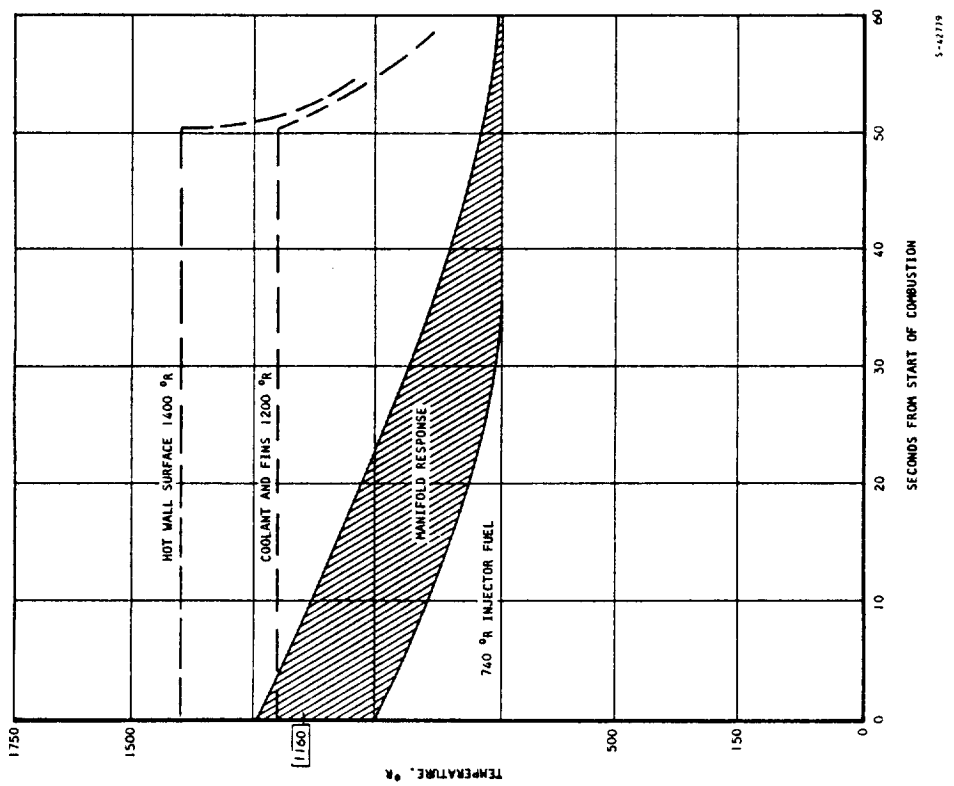

Figure 5.1-10. Temperature Histories at Innerbody Subsonic Manifold During Mach 4 Combustion

5.1.5 Mission Coolant Requirements

Analyses were performed to determine minimum hydrogen coolant requirements for ascent and descent to and from a Mach 8 (flight and engine local) 88,000-ft flight profile. These results established requirements for control of flow in each of the four flow routes as a function of time during mission. Ascent and descent coolant requirements for three methods of flow control are presented in Table 5.1-3 and are discussed below. These hydrogen consumptions are required above Mach 4 where the freestream total temperature is above the engine structural temperature limit of 1600°R. The flight profile used in the analyses is shown in Figure 5.1-12 (proposed AiResearch modification). Though not included in Table 5.1-3, the hydrogen requirement at the operating point (Mach 8 freestream and local) was calculated from the required coolant rate in Table 5.1-2 and the operational time of 20 sec indicated in Figure 5.1-12, at 43.8 lb (i.e., 2.19 lb/sec x 20 sec).

Method 1. Outlet Temperature Control (No Insulation)

A hydrogen consumption of 28.2 lb can be approached if four separate modulating valves regulate flow in each of the four flow routes so that an outlet coolant temperature of 1600°R is maintained. A 1600°R outlet coolant temperature can be achieved in all but the spike flow route. In the double-sandwich plate-fin section of the aft spike, coolant is heated to 1600°R at the end of the passage adjacent to the hot gas, but is cooled below 1600°R after making a 180-deg turn and flowing through the inner passage of the double-sandwich section. The coolant outlet temperature of the spike for design combustion conditions is about 1300°R. During non-lit, spike closed conditions, the outlet coolant temperature can be slightly higher than 1300°R, but to have a single value of spike outlet temperature, a 1300°R spike coolant outlet appears desirable for all flight phases. For 1600°R outlet coolant temperature in three of the four routes and 1300°R in the spike route, the hydrogen consumption for non-lit, spike closed conditions is increased 3.2 lb to 31.4 lb.

The above coolant consumption does not provide for adequate cooling of the outerbody leading edge design as shown in Figure 5.1-3. During ascent and descent, the outerbody leading edge heat flux is a higher percentage of its design point combustion level than is the overall leading edge route heat load. The leading edge flow route outlet control temperature could not detect an overheated leading edge tip. A leading edge tip cooling design reservoir which would provide for separately routed leading edge tip coolant passages of small cross-sectional area could alleviate this problem. This alternate design is discussed in Section 5.5.4. The coolant required for this separate route was estimated at about 20 percent of the total ascent-descent coolant consumption, or an increase of about 6 lb in the total hydrogen required. A 6-lb increase is associated with connection of the separate leading edge passages in parallel with the spike flow.

TABLE 5.1-3

SUMMARY OF ASCENT AND DESCENT COOLANT REQUIREMENTS

Method 1:	Outlet Temperature Control (No Insulation)	
	Thermodynamic minimum consumption	28.2
	Increase in consumption due to 1300°R spike outlet coolant temperature	3.2
	Increase due to separate cooling of outerbody leading edge tip	6.0
	Total	37.4 lb
Method 1a:	Outlet Temperature Control (Rockide Z Insulation on Spike)	
	Thermodynamic minimum consumption	24.3
	Increase in consumption due to 1300°R spike outlet coolant temperature	2.6
	Increase due to separate cooling of outerbody leading edge tip	6.0
	Total	32.9 lb
Method 2:	Fixed Orifice Control (No Insulation)	
	Minimum flow as detected by highest coolant outlet temperature	73.0
	Increase due to separate cooling of outerbody leading edge tip	6.0
	Total	73.0 lb
Method 3:	Leading Edge Tip Temperature of 1500°R with Fixed Orifice Flow Control	150.0 lb

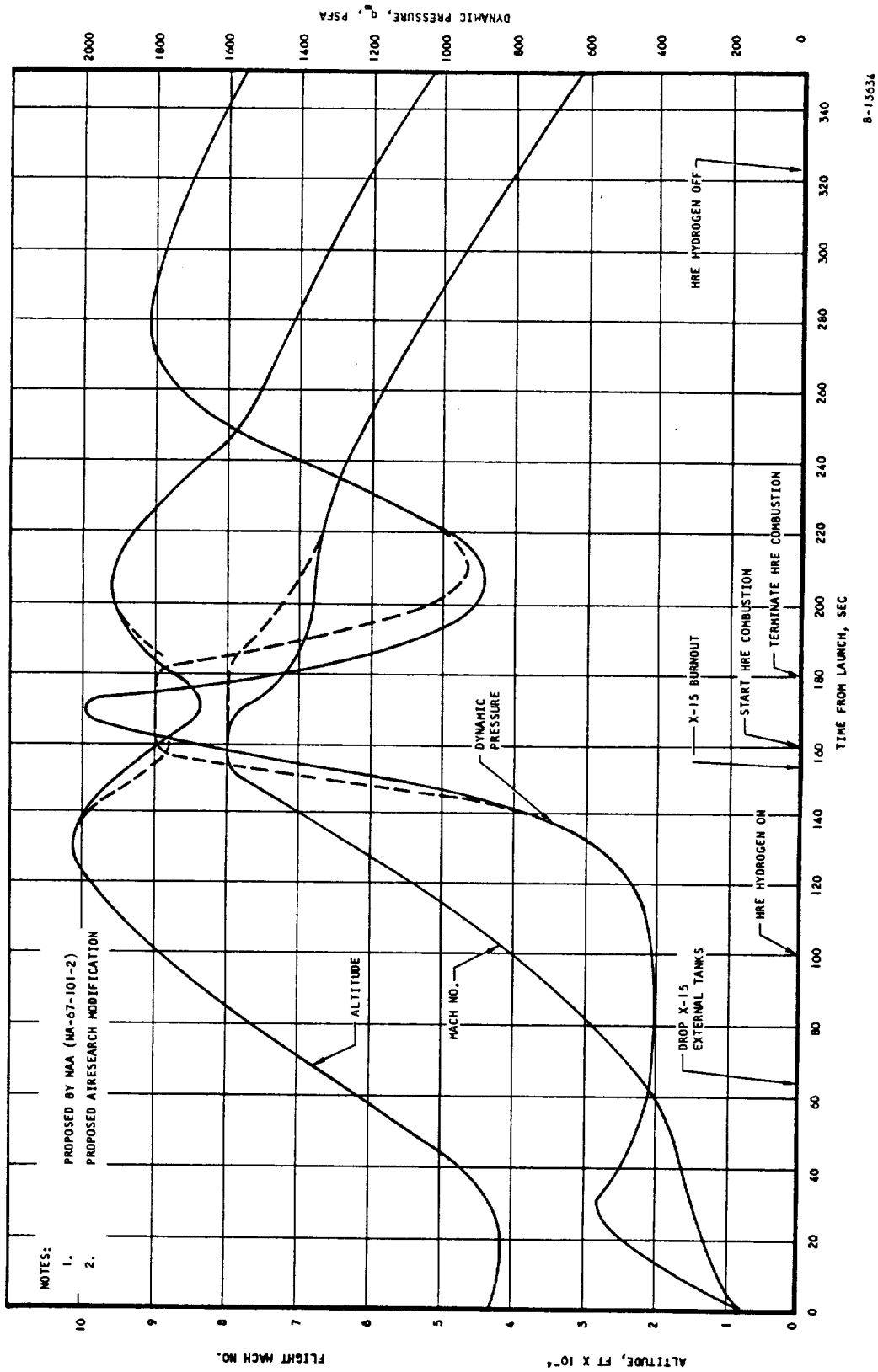

Figure 5.1-12. Proposed X-15A-2 Trajectory for HRE Mission to Mach 8

Method 1a. Outlet Temperature Control (Insulation)

Application of Rockide Z (zirconium oxide) to external surfaces of the spike and outer body leading edge flow routes (0.030 in. thick on the spike fore body, 0.015 in. on the spike aft body, and 0.020 in. on the outerbody) can reduce the uninsulated thermodynamic minimum for ascent and descent from 28.2 to 24.3 lb. Rockside Z insulation can reduce hot gas heat absorption in metal surfaces by (1) creating an additional thermal conduction resistance in the heat path from hot gas to coolant, and (2) dissipating hot gas heat input by radiation, because Rockide Z surface temperatures of up to 3500°R appear feasible. The reduction in coolant consumption on internal surfaces during combustion is much greater than on external surfaces because internal combustion heat fluxes are much greater. The net combustion coolant rate could be 50 percent lower than for uninsulated surfaces because of the large ΔT in Rockide Z with metal surfaces maintained at 2060°R maximum. On external surfaces, the heat flux is lower, the ΔT through Rockide Z is correspondingly lower, and the net reduction in coolant consumption is only 15 percent (28.2 to 24.3 lb). The increase in consumption due to a 1300°R spike outlet temperature with insulation was estimated at 2.6 lb. The 6-lb increase due to separate cowl leading edge cooling is also applicable.

Method 2. Fixed Orifice Flow Control

Fixed-geometry orifices in all but the pressure-drop-controlling route was investigated as a means of coolant flow control. This method eliminates the use of modulating valves at the route inlets, but results in a considerable increase in hydrogen consumption during non-lit, spike closed conditions. Outlet temperature sensors adjust the flow rate in all four routes, so that the maximum allowable coolant outlet temperature in any route is never exceeded. The orifice sizes would be selected to give best coolant usage during design combustion conditions. Under these conditions, the coolant consumption for non-lit spike closed conditions is 73 lb. This more than twofold increase in coolant consumption over individual flow control results from the relationship of the heat load on each flow route during non-lit, spike-closed conditions and during combustion at Mach 8, 88,000 ft. During design combustion conditions, the inner shell, outer shell, trailing edge, and nozzle, receive 37 percent of the total heat load. During non-lit, spike-closed conditions, these surfaces receive less than 10 percent of the total heat load. Because fixed-orifice flow regulation will give approximately the same spike flow for all heating conditions, the inner shell, outer shell, trailing edge, and nozzle will be overcooled during non-lit, spike-closed conditions. In fact, the coolant in the highly heated routes will be more dense and a higher percentage of the total coolant will flow through these routes during non-lit conditions than during combustion.

The 6-lb increase due to separate leading edge cooling is also applicable for this method.

Method 3. Leading Edge Tip Temperature Control

In order for the coolant requirements by the above methods to be realistic, a separate leading edge circuit is required. A third method was employed with

the existing leading edge flow routing shown in Figure 5.1-3. To provide leading edge tip cooling by this method, it was assumed that a thermocouple mounted in the leading edge metal tip regulated coolant to all flow routes with fixed-geometry orifices (as in Method 2 above) such that the tip metal temperature was maintained at 1500°R. The resulting ascent and descent coolant consumption is 150 lb. This coolant consumption is higher than determined by the above methods because the consumption reflects a hydrogen conductance at the outerbody leading edge that was increased by increasing leading edge passage flow rate, and thereby increasing flow rate in all engine flow routes. Hydrogen conductance at this leading edge could also be increased by decreasing the hydrogen passage height at the outerbody leading edge so the leading edge would be adequately cooled during ascent and descent. However, during combustion the increased flow rate required in the leading edge flow route would result in a large pressure drop in this reduced-clearance region.

5.2 SYSTEM STRUCTURAL ANALYSIS (FLIGHT)

5.2.1 Loads

The sign and coordinate convention used to express loads acting on the HRE is shown on Figure 5.2-1. It is assumed that the acceleration directions are positive in the positive coordinate direction, but the forces due to the acceleration are reversed by virtue of D'Alembert's principle.

Inertia loads are assumed to act in the center of gravity of the engine. The position of the center of gravity is a function of the spike position. Movements of the spike change the location of the center of pressure. The positions of the center of gravity and the center of pressure for normal loads in the fully extended and retracted positions of the spike are shown on Figure 5.2-2. Aerodynamic, inertia, vibratory and thermal load were based on flight envelope and operational characteristics of the X-15A-2 aircraft. The most significant load cases either with the engine operating or inoperative are shown on Table 5.2-1. This table presents a comprehensive listing of operating conditions, aerodynamic external drag forces, engine net internal thrust forces, and acceleration loads for Mach numbers of 8.0, 6.5, and 5.0 at different dynamic pressures, flight angles of attack, and flight yaw angles.

A fuel flow limitation, w_f = 3 lb per sec, has been established for the first flightweight engines, which precludes stoichiometric engine operation over a portion of the flight spectrum indicated in the Statement of Work (L-4947-B, dated January 1967). The following constraints are imposed by structural limitations of the X-15A-2 aircraft:

- Maximum airplane angle of attack, α = 10 deg
- Maximum normal acceleration, N_z = 4.25 g

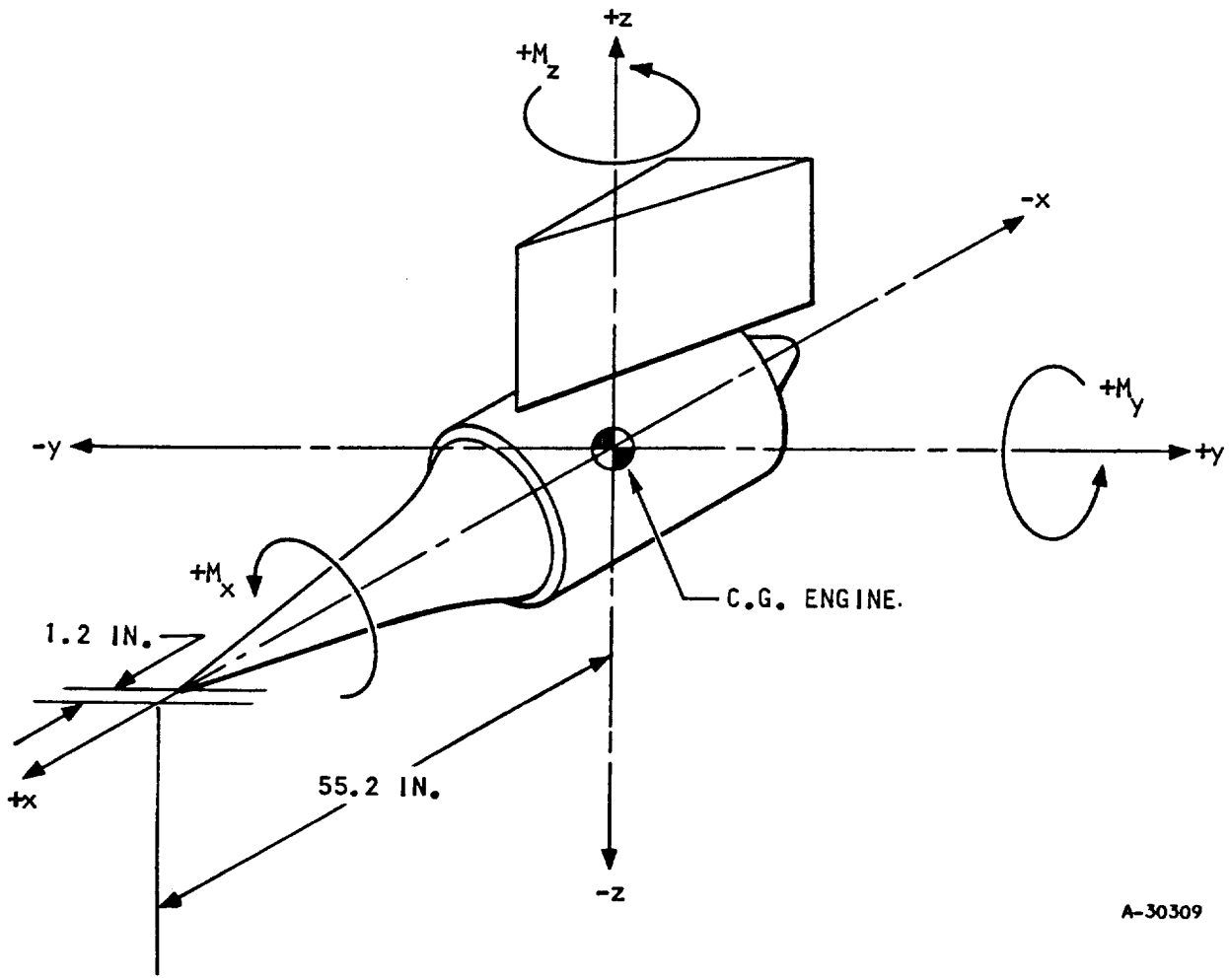

Figure 5.2-1. HRE Coordinate System and Sign Convention

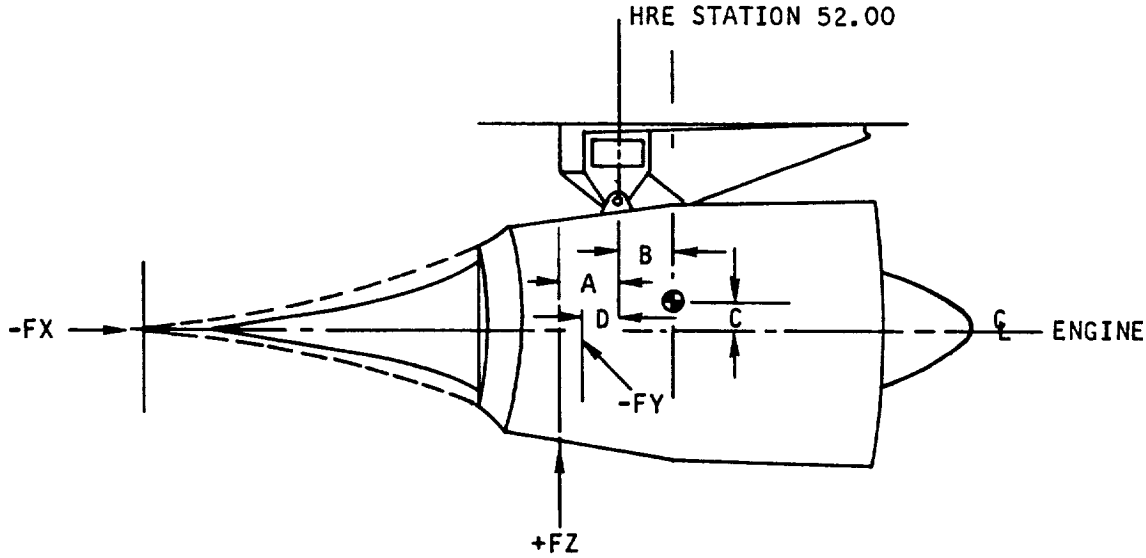

NOTE: The vertical centerline of the thrust block mount is located at HRE Station 52.00 which is established by a plane perpendicular to the axial centerline of the HRE intersecting that centerline 52.00 inches aft of the theoretical apex of the inlet spike cone, when the spike is in the fully retracted position. For convenience in structural design, station 52.00 is the datum for location of center of gravity, and centers of pressure. All locations forward of station 5200 are negative, and all locations aft of station 52.00 are positive.

		ENGINE OPERATING (SPIKE RETRACTED), in.	ENGINE NOT OPERATING (SPIKE EXTENDED), in.
A	Center of Pressure, FY Load	-13.23	-15.43
B	Center of Gravity	+ 4.50	+ 3.4
C	Center of Gravity above ℄	+ 1.20	+ 1.20
D	Center of Pressure, FZ Load	-13.23	-15.43

S-72682

Figure 5.2-2. HRE Center-of-Gravity and Center-of-Pressure Locations

TABLE 5.2-1

FLIGHT CONDITIONS AFFECTING STRUCTURAL DESIGN OF HRE

Case No.	Operation Mode	M_∞	q_∞, psf	α_∞, deg	β_∞ deg	N_z, g	N_x, g	N_y, g	M_L	q_L, psf	α_L, deg	β_L, deg	HRE Net Internal Thrust, lb	External Drag	Normal F_z	Side F_y	Axial
1	n	8.0	2000	10.0	2	4.25	4.5	-1.0	6.5	3600	4.0	2.0	0	1807	1297	862	-2036
2	n	8.0	2000	10.0	2	4.25	-3.0	-1.0	6.5	3600	4.0	2.0	0	1807	1297	862	-2036
3	n	8.0	1800	10.0	2	4.25	4.5	-1.0	6.5	3240	4.0	2.0	0	1626	1167	776	-1832
4	o	8.0	1800	6.8	2	3.0	2.0	-1.0	6.8	2760	4.0	2.0	3690	654	826	552	2851
5	n	8.0	1800	10.0	2	4.25	-3.0	-1.0	6.5	3240	4.0	2.0	0	1626	1167	776	-1832
6	o	8.0	1800	6.8	2	3.0	-3.0	-1.0	6.3	2760	4.0	2.0	3690	654	826	552	2851
7	n	8.0	835	10.0	7	1.7	4.5	-1.0	6.5	1500	4.0	7.0	0	741	527	1280	-835
8	n	8.0	835	10.0	7	1.7	-1.0	-1.0	6.5	1500	4.0	7.0	0	741	527	1280	-835
9	n	8.0	2000	-1.0	2	-0.5	4.5	-1.0	7.5	1800	-1.0	2.0	0	904	649	431	-1018
10	n	8.0	2000	-1.0	2	-0.5	-3.0	-1.0	7.5	1800	-1.0	2.0	0	904	649	431	-1018
11	n	8.0	1300	-1.0	2	-0.5	4.5	-1.0	7.5	1620	-1.0	2.0	0	813	584	389	-916
12	n	8.0	1800	-1.0	2	-0.5	-3.0	-1.0	7.5	1620	-1.0	2.0	0	813	584	389	-916
13	o	8.0	1800	-1.0	2	-0.5	3.0	-1.0	7.5	1620	-1.0	2.0	1900	374	485	324	+1423
14	o	8.0	1800	-1.0	2	-0.5	-2.0	-1.0	7.5	1620	-1.0	2.0	1900	374	485	324	+1423
15	n	6.5	2000	9.7	2	4.25	4.5	-1.0	5.4	3200	-1.0	2.0	0	1606	1153	766	-1809
16	n	6.5	2000	9.7	2	4.25	-3.0	-1.0	5.4	3200	-1.0	2.0	0	1606	1153	766	-1809
17	n	6.5	1800	10.0	2	4.25	4.5	-1.0	5.4	2880	4.0	2.0	0	1446	1037	389	-1629
18	o	6.5	1800	9.0	2	2.0	2.5	-1.0	5.45	2790	4.0	2.0	5110	704	835	558	4228
19	n	6.5	1800	10.0	2	4.25	-3.0	-1.0	5.4	2880	4.0	2.0	0	1446	1037	389	-1629
20	o	6.5	1800	9.0	2	2.0	-2.0	-1.0	5.45	2790	4.0	2.0	5110	704	835	558	4228
21	n	6.5	2000	-1.0	2	-0.5	4.5	-1.0	5.8	1800	-1.0	2.0	0	904	649	431	-1018
22	n	6.5	2000	-1.0	2	-0.5	-3.0	-1.0	5.8	1800	-1.0	2.0	0	904	649	431	-1018
23	n	6.5	1800	-1.0	2	-0.5	4.5	-1.0	5.8	1620	-1.0	2.0	0	813	584	389	-916
24	o	6.5	1800	-1.0	2	-0.5	3.0	-1.0	5.8	1620	-1.0	2.0	2740	397	485	324	+2240
25	n	6.5	1800	-1.0	2	-0.5	-3.0	-1.0	5.8	1620	-1.0	2.0	0	813	584	389	-916
26	o	6.5	1800	-1.0	2	-0.5	-2.0	-1.0	5.8	1620	-1.0	2.0	2740	397	485	324	+2240
27	n	5.0	2000	8.0	2	4.25	4.5	-1.0	4.2	2800	4.5	2.0	0	1405	1009	670	-1583
28	n	5.0	2000	8.0	2	4.25	-3.0	-1.0	4.2	2800	4.5	2.0	0	1405	1009	670	-1583
29	n	5.0	1800	8.8	2	4.25	4.5	-1.0	4.2	2520	4.5	2.0	0	1265	908	603	-1425
30	o	5.0	1800	8.8	2	2.5	3.0	-1.0	4.2	2520	4.5	2.0	5950	699	784	504	+5091
31	n	5.0	1800	8.8	2	4.25	-3.0	-1.0	4.2	2520	4.5	2.0	0	1265	908	603	-1425
32	o	5.0	1800	8.8	2	2.0	-2.0	-1.0	4.2	2520	4.5	2.0	5950	699	754	504	+5091
33	n	5.0	2000	-1.0	2	-0.5	4.5	-1.0	4.9	1900	-1.0	2.0	0	954	684	455	-1075
34	n	5.0	2000	-1.0	2	-0.5	-3.0	-1.0	4.9	1900	-1.0	2.0	0	954	684	455	-1075
35	n	5.0	1800	-1.0	2	-0.5	4.5	-1.0	4.9	1710	-1.0	2.0	0	858	616	409	-967
36	o	5.0	1800	-1.0	2	-0.5	2.0	-1.0	4.9	1710	-1.0	2.0	3310	443	511	342	+2758
37	n	5.0	1800	-1.0	2	-0.5	-3.0	-1.0	4.9	1710	-1.0	2.0	0	858	616	409	-967
38	o	5.0	1800	-1.0	2	-0.5	-2.0	-1.0	4.9	1710	-1.0	2.0	3310	443	511	342	+2758

q - dynamic pressure
α - angle of attack
β - angle of yaw
N - acceleration
M - Mach number
o - operating
n - nonoperating

Subscripts
x - longitudinal
y - lateral
z - normal
∞ - freestream
L - local

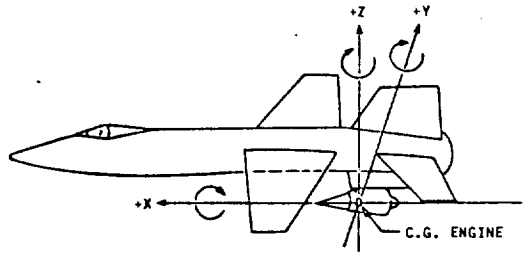

X-15 COORDINATE SYSTEM

The resulting permissible mission envelope is shown in Figure 5.2-3. Some of the salient features of this envelope are:

- At q_{max} of 2000 psf, α_{max} = 8.8 deg at M_∞ = 5.8

  Below M_∞ = 5.8, the α_{max} at q_∞ = 2000 is N_z limited

- At q_{max} = 1800 psf, α_{max} = 10.0 deg at M_∞ = 6.3

  Below M_∞ = 6.3, the α_{max} at q_∞ = 1800 is N_z limited

- Maximum angle of attack α_{max} = 10.0 deg is limited to

  $q_{max} \cong 1600$ psf and $M_\infty \cong 7.5$

The engine is designed structurally for operation with the X-15 angle of attack ≤ 10 deg and the dynamic pressure ≤ 2000 psf, but with the combustor not lit.

The tabulation of the flight conditions affecting the structural design of the HRE was revised to reflect the effect of the symmetrical and the asymmetrical inlet unstart and the effect of limitations shown in Figure 5.2-3.

5.2.1.1 Aerodynamic

Engine external drag and internal thrust for different Mach-number and flight-maneuver conditions are tabulated in Table 5.2-1. Wind tunnel tests using a one-third-scale inlet model indicated that an unsymmetrical unstart of the inlet is possible at the maximum design Mach number. This condition results in high normal loads when the engine is in the X-15A-2 shock field. Similarly, a symmetrical unstart in the shock field results in high axial loads. The nondimensionalized pressure distribution due either to partial or symmetrical unstart for M_∞ = 8.0, M_L = 6.5 condition is shown in Figure 5.2-4.

This pressure distribution was integrated to obtain the freebody loads on the HRE. Table 5.2-2 presents these loads for the most critical fuel ON and fuel OFF conditions and shows the axial freebody loads due to asymmetrical inlet unstart that act concurrently with the peak normal force of 16,800 lb. Engine forces for the engine-operating and the inlet-started conditions are shown for q_∞ = 1600 psf in the last column.

The maximum axial load, P_{xa} = 14,190 lb, at the strut attachment at the outerbody occurs at M_∞ = 8.0, M_L = 6.5, q_∞ = 2000 psf due to symmetrical inlet unstart. The maximum normal force, P_{zn} = 16,800 lb, occurs in case of an asymmetrical engine unstart condition at M_∞ = 8.0, M_L = 6.5, and q_∞ = 2000. Both of these load cases occur in a non-lit condition of the engine, outside of the engine-lit flight envelope.

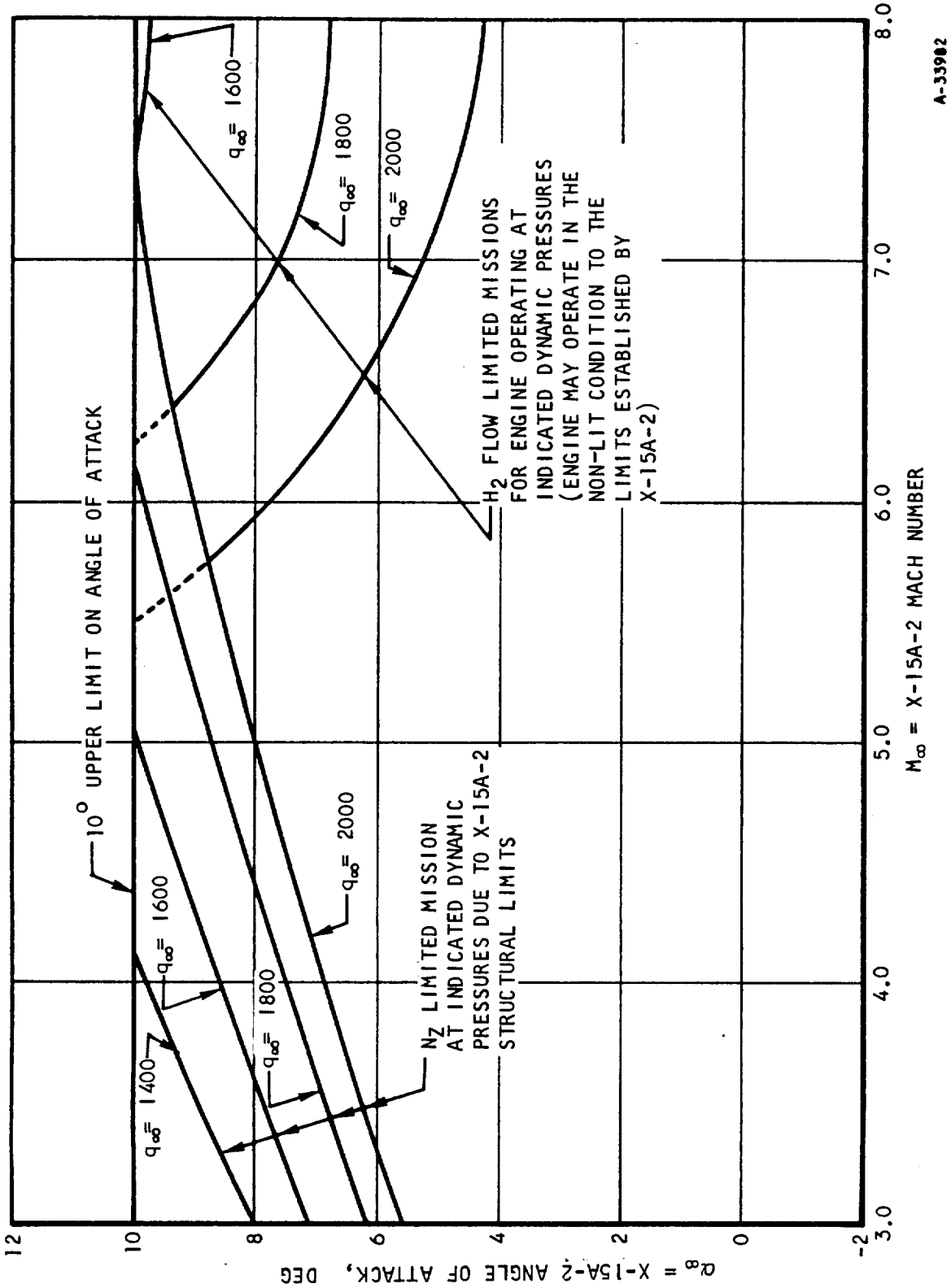

Figure 5.2-3. X-15A Engine-Lit Mission Envelope

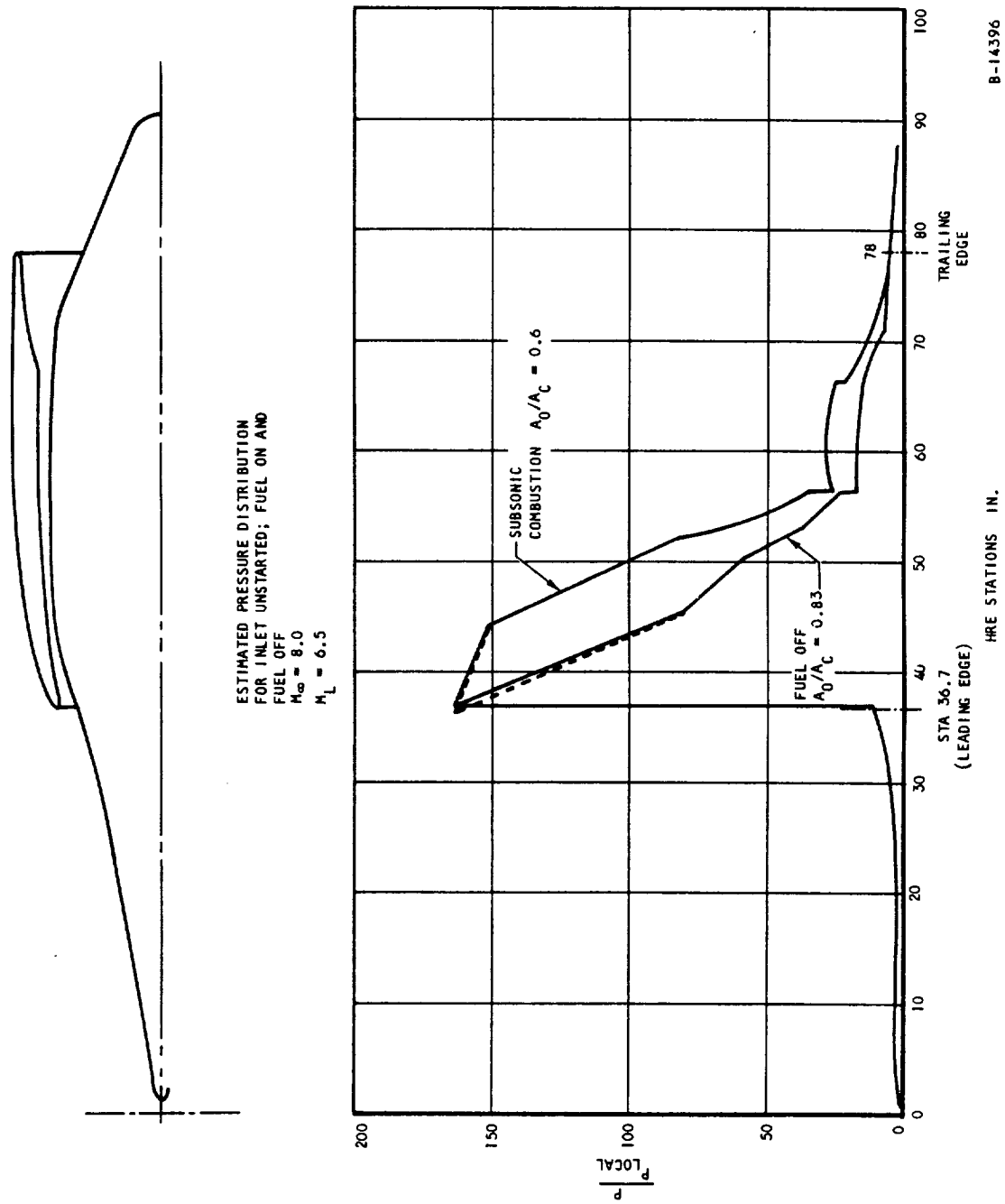

Figure 5.2-4. HRE Pressure Distribution at $M_\infty = 8.0$

TABLE 5.2-2
HRE FREEBODY AERODYNAMIC LOADS

	Fuel Off	Fuel On (Subsonic Combustion)	Asymmetrical Inlet Unstart	Fuel-Limited Mission, Fuel on, Inlet Started
q_∞	2,000	1,600	2,000	1,600
Max P_L (psi)	0.845	0.68	0.845	0.68
F_1	15,000	14,500	5,650	2,500
F_2	200	250	75	435
F_3	805	1,120	303	1,855
F_4	9,600	10,600	3,620	4,770
F_5	195	170	195	135
F_6	1,260	1,010	1,260	1,010
F_a	13,130	13,130	5,270	210
F_b	13,300	13,300	5,465	395
F_c	3,710	3,710	3,105	-3,155

$M_\infty = 8.0$
$M_L = 6.5$

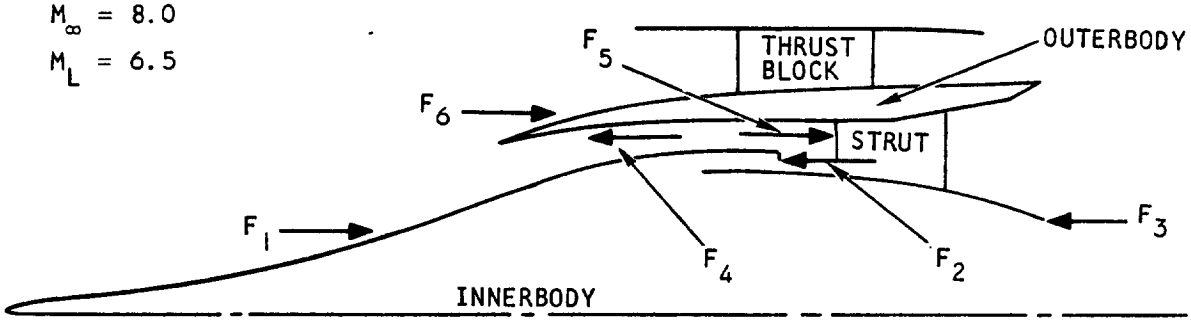

LOADS TRANSMITTED

(a) STRUT ATTACHED AT INNERBODY
$F_a = F_1 - F_2 - F_3$

(b) STRUT ATTACHED AT OVERBODY
$F_b = (F_1 - F_2 - F_3) + F_5$

(c) THRUST BLOCK
$F_c = (F_1 - F_2 - F_3 + F_5) - F_4 + F_6$

S-72668

5.2.1.2 Dynamic and Vibration

External loads, such as aerodynamic pressure and inertia loads are dynamic in nature. The values tabulated in Table 5.2-1 are calculated on a statistical basis and used as static equivalent loads representing certain extreme cases of the aircraft in operation.

The HRE must withstand vibrational forces simultaneously with the aerodynamic and acceleration loads. The best information available indicated that the maximum X-15A-2 output at the engine mount points does not exceed 0.3 g. Employing this input level and further assuming an amplification factor of 10 at the engine fundamental frequency, leads to a 3.0 g load factor (0.3 x 10) in all directions, which must be applied in conjunction with the acceleration and aerodynamic forces. The fundamental axial response was assumed to be 20 g; the transverse and lateral response--based on the expected structural damping--was 7.5 g for the engine. Amplification factors for certain parts of the engine were established based on the structural features of each part.

5.2.1.3 Pressure-Containment

Regeneratively cooled surfaces, manifolds and fittings are exposed to coolant pressure. Maximum operating pressure was assumed to be 700 psi. All plate-fin shell assemblies and manifolds were designed to contain this pressure during the 10-hr design life of the engine. All shells at the subassembly and final assembly levels (i.e., after the installation of the manifolds) were subjected to proof pressure of 1050 psi. These pressure tests were to provide verification of manifold containment-strength and prove leak-tightness of all final assemblies.

This test pressure in general is inadequate to confirm shell-containment strength of the various shell assemblies. Each shell assembly was pressure tested prior to the addition of manifolds to provide a realistic evaluation of shell fin assemblies without inducing damage in a sound part. Experience on the sub-element panels has shown that a higher proof pressure is required to pinpoint local braze voids which could subsequently cause premature failure under creep-rupture or thermal cycling conditions. Such pressure tests permit possible repairs to locally defective shells in some instances, and it also permits timely rejection of nonrepairable defective shells prior to additional fabrication steps.

5.2.2 Stress Analysis

5.2.2.1 Design Loads

External loads acting on the HRE installed on the X15 aircraft were described in Section 5.2.1. Loads acting on the major assemblies of the engine are described in the following paragraphs.

5.2.2.1.1 Spike-Actuator Assembly

Loads on the actuator are produced by external aerodynamic forces acting on the spike, bellows spring forces, pressure forces within the bellows cavity, acceleration forces acting on the spike, and aerodynamic unstart loads.

The maximum aerodynamic axial force is produced by a symmetrical unstart with $M_L = 6.5$, $q_L = 3600$ psfa, and $\alpha_L = 0$. The axial force for this condition is 15,000 lb aft. Normal and transverse aerodynamic loads for this condition are negligible.

The maximum aerodynamic normal force occurs with an asymmetrical unstart with $M_L = 6.5$, $q_L = 3600$ psfa, and a local angle of attack of 4 deg at the engine centerline. The normal force is 16,800 lb upward for this condition, and it is accompanied by an axial force of 5600 lb aft.

The bellows spring force varies from 2500 lb aft for the fully extended spike position, to zero with the spike fully retracted. Pressure forces within the bellows cavity vary from 6300 lb forward to 400 lb forward, with the spike in the fully retracted position.

Vibrational response acting simultaneously with these loads may be 3.0 g in any direction. The acceleration loads that may occur are listed in Table 5.2-1. Engine thrust forces and external drag forces do not contribute to the actuator loading.

The actuation system sizing is based upon the axial load profile shown in Figure 5.2-5 for a typical inlet unstart sequence. Normal load for this operating mode is taken as zero. The unstart occurs in the fully retracted position, and the axial aerodynamic force increases from the normal operating value to 15,000 lb within approximately 6×10^{-4} sec. The bellows pressure force tends to counteract this load, but its buildup time requires approximately 0.1 sec. The transient load for actuator force was reduced by allowing for partial buildup of the pressure force, based on a 0.05-sec lag in actuator response. The design loads that occur during the unstart are summarized below.

Loads Tending to Open	lb
Aerodynamic load	15,000
Bellows (mechanical)	200
Innerbody seal	500
Actuator support structure bearings	1,040
Actuator friction	100
	16,840

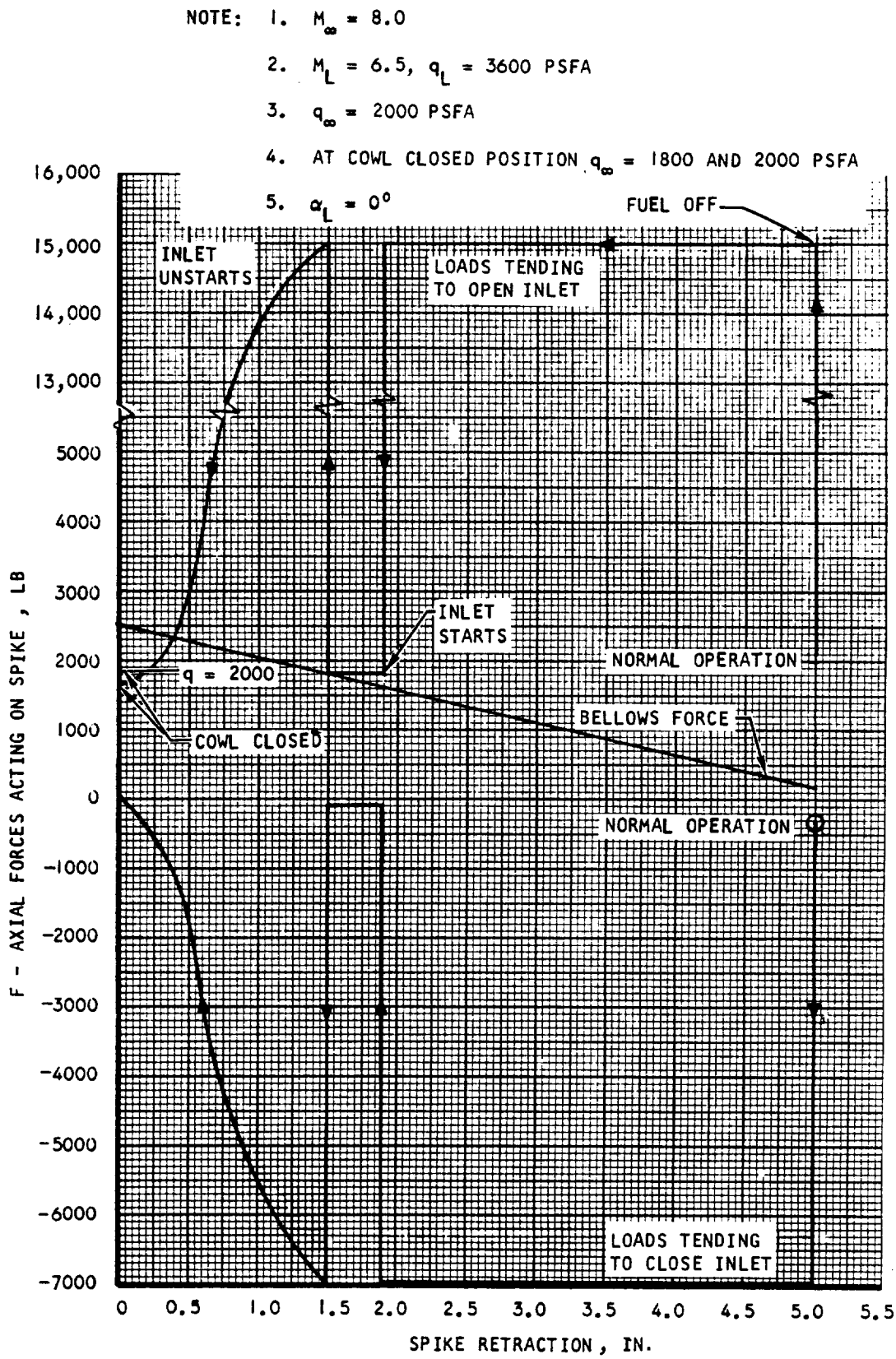

Figure 5.2-5. Estimated Axial Load Profile on Spike During a Typical Inlet Unstart Sequence (Shock Expelled)

Load Tending to Close	lb
Bellows pressure load (0.05-sec lag)	4,200
Net force required to close	12,640

The available force for the minimum stall pressure is

F_A = 16,700 lb

The design load margin is about 4060 lb.

The load conditions improve considerably after 100 msec when the hydraulic system can provide the maximum position rate. The following loads occur during closing:

Loads Tending to Open	lb
Aerodynamic load	15,000
Bellows (mechanical)	300
Innerbody seal	500
Actuator support-structure bearings	520
Actuator friction	100
	16,420

Loads Tending to Close	
Bellows pressure load	7,000
Net Force Required to Close	9,420

The force available from the hydraulics at maximum position rate is 11,900 lb, resulting in a margin of 2480 lb.

The maximum normal load condition occurs during an asymmetric unstart as shown in Figure 5.2-6.

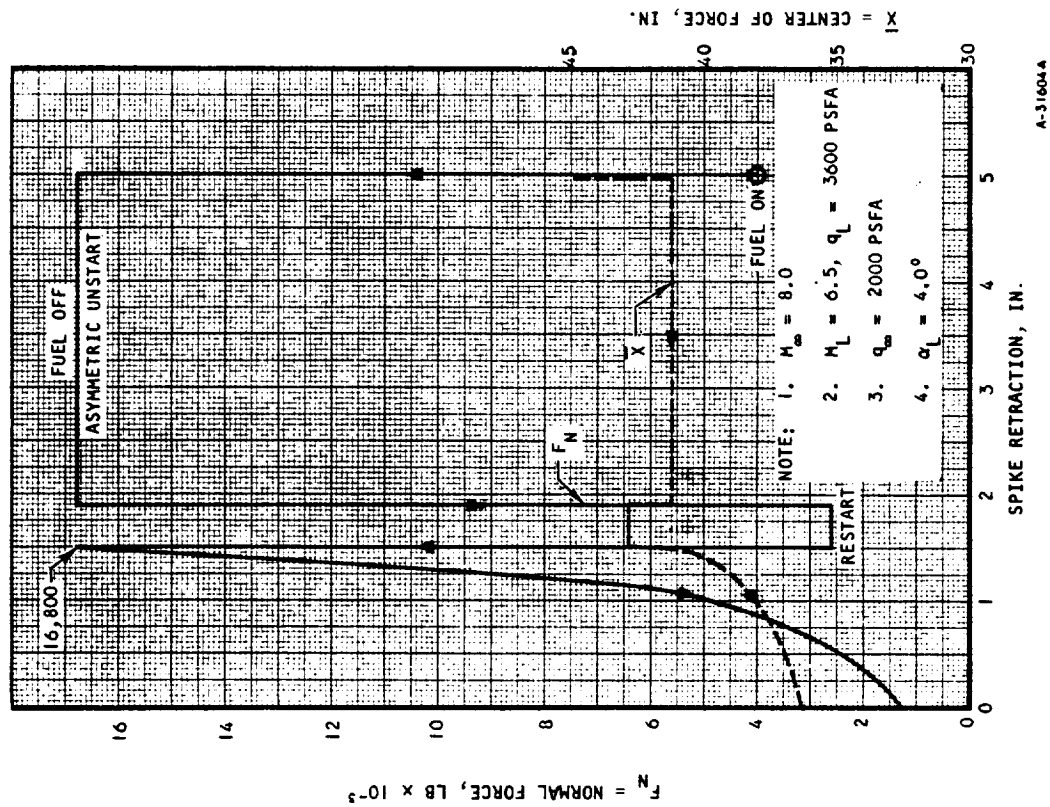

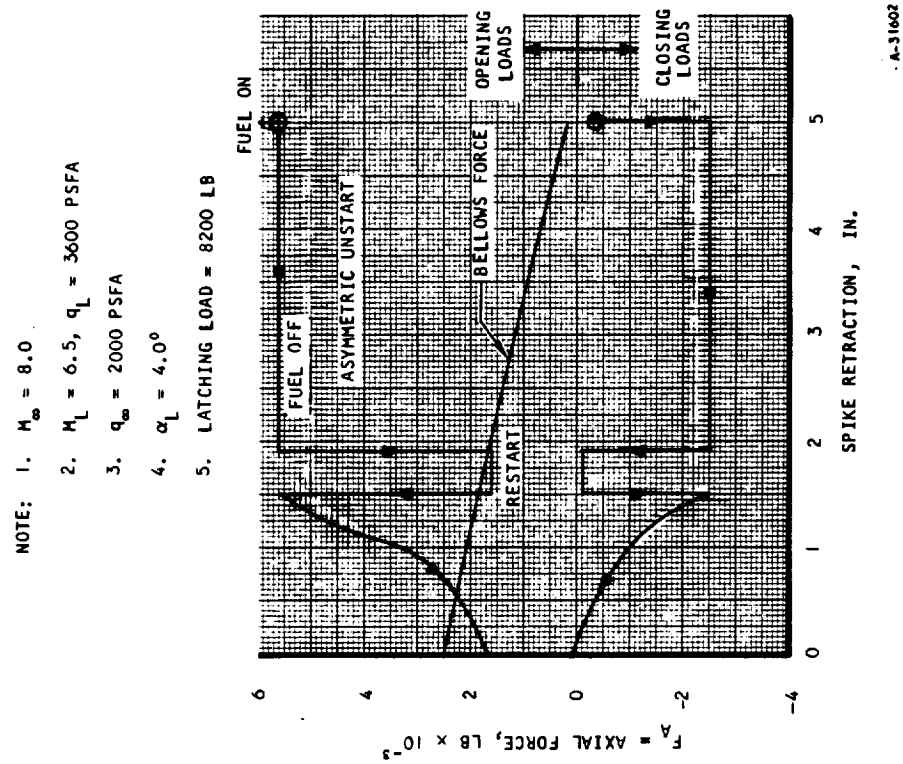

Figure 5.2-6. Estimated Load Profiles on Spike During a Typical Asymmetric Inlet Unstart Sequence (Shock Expelled)

These particular load conditions occur simultaneously, producing the governing structural design loads for the actuator support structure and legs. The actuator loads during this case are summarized as follows:

Loads Tending to Open	lb
Axial force	5,600
Bellows (mechanical)	200
Innerbody seal	900
Actuator support structure bearings	2,790
Actuator friction	100
	9,590
Loads Tending to Close	
Bellows pressure force (0.05-sec lag)	1,400
Net force required to close	8,190

This force is considerably less than the preceding design load; an approximate 8510-lb margin is allowed for minimum stall pressure.

The opening loads required by the spike actuator during flight are always less than those during ground checkout of the engine. Loads that must be overcome in ground checkout of the actuator are as follows:

	lb
Internal differential pressure across the piston to unlock the actuator	50
Innerbody seal friction	500
Actuator support structure bearing friction	1,040
Actuator friction	100
Total force	1,690

The available force for maximum position rate is 7120 lb. The need to provide for latching and snubbing determines piston area for the opening stroke and results in a margin of 5430 lb for opening.

5.2.2.1.2 Strut

The unsymmetrical inlet unstart condition creates the governing load condition for the innerbody-outerbody strut design. Loads acting on the innerbody spike, actuator, and nozzle are shown on Figure 5.2-7a. Strut design loads based on these loads are shown on Figure 5.2-7b. These design loads are the result of deflection compatibility studies which take into account the flexibility of the major engine components.

5.2.2.1.3 Innerbody/Outerbody Shells

Aerodynamic parameters of the innerbody/outerbody surfaces exposed to the gas flow are shown in Figure 5.2-8 and Figure 5.2-9 for Mach 8, q_∞ = 2000 psfa, M_L = 6.5, q_L = 3600 psfa condition. The static pressure profiles are representing this pressure load on the regeneratively cooled shells. Inertia loads conform with Table 5.2-1. The effects of vibration are 3.0 g load in any direction.

5.2.2.1.4 Mounting Frame

The design loads for the mounting frame stress analysis are described in para. 5.5.8.1.

5.2.2.1.5 Ablatively Cooled Cowl

Aerodynamic pressures acting on the cowl were integrated over four segments of the shell, and the three most significant cases are listed on Figure 5.2-10a. A shockwave starting from the leading edge of the X-15 lower vertical stabilizer creates a localized high pressure area shown on Figure 5.2-10b. The weight of the ablatively coated (Martin Company MA-25S ablative) cowl is calculated as 64.8 lb. The temperature of the cowl will not exceed 600°F.

5.2.2.1.6 Fuel Control Valves

The three fuel control valves are mounted 120-deg apart to the No. 2 fuel injector manifold of the innerbody. Since the spike is retractable, the piping connection from the spike coolant-outlet manifold to the collector manifold, and from the No. 1 fuel injector manifold in the spike to the No. 1 fuel control valve require bellows to absorb the total spike stroke.

Two bellows connect the spike and the control valve collector manifold system. The first, connecting the spike coolant-outlet manifold, produces 1353 lb total thrust load, and the second, connecting the No. 1 injector manifold produces 1027 lb total thrust load. Both loads are in the engine axial direction (X-axis). These thrust loads are due to pressure forces acting on the bellows and the 40-lb/in. force required to compress the bellows 5.3 in.

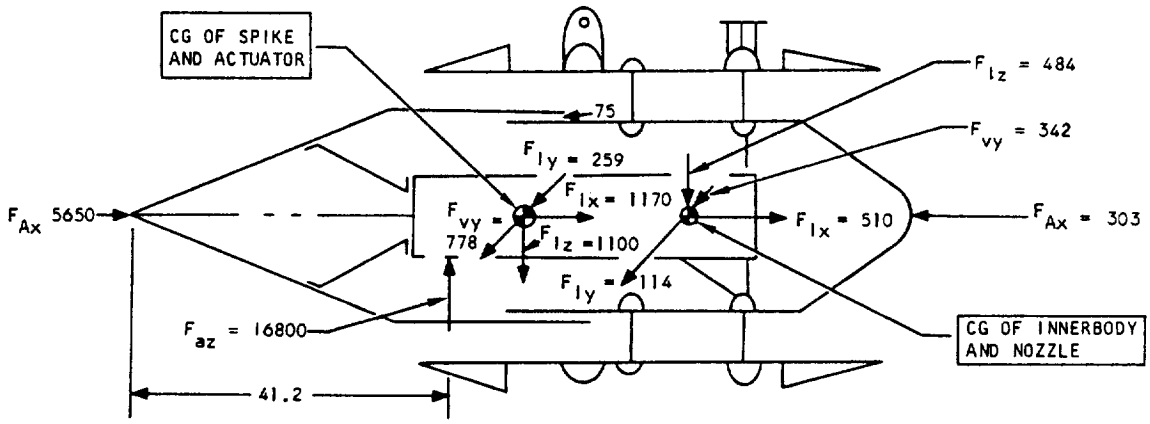

NOTES: 1. ONLY LOADS ON SPIKE, ACTUATOR, INNERBODY AND NOZZLE ARE SHOWN

F_V - VIBRATION LOAD
F_I - FRAME ACCELERATION LOAD
F_A - AERODYNAMIC PRESSURE LOAD

a. OUTER-INNERBODY STRUTS CRITICAL LOAD CONDITION (CRITICAL FLIGHT CONDITION: TRANSIENT, UNSYMMETRIC UNSTART)

A-33848

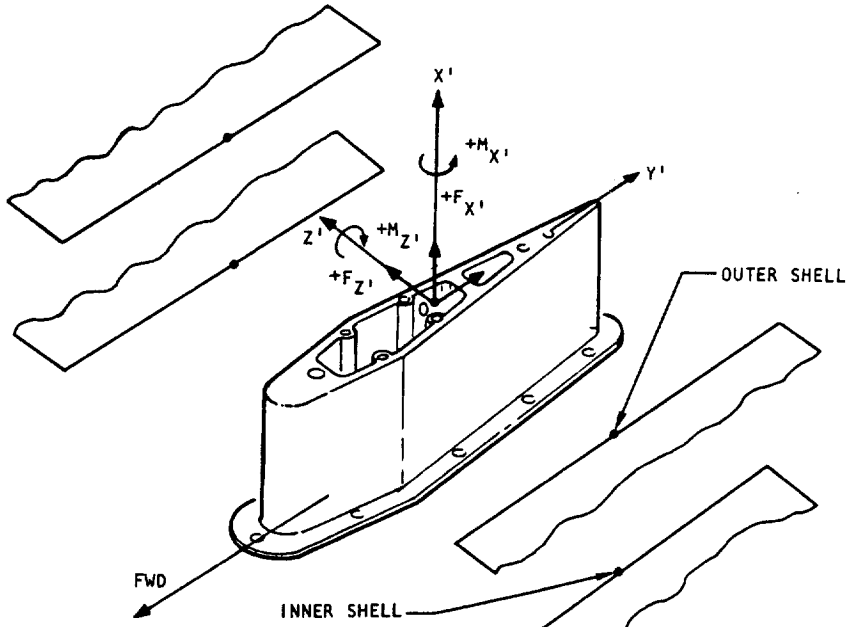

REACTION	OUTER SHELL (-0)	INNER SHELL (0)
$F_{X'}$ (LB)	-4333	4333
$F_{Y'}$ (LB)	16072	-16072
$F_{Z'}$ (LB)	8116	-8116
$M_{X'}$ (IN. LB)	53333	-53333
$M_{Y'}$ (IN. LB)	8901	4867
$M_{Z'}$ (IN. LB)	-15930	20196

A-33859

b. STRUT DESIGN LOADS

Figure 5.2-7 Strut Design Loads

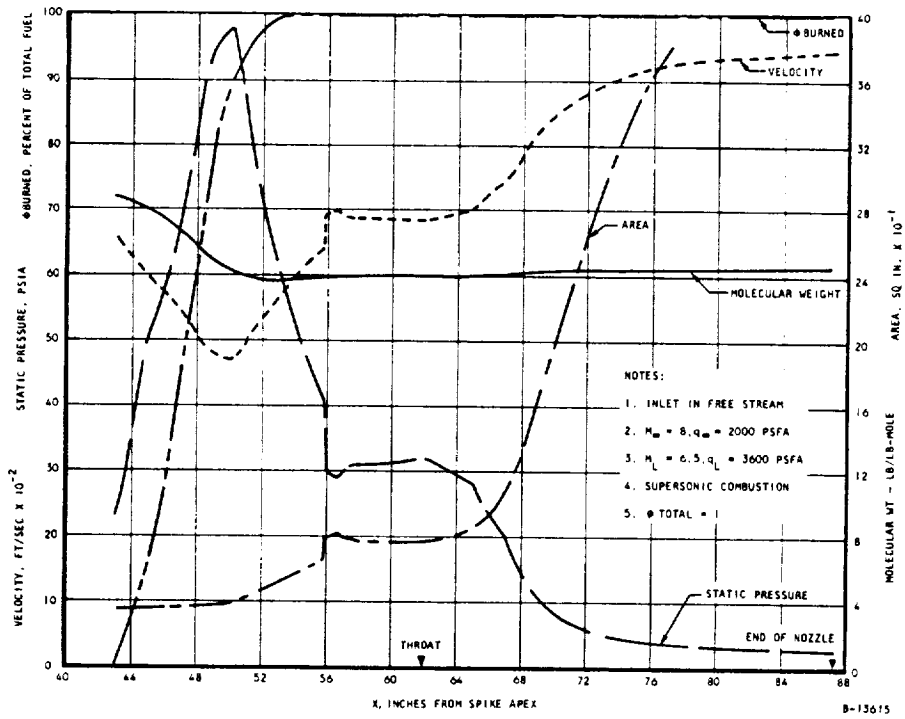

a. INNERBODY-OUTER SHELL MACH 8 AERODYNAMIC PARAMETERS

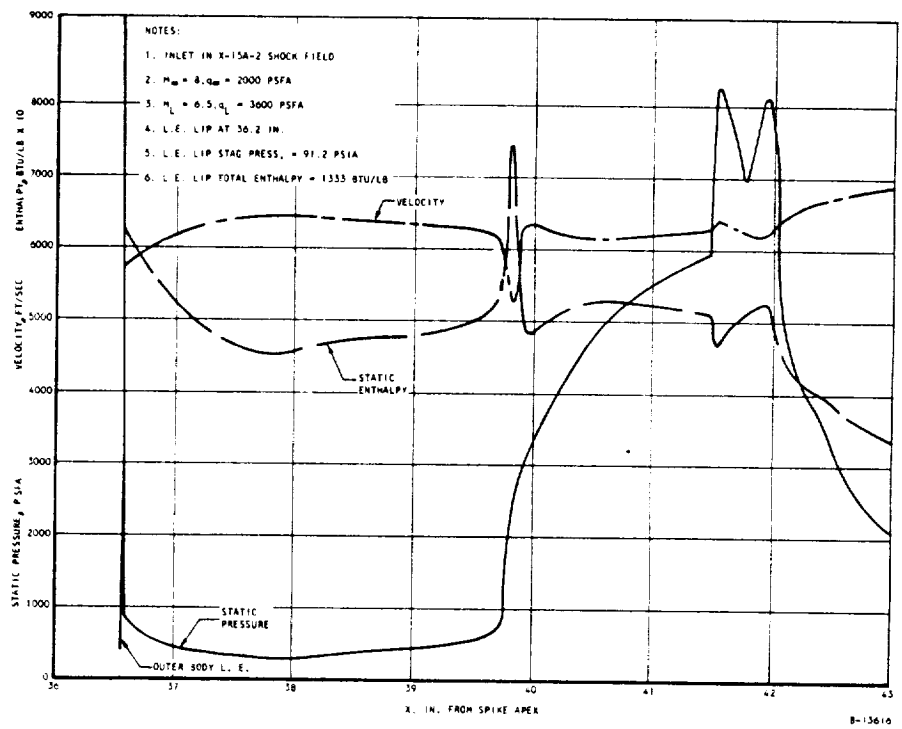

b. OUTERBODY MACH 8 AERODYNAMIC PARAMETERS

F-15299

Figure 5.2-8. Innerbody-Outerbody Aerodynamic Parameters

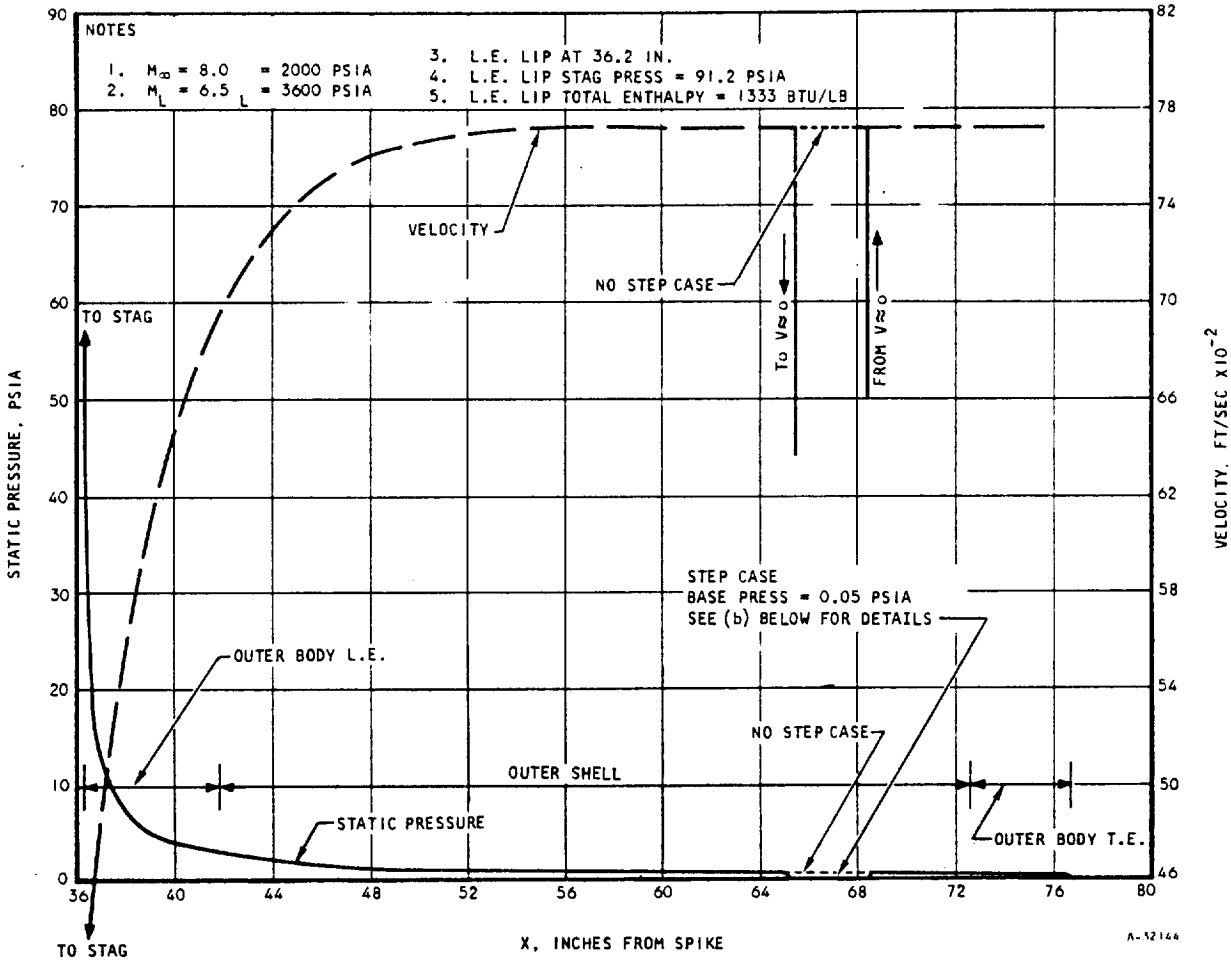

a. ESTIMATED OUTERBODY MACH 8 AERODYNAMIC PARAMETERS

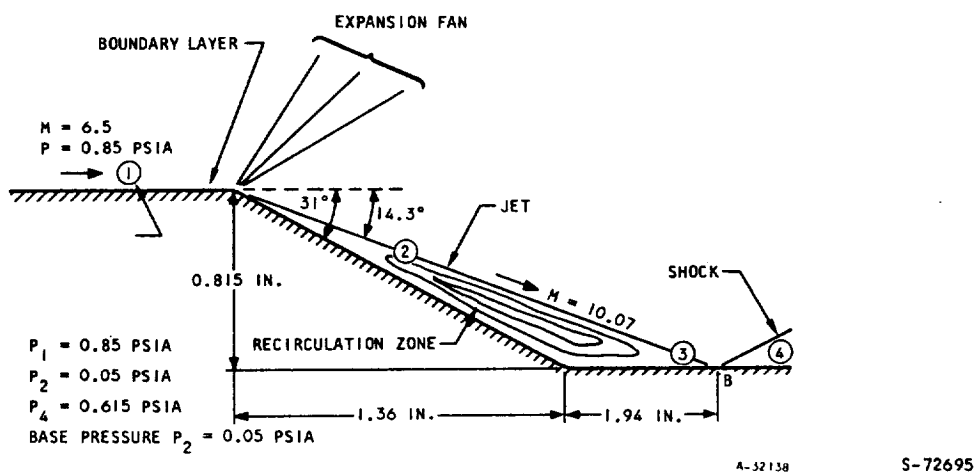

b. DETAIL FLOWFIELD AROUND THE STEP CONFIGURATION

Figure 5.2-9 Outerbody Aerodynamic Parameters

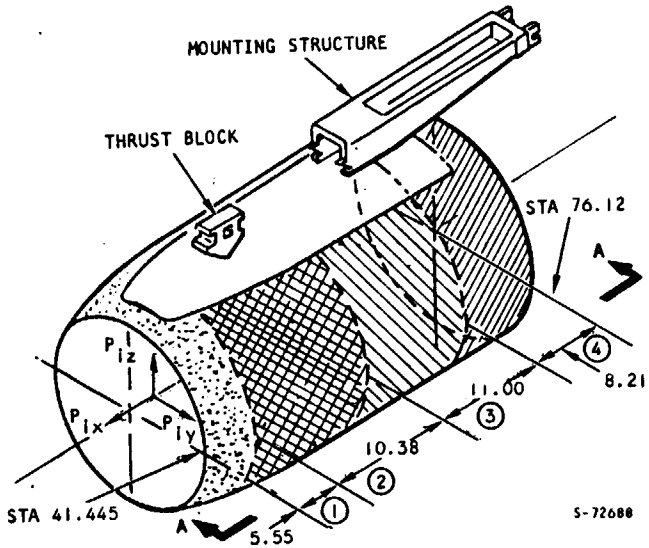

a. COWL PRESSURE LOAD

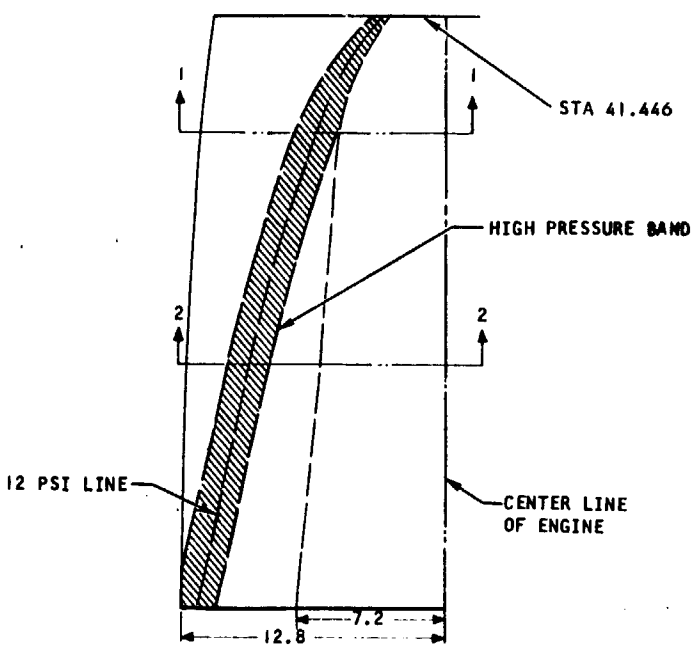

P_i		CONDITION 1	CONDITION 4	CONDITION 6
P_1	P_{1_x}	365	688	283
	P_{1_y}	134	171	249
	P_{1_z}	486	258	106
P_2	P_{2_x}	45	83	34
	P_{2_y}	113	145	211
	P_{2_z}	396	218	89
P_3	P_{3_x}	78	146	60
	P_{3_y}	82	104	150
	P_{3_z}	284	144	59
P_4	P_{4_x}	0	0	0
	P_{4_y}	9	18	35
	P_{4_z}	118	8	7

CONDITION 1
$M_\infty = 8.0$, $q_\infty = 2000$ PSFA
$M_L = 8.0$, $q_L = 2000$ PSFA
$\alpha_\infty = 10.4$ DEG, $\beta_\infty = 2.9$ DEG
$\alpha_L = 10.4$ DEG, $\beta_L = 2.9$ DEG

CONDITION 4
$M_\infty = 8.0$, $q_\infty = 2000$ PSFA
$M_L = 6.5$, $q_L = 3600$ PSFA
$\alpha_\infty = 10.4$ DEG, $\beta_\infty = 2$ DEG
$\alpha_L = 3$ DEG, $\beta_L = 2$ DEG

CONDITION 6
$M_\infty = 8.0$, $q_\infty = 835$ PSFA
$M_L = 6.5$, $q_L = 1500$ PSFA
$\alpha_\infty = 10$ DEG, $\beta_\infty = 7$ DEG
$\alpha_L = 3$ DEG, $\beta_L = 7$ DEG

A-52173

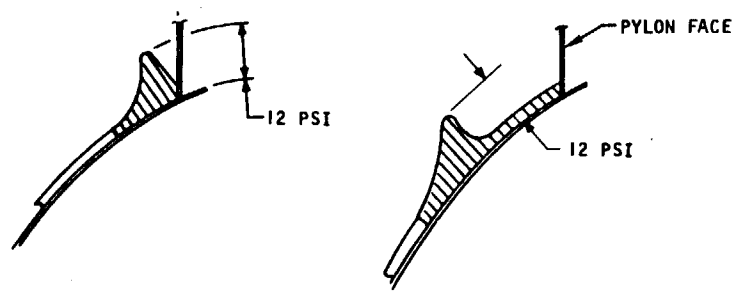

PRESSURE DISTRIBUTION 1-1

PRESSURE DISTRIBUTION 2-2

A-52194

b. LOCALIZED HIGH PRESSURE BAND ACTING ON COWL, MACH 8

S-72689

Figure 5.2-10 HRE Cowl Aerodynamic Loads

In addition to these mechanical loads, a 20-g load was applied to each valve at its c.g. location. This load was separately applied in the axial, vertical, and lateral axes in combination with the bellows forces. The most severe thermal stresses are caused by the condition when the temperature difference between the No. 1 and No. 3 fuel control valve is 1205°F.

5.2.2.1.7 Spike Bellows

The spike bellows will perform two principle functions: (1) it is a seal between the air, or combustion gases, and the innerbody; and (2) it forms an annular cavity with the spike which is used as a piston to assist the actuator during inlet unstart. In the event of an unstart, the static pressure at Station XX = 44.6 will provide a maximum axial thrust of approximately 2000 lb to aid the actuator extension stroke. This axial thrust magnitude is based upon a static pressure of 70 psi in the bellows cavity.

The bellows must be adequate to sustain stresses due to applied pressure and due to actuator stroke. The maximum operating pressure in the bellows-spike cavity has been established as 80 psi at a maximum operating temperature of 1200°F for design. The total available actuator stroke of 5.3 in. has been used to determine bellows deflection stresses.

Since the engine is designed for one restart per test, two full bellows cycles per engine cycle are possible. In order to safeguard against bellows failure during the rated life of the engine (100 test cycles), the bellows minimum life has been specified as 500 cycles.

Bellows spring rate is another parameter that must be carefully controlled. Accordingly, the total bellows force to produce full stroke was limited to 1900 lb. For the rated bellows stroke of 5.3 in., this results in a spring rate limitation of 360 lb/in.

5.2.2.1.8 Spike Actuator

Allowable deflections rather than stresses governed the structural design of the spike actuator assembly.

The aft portion of the outer housing and the array of support legs were analyzed with the MIT STRUDL space-frame computer program. The front portion of the outer housing and the inner shell structure were analyzed using ordinary beam calculations. The front conical portion of the inner shell was checked by a straightforward membrane analysis. The gusseting and thickness of the support leg mounting-pads were sized on the basis of the computed load flow.

The peak stress in the actuator was determined to be 58,000 psi. Allowing for a 1.5 stress concentration factor due to localized filleting effects, cutouts, and any other irregularity, the peak actual stress should not exceed 90,000 psi. The actuator structure is constructed from AISI type 4340 steel with a heat-treat procedure to attain minimum strength properties in excess of 132,000 psi for f_{ty} and 170,000 psi for f_{tu}. This leads to an allowable stress of 112,000 psi, which still provides an adequate safety margin for the structure of 0.25.

5.2.2.1.9 Strut Attachment

The attachment margins of safety for the critical loads as previously shown in Figure 5.2-8 are indicated below. They are based on a design which incorporates heavier ribs and a forward manifold.

Element	Stress, psi	Margin of Safety
Rib, aft end	31,700	0.27
Socket, aft end	39,800	0.01
Rib, forward end	31,400	0.10
Manifold, forward	26,400	0.13

Another analysis utilizing a more complete model indicated higher shear loads on the studs which attach the strut to the outer shell than had previously been considered. The stud pattern was reanalyzed, assuming that (1) a coefficient of friction equal to 0.20 existed between the strut flange and the socket, and (2) the studs were torqued up to develop 85 percent of their yield load. The minimum shear margin of safety occurs at the aft-most stud and is equal to 0.02.

5.2.2.1.10 Engine-Mount Manifolds

The engine-mount manifolds were stress-analyzed for the design loads as indicated in Figure 5.2-11. For in-plane loads, a simple conservative model was used. It was assumed that the manifolds are very rigid compared with skin, i.e., the effects of ring and skin deformation were neglected. For out-of-plane forces on the forward mount, the model used was a beam on an elastic foundation. The beam moment of inertia equals that of the manifold about a radial axis, and the foundation modulus is based on the axial shell flexibility between the support manifold and the adjacent manifold just aft of it. The solution of the out-of-plane bending stresses for the longitudinal input vibration condition is given in Figure 5.2-11, and the results of the analysis are shown in Table 5.2-3.

5.2.2.1.11 Ablatively Cooled Cowl

The stress analysis of several different cowl design configurations revealed that the selection of the proper design configuration is primarily governed by deflection limitations.

The recommended geometry consists of a 0.040-in.-thick beaded Hastelloy X shell supported by two hat section rings and stiffened by two rings at the leading and trailing edge. These are needed to prevent local buckling of the cowl shell from the front edge to the front stiffening ring and from the aft stiffening ring to the aft edge of the cowl.

The maximum deflection of the beaded panels between the rings is 0.1 in. The design of the ring is governed by the deflection criteria and the stresses are quite low ($\sigma_{bending}$ = 7400 psi, σ_{axial} = 1600 psi). All of these values were computed using elastic properties of the materials at 600°F and neglecting the stiffness contribution of the ablative coating.

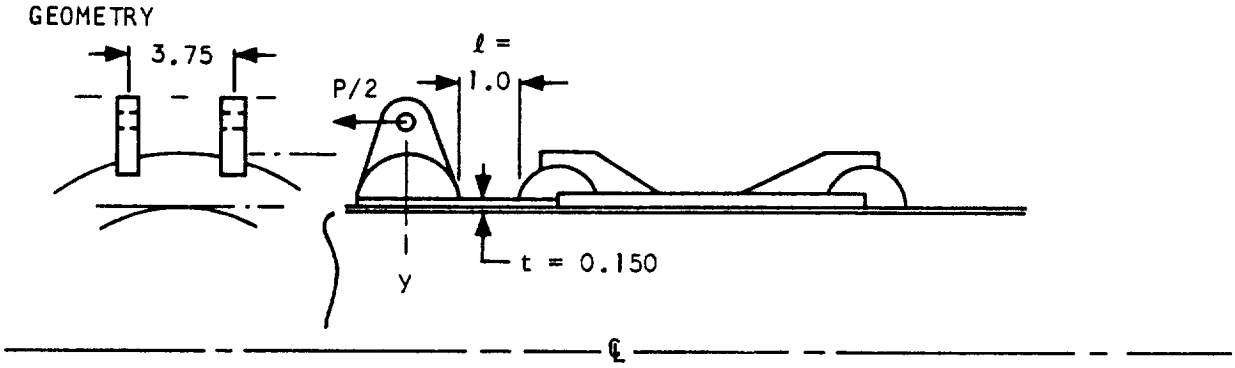

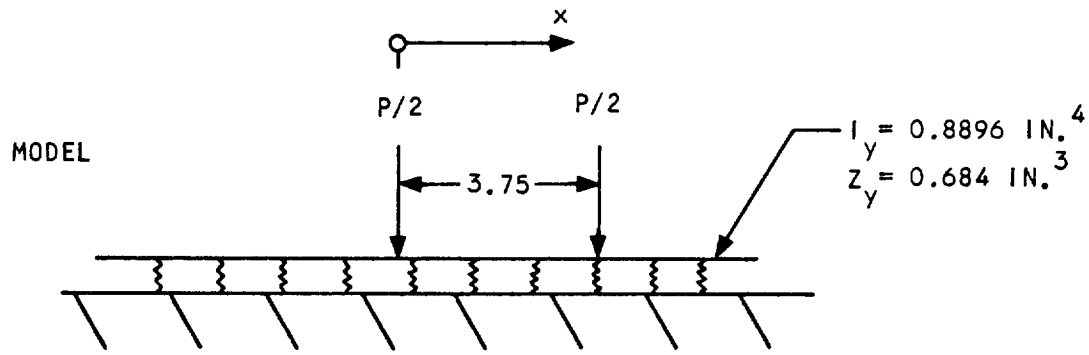

$$M_{(z)} = \frac{P/2}{4\lambda}[1 + e^{-\lambda x}(\cos \lambda x - \sin \lambda x)]$$

A-33849

where M = moment in beam (in.-lb)

λ = characteristic of system (in.$^{-1}$)

$$\lambda = \sqrt[4]{k/4EI_y}$$

and

k = foundation modulus (lb per sq in.)

EI_y = beam flexural rigidity (lb per sq in.)

$$k = \frac{AE}{l} = \frac{(0.15 \times 1)\ (27 \times 10^6)}{1.0} = 4.05 \times 10^6 \text{ lb per in.}$$

$$\lambda = \sqrt{k/4EI_y} = \sqrt[4]{\frac{4.05 \times 10^6}{4 \times 27 \times 10^6\ (0.8896)}} = 0.452$$

Figure 5.2-11. Engine-Mount Manifolds Stress Analysis

TABLE 5.2-3

SUMMARY OF ENGINE-MOUNT MANIFOLDS STRESS ANALYSIS

GEOMETRY	FORWARD MOUNT MANIFOLD 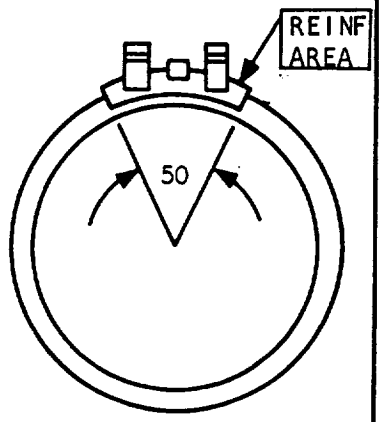		AFT MOUNT MANIFOLD 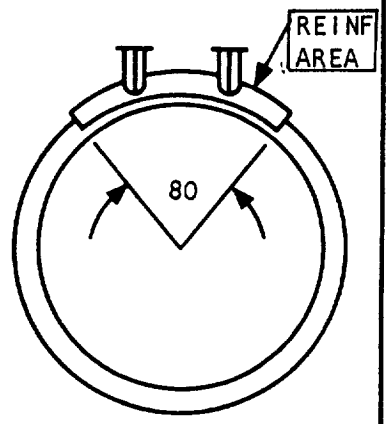	
	REINFORCED AREA	UNREINFORCED AREA	REINFORCED AREA	UNREINFORCED AREA
DESIGN TEMPERATURE (°F)	1140	1140	100	100
ALLOWABLE STRESS (PSI)	34600	34600	43200	43200
MINIMUM SECTION MODULUS (IN.^{3})	0.747	0.432	0.472	0.353
CRITICAL FLIGHT CONDITION (UNSYMMETRICAL, UNSTART) MAXIMUM STRESS (PSI) MARGIN OF SAFETY	34500 0.0	31610 0.09	37300 0.16	14180 2.05
CRITICAL VIBRATION QUALIFICATION CONDITION LONGITUDINAL INPUT MAXIMUM STRESS (PSI) MARGIN OF SAFETY	31320 0.10	28810 0.20	42040 0.03	25760 0.68
LATERAL INPUT MAXIMUM STRESS (PSI)	23100	31680	41050	39480
MARGIN OF SAFETY	0.50	0.09	0.05	0.09

A-33861

5.2.2.1.12 Suspension Frame

The structural design and stress analysis results of the suspension frame are described in para. 5.5.8.2.

5.2.2.1.13 Fuel Control Valves

The fuel valve system was treated as a space-frame, supported externally at twelve points (the valve mounting bracket attachments to the No. 2 fuel injector manifold); loaded externally at five points with the design loads in three load cases; and loaded externally at one point with the proof-pressure load in one load-case. An idealized model of this frame is shown in Figure 5.2-12. Joints 1 to 4 and 9 to 12 are fixed supports, while joints 5 to 8 are fixed against lateral movement, but allowed to slide in the Y-direction (no support in Y-direction). Axial (Z-directional) forces are applied at joints 27 and 37 in three cases, and axial force is applied at joint 27 only in the fourth case. Axial, vertical and horizontal forces were applied at joints 33, 34, and 35, in Cases 1, 2, and 3, respectively. These represent the acceleration loads acting on the valves.

Members 19 and 42 are rigid members to represent the physical geometry of the valve bodies. The maximum stresses and the safety margins against allowable stress for each member are as follows:

Member Number	Critical Load Combination	σ_{max}	Safety Margin
9	1	18,900	0.75
5	1	21,500	0.55
15	1	20,700	0.60
4	2	14,600	1.28
5	2	19,600	0.70
15	2	20,700	0.60
5	4	26,700	0.66
15	4	29,300	0.52

These results for loading Cases 1, 2, and 3 are based on the governing allowable stress for Hastelloy X at 1240°F (1140° + 100° overtemperature allowance) being $0.85 \times F_{ty} = 33{,}200$ psi, and on the STRESS computer program output results.

The fourth case represents the proof-test condition for the spike-cooling system. In loading Case 4, only the spike coolant bellows is pressurized to 1050 psi, and the governing allowable stress for Hastelloy X at room temperature was used ($0.85 \times F_{ty} = 44{,}400$ psi). Forces and moments used are also taken from the STRESS computer program output.

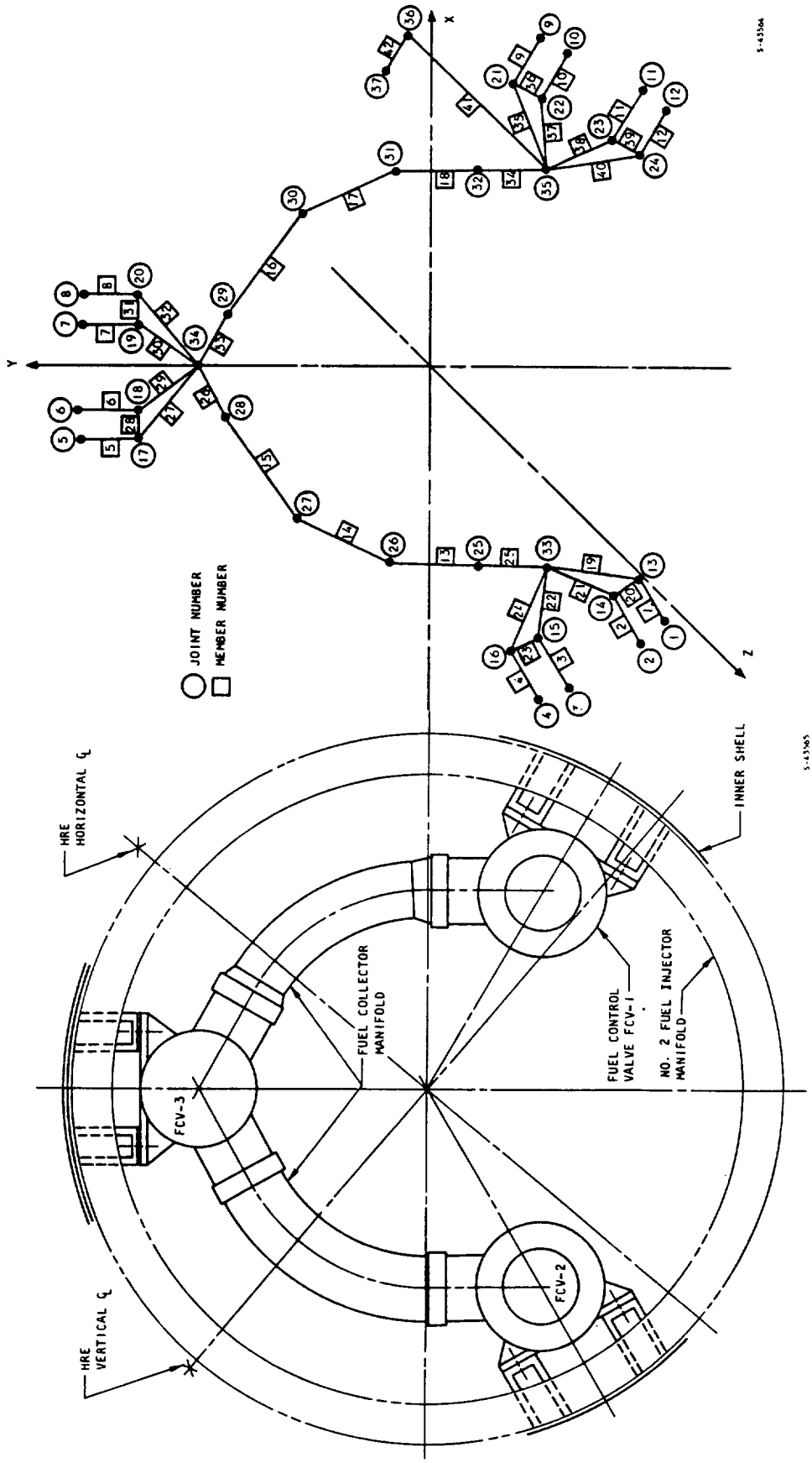

a. VALVE AND MANIFOLD ARRANGEMENT

b. IDEALIZED GEOMETRY

F-15291

Figure 5.2-12. HRE Fuel Control Valve Manifold System

5.2.2.1.14 Spike Bellows Analysis

Stresses due to pressure and stroke were computed in the four different designs submitted by vendors. The results of the analysis are tabulated on Table 5.2-4. Alternates 2, 3, and 4 were found acceptable and a slightly modified version of the design submitted by Vendor 2 was used.

5.2.2.2 Pressure Containment

5.2.2.2.1 Fins

The design objective for all of the plate-fin shell assemblies was the attainment of the desired design life of 10 hours based upon 700 psi containment capability at operating maximum fin temperatures at the M8 (local) design point. An overtemperature allowance of 100°F has also been employed to account for short duration transients and to allow for deviation between calculated and actual operating metal temperatures. In all cases, the fin strength efficiency factor (ν) of 0.333 has been used to determine fin pressure capability for both the short time and for the elevated temperature conditions. It is known from actual pressure tests that the fins will perform somewhat better than this.

Fin stresses have been computed by first determining the ratio of pressure area to nominal fin metal area. This quantity has been denoted as the "fin stress multiplier."

$$\text{FIN STRESS MULTIPLIER} = \frac{1}{Nt_{fin}} - 1$$

where N = fins per inch

t_{fin} = fin thickness

This quantity is therefore equal to the ratio of nominal fin stress divided by applied internal pressure. The maximum fin stress is then the "fin stress multiplier" divided by the fin strength efficiency. The expression for maximum fin stress due to internal pressure is:

$$\sigma_{fin} = \frac{p}{\nu}\left(\frac{1}{Nt_{fin}} - 1\right)$$

The stress criteria for each particular fin has been to use the lesser value of

$$\sigma_{all} = 0.85 \times \sigma_{0.2_y}$$

$$\sigma_{all} = 0.667 \times \sigma_{10\text{ hr. rupture}}$$

TABLE 5.2-4

BELLOWS STRESS ANALYSIS SUMMARY

		Convolution Data				Calculation Results		
Vendor Number	Bellows Type	Convolutions	Height, in.	Thickness, in.	Material	Spring Rate, lb/in.	Deflection Stress, psi	Pressure Stress psi
1	"U"	23	1.0	0.016	Inco 718	137	172,000	156,200
2	Nested Ripple, Welded	31	1.0	0.021	Inco 718	317	201,000	90,300
3	Nested Ripple, Welded	43	1.0	0.021	Inco 625	265	159,000	77,500
4	Nested Ripple, Welded	50	0.6	0.012	A286 Steel	240	239,000	65,700

at the fin design temperature. Margin of safety for each fin has been computed by comparing the operating stress to the allowable stress:

$$M.S. = \frac{\sigma_{all}}{\sigma_{op}} - 1$$

A complete tabulation of fin stresses and margins of safety is presented in Table 5.2-5, including fin allowable stresses, fin stresses at 700 psi internal pressure, and fin temperature data.

All shells at the subassembly and final assembly levels (i.e., after the installation of manifolds) were subjected to proof pressures of 1050 psi. This test pressure in general was inadequate to confirm shell containment strength of the various shell assemblies. Prior to the addition of manifolds each shell assembly was pressurized to provide a realistic evaluation of shell-fin assemblies without inducing damage in a sound part. Experience on the sub-element panels has shown that this higher proof pressure is required to pinpoint local braze voids which could subsequently cause premature failure under creep-rupture or thermal cycling conditions. This would permit possible repairs to locally defective shells in some instances, and it would also permit timely rejection of nonrepairable defective shells prior to additional fabrication steps.

The room temperature 0.2 percent yield offset strength of 52,400 for Hastelloy X was used to compute the yield pressures of the various fins. Then, by direct scaledown, the pressures to produce 0.85 x $\sigma_{0.2y}$ were also calculated. These latter pressures could safely be applied to perfectly brazed shells without producing permanent deformations of the fins or shells. The results of these calculations are summarized in Table 5.2-6. A final column is shown in this table listing the recommended proof pressures.

For the nozzle, the forward leading edge section and the forward spike section, the room temperature pressures to produce equal safety margins at 0.2 percent yield stress compared to operating conditions were all quite low, and in fact less than 1050 psi. Rather than use these low values, target proof pressures corresponding to 85 percent of $\sigma_{0.2y}$ were established. These pressure magnitudes would not damage well-brazed shells, but they would materially aid in locating braze voids. In any case, a minimum proof pressure of 1050 psi was applied to each of these shells to verify usability at their respective design conditions.

The innerbody, outer shell, and the aft spike all operate at high temperatures at their most critical locations. All of these shell assemblies utilize 28 fins per inch, 0.006-in. thick structure. At room temperature, the pressure to reach 85 percent of $\sigma_{0.2y}$ would be 3000 psi. The pressures at room temperature corresponding to the operating safety margins ranged from 1840 to 2170 psi. A room temperature proof-pressure target of 2200 psi was selected for these shells. This pressure level was sufficient to verify shell strength capability or to locate any braze voids that would seriously degrade containment performance.

TABLE 5.2-5

FIN-CONTAINMENT DATA

Shell Location	Fin Geometry*	Fin Stress Multiplier	Fin Stress @ 700 psi	Operating Temp, °F	Design Temp, °F	σ_{all}, psi	Margin of Safety
Nozzle	20-0.006	7.33	15,400	500	600	39,000	1.53
Innerbody	28-0.006	4.95	10,400	1350	1450	17,000	0.63
Outer Shell	28-0.006	4.95	10,400	1300	1400	20,000	0.92
Leading Edge Tip	20-0.004	11.5	24,100	100	200	43,000	0.79
Leading Edge Shell	20-0.006	7.33	15,400	900	1000	35,500	1.30
Forward Spike	16-0.006	9.42	19,800	300	400	41,000	1.07
Aft Spike	28-0.006	4.95	10,400	1300	1400	20,000	1.92
Strut	20-0.004	11.5	24,100	1200	1300	28,700	0.19

*Fins per inch and fin thickness, inches.

TABLE 5.2-6

SHELL PROOF-PRESSURE TARGETS

Shell Location	Pressure to $\sigma_{0.2y}$*, psi	Pressure to 0.85 $\sigma_{0.2y}$, psi	$\left(\frac{1}{M.S.+1}\right)$ Pressure to $\sigma_{0.2y}$, psi	Target Proof Pressure, psi
Nozzle	2380	2020	940	2000
Innerbody	3530	3000	2170	2200
Outer Shell	3530	3000	1840	2200
Leading Edge Tip	1520	1290	850	1200
Leading Edge Shell	2380	2020	1040	1800
Forward Spike	1860	1580	900	1500
Aft Spike	3530	3000	1840	2200
Strut	1520	1290	1280	1300

*Accounts for fin-strength efficiency factor

For the aft section of the leading edge, a target proof pressure of 1800 psi was chosen, which is nearly the room temperature pressure to produce 85 percent of the yield stress. Finally, the strut calculation indicated that a target proof pressure of 1300 psi was appropriate.

It had already been experimentally determined that fin-voids as small as a single fin could be detected for the range of fin spacings used in these shells by pressures ranging from 800 to 1400 psi. For the inner shell, outer shell, and the aft spike, pressurization to the target proof pressure of 2200 psi without cracking the Stress Coat would provide positive assurance of completely successful brazing, (i.e., zero voids). In the event of voids, Stress Coat cracking will occur before reaching 2200 psi, and the pressure required to initiate cracks will provide a direct measure of void size and pressure containment degradation in the immediate void areas. Each of these three shells (inner shell, outer shell, aft spike) will actually operate with substantial axial temperature rises, whereas the computed safety margins shown in Table 5.2-5 apply only for the hot end-fin temperature. If voids were detected in the colder operating zones of these shells during the proof test, they did not necessarily locally degrade the containment capability for operational purposes, but they may have prevented achievement of the target proof pressures. The desirable minimum pressure to confirm shell suitability would then be 1500 psi in order to locate potential braze voids at the hot end of each shell during operation.

Due to the increased fin spacing in the leading edge shell as well as lower operating temperatures and higher calculated safety margins, a minimum proof test pressure of 1200 psi would locate a single braze void and would constitute a sufficient test to verify suitability. Similarly, 1200 psi would also suffice for the strut. As previously noted in this section, satisfactory passing of a minimum 1050 psi proof pressure was adequate verification for the nozzle, leading edge tip, and forward spike shells.

5.2.2.2.2 Manifold

The regeneratively cooled shells of the HRE are stiffened by several manifolds. These manifolds distribute or collect the coolant, and also serve as reinforcing or supporting members to the shells. Figure 5.2-13 gives the location and the identification of those manifolds which fulfill a dual purpose of structural supporting or stiffening elements and coolant containers. All of these manifold rings are fabricated from Hastelloy X material. All of the coolant manifold rings must contain the 700-psi operating pressure at the operating temperature of each ring. The pressure-containment capability will be verified by pressure testing each ring at 1.5 x 700 = 1050 psi at room temperature, after the manifold is brazed to the shell. Space limitations, feasibility of fabrication and assembly, strength, and stiffness considerations dictated the design of each cross section. These sections, shown in Figure 5.2-14 are not necessarily the optimum shapes for pressure containment, but they represent the best compromise to satisfy each of the design requirements. Table 5.2-7 shows the cross-sectional areas and the moments of inertia of each significant cross section of every ring.

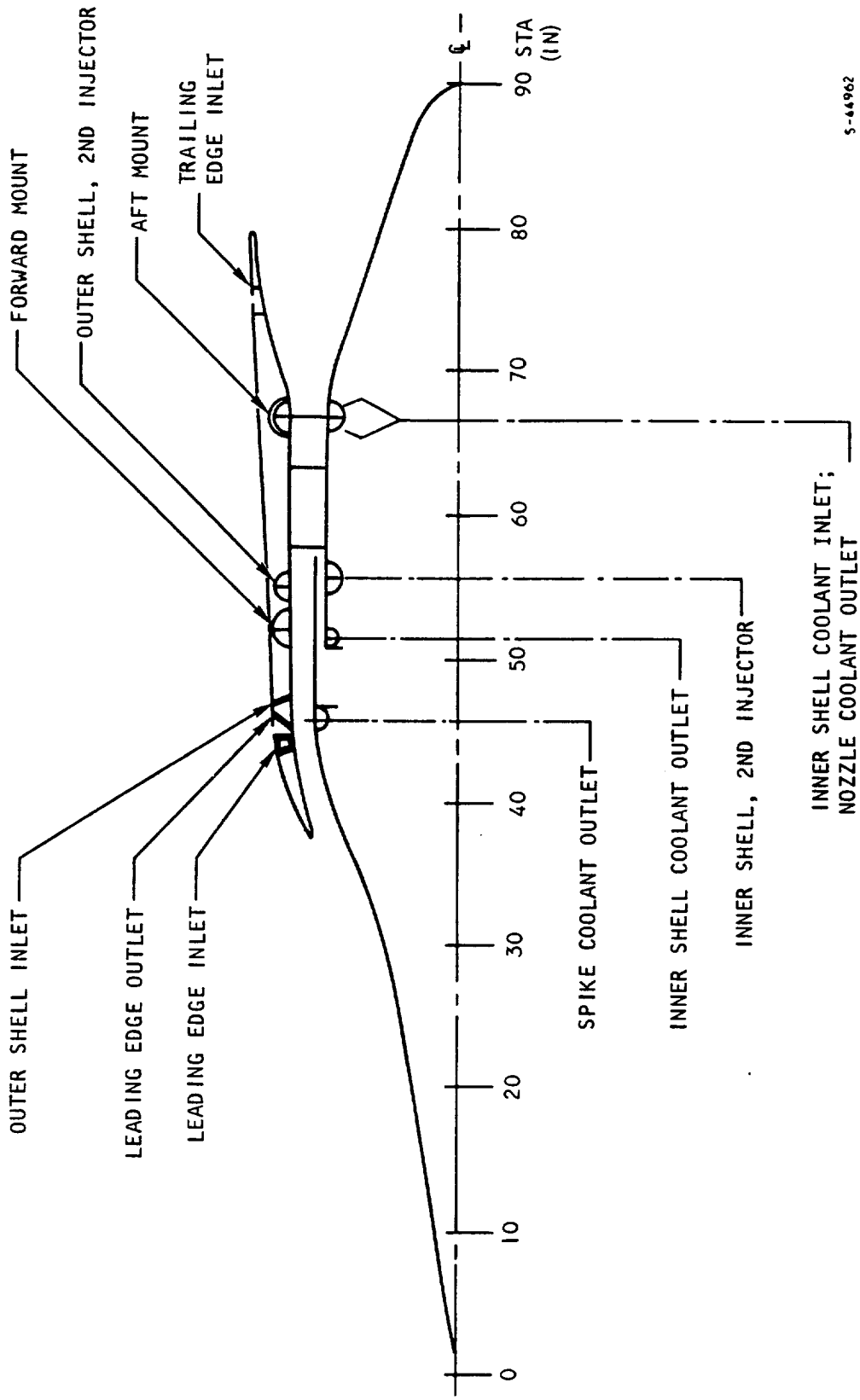

Figure 5.2-13. HRE Manifold Locations

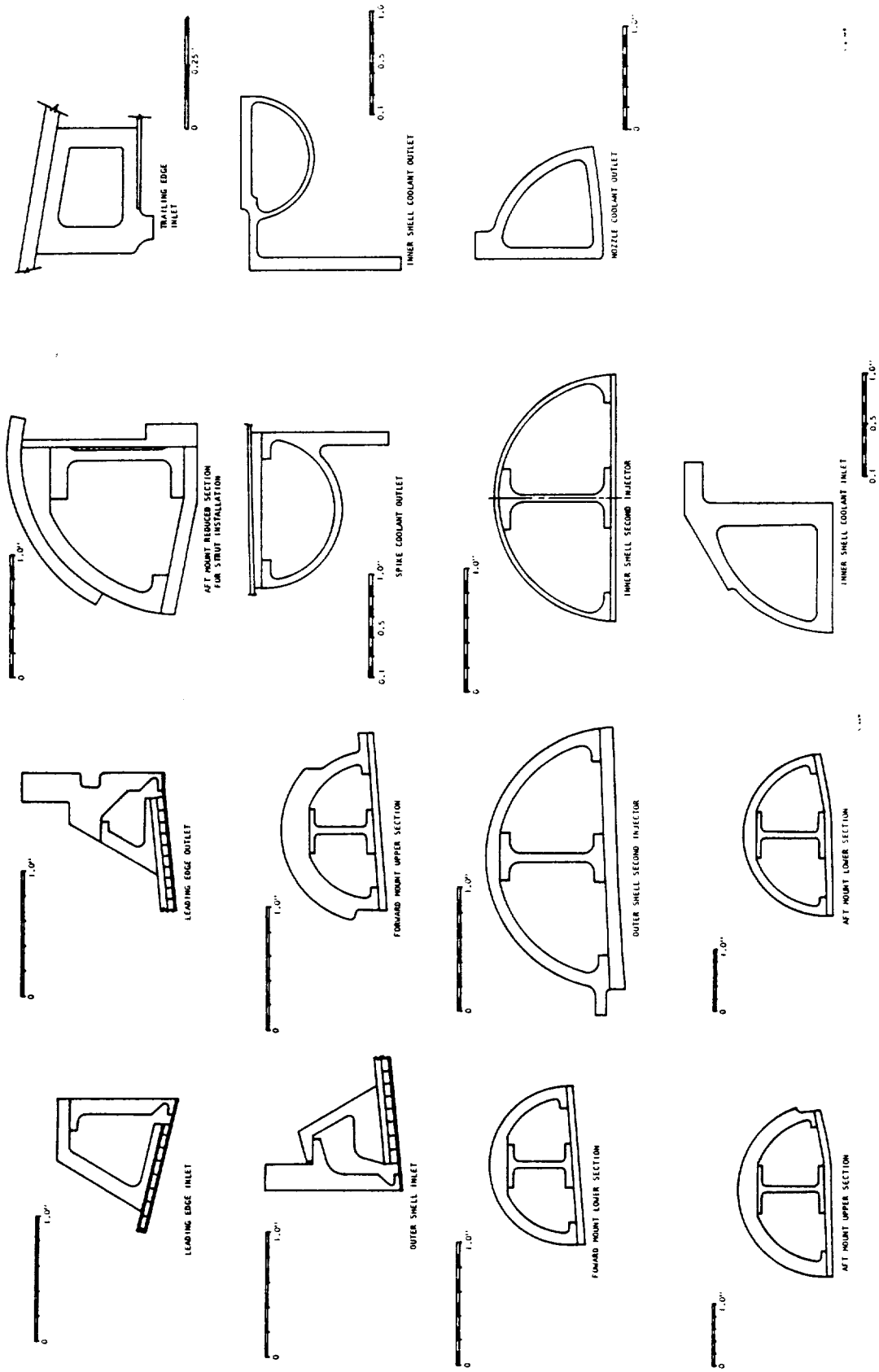

Figure 5.2-14. Manifold Cross Sections

TABLE 5.2-7

HRE MANIFOLD STRESSES AND SECTIONAL PROPERTIES

Manifold	Sectional Properties: Area A, in.^{2}	Sectional Properties: Moment of Inertia I_x, in.^{4}	Sectional Properties: Moment of Inertia I_y, in.^{4}	Stresses Due to Coolant Pressure: Bulk Operating Temperature (T), °F	Stresses Due to Coolant Pressure: Allowable* Stress at Operating Temperature, psi	Stresses Due to Coolant Pressure: Maximum Stress Due to 700 psi Operating Pressure, psi	Stresses Due to Coolant Pressure: Margin of Safety
Leading Edge Inlet	0.2940	0.0211	0.0233	-360	44,200	18,400	1.4
Leading Edge Outlet	0.4002	0.0421	0.0193	250	42,500	36,238	0.17
Outer Shell Inlet	0.4303	0.0363	0.0243	250	42,500	30,350	0.40
Forward Mount, Upper Section	2.1463	0.6036	1.4321	1140	35,200	17,160	1.05
Forward Mount, Lower Section	1.4716	0.3689	0.8418	1140	35,200	21,400	0.64
Outer Shell, Second Injector	0.6443	0.0841	0.2509	1140	35,200	31,184	0.13
Aft Mount, Upper Assembly	1.5461	0.4821	0.9359	0	44,200	20,700	1.14
Aft Mount, Lower Assembly	1.1972	0.2539	0.6562	0	44,200	37,400	0.18
Aft Mount, Reduced Section	1.0250	0.2483	0.2660	0	44,200	31,960	0.38
Trailing Edge Inlet	0.1519	0.0037	0.0045	-360	44,200	9,500	3.66
Spike Coolant Outlet	0.4542	0.0466	0.1231	840	37,400	30,614	0.22
Inner Shell Coolant Outlet	0.4906	0.0869	0.1491	1140	35,200	31,600	0.11
Inner Shell, Second Injector	1.0054	0.0388	0.2254	1140	35,200	29,990	0.17
Inner Shell Coolant, Inlet	0.6284	0.1142	0.0997	70	44,200	39,881	0.11
Coolant Outlet, Nozzle	0.3647	0.0690	0.0459	70	44,200	42,700	0.03

*Allowable stresses = $\begin{matrix} 0.85\ F_{ty} \\ 0.667\ F_{tu} \end{matrix}$, whichever is lower

Each manifold cross section was considered to be a rigid-plane frame. The effect of the curvature perpendicular to the plane of the cross section was neglected. Uniform loads of 700 lb/sq in. and 1050 lb/sq in. were applied to each member surrounding the coolant containment areas. The idealized structures were analyzed using the MIT STRUDL program. This program computes the stresses in each member at several points and lists the magnitude and location of the maximum stress. The geometry of most of the cross sections is such that substantial bending stresses were developed. Since the method of stiffness analysis used by the STRUDL program is a linear, elastic, static small-displacement-frame analysis, the results were conservative. As a basic requirement, allowable stresses in the prime structural components, including the manifolds, were limited to 0.85 x 0.2 percent yield strength. If plastic deformation is allowed to occur, test data reported in Reference 5.1-1 shows a containment capability of 3000 psi for 1000 cycles in the nozzle coolant outlet manifold (M.S. = 0.03 at 700 psi for elastic analysis).

Maximum stresses due to 700-psi coolant pressure are also shown on Table 5.2-7. Injection manifolds are rated at the same pressure, even though maximum injection pressures are always less than 400 psi. The fifth column of the table shows the bulk metal temperature of each manifold. Allowable stresses are listed in the sixth column, based on 85 percent of the 0.2 percent yield strength ($0.85\ F_{ty}$) of the Hastelloy X material at the bulk temperature of the metal. These values were always lower than two-thirds of the ultimate strength ($0.667\ F_{tu}$) at elevated temperature. Safety margins, calculated as

$$M.S. = \frac{0.85\ F_{ty}}{\sigma_{max}} - 1.0$$

are listed in the last column. All safety margins are positive, indicating that manifold pressure containment is not a problem. Maximum stresses due to coolant containment are rather low in the support manifolds, but these manifolds will carry sizeable additional aerodynamic and inertia loads.

5.2.3 Low-Cycle Fatigue

Differential temperatures between the hot skin and the prime load carrying structure of the engine lead to the generation of stresses in the hot skin well beyond the material yield strength. For Hastelloy X plate-fin construction, repeated cycling with differential temperatures in excess of 400°F will cause a plastic strain loop to occur during each cycle, and for the cyclic life to be finite.

Figure 5.2-15 shows a typical temperature-time history, the stress history, and the resulting plastic stress-strain loop that would occur in an operating cycle. The hot skin starts each cycle in a state of residual compressive stress from the previous usage cycle. At point 1 in all three figures, the temperature is the same in both the prime structure and the heated surface. As the heat load is applied, the hot skin develops a large temperature increase relative to the prime structure. The rate at which the heat load is applied determines when the maximum ΔT occurs. The maximum compressive stress and strain occur at point 2 in the cycle when the maximum positive ΔT is achieved.

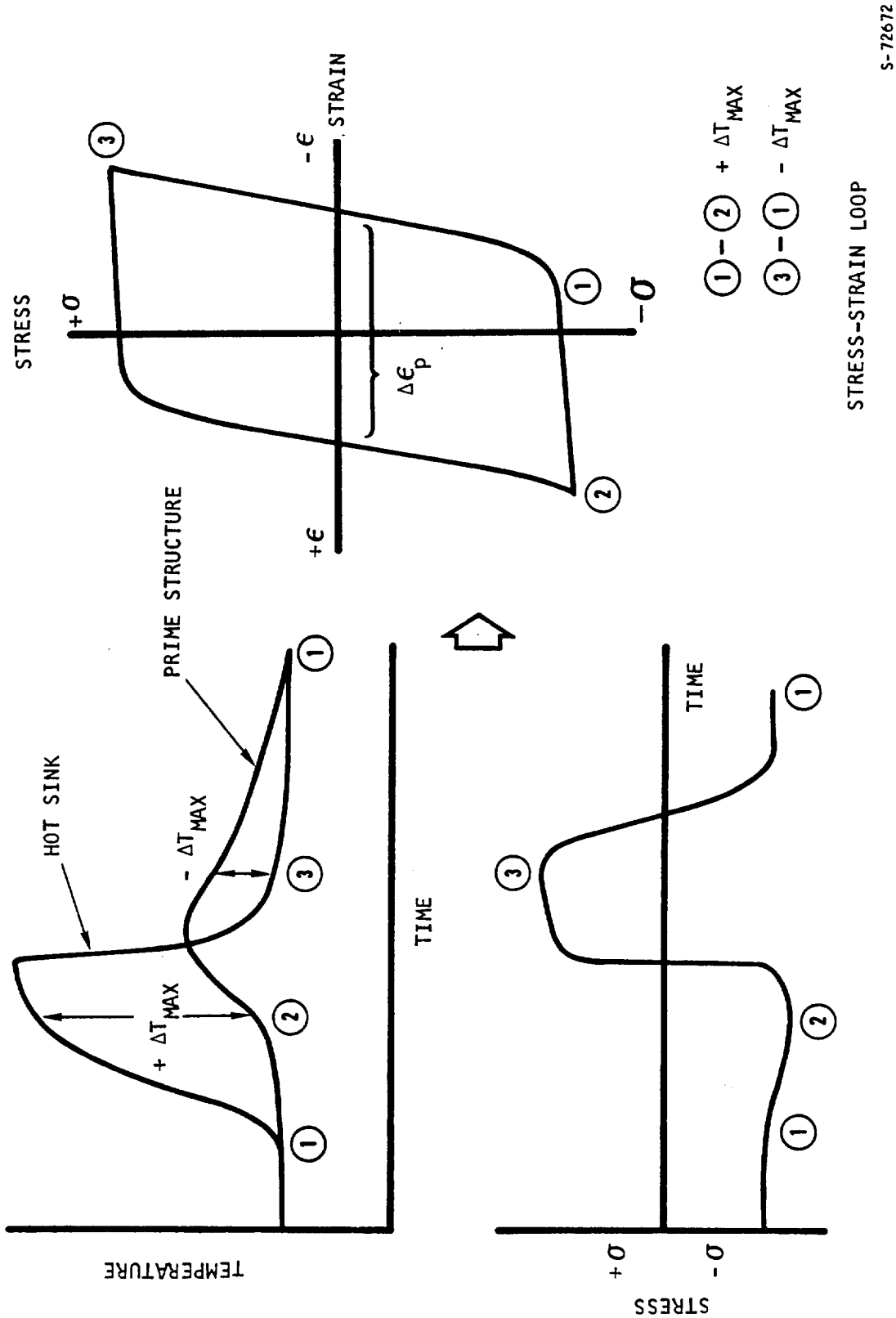

Figure 5.2-15 Typical Hot-Skin Plastic Strain Loop

The increase in compressive stress from point ① to point ② is small because the hot skin will generally be past the knee of the stress-strain curve at the start of each operating cycle. Immediately after the heat load is removed entirely or reduced in intensity, the hot skin stresses decrease rapidly, go through zero, and achieve peak tensile values at point ③, the time at which the maximum ΔT reversal takes place. For some parts of the engine, the cooldown is relatively slow, and no reversal in ΔT occurs. In the combustor section, the heat load can be rapidly removed, and it is possible to develop an appreciable negative ΔT.

For the loop illustrated in Figure 5.2-15, the total ΔT is the summation of the positive and negative ΔT's during the full operating cycle. The cycle life is related to the plastic loop caused by the total ΔT. The design goal of 100 cycles at 800^0 ΔT was based upon peak steady-state conditions.

The quantity of interest is the plastic strain amplitude $\Delta\epsilon_p$, which is a direct measure of thermal fatigue damage during each usage cycle. The stresses and strains are determined by the differential expansion history during each cycle. In the actual calculations the expansion data as a function of temperature is used for this calculation. Since the expansion coefficient of Hastelloy X increases with increased temperature, ΔT differences produce much more differential growth at elevated temperatures, and hence larger plastic strain loops. For instance, the differential growth from 70^0 to 870^0F is 0.0066 in./in., whereas from 800^0 to 1600^0F the differential expansion is 0.00785 in./in. The engine design is based upon this latter magnitude.

5.2.3.1 Basic Approach

The basic formulation for low cycle fatigue analysis relates cycles-to-failure to material ductility and plastic strain range. The expression is

$$N = C/\Delta\epsilon_p^{\,k}$$

where N = cycles to failure

$\Delta\epsilon_p$ = plastic strain range

C = ductility constant

k = exponent $\cong 2$

The ductility constant is related to material reduction of area (RA) in the fabricated form, which takes into account material thickness and manufacturing processes such as forming, brazing, welding, and annealing. The plastic strain range is determined from the total applied strain and accounts for multi-axial effects, elastic strain of the hot skin, elastic strain of the prime structure and local strain concentration effects. A value of 2.0 for the exponent, k, was found to be valid over the strain ranges of interest for Hastelloy X.

The data from the mechanical bending tests on plate-fin specimens constructed with Palniro I braze alloy are illustrated in Figure 5.2-16. The tests were conducted at RT, 1340°F, and 1540°F. It can be seen that operation at elevated temperature leads to reduced life. This is due to reduced ductility, reduced strength, and material creep. Material creep at elevated temperature uses up a portion of the creep-rupture life. In addition, the plastic flow due to creep relaxation of thermal stress leads to an increase in plastic strain range for the same magnitude of total applied strain range. It can be noted from Figure 5.2-16 that the measured cyclic life at 1540°F is not appreciably reduced from the 1340°F results. Although the creep effects are increased at the higher temperature, this has been substantially offset by the improved ductility for Palniro I- coated Hastelloy X at 1540°F (RA = 34 percent) as compared to 1340°F (RA = 29 percent).

In an operational thermal cycle the compressive plastic strain essentially takes place at elevated temperature, while the tensile strain occurs during cooldown of the hot skin. An average line has been constructed in Figure 5.2-16 to be representative of the overall behavior during each thermal cycle. For purposes of data reduction, the effects of creep and ductility variations have been absorbed into the ductility constant (C). The effective ductility constant is 0.150 at RT, and for a thermal cycle with a maximum cycle temperature of 1340°F (1800°R) to 1540°F (2000°R), the effective ductility constant is 0.100. Over the temperature range from RT to 1340°F (1800°R), the ductility constant is taken to decrease as a straight line function of temperature. A plot of (C) vs temperature and the effect of temperature on cycles-to-failure is illustrated on Figure 5.2-17.

The introduction of elevated temperature effects into the basic low-cycle fatigue formula leads to the formulas for fatigue life given below.

$$N = \left[\frac{0.150 - 0.050 \left(\frac{T_{max} - 530^\circ R}{1270} \right)^2}{\Delta\epsilon_p} \right] ; T_{max} \leq 1800^\circ R$$

$$N = \left[\frac{0.100}{\Delta\epsilon_p} \right]^2 \qquad ; 1800^\circ R \leq T_{max} \leq 2060^\circ R$$

The first formula is valid over the temperature range from RT to 1340°F (1800°R), and it accounts for the linear reduction in ductility constant over this range. The second formula is valid over the temperature range from 1340°F (1800°R) to 1600°F (2060°R). The maximum metal temperature during the entire test cycle is denoted by T_{max}.

An expression was developed to convert the applied total differential expansion of the hot skin directly into plastic strain. The expression makes allowance for the biaxial effects, hot skin elastic strains, and cold skin elastic strains. This takes the form of a linear function as follows

$$\Delta\epsilon_p = -0.0050 + 1.75 \Sigma (\alpha \Delta T)$$

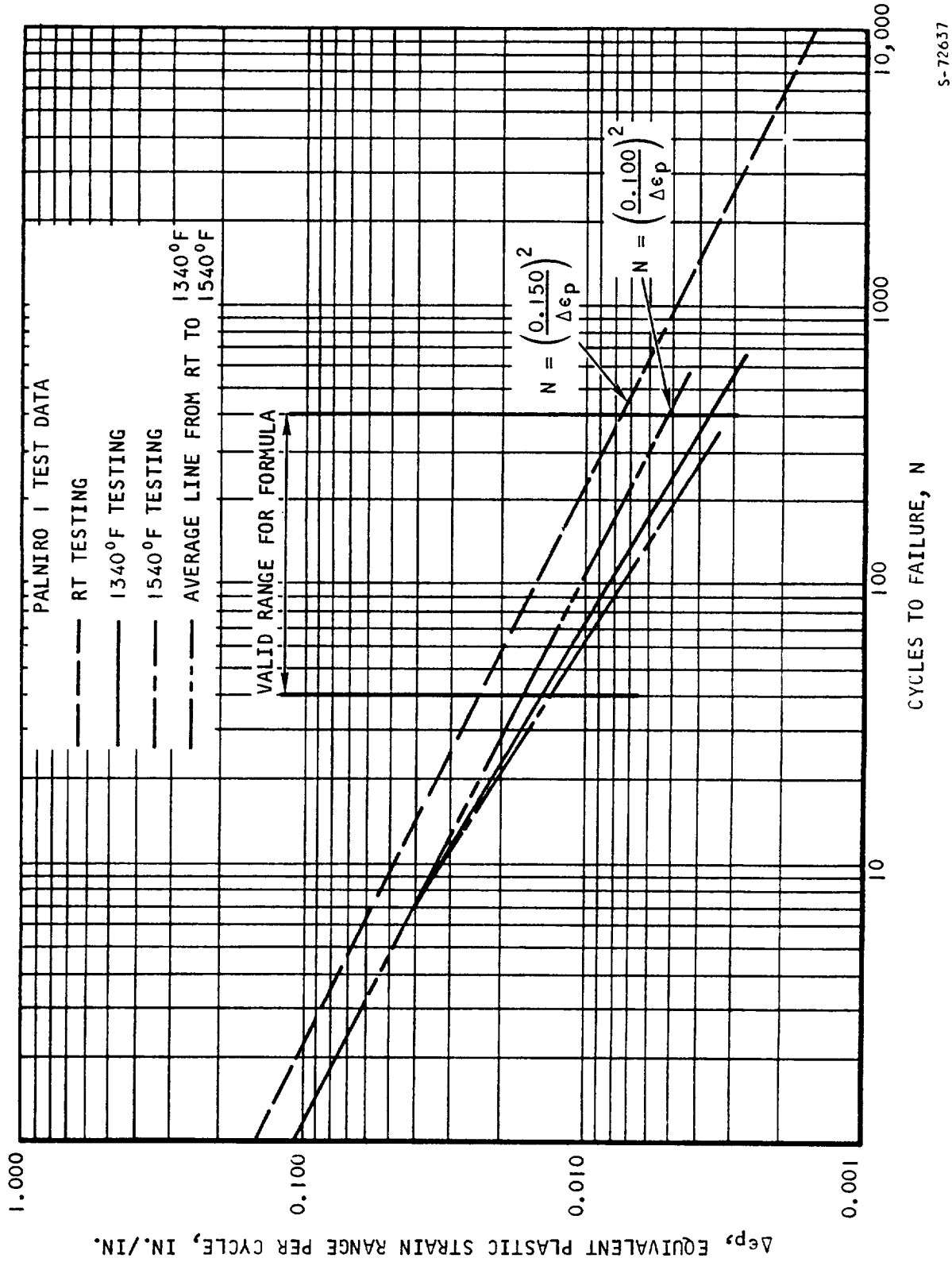

Figure 5.2-16. Hastelloy X Plate-Fin Low-Cycle Fatigue Test Results

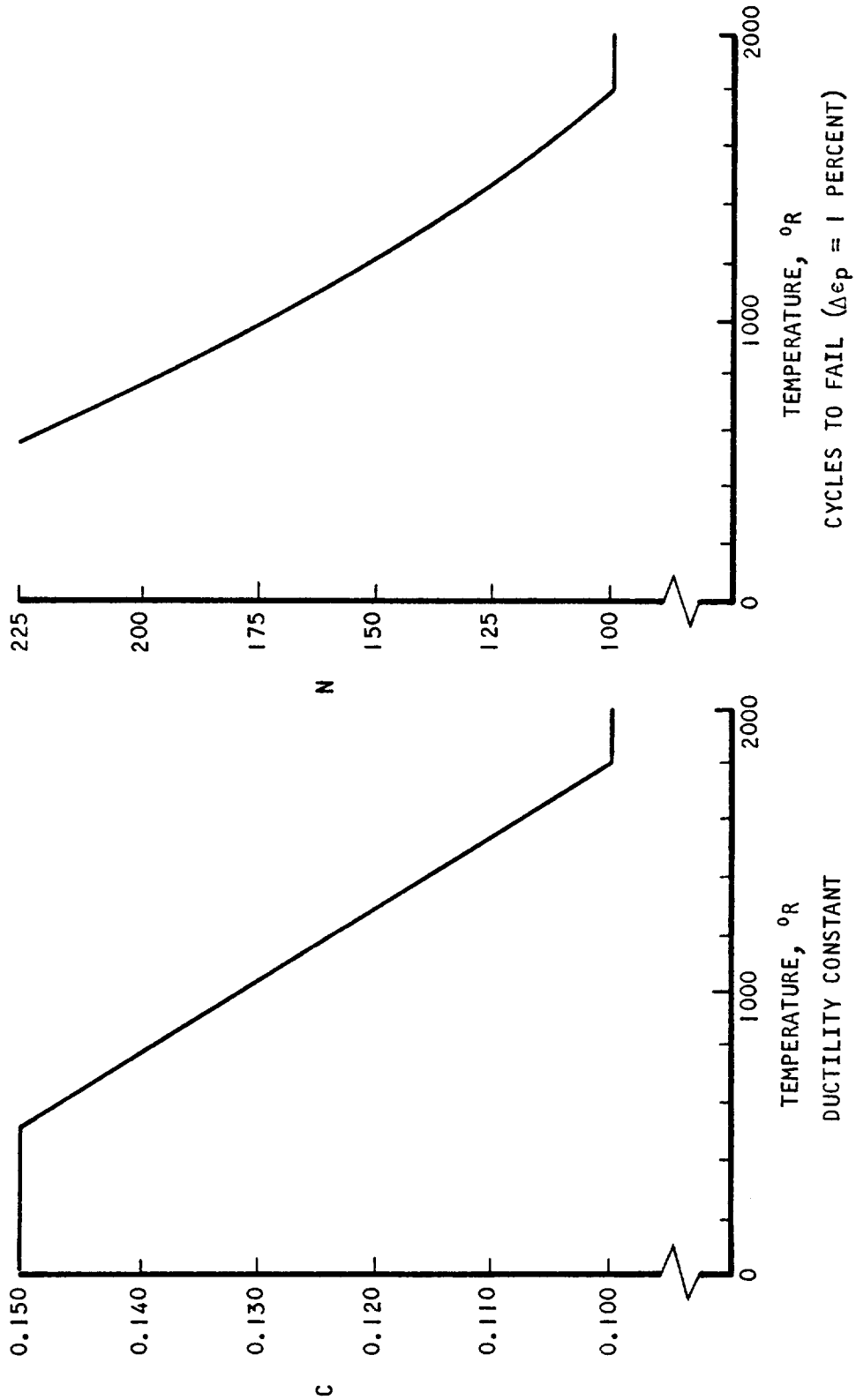

S-72639

Figure 5.2-17. Effects of Elevated Temperature Fatigue Life

where the differential expansion is the summation of the positive and negative differential expansions between the hot skin and the prime structure. This linear formula is valid for total thermal expansions ranging from 0.005 in./in. to 0.0200 in./in.

5.2.3.2 Engine Fatigue Life

The design objective for the engine was a life of at least 100 operating cycles at the Mach 8 design point. This was based upon a maximum hot skin metal temperature of 1600°F at a ΔT of 800°F between the hot skin and the prime structure. From the mechanical plate-fin test data, and the thermal fatigue flat panel test results described in Section 8.3.3 of this report, the calculated hot skin life was determined to be 136 cycles. Other critical areas of the engine such as the cowl leading edge and the struts have also been analyzed, and these results are discussed in the report sections that treat these components.

5.3 ENGINE STRUCTURAL DYNAMICS

5.3.1 Objectives

The main objective of the analysis was to develop a suitable mathematical model of the engine structure to compute structural response for various types of loadings. This analysis involved computation of resonant frequencies, mode shapes, and response to sinusoidal inputs at the engine attachment points to the X-15A-2. Basically the mathematical model had to be a simplified analog of the actual structure. There had to be sufficient dynamic similitude to compute the response of critical engine component parts.

The main area of concern was the dynamic response for low frequency inputs to the HRE. The analysis model that was selected produced an accurate description of total system mass, system mass distribution, and flexibility between the major mass elements. This approach produced a dynamic matrix size appreciably larger than the number of significant resonant frequencies and mode shapes. The reason for the large matrix size was to obtain good accuracy for the lower structural frequencies. The higher frequencies and mode shapes obtained from this computation have no significance. The analysis results were to have been used in conjunction with an engine vibrational test model to confirm design adequacy of the actual engine structure.

Whereas calculation of engine overall mass properties was relatively easy, the determination of system flexibility between the distributed mass elements of the engine was recognized to be more difficult. The structural model was modified several times during the program before a suitable representation of engine structure was obtained.

The principle difficulty in predicting the amplitudes of structural response to dynamic inputs at or near resonant frequencies is largely due to the difficulty in estimating structural damping. The test results from the vibrational test model were expected to yield valuable data in connection with this problem. In order to evaluate damping coefficients, it was necessary to

have good information for mode shapes. Since there would be several significant structural resonant frequencies, it was thought to be possible to obtain reasonable estimates of local damping between the major structural elements by using the test response information and comparing this data to the computer results from the mathematical model.

With the combined data from the dynamic analysis model and the vibrational test model, calculations were to have been made on the critical joint connections in the HRE due to sinusoidal and random input loading as well as for static loads.

The engine structural design loads have been summarized in Section 5.2. The engine design had to be adequate for a variety of load conditions. The design had to satisfy combined external aerodynamic acceleration and vibratory loads during flight as well as engine operation in the X-15A-2 flow field with axisymmetric and asymmetric inlet unstarts. The controlling design load condition varies from part to part; however, it was determined that loads due to maximum operating conditions were closely comparable to the loads generated from the Statement of Work qualification vibration inputs at the engine suspension frame attachment points.

The estimated longitudinal axial load factor due to the qualification vibration inputs was assumed to be a 20-g longitudinal response for the entire engine for a 3-g input. The output response for lateral and vertical inputs of 3 g was estimated to be 7.5 g for the outerbody, innerbody, and actuator, and 20 g for the spike. If the actual engine were to have critical resonances within the qualification test frequency range and the amplification factors proved to be appreciably higher than these estimates, the structural loads applied to the engine would be significantly higher during the qualification testing than those imposed by the operating conditions. Therefore, an important objective of the analysis and testing program was to assess the validity of the qualification test levels as a realistic measure of structural adequacy.

5.3.2 Approach

The analysis approach was to treat the engine as a system of elastically connected rigid-mass elements. Each rigid-mass element has 6 deg of freedom to describe the three displacement and rotational elements of motion, and the total number of degrees of freedom in the dynamic model will then be 6-times the number of mass elements selected to represent the engine structure. In order to achieve a suitable representation of mass distribution and of elastic coupling between different regions of the engine, the final dynamic model consisted of twelve discrete lumped masses. This resulted in a 72-deg-of-freedom system, but by virtue of the engine axisymmetric configuration and mass distribution, the in-plane and out-of-plane responses were independent of each other. Hence, the 72-deg-of-freedom problem reduced to two 36-deg-of-freedom calculations. Despite the relatively large number of mass elements, great simplicity was accomplished by choosing discrete elements that permitted the greatest ease of definition and computation.

5.3.3 Analysis Model

A block diagram of the analysis model is shown in Figure 5.3-1, and a sketch of the engine structure is shown in Figure 5.3-2. The mounting frame is denoted as mass element No. 1, and it is shown with a flexible coupling to relative ground and to element No. 2. Element No. 2 is the key component in the entire model. It consists of the portion of the outer shell that runs from the front mounting ring to the aft mounting ring, and combines with the six struts and the portion of inner shell from the inner manifold ring at the front end of the struts to the aft manifold ring located at the aft end of the struts. This multiple-ring construction is essentially rigidly connected radially by the six struts, and axially by the shear stiffness of the shell sections between the rings. Element No. 3 is the trailing edge portion of the outer shell. Element No. 4 is the nozzle structure. Element No. 5 is the leading edge portion of the outer shell, and element No. 6 is the fore portion of the inner shell. The aft spike, spike mounting cone, and the fore spike are considered as separate elements, and they are denoted as element Nos. 7, 8, and 9 respectively. The inner actuator and outer actuator parts have been separated and are denoted as element Nos. 10 and 11 respectively. Finally, element No. 12 is the control computer.

The mass properties of each element included all equipment rigidly attached to the element. The flexibility properties between the elements were intended to account for the flexibility of connecting members between the elements as well as local flexibility of the mass elements themselves. The mass properties of the entire engine would be represented by two separate 36 x 36 diagonal matrices representing the in-plane and out-of-plane mass properties respectively. The 36 x 36 in-plane and out-of-plane flexibility matrices were to be obtained by expansion of the individual 3 x 3 in-plane and out-of-plane flexibility matrices of each element in accordance with the location of the interconnections between the elements. Work on the total development of these matrices was discontinued prior to the completion of this analysis.

The system of axes chosen for the analysis was oriented with the x-axis directed in the longitudinal engine direction, the y-axis directed in the engine transverse (i.e., lateral) direction, and the z-axis directed in the engine vertical (i.e., normal) direction. Both in-plane (x-z plane) and out-of-plane (x-y plane) deformations can be written as

$$[V] = [A][Q]$$

where $[V]$ = 36 x 1 displacement matrix

$[Q]$ = 36 x 1 force matrix

$[A]$ = 36 x 36 flexibility matrix

The resonant frequencies of the system would then be obtained from the eigenvalues of the dynamic matrices $[A][M]$, where

$[M]$ = 36 x 36 diagonal mass matrix

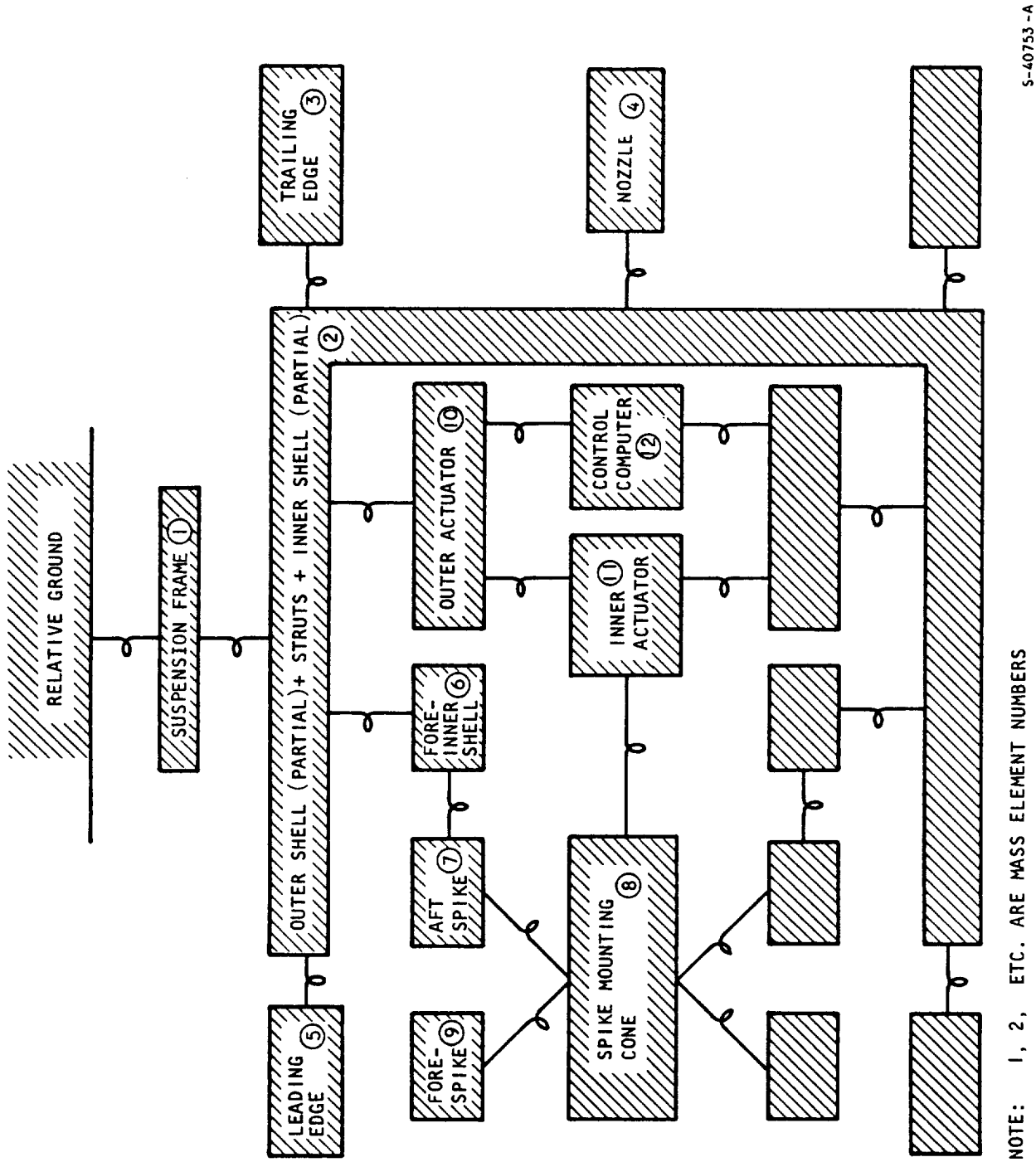

NOTE: 1, 2, ETC. ARE MASS ELEMENT NUMBERS

Figure 5.3-1. Schematic of HRE Vibration Analysis Model

ISACS

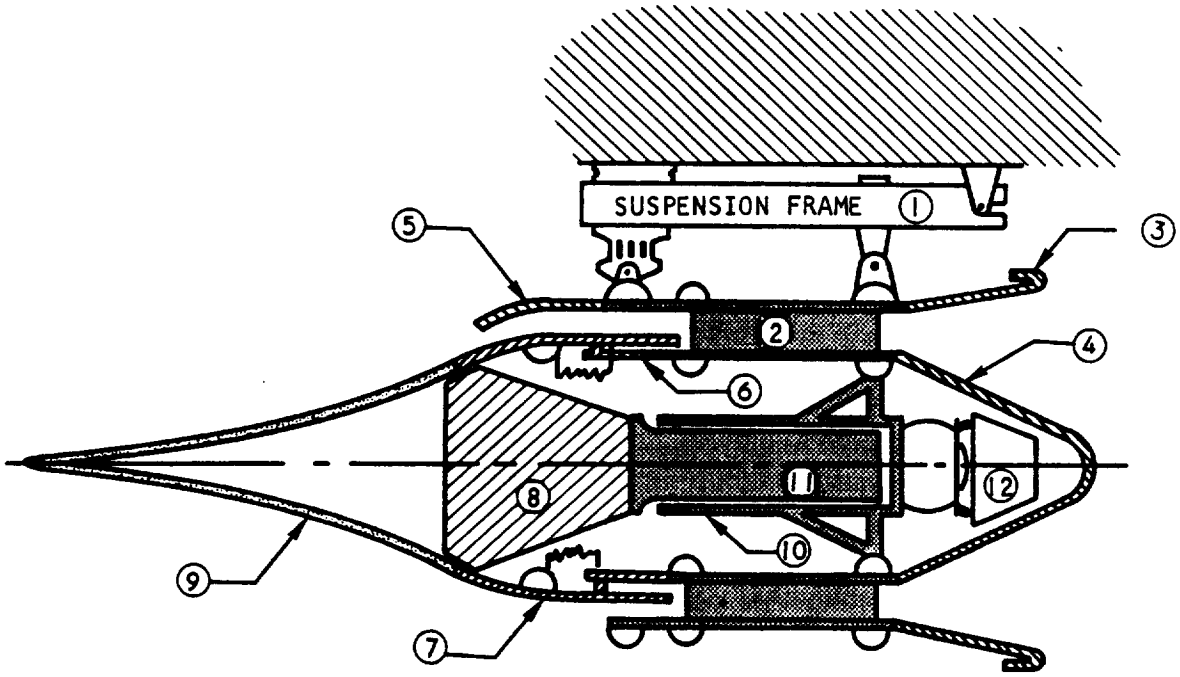

S-40763-A

① SUSPENSION FRAME
② OUTER SHELL-STRUTS-INNER SHELL
③ OUTER SHELL TRAILING EDGE
④ NOZZLE
⑤ OUTER SHELL LEADING EDGE
⑥ FORE-INNER SHELL
⑦ AFT-SPIKE SHELL
⑧ SPIKE MOUNTING CONE
⑨ FORE-SPIKE SHELL
⑩ INLET SPIKE ACTUATION SYSTEM SUPPORT HOUSING
⑪ INLET SPIKE ACTUATION SYSTEM SLIDE HOUSING
⑫ CONTROL COMPUTER

Figure 5.3-2. Vibration Analysis Model

5.3.4 Typical Dynamic Analysis

Vibration analysis for both the in-plane and out-of-plane responses was carried out for the fore spike-aft spike-mounting cone assembly by treating it to be fixed at the actuator end of the mounting cone. The output results are shown on Table 5.3-1 for the in-plane solution. The bending modes were identical for both solutions, and the only differences that were noted was the longitudinal mode for in-plane response and the torsional mode for out-of-plane response. By comparison, the resonant frequency of the fore spike by itself was previously determined to be 750 Hz. The spike cone assembly was the only portion of the engine that might respond to vibrational input as an individual component. This was an area of attention during the SAM test program.

5.3.5 Engine Vibration Model

An engine vibration test model was designed during the program using simulated components with equivalent inertia properties and flexibility properties (where applicable) to the full scale engine components. Individual structural members (struts, ring manifolds, actuator) were to be identical to those used on the actual engine. This approach was adopted to expedite construction of the model and to evaluate the principle structural members in the engines independently of the development of the full scale plate-fin sandwich shells. The main goal was the early resolution of potential problems under vibration loading conditions.

5.3.5.1 Test Objectives

Several important objectives were to have been satisfied with this test program. These were:

- Determination of structural resonant frequencies and mode shapes
- Evaluation of amplification factors at these resonant frequencies
- Evaluation of load flow through the outer shell/struts/inner shell region.
- Measurement of stresses in the manifold ring structures
- Determination of functional performance of spike actuation system under applied load
- Verification of spike seal and bellows behavior

5.3.5 2 Design Approach

The approach taken in the design of the vibration test unit is summarized in the following paragraphs. The engine vibration model was to be constructed

TABLE 5.3-1

OUTPUT FOR SPIKE-MOUNTING CONE ASSEMBLY

MOUNTING CONE	X 1 =	0.378460 00
	X 2 =	0.0
	X 3 =	-0.339090-01
FORE SPIKE	X 4 =	0.912240 00
	X 5 =	0.0
	X 6 =	-0.358750-01
AFT SPIKE	X 7 =	0.144890 00
	X 8 =	0.0
	X 9 =	-0.339910-01

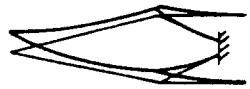

n = 140 Hz

EIGENVALUE NO. 2 = 0.692030 00

EIGENVECTOR

X 1 =	0.0
X 2 =	0.506010 00
X 3 =	0.0
X 4 =	0.0
X 5 =	0.515060 00
X 6 =	0.0
X 7 =	0.0
X 8 =	0.691860 00
X 9 =	0.0

TORSIONAL MODE

n = 193 Hz

EIGENVALUE NO. 3 = 0.111830 00

EIGENVECTOR

X 1 =	0.277550 00
X 2 =	0.0
X 3 =	0.273010-01
X 4 =	-0.232290 00
X 5 =	0.0
X 6 =	0.443410-01
X 7 =	0.929810 00
X 8 =	0.0
X 9 =	0.417300-01

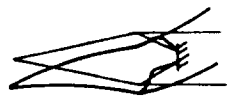

n = 476 Hz

EIGENVALUE NO. 4 = 0.305730-01

EIGENVECTOR

X 1 =	0.861950 00
X 2 =	0.0
X 3 =	-0.669240-01
X 4 =	0.105190 00
X 5 =	0.0
X 6 =	0.442440 00
X 7 =	-0.185910 00
X 8 =	0.0
X 9 =	-0.105750 00

n = 910 Hz

EIGENVALUE NO. 5 = 0.281060-01

EIGENVECTOR

X 1 = 0.0

S-72599

using both actual components and simulated structural elements; i.e., elements with inertia properties and flexibility characteristics (where applicable) similar to those of the full-scale HRE components. The major individual structural members, such as the struts, manifold rings, wishbone frame, thrust block, rear engine mounts, and spike actuator were to be actual full-scale hardware. This approach allowed evaluation of most of the critical portions of the engine structure during vibration and makes this effort independent of full-scale multi-layer shell development. A sketch of the test unit is shown in Figure 5.3-3.

The shell simulation was accomplished by the use of single-wall inner and outer shells in place of the actual sandwich shells for the full-scale HRE. The spike and nozzle shell assemblies were simulated by single-shell assemblies that achieve suitable similitude for the mass, cg and inertia properties.

The actual spike bellows was to have been installed in the test unit, and to have been connected to the spike simulator and the fore inner shell simulator with flanges that closely resemble the full-scale HRE parts. The spike seal-assembly and preload arrangement would also closely simulate the full-scale HRE design. Other component parts of the engine, such as ducting, valves, and instrumentation packages would be simulated by metal parts that duplicate component weights and cg locations in the full-scale HRE.

5.4 VIBRATION FIXTURE

A vibration fixture was designed and fabricated to test the engine vibration model. The fixture design and method of supporting the fixture were studied in some detail. The mounting fixture was designed with sufficient stiffness to preclude low frequency lateral bending response due to the combined weight of the fixture and the engine model over the test frequency range of 10 Hz to 500 Hz. This was done to prevent excessive cross-talk response in the direction normal to shaker input motion, and also to prevent breakdown of the adhesive forces in the oil film between the bottom of the fixture and the slip-table surface. This design feature was accomplished by using a thick fixture, having a minimum thickness of 10 in. with an average of not less than 11 in. at any cross-section. The design objective was to obtain a fundamental lateral bending frequency in excess of 500 Hz.

5.4.1 Design Approach

The fixture was constructed from a solid block of cast K-1A magnesium with overall dimensions of 67 in. long x 43 in. wide x 18 in. deep. A cavity was machined out of the fixture to permit installation of the test engine on elevated bosses. The recessed cavity provided space for equipment and plumbing that would have been attached to the engine suspension frame.

In all cases, the fixture input motion would have been in the horizontal direction. Vibration input to the three engine co-ordinate directions would have been achieved by reorienting the engine on the fixture for each input axis. Input in the engine longitudinal axis (X-axis) would have been produced by installing the engine on the top surface of the fixture upside down on the

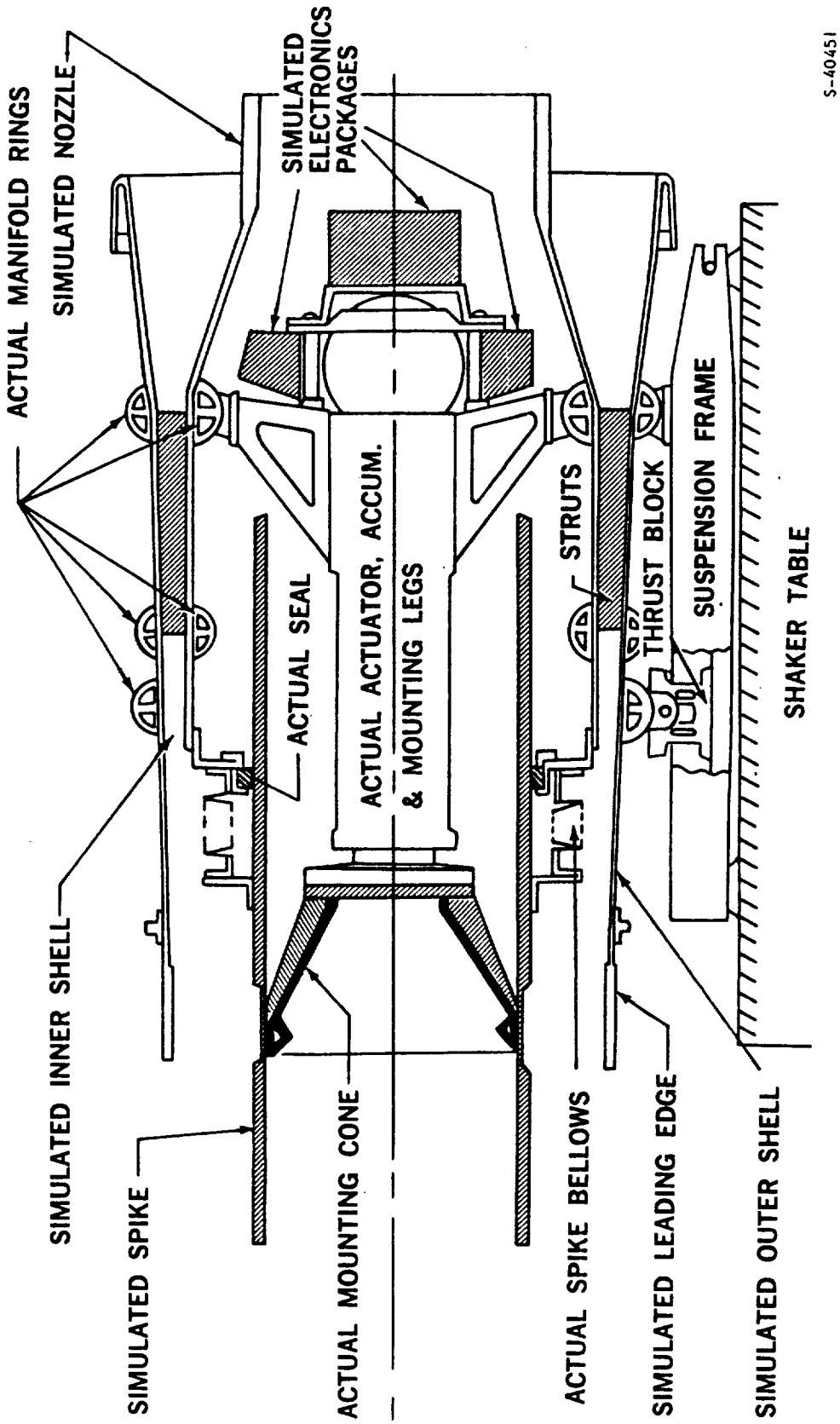

Figure 5.3-3. HRE Vibration Test Unit

suspension frame, and by orienting the engine longitudinal axis to coincide with the shaker input direction. The forward end of the spike was to be pointed away from the shaker. For lateral input, the engine would be rotated 90 deg from the position just described, and this would align the engine lateral axis (Y-axis) with the shaker input motion. Finally, for vibrational input in engine vertical direction (Z-axis), the engine would be installed at the far end of the fixture with the engine Z-axis aligned with the direction of shaker input and the engine longitudinal axis aligned along the width direction of the fixture.

The weight of the finished magnesium block plus accessory hardware was approximately 2000 lb. The flight engine, including the suspension frame and all equipment mounted from the frame, would have been 900-1000 lb.

5.4.2 Vibration Response Analysis Method

Various problem areas were investigated to insure workability of the fixture. The use of a team-bearing support system at the ends of the fixture was considered first. Accordingly, the critical fixture lateral bending modes were analyzed. The analysis was carried out first with the specimen mass on top of the fixture and then with the specimen mass at the end of the fixture. The following major assumptions were made:

(a) For lateral modes, the test engine was treated as a rigid mass attached to the fixture.

(b) The test specimen did not add rigidity to the fixture.

(c) With the engine mounted at the extreme end of the fixture, the engine was assumed to be elastically coupled to the fixture end using the estimated suspension frame and internal engine flexibility.

The analysis was performed by using lumped-parameter models for the several configurations. A computerized eigenvalue method was used to obtain the resonant frequencies and mode shapes.

A schematic of the shaker fixture system is shown on Figure 5.4-1. This setup represents the installation with team bearings at locations A and B. The figure is also equally applicable to an oil-film continuous support system with restraining flexures at A. With the oil-film and flexure support, the additional lateral support introduced by the oil would slightly raise the fundamental lateral frequencies, but the mode shapes would be substantially the same as with the team bearings. The principal advantages of the oil-film support system would be the more uniform support afforded to the fixture and the greater damping effectiveness.

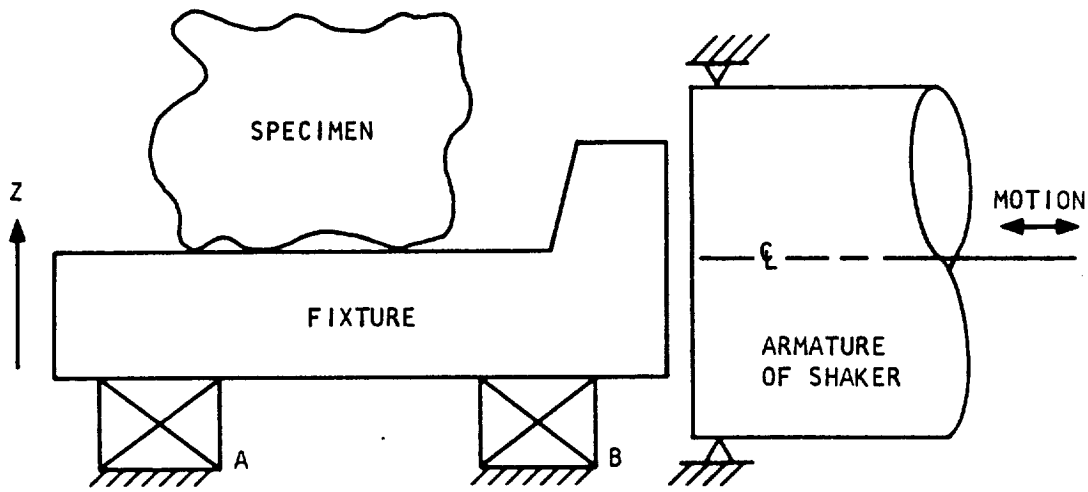

Figure 5.4-1. Shaker, Fixture and Specimen Schematic - Team Bearing Support or Oil Film With Flexures

Calculations were also performed for oil-film support without the use of flexures. In this case the entire fixture load would be borne by the continuous oil film that would be several mils thick. By neglecting the support stiffness of the oil film, the system would operate as a hinged free beam structure as depicted in Figure 5.4-2. The analysis was conducted for the three different engine orientations.

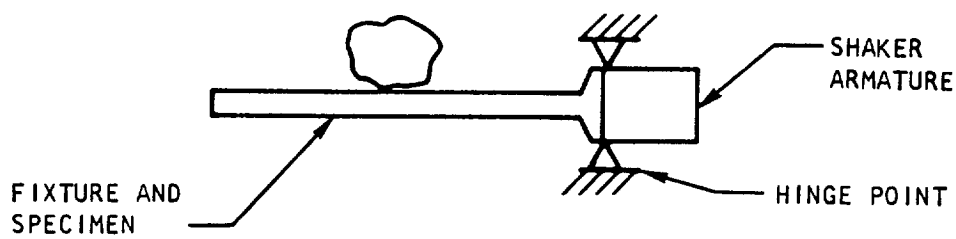

Figure 5.4-2. Dynamic Structural Model with Oil Film Support and Without Flexures

The longitudinal response characteristics of the fixture alone, and the fixture combined with an end-mounted test specimen were also investigated. This was done to determine the force transmissibility from the shaker input end out to the far end of the fixture. The analysis model is shown in Figure 5.4-3. Mass elements W_1 and W_4 represent the fixture, and W_5 plus W_6 represented the engine in this structural model.

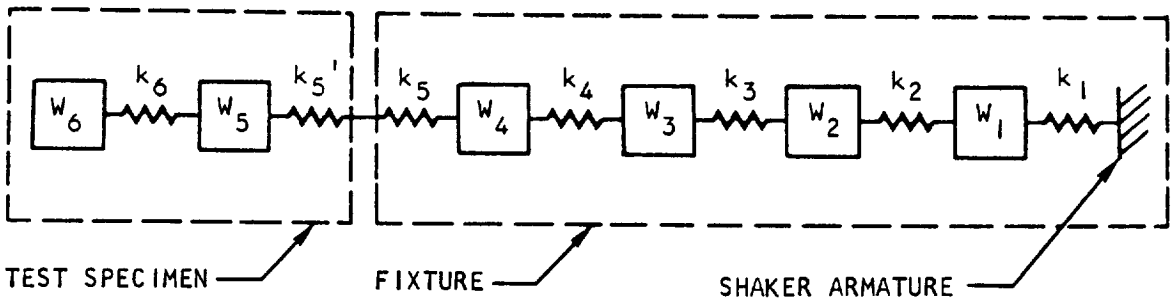

Figure 5.4-3. Extensional-Mode Lumped-Parameter Model

5.4.3 Results and Conclusions

The lateral bending mode shapes for the team-bearing or the oil-film supports with flexures are shown on Figure 5.4-4a and 5.4-4b, which represent the engine on top of the fixture and the engine at the end of the fixture respectively. With the engine on top of the fixture, the first two resonant frequencies were 83 Hz and 1035 Hz. With the engine at the end of the fixture the first three resonant frequencies were 110 Hz, 513 Hz, and 1364 Hz.

In both cases, the first mode occurred within the test frequency range. Due to the low resonant frequency, loading at the team-bearing supports would have been excessively large, thus necessitating an oil-film slip-table mounting system. The higher frequencies were outside the test range and of no concern.

The additional analysis for an oil-film support system without the flexures was carried out to determine whether the flexures could be deleted. The analysis was carried out for the engine on top and at the end of the fixture. In these various cases, the first resonant frequency ranged from 28 to 71 Hz with a hinged-free mode shape. The combination of the low resonant frequency and the adverse mode shape was considered a serious problem that could have led to fixture chatter and a heavy peeling load on the oil film. It was concluded that flexures would be needed beyond the end of the fixture to enforce a mode point at this location and to eliminate peel-away or chatter.

Finally, the solution for longitudinal response was obtained. The total engine weight of 1000 lb was equally distributed between W_5 and W_6 on Figure 5.4-3 and stiffnesses of 100,000 lb/in. were used for k_5 and k_6 representing the engine suspension frame and the internal engine springrates. The first two resonant frequencies were 39 Hz and 101 Hz, and the mode shapes indicated that these were test specimen resonant frequencies. The next two response frequencies of 755 Hz and 2140 Hz were fixture-response resonances. These were outside the test frequency range and would not have created a test difficulty.

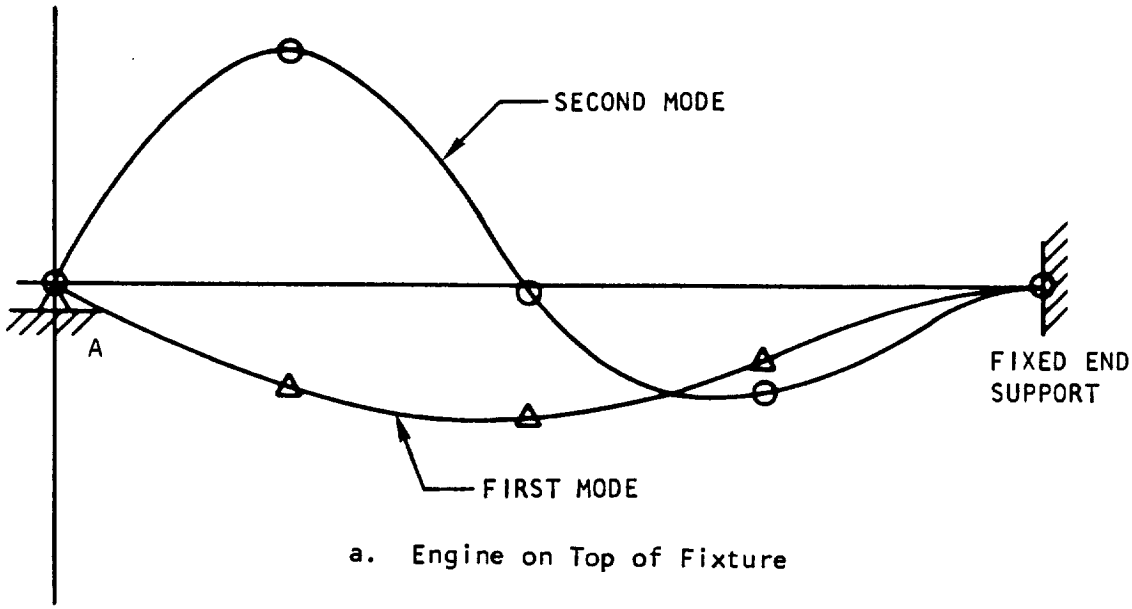

a. Engine on Top of Fixture

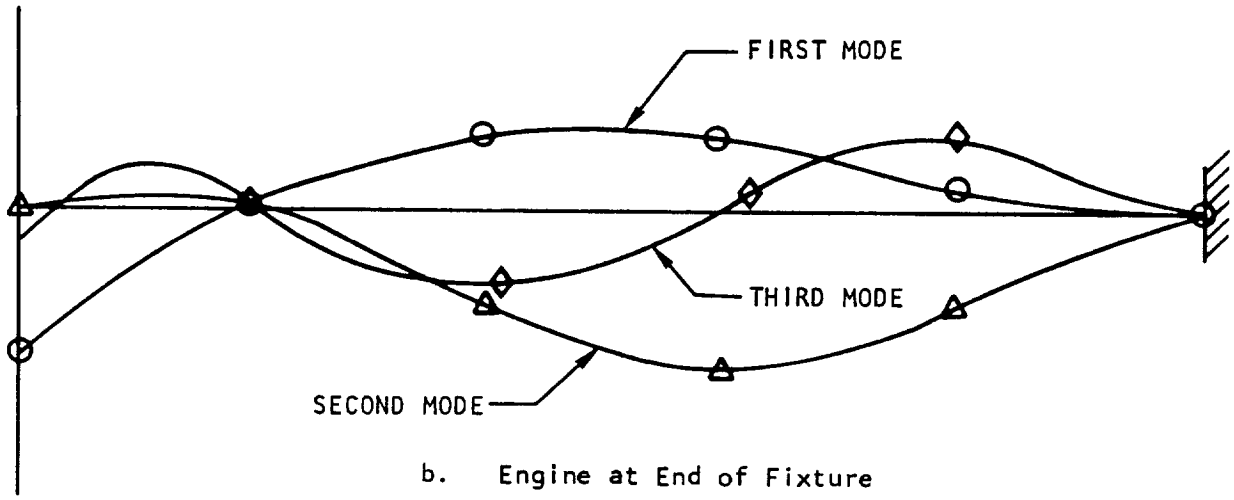

b. Engine at End of Fixture

Figure 5.4-4. Lateral Bending Mode Shape

Based on the analysis, the fixture was shown to be adequate for the planned test program. The analysis also demonstrated the need for a slip-table oil-film test setup to be supplemented with flexures at the end of the test fixture to prevent oil-film peeling.

5.5 ENGINE COMPONENTS

5.5.1 Inlet Spike

5.5.1.1 Cooling Design and Analysis

5.5.1.1.1 Spike Tip Cooling

The spike tip will be cooled with 100°R hydrogen impinging on the inner surface of the tip as shown in Figure 5.5-1. The impinging hydrogen is a fixed 4.5-percent of the spike coolant rate and is routed in parallel with the remainder of the spike flow in the region of the tip. The coolant flow control orifices were sized by calculating the pressure drop for the spike tip route based on a flow of 0.02 lb per sec. To account for pressure drop calculation uncertainties in complex passages with several turns and area changes, the flow-control orifices were sized for twice the pressure loss calculated for the tip route, which was based on a loss coefficient of 1.5. The design pressure drop for the orifices is based on a more realistic loss coefficient, 2.8.

Placement of the flow control orifices for the spike at Station 4.0 was based on pressure drop and fabrication considerations. To match the design pressure drop in the tip, an adequate orifice area was needed for the main flow to the spike cooling jacket. Forward of Station 4, the small circumference would not accommodate the number of holes (0.125 in. dia) necessary for the total orifice area. If the flow control orifices were moved aft of Station 4, the pressure drop in the spike is essentially unchanged. The pressure drop in the fins is reduced, but the pressure drop in the spike tip is increased by a comparable amount.

At Mach 8 local, 88,000-ft altitude, the aerodynamic heat flux at the tip stagnation point is 560 Btu/sec-ft^2 as calculated by the method of Fay and Riddell (Reference 5.5-1). With an impinging hydrogen rate of 0.0295 lb/sec (4.5 percent of total spike coolant rate of 0.655 lb/sec) a tip outer surface temperature of 755°R was calculated. The corresponding inner surface temperature of the tip is 325°R. The convective heat transfer coefficient for coolant hydrogen impinging on the inner surface was calculated at 2.6 Btu/sec-ft^2 from a correlation presented in Reference 5.5 -2.

When the inlet is closed at Mach 8, 88,000-ft altitude, the spike coolant demand is 25 percent of that required during design point operation, 0.655 lb/sec. The spike tip flow rate will be 25 percent of 0.0295 lb/sec, or 0.0076 lb/sec, but the aerodynamic heating rate at the tip will be the same as with inlet open and with combustion. At this condition, the predicted outer surface temperature is 1250°R and the inner surface temperature is 1010°R.

5.5.1.1.2 Spike Folded-Flow Section

The cooling design of the folded-flow section of the aft spike (Stations XX = 46.00 to 55.76 in.) and analytical results for the Mach 8 local, 88,000-ft altitude flight condition are presented in Figure 5.5-2. This double-sandwich

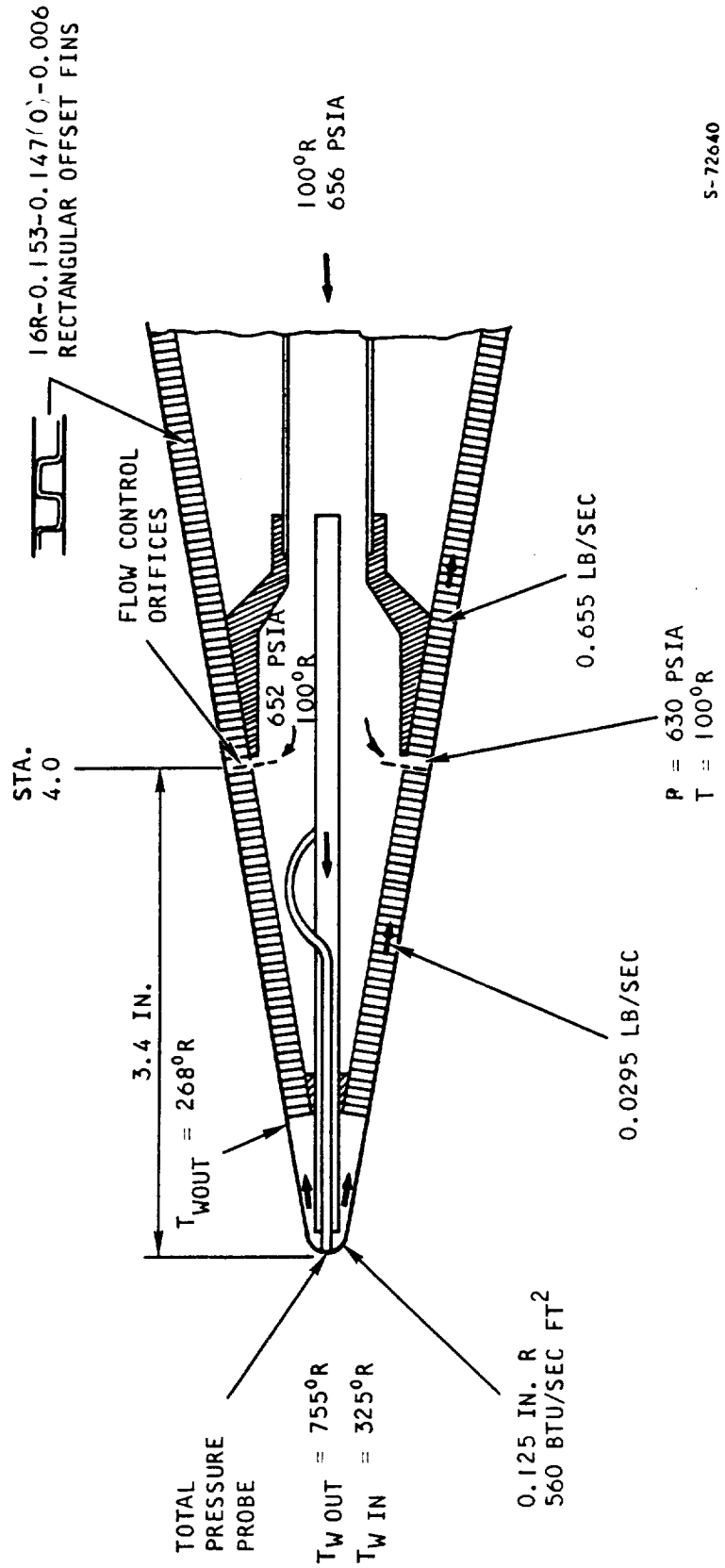

Figure 5.5-1. Spike Tip Coolant Conditions (Mach 8, 88,000 ft)

counter flow design provides a means of exhausting hydrogen coolant from the inner shell-overlapping portion of the spike. The hydrogen flow rate of 0.655 lb/sec was selected to give maximum structural temperatures T_{MIDC}, T_{MIDH}, T_{H2H} in Figure 5.5-2) of 1600°R at the end of the spike (Station XX = 55.76 in.) as per the thermal design ground rules in Section 5.1. After making a 180-deg turn and flowing through the inner passage of the double-sandwich section, the hydrogen is cooled down from 1600°R to 1350°R by heat transfer from the inner to outer passage (T_{H2H} in Figure 5.5-2). This 250°R loss in available heat sink requires a 0.655-lb/sec rather than a 0.546-lb/sec spike flow requirement with 1600°R outlet temperature, as in the other flow routes. The hot wall temperatures and hot wall-to-structure temperature differences are maintained below 2060°R and 800°R, respectively.

A transient thermal analysis of the spike folded-flow section was performed at the start of the Mach 8 freestream (Mach 6.5 local) operating condition. The primary object of the analysis was to determine the coolant flow-rate-control method (outlet coolant temperature sensing or preprogrammed flow rate scheduling) required to maintain metal temperatures at or below acceptable design limits. A second objective was to determine whether metal ΔT's in the folded-flow section during transient startup conditions exceeded the design steady-state values. Results indicate that the spike coolant must be preprogrammed to increase from 0.20 lb/sec (the spike latched-closed value prior to startup) to 0.78 lb/sec (the steady-state operating value) within 0.80 sec after the start of spike retraction. When the coolant is scheduled in this manner, transient startup metal temperatures and ΔT's are no higher than those reported for steady state.

5.5.1.2 Structural Design and Analysis

The inlet spike is a regeneratively cooled shell structure. A 10-deg cone forms the forward section between Station 1.189 and Station 27.259. The next section, up to Station 50.506 is a compound curved part, followed by an almost straight cylindrical section. A truncated cone (reinforced with welded stiffeners) attaches the spike to the actuator housing.

The spike was analyzed as a sandwich shell with isotropic faces and an orthotropic core. A structural model was prepared and analyzed using A. Kalnin's "Static, Free Vibration and Stability Analysis of Thin, Elastic Shells of Revolution." (AFFDL-TR-68-144) computer program. The shell elements, thicknesses, and other details are shown in Figure 5.5-3.

Certain parts of the spike were known in advance to be low-fatigue, cycle-limited. The following problems were investigated during the design of the spike:

(a) The effect of external pressures and temperatures due to symmetrical hot gas flow.

(b) Stresses and deformations due to asymmetric inlet unstart.

(c) Pressure-containment capability of the coolant passages, manifolds, etc.

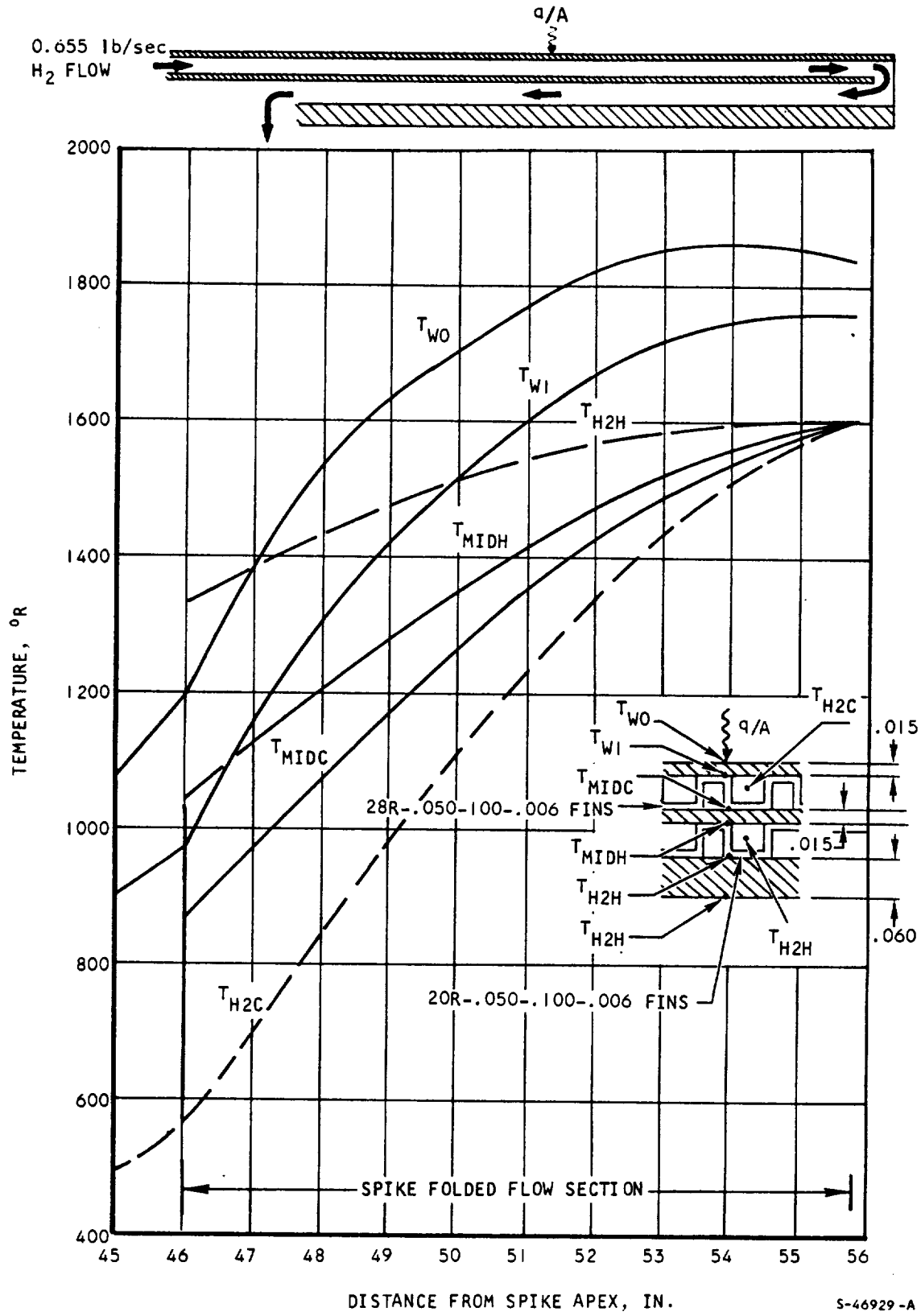

Figure 5.5-2. Spike Folded-Flow Section Thermal Performance

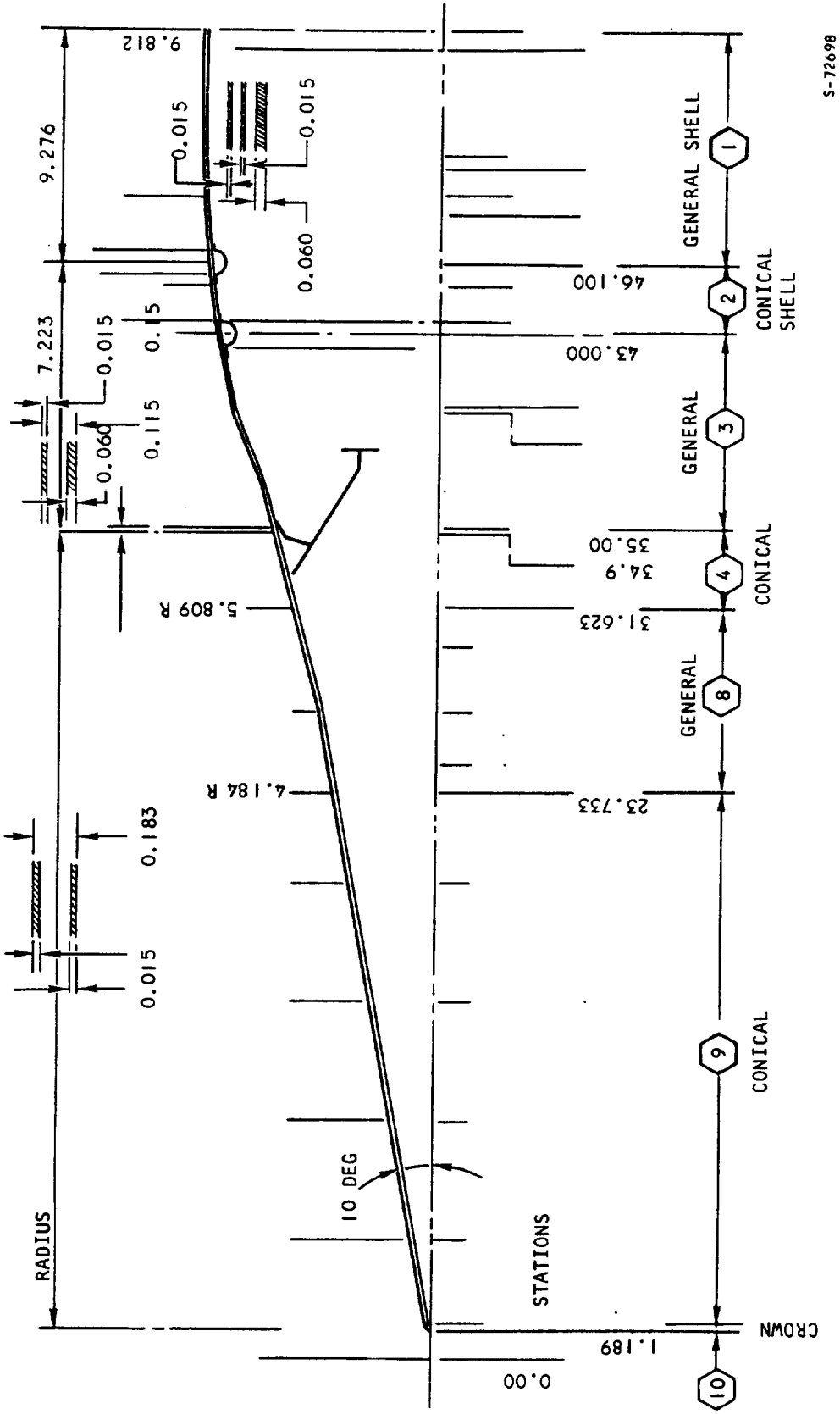

Figure 5.5-3. Spike Analytical Model

(d) Calculation of the expected cycle life where high thermal stresses were present.

The inlet spike is exposed to the following loads:

(a) Aerodynamic: Pressure
Heating

(b) Inertia

(c) Environmental loads due to ground handling, fabrication, and miscellaneous

These loads are presented in Section 5.2. A summary of the analytical results is tabulated below:

	Distance From Spike Tip, in.			
	4.0 to 36.5	37.8 to 43.0	43.0 to 45.3	46.8 to 55.8
Critical buckling pressure, psi	66.5	169	211	55
Buckling pressure load, psi	10.0	102	74	36.4
Safety factor against buckling	6.65	1.66	2.85	1.51
Shear stress, psi	2020	-	-	-
Bending stress, psi	2580	-	-	-
Hoop stress, psi	-	16,900	-	23,100
Cycles-to-failure	390,000	2,000	-	-

Buckling strength and cycle life of the aft spike governed the design.

5.5.2 Inner Shell

5.5.2.1 Cooling Design

Hardware changes, which improve the coolant hydrogen flow distribution around the strut cutout headers in the inner shell as well as the outer shell, were designed and are summarized in Figure 5.5-4. These were made after hot gas strut test results (Section 8.1) showed local hot skin blackening of the test support panels adjacent to the coolant cutout headers. The support panels cooling design was similar to the previous inner and outer shell design. In the previous design, coolant crossflow around the strut cutout header bars was limited by the finned surfaces adjacent to the header bars (28R-0.050-0.100 (0)-0.006 offset fins). This created low coolant flow regions directly upstream

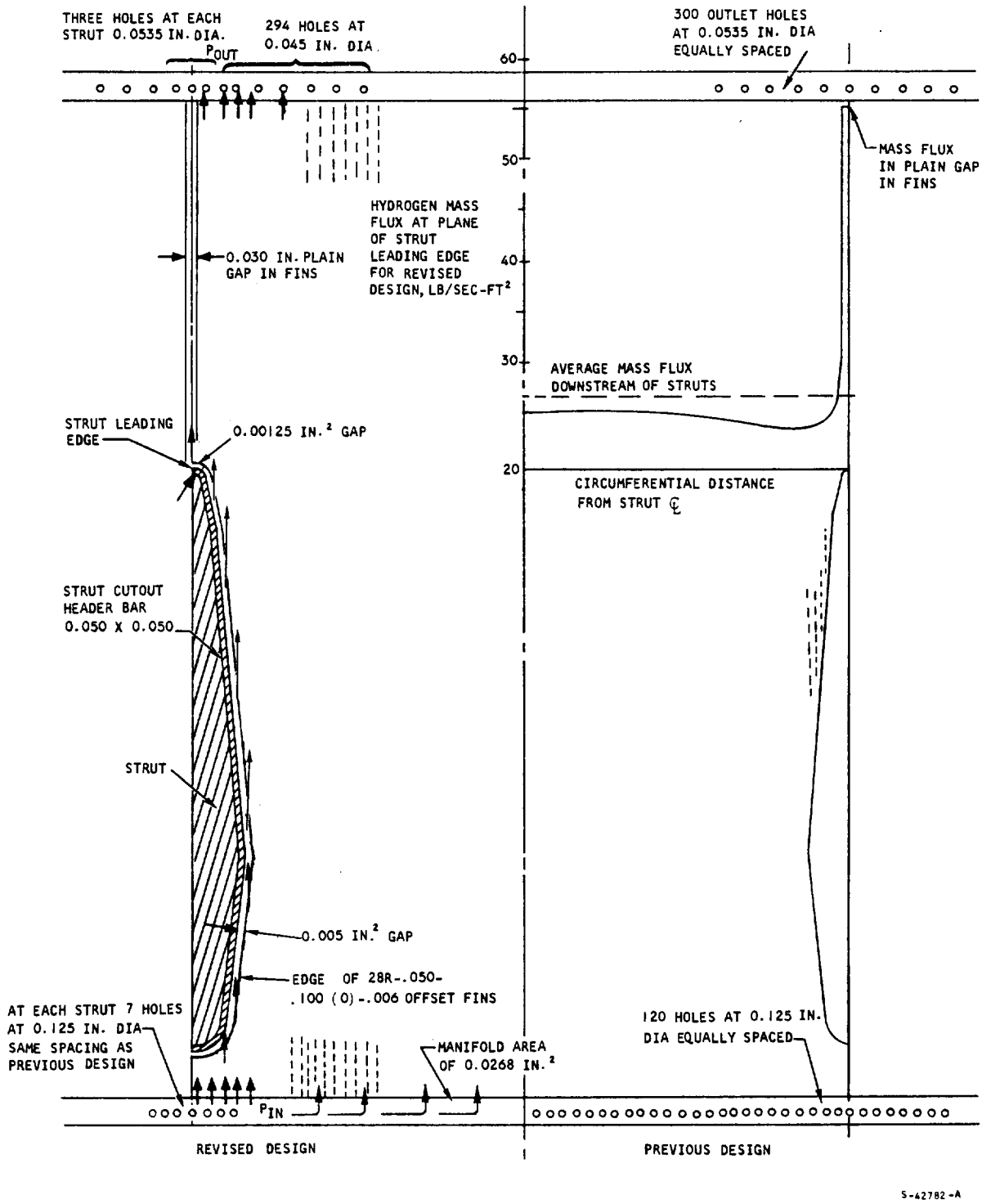

Figure 5.5-4. Summary of Special Cooling Design Features of Inner Shell

and downstream of the struts. Depending upon the amount of flow maldistribution and heat flux distribution, these low-flow regions could degrade thermal fatigue performance. At $M_L = 6.5$ ($M_\infty = 8$, B-B line), a heat flux spike of 900 Btu/sec ft^2 was predicted on the header bar, while the average heat flux on shell surfaces between the struts at this axial location is 350 and 500 Btu/sec ft^2, respectively, on the inner and outer shells.

To improve coolant flow distribution around the header bars, two general techniques were used, including (1) a reduction in flow resistance directly in line with the struts, and (2) an increase in flow resistance in the finned passages that are not in direct line with the struts. The criteria for adequate flow distribution are (1) a coolant mass flux in the fins directly in line with the struts that is approximately equal to the mass flux in the fins not in line with the struts, and (2) a coolant heat transfer coefficient that is adequate to cool the header bar, particularly near the leading edge of the strut.

The flow resistance adjacent to the header bars on the inner and outer shells was reduced by introducing a plain passage gap between the offset fins and the header bar with free flow area of 0.005 in.^{2}. Flow resistance of passages in line with the struts was further reduced by providing a plain unfinned gap of 0.030 in. (nominal) by 0.050 in. between offset fins located on strut centerlines and extending from strut leading edge to inner and outer shell outlet holes.

Inlet and outlet holes of the inner shell were modified to increase flow resistance of flow paths not in line with the struts relative to flow paths in line with the struts. Instead of the 120 holes at 0.125 in. dia and equally spaced, the number of inner shell inlet orifices was reduced to 42 at 0.125 in. dia and placed symmetrically in groups of seven about the centerline of each of the six struts. The hole spacing is still 3 deg as in the previous design. Inner shell inlet holes can be eliminated between struts because there is a manifold-like passage (0.0268 in.^{2} cross-sectional area) between the holes and finned passage inlet that will distribute the flow circumferentially to finned passages between the struts. At the inner shell outlet, the previous hole configuration (300 holes, 0.0535 in. dia, equally spaced) was replaced by 294 holes, 0.045 in. dia (same spacing as previous configuration) and 18 holes, 0.0535 in. dia, in groups of three, symmetrically located about the centerline of each strut at one-half of the previous spacing. These inner shell orifice modifications create an overall pressure drop increase of 56 psi in the innerbody flow route. This pressure drop increase can be tolerated by adjusting the upstream coolant regulating valve to expend a pressure drop of 56 psi less than the present value of 282 psi.

The number of strut-sides flow-inlet-manifold orifices on the outer shell was reduced from 240 (0.055 in. dia) equally spaced, to 204 on the same spacing. This represents a deletion of six holes symmetrically located about the centerline of each strut. This reduction provides a 20-percent increase in coolant-rate, flowing around the strut-cutout header bars on the outer shell. The outerbody outlet-manifold orifices were not modified because these orifices also provide the outlet of the leading edge flow rate.

5.5.2.2 Structural Design

5.5.2.2.1 Applied Structural Loads

The inner shell was analyzed for the following applied structural loads:

Coolant Pressures:

(a) Maximum operating 700 psi

(b) Proof 1050 psi

Gas Pressure Loads:

(a) Symmetric - external

1. Maximum operating steady state pressure: 105 psi ($M_\infty = 4$, $q_\infty = 2000$ psf, subsonic combustion)

2. Maximum pressure after shock is expelled: 150 psi ($M_\infty = 8$, $q_\infty = 2000$ psf)

3. Maximum transient pressure during inlet unstart: 390 psi ($M_\infty = 8$, $q_\infty = 2000$ psf, duration less than 0.002 sec)

(b) Symmetric - internal

1. Design: 30 psi (due to possible stoichiometric burning of unvented hydrogen)

(c) Unsymmetric - external

1. 10 deg engine angle of attack ($q_\infty = 2000$ psf)

2. 7 deg engine yaw ($q_\infty = 2000$ psf)

Inertia Loads:

(a) Operating

1. Vibration: 0.3 g input in any direction (assumed amplification of 10)

2. Static acceleration

Transverse: ±1.0 g

Longitudinal: +4.5, -1.0 g

Normal: +4.25, -0.5 g

5.5.2.2.2 Stresses and Safety Margins

Hoop stresses due to external gas pressure in the shell are:

σ_h = 23,600 psi, and at 1615°R this corresponds to a margin of safety of +0.30

Buckling analysis of the inner shell revealed that the lowest margin of safety against buckling is +0.55.

Maximum fin stresses due to coolant pressure occur at the exit to the manifold, where the metal temperature is approximately 1616°R, and 2 in. aft, where the gas-side thermal wall temperature is 1920°R. At the exit, the fin stresses (σ) are for the 25R-0.05-0.065-0.006 fin at a proof pressure of 1050 psi (governing):

$$\sigma_{fin} = 18{,}000 \text{ psi}$$

$$S = 0.85\ F_{ty} = 44{,}200 \text{ psi}$$

$$MS = \frac{44{,}200}{18{,}100} - 1 = 1.44$$

Since a gap of 0.08 in. long exists between the end of the fins and the header ring, a check was made of the effect on the fins of the gap pressure load. The model assumed was half the gap pressure load acting as the shear on a semi-infinite beam on an elastic foundation. The additional maximum local stress equals 19,800 psi, assuming that the fin efficiency factor does not apply for local stress.

$$\sigma_{total} = 18{,}100 + 19{,}800 = 37{,}900 \text{ psi}$$

$$MS = \frac{44{,}200}{37{,}900} - 1 = 0.17$$

For fins 2 in. aft of the exit, the 10-hr creep rupture stress governs the design. Fin stress, σ_{fin} = 9400 psi and the margin of safety against stress rupture, M.S. = 0.62.

5.5.2.2.3 Strut Sockets

The strut sockets were analyzed for the following structural load conditions:

Longitudinal load	+4.5, -1.0 g
Normal load	+4.5, -0.5 g
Transverse load	±1.0 g

Vibration	±3.0 g (any direction)
Aerodynamic loads	due to 10-deg-engine angle of attack, q_∞ = 2000 psf
Yaw loads	0

The spike and actuator loads are reacted at the mount pads, and the center of gravity of the innerbody is approximately at the same station. For purposes of strut structural design, the reactions were all taken at the six pads. Moments about the transverse axes were reacted by axial forces at the pads. Transverse forces were reacted by radial forces in the struts. The mount pads, struts, and sockets are designed to transmit the total load directly into the outer shell.

The maximum stress in the socket occurs at the scalloped bolt flange and is equal to 39,900 psi, which is within the allowable stress limit.

5.5.3 Nozzle

5.5.3.1 Nozzle Cap Cooling Design

The design objectives were to evolve a cooling method that would (1) generally maintain exterior surfaces below 1000°R; (2) keep temperature difference between metal surfaces below 400°R, though localized values higher than 400°R can be tolerated; and (3) maintain a low coolant pressure drop, preferably under 10 psi. Aerodynamic heating parameters used in the analysis corresponded to the Phase I design flight condition of Mach 8, 81,000-ft altitude. The nozzle cap was designed prior to full definition of the current Mach 8 (local), 88,000-ft altitude design aerodynamic heating conditions and cooling requirements, so the conditions discussed below do not correspond exactly with those presented in Section 5.1. The hot gas convective heat transfer coefficient in the nozzle cap vicinity is 0.01 Btu/sec-sq ft-°R and the adiabatic wall temperature is 5300°R. A hydrogen flow of 0.34 lb/sec at 120°R and 600 psia is available to cool the nozzle cap surfaces. With these conditions, the pressure drop for the cap passages is 10 psi. This coolant subsequently cools the innerbody surfaces.

A cross section of the nozzle cap is shown in Figure 5.5-5. A coolant flow rate of 0.34 lb/sec is fed to the cap through a 5/8-in.-ID tube. Eight oval holes (total area = 0.070 sq in.) near the end of the tube allow most of the coolant to flow directly into a channel formed by the cap hemispherical surface and a 0.025-in.-thick baffle placed nominally 0.10 in. from the cap surface. The remainder of the coolant in the tube is fed through six 0.050-in.-dia holes drilled through the solid end section of the tube. This coolant impinges on the inner surface of the nozzle cap tip, adjacent to the bolt, and provides forced convection coolant in the gap between tube and inner cap surfaces that would otherwise be filled with near-stagnant coolant. Coolant leaves the nozzle cap through sixty holes of 1/8 in. dia adjacent to the threaded flange section and enters the rectangular offset fins in the aft innerbody flow route.

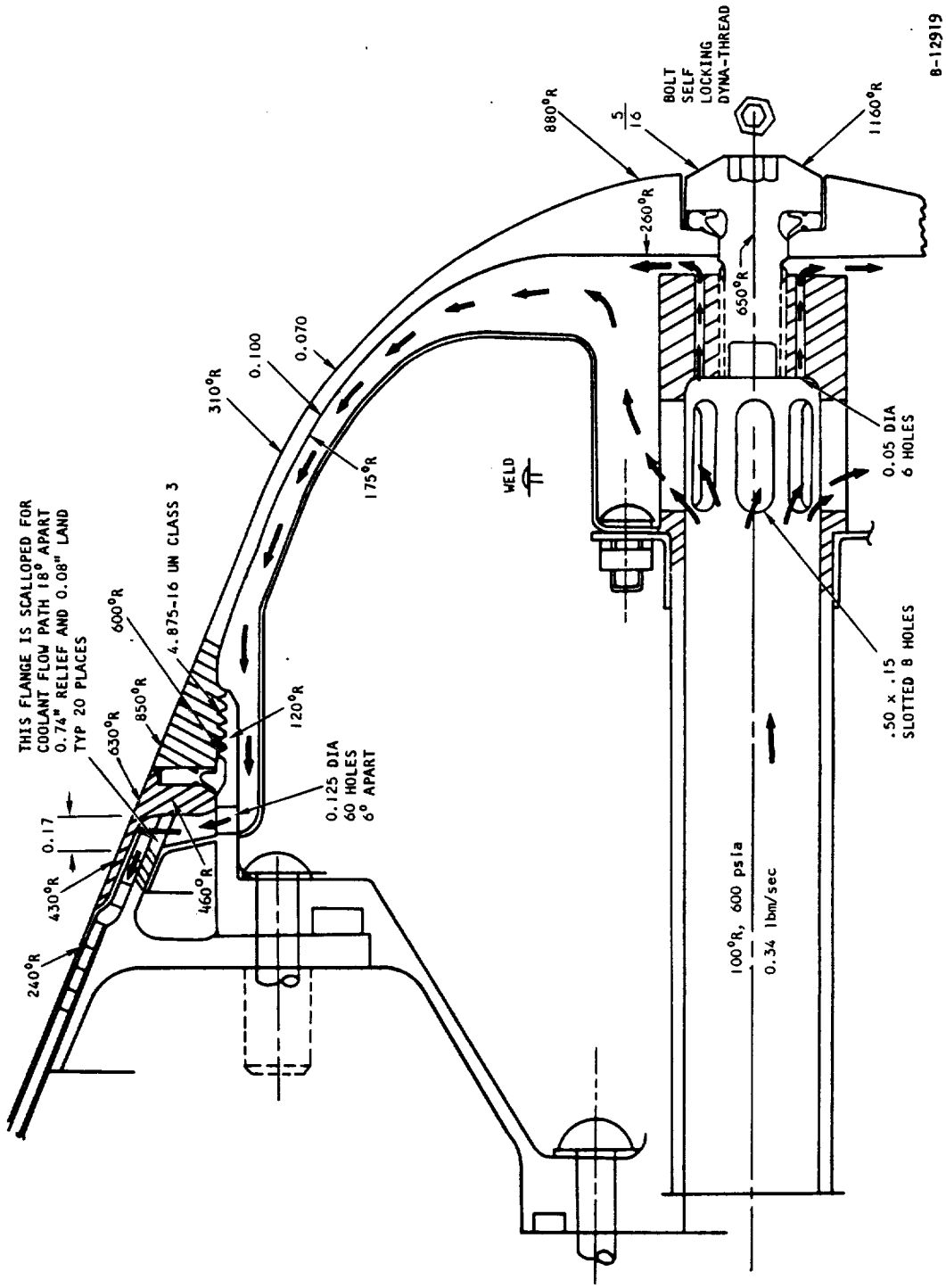

Figure 5.5-5. Cross Section of Nozzle Cap

Metal temperatures and coolant temperature and pressure are indicated in Figure 5.5-5. The maximum metal temperature (1160°R) occurs on the surface of the bolt exposed to the hot gas, and the maximum metal temperature difference (700°R) occurs at the thick section of the threaded flange. A similarly high metal temperature difference of 620°R occurs at the thick-wall section adjacent to the bolt. Although these temperature differences exceed the objective of 400°R, they are localized values. Generally, nozzle cap temperature differences are much less than 400°R, as indicated for the 0.070-in.-thick metal section midway between the bolt and thread flange. The bolt temperature of 1160°R is not critical.

5.5.3.2 Structural Design

The nozzle cap was analyzed for the following conditions:

Normal operating condition

Pressure	700 psia
Temperature	Outside surface metal ranging from 400° to 900°R, as indicated by thermal analysis

Proof pressure condition

Pressure	1050 psi
Temperature	ambient

The proof pressure condition proved critical and formed the basis for the detail design.

The skin and tube structure is fabricated from Hastelloy X.

A brief description of two nozzle cap designs that were investigated is given below.

(a) The initial design proposed was such that the force required to react the pressure thrust on the cap and to seat the main seal, be applied through the center of the cap. This would be done by structurally connecting the cap center to the inner shell through a bolt-tie bar arrangement.

(b) The second design utilized a threaded flange connection between the end of the nozzle cap and the inner shell. The pressure thrust and the gasket seating load would be reacted through the total periphery of the inner shell (Reference Drawing L-980604).

Transmission of the reacting loads through the center of the cap (design (a) above) resulted in a high axial concentrated load in the cap and in the connecting bolt and tie bar, causing excessive stresses in the skin. In addition, the accumulated axial deflection in the skin and tie bar would have exceeded, by a considerable amount, the compression on the main "K" seal (0.012 in.). The amount of skin reinforcing and additional tie bar metal cross section required to reduce the stresses and deflections to acceptable levels would have resulted in higher temperatures and temperature gradients in the skin, as well as considerably increased component weight.

The second design (b), which carries the thrust load in the total periphery of the skin, proved to be far better. The center bolt and tie bar become essentially nonstructural, and the size is governed purely by design considerations (i.e., flow passage required, locking device required, etc.). This, in turn, reduced the size of the hole required in the end of the cap (a 1/4-in. bolt can be used rather than the 5/8-in. bolt, which would have been required in design (a), which results in less reinforcing at the center of the cap. There is no tendency for the pressure thrust to open up the seal because the load path is short and stiff.

The sealing load required for the main "K" seal is approximately 2300 lb. The inner shell ring mating with the seal was stiffened in order to resist this load. The maximum pressure (circumferential) stress in the 0.070-in. wall of the skin is 41,200 psi, which is well within the allowable. The threaded end of the cap was reinforced slightly, in order to accommodate the additional local bending stresses. The maximum axial stress (membrane plus bending) in the threaded end is 38,600 psi. The shear stress in the threads is less than 15,000 psi; again, well within the allowable.

5.5.4 Leading Edge

5.5.4.1 Full Scale Cooling Design

The purpose of the outerbody leading edge thermal design was to find a leading edge tip configuration that was acceptable for temperatures, stress, and fabrication at the Mach 8, 88,000-ft design point. The candidate designs and flow routings are shown in Figure 5.5-6. These two design concepts have the entire outerbody forward flow of hydrogen perpendicular to the leading edge. Concept 2 has an additional flow in each of two or four segments parallel to the leading edge.

Both concepts in Figure 5.5-6 have beneficial features not available in the other. The Concept-2 configuration has no need for a small clearance at the 180-deg bend where the flow is first toward the leading edge and then awav from the leading edge in the finned passages, because the leading edge heat flux is handled by the flow parallel to the leading edge in the separate passage. This feature is important for coolant conservation during ascent and descent as stated in Section 5.1.5. Coolant flow perpendicular to the leading edge, Concept-1 configuration, offers simpler fabrication and flow routing, and coolant pressures required for equal metal temperatures are lower. Both concepts can be improved by using nickel instead of Hastelloy X for the skin. Nickel has a higher thermal conductivity (lower wall ΔT and outer wall temperature) and a higher low-cycle fatigue life.

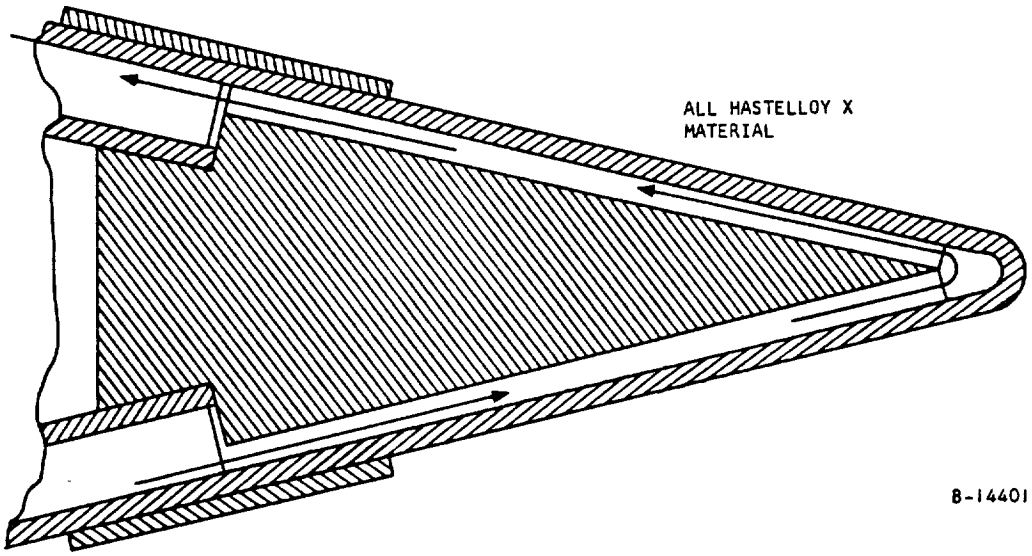

LEADING EDGE CONFIGURATION NO. 1

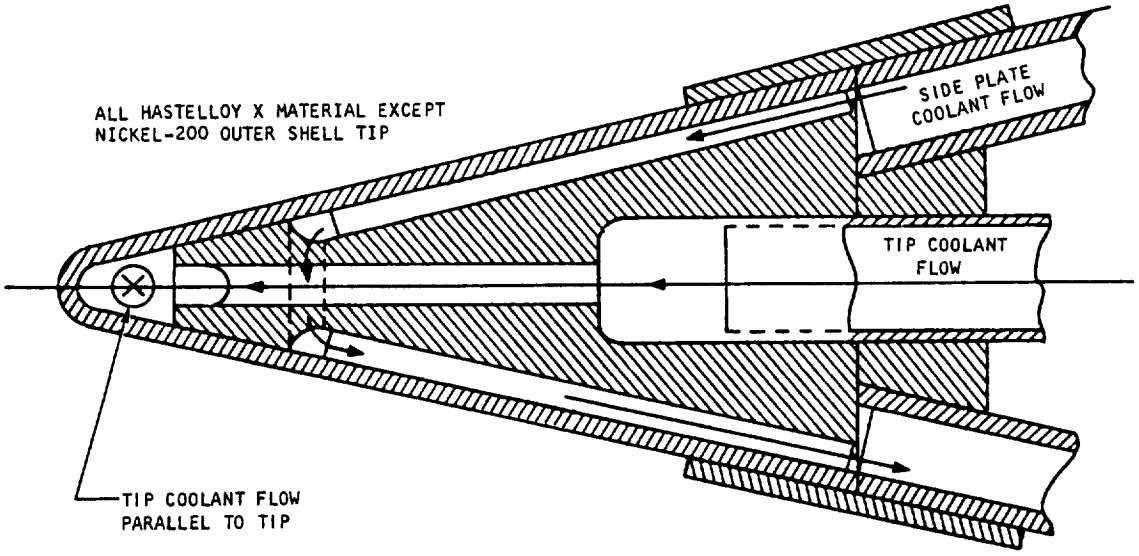

LEADING EDGE CONFIGURATION NO. 2

Figure 5.5-6. Cowl Leading Edge Tip Configurations and Coolant Flow Paths

A Nickel-200 leading edge tip with coolant flowing perpendicular to the stagnation line, Concept 1, was selected for the flightweight engine leading edge design. In addition to the above considerations, this design was selected because leading edge straight section test results summarized in Section 8.2 indicated that coolant flow distribution was acceptable and the internal coefficient in the 154-deg turn was acceptable for cooling, even when high shock-impingement heat flows on the leading edge tip are considered.

Results of a thermal analysis performed to determine the internal and external surface temperatures of the selected leading edge design at the 88,000-ft altitude, freestream Mach 8 design point are presented in Figure 5.5-7. Coolant hydrogen heat transfer coefficients were calculated with the correlation for the 154-deg turn reported in Section 8.2. A 70 node, two-dimensional steady-state thermal analysis of the 15-mil-thick nickel wall with 30-mil outside leading edge radius was conducted. Curves labeled "no shock" are the inside and outside surface temperature distributions, assuming the spike shock falls outside of the leading edge. Curves labeled "shock" are the inside and outside surface temperatures, assuming the spike shock impinges on the leading edge. The heat transfer coefficient for a shock impinging on a leading edge was calculated on the basis of data from Reference 5.5-3 to be 15.4-times the value for the shock located inside of the leading edge. This area with high heat transfer has a width of 4 mils and extends around the entire 56.7-in. circumference of the leading edge. Although the maximum local heat flux for the Mach 8 design increases from 2050 to 10,200 BTU/sec-sq ft when shock impingement is assumed, conduction in the nickel wall permits a maximum metal temperature increase of only 470°R and an acceptable overall temperature difference increase from 990° to 1460°R.

5.5.4.2 Leading Edge Straight Section Thermal Design

Leading edge straight section test specimens were designed and subsequently tested for the purpose of evaluating the thermal performance of the two candidate leading edge tip coolant configurations discussed above. A high-temperature subsonic gas test tunnel was designed so that the test specimens would experience the same level of heating as the flight engine at the design condition of Mach 8 local, 88,000-ft altitude.

The leading edge straight section test specimens were directly applicable to the flight engine axisymmetric outerbody leading edge. The use of a straight section, instead of a compound-curved section, greatly simplified the fabrication and testing. The two types of specimens used in the test program were designated configuration No. 1 and configuration No. 2, as previously shown in Figure 5.5-6. Both types have the same overall dimensions (8-in. span, a 4-in. length), approximately equal to 1/7 of the outerbody circumference at the leading edge tip. The features that distinguish the two types of specimens are described below.

Configuration No. 1 test specimens had leading edge tip-coolant flows perpendicular to the specimen stagnation line through a 154-deg turn. The tip-coolant also provides coolant to the sides of the specimen. All face sheets, fins, and structure were Hastelloy X. The tip, which was fabricated separately

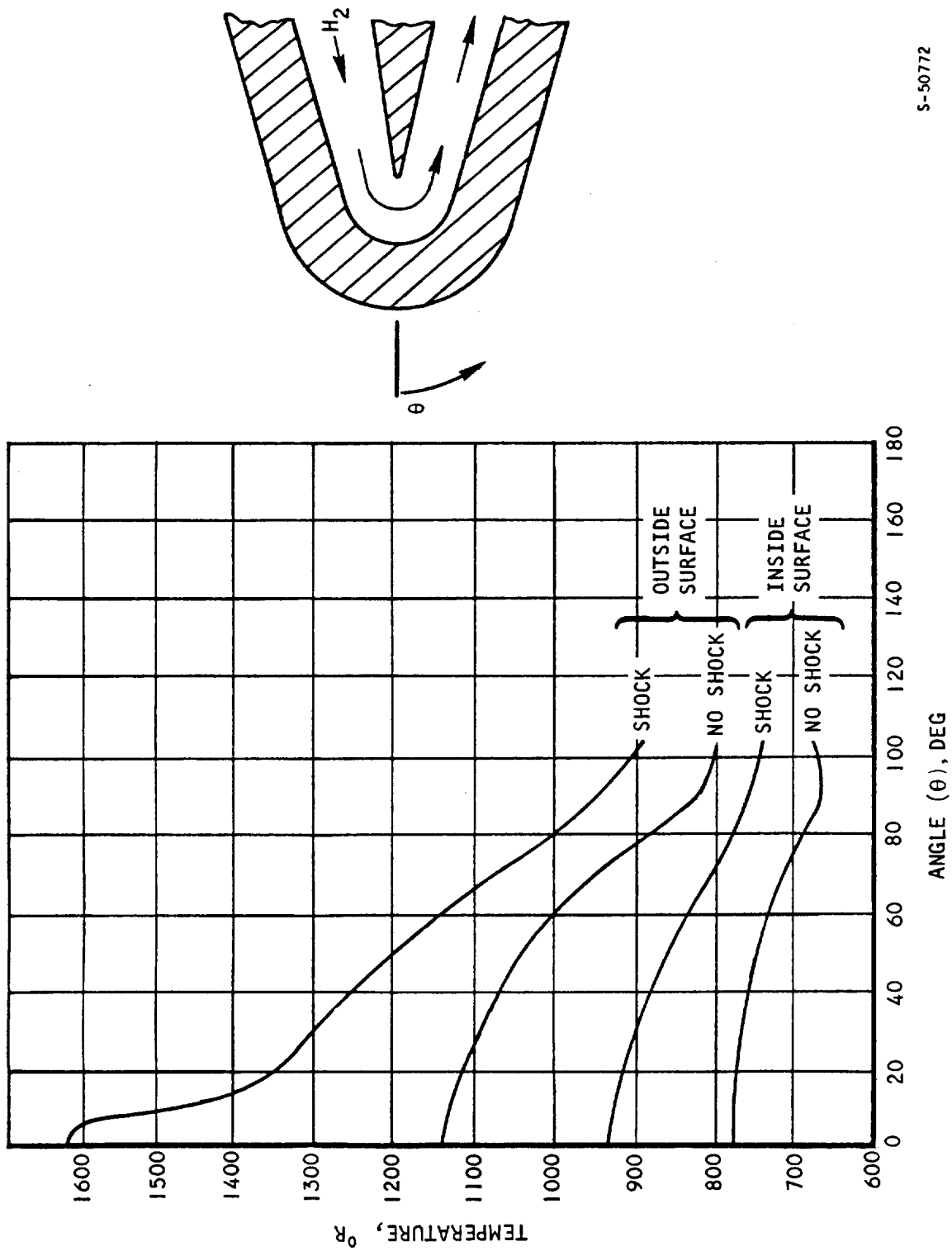

Figure 5.5-7. Leading Edge Design Thermal Performance

from the sides, had 20R-0.020-0.004 plain rectangular fins brazed to the 1/2-in.-length arrowhead piece, and the 0.015-in. V-shaped surface sheet. The side subassemblies consisted of 20R-0.075-0.100(0)-0.006 rectangular offset fins brazed between two 0.015-in.-thick sheets. The sides were brazed to the tip at the arrowhead piece and two outer skin joint covers. Coolant enters and exits from the specimen side fins through manifolds located at the base of the 26-deg wedge, as shown in Figure 5.5-8. The manifolding was selected to simulate the manifolding in the flight engine.

Configuration No. 2 test specimens had leading edge tip coolant flows parallel to the stagnation line and separate from the sides coolant flow. The construction details are similar to the configuration No. 1 specimen except at the leading edge tip, where the construction detail shown in Figure 5.5-6 was used. All material is Hastelloy X except the tip outer sheet where Nickel-200 was used.

The test tunnel is a two-dimensional channel with a 6-in. straight section of 2 in. by 8 in., followed by an 18-1/2-deg half-angle divergent channel (Figure 5.5-9). The 6-in. straight section serves two purposes: (1) to allow the inviscid portion of the flow to settle any upstream distance, and (2) to permit the boundary layer in the tunnel wall to develop a turbulent flow at the test section. This latter condition will permit side wall radiation to contribute approximately 24 Btu/sec-sq ft of net heat flux to the flat surfaces of the test unit.

Subsonic air, heated by a hydrogen/oxygen combustor to temperatures between 2500° and 4000°F, was flowed over the test unit at rates between 2 lb/sec and 6.5 lb/sec. The test unit was cooled with gaseous hydrogen at inlet temperatures between 200° and 520°F, at inlet pressures between 400 psia and 700 psia, and at flow rates between 0.02 lb/sec and 0.12 lb/sec.

The maximum flow rate of 6.5 lb/sec produces a velocity of 890 ft/sec at the leading edge in the test section. The stagnation line heat flux is 670 Btu/sec-sq ft based on a wall temperature of 2000°R. The test unit boundary layer will be laminar and the predicted average convective heat flux is approximately 50 Btu/sec-sq ft. Since the tunnel wall is made of zirconium oxide, ZrO_2, there is little conduction loss. Hence, the convective heat load incident on the tunnel wall was rejected primarily through radiation to the test unit. At a steady state, the net radiative heat flux of 24 Btu/sec-sq ft equals the convective heat flux to the tunnel wall. The test conditions which meet the requirements of the stagnation line do not produce the flight condition heating to the flat surfaces. By having a 6-in. straight section upstream of the test sections so that $Re \simeq 5 \times 10^5$, turbulent conditions increased convective heating. The tunnel wall equilibrium temperature was 3320°R and a net radiative heat flux of 24 Btu/sec-sq ft occurred. The total net heat flux to the side wall of the test unit will be 64 Btu/sec-sq ft, which is very close to what the outer surface of the flight engine cowl will receive. No attempt was made to simulate the higher heat flux encountered on the interior cowl surface.

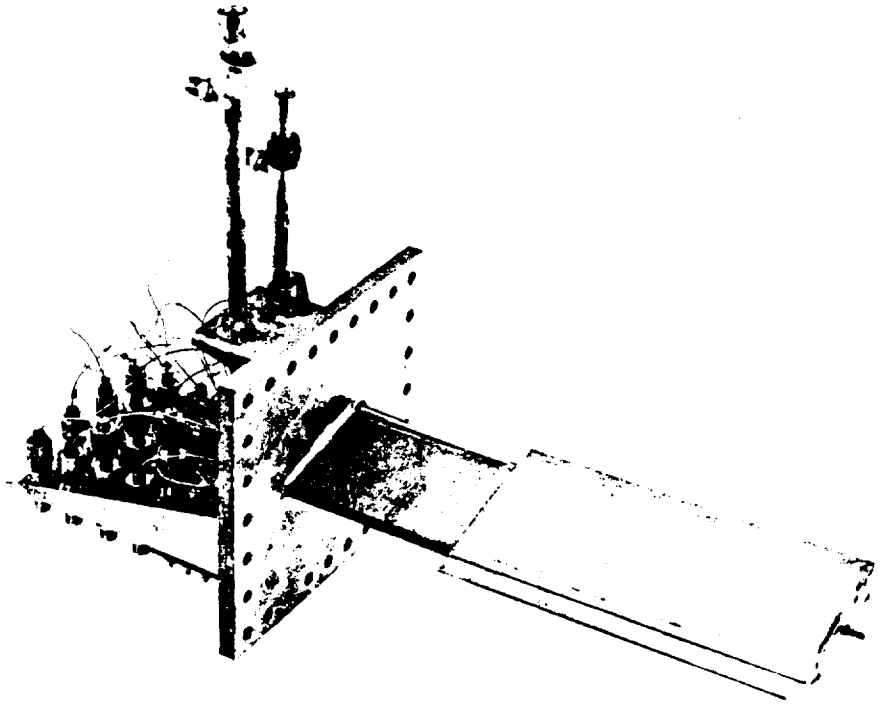

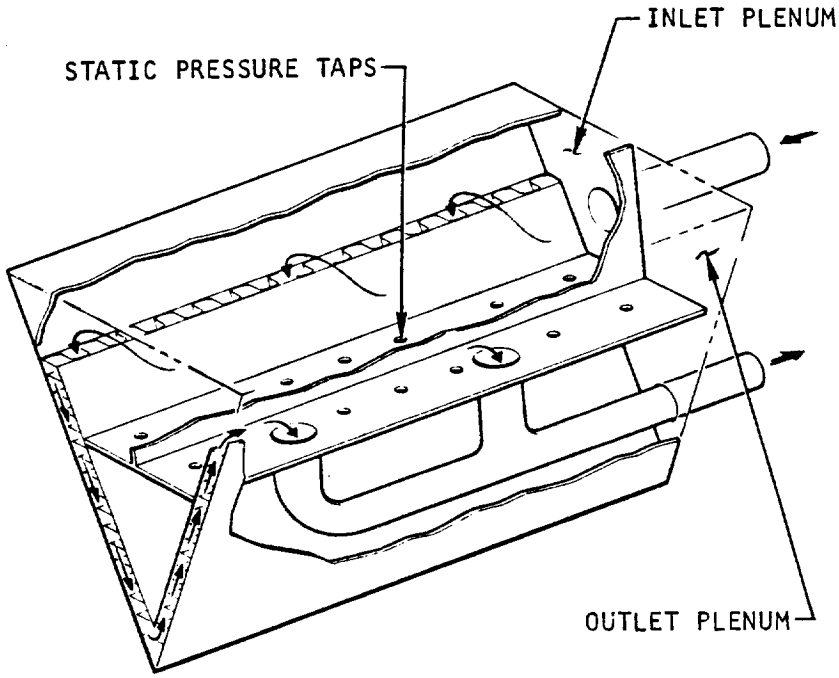

S-72424

Figure 5.5-8. Leading Edge Test Section

UNCLASSIFIED

NOTES:
1. ALL DIMENSIONS ARE IN INCHES
2. INTERIOR WALLS (EXCEPT THE MODEL) ARE TO BE LINED WITH ZrO_2 OR EQUIVALENT
3. WIDTH OF CHANNEL = 8 INCHES
4. ZrO_2 WALL NOT TO SCALE

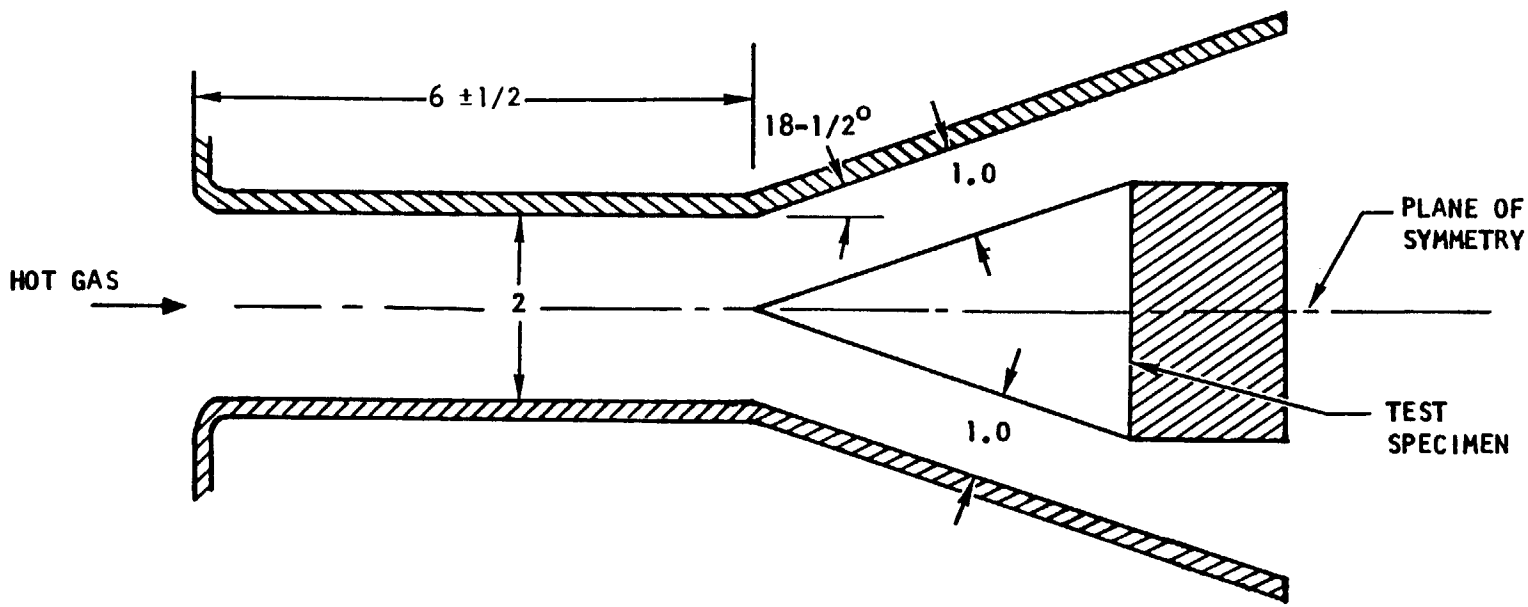

Figure 5.5-9. Schematic of Test Apparatus

UNCLASSIFIED

5.5.4.3 Structural Design

The outerbody leading edge test section was analyzed in order to evaluate possible configurations. Figure 5.5-10 shows the results of the investigation. Cases 1 and 5 can support the 100-psi external pressure while the other combinations are not satisfactory.

Combined axial and bending stresses due to 700 psi internal coolant pressure at the leading edge in the vicinity of the stagnation point will be around 8140 psi. Temperatures during testing will create plastic strains, but the magnitude of these strains will be such that the expected number of allowable cycles will exceed 4000 if the maximum ΔT does not exceed 300°F, and the maximum metal temperature will be below 1550°F.

Fins at the leading edge will be 20R-0.020-0.003. The margin of safety is 0.112 based on the combined loads due to 700 psi internal pressure and the differential radial expansion of the face metal and using a fin efficiency factor of 0.33.

The analysis revealed that the maximum allowable span of 0.015-in.-thick Hastelloy X sheet would be less than 0.1 in.

5.5.5 Outer Shell

5.5.5.1 Cooling Design

Hardware changes, which improved the coolant hydrogen flow distribution around thestrut cutout headers in the outer shell, were discussed in conjunction with similar changes on the inner shell (Section 5.5.2.1).

5.5.5.2 Structural Design

The maximum tensile strength due to circumferential gas pressures is 27,500 psi which results in a margin of safety of +0.14.

An analysis was performed to ascertain the adequacy of the 0.06-in. primary wall in resisting shear buckling.

For a maximum ℓ = 10.4 in. and a design T = 1200°F, the calculated value of the buckling stress, S_s, is 20,000 psi; the allowable value of S_s is 13,400 psi.

The maximum shell shear stress occurs at the forward mount ring, assuming simple sinusoidal shear flow distribution; the maximum actual shear stress,

$$\tau_{max} = 4960 \text{ psi} \ll 13{,}400 \text{ psi}$$

the margin of safety,

$$M.\ S. = \frac{13400}{4960} - 1 = +1.7$$

OUTERBODY LEADING EDGE TEST SECTION

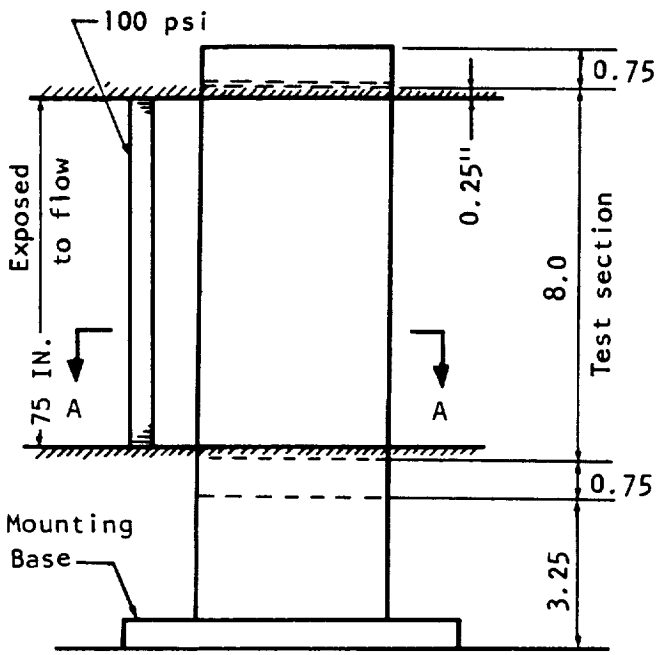

SIDE VIEW

CASE		CONFIGURATION	MARGIN OF SAFETY
0.015 0.015	1		0.03
	2		-0.762
	3		-0.362
0.015 0.060	4		-0.512 (0.065) -0.646 (0.015)
	5		0.96 (0.060) 0.43 (0.015)

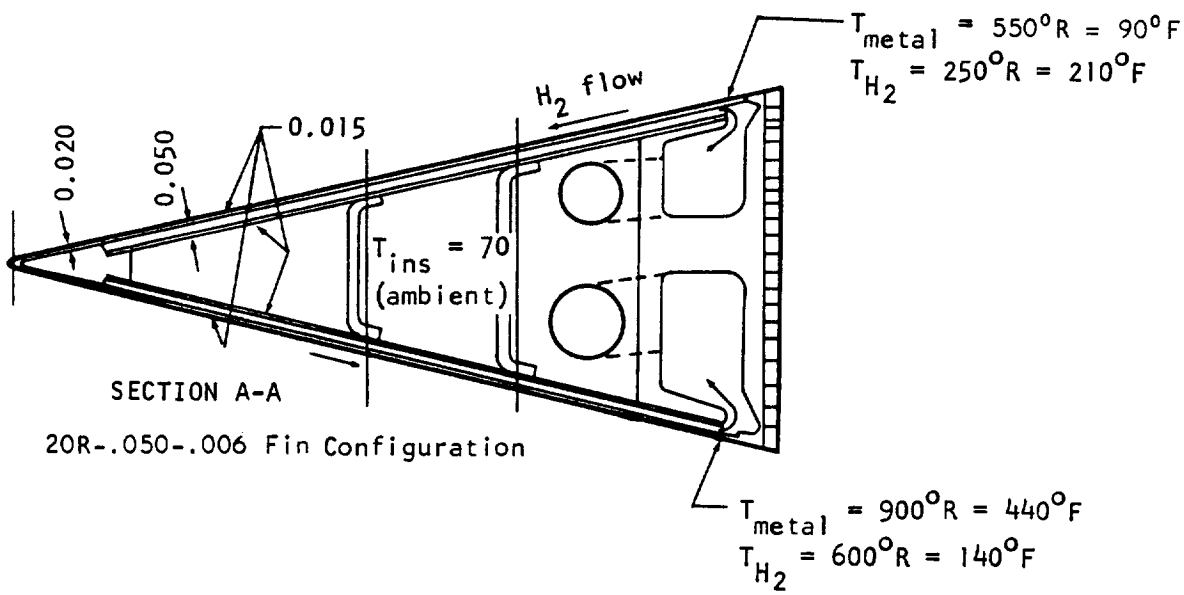

A-27910

Figure 5.5-10. Outerbody Leading Edge Test Section

The critical stresses due to pressure occur where the coolant exits to the collector manifold. The geometry in this area and the calculated metal temperatures are shown below.

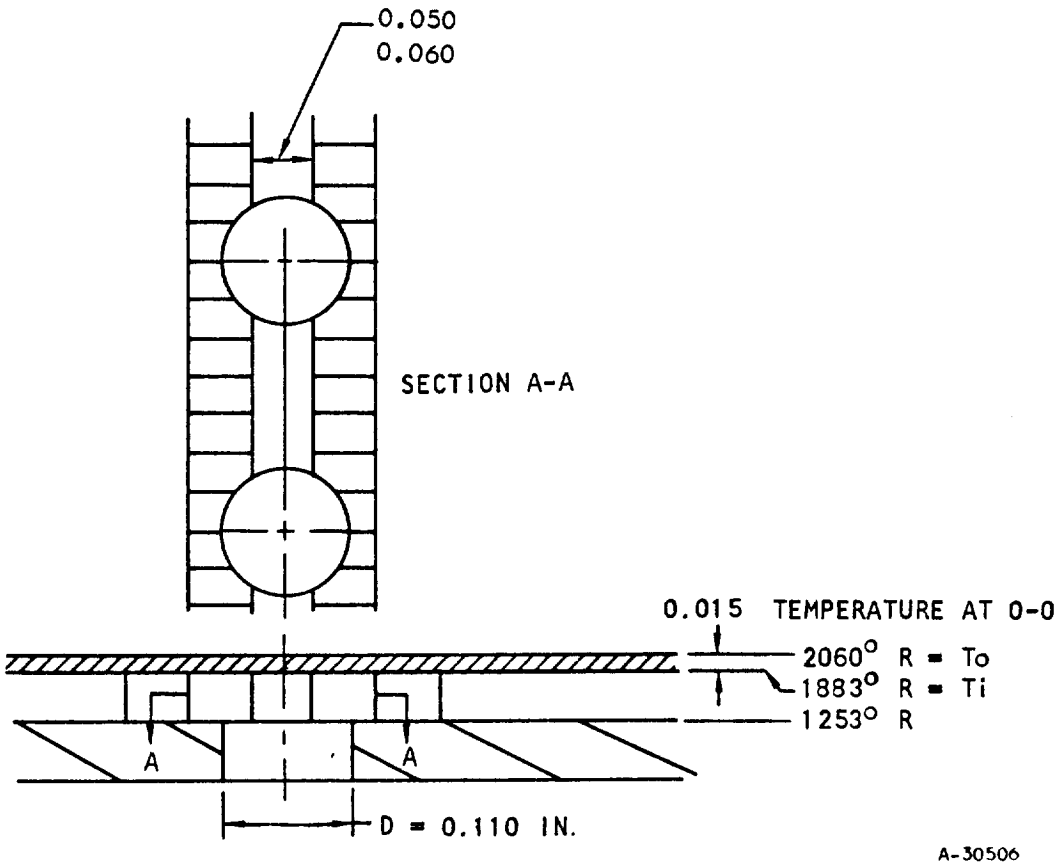

The pressure and temperature conditions are as follows:

(a) Operating (critical and used in design)

P = 628 psi

T = as indicated in above sketch

(b) Proof pressure

P = 1050 psi

T = room temperature (RT)

The conditions for Hastelloy X are tabulated below.

Design Temp, °R	Design Temp, °F	F_{tu}, psi	F_{ty}, psi	10-hr Creep-Rupture Stress, psi	Allowable Stress, psi
RT	RT	120,000	52,000	-	44,200
1923*	1463	62,000	32,000	26,000	17,300
2081**	1621	40,000	26,000	15,000	10,000

*Design temperature = T_{calc} + 100°F

**Design temperature = T_{out} -1/3 (T_{out} -T_{in}) + 100°F

The maximum bending stress in the thermal wall is equal to 10,000 psi, which results in a zero margin of safety. The fin stress is equal to 12,600 psi, with a resulting margin of safety of 0.38. A test section with the indicated gap-fin geometry was pressure tested to verify the design and found satisfactory.

5.5.6 Support Struts

5.5.6.1 Engine Assembly Struts Cooling Design

The purpose of cooling design and analyses for the strut was to determine the simplest hydrogen coolant flow routing and passage geometry required to (1) maintain all aerodynamically heated surface temperatures below 2060°R, (2) maintain structural temperature differences between strut and adjacent innerbody and outer shell below 300°R, (3) provide a coolant pressure drop less than 100 psi, and (4) keep fin temperature differences generally below 400°R (higher localized fin temperature differences are acceptable).

The selected strut design (Phase II, Concept II) is shown schematically in Figure 5.5-11. This design was developed from two previous designs (1) the Phase I strut design, and (2) a design considered at the start of Phase II (Concept 1). Coolant for strut sides is taken from the aft outer shell at the structural support torus, which is located at axial Station 69 in the Mach 8 geometry, and delivered to the aft of each of the six struts. The flow to the strut sides is distributed to 20R-0.020-plain-0.004 rectangular fins that are oriented parallel to the engine axis. Coolant flow paths on the sides are not identical with respect to the strut innerbody because of space limitations. The trailing edge is cooled with coolant flowing through 0.020-in.-deep grooves milled into the 3/8-in.-radius semi-cylindrical trailing edge. The trailing edge coolant subsequently provides coolant for one strut side. Coolant leaves the strut sides at about one inch aft of the leading edge and is routed directly to the innerbody fuel plenum. The strut leading edges are cooled separately from the sides with 100°R coolant flowing through a 0.13-in.-dia circular passage adjacent to the 0.015-in.-thick leading edge wall. Coolant from the

Design Schematic	Advantages	Disadvantages	Aero Heating Parameters Used in Analysis	Coolant and Pressure Drop Requirements
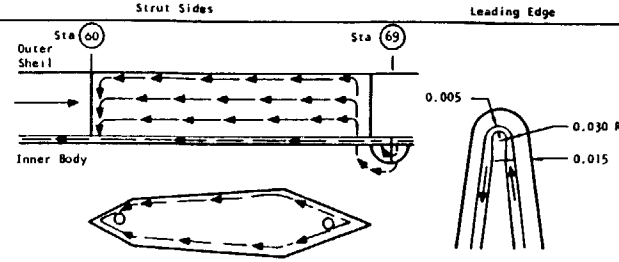 Phase I (Dwg No. 950007)	1) Acceptable structural ΔT's with inner body and outer shell (<300°R) 2) Surface temperature and fin ΔT's OK except at L.E. with 2180 Btu/sec ft^2 L.E. heat flux	1) 0.005" gap at L.E. unacceptable to manufacturing 2) Coolant concept cannot cool L.E. under new heat flux conditions (2180 Btu/sec ft^2) 3) Recombination of strut flow and inner body flow at station 60 unacceptable to manufacturing	1) At L.E. tip, q = 1080 Btu/sec ft^2 2) H_{avg} = 0.065 Btu/sec ft^2 °R T_{aw} = 5400°R on sides. See ref 1 for details	1) 0.07 lb/sec total for six struts including leading edges. Pressure drop = 50 psi. 2) 0.21 lb/sec in adjacent inner body passages or 0.28 lb/sec total in aft inner body route.
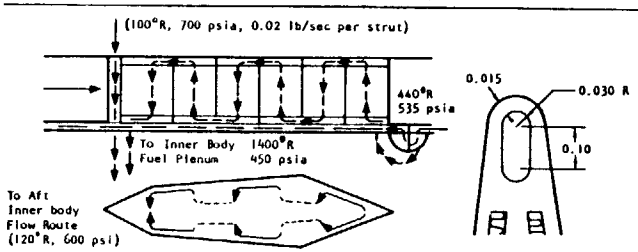 Phase II, Concept I (Dwg No. L-980606)	1) Acceptable structural ΔT's with inner body and outer body (315°R maximum excluding the effect of 100°R hydrogen in L.E. passage). 2) Surface temperatures and fin ΔT's OK	1) Leading edge tip temperature marginal (1980°R) 2) Strut manifolds reduce structural strength 3) Leading edge pressure drop marginal (OK if smooth transitions are made) 4) L.E. flow in parallel with remainder of aft inner body flow 5) L.E. metal ΔT's are approximately 1000°R	1) At L.E. tip, q = 2180 Btu/sec ft^2 2) H_{avg} = 0.085 Btu/sec ft^2°R T_{aw} = 5800°R on sides No details available	1) Side coolant = 0.094 lb/in. for six struts or 27% of aft inner body flow rate (0.34 lb/sec) Pressure drop = 85 psi 2) L.E. coolant = 0.12 lb/sec for six struts. Pressure drop = 100 psi if smooth transitions are used
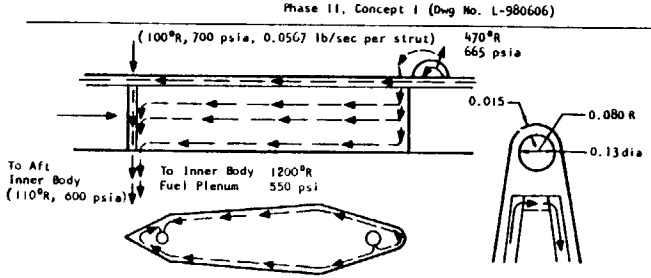 Phase II, Concept II (Dwg No. L-980608)	1) Acceptable structural ΔT's (>200°R, excluding 100°R hydrogen in L.E. passage 2) L.E. temperatures and pressure drop OK (no smooth transitions needed) 3) L.E. carries entire aft inner-body flow. 4) Surface temperature and fin ΔT's OK 5) L.E. metal ΔT's are reduced to approximately 600°R.	1) Design problem to equalize flow on strut sides	1) At L.E. tip, q = 1350 Btu/sec ft^2 2) H_{avg} = 0.093 Btu/sec ft^2 T_{aw} = 5800°R on sides See Table I for details	1) Side coolant = 0.165 lb/sec for six struts or about 25% of aft outer shell flow rate (0.64 lb/sec) Pressure drop = 115 psi 2) L.E. coolant = 0.34 lb/in. for six struts or 100% of aft inner body flow rate. Pressure drop = 100 psi without smooth transistors

B-12922

Figure 5.5-11. Summary of HRE Strut Cooling Design

six strut leading edges is collected and delivered to the aft innerbody at the nozzle cap. The leading edge radius was increased to 0.08 in. from 0.03 in. used in the two previous designs. An increased leading edge radius reduces the hot gas stagnation point heat flux, provides more coolant passage free-flow area and reduced coolant pressure drop. Neither coolant from the strut side nor adjacent innerbody or outer shell flow routes can be used to cool the strut leading edge because the coupled effects of high temperature and low pressure of these coolant sources is insufficient to guarantee an acceptable leading edge maximum temperature and coolant pressure drop.

The Phase I design point flight condition of Mach 8, 81,000-ft altitude (which the operating parameters in Figure 5.5-11 are based on) was superseded by the Phase II design condition of Mach 8 local, 88,000 ft altitude. The strut sides thermal performance and operating parameters for this condition are presented in Figures 5.5-12 and 5.5-13 and are acceptable from the design goal standpoint.

Strut component wind tunnel tests performed with the above selected strut design (Section 8.0) indicated that hot gas heat fluxes on the strut leading edges could be about 1.8-times heat flux values predicted by the methods used in the design analyses. This increase is thought to be due to a high freestream turbulence level and leading edge surface roughness, both of which may be present at the Mach 8 local, 88,000-ft altitude flight condition. If so, a plain round passage in the strut leading edge is not able to provide adequate cooling of leading edge metal temperatures. As discussed below, a nickel fin brazed into the leading edge passage provided acceptable metal temperatures.

A two-dimensional thermal analysis was performed on the leading edge for the Mach 8 local, 88,000-ft altitude condition with a strut leading edge coolant rate of 0.057 lb/sec at 100°R (one-sixth of the strut leading edges/innerbody flow rate of 0.34 lb/sec). Results for a round passage without a fin indicate a maximum outer wall temperature of 2600°R and an inner wall temperature of 2270°R.

To reduce strut leading edge temperature, a nickel fin was brazed in the coolant passage as shown in Figure 5.5-14. Two-dimensional thermal analyses have been performed with 0.020- and 0.040-in.-thick nickel fins. Maximum metal temperatures were reduced to 1790°R for the 0.020-in. fin and 1600°R for the 0.040-in. fin. The finned leading edge design offers high local pressure drop. In addition, the coolant heat transfer coefficient is increased because free-flow area is reduced, the coolant side wall temperatures are lower, and the hydraulic diameter is smaller. A 0.030-in.-thick nickel fin was used to yield temperature distributions between those for the 0.020- and 0.040-in.-thick fins. The pressure drop for the leading edge with a 0.030-in.-thick fin will be double that for a plain round passage. A pressure drop of 67 psi and outlet Mach number of 0.29 will result for Mach 8 design point conditions. Both of these values are acceptable.

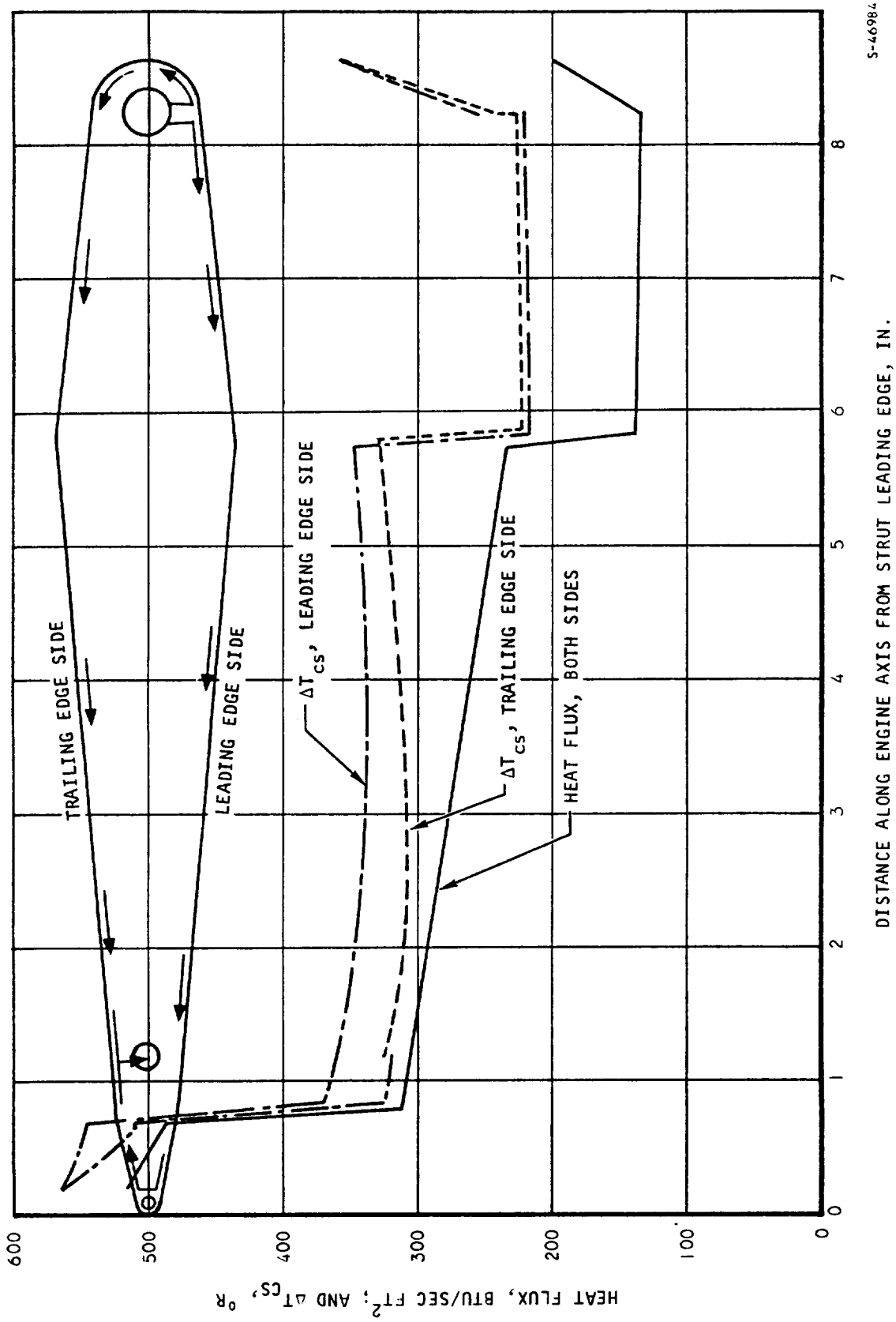

Figure 5.5-12. HRE Struts Thermal Performance

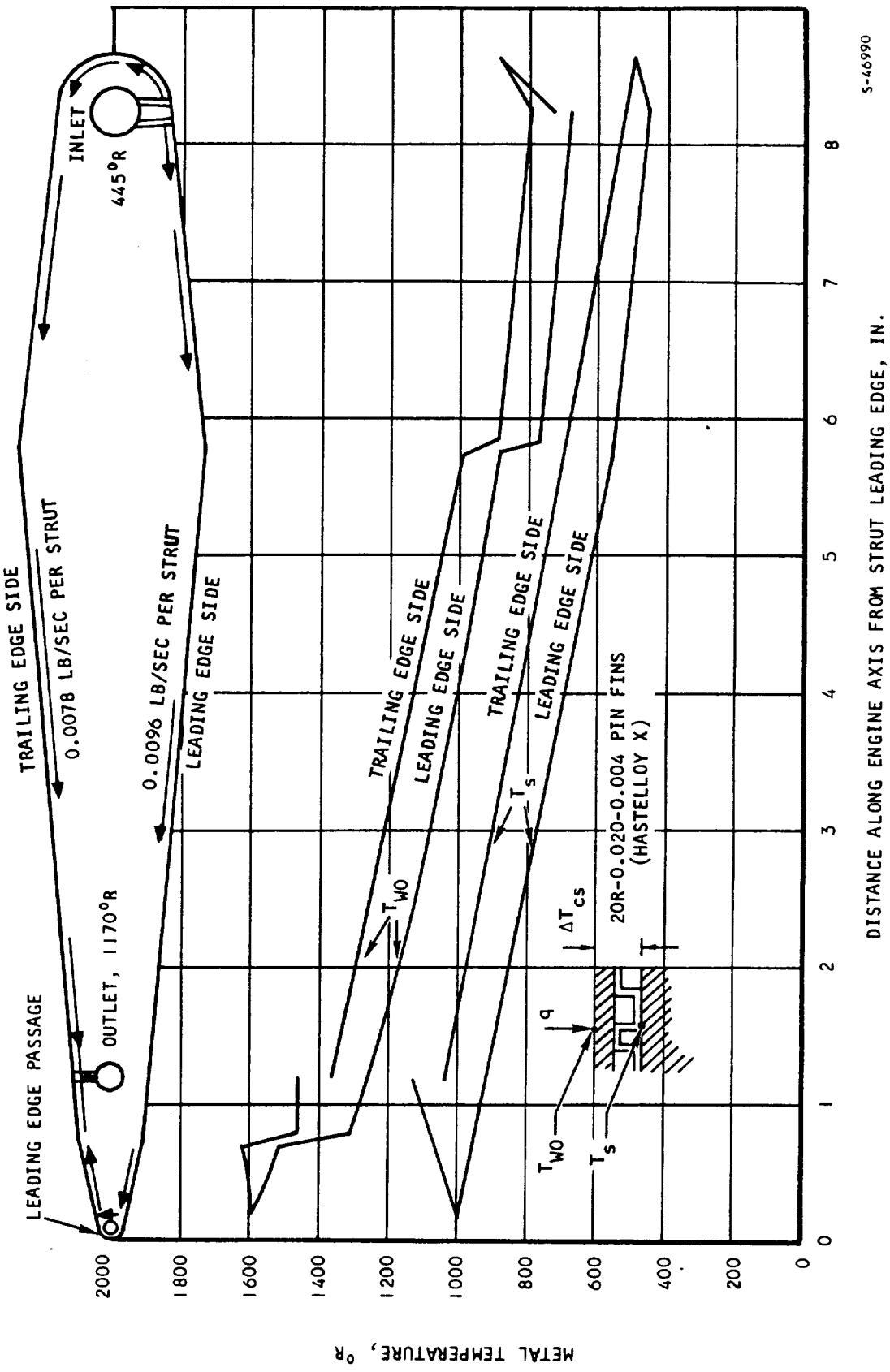

Figure 5.5-13. HRE Struts Thermal Performance

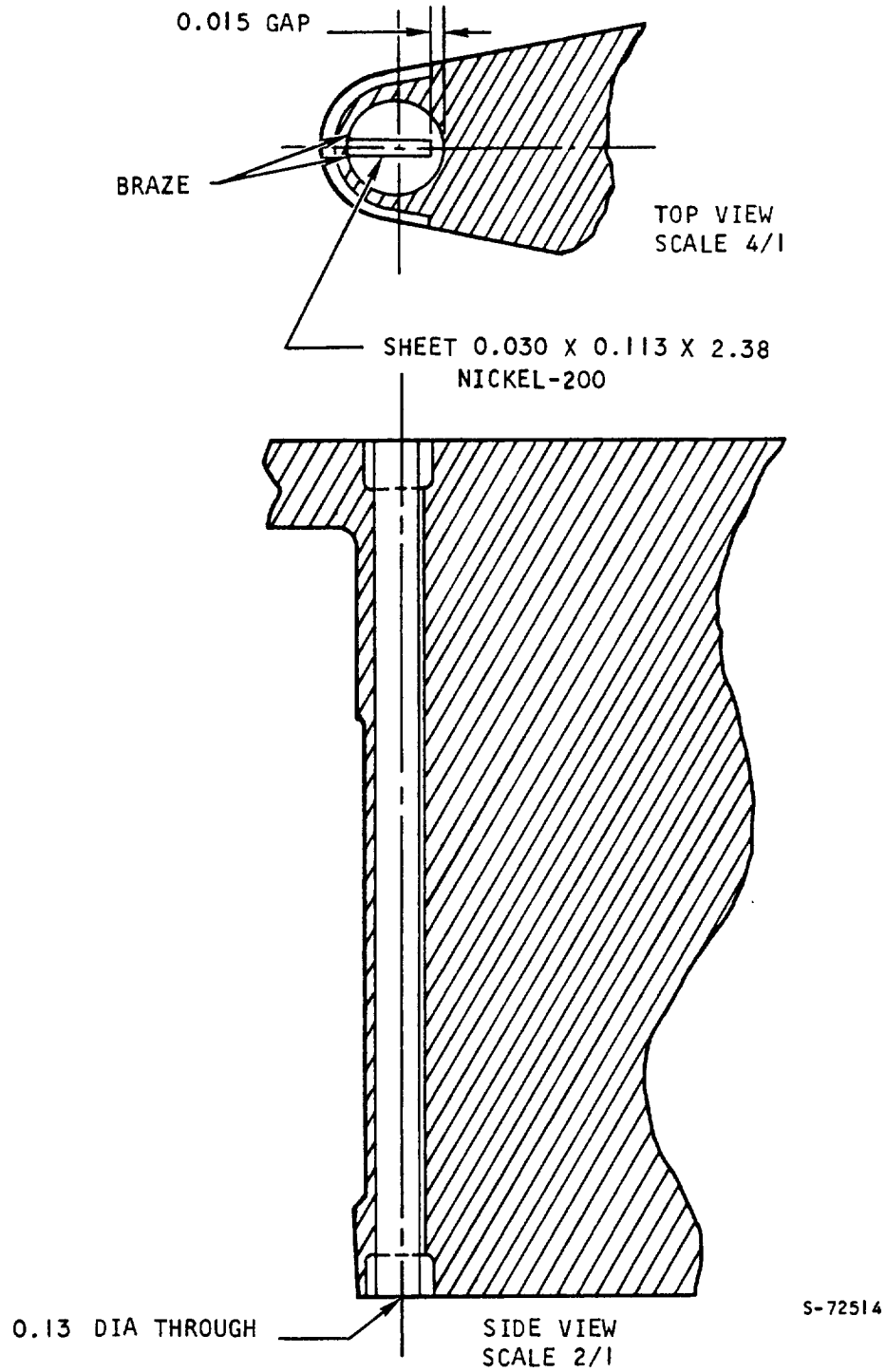

Figure 5.5-14. HRE Strut Leading Edge Fin Geomerty

5.5.6.2 Strut Test Section Cooling Design

Strut assemblies were subjected to aerodynamic heating tests. The tests were conducted in a 1.5-in.-high by 6-in.-wide Mach 2 tunnel. Confirmation and improvement of analytical techniques for leading edge heating, shock boundary layer interaction, and general heat transfer in the environment of hydrogen combustion products was obtained with a wall-to-hot-gas total temperature ratio of about 0.25. Test data, however, was limited by tunnel width, total temperrature, and incomplete simulation of fuel-injection conditions.

The tunnel nozzle was approximately 12 in. long, as measured from the sonic throat to the exit. Butted against the exit was the test section, which consisted of a 2-in.-long adapter section, a strut supported between two 6-in. by 4 in. panels, and two side walls. A water-cooled test section, formed from four separate walls and sealed at the corners, was used to obtain good quality aerodynamic heating data with a water-cooled strut. Hydrogen-cooled strut support panels and hydrogen cooling in the strut were substituted for the water-cooled top and bottom panels during thermal cycling tests.

The maximum operating reservoir pressure and temperature available for this test were 300 psia and 4500°R, respectively. The corresponding flow rate was 6.2 lb per sec. A small amount of leakage at the joint between the tunnel and the test section and at the corners was deemed permissible. The tunnel geometry and instrumentation are shown in Figure 5.5-15 and the heating distribution on the supporting panels is shown in Figure 5.5-16. In Figure 5.5-16, the centerline wall heating is shown as a dashed line, marked Y = 0, and the heating distribution at midway between the centerline and the side wall is shown as a solid line, marked Y = 1-1/2. The trough and peak heat fluxes reflect the effects of the shock-induced flow separation. The peak heating is a conservative value because theory indicates that the flow separation at Y = 1-1/2 is marginal.

Since the tunnel is 6 in. wide, the reflection of the strut/leading edge shock from the tunnel walls will impinge at about 70-percent chord of the 9-in.-long full-scale strut, if full-length side walls are used. Short side walls extending only 2.75 in. aft of the strut leading edge appear to be beneficial. In this arrangement of the wall, the strut leading edge shock will not be intercepted and reflected; the exit wave produced by the walls (assuming the system is underexpanded), however, will impinge on the strut at approximately the 90-percent chord.

The maximum heat flux during the test was produced when the tunnel was operated at its peak pressure and temperature (P_t = 300 psia, T_t = 4500°R). At this operating condition, the leading-edge heat flux is 690 Btu/sq ft-sec, which is approximately half of that estimated for the flight engine at the critical heating conditions of Mach 8, local 88,000-ft altitude. The average flux on the strut supporting panels under the same test conditions will be 300 Btu/sq ft-sec, which is higher than the 250 Btu/sq ft-sec predicted for the flight engine at Mach 8, 88,000-ft altitude.

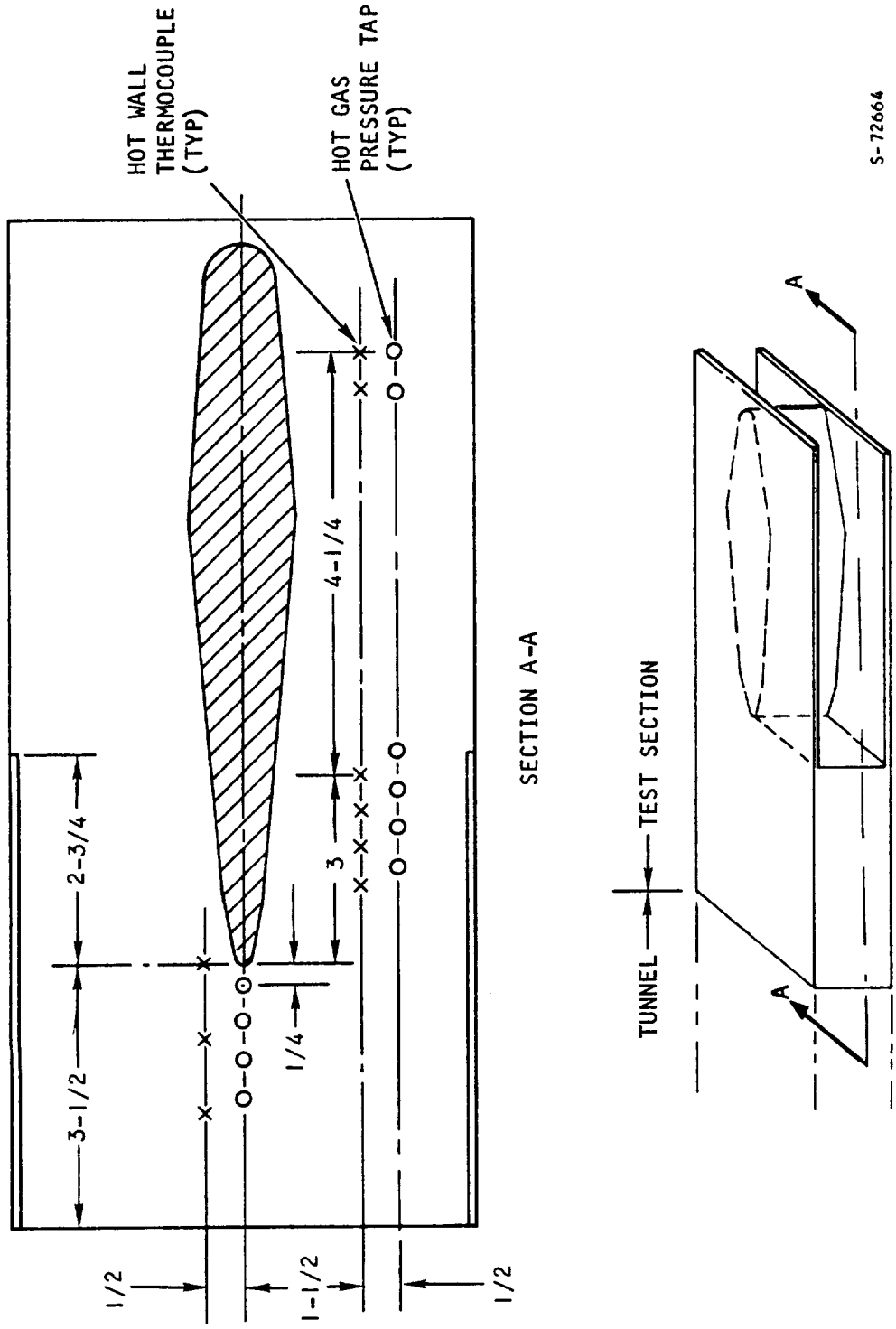

Figure 5.5-15. Strut Test Section Instrumentation

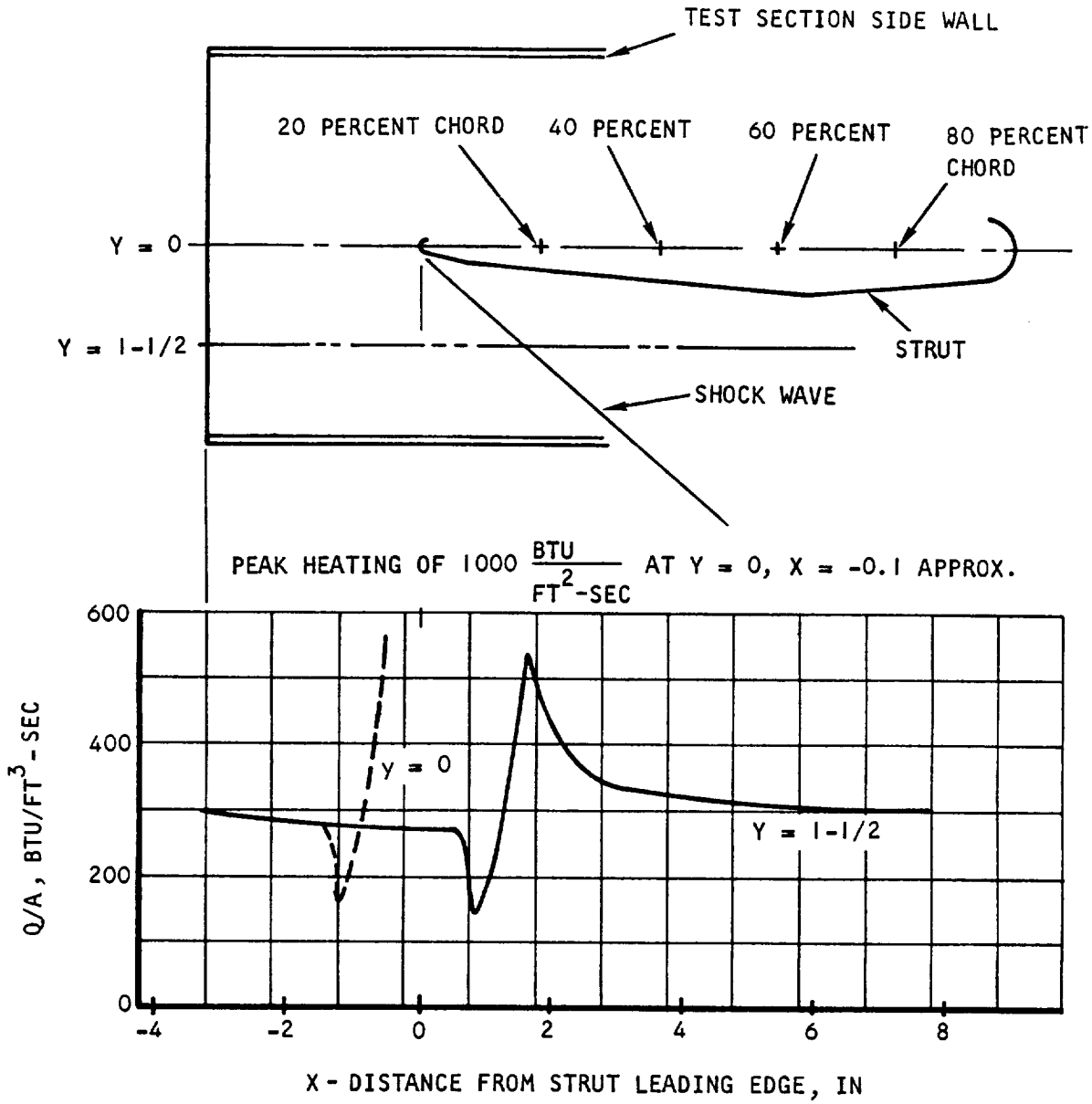

P_{TO} = 300 PSIA

T_{TO} = 4500 °R

M = 2.3

GAS COMPOSITION

40 PERCENT H_2O

24 PERCENT O_2

36 PERCENT N_2

S-72671

Figure 5.5-16. Strut Support Panels Hot Gas Heat Flux Distribution

All metal temperatures and metal ΔT's predicted for test were satisfactory, with the possible exception of those along the line of shock impingement on the support panels caused by the strut/leading-edge bow shock. Along this line, the predicted hot-gas heat flux is a minimum of 1000 Btu/sq ft-sec at about 0.10 in. upstream of the leading edge and decreases to 530 Btu/sq ft-sec at 1-1/2 in. from support panel centerline (see Figure 5.5-16). A one-dimensional heat transfer analysis indicates that the fin ΔT could be 1000°R on the support panel where the heat flux is 1000 Btu/sq ft-sec. Two-dimensional conduction effects in the 0.015-in. skin and in the 20R-0.075-0.100(0)-0.004 fins in the support panel will decrease the fin ΔT slightly from 1000°F. The region of the strut leading edge received close observation during testing. Hot surface thermocouple data and discoloration of temperature-indicating paint on panel surfaces were expected to indicate whether the level of predicted high heat flux did occur.

5.5.6.3 Engine Assembly Struts Structural Design

A series of unit load flexibility analyses were performed to obtain an accurate picture of the internal reactions at the actuator supports and at the connection of the struts to the inner and outer shells. Unit forces and moments were assumed to act on the actuator at its forward mount face (Station 42.10). An equivalent ring was determined which accounted for the rigidity contributions of the inner and outer shells and manifolds in the strut area. Zero deflection and rotation were assumed at the top of this ring. The model became:

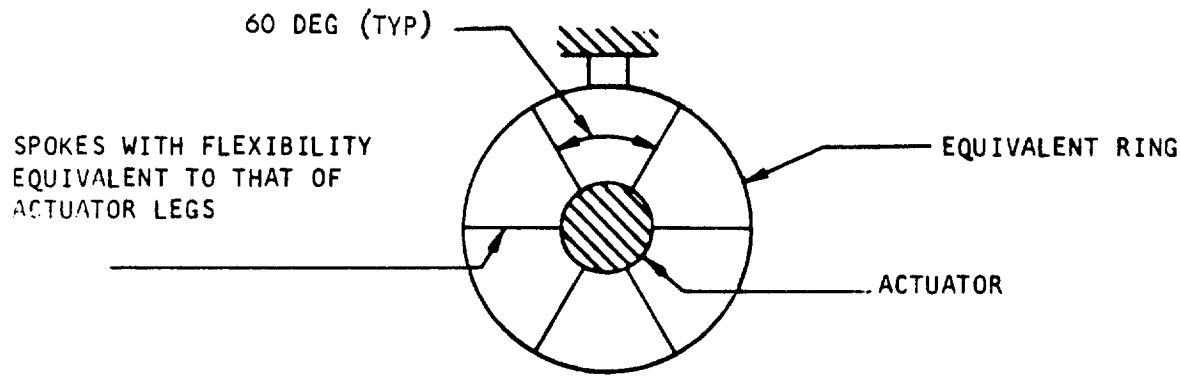

Figure 5.5-17a shows the structure reactions to the critical applied load condition. These reactions are located at a radius of 10.4 in. and at Station 65.05. Figure 5.5-17b shows the loads at the top and bottom strut resolved into radial and tangential components. In Figure 5.5-18, the significant components of these loads are translated to the plane of the actuator support pad and become the design loads for the actuator support structure.

a. REACTIONS

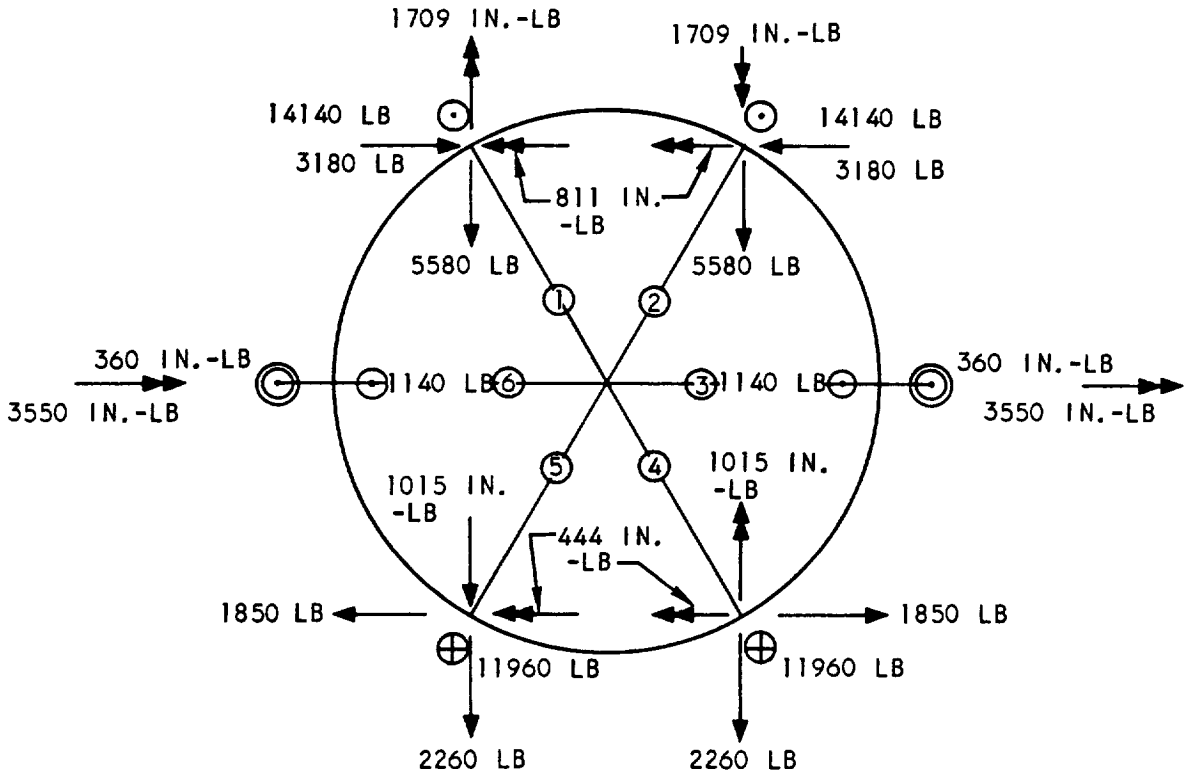

b. RADIAL AND TANGENTIAL COMPONENTS OF REACTIONS AT STRUTS ① AND ⑤ (INCREASED BY DYNAMIC LOAD FACTOR 1.2)

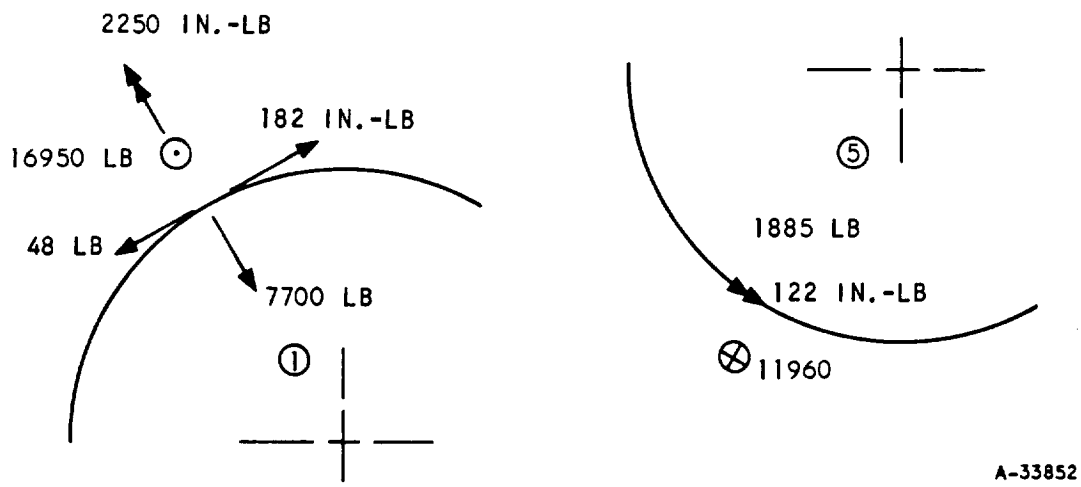

Figure 5.5-17. Reactions to Unsymmetrical Unstart Loads (Radius) 10.4 in., Sta 65.05)

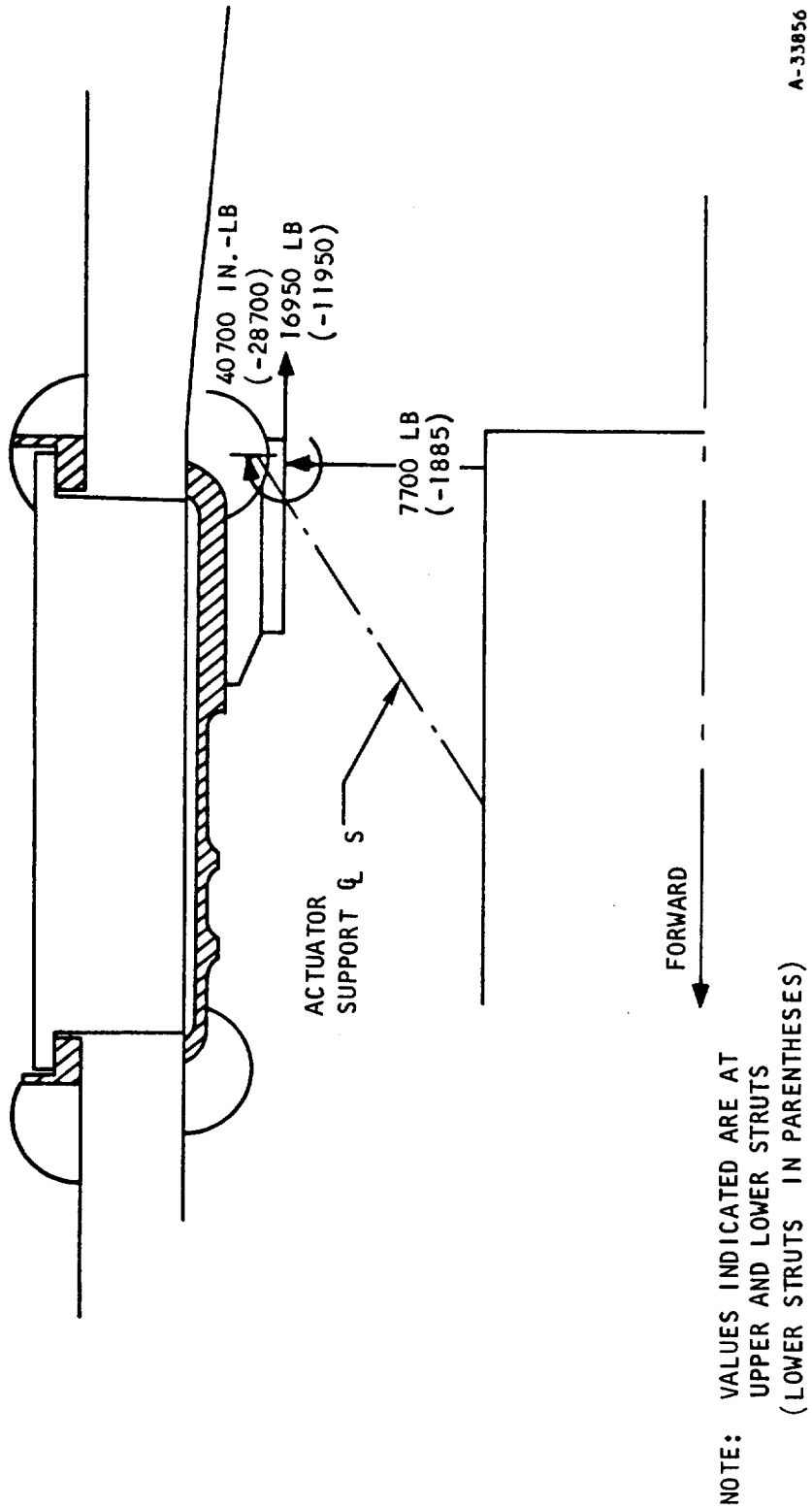

Figure 5.5-18. Design Loads-Actuator Support Structure

Once the unit load reactions were found for the single equivalent ring, the opposite action values were applied to a system of two rings and struts. Each ring is an equivalent ring which takes into account the flexibility of the corresponding shell-manifold combination. The model is indicated below.

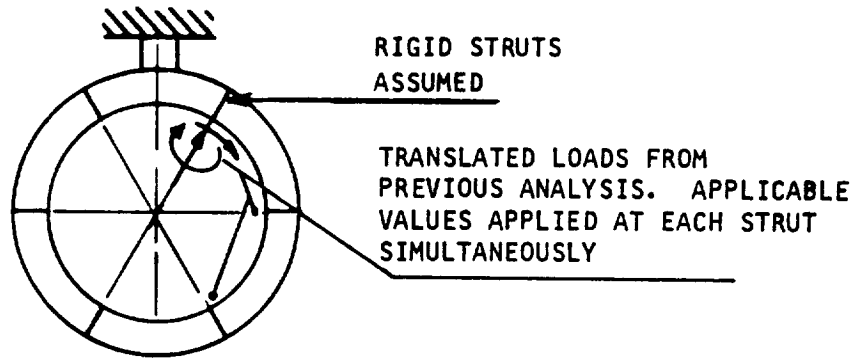

Figure 5.2-7b (see Section 5.2.2.1.2) showed the design loads for the strut and attachments at the inner and outer shells which result from this analysis.

The strut structural analysis was concentrated on the two most significant areas:

(a) Leading edge pressure containment, and low-cycle fatigue analysis

(b) Strut attachment flanges and bolting

Three leading edge configurations and radii were investigated. The number of expected life cycles was quite low (around 230) making the strut leading edge one of the shortest life-cycle limited items of the engine.

The analyses of the strut flanges indicate that high torsional moments (approximately 53,000 in.-lb) were developed in the upper two struts. This moment, combined with the other shear loads, required that the bolts attaching the strut to the innerbody socket be made of Inconel 718 (or equivalent strength material). In addition, the two end bolts, i.e., those at the forward and aft attaching innerbody manifolds should be made 3/8 in. and 1/2 in. dia, respectively. The sockets had to be strengthened so that the highly loaded bolts did not shear through. Increased bending loads in the plane of the struts required that the actuator mount pad bolts be made of Inconel 718 with the diameter increased to 3/8 in. The same bending load also required that the ribs from the socket to the attaching manifolds be made stronger. The loads in the remaining four struts were lower, and these portions of the structure could be made lighter.

5.5.7 Inlet Spike Actuation Control System

A structurally integrated support structure and actuator system controls the spike position as commanded by the control system computer.

5.5.7.1 Design Concept

Four concepts were investigated as potential candidates for use with a hydraulic servoactuator. These systems included (1) a solid-propellant gas generator exhausting through a pressure control valve, (2) X-15 hydraulic system to drive a motor/pump, (3) X-15 hydraulic system without the interfacing motor/pump, and (4) the selected system, which consists of a 5750-psi nitrogen supply blowing down through a pressure regulator to 3000 psi. Hydraulic oil is then expelled from the accumulator to drive the servoactuator. A schematic diagram of the complete system is shown in Figure 5.5-19.

Table 5.5-1 compares the relative merits of each system. In view of the most critical tradeoffs, the selected system is the least complex, has the least volume, and is second in overall weight to the hot gas system.

TABLE 5.5-1

COMPARISONS OF INLET SPIKE ACTUATION SYSTEMS

Item	System (1)	System (2)	System (3)	System (4) (Fig. 5.5-15)
Weight (less servo and actuator)	21.84	35.0	45.0	29.29
Complexity	3rd	Most	2nd	Least
Component volume required	2nd	Most	3rd	Least
Reliability	Least	3rd	2nd	Most
X-15 power required				
a) Electrical*	Yes	No	No	Yes
b) Hydraulic	No	Yes	Yes	No
Growth potential (extended operation)	(Requires resize)	(Indefinite as is)		(Requires resize)
Checkout capability	Partial	Standard	Standard	Partial

*Not including servo or systems which require 28 vdc, 8 to 10 ma

5.5.7.2 Design Loads

The critical structural loads and actuator forces produced are due to symmetrical and asymmetrical engine unstart operation at $M_\infty = 8.0$ and $M_L = 6.5$, based upon operation at the $q_\infty = 2000$ psf and $q_L = 3600$ psf condition.

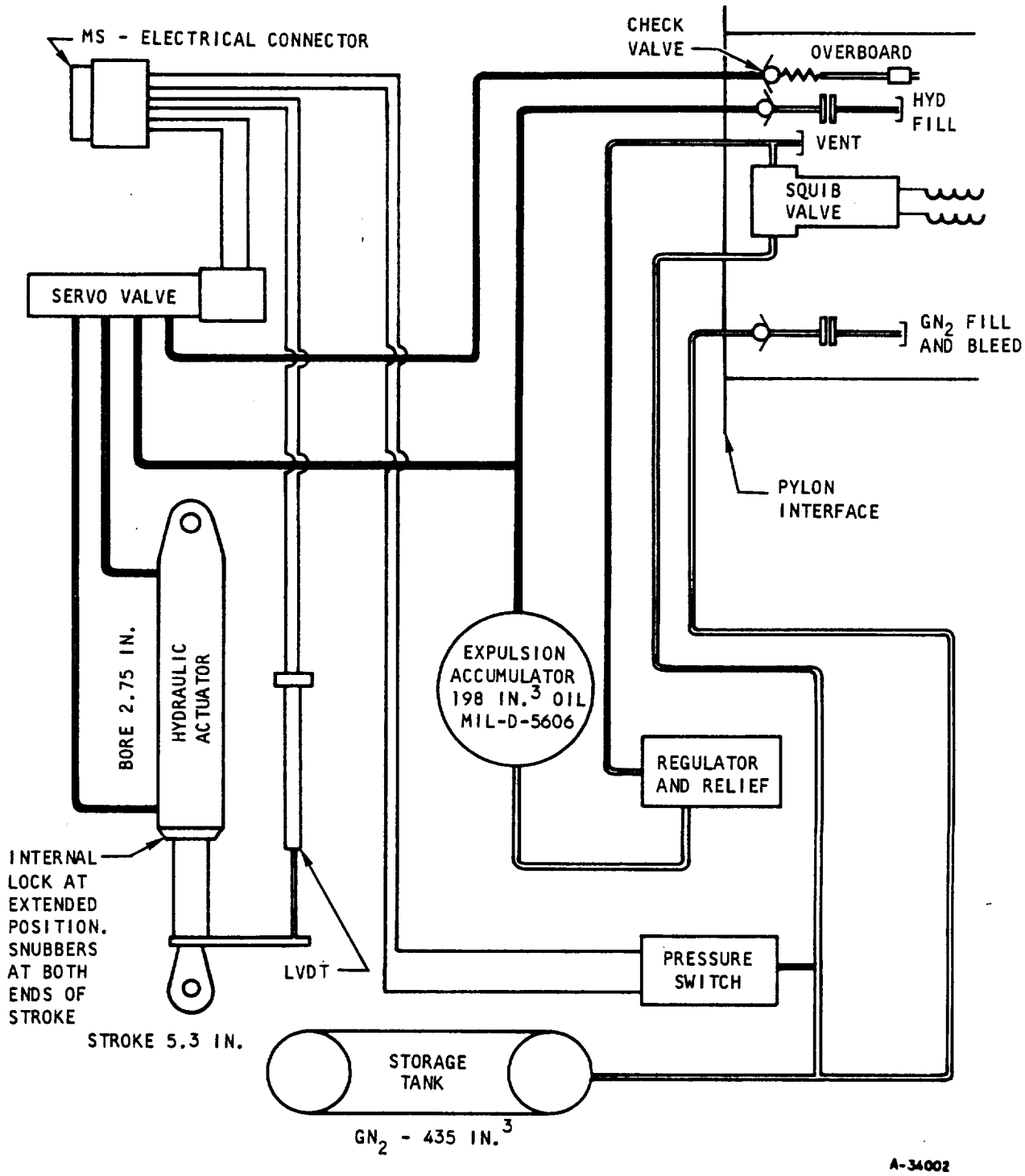

Figure 5.5-19. Inlet Spike Actuation System - Nitrogen Blowdown System

Since the opening loads in flight always exceed the closing loads, the design criteria for opening are established by the friction forces during ground checkout. The axial design load for closing during flight occurs during the symmetrical unstart.

The actuation system sizing is covered in detail in Section 5.2.2.1.1.

5.5.7.3 Structural Design

5.5.7.3.1 Stresses in Actuator Support Structure

The actuator support structure and superimposed loads for the asymmetric unstart condition are shown in Figure 5.5-20. Similarly, Figure 5.5-21 shows the loads for symmetric unstart.

The analysis was carried out by applying unit loads and moments of 1000 lb to 1000 lb-in., respectively, at the mounting plane of the actuator. The load flow results for these unit loads are presented in Figures 5.5-22 and 5.5-23.

Since the unstart loads are applied suddenly, a shock magnification factor of 1.6 was used for these loads, and stresses were computed at the various critical locations of the actuator structure. The cylinder thicknesses were reduced to 0.300 in. (as compared to 0.450 in. previously). Consideration of seal stiffness in the analysis has shown that the aft spike will not contact the innerbody in spite of the reduction in actuator shell thicknesses.

The maximum stress in the cylinder occurs at the intersection between the support legs and the outer cylinder shell. This stress is 90,000 psi, and it includes consideration of the localized stress concentration. The front conical element which picks up the front end of the actuator rod was analyzed with the Sabor III (MIT) computer program. The peak stress in this part was less than 54,000 psi. The pivot lug was analyzed, and the maximum principal stress was 101,000 psi. The support legs were checked, and a maximum stress of 72,000 psi was computed. The flange mounting of the spike cone to the actuator uses 12-3/8-in.-dia bolts.

The actuator material for the cylinders and the mounting legs is 4330 alloy steel that is heat-treated to produce the following material properties at 300°F:

$$f_{tw} = 192{,}000 \text{ psi}$$

$$f_{ty} = 167{,}000 \text{ psi}$$

The allowable stress based upon the lower value of 0.667 f_{tu} or 0.85 f_{ty} is σ_{all} = 128,000 psi. All of the highly stressed actuator parts have less than this stress level and therefore have a positive margin of safety.

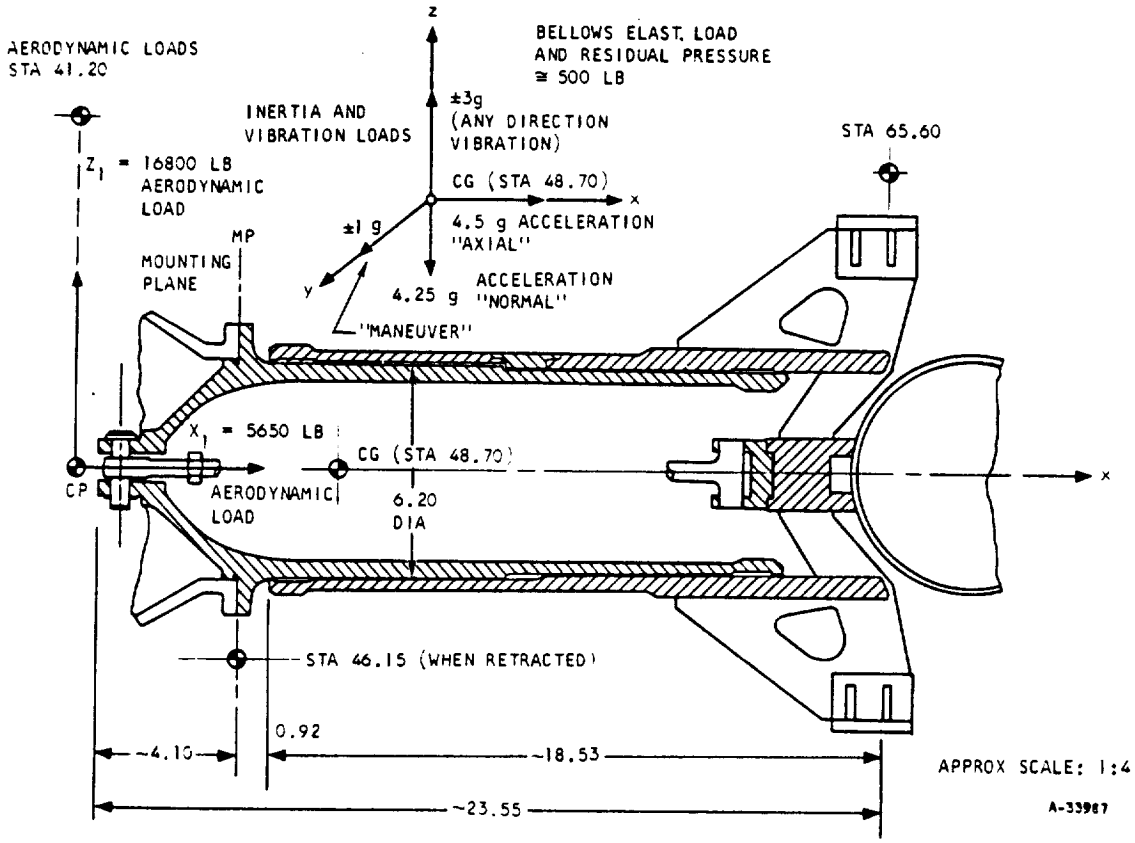

Figure 5.5-20. Actuator Loading With Unsymmetric Unstart

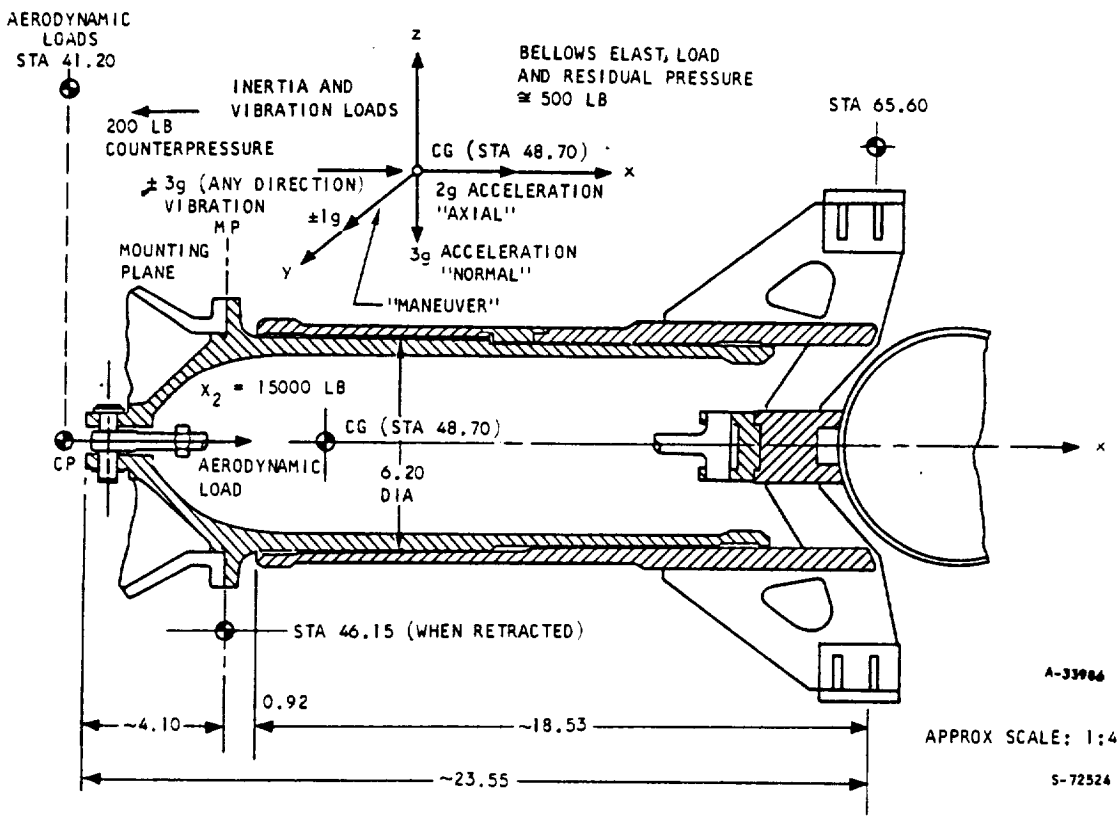

Figure 5.5-21. Actuator Loading With Symmetric Unstart

LOAD FLOW THROUGH INNER-OUTER SHELL
CONDITION: $\bar{Z}$ = 1000 LB

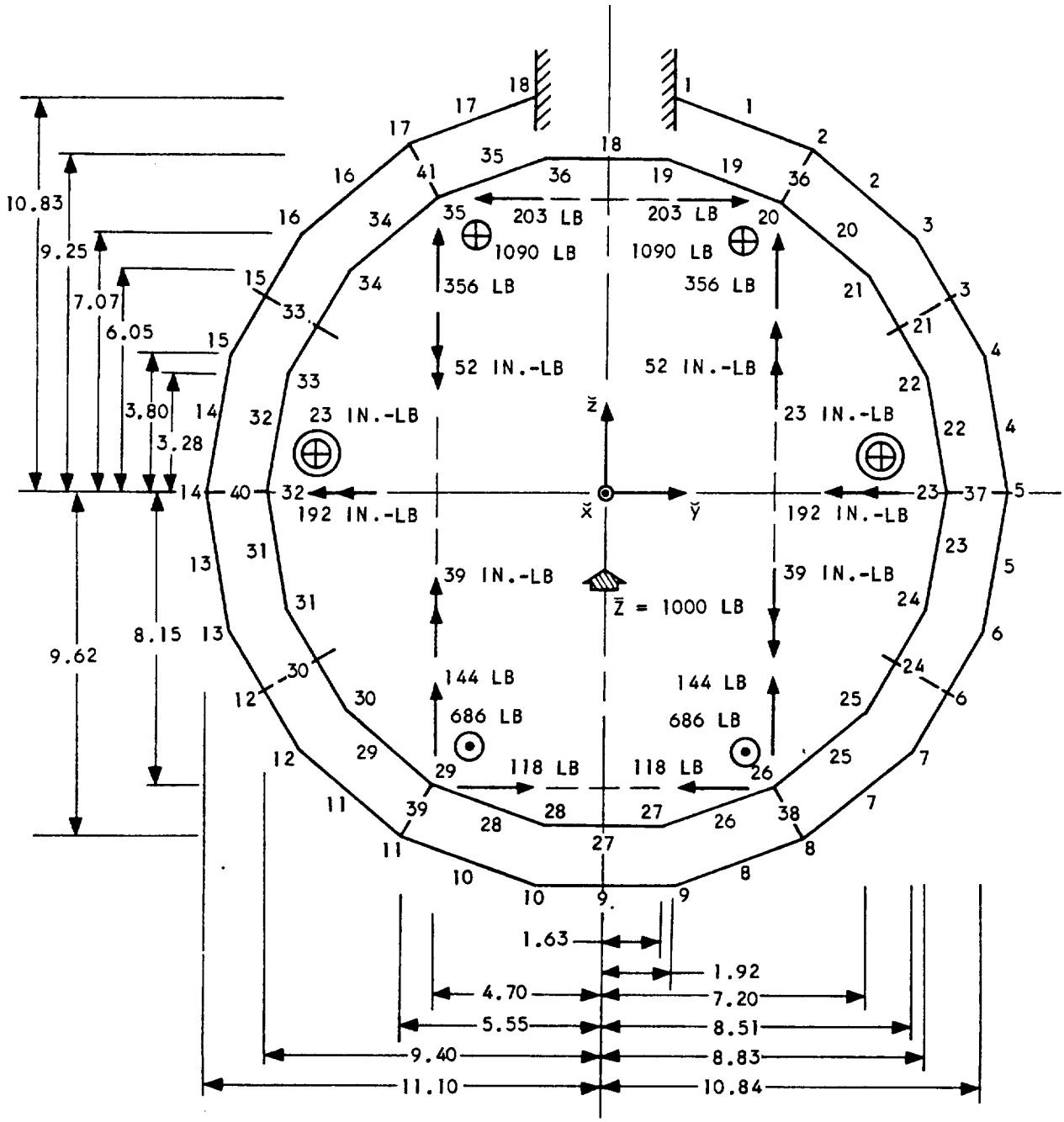

(THIRD ESTIMATE)

NOTE: ALL DIMENSIONS ARE IN INCHES

A-34005

Figure 5.5-22. Actuator Load Flow Due to 1000-lb Unit Load

LOAD FLOW THROUGH INNER-OUTER SHELL
CONDITION: $\bar{M}_y$ = 1000 IN.-LB

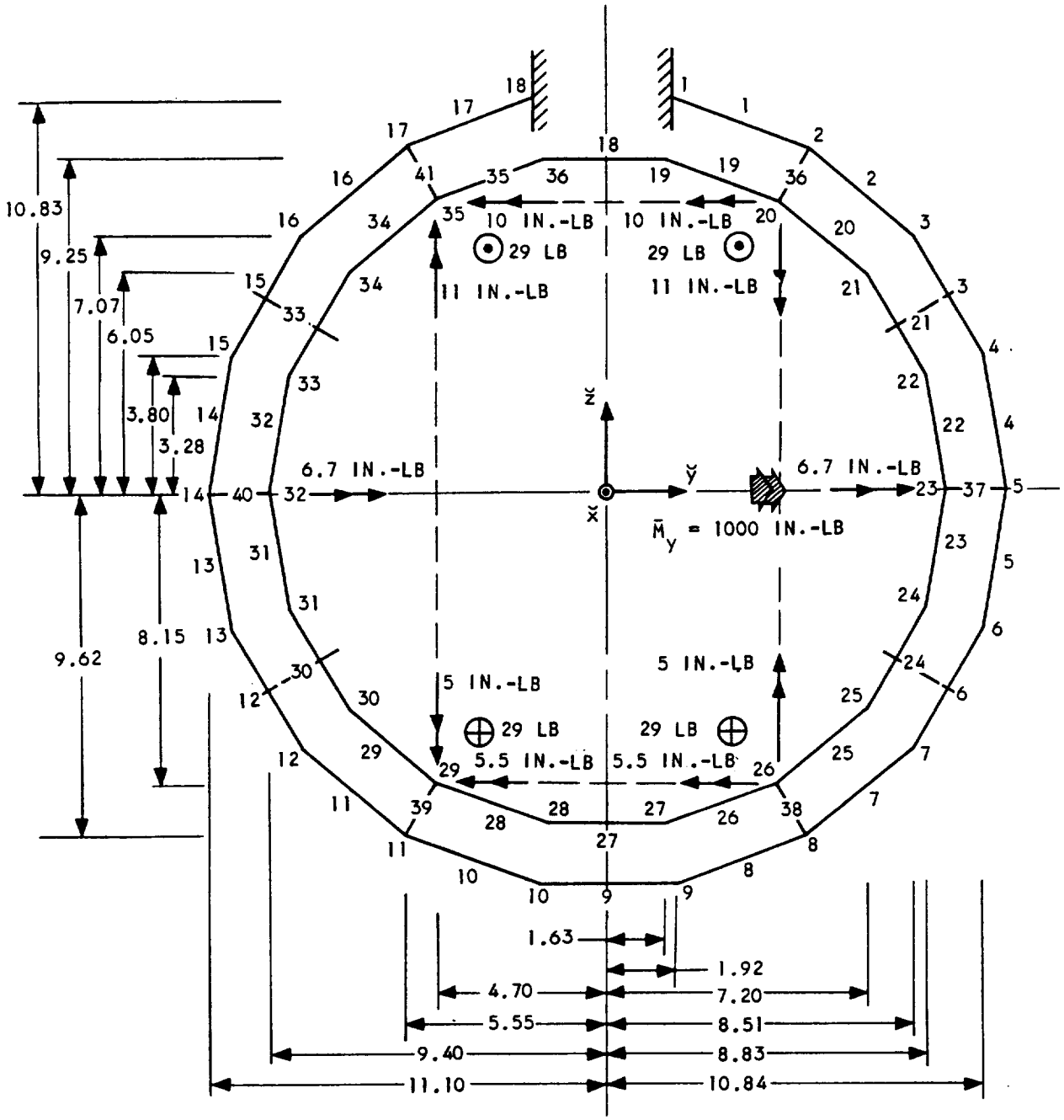

(THIRD ESTIMATE)
NOTE: ALL DIMENSIONS ARE IN INCHES

A-34003

Figure 5.5-23. Actuator Load Flow Due to 1000 lb-in. Unit Moment

5.5.7.3.2 Deflections

Spike deflections and rotation at the cowl lip and at the aft end are increased over the previously published values due to increased loads and decreased actuator shell thickness. Numerical data were developed at the seal locations for use with the seal analysis. For the unstart normal load of 16,800 lb, the spike deflection at the seal would be 0.077 in., and at the aft end of the spike which is 1.5 in. beyond the seal with the spike in its most extended position, the estimated relative displacement would be 0.083 in. This deflection would exceed the initial clearance of 0.053 in.; it exceeds the design goal of 0.040 in. to allow for noncircularity and misalignment of the spike shell and the innerbody. As discussed below, the seal will prevent the excessive deflection when it is adequately preloaded between the spike and the innerbody, and it will, in fact, limit deflections to 0.030 in. or less.

5.5.7.3.3 Bearing and Friction Loads

A bearing load and friction load estimate was made for the actuator structural shells. Values for this estimate were based on metal/metal sliding surfaces and on a friction coefficient of 0.15. Use of teflon-impregnated bearings conservatively reduces this coefficient to 0.02 to 0.03 and the friction loads accordingly.

The spike seal will pick up 2000 to 4000 lb of normal load depending upon spike position. The seal will consist of two packing strips which will have free, uncompressed cross-section dimensions of approximately 1/4 x 1/4 sq in. An estimated seal strip preload of approximately 15 to 20 lb per in. for each seal will be needed to prevent deflections in excess of 0.030 in. at the seal. The total radial force acting on the spike inside surface will be approximately 900 to 1200 lb. When the asymmetric unstart force deflects the spike, one side of the seal increases in loading while the other side relaxes. The seal behavior is nonlinear, and it also has an appreciable hysteresis loop. Based upon the above-mentioned precompression level, the seal will deflect 0.020 in. due to the unstart load, it will carry nearly 4000 lb of load, and the total radial load on the spike surface will be from 4500 to 5000 lb. For a friction coefficient of 0.2, the seal axial friction force would be 900 to 1000 lb. Since this loading reaction in the seal alleviates normal forces in the actuator, the total friction force will be less than the algebraic sum of the seal friction load plus the peak actuator friction load of 2890 lb. For design purposes, a maximum combined friction force of 3790 lb is being used.

5.5.7.4 Dynamic Simulation

The simulation of the inlet spike actuation system using the IBM 1130 digital computer was based on the nonlinear model described in Figure 5.5-24. The response of the servoactuator was analyzed by two techniques. The first assumed the system operating at some specified position and introduced a small position command. The second technique assumed a fully closed spike inlet.

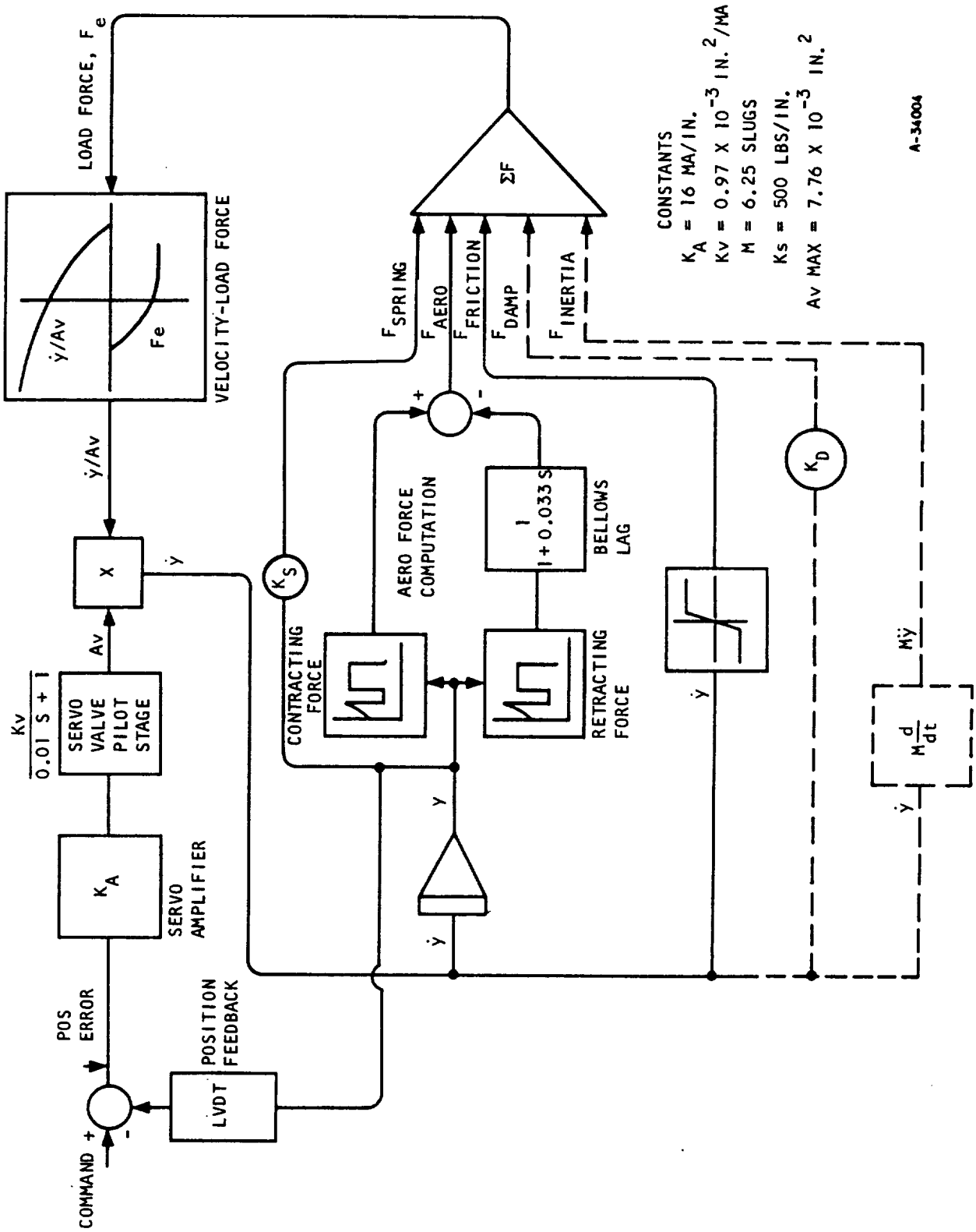

Figure 5.5-24. Diagram of Inlet Spike Actuation System

A command signal was issued to open the spike 5 in. After completing full retraction, an unstart signal would command the spike back to the closed position. The present system configuration was simulated with the following simplifications:

(a) Structural and hydraulic compliance effects were neglected.

(b) Pneumatic system characteristics were neglected.

(c) The hydraulic actuator snubbing and locking devices were omitted.

A block diagram of the simulated system is shown in Figure 5.5-24. Figures 5.5-25 and 5.5-26 show the response for small position command signals. Spike position, velocity, and valve area vs time are plotted. Figure 5.5-25 assumes an operating point of 0.45-in. retraction. At this point, the rate of change of the aerodynamic force with spike position is large. A perturbation of 0.2-in. step is used as the disturbance signal. The servo is well behaved, with a response time of 150 ms to achieve its final value. The maximum retraction rate is about 2.8 in. per sec, and the effective valve area attains about one-third its maximum.

The inertia force was initially ignored in this analysis. This exclusion was justified by the negligible effect the inertia force would have on the actuator performance compared with that of the aerodynamic forces. The validity of the assumption was subsequently verified.

Figure 5.5-26 assumes an initial operating point of 1.45-in. retraction. At this point, the aerodynamic forces are approaching their maximum value. A 0.2-in. step commands the system to a new equilibrium position of 1.65-in. retraction. At 1.5-in. retraction, the aerodynamic forces reach their maximum, then abruptly drop to their minimum values when the inlet starts. Since the aerodynamic forces dominate the load profile, they will have the greatest effect on the servo behavior. Hence, this point should represent the largest disturbance function on the servo. The inertia force was neglected. The transient indicates an overdamped system with a response time of 190 ms. The maximum retraction rate is about 3.1 in. per sec, with a maximum value area of one-third its maximum.

Figure 5.5-27 shows the servo response for a full-retraction sequence. The curves show spike position, velocity, load force, and valve area vs time. This analysis considered the inertia force. The position transient indicates a Type 1 servo response requiring 700 ms to achieve the fully retracted position. The maximum retraction rate is 11.1 in. per sec and occurs when the spike has retracted approximately 1.5 in.; the load force is thus large and tends to aid the retraction process. The effective valve area saturates after 20 ms and continues in this condition until the spike has retracted to 90 percent of its final value. If no valve leakage is assumed, the total amount of fluid consumed is 17.5 cu in. The maximum inertia force on this transient is only 151 lb, which justifies the original assumption.

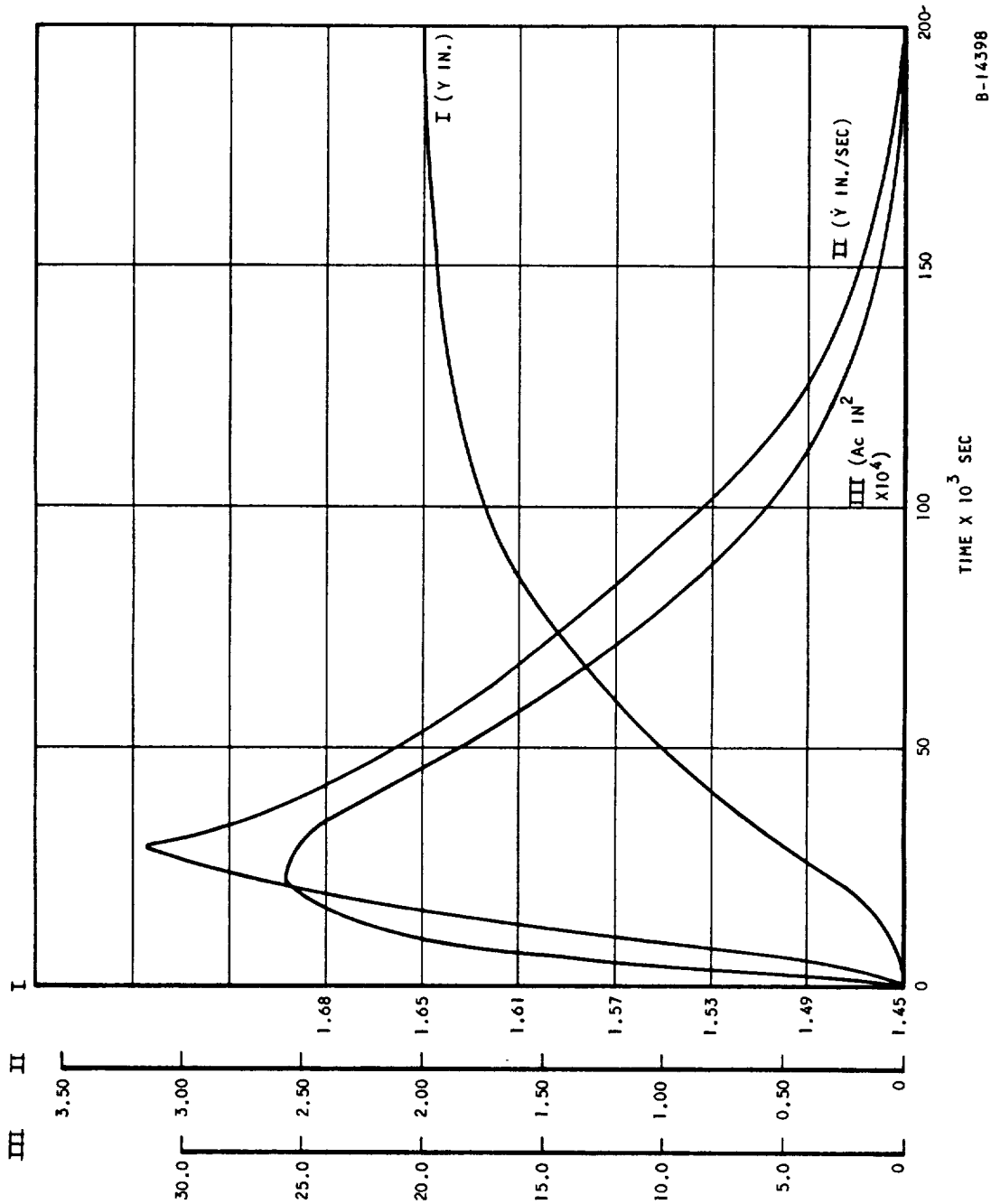

Figure 5.5-25. Transient Response to a Step Command Signal of +0.2 in. From the Initial Position of 0.45 in.

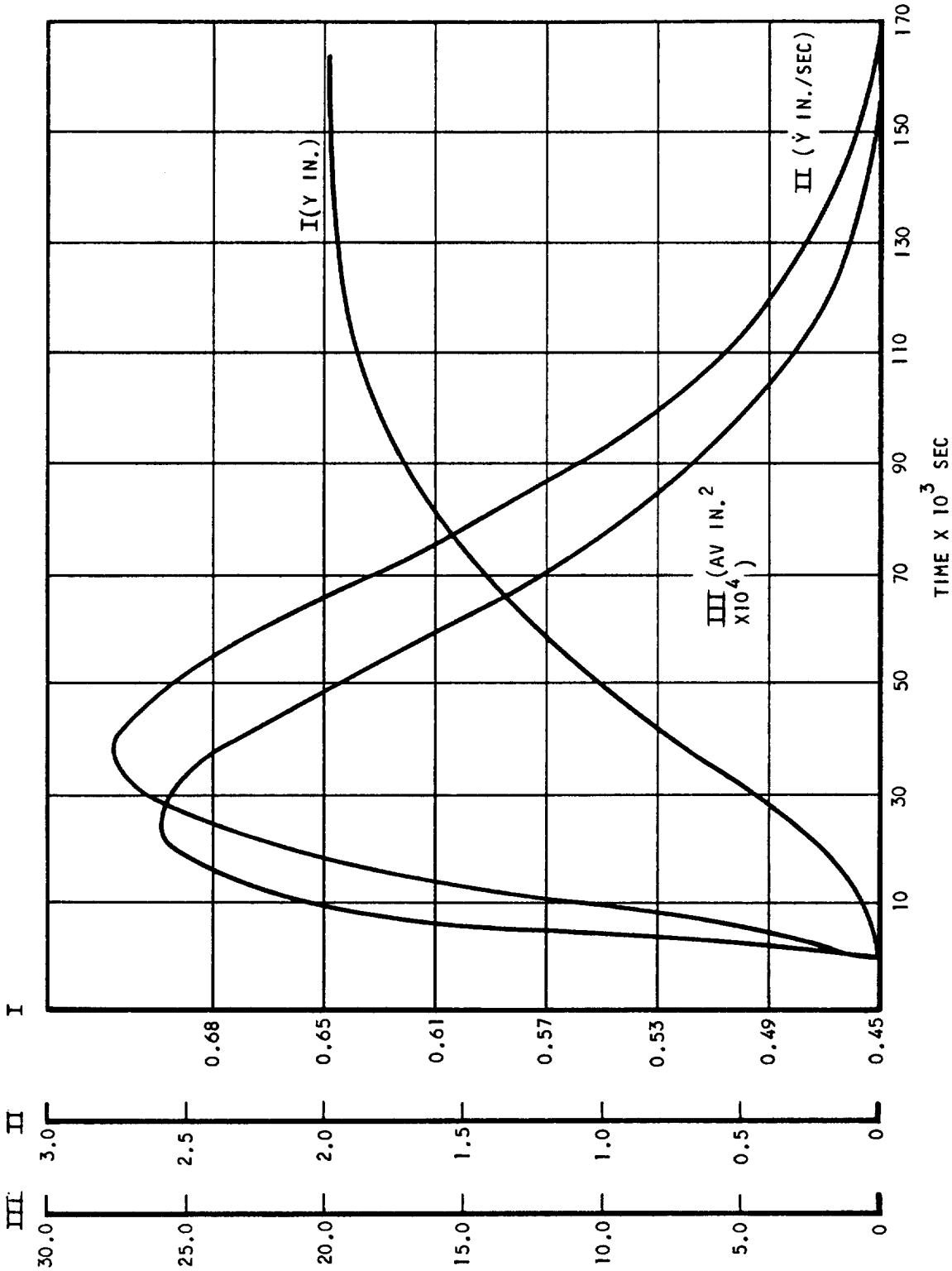

Figure 5.5-26. Diagram of Inlet Spike Actuation System Transient Response to a Step Command Signal of +0.2 in. From the Initial Position of 1.45 in.

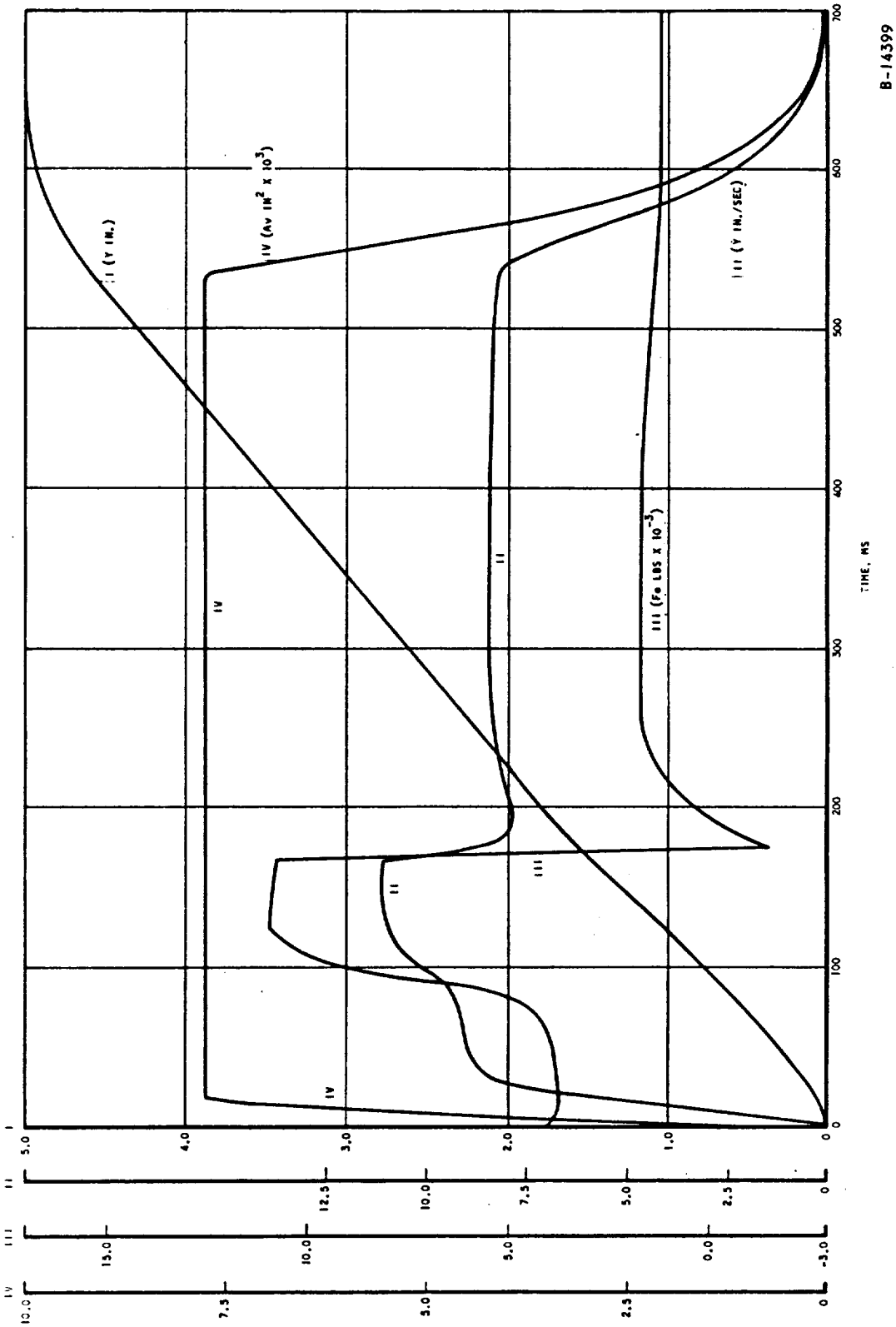

Figure 5.5-27. Transient Response During Retraction of Spike

Figure 5.5-28 illustrates the transient response for an extension sequence. The initial state of the servo is in the fully retracted position. An unstart signal is introduced which immediately increases the aerodynamic forces. The command signal from the HRE computer which causes the servo to react to this situation is delayed 50 ms, as indicated by the velocity and valve area curves of Figure 5.5-28. The position transient (Curve I) again shows an overdamped characteristic with a response time of 825 ms (to attain a fully extended position). The highest spike velocity (Curve II) is 9.85 in. per sec. Again, the valve is saturated (Curve IV) during 90 percent of the transient. The negligible maximum inertia force of 110 lb was obtained. The total fluid consumed is 30 cu in.

A comparison of the last two figures shows that the response time of Figure 5.5-28 is approximately 125 ms longer. This condition is largely due to the loading which normally tends to retract the spike. Therefore, during retraction, the response time is an aiding factor; during the extension process, it is a retarding one. This effect is again demonstrated by the spike velocity curves. The fluid consumption is greater for the extension case because the effective piston area is larger.

5.5.8 Suspension Frame

The HRE is attached to a suspension frame which is fastened to the X-15A-2 aircraft. The structure is made of built-up welded sections of Inco 718 alloy. It supports the turbopump, fuel piping, valves, etc. on its upper surface, while the thrust block is attached to its lower surface. The HRE is attached to this suspension frame in such a manner that fore and aft loads are transferred only through the thrust block. General arrangement of the suspension frame is shown in Figure 5.5-29a. Layout Drawing L980619 presents additional details.

5.5.8.1 Design Loads

The engine loads are directly transmitted to the thrust block and the aft mounting. Three external load conditions govern the design of the mounting structure. Condition "a" is the critical flight condition, symmetrical engine unstart at $M_\infty = 8.0$, $q_\infty = 2000$, $\alpha_\infty = 10$ deg. Load conditions "b" and "c" are the critical vibration qualification loads. The magnitude and direction of these three load cases are shown on Figure 5.5-29c.

5.5.8-2 Structural Design

The suspension frame is basically a space-frame with rigid joints, supported externally at three points. An idealized model of this frame is shown on Figure 5.5-29b. Joint 1 represents a fixed support, while joints 8 and 10 are considered sliding in the x-direction, but pinned in the y- and z-directions, transmitting only y- and z-directional loads to the aircraft. The vertical legs of the aft mount are attached to the sides of the longitudinal members of the mounting structure. Dummy members 4 and 12 are introduced to simulate this eccentric attachment. The MIT STRESS computer program was used for the analysis of the structure.

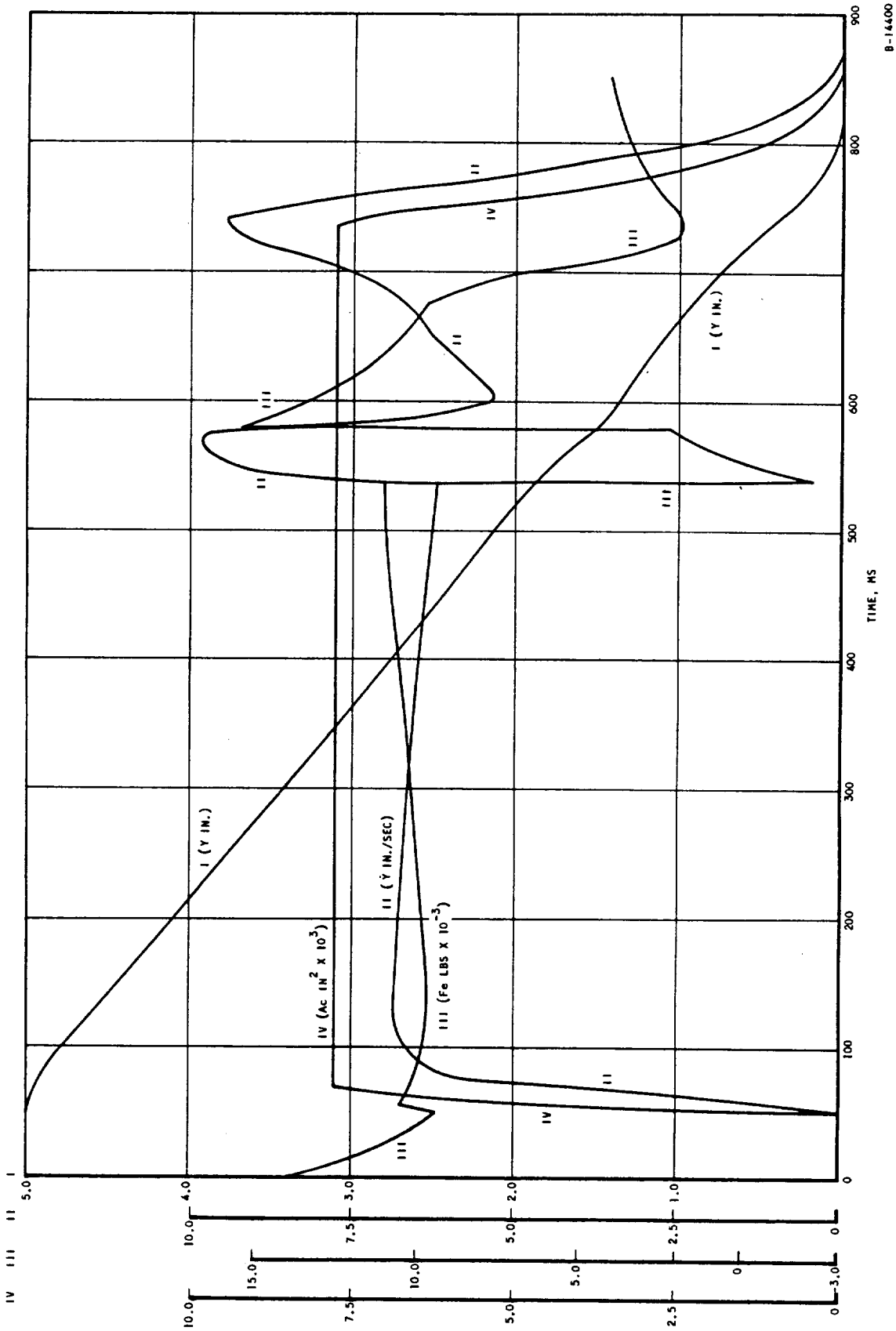

Figure 5.5-28. Transient Response During Extension of Spike

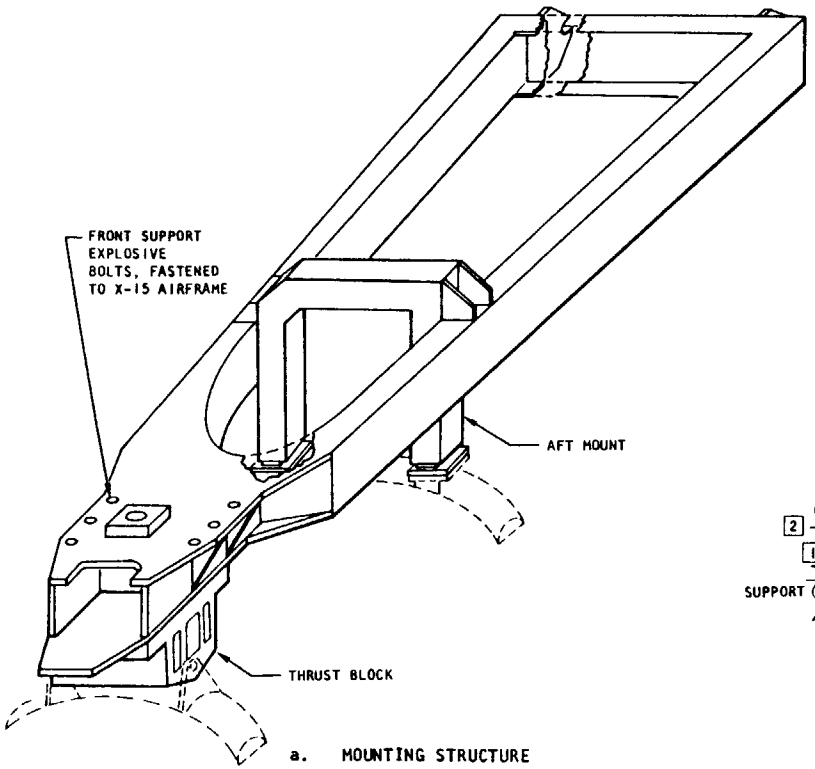

a. MOUNTING STRUCTURE

S-40757

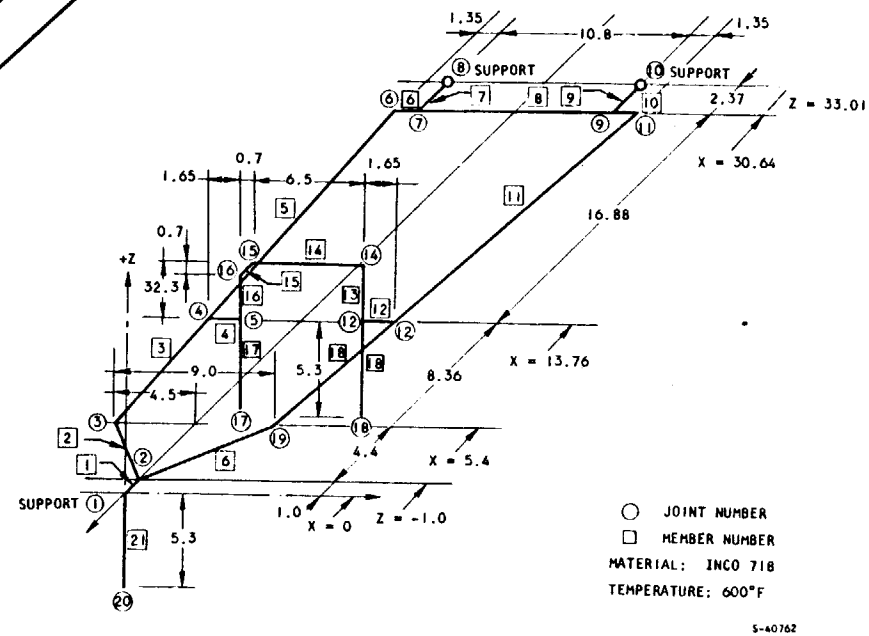

S-40762

b. IDEALIZED GEOMETRY

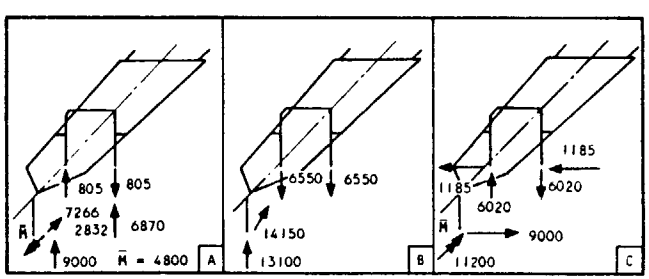

S-40758

c. GOVERNING LOAD CASES

MEMBER	LOAD COMBINATION	MAXIMUM STRESS, LB	SAFETY MARGIN
1	B	41300	1.8
2, 3, 5, 11, 19, AND 20	B	51000	1.28
6, 8, AND 10	B	12120	8.5
7 AND 9	B	7120	15.3
14	A	41896	1.77
15	B	37600	2.1

d. MAXIMUM STRESSES

S-72685

Figure 5.5-29. HRE Suspension Frame

The maximum stresses and the safety margins against allowable stress for each member are shown in Figure 5.5-29d. These stresses are based on the governing allowable stress for Inco 718 at 600°F being 0.667 F_{tu} = 116.0 ksi. The aft mount is a brazed-leaf assembly (see Layout Drawing L980619), with an X-directional spring constant of 339 lb per in., which is within the 400-lb-per-in. limit established for instrumentation requirements. Maximum stress in the leaves of the aft mount is 56,200 psi.

5.5.9 Ablatively Cooled Cowl Thermal Analysis

A preliminary study of the boundary conditions required to define the ablatively cooled cowl surface was performed. The cowl surface heat flux was calculated using the Eckert flat-plate heat transfer equation, the aerodynamic data at Mach 8 local, 85,000 ft (q_∞ = 2000 psf), and the proposed X-15A-2 flight trajectory for the HRE mission to Mach 8. The variation of the heat flux with the flight time is shown in Figure 5.5-30 at the beginning and end points of the cowl surface (Station 45 and 76). The local heat load, which is the result of numerical integration of local heat flux over the entire flight time is tabulated in Table 5.5-2 at various locations on the cowl surface. Both laminar and turbulent flow fields were assumed. The heat loads on the entire ablative cowl surface at Mach 8 and 85,000 ft are 120 and 600 Btu/sec for laminar and turbulent flows, respectively. It is noted that the heat fluxes or heat loads are so-called "cold wall" values using a base temperature of 0°R.

Flow field results were determined for both laminar and turbulent flows. Marked differences occur. The local Reynolds number along the cowl contour at M = 8 and 85,000 ft in Table 5.5-2 indicates that the flow in the forward portion of the cowl may be laminar, while the flow in the aft region of the cowl may be turbulent. As the freestream Mach number decreases, Reynolds number increases, and hence the flow is more likely to be turbulent for most of the flight time. Also, for the range of the Reynolds number under discussion, freestream disturbance, local discontinuities on the cowl contour, and surface roughness due to char formation of the ablative material may produce early transition to turbulent flow. To insure against local overheating, the results based on turbulent flow were selected.

Local protuberances on the cowl surface induce boundary layer separation and a shock near Station 72. An aerodynamic analysis indicates that the ratio of the pressure rise across this shock is 12.3 at M = 8 and 85,000 ft. The associated rise in heat flux may be determined by the relation

$$\frac{(q/A)_{max}}{(q/A)_o} = \frac{P_2}{P_1}^n$$

where $(q/A)_o$ is the heat flux in the shockless system, (P_1) and (P_2) are the upstream and downstream pressures of the shock, respectively, and (n) is a constant with a value between 0.80 and 0.93. With use of n = 0.9, the local maximum (or peak) heat flux becomes approximately 10-times as great as the heat flux in the corresponding shockless system. This requires thickening of the ablative material in the region.

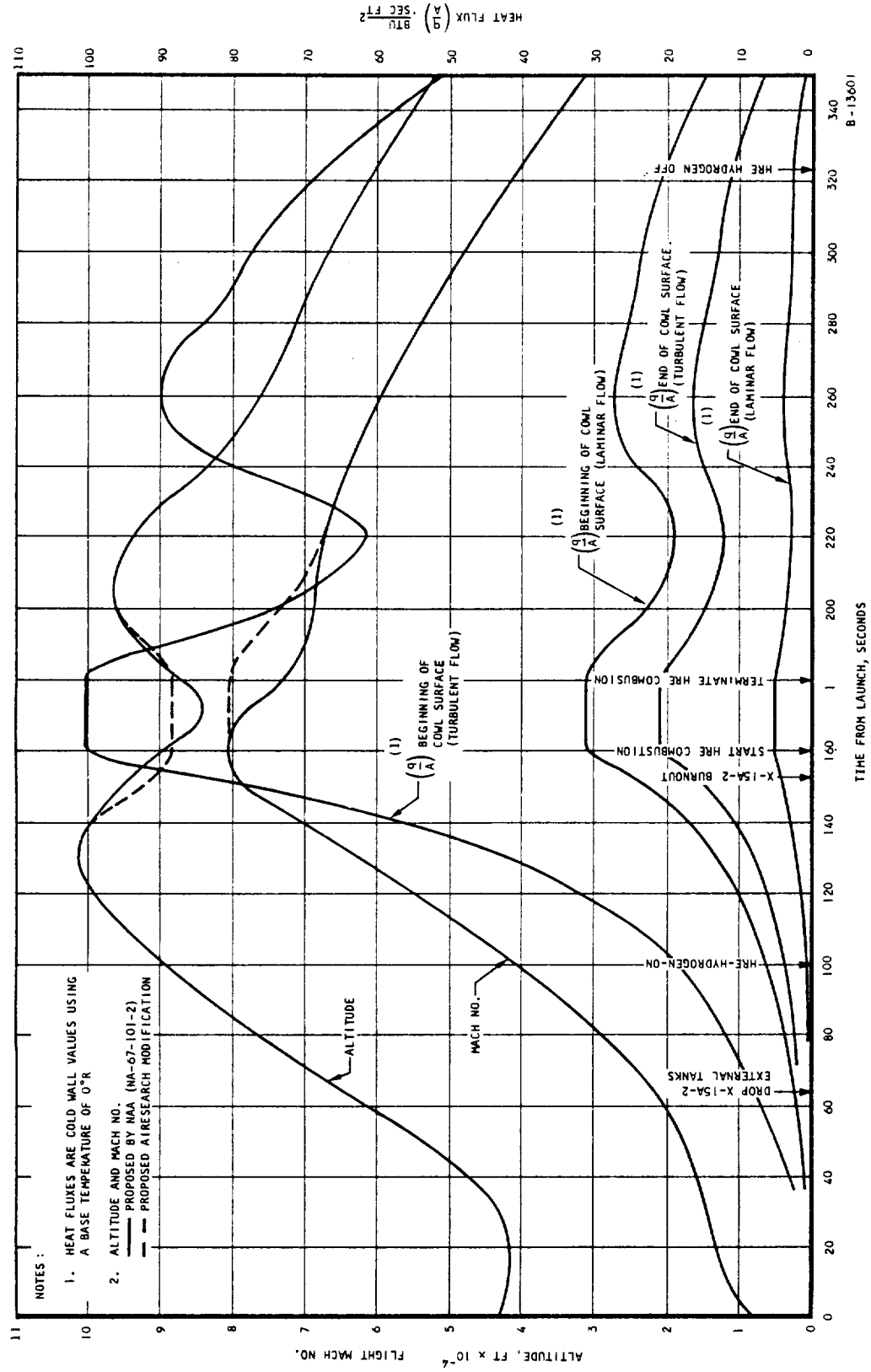

Figure 5.5-30. Ablative Cowl Heat Loads at Mach 8

TABLE 5.5-2

ABLATIVELY-COOLED COWL AERODYNAMIC HEATING SUMMARY

Station No.	Reynolds Number, Re, x 10^{-6}	Flow Pattern	Heat Flux, q/A, Btu/sec ft^2	QT = (1/A)dt, Btu/ft^2
45 (Beginning of ablative cowl)	0.75	Laminar Turbulent	20.8 102	3,700 20,500
49	2.5	Laminar Turbulent	11.7 59.0	2,080 11,900
65	5.2	Laminar Turbulent	5.7 33.6	1,010 6,500
72 (Position of bump-induced shock)	---	Laminar Turbulent	47 304	8,350 58,200
76 (End of ablative cowl)	7.5	Laminar Turbulent	4.64 31	830 5.930

NOTES:

$$Re = \frac{\rho v x}{\mu}$$

Re and q/A, as shown, are based on M_∞ = 8, 85,000 ft

5.6 SHELL ASSEMBLY FLOW TEST ADAPTERS

Full scale engine components and adapters were defined for the purpose of evaluating the component thermal and structural performance during tests with subsonic hot gas heating and hydrogen cooling. The test plan was to simulate design point flight thermal conditions (metal temperatures and metal temperature differences) during subsonic (Mach No. < 0.30) annular duct flow tests using the hot-gas combustion products of oxygen-enriched air and hydrogen. The design point selected for the test setup was the temperature and ΔT conditions predicted for combustion at Mach 8 freestream and local, 88,000-ft altitude.

5.6.1 Thermal Design

The objectives of the component thermal simulation were:

(a) A cross-section ΔT distribution in the plate-fin cooling jackets within $\pm 50^{\circ}R$ of the predicted design values (the cross-section ΔT is the sum of the ΔT's through the 0.015-in.-thick skin and the 0.050-in.-high fins).

(b) A maximum metal surface temperature within $50^{\circ}R$ on the low side of $2060^{\circ}R$.

(c) A structural temperature distribution within $100^{\circ}R$ of flight conditions, but not exceeding $1600^{\circ}R$.

The predicted test conditions that gave the best simulation of the flight conditions within the stated objectives are shown in Table 5.6-1. The test adapter support structures were water cooled and were axially contoured with the components to produce the simulated heating distribution. The contours were selected for hot operating conditions and therefore included the effects of thermal radial expansion of both component and adapter. Since the support structures are water cooled, all water circuits were designed to obviate separate flow controls. All metal temperatures of the test equipment are less than $500^{\circ}F$; most of them below $200^{\circ}F$. The maximum metal temperature in the water passages is about $300^{\circ}F$. The inlet spike test adapter is the same piece of hardware that will support the innerbody test unit. Heating conditions on the adapter during spike testing were equal to or less than those during innerbody testing.

Two types of component testing were planned, (1) thermal performance testing, and (2) thermal cycle testing. Thermal performance testing was planned to establish the above thermal simulation objectives on the components. Evaluation of the component cooling capability was to be based on visual observations of temperature-sensitive paints on component surfaces and on wall temperature thermocouple readings. In addition, these test runs would permit adjustment of test conditions for the thermal cycle test and provide response of the component test unit to heat load, heat flux, and coolant hydrogen flow rate with heat transfer.

TABLE 5.6-1

FULL SCALE COMPONENT TEST CONDITIONS

Component	Hot Gas			Hydrogen Coolant			Test Unit Dwg. No.
	Temperature, °R	Pressure, psia	Flow Rate, lb/sec	Inlet Temperature, °R	Inlet Pressure, psia	Flow Rate, lb/sec	
Spike	4500	300	7	200	700	0.53	L980617
Innerbody	4500	300	12	200	700	0.44	L980614
Leading Edge	4500	300	8.7	200	700	0.56	L980618
Outer Shell	4500	300	12	540	700	1.09*	L980622

*0.43 lb/sec for forward outer shell and 0.66 lb/sec for aft outer shell.

The objective of the thermal cycle test was to evaluate the low cycle thermal fatigue performance of the full-scale components at the simulated design point operating condition. The hot gas and hydrogen conditions required to produce the thermal performance simulation objectives (maximum tunnel heating condition of 4500°R) were to be established. The hot gas temperature was to be then reduced from 4500° to 2500°R in approximately 2 min (constant hot gas flow rate), maintained at 2500°R for 1 min, increased to 4500°R in 2 min and maintained at 4500°R for 1 min. This cyclic pattern in hot gas temperature was to be repeated a maximum of 100 times or until a failure of the test unit occurred.

5.6.2 Structural Design

In order to verify the analytically derived performance of the major subassemblies, the following test adapters were designed:

Inlet spike

Innerbody

Leading edge

Outer shell

These adapters were designed as water-cooled units fabricated from SAE 1020 mild steel, except certain coolant pipes and tubes which were made of type 321 corrosion resistant steel. The following mechanical properties were used for the design:

	SAE 1020			Type 321 CRES (0.2 Percent YS)
Temperature, °F	Ambient	200	1600	< 200
E, psi	-	-	-	28×10^6
F_{tu}, psi	70,000	-	-	55,000
F_{ty}, psi	40,000	35,000	30,000	36,000
α, in./°F	-	-	-	6.5×10^{-6}

The maximum allowable mechanical stress used during the design was limited to 0.5 F_{tu} or 0.75 F_{ty} (whichever was less).

5.6.2.1 Inlet Spike

This adapter was designed primarily for the innerbody testing (see para. 5.6.2). Only minor modifications were required to use the adapter (shown on Drawing L980614) for the inlet spike tests. These tests were not intended to simulate the primary design loads on the spike, i.e., unsymmetrical unstart

and high external net pressures. A heavy-duty conical spool part made from SAE 1020 mild steel was designed to support the spike mounting cone to the test ducting. Minor plumbing modifications were required; however, they did not affect the structural integrity of the test fixture.

5.6.2.2 Innerbody

5.6.2.2.1 Design Conditions

The innerbody test adapter was designed to meet the following operating and proof test conditions:

	Temperature, °R	Pressure, psi
a. Operating Conditions		
Tunnel gas flow	≤ 4500	300
Cooling hydrogen in	200	700
Cooling hydrogen out	1600	-
Cooling water in	530	100
Cooling water out	560	-
Pressurizing nitrogen	560	320
Nitrogen, hot gas press. diff		30 psi
b. Proof Test Conditions	Ambient	300 (water pressure in each flow path)

5.6.2.2.2 Structural Analysis

5.6.2.2.2.1 Two-Plate Door Assembly

Under operating conditions, this assembly, consisting of two parallel plates, is designed to resist a 30-psi ΔP across the door. The internal water pressure being 50 psi, the assembly must simultaneously resist a (300 - 50) = 250-psi ΔP across each plate. It must also resist a 300-psi internal proof pressure at room ambient pressure and temperature.

Pins and, whenever necessary for assembly and disassembly, short tubes were used to maintain plate spacing and to maintain the bending stresses, due to the ΔP between the coolant and the internal gases, within allowable limits. The maximum allowable distance between the pins, if these were placed in the common square pattern, would be about twice the mean pin distance that is being used in an axisymmetrical pattern. This provides a high margin of safety. The door assembly will assume some bowing under the 30 psi ΔP, but the stresses due to this effect will remain within allowable limits.

5.6.2.2.2.2 Duct Assembly

The flanges of the duct assembly are bolted to the test tunnel with 24 bolts, preloaded to 10,000 lb per bolt, which is considered adequate to prevent separation of the duct assembly from the tunnel under a 300-psi pressure.

5.6.2.2.2.3 Pipes and Tubes

Of all pipes and tubes, the hydrogen outlet central tube, which operates at 1600°R and 700 psi, experiences the highest loading, resulting in a stress of 15,000 psi. The margin of safety equals $\frac{22,500}{15,000} - 1 = 0.5$.

5.6.2.3 Leading Edge

5.6.2.3.1 Design Conditions

The leading edge test adapter is designed to meet the following operating and proof test conditions:

	Temperature, °R	Pressure, psi
a. Operating Conditions		
Hot gas	≤ 4500	300
Cooling hydrogen in	200	700
Cooling hydrogen out	690	-
Cooling water in	530	100
Pressurizing nitrogen	560	302
Pressure differential (maximum)	-	15
b. Proof Test Conditions	Ambient	300 (water pressure)

5.6.2.3.2 Structural Analysis

Proof pressure load on the circular flat plate on the forward plug created high stresses. Even with 1/2-in. plates, it was necessary to tie the two plate halves together with eight 1/2-in. tie pins at a radius of approximately 3.0 in., and with 15 pins at $r \simeq 6.8$ in. The maximum bending stress in the plate was then equal to 13,000 psi, with a resulting margin of safety against yield of 1.11.

The design of the conical and cylindrical double-wall shells was governed by buckling of the inner shell under proof pressure. An approximate formula for buckling of these shells is:

$$p = 0.807 \frac{Et^2}{r} \sqrt[4]{\left(\frac{1}{1 - \nu^2}\right)^3 \frac{t^2}{r^2}}$$

where p = buckling pressure, psi

t = wall thickness, in.

r = radius, in.

l = distance between ends held circular

For an ultimate factor of safety of 2.0, i.e., a design buckling pressure of 600 psi, it was necessary to weld spacers between the inner and outer wall for the two aft shells. The forward plug is sufficiently rigid and does not require any connecting spacers.

The flange connection to the main duct was designed to react to a pressure thrust of

$$\text{thrust} = \rho_o \pi r^2 = 300\ (\pi)\ (15)^2 = 212{,}000 \text{ lb}$$

The flange was designed with the mating surface relieved approximately 1/2 in. in from the inner and outer diameter. This ensured that 1/2 of the clamping load acts in the seal area. The sealing element is a rubber O-ring which requires minimum pressure to seal. Flanges were fastened with 32-3/4-in.-dia bolts (F_{tu} > 125,000 psi) torqued to 85 percent of the yield which created 18,700 lb tension in each bolt. Maximum bending stresses in the flange were 22,000 psi (MS_{yield} = 0.21).

5.6.2.4 Outer Shell Structural Design

A schematic representation of the outer shell test unit is shown on Figure 5.6-1a. The unit consists of the following major items:

Forward spool (A)

Outer shell test specimen

Aft spool (B)

Plug

The design was based on the assumption that the spools A and B are externally supported for deadweight while still allowing radial and axial thermal growth of the whole assembly. Stresses due to the dead load of the assembly were then negligible.

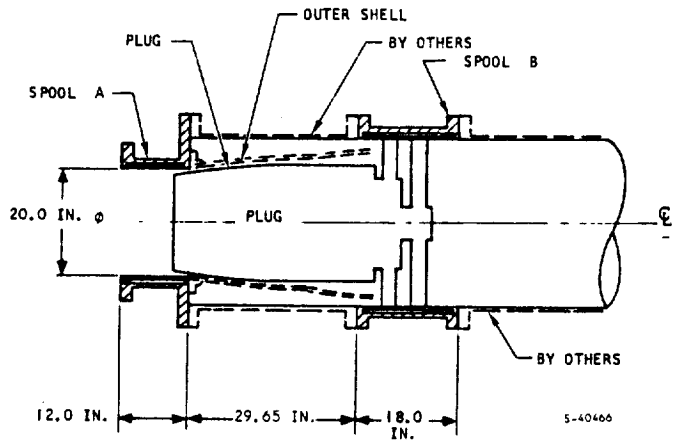

a. OUTER SHELL TEST FIXTURE, GENERAL ARRANGEMENT

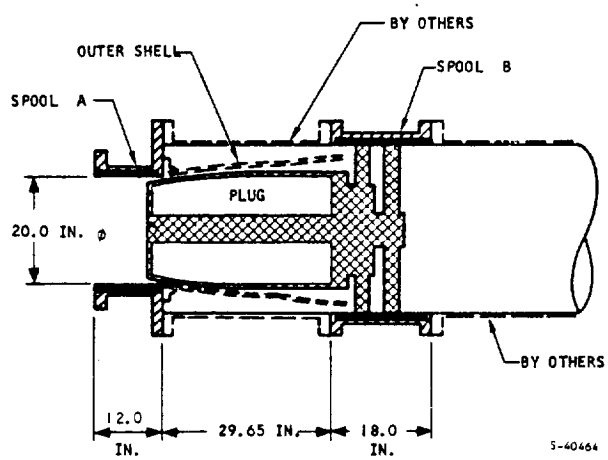

PROOF PRESSURE: 300 PSI ON SURFACES SHOWN

b. OUTER SHELL TEST FIXTURE, LOAD CASE 1

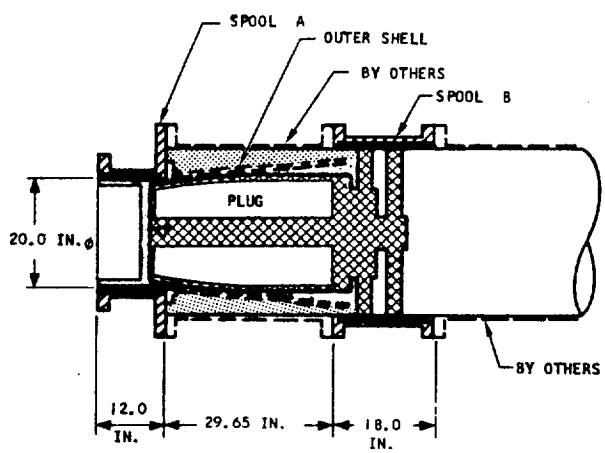

OPERATING CONDITION:

A. COOLANT PRESSURE ≤ 100 PSI B. GAS PRESSURE 300 PSI C. GAS PRESSURE 315 PSI

c. OUTER SHELL TEST FIXTURE, LOAD CASE 2

5-40465

Figure 5.6-1. Outer Shell Test Fixture Configuration and Loads

F-15401

The assembly was designed for two different loading conditions:

(a) A 300 psi hydrostatic proof pressure on the coolant passage areas shown in Figure 5.6-1b at room temperature.

(b) Operating coolant pressure of 100 psi in the coolant passages of the assembly and 300 psi hot-gas pressure in the gas-annulus area as shown in Figure 5.6-1c.

All parts of the assembly (except the outer shell) were to be fabricated from SAE 1020 steel. The inside plug will be insulated. Maximum hot skin temperature of the plug will be 680°F, maximum ΔT, 370°F.

The inner plug is supported by a 5.0-in.-dia pipe. This pipe is in turn connected by an array of six equally spaced radial pipes (2.5 and 3.0 in. dia) to the aft spool. External loads are 3300-lb axial load due to the drag of the gas flow, and 491.0 lb due to the weight of the plug and the coolant during operation. Stresses in the members due to the combined effect of these loads are small. The peak stress in this assembly is 4580 psi and the margin of safety is 4.0. Maximum vertical deflection of the tip of the plug is 0.0023 in. while the horizontal displacement is 0.0019 in. (axial direction).

The double shell of the plug is formed by two truncated cones and a straight cylindrical section. These shells are closed near Station 40.44 by two flat plates tied together with 0.5-in.-dia pins. Maximum bending stress in the 0.5-in.-thick plate is 13,500 psi, giving a margin of safety of 0.79 at 565°F.

Critical buckling pressure of the 0.1-in.-thick outer shell is 64 psi. This is much less than the actual net external pressure during operation (200 psi). Six rows of 0.375-in.-dia pins between the inside and the outside shells raise the critical buckling pressure to 400 psi if the rows are spaced at 5-in. axially. The outside shell is not welded to these pins to allow for axial expansion. The front spool is a 20-in.-dia straight section with brazed 20R-0.075-0.004 stainless steel fins, a 0.065-in.-thick inside shell, and one 0.25-in.-thick outside shell. Two 1-in.-thick flanges connect this section to the tunnel. These two flanges are interconnected by twelve 0.5-in.-thick gussets to transmit the axial load due to the duct diameter change from 20.0 to 30.0 in. The flanges are connected with 24-3/4-in.-dia bolts. Using 85-percent yield load on these bolts (125,000 psi ultimate strength material), the flange sealing load is 13,000 lb, which is adequate for a rubber O-ring, requiring minimum pressure to seal. The safety margin over yield due to bending in the flange is 0.06.

Maximum temperature of the front spool is 850°F at the inside tip of the flange. Low-cycle fatigue analysis of this area indicates that the assembly has sufficient strength for approximately 3,000 cycles. Planned operation of the test assembly is 20 hr of 5-min-long cycles, (240 cycles).

The aft spool is an 18-in. long, 30-in.-I.D. spool with 0.25-in.-thick welded inner and outer surfaces. Maximum stresses are 34,600 psi at proof pressure, giving a safety margin over yield of 0.04, without deducting the relieving effect of the six inner plug support pipes. The inner shell is exposed to a maximum hot surface temperature of 425°F and a ΔT of 70°F, creating thermal stresses well below the yield point of the SAE 1020 material.

5.7 SYSTEM WIND TUNNEL ANALYSIS

5.7.1 Aerodynamic Heating

Heat transfer analyses were performed for SAM hydrogen-cooled surfaces at maximum wind tunnel conditions. The calculations were based on equilibrium expansion to Mach 7.34 of methane-vitiated gas ($\phi = 0.8$). The analysis was for the case of no injection of gases through engine fuel injectors into the methane products stream during operation.

The aerodynamic data for methane-vitiated gas flowing adjacent to centerbody and outerbody surfaces, and the analytical heat flux distribution is shown in Figure 5.7-1.

The cone-rule modification factor ($3^{0.5}$ for laminar flow and $2^{0.2}$ for turbulent flow) was used on the spike for just aft of the tip to Station XX = 39.4 in. The cone rule was not used on other engine surfaces. A transition Reynolds number (based on surface length from leading edges) of 1×10^7 was used on the spike, and 1×10^5 on the inner surface of the outerbody. The resultant transition locations are shown in Figure 5.7-1.

Combustion products gas radiation to cooled surfaces was not considered. A review of hot-gas heating at Mach 8, 88,000-ft flight conditions indicated that gas radiation contributed less than 1 percent of the hot-gas radiation of hydrogen combustion products for Mach 8 flight at 4300°R. The average hot-gas static temperature of methane combustion products for SAM wind tunnel conditions is 1200°R. In addition, the radiation emissivity for methane combustion products (CO_2 and H_2O) is less than that for hydrogen combustion products of Mach 8 flight (H_2O). First, the static pressure for SAM wind tunnel conditions is less than Mach 8 flight, and second, when carbon dioxide and water vapor are present together the total radiation due to both is somewhat less than the sum of the separate effects because each gas is somewhat opaque to the other.

The aerodynamic heat transfer analyses were performed with a constant hot-gas total enthalpy (1095.3 Btu/lbm) corresponding to a total temperature of 3600°R. Based on a net heat transfer rate to the centerbody and to the inner surface of the outerbody of 2550 Btu/sec and an estimated hot-gas rate through the annular section of the engine of 28.7 lb/sec, the hot gas total temperature will decrease to 3350°R at the end of the engine.

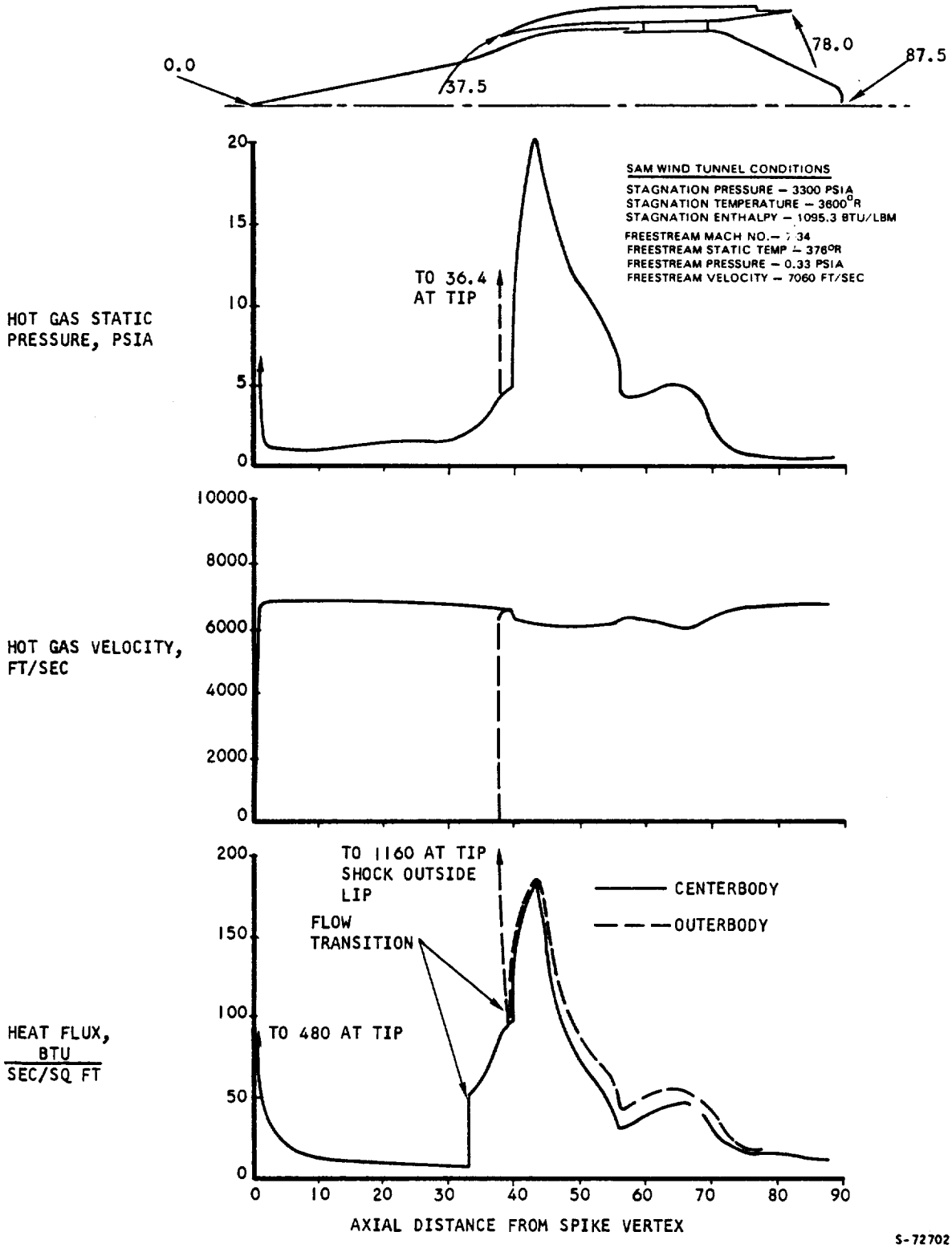

Figure 5.7-1. Aerodynamic Parameters and Heat Flux Distribution for SAM Wind Tunnel Conditions

5.7.2 Structural Loads

Wind tunnel testing of the SAM exposed the engine-tunnel adapter system to loads generated by the tunnel operation. These were due to:

(a) Insertion and retraction of the SAM into the tunnel, a 2.0 g vertical inertia load. Weights and weight distribution used for inertia load calculation are shown on Figure 5.7-2.

(b) Aerodynamic loads due to tunnel unstart. The symmetrical and asymmetrical inlet unstart governed the design of many components of the engine. The five aerodynamic load cases governing the design of the SAM and its tunnel adapters are shown on Figure 5.7-3. These loads occur while the model and its adapters are at elevated temperature. Side plates of the assembly were designed to withstand a 15-psi pressure load.

The effect of the following additional loads was studied:

(a) Loads due to transportation and handling were taken as 5.0 g inertia with the unit at room temperature.

(b) Coolant pressure is 90 psig maximum in the leading edge coolant circuit of the support structure during operation, while in the side panels it is 180 psig. Proof pressure is 1.5-times operating pressure (135 and 270 psig).

5.7.3 Thermal Performance

5.7.3.1 Steady State Performance

Metal temperatures and temperature differences along the hydrogen-cooled plate-fin surfaces are presented in Figure 5.7-4 for the centerbody and Figure 5.7-5 for the outerbody. Plate-fin panel cross-section temperature differences are 490°R or less. The maximum ΔT of 490°R occurs at Station 40.4 (cowl lip at Station 37.44) on the leading edge. Other relatively high ΔT's are 405°R at Station 35.0 on the spike, 380°R at Station 42.0 on the spike, and 360°R at Station 57.4 on the inner shell. A ΔT of 450°R was calculated on the strut sides. All other ΔT's are less than these. For Mach 8 flight, the predicted ΔT's were 950°R on leading edge and outer shell surfaces, and 1200°R (caused by shock impingement) for localized areas of the outer shell.

The maximum panel heat flux of SAM wind tunnel conditions is 170 Btu/sec-ft^2 at Station 40.4 on the leading edge, compared with 700 Btu/sec ft^2 on the outer shell (excluding localized shock impingement) at Mach 8 flight conditions. The effect of cowl leading edge shock impingement on the spike at Station 39 has been included in Figure 5.7-4. Shock impingement which occurs at Station XX = 57.4 on the inner shell is caused by the rearward-facing step at the end

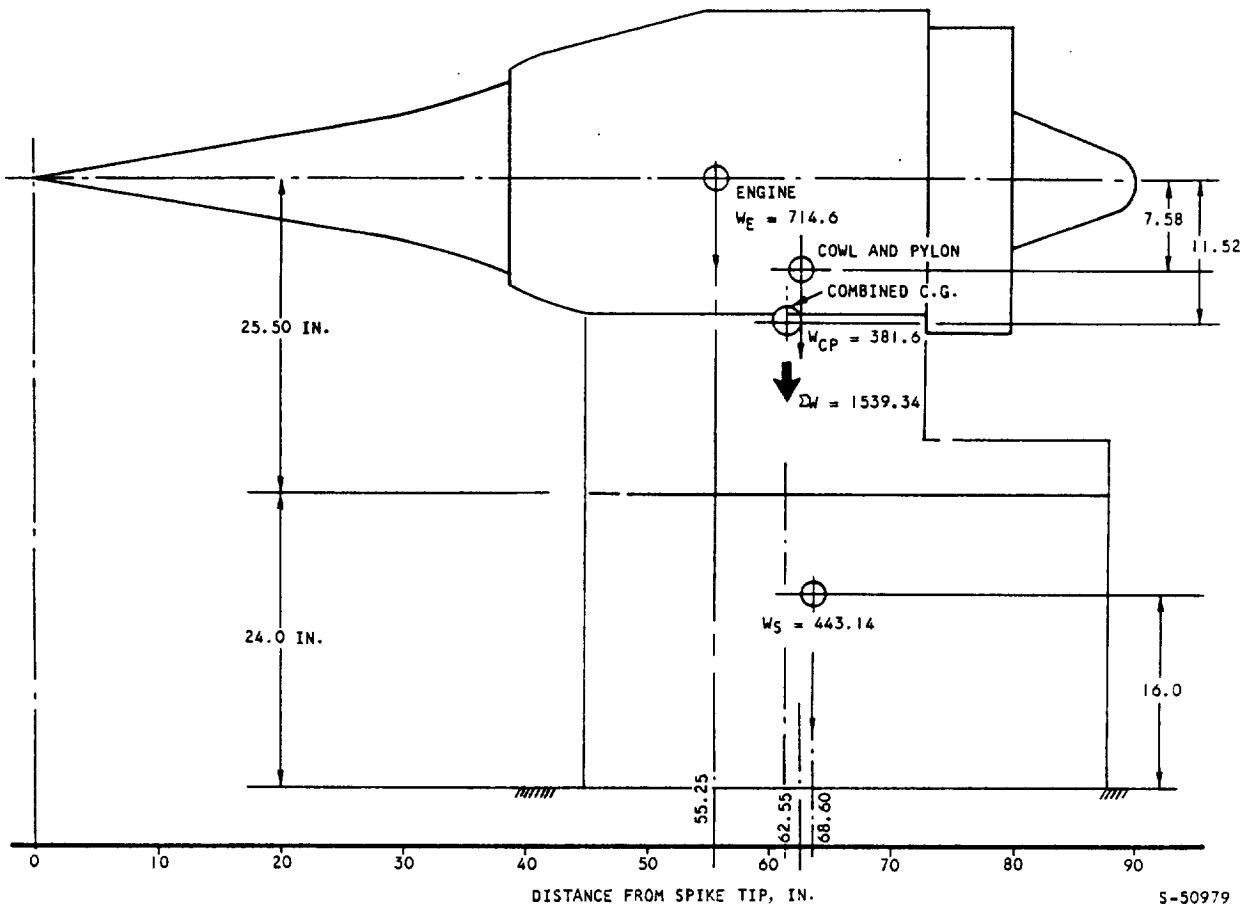

Figure 5.7-2. Sam Weight Distribution, Spike Retracted

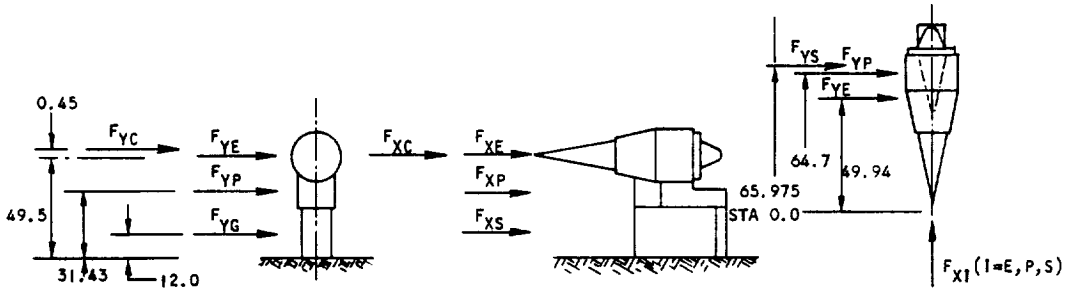

LOAD CASE NO.	LOAD CASE DESCRIPTION	F_{XE}	F_{XC}	F_{XP}	F_{XS}	$F_{YE} + F_{YC}$	F_{YP}	F_{YS}
1	SYMMETRICAL INLET UNSTART	4005	230	2500	1360	0	0	0
2	ASYMMETRIC INLET UNSTART	5350	230	2500	1360	~2000	0	0
3	SYMMETRICAL TUNNEL UNSTART	-8000	-1253	- 500	-3400	0	0	0
4	ASYMMETRICAL TUNNEL UNSTART	960	230	2500	1360	18860	8017	15615
5	INLET AND TUNNEL STARTED	960	230	2500	1360	0	0	0

S-72684

Figure 5.7-3. Sam Aerodynamic Loads

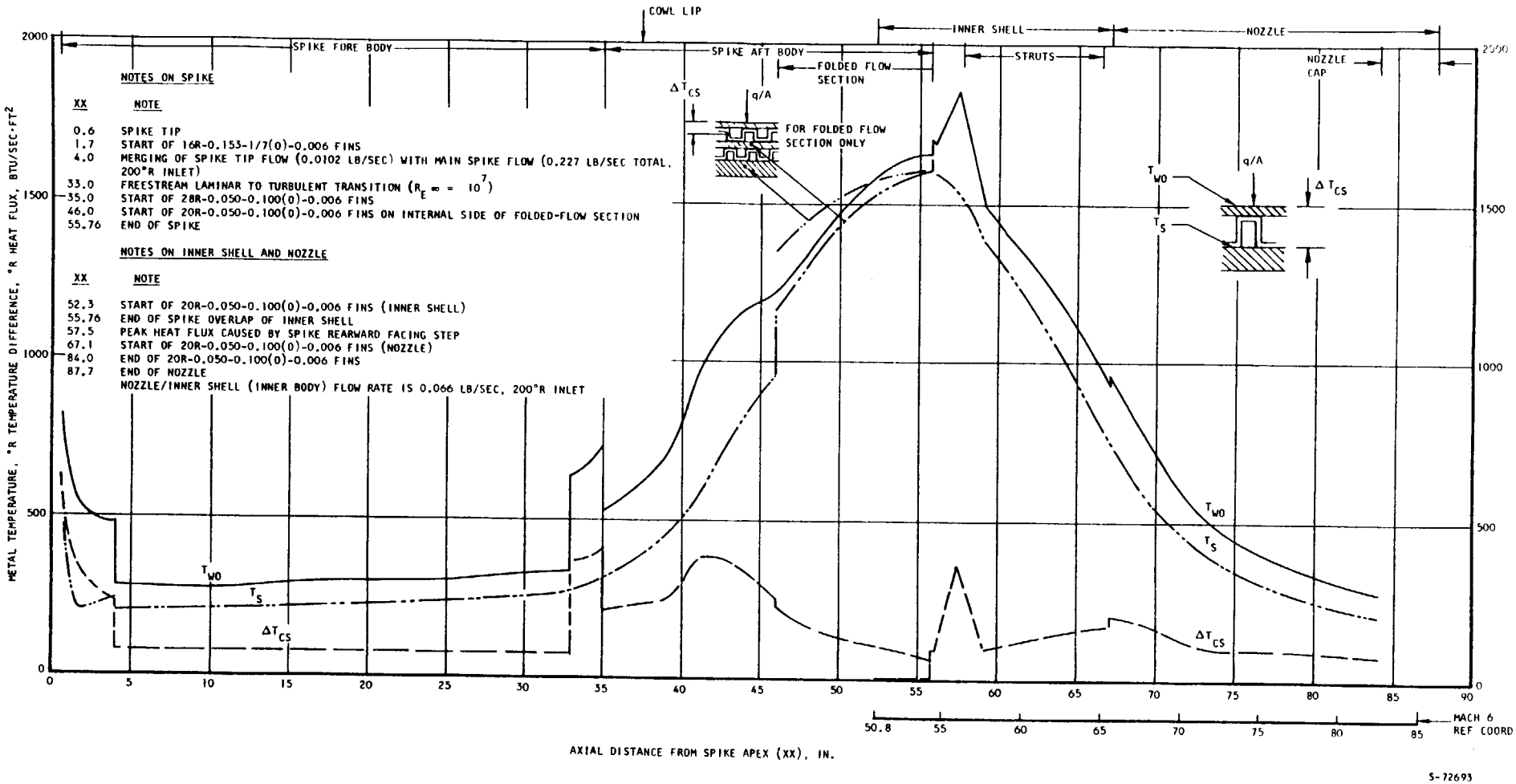

Figure 5.7-4. SAM Centerbody Thermal Performance

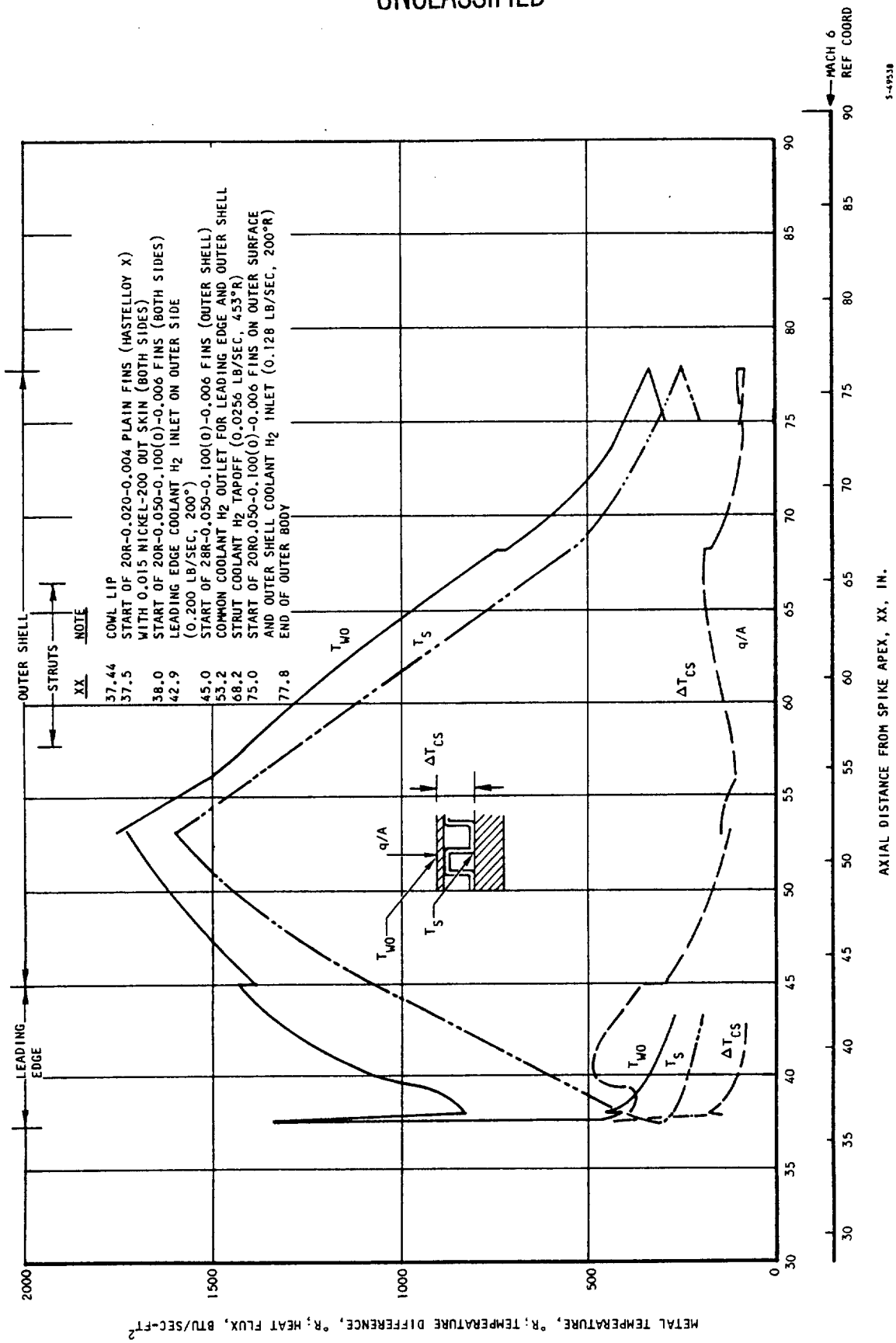

Figure 5.7-5. SAM Outerbody Thermal Performance

of the spike, Station 55.76. A heat flux of four-times the local flat-plate value of 40 Btu/sec ft^2 was estimated for this shock impingement.

The normal hydrogen flows, which were selected to give 1600°R maximum structural temperature and outlet temperature for each flow route are summarized below. The inlet temperature is 200°R.

	Flow Rates, lb/sec	Outlet Temp, °R
Spike	0.227	1347
Innerbody	0.066	1600
Leading edge	0.200	1600
Aft outer shell (at inlet)	0.128	-
Strut sides (from outer shell) 0.026	-	1430
Aft outer shell (at outlet) 0.102	-	1600
Total	0.621	-
Average	-	1500

5.7.3.2 Transient Thermal Performance

Transient heat transfer analyses of the SAM during the starting sequence in the tunnel were performed. The object of the analyses was to determine structural cross-section temperature differences during startup so that thermal stresses resulting from these temperature differences could be evaluated. In general, thermal stresses resulting from structural temperature differences greater than 800°R will reduce the engine life below the design objective of 100 cycles. Results of the analyses were also used to establish test conditions that were within the design range of the engine assembly.

The locations where startup transient metal temperatures were analyzed are listed in Table 5.7-1 along with the maximum calculated cross-section temperature differences. Two values are given--"one-way" and "reversal"-- where the latter is the absolute sum of differences to either side of a base temperature. A reversal of temperature gradient effectively increases temperature difference in terms of structural loading to a value equal to the sum of the differences. Included in Table 5.7-1 are the steady-state cross-section differences.

Modification of the tunnel startup sequence used in the transient heat transfer analyses can result in more severe transient conditions than reported. The total startup time used was 4 sec (start of engine hydrogen flow, engine

TABLE 5.7-1

SUMMARY OF SAM TRANSIENT STRUCTURAL TEMPERATURE DIFFERENCES

Location	Max. Transient ΔT, °R				Maximum Steady State ΔT, °R		
	One Way	Reversal	From	To		From	To
Outer Shell Inj. Manifold	560	1105	Manifold Tip	Hot Wall	115	Hot Wall	Struct. Wall
Inner Shell Inj. Manifold	610	1175	Hot Wall	Manifold Tip	90	Hot Wall	Struct. Wall
Outerbody Outlet Manifold	800	1400	Manifold Tip and Hot Wall	Hot Wall and Manifold Tip	160	Hot Wall	Struct Wall
Spike Injector Manifold	<760	1100	-	-	760	Manifold	Struct. Wall
Outer Shell	<385	-	-	-	385	Injectors	Struct. Wall
Innerbody Cross-Over Manifold	<425	585	-	-	425	Hot Wall	Actuator Pad
Actuator Support Interface on Spike	<125	-	-	-	125	Actuator	Struct. Wall
Spike Folded-Flow Section	<525	-	-	-	525	Struct. Wall	Struct. Wall
Plate-Fin Panel Structure	600	-	Hot Wall	Struct. Wall	335	Hot Wall	Struct. Wall
Strut Sides	1250	-	Hot Wall	Struct. Wall	380	Hot Wall	Struct. Wall

insertion into tunnel, and spike retraction). With the present sequence, the valves are opened at time zero and hydrogen at 200°R starts to flow through the engine. Hot-gas heating starts at 1 sec and steady-state heating is established at 4 sec. This quick sequence does not allow a substantial cooldown of the engine structure prior to insertion into the hot-gas stream.

If, instead of the operational sequence described above, the hydrogen flow were started at time zero and the engine allowed to linger in the pod for 5 to 10 sec prior to injection into the hot-gas stream, the engine structure would cool down to a temperature slightly above the inlet hydrogen temperature of 200°R. Injection into the hot-gas stream at this point would still result in fast-responding outer walls (0.015 in. thick) as resulted from the above startup sequence. The structural walls (0.060 in. and thicker) would also respond similarly. However, the structural walls are 200° to 300°R cooler at the start of heatup. This would create temperature differences that are 200° to 300°R higher than reported. The timing of the startup sequence can, therefore, be used as a means of adjusting the severity of the thermal cycle conditions.

Results in Table 5.7-1 indicate that the structural temperature difference of the strut sides reaches 1250°R during transient startup to the SAM maximum tunnel total conditions of 3300 psia and 3600°R. Additional thermal transient analyses were performed to determine the SAM test operating conditions required to limit strut-sides structural temperature differences to 900°R during thermal cycling testing. It was determined that structural temperature differences could be limited to 900°R with 1350 psia, 2640°R tunnel total conditions, and with room temperature inlet hydrogen coolant. In addition, it was determined that a two-cycle test (engine withdrawal and reinsertion into the tunnel during one tunnel blowdown) could be conducted to obtain approximately the same temperature differences during the second cycle as the first.

5.8 WATER-COOLED WIND TUNNEL ADAPTERS

The cowl/pylon and support structure assembly of the SAM is water-cooled. The design is shown schematically in Figure 5.8-1. In order to determine the coolant and structural design of the assemblies, aerodynamic, heat transfer, water coolant pressure drop, and stress analyses were performed. These are summarized below.

5.8.1 System Configuration

The cooling system of the cowl/pylon consists of four separate flow routes as shown schematically in Figure 5.8-1. Combined water-flow rates of 160 gpm at 90 psig inlet pressure and 60 gpm at 180 psig inlet pressure are required for cooling. Route No. 1 cools the leading edge of the pylon; route No. 2 cools the main portions of the pylon and cowl; route No. 3 cools the forward portion of the cowl, a 3-in.-long section between Station 41.455 (forward edge of the cowl) and Station 44.455 (where the cowl meets the pylon leading edge), and also the box-like surface of the rear pylon; and route No. 4 cools a 2.4-in.-long cowl section between Station 44.455 (end of route No. 3) and Station 46.855 (beginning of route No. 2), and also the aft end cowl/outerbody seal.

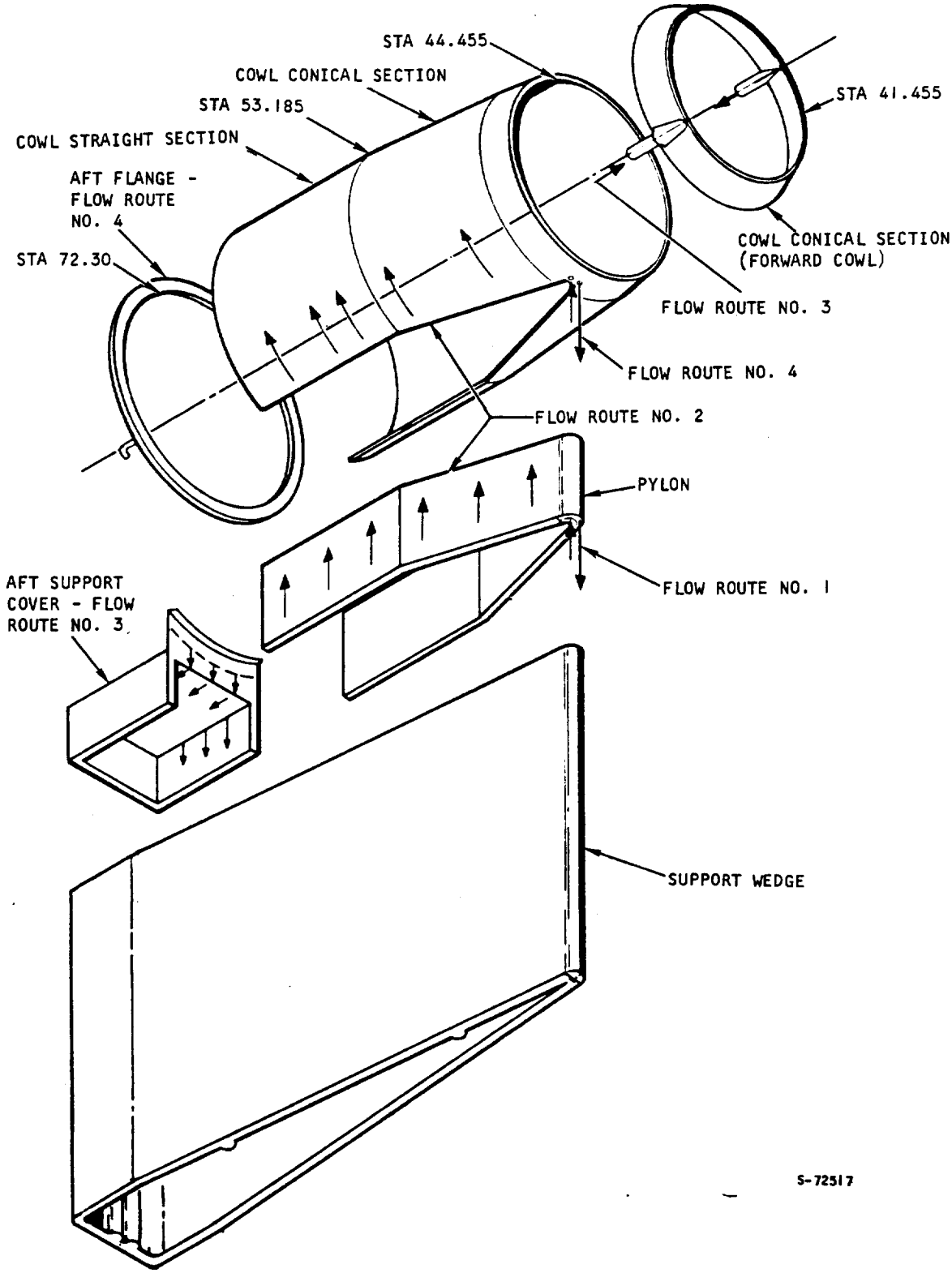

Figure 5.8-1. SAM Water-Cooled Wind Tunnel Adapters

The coolant water requirements for these routes as well as the support structure described below are tabulated in Table 5.8-1.

The support structure and the flat bottom surface of the pylon are cooled together by a single coolant water route as shown in Figures 5.8-2 and 5.8-3. The leading edge of the wedge-shaped mounting structure is cooled by water flowing through a stainless steel tube and parallel to the leading edge.

5.8.2 Heat Transfer Analysis

The SAM was tested in a methane-initiated gas flow. The freestream gas conditions in the wind tunnel upstream of the engine, as used for heat transfer analyses are Mach 7.34, 3300 psia total pressure, 5600°R total temperature and $\phi = 0.8$. Using the local aerodynamic conditions, the heat fluxes were computed. The external flow for the entire cowl was assumed to be turbulent because the Reynolds number, based on the integrated length from the outerbody leading edge, is about 0.76×10^6.

The effects of the shocks from both the outerbody and pylon leading edges were taken into consideration. Where the outerbody leading edge shock intersects the cowl surface, a pressure differential will be produced across the line of intersection and thus may result in a local flow separation. With use of the empirical correlation that the heat transfer coefficient ratio is equal to the static pressure ratio across the shock to the 0.9 power, the heat flux along the shock-sweeping lines was estimated. The maximum wall temperature is 1370°F for the cowl and 1088°F for the pylon side surface, both near the beginning of the shock-sweeping lines.

The impingement of a shock on the leading edge of a blunt body in a supersonic stream produces a localized peak-heat flux near the shock impingement point, but the magnitude and width of the peak-heat flux are not well established. With application of the shock structure and correlation for peak-heat flux reported in Reference 5.5-3, the shock structure for the interaction of the outerbody and pylon leading edge shocks was established as 20-times larger than the Fay-Riddell laminar stagnation heat flux on the outerbody shock-free leading edge. A gas surface temperature of 1590°F resulted. The width of this intense heating was estimated to be 0.112 in., one-twentieth of the pylon leading edge radius.

The pressure of surface protuberances causes separation of the oncoming attached boundary layer flow, and the heat flux in the interference region is generally higher than that in the upstream undisturbed flow region. The pylon will induce this type of interference flow, locally, on the cowl, upstream of the pylon leading edge. In general, the magnitude of the resultant interference heat flux depends on the shape of the protuberance and the upstream flow conditions such as Mach number, Reynolds number, and boundary layer thickness. The maximum heat transfer coefficient in the interference region was estimated at 17.3-times larger than that in the undisturbed flow at 9 in. from the outerbody leading edge. This peak-heating produces a local maximum temperature of 1700°F on the water-cooled cowl.

TABLE 5.8-1

SAM COOLANT WATER REQUIREMENTS FOR SAM ADAPTERS

Flow Route	Flow Rate, gpm	Temperature, °F		Pressure, psig		Flow Route ΔP, psi
		Inlet	Outlet	Inlet	Outlet	
1 Pylon Leading Edge	35	80	95	90	20	70
2 Main Parts of Pylon and Cowl	125	80	160	90	10	80
3 Forward Cowl and End Pylon Box	45	80	180	180	20	160
4 Cowl--2.4-in. long--Between Routes No. 2 and 3, and Cowl End Seal	15	80	150	180	40	140
5 Support Structure and Pylon Bottom Surface	70	80	165	180	20	160

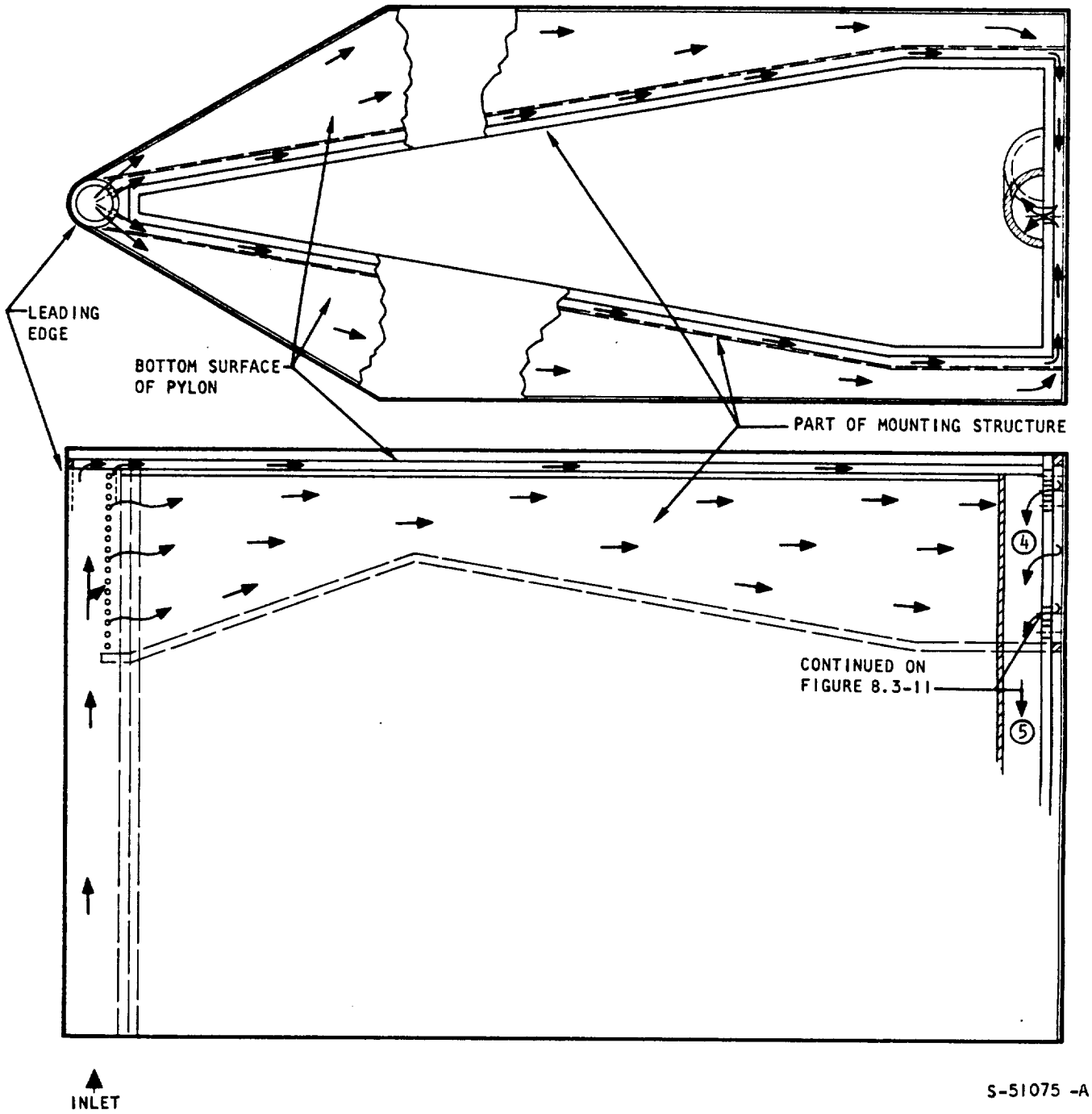

Figure 5.8-2. Support Wedge (Route 5) - Cooling of Mating Surface with Pylon, Leading Edge, and Part of Sides (Reference Figure 5.8-3.)

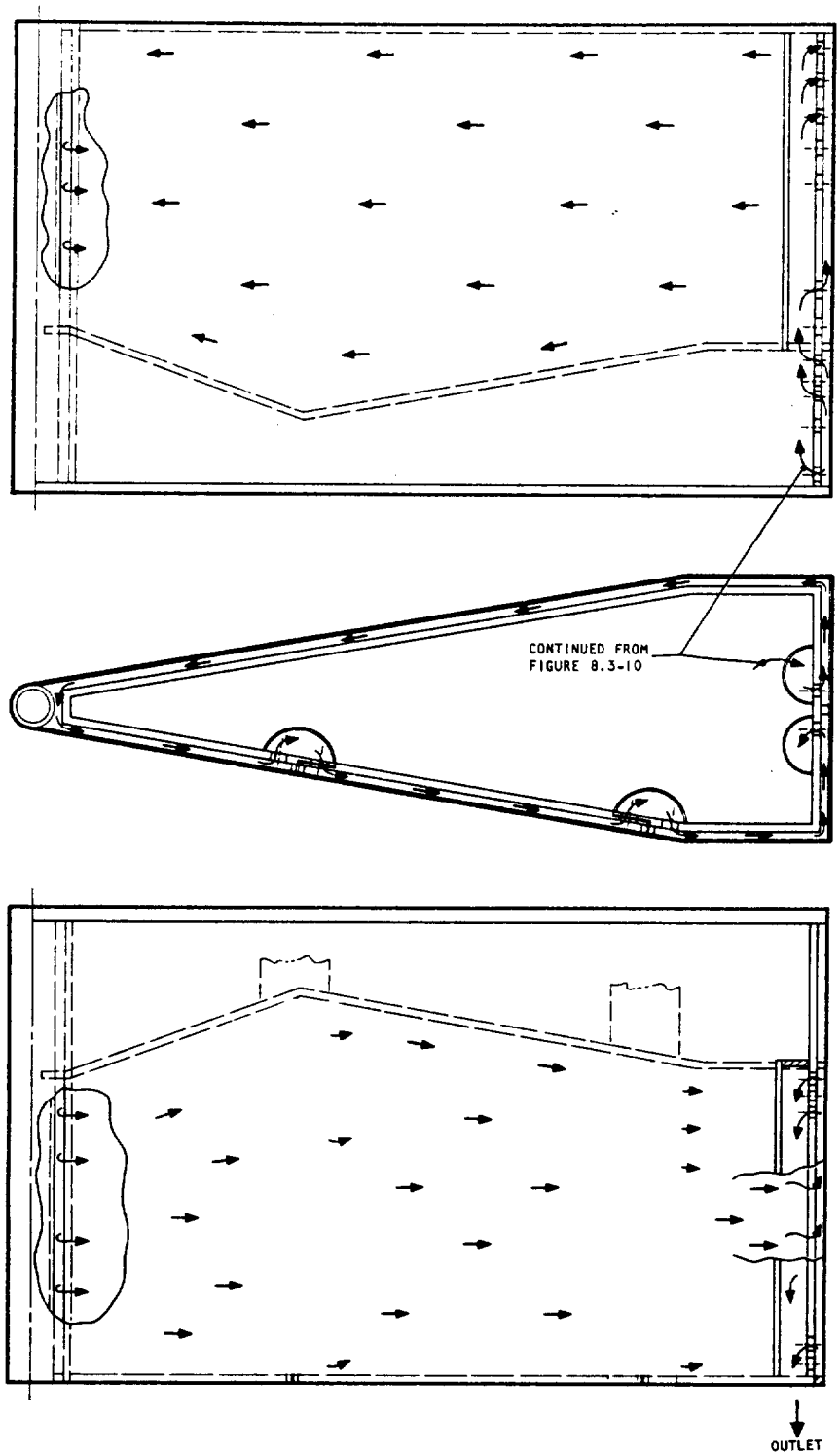

S-51076 -A

Figure 5.8-3. Support Wedge (Route 5) - Cooling of Remaining Part of Sides (Reference Figure 5.8-2.)

A one-dimensional radial heat flow analyses on the leading edge of the wedge-shaped support structure indicated a maximum surface temperature of 940°F. The effects of the shock from the support structure leading edge on the pylon bottom surface were taken into consideration. The maximum calculated gas-side wall temperature on the surface was 370°F.

5.8.3 Structural Analysis

3.8.3.1 Cowl/Pylon

The cowl/pylon of the SAM is a water-cooled, double-walled structure. The cowl consists of a tapered-truncated cone and a cylindrical section. Leading edge of the pylon is a 30-deg wedge which is attached to a straight section and to the aft support cover.

The pylon outer (hot) wall is 0.090 in. thick, while the thickness of the inner wall is 0.125 in. Coolant passages are 0.1-in.-high straight fins 0.004 in. thick, 10 fins per in. Walls and fins are fabricated from CRES Type 347 stainless steel. Both the pylon and the aft box are brazed.

The cowl is a welded assembly fabricated from CRES Type 321 steel. Steel plugs, 0.1 in. high, welded between the 0.125-in. outer shell and the 0.1875-in.-thick inner shell on a 2.5-in. radius, tie the two shells together and form the coolant passage. Between Stations 41.455 and 44.455, the shell thicknesses are 0.080 in. (outer) 0.12 in. (inner). Welded spacer bars keep the two shells tied together and form the coolant passages in this area.

Stress analysis of the structure was performed using the EASE (Elastic Analysis for Structural Engineers) digital computer program. A combination of triangular shell elements and beams are used in this program to represent the structure in the analysis. An isometric plot of the beams and the shell elements generated during execution of the computer program is shown in Figure 5.8-4a. The cowl/pylon was represented by 786 shell elements and 88 beam elements. Some of the beam elements are marked with an asterisk in Figure 5.8-4a; these are the imaginary beams simulating effect of the aft support cover. Loads acting on the SAM were discussed in Section 5.7.2.

A summary of aerodynamic, thermal and coolant pressure containment loads is shown in Figure 5.8-5. Aerodynamic load Case 4 is based on the assumption that 15 psi is acting on the vertical projected area of the cowl/pylon. Since such a load is of extremely short duration, any analysis considering it as a static load is considered conservative. Pressure during normal operation of the tunnel is 2.0 psi or less.

The results of the analysis are shown in Figure 5.8-4b. Only the maximum stresses are shown. The high, but localized temperature differences across the hot-gas exposed metal cause plastic deformation, but the calculated maximum cycle life is above 100.

The cowl/pylon is attached to the HRE suspension frame (wishbone) at four places. Stresses due to the loads transmitted to the suspension frame by the cowl are well within allowables.

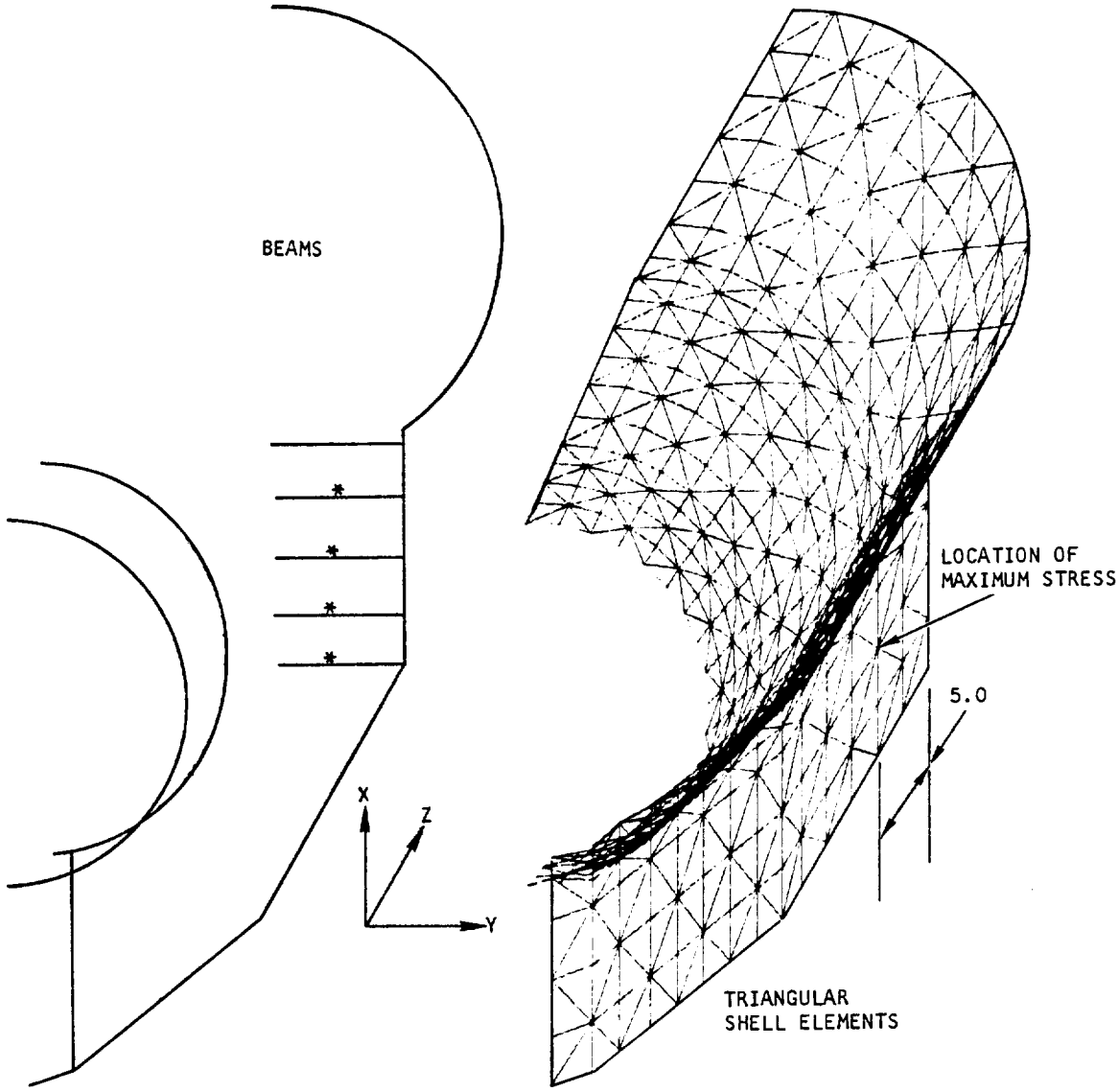

a. SAM Cowl/Pylon Structural Model

	Pressure Loads, psi		5 g Inertia Load		
	2.0 Uniform	Tunnel Unstart	X	Y	Z
Maximum stress, psi	10,500	37,200	10,000	5,040	-16,300
Yield strength at temperature	33,700	36,750	39,500		
Margin of safety	2.11	-0.01	2.95	6.83	1.42

b. SAM Cowl/Pylon Maximum Stress Due to Pressure and Inertia Loads S-72691

Figure 5.8-4. SAM Cowl/Pylon Stress Analysis

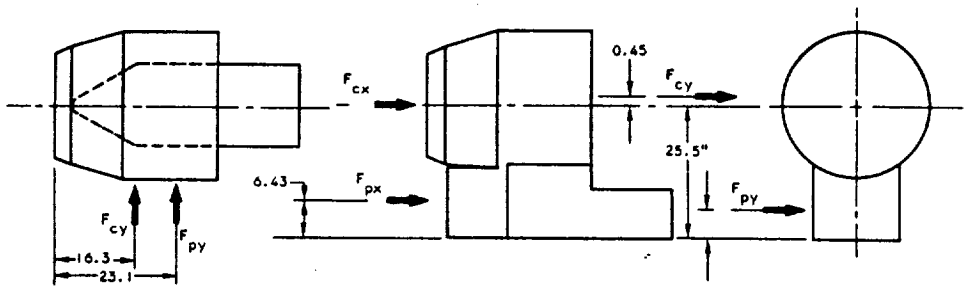

LOAD CASE NO.	LOAD CASE DESCRIPTION	F_{cx}	F_{px}	F_{cy}	F_{py}
1	SYMMETRICAL INLET UNSTART	230	2500	0	0
2	ASYMMETIC INLET UNSTART	230	2500	0	0
3	SYMMETRICAL TUNNEL UNSTART	-1253	-500	0	0
4	ASYMMETRICAL TUNNEL UNSTART	230	2500	12100	8017
5	INLET AND TUNNEL STARTED	230	2500	0	0

a. SAM COWL/PYLON AERODYNAMIC LOADS

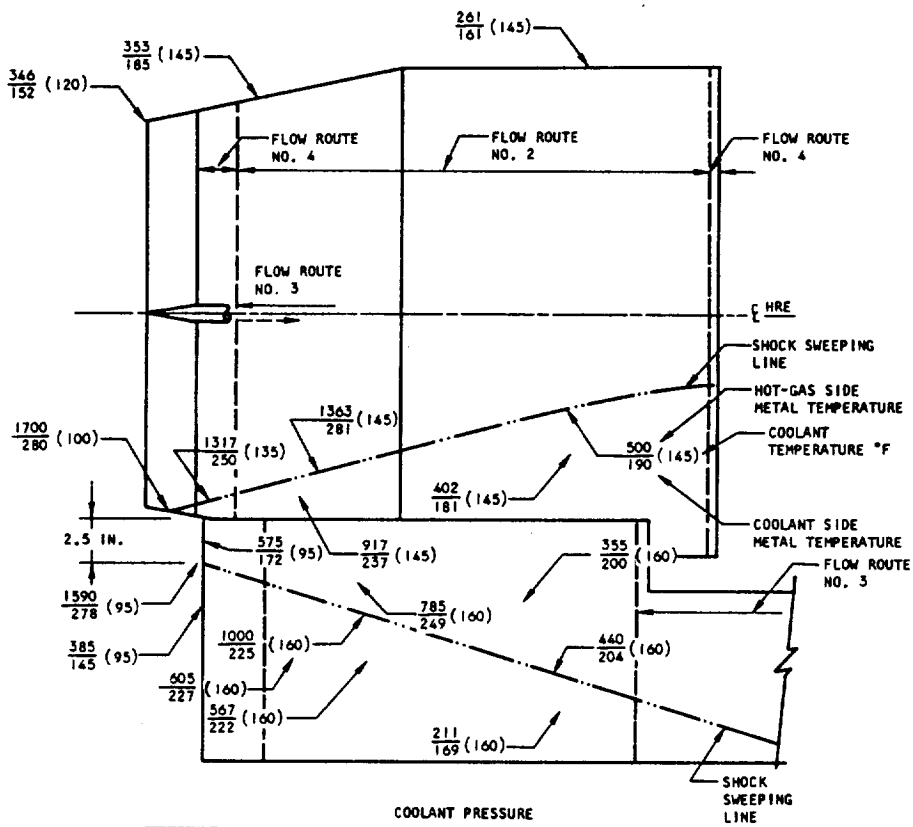

COOLANT PRESSURE

FLOW ROUTE	PRESSURE, PSIG OPERATING	PRESSURE, PSIG HYDROTEST
1	90	135
2	90	135
3	180	285
4	180	285

b. SAM WATER COOLED COWL/PYLON METAL TEMPERATURE AND COOLANT PRESSURES

Figure 5.8-5. Sam Cowl/Pylon Aerodynamic, Thermal, and Coolant Pressure Load Summary

The hoop stress due to coolant pressure in the outer CRES 321 shell between Stations 53.185 and 72.30 (cowl straight section) is:

$$\sigma_h = \frac{pR}{t} = \frac{1.5 \times 90 \times 13.95}{0.125} = 15{,}066 \text{ psi}$$

$$M.\ S_{yield} = \frac{0.85\ Fy}{\sigma_h} - 1 = \frac{0.85 \times 33000}{15066} - 1 = 0.86$$

The compressive hoop stress in the inner CRES 321 shell is

$$\sigma_h = \frac{pR}{t} = \frac{1.5 \times 90 \times 13.65}{0.1875} = 9828 \text{ psi}$$

The safety factor against buckling of the cylinder was calculated on the basis of the method presented in the 1965 NASA Report SP-8007, and was found to be 0.59; therefore the two shells must be connected. The space between connections welded between the shells is

$$\sqrt{Rt} = \sqrt{13.65 \times 0.1875} = 1.6 \text{ in.}$$

0.125-in. pins welded at 1.75 in. on center were used.

The proof pressure between Stations 41.455 and 44.455 (forward cowl) is 220 psi. Bars are welded between the outer and inner shells in order to utilize the load-carrying capability of the inner shell. Both shells are 0.08 in. thick. The spacing of these bars connecting the two shells is calculated as

$$\sqrt{Rt} = \sqrt{11.75 \times 0.8} = 0.97 \ (1.0 \text{ in.})$$

Thus, two connecting bars were used.

5.8.3.2 Support Structure

The SAM is supported on a 24-in.-high, 19-deg wedge-shaped structure. This support structure is a double-walled, brazed structure fabricated from Type 347 stainless steel. The outer surface, which is exposed to the hot gas flow, is 0.1 in. thick. Coolant passages between the outer surface and the inner wall are formed by 0.1-in.-high plain fins. The inner wall is 0.31 in. thick. Figure 5.8-6 shows the basic geometry of the structure. The assembly is anchored to its base by 11-5/8-in.-dia bolts. The loads acting on the complete system are described in Section 5.7.2.

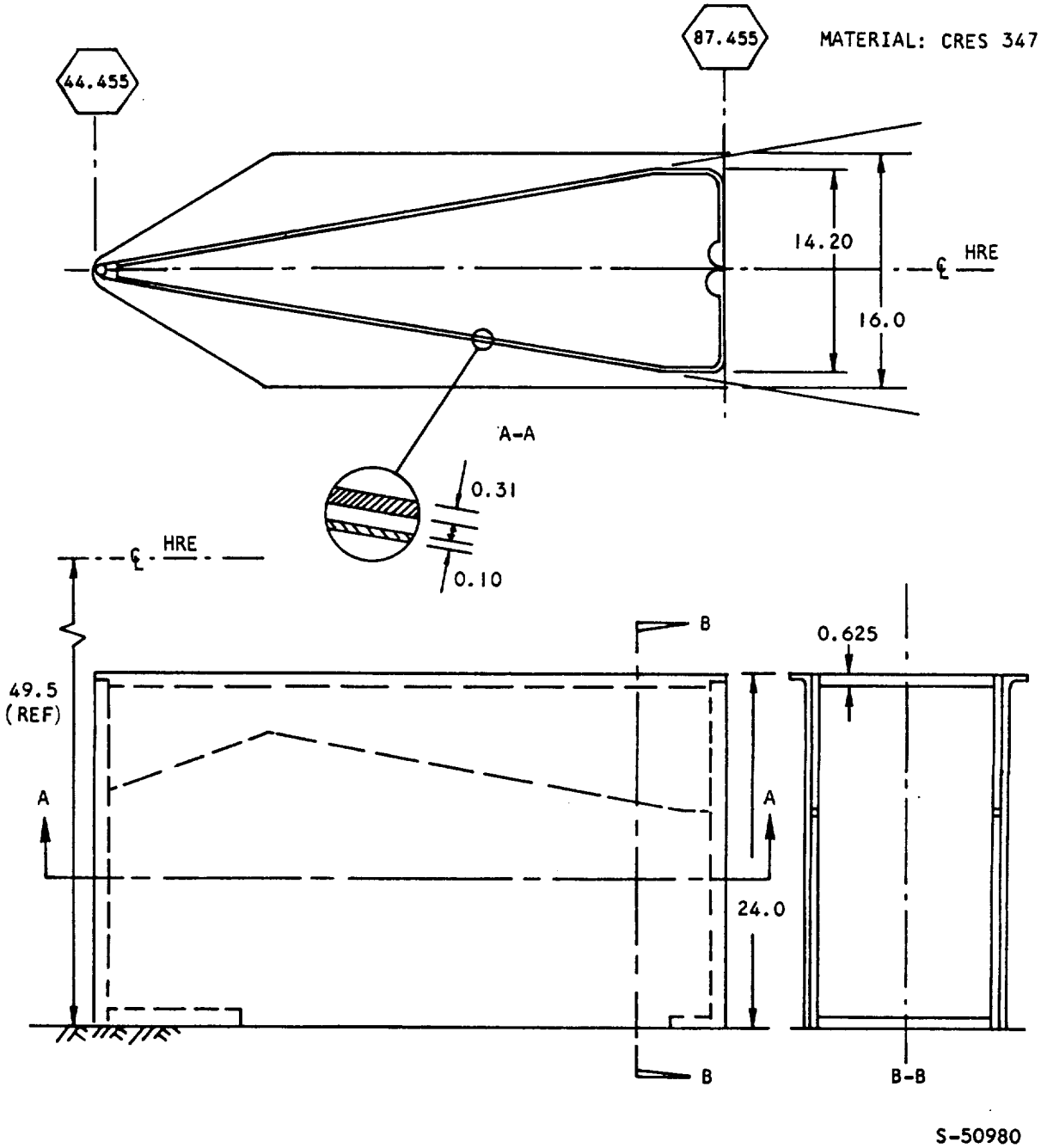

Figure 5.8-6. SAM Support Structure

The maximum bending stress due to the combination of aerodynamic load Case (d) and the 2.0g inertia load is 17,952 psi. Using 85 percent of the 0.2-percent yield strength as maximum allowable stress, the margin of safety, M.S. $= \frac{0.85\ Fy}{f6} - 1 = 0.7$ (quite high). The deflection of the structure perpendicular to the ℄ of engine is 0.000296 in., which is entirely acceptable.

Stresses in the leading edge due to pressure containment of the coolant are 1780 psi. Thermal stresses in the side panels will be below the elastic limit, but the leading edge will undergo some plastic deformations. The expected number of life cycles will exceed 5000. The natural frequency of the support with the model in place is 181 Hz, which is well above an expected 27-Hz wind tunnel input.

5.9 TEMPERATURE CONTROL SYSTEM

The design and fabrication of a temperature control system for the HRE SAM differed from the earlier work on the HRE control system, the objective of which was a controller to be mounted within the engine and handle engine operation for a wide variety of flight operating conditions. The objective of the later effort was a control console to be located in the control room of the hypersonic wind tunnel at NASA Langley. In addition, the intended functions of this control system differ from those of the flight system in that the flight control system was intended to control the spike, combustors, engine temperature, and several other variables in order to achieve best operating conditions at a given Mach number and altitude. The present system is, in contrast, a set of test support equipment which provides for engine temperature control in the= relatively stable operating environment of a wind tunnel.

The functions of the SAM control system can be grouped in three categories:

(a) It provides the necessary interface with the test facility. A set of switches and interlocks will permit safe start-up operations, and shut-down of the HRE SAM in step with the operation of the wind tunnel.

(b) It provides manual control and visual monitoring of the total hydrogen flow rate and the ratios of the flow through the different parallel coolant paths.

(c) It contains an automatic temperature controller which increases the total hydrogen flow rate if any of 27 temperatures in the engine structure exceeds a preset value. Test data acquisition is accomplished by means of output lines from the SAM control system to the facility DAS.

The design approach of the present system was to use analog computing circuits, rather than the digital circuits which were to be employed in the flight control system. This approach is expedient here since the device becomes a piece of control room equipment for which the local environmental factors and package size are much less restrictive.

5.9.1 System Configuration

A functional diagram of the temperature control system is shown in Figure 5.9-1. Gaseous hydrogen at about 1000 psia and 200°R enters the pressure control valve (PCV). A simple pneumatic controller, not shown, modulates the PCV to maintain a constant gas pressure in the plenum. Hydrogen leaving the PCV goes through the main flowmeter, which measures the total mass-flow rate of gas, then splits into four parallel flow paths. The volume flow rate in each path is measured by a flowmeter, whose output is ratioed with the volume flow rate through the main flowmeter, in order to display percentage flow through each flow path. After passing through the cooled structures components, the hydrogen arrives at the fuel plenum, from which the flow again divides. One path goes through two fuel dump valves (FDV), operated in parallel, and thence to a facility vent line. The other path goes through the injection control valve (ICV) to the injectors.

5.9.1.1 Temperature

Temperature is sensed at 27 locations in the SAM by means of chromel-alumel thermocouples. Each pair of thermocouple leads is brought to a reference junction, maintained at 150°F, where connections to copper wires are made. The 27 pairs of copper leads are connected to 27 buffer amplifiers in the controller console. Each buffer has two outputs; one goes to the data acquisition system and the other to one channel of a 27-channel auctioneering circuit. The outputs of five set-point generators are also fed to the auctioneering channels. These set-points correspond to the five zones of the SAM. Each channel has as its input the difference between the temperature and the zone set-point for a given thermocouple. The auctioneering circuit picks out the greatest of these error signals and operates on it in the manner of a process controller. The output signal is suitably amplified and applied to the FDV.

5.9.1.2 Fuel Injection

During the changeover to the fuel injection operating configuration, a summing amplifier within the controller is used to provide a smooth transition of flow between the FDV and the ICV. This amplifier has several inputs; namely, the control signal, the FDV bias signal, the derivative of the volume-flow rate, and the purge command signal. The sense of the flow rate deviation signal is to cause FDV to move toward a closed position if the flow rate increases, and vice versa. This type of control is often called "feed-forward" in process control. The bias signal serves to keep the FDV open when the ICV is closed and all temperatures are below their set-points. In the absence of this bias signal, the FDV would remain closed until one of the 27 temperatures reached its set-point. Precooling before insertion into the hypersonic wind stream requires that the FDV be biased to remain open in such a condition. The bias signal is removed when the ICV is opened.

5.9.1.3 Flow Management

The flow management system comprises four CRV's, five turbine flowmeters, a pressure transducer, and a temperature transducer--all mounted on the hydrogen piping on the carriage beneath the SAM--and signal conditioning equipment,

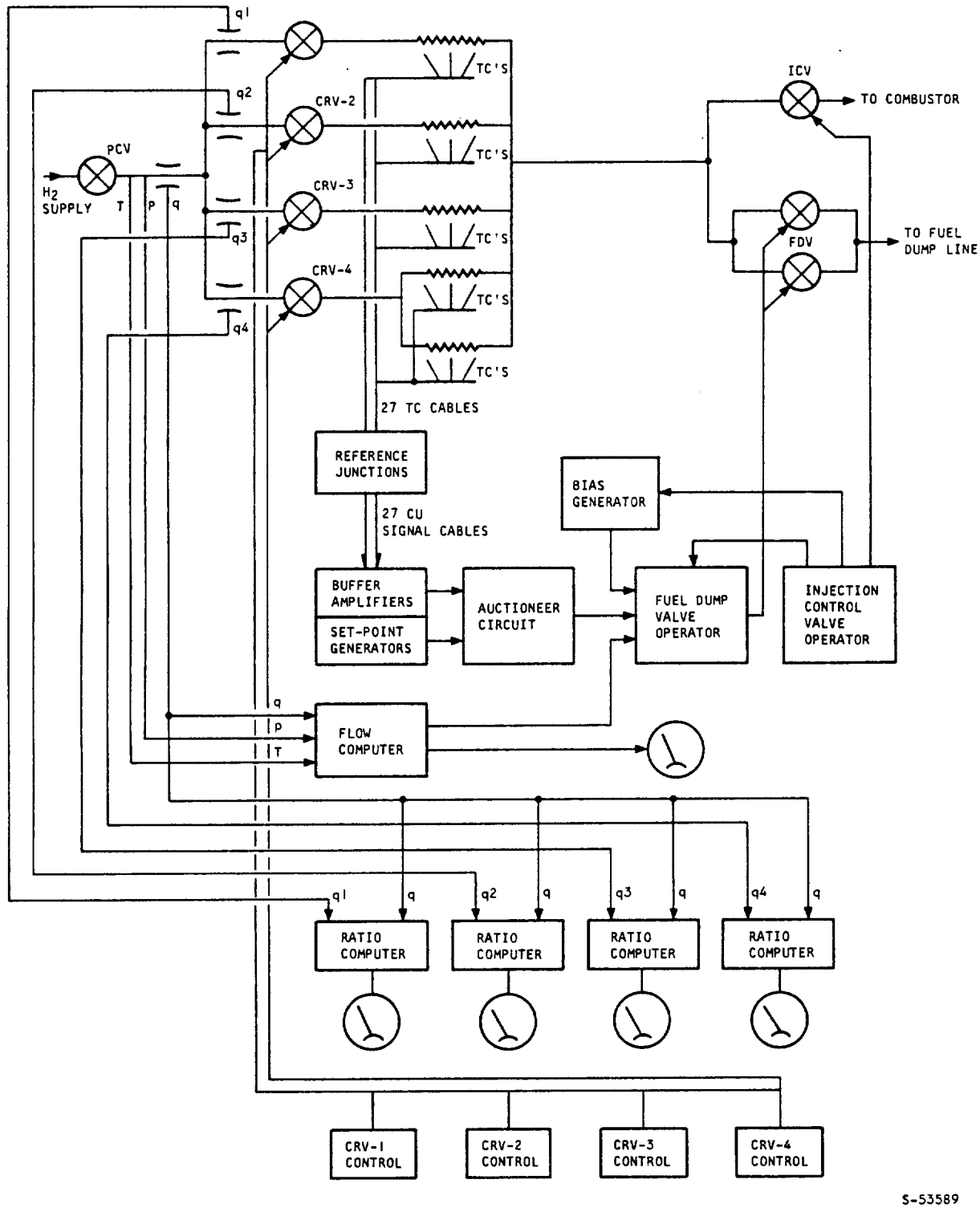

Figure 5.9-1. Functional Diagram of Temperature-Control System

meters for displaying flow rate, CRV control amplifiers, and CRV adjustment controls--all mounted in the console. The main flowmeter is located between the pressure control valve (PCV) and the branching manifold. The four branch flowmeters are located just downstream from the same branching manifolds and upstream from the four CRV's.

Mass flow rate is computed by an analog computer according to the following equation:

$$\dot{m} = kpq/T$$

In this equation, ($\dot{m}$) is the mass flow rate (e.g., in lb/min), (p) is the absolute pressure, (q) is the volume flow rate, and (T) is the absolute temperature. The coefficient, k, includes the gas constant and the various scaling factors between the electrical signals and the actual values of (p), (q), and (T).

The flowmeter sizes have been selected to cover the expected range of hydrogen volume flow in each branch as well as in the main flow section. Calculations have been made of the nominal, maximum, and minimum mass flow rates at each of the five flow-measuring points shown in Figure 5.9-1. The maximum total flow rate has been established as 1.25 lb/sec at a pressure of 900 psia and a temperature of 200°R. The nominal or design point total flow rate is 0.622 lb/sec at a pressure of 735 psia and temperature of 200°R. Minimum flow is one-third of nominal mass flow rate, and occurs at an assumed pressure of 700 psia and temperature of 200°R. The volume flow rates for the three conditions and the flow rate range of the turbine flowmeter selected for each of the five locations are tabulated below.

Flow Location	Flow Rates, cfm		Flowmeter, cfm	
	Minimum	Nominal	Maximum	Range
Inlet (total)	19.2	54.9	90.7	10.0 - 125
Through CRV-1	7.05	20.1	33.1	4.0 - 50.0
Through CRV-2	2.04	5.83	9.65	1.5 - 10.0
Through CRV-3	6.19	17.68	29.2	4.0 - 50.0
Through CRV-4	3.97	11.31	18.65	2.5 - 25.0

Each of the five flowmeters covers a greater flow range than that predicted by the analysis. In addition to the ranges listed, each flowmeter has an overspeed capability of at least 50 percent.

The primary signal generated by each flowmeter is a frequency determined by the rotor speed. The nominal maximum of the range corresponds to a frequency of approximately 1200 Hz for each meter. For example, suppose that a flow rate of 50 cfm through CRV-1 would generate a frequency of 1200 Hz. The

three calculated flow rates listed above for that flow path would generate frequencies of 169, 483, and 795 Hz, respectively. This frequency signal is converted to an analog voltage for use by the flow computer or the data acquisition system. This signal conditioning is accomplished by means of five digital-to-analog converters, one for each flowmeter, located in the flow management section of the control console.

The performance of the flowmeters with nitrogen instead of hydrogen was examined. The conclusion was reached that the volume-flow rate would be less with nitrogen than with hydrogen. The greatest nitrogen flow rate occurs during purge condition. In this condition, both of the FDV's and the ICV are opened. In addition, the safety bypass valves around the PCV and the FDV's are opened in order to clear their connecting lines of any hydrogen. (These bypass valves are not shown in Figure 5.9-1).

5.9.1.4 Interface Logic

A functional block diagram of the interface logic system is shown in Figure 5.9-2. The system provides appropriate responses to signals from the wind tunnel facility and generates signals to the facility, enables the operator to start up and shut down the model, and initiates appropriate action in case of an alarm condition.

The following conditions constitute alarms, any one of which causes shutdown, if:

(a) A high temperature causes the FDV to go completely open, so that there is no longer any ability to control or reduce temperature.

(b) The mass flow rate of hydrogen falls below a low-flow limit, a condition which implies a valve malfunction, obstruction in the line, or lack of sufficient hydrogen supply pressure. This alarm is inhibited unless the carriage is in the raised position.

(c) Cooling water flow to the supporting structure connecting the SAM to the carriage falls below a safe value.

(d) The operator presses the manual shutdown switch.

Any of these shutdown alarms causes the spike to close and signals the wind tunnel operator to lower the carriage, withdrawing the SAM from the hypersonic air stream. In addition, the high-temperature and low-hydrogen-flow alarms cause the bypass valves to open, in order to increase the gas flow rate through the SAM.

The logic system operates to provide a safe startup procedure. The startup sequence commences with the carriage in the lowered position and no gas flow through the SAM. The operator clears all alarms that are still in effect (alarms are held in by latching relays until manually cleared) and operates the CALIBRATE RUN switch to the RUN position. He adjusts the FLOW PRESET control to set the FDV at some opening, then requests gas flow (hydrogen or nitrogen) from the facility.

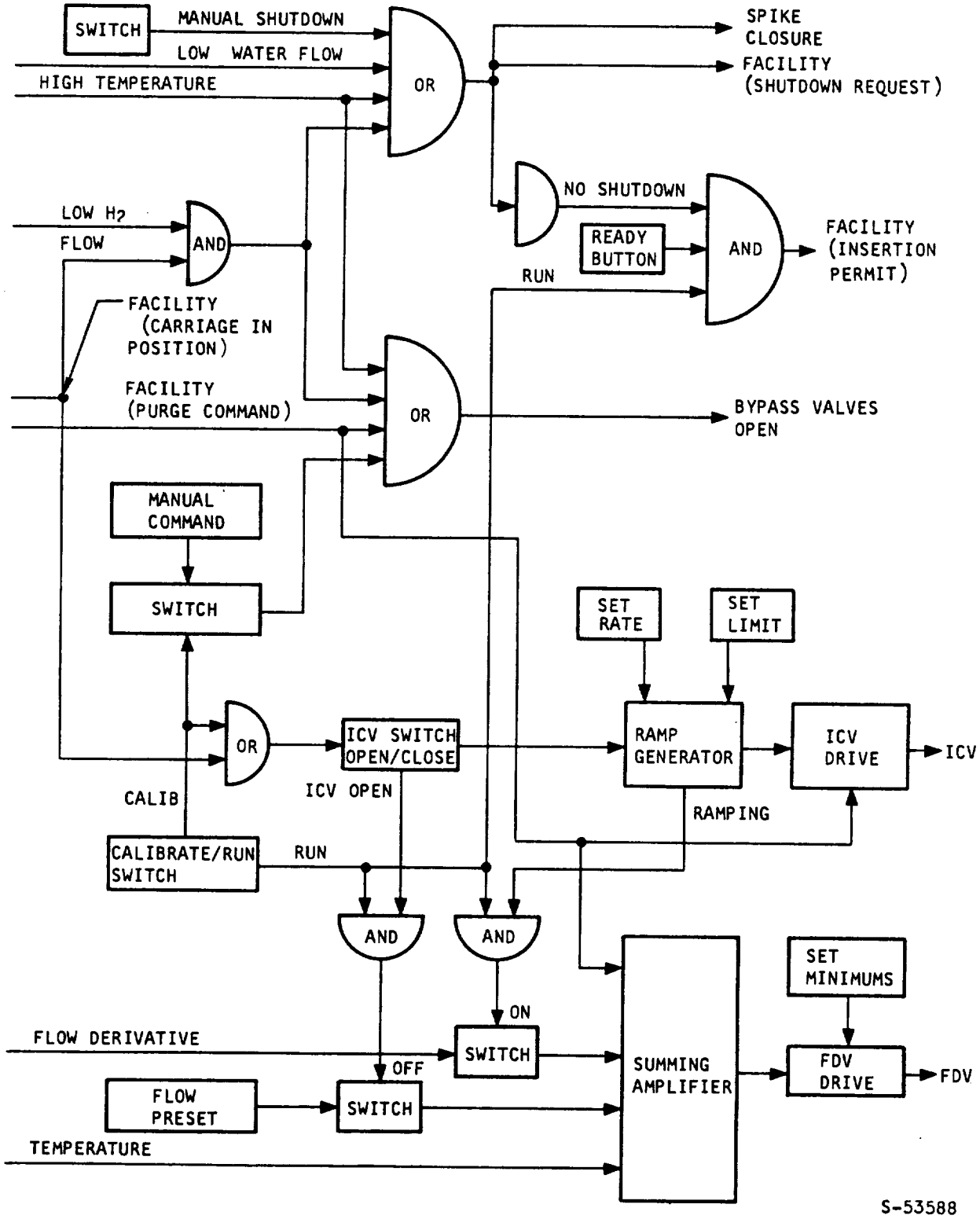

Figure 5.9-2. Logic Diagram for SAM Temperature-Control System

When the tunnel is started and hydrogen flow is established, the operator satisfies himself that the flow rate values are correct. He then presses the READY (carriage insertion) button. The carriage insertion circuit is closed by this action, and the tunnel operator is then able to raise the carriage. When the carriage is in position, a signal is received from the tunnel facility. This signal enables the Low-H_2-Flow alarm and enables the ICV switch.

The operator then operates the ICV switch to the OPEN position if desired. A ramp generator is started which sends a command to the ICV to open at the ramping rate. Simultaneously the FLOW PRESET signal is turned off, in order to permit the FDV to close. To prevent the FDV from closing immediately, a signal derived from the main flowmeter is switched on. This signal is proportional to the rate of change of the volume flow rate. The FDV is thus constrained to move in such a way that the total flow rate through the SAM remains nearly constant while the ICV is opening. When the ramp generator reaches its limit, the flow-derivitive signal is turned off and only the temperature control signal has any effect on the FDV.

In a controlled shutdown, the operator would operate the ICV switch to the CLOSE position. He would manually close the inlet spike as a separate step, or could cause spike closure by pressing the MANUAL SHUTDOWN switch. This switch also signals the tunnel operator to lower the carriage. In a manual emergency shutdown, the operator would simply press the MANUAL SHUTDOWN switch.

Another condition is the one which results from a purge command from the facility. This command may be given at any time, although it will not occur in the middle of a test except in an emergency. The purpose of purging is to replace all hydrogen in the SAM piping by nitrogen. In order to accomplish this, all outlet valves and the bypass valves are opened and the system is flushed with nitrogen gas. Referring to Figure 5.9-2, it can be seen that a purge signal opens the bypass valves, the ICV, and the FDV.

The function of the CALIBRATE/RUN switch is to permit manual operation of each of th e valves, including the bypass valves. In the CALIBRATE position, the various interlocks between valves are turned off. The carriage cannot be raised unless this switch is in the RUN position.

5.9.2 Circuits

Solid-state electronic circuits are used throughout the temperature control console, except that some latching and switching functions are accomplished with relays. The electronic solid-state circuits consist of discrete components and operational modules. These are mounted on printed circuit boards for ease in servicing and replacing faulty units.

5.9.3 System Dynamics

An analog computer simulation of the SAM coolant system and pressure and temperature controls was prepared for analysis of the system dynamics. The analog computer simulation was for the purpose of conducting transient analyses for determination of:

(a) Cooling system transient operation relative to wind tunnel test conditions

(b) Mathematical descriptions for electronic compensation networks as required to produce safe operation for all tunnel operating conditions and stable operation for tunnel nominal test conditions

5.9.3.1 Computer Run Conditions

Various runs were made on the computer, in which component parameters were varied over their expected ranges, to determine relative effects of the individual loop response-frequencies of the temperature control, pressure control, and cooling system. The range of parameter variations is noted below.

Pressure Control

(a)	Control gain:	Gains to provide a droop-band of 25, 50, and 100 psi.
(b)	Valve natural frequency:	1, 3, and 5 Hz
(c)	Damping coefficient:	0.3, 0.7, and 1.0
(d)	Plenum volume:	1000 to 5000 cu in.
(e)	Sensing time constant:	0 to 3.0 sec

Temperature Control

(a)	Control gain:	Gains to provide a droop-band of 50, 100, and 200 deg.
(b)	Valve natural frequency:	1, 3, and 5 Hz
(c)	Damping coefficient:	0.3, 0.7, and 1.0 Hz

5.9.3.2 Computer Results

The computer results indicated there was a strong interaction between the temperature and pressure control loops at low natural frequencies. The most noticeable effect appeared at valve frequencies close to the resonant frequency of the cooling system. For the pressure control loop, noticeable instabilities were present at a frequency of 1 Hz. At a frequency of 5 Hz they were substantially reduced with adequate valve damping.

Similar effects were noted with variations in natural frequencies of the temperature control valve, although they are of a lesser magnitude. Incorporation of temperature control feedback, however, further decreased the damping of the pressure control.

Increasing plenum chamber volume has a stabilizing effect upon the pressure control, although not sufficient by itself to achieve the stability required.

To provide stability it was necessary to add electronic compensation in the temperature control and also to orifice the pressure-sensing line.

The compensation added was of the form $\frac{A_s}{\tau s + 1}$. For various valve frequencies and control gains there is an optimum value of the parameters A and τ which will provide adequate performance. Values selected are, however, very dependent upon the control valve response characteristics. It was therefore necessary to determine these characteristics through actual valve testing and incorporate these in the computer simulation prior to finalization of the network parameters.

6. DESIGN FEATURES

The specific designs adopted for fabrication of components and assemblies required consideration of numerous constraints. Underlying all else were the requirements imposed by the aerodynamic design and performance objectives. The thermal and structural design occurred within the aerodynamic constraints. Although manufacturing considerations were clearly important, they governed the aerodynamic design only in the case of the outerbody and strut leading edge radii. Performance objectives and survivability requirements were governing in all other areas.

In the following, the design features of the flightweight engine structures are discussed. The water-cooled test adapters for SAM, as well as other equipment required in the SAM tests, are also reviewed. Shell assembly flow test adapters and a vibration model were designed, but not fabricated to completion. The features of the vibration model are summarized; the flow test adapters are discussed in both Sections 5 and 7 and are not further reviewed in this section. Layout drawings are generally used as the basis for the following discussion and are included at the end of the report. These layout drawings occasionally differ in detail from the final design as fabricated. Since they display all of the features of the components on a single sheet, they are used, and the important differences are noted. All designs shown were expected to meet the thermal and structural requirements that would have been encountered in engine flight testing.

Design of the flightweight components was derived from the engine designs evolved during Phase I of the program. The layout design of a qualification test engine derived from this effort is presented. In the following, however, the SAM assembly is generally used as the reference design, since it closely reflects the initial engine design concepts and was fabricated and tested. The hydrogen-cooled engine assembly for SAM is discussed in detail following discussion of the components.

A mock-up of the engine assembly, discussed in Section 7, was used to investigate assembly requirements, packaging of subsystems, and routing of fluid and electrical lines. Data derived from the mock-up was incorporated into the designs as required. Since most of the subsystems required for flight testing did not become a part of the SAM or were not required to be internally packaged, no serious packaging problems were encountered in design of the SAM.

6.1 INLET SPIKE

The inlet spike has interfaces with the inner shell and with the actuator. From a design standpoint, the most critical of these is the interface with the inner shell.

6.1.1 Design Ground Rules

The requirements imposed on the design of the inlet spike included the following:

1. Zero leakage sealing at the interface with the inner shell or leakage flow that can be vented to low-pressure ambient. This requirement is imposed so that low pressure levels can be maintained in the engine cavities. Low pressure levels are advantageous for two reasons. The first reason is to eliminate the need for a large gas supply to inert the cavities. If cavity pressure is maintained near nozzle base pressure, the structure will contain any explosions resulting from hydrogen leakage into the cavity. The second reason is to avoid large blowoff loads on the spike, which would result from high pressure in the cavity, either due to high leakage flows or inerting. These blowoff loads, in turn, would be imposed on the spike actuator.

2. Fabrication of the spike in three sections to accommodate the large change in diameter in forming operations.

3. Smooth aerodynamic surface. Initially, it was thought that external doublers would be acceptable in terms of inlet performance. Inlet testing, however, showed a potential starting problem at low Mach numbers as a result of such doublers.

6.1.2 Features

Drawing L-980612 depicts the layout of the inlet spike. Sandwich shells are used as the cooling jackets and ring-stiffening in the form of manifolds is used to resist buckling loads in areas of high external pressure. Hastelloy X is used throughout, except for instrumentation and coolant plumbing tubes, which are CRES.

6.1.2.1 Spike Tip Cooling

The spike tip is shown as an enlarged detail on the drawing. Coolant enters from the rear and distributes itself into the plenum and through a central tube, which provides ducting to the hemispherical tip. The two coolant streams combine and flow aft along the spike jackets. The tip of the cooling tube is supported by the spike tip, but is not brazed to allow accommodation of differential thermal expansions. An additional support for the tube is provided near Sta. 4.40 to prevent the tube from vibrating. For the same reason, the total-pressure tube from the spike tip is brought out of the central tube at the first opportunity to limit the unsupported length of this tube. As shown, the spike tip assembly forward from Sta. 7.00 is fabricated from two sandwich sections. The final design used one sandwich section from Sta. 7.00 to Sta. 1.56 and a single-skin nose cone for the remainder.

6.1.2.2 Inner Shell-Inlet Spike Interface

The selected configuration for this interface uses a combination of bellows and seals. Graphite-impregnated asbestos seals were used for the sliding-seal application. The purpose of this seal is to provide a high pressure-drop flow path into the cavity between the bellows and the spike shell rather than to provide zero leakage. The leakage flow is then vented overboard to a point of low pressure. In this way, the pressure loading on the bellows is considerably reduced over that which would occur without a seal. This design accomplishes two things: (1) it permits the use of a lighter weight bellows and (2) it reduces the blowoff load that must be carried by the actuator. The bellows material is Inconel 718, although the drawing bill of materials indicates Hastelloy X.

6.1.2.3 Manifolds

The spike assembly uses two manifolds, one at Sta. 43.00 for fuel injection and another at Sta. 46.00 for the spike coolant outlet. The fuel injection manifold is made as light weight as possible to accommodate temperature differences that will exist between the cooled shells and the fuel being injected. At the same time, this manifold serves as a ring stiffener for the shell. The coolant outlet manifold is similarly used for ring stiffening. Although pressures between Sta. 50.50 and 55.76 are high, the pressure difference across the shell in this area will be essentially zero, since the back of the spike shell is open to engine pressure. Buckling loads here are carried by the inner shell.

6.1.3 Fabrication Requirements

The inlet spike is fabricated from three main subassemblies. These are described below:

1. The spike tip, extending to Sta. 7.00 is shown to consist of two separate plate fin assemblies. In the final design, one sandwich section extends from Sta. 1.56 to Sta. 7.00, and a single-skin, machined cone is used for the nose.

2. The spike fore body, extending from Sta. 7.00 to Sta. 35.00, consists essentially of the conical portion of the spike. The break point at Sta. 7.00 was established by forming considerations, that is, by the diameter ratios at the two ends. The break at Sta. 35.00 permits a change in fin height from 0.153 in. to 0.050 in. The use of a single fin height for the inlet spike is not practicable. A low-height fin is required in the aft spike for satisfactory cooling. If this fin were used in the fore body, the pressure drop would be too high.

3. The spike aft body, extending from Sta. 35.00 to Sta. 55.76, consists of the cooling surface proper and the flow return to permit translation of the spike over the inner shell. The internal shell for the reverse flow section is fabricated from heavy sheet (0.090-in. thickness), which was machined to ensure a smooth surface for the sliding seal.

The doublers used at the joints of the shell subassemblies are shown to be external in the layout. As noted above, it was subsequently required that the aerodynamic surface be smooth. The doublers at all three shell joints were, therefore, made internal by providing relief in the fin passages.

6.2 INNER SHELL

The inner shell has interfaces with the nozzle, the inlet spike, the inlet spike actuator, and the struts. Consideration of each of these areas was required to define the final design.

6.2.1 Design Ground Rules

The critical design problems for the inner shell occur at the interfaces. The interface with the inlet spike is governed by considerations of assembly and accessibility. The interface with the strut must provide the requisite structural strength and must accommodate the subsonic fuel injection manifolds and the inner shell/nozzle coolant crossover manifold and connection. The interface with the nozzle must have provisions for sealing both the coolant crossover and the internal cavity from the propulsion stream and also must permit attachment of the nozzle. The interface with the actuator must permit sliding the actuator into the inner shell (after strut assembly and alignment of the actuator centerline relative to the shell center line), by using shims for custom fitting.

6.2.2 Features

Drawing L-980609 depicts the layout of the inner shell. A sandwich shell is used as the cooling jacket, with ring stiffening in the form of manifolds being used to resist buckling loads. In addition, the shell is shown reinforced between the manifolds at Sta. 50.46 and 55.67 by the use of four sheet metal segments around the internal periphery. This reinforcement was deleted from the final design. Three of the four separate manifold rings are used as structural members. These are:

1. The forward manifold at Sta. 50.46 which is the coolant outlet for the innerbody flow route. It carries a flange for attachment of the sealing bellows between the inlet spike and the inner shell. Details of the actual interface are shown in the spike layout, Drawing L-980612.

2. The fuel injection manifold at Sta. 55.67. Several design approaches were considered for this manifold. Four of these approaches are described below.

   (a) The use of individual fuel tubes to each of the fuel injection ports. These tubes would penetrate the manifold shown on Drawing L-980609, which would then act only as a ring stiffener. To control thermal lag, coolant could be bled from the shell through the manifold and back to the shell.

(b) The use of a dual manifold (one manifold within the other). The inner manifold would be used as a fuel injection manifold. Coolant would flow in the space between the two manifolds to ensure temperature equalization.

(c) Attachment to the manifold of small diameter lines carrying coolant. Coolant from the inlet spike exhaust could be used in these lines to ensure temperature equalization between the manifold and the shell. The small quantity of coolant required to achieve this purpose would be routed to the fuel plenum after passing around the manifold.

(d) The design shown in the layout drawing, which was used in the final design. This design assumes that the temperature differences encountered at this location are acceptable in terms of thermal loading and fatigue life.

3. The fuel injection manifold at Sta. 59.53. This is a nonstructural component fabricated in six segments. The mass of the structure has been minimized to reduce loads resulting from thermal lag and to reduce weight.

4. The crossover manifold at Sta. 65.6, which serves as the coolant inlet for the inner shell.

All manifolds are fabricated from Hastelloy X. The crossover manifold and the forward fuel injection manifold are locally cut out and reinforced by doublers to accommodate the strut mounts and to transmit the strut loads.

6.2.3 Fabrication Requirements

The assembly sequence reflected in the design for the inner shell and used in the fabricated assemblies is as follows:

1. Braze the shell assembly (hot shell, fins, and cold shell).

2. Machine the ports into the shells for the fuel injection nozzles at the manifolds and for the instrumentation fittings.

3. Machine the cutout for the struts.

4. Install and braze the fuel injection nozzles and the instrumentation inserts.

5. Install, tack in place, and braze the various manifolds, the strut socket, and its doublers and gussets.

The crossover manifold at Sta. 65.6 is a prebrazed assembly which is installed as a unit. Similarly, the fuel injection manifolds at Sta. 59.53 and 55.67 are prebrazed. A separate braze cycle for the gussets that tie the

strut mounting to the manifold rings exists as an option, but was reserved for repair rather than primary brazing in the final design. Since this part of the structure operates at temperatures below 1600°R, considerable flexibility exists in the selection of braze filler alloys.

6.3 NOZZLE

The nozzle involves two critical design problems; (1) provisions for assembly of the nozzle to the inner shell must be made, and (2) access to permit such assembly must be provided.

6.3.1 Design Ground Rules

Design of the nozzle proceeded on the assumption that all of the nozzle, and structure brazed directly to the nozzle, would soak to temperatures of approximately 1600°R prior to start of coolant flow in flight. This assumption is the most pessimistic that could be made. The importance of this assumption is that metal seals only were acceptable. Many of the design features adopted stem directly from this basic assumption. Subsequently, detailed analysis showed that the use of spring-loaded Teflon seals ("Omni-seals") was feasible. Such seals were used for the SAM tests and performed well.

6.3.2 Features

Drawing L0980604 is the completed layout of the nozzle.

6.3.2.1 Nozzle Cap

The nozzle cap is used to make the final engine closeout. It is threaded into the brazed mounting provided on the shell and is locked into position using the center bolt. Although the locking bolt picks up load by its mere presence, its primary function is to lock the nozzle cap against rotation. The metallic seal at the bolt end is a standard part suitable for use with threaded fittings. As shown, the large seal at the interface with the shell is specially fabricated to be of the same type as the one used under the bolt. Metallic "K" seals are used to seal the nozzle cap cavity from the remainder of the nozzle. As noted above, "Omni-seals" were used in all these locations, except under the bolt, on the SAM. Removal, in turn, of the bolt, the cap, the male thread supporting the cap, and the central tube, gives access to the nozzle cavity. Connections for instrumentation of the nozzle can be made through the nozzle cap opening, which also provides access to the bolts with which the nozzle is mounted to the inner shell.

6.3.2.2 Bolted Flange/Manifold

The flange/manifold consists of the manifold itself, fabricated as a weldment from two machined pieces, and a brazed face. The coolant crossover connection to the inner shell is provided by ports sealed with conventional, metallic "K" seals (later changed to "Omni-seals"). Fastening occurs on either side of the seal using blind inserts in the flange/manifold assembly of the inner shell. The tubes shown extending from the manifold serve to guide the wrench used to torque the bolts. These tubes are welded into the manifold to eliminate possibility of leakage.

6.3.2.3 Shell

The thermal design of the shell had as its objective the use of a single fin height along the entire length of the nozzle shell. During Phase I, different fin heights were used to reflect variations in heat flux. Analysis showed that use of a single fin height is feasible and even desirable. The resulting increase in pressure drop was within acceptable limits and aids in assuring better flow distribution than could be obtained with the very low pressure drop encountered in the two-fin approach. Use of a single fin also was expected to simplify manufacture and assembly of the shell.

6.3.2.4 Nozzle Cap Purging

Because of its configuration and flow arrangement, the nozzle cap cannot be readily swept by the purging fluid. In the final design, as used on the SAM, the center tube was ported near the door assembly (Item 12 in the layout). This provides for a small amount of flow directly into the nozzle cap cavity.

6.3.3 Fabrication Requirements

Fabrication of the nozzle assembly involved no special considerations. It was arranged in steps paralleling those used for the inner shell.

6.4 LEADING EDGE

The leading edge has interfaces with the outer shell and with the ablatively cooled cowl. In contrast to the interface problems encountered with other cooled-structure components, the design problems of the leading edge are primarily associated with assembly of the leading edge itself.

To evaluate the thermal fatigue and coolant-side heat transfer in the region of the leading edge stagnation line, straight sections of the leading edge were designed, fabricated, and tested. The design features of these straight sections are discussed below, following discussion of the full-scale leading edge design.

6.4.1 Full-Scale Leading Edge

6.4.1.1 Design Ground Rules

The general objectives sought in design of the leading edge were:

(a) Use of the largest possible gap for coolant flow at the leading edge stagnation line. It is considered that reliable manufacture requires minimum gap of approximately 0.020 in. Gaps less than this are subject to plugging by braze alloy and require extremely careful control of braze alloy quantity and braze cycles.

(b) A manifolding arrangement into and out of the leading edge which permits flexibility in the selection of manifold cross-sectional area and number of inlet and outlet lines. This flexibility, in turn, assures opportunity for control of leading edge flow distribution.

(c) Temperature matching at the inlet and outlet stations of the leading edge section. Temperature differences up to about 300°R at these sections are acceptable. Much larger temperature differences were expected to lead to thermal stress problems.

(d) Detail configurations and assembly sequences that would permit verification of the structural integrity under internal pressure loading at various stages during manufacture.

(e) Avoidance, if possible, of weld joints at the stagnation line or of brazed joints in the immediate area of the stagnation line. Both were deemed risky.

6.4.1.2 Features

Drawing L-980611 depicts the layout of the leading edge. The design shown was expected to meet the thermal and structural requirements predicted for flight engine testing. The leading edge is fabricated from Hastelloy X, except for the coolant and pressure-sensing tubes, which are CRES. The final design as used for SAM incorporated a Nickel 200, as opposed to Hastelloy X, tip section.

The crossover arrangement for coolant from the leading edge to the outer shell, at Sta. 43.44, requires that the manifold flanges be scalloped. The flange ring, Item 19, is preheated for clearance over the internal hot shell during installation. This is done in preference to providing a joggle in this shell.

The leading edge tip from approximately Sta. 36.4 forward was designed as a separate multipart assembly, consisting of eight tip segments. Fins are shown machined into the surface of the tip segments in Section E-E of Drawing L-980611. The final design used sheet metal fins brazed in place. Because of the conical shape of the internal and external hot skins, installation of the tip as a single circular part is not possible. The use of multiple tip-sections permits installation of the tips with minimum flexing of the hot skins. At the same time, fabrication of the tip portion of the leading edge as a separate subassembly permits use of positive loading during brazing to ensure the required fitup for brazing. The tip portion is joined with the main body of the leading edge in three places. The wedge-shaped joint at the center acts as a seal, as well as the principal structural joint. The outer skins are butted together and closed out with brazed strips. For aerodynamic considerations, the brazed strip on the leading edge internal surface is then feathered to minimize blockage in this critical area.

6.4.1.3 Fabrication Requirements

The design assembly sequence for the leading edge is described below. This sequence was followed in fabrication of the hardware, as discussed in Section 7.

1. First brazing operations:

   (a) Inner shell assembly, consisting of the hot shell, fins, and cold shell.

   (b) Outer shell assembly, consisting of hot shell, fins, cold shell, and support ring.

   (c) Leading edge tip assembly, consisting of the leading edge tip segments and the formed shell.

2. Machining Operations:

   Drill holes in shells to accept instrumentation fittings. Final-machine manifold components and support ring segments to fit brazed shells.

3. Second brazing operation:

   (a) Install and braze the outlet manifold and instrumentation fittings on inner shell.

   (b) Install and braze support ring segments, the inlet manifold forward ring, and instrumentation fittings on the outer shell.

   (c) Install and braze crossover tubes and doublers in the outlet manifold.

   (d) Leak test each of the shell assemblies.

4. Third brazing operation:

   Install the aft ring of the inlet manifold on the outer shell subassembly; assemble and braze the two shell assemblies.

5. Fourth brazing operation:

   Assemble and braze the leading edge tip assembly to the leading edge main body.

The reason for the four braze cycles is to permit leak-checking and repair of each of the subassemblies. The entire leading edge assembly can otherwise be fabricated in two braze cycles.

6.4.2 Leading Edge Straight Section

Two leading edge designs were evaluated by means of straight sections representing the full-scale leading edge tip regions. In the one, flow of coolant was perpendicular to the stagnation line and centrifuged around the stagnation area. This is the configuration that was used in the SAM. The second configuration used coolant flow parallel to the stagnation line. This configuration was evaluated as a straight section only.

6.4.2.1 Perpendicular Flow

Figure 6.4-1 schematically shows the test section as used for the wind tunnel tests. It was fabricated entirely from Hastelloy X. The same test section was also used in the thermal cycling tests. For the wind tunnel tests, the internal portion of the test section was sealed against gas pressure to simplify instrumentation and plumbing connections. The webs shown in Figure 6.4-1 provide buckling strength to the surface panels. Cast zirconia pieces are shown on the manifold and at top and bottom to protect these uncooled areas. Cracking of the zirconia in the tests led to replacement of the zirconia by water-cooled shields.

6.4.2.2 Parallel Flow

This test section is shown schematically in Figure 6.4-2. The coolant for the aft portion of the test section enters through the manifolds, flows forward to the crossover slots, and returns to the outlet manifold along the fin passages. The coolant for the tip section enters at the center through two tubes, flows to either side of the inlet parallel to the leading edge, and exits at the ends of the tip section through the outlet tubes shown. Individual control of the flow rate in the two flow routes was provided during test.

In this configuration, the hot skin of the tip was fabricated from Nickel 200 alloy. Hastelloy X was used for the perpendicular flow configuration. The nickel hot skin was used to reduce the stagnation-line surface temperature and was expected to provide increased thermal fatigue performance. Hastelloy X was used for all other parts of the assembly.

6.5 OUTER SHELL

The outer shell of the flight engine had interfaces with the leading edge, the struts, the ablatively cooled cowl, and the aircraft pylon mounting structure. Additionally, there are plumbing and electrical connections. The outer shell design effort discussed here was carried to the engine mount points with appropriate assumptions regarding the interaction between the aircraft structure and the engine mounting. No provisions were made for installation of the cowl. An assumed inside cowl contour was used to design the outer shell envelope.

6.5.1 Design Ground Rules

The critical design problems for the outer shell occur at the mount points, at the interface with the leading edge, and in the fuel injection manifolds. The use of multiple connections between the outer shell and the leading edge led to the decision to use brazed connections for the crossover tubes and for leading edge inlet tubes, rather than threaded connections or sealed crossover ports (as used for the inner shell-nozzle coolant crossover).

A single-height fin was selected for the entire length of the outer shell. This ground rule was aimed at improving the reliability of the basic shell assembly by avoiding a step in the cold shell and the resulting fitup and potential leakage problems.

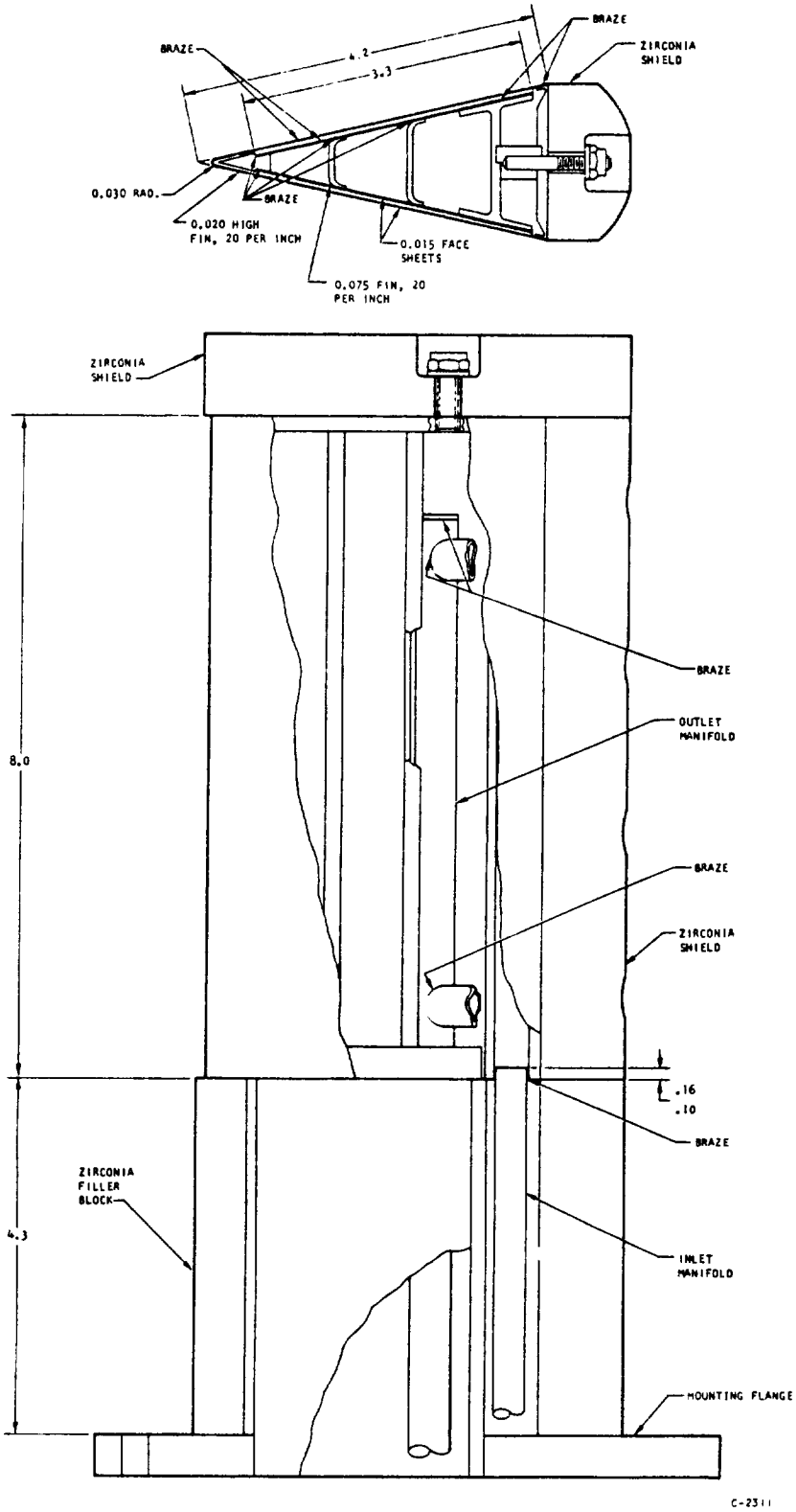

Figure 6.4-1. Outerbody Leading Edge Straight Section

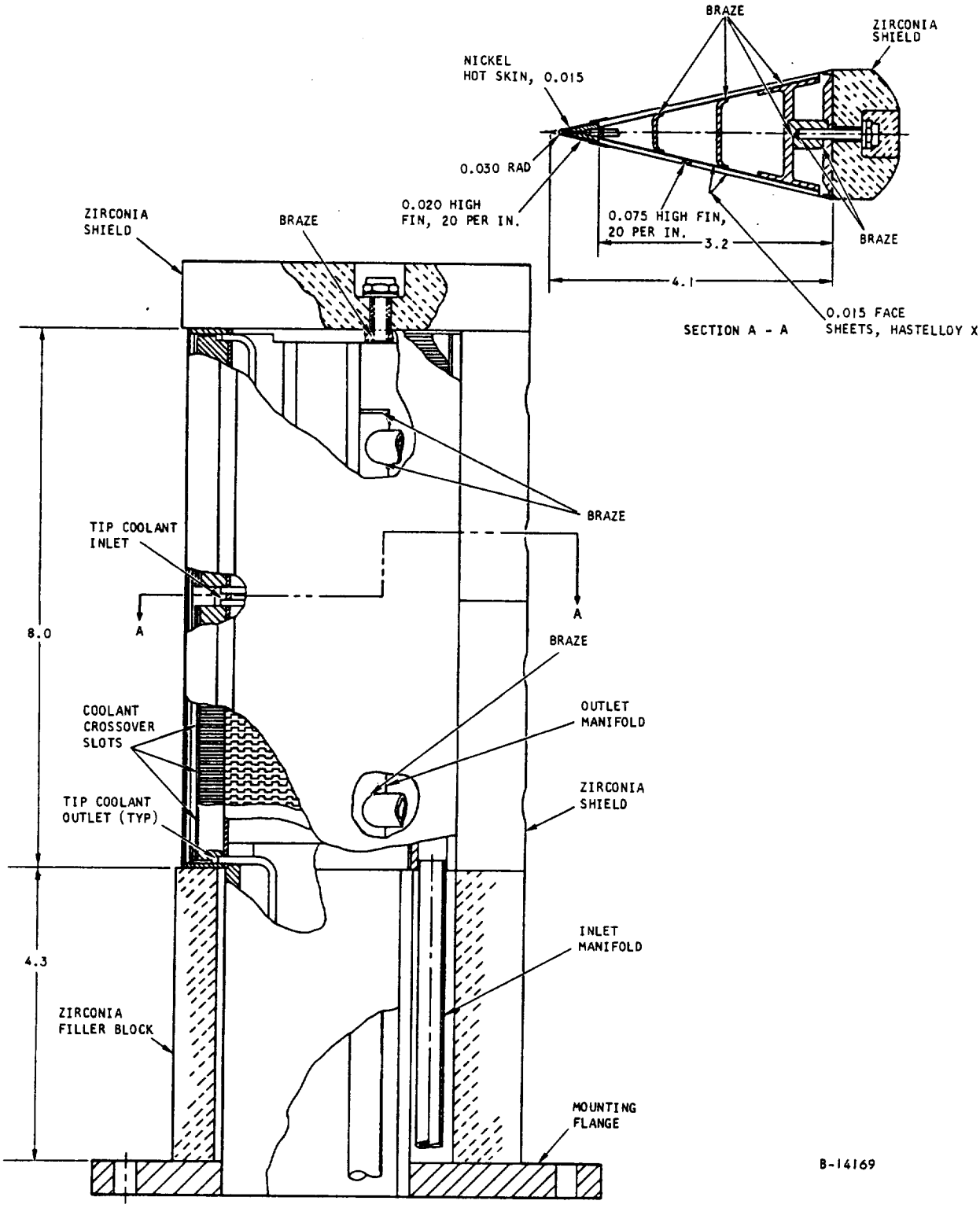

Figure 6.4-2. Leading Edge Straight Section With Separate Tip Cooling Circuit

Hastelloy X was selected as the material for structural components to ensure thermal growth compatibility of individual parts during the brazing operation. The use of high strength materials, such as Inconel 718, would have resulted in a significant reduction in cross-sectional areas, particularly those of the manifolds which also serve as engine mounting rings. However, the coefficient of thermal expansion for Inconel 718 is somewhat higher than for Hastelloy X. Although this difference is not particularly objectionable at engine operating conditions, it becomes significant during the brazing operation, in which the assemblies will reach temperatures of 2000°F. Certain of the coolant distribution manifolds were fabricated from CRES, where no thermal expansion problem existed and where material strength was adequate.

6.5.2 Features

Drawing L-980610 depicts the layout of the outer shell. The design shown was expected to meet the thermal and structural requirements encountered during engine flight testing.

6.5.2.1 Leading Edge Coolant Crossover

The coolant crossover at the leading edge is a flanged and bolted configuration, using brazed individual tube connections. Sealing of the propulsive stream is by means of a seal set between flanges. The connection for the leading edge coolant inlet lines similarly occurs in the outer shell cavity.

The location of the fuel injection station for supersonic combustion (Sta. 43.82) coincides with the location of the outer shell crossover manifold. The injection ports have been integrated with the coolant crossover by use of individual tubes brazed into the manifold, as shown in Section L-L of Drawing L-980610.

6.5.2.2 Manifolds

The various manifolds will be discussed in sequence from left to right as shown on L-980610. The toroidal manifold at Sta. 48.45 serves as a distribution point for the fuel injector nozzles. The space limitations, which also lead to the use of individual tubes to feed the fuel injectors, require the use of this additional manifold. This configuration was retained for SAM, using two inlets to the manifold. In the flight engine, six inlets were used to supply fuel from the control valve located in the centerbody cavity, i.e., one running through each strut.

The adjacent manifold is supplied with coolant directly from storage. This manifold, which distributes coolant to the individual leading edge inlet lines, is used in order to limit the number of branch lines from the pump.

The manifold at Sta. 52.01 serves as the outlet for both the forward flow route (leading edge and outer shell up to this manifold) and the aft flow route (around the trailing edge and forward to this manifold). To reduce the pressure drop in this manifold and improve flow distribution, a Hastelloy X collector tube with six inlets from the main manifold is used.

The fuel injection manifold at Sta. 55.32 has provisions for installing the strut mounting flange. A thermal lag problem exists with this manifold. The considerations outlined for the fuel injection manifold at Sta. 55.67 of the inner shell are equally applicable to this manifold.

The fuel injection manifold at Sta. 59.53 is a nonstructural component of the same design, requiring the same considerations as the inner shell manifold.

The manifold at Sta. 65.75 is introduced into the outer shell design primarily as a structural member. It is in the direct path of loads entering the innerbody crossover manifolds and the strut. Its existence as a structural member led to its use as a coolant manifold. As shown, coolant is tapped from the shell and ducted to the strut for cooling the strut sides. Subsequently, on the SAM, the strut sides were made an independent flow route to facilitate control of flow splits.

The manifold noted as Item 11 on Drawing L-908610 serves as the distribution point for inlet coolant to the aft shell flow route. It is supplied directly from storage and is used to avoid multiple supply tubes. Envelope restrictions limit the size of the shell inlet manifold at the trailing edge to the extent that a relatively large number of small tubes are required to ensure good flow distribution.

6.5.3 Fabrication Requirements

The anticipated assembly sequence for the outer shell was as follows:

1. Braze the shell assembly (hot shell, fins, and cold shell), including both the shell proper and the trailing edge assembly.

2. Drill holes in the shell for the fuel injection nozzles.

3. Braze the fuel injection nozzles into the shell.

4. Grind fuel injection manifolds flush with the external shell surface.

5. Drill holes in the shell for instrumentation fittings and finish-machine manifold subassemblies and strut flanges to fit.

6. Install and braze all manifolds in place, including the toroidal manifolds and the trailing edge external shell assembly manifold, but not the mounting flange at the leading edge coolant crossover.

7. Install and braze the leading edge mounting flange in place. (This braze operation is being performed separately to permit leak checking of the injector nozzles.)

8. Electro-discharge machine cutouts for the struts in the shells.

9. Final-machine the engine mounts, the leading edge mounting flange, and strut flanges.

This sequence was followed in actual fabrication of the outer shell assemblies. Specifics are further discussed in Section 7.

6.6 SUPPORT STRUTS

Support struts were designed for use in the flight engine application and for evaluation of heat transfer and structural characteristics in a wind tunnel. The test struts were full-scale and fabricated by the same procedure planned and used for the SAM. They were tested as individual struts mounted between flat panels simulating the installation in the engine assembly. In the following, no distinction is made between the struts used in the two applications.

6.6.1 Design Ground Rules

One of the primary objectives of the design work accomplished on the struts was to achieve a bolted assembly, as opposed to a brazed assembly, of the strut to the inner shell and the outer shell. The advantages afforded by the possibility for assembly and disassembly were one factor leading to this approach; the advantages expected in accomplishing the initial assembly were a more important consideration. While the brazed assembly represents a basically feasible concept, it entails requirements for relatively complex fixturing during brazing to ensure that the required tolerances and concentricities are maintained. The use of a bolted assembly offers an opportunity for mechanical adjustment to obtain the necessary alignments and concentricities. The bolted assembly that evolved from this study was evaluated for structural and thermal performance and found adequate. In its application to the SAM, the expected flexibility during assembly was realized.

Another basic requirement imposed on this design was that the flow in the two routes along the strut sides be adjustable by positive and repeatable means. In addition, it was required that pressure drop and flow relationships in each of the routes be separately measurable in the test unit. Features devised to achieve this were such that they could be eliminated from the flightweight hardware without altering performance. This requirement, in turn, resulted from data obtained in wind tunnel tests using struts that had a common inlet to the two routes along the strut sides, an arrangement which proved unsatisfactory.

6.6.2 Features

Figure 6.6-1 shows the strut design in the test configuration. Inlet to the strut sides is by two separate tubes. During calibration, each of these tubes was connected to a separate gas source for independent flow measurement. The two manifolds drilled into the strut body are connected to the surface by drilled holes, the holes being separated at the surface by a brazed strip. With one of the manifolds plugged, the flow/pressure drop characteristic of the other manifold and flow route were determined.

The drilled manifolds were so located that they could be replaced by a single hole supplying both flow routes. The pressure-drop characteristics in the two circuits are changed in a negligible manner by this approach due to a slight change in length of the passages leading to the strut surface.

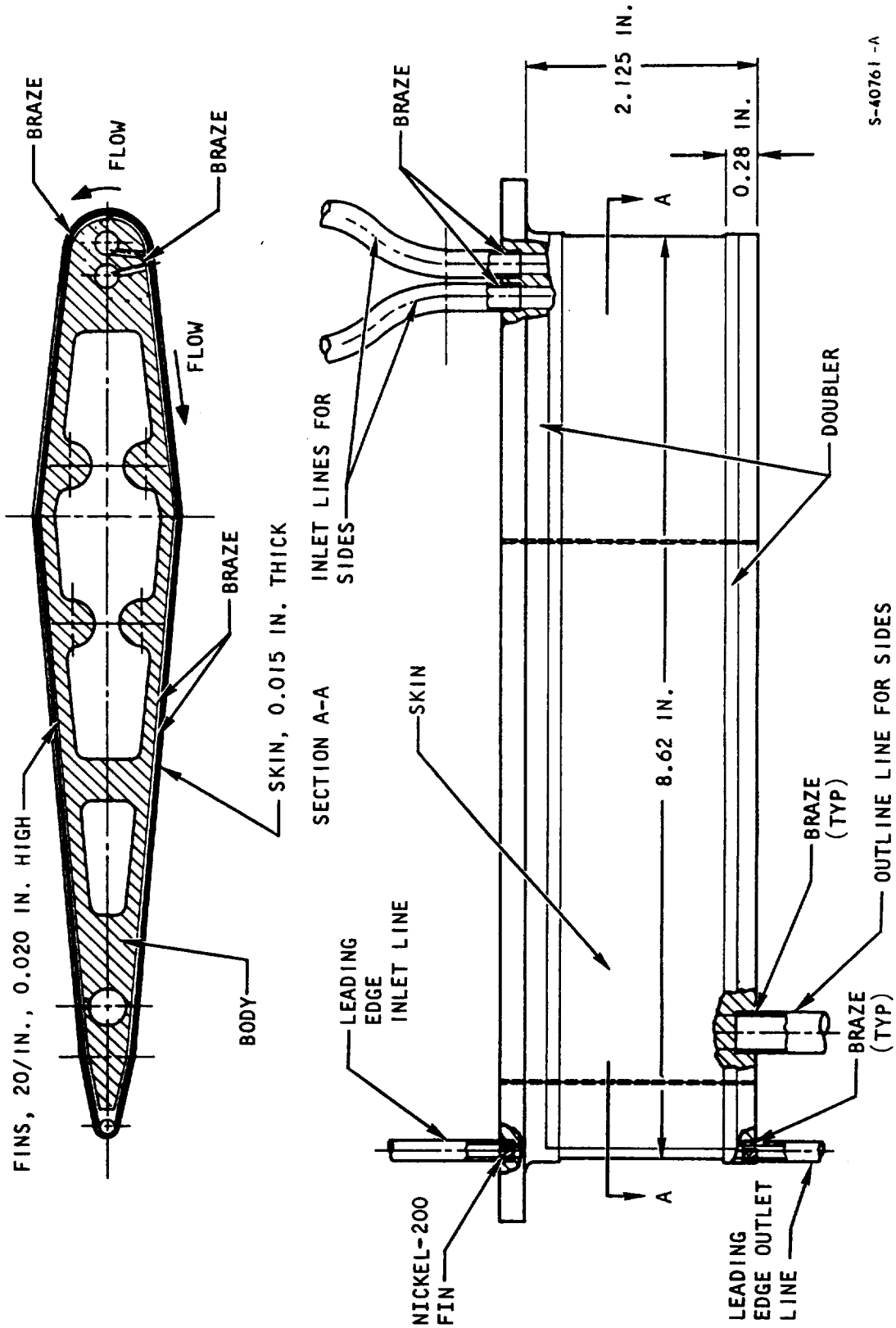

Figure 6.6-1. Innerbody-Outerbody Strut--Separate Inlets to Flow Routes

General features that are part of the strut design and affect the various interfaces with other components are discussed below. Reference to inner shell and outer shell layout drawings will show particular areas of interest.

6.6.2.1 Assembly

Assembly of the inner shell and outer shell by the support strut will involve, first, the placement of the two shells and alignment of the cutouts in the shells. The strut is then inserted from outside and bolted to the socket in the inner shell. The bolts are tightened to predetermined torque values. The mounting flange on the outer shell has brazed, threaded studs which pass through clearance holes in the strut flange. The nuts used on these studs are again tightened to preselected torque values. The air seal is formed by a flat nickel gasket.

The exit tube for the leading edge has its own seal which is formed by a ferrule fitting after assembly. Use of this separate seal avoids the need to extend the flat gaskets into the leading edge area.

6.6.2.2 Manifolding and Structural Attachment

Adequate cooling of the strut requires two externally separate flow routes, one for the leading edge and one for the main portion of the strut. The leading edge is cooled with flow used to provide cooling to the entire innerbody. The main strut forms its own route, with flow axially along the strut and then discharged into the fuel plenum.

Structural loads are reacted at the fuel injection manifolds near the leading edge of the strut and at the manifolds near the trailing edge of the strut. The basic structural design problem is the attachment of the strut mounting to these manifold rings. The fuel injection manifold at the center of the strut is not necessary as a structural member and has, therefore, been made lightweight and is not tied to the strut mountings.

All hydrogen plumbing connections that are required to pass through the strut will be metallurgically joined to their mating lines. Disassembly of the shells, therefore, will require cutting of the lines. This is considered preferable to the use of a multiplicity of threaded connections.

6.6.3 Fabrication Requirements

The strut design itself involves fabrication problems primarily related to brazing. The critical areas concern fixturing for brazing and control of braze filler alloy flow to prevent plugging of the 0.020-in.-high fin passages. The sequence of brazing operations is discussed in Section 7. The machining operations on the strut, although numerous, can be accomplished with conventional machine tools or by electrical-discharge machining.

6.7 ENGINE ASSEMBLIES

The basis for the cooled-structures design work performed as part of the program was an engine suitable for testing with the X-15A-2 aircraft. The layout design of such an engine was performed and the SAM derived from this engine design. In the following, both the flight engine design (qualification test engine) and the SAM are discussed.

6.7.1 Qualification Test Engine

This layout constituted the basis for establishing component interfaces, packaging of subsystems and components, assembly and disassembly procedures, and plumbing arrangements for the engine. It was mocked up as shown in Section 7 to further verify detail features.

6.7.1.1 Design Ground Rules

Layout Drawing L980615, Sheets 1 and 2, shows the completed layout for the qualification test engine, configuration No. 1. This drawing reflects the following considerations:

(a) The engine operates on the X-15A-2, at M = 8, 88,000 feet.

(b) The interface of the engine with the thrust measuring system, that is, with pylon-mounted structure, occurs on the engine side of the engine mounts, as shown in the layout drawing. This interface is arbitrary and was used only to define the interface of the Structures and Cooling Development effort. It reflects a drawing rather than a functional arrangement.

(c) As an objective, all hydrogen plumbing connections are made by either welding or brazing. The use of seals and threaded fasteners is limited to the minimum required for assembly and disassembly of major components, and access to the various subsystems. Replacement of certain of the components is complicated by this approach, but the chance for hydrogen leakage is considerably reduced.

(d) Hastelloy X is used on all regeneratively cooled structures. All connecting tubing used in the engine is made from Type 347 corrosion resistant steel since the maximum temperature expected in any of the tubing lines is below 1200°F.

6.7.1.2 Features

The engine layout drawing shows the arrangement of equipment in the engine. Sheet 2 of the layout drawing shows sections through the innerbody cavity that were used to establish packaging configuration and plumbing

arrangements. In the following discussion, reference will be to Sheet I of this drawing. The engine assembly procedure of completed full-scale components and the various features of the engine are described in the following steps:

Step 1. The outer shell is positioned over the inner shell and the strut cutouts are aligned. After this, the struts are installed with their gasketing (nickel) and bolted in place. This assembly constitutes the backbone for all subsequent assembly work.

Step 2. The fuel valves are installed as an assembly and bolted to individual mounting brackets on the manifold serving the second injector station. These valves are interconnected by tubing which forms the fuel plenum. This tubing is provided with bellows corrugations between the valves to allow for differential expansion between the inner shell and the valve assembly. Connecting lines to the fuel plenum and the valve outlets are welded in place as part of the valve assembly.

Step 3. All plumbing lines connecting the outer shell to the fuel plenum and valves are installed through the struts and fitted up to the mating lines. Lines from the inner shell to the fuel plenum are similarly fitted. All lines have brazed sleeves preinstalled with braze rings in place. Connections are then bonded using a hand-held induction brazing tool.

Step 4. The asbestos packing on the forward end of the inner shell is installed.

Step 5. The inlet spike is installed in place over the inner shell. The sealing bellows flange is bolted to the inner shell. Bellows serving the spike (spike coolant inlet, spike coolant outlet, and injector manifold) will have been preinstalled in the inlet spike and are now connected to the fuel plenum or valve, as required, using a clamped connection ("Conoseal" type).

Step 6. The inlet spike actuator is bolted to the inner shell mounting pads and the inlet spike mounting cone is bolted to the actuator flange. At this time, the position of both the inlet spike and the actuator itself are adjusted to assure concentricity between the inlet spike and inner shell and to true the axial travel of the inlet spike and actuator relative to the inner shell. Shims are used to accomplish this at the actuator mounting pads, while the spike adjustment relative to the actuator is accomplished by providing suitable clearance holes in the mounting flanges. The instrumentation package shown at the forward end of the actuator is preinstalled.

Step 7. The leading edge assembly is bolted to the outer shell and the tubing connections from the leading edge to the manifolds provided in the outer shell are braze-joined.

Step 8. The nitrogen storage tank is bolted to the mounting ring provided on the inner shell and the nitrogen supply and pressure regulator lines are connected to the tank.

Step 9. The controls components are installed on the mounting plate provided on the nitrogen tank.

Step 10. The nozzle is bolted to the inner shell using the access provided through the nozzle cap. At this time, the nozzle instrumentation connections (connector installation not shown) also are made.

Step 11. The nozzle components are installed.

Upon completion of these operations, the engine is ready for mounting to the thrust measuring system and for joining the hydrogen lines to the pump discharge line, and the turbine inlet and dump lines. Electrical lines will already be installed with quick disconnect fittings for attachment to aircraft wiring. All required wiring must pass through the strut cavity and is installed simultaneously with the plumbing (Step 3). The ablatively cooled cowl is installed after mounting the engine to the thrust-measuring system. The cowl is mounted directly to the structure above the thrust-measuring system to avoid drag inputs to thrust measurements. The cowl outline is indicated on the drawing for reference, but is not considered to represent a final configuration.

Details of the routing of hydrogen lines through the struts are shown in the drawing for each of the six struts. The remaining space in the struts is reserved for wiring. The reserved area is near the coolant inlet to the strut and is, therefore, the coolest area, with metal temperatures near room temperature at design conditions. Wiring is run here to reduce the need for thermal shielding.

The interface of the engine with the pylon leading edge is indicated in the drawing. The joint between the pylon and adjacent structure requires sealing and ablative protection. Restraint on the engine due to this joint would introduce inaccuracies into the thrust measurement and must be avoided. Alternatively, the pylon leading edge could be repositioned relative to the engine to intersect the ablatively cooled cowl.

6.7.1.3 Maintenance and Refurbishment

The basic approach to engine assembly and disassembly assumed that refurbishment and maintenance of the type requiring replacement of hydrogen system components generally would be accomplished at the factory level.

Access to all electrical components, however, is possible in the field. The procedures involved in replacement or maintenance of various components are described in the following paragraphs:

(a) Refurbishment of the leading edge--Inlet and outlet lines must be cut (brazed connections) and the leading edge removed after unbolting of the flange connection with the outer shell. Installation of a new leading edge requires that new braze connections to the manifolds be made. The induction brazing operation required here can be accomplished with relative ease using portable equipment and could be done in the field, if necessary.

(b) Replacement of strut--This requires that lines and electrical wires passing through the strut be cut or unsoldered, as required, and removed. To permit cutting of the lines in the innerbody, disassembly of the control equipment, the nitrogen tank, and the actuator is required. This work would be performed at the factory level.

(c) Access to instrumentation mounted in the spike--The control and instrumentation packages mounted in the nozzle area, the nitrogen tank, and the inlet spike actuator must be removed. No cutting of hydrogen lines is required. This work can be performed in the field.

(d) Removal of the inlet spike--The leading edge must be removed, as described above, the inlet spike actuator must be removed along with equipment to the rear of the actuator, the bellows clamps connecting spike hydrogen lines to the fuel plenums and valves must be removed, and the sealing bellows must be unbolted. All joints involved in this operation, except the leading edge hydrogen lines, are mechanical.

(e) Replacement of inner or outer shells--As may be deduced from the description of the assembly sequence, this requires complete stripping of the engine and involves a rebuilding operation.

All operations requiring access to the centerbody cavity are performed with the nozzle removed in a sequence which is the reverse of that used on assembly. No lines must be cut to accomplish this.

6.7.2 SAM Engine

The hydrogen-cooled engine assembly of the SAM is shown in Drawing 980801. Of the subsystems associated with the qualification test engine, only the inlet spike actuator is retained in the centerbody cavity. The complete SAM assembly is shown in Drawing 980800. The SAM test systems and adapters are discussed in separate sections.

6.7.2.1 Design Ground Rules

The SAM assembly reflects the ground rules for the components, as well as the following considerations:

(a) The basic assembly shown on Sheet 1 of Drawing 980800 is delivered to the wind tunnel facility as a unit ready for installation.

(b) Assembly and disassembly of the basic assembly, Drawing 980801, in the field is not required. In line with this, all internal hydrogen line connections are either welded or brazed. Water lines, which are subject to limited thermal cycling by comparison with the hydrogen lines, use threaded or flange-type joints.

(c) The complete basic assembly, and in particular, the cowl/pylon assembly must be capable of being inerted at pressures greater than those occurring in the cowl/pylon shock-interaction region.

(d) Even though assembly or disassembly in the field are not basic design requirements, the capability of at least partial disassembly of the water-cooled test adapters was considered desirable.

(e) Model alignment in the wind tunnel will be accomplished by appropriate shimming between the base plate and the wind tunnel test adapter. In other words, the complete assembly will be adjusted as a unit. Adjustment of the various model components relative to each other is accomplished as part of the SAM assembly process.

6.7.2.2 Assembly Features

The major components that make up the basic assembly shown in Drawings 980800 and 980801 are the (1) engine assembly, (2) cowl/pylon assembly, (3) structural support assembly, (4) panel assembly, and (5) cover assembly.

The engine assembly constitutes the hydrogen-cooled structure being evaluated in wind tunnel testing. All other components of the basic assembly are water-cooled test adapters. The assembly of components is performed in the following sequence with reference to Drawing 980800:

(a) The bulkhead, Item 15, is attached to the plumbing of the engine assembly. The necessary mechanical connections are made prior to the next step, which involves installation of the cowl/pylon. These mechanical connections involve the water lines and certain of the instrumentation lines.

(b) The cowl/pylon assembly is installed as a unit onto the engine assembly. Installation is axial and dimensions are such that this assembly, when slipped on from the front, will clear the basic engine assembly. The cowl/pylon is bolted to the engine suspension frame as shown in Section B-B of the drawing. No other supports to

the engine are provided. A number of stops on the engine assembly manifolds, however, prevent undesirable deformation of the cowl.

(c) The panel assembly, Item 4, at the front of the cowl and its seals are installed. These assemblies are fabricated as split cones and bolted in place, both to the cowl and to each other.

(d) The ring assembly, Item 11, is installed between the cowl and the engine trailing edge.

(e) The forward and aft support assemblies are attached to the engine assembly suspension frame.

(f) The cover assembly is installed in place and its plumbing connected. This includes plumbing for its own cooling circuits as well as the lines passing through it and cooling the panel assembly, Item 4, and the ring assembly, Item 11. These tubes are supported by a clamp mechanically attached to the cowl, Section N-N.

(g) The previously completed assembly is set on the structural support assembly and bolted in place. Shimming is provided for under the fore and aft supports, Items 12 and 13. To ensure control over the final fitup, all surfaces are machined with respect to the engine suspension frame (X-surface). The interface between the pylon and the support structure is sealed by means of a silicon rubber O-ring.

Sealing of the engine and cowl/pylon cavities against the tunnel gas is basically not required. The cavities are inerted at pressures sufficient to ensure outward flow of nitrogen. Sealing was introduced at all external joints, however, to limit the amount of nitrogen flow to the model cavities. Since neither thrust- nor drag-force measurements were planned for the wind tunnel test, the restraints imposed by this approach on the engine are not objectable.

Only limited provisions are made for handling of the assembly as shown in the drawing. Specifically, four tapped bosses are provided at two locations for use with either yokes or eyebolts. The general mode of handling the assembly will be by means of its baseplate.

The interface between the tubing terminations shown on Sheet 1, and the manifold systems shown on Sheet 2 of Drawing 980800 are such as to permit removal of the support wedge without requiring cutting of tubes. Removal of the cover assembly is also possible without requiring tube cutting. Finally, removal of the cowl/pylon requires cutting of only four water tubes. In this way, the outer surface of the outer shell and the hydrogen tubing in this area can be made accessible.

6.8 SAM FUEL/COOLANT SYSTEMS

The hydrogen and water systems required for SAM testing reflect the model-facility interfaces, fail-safe features aimed at preventing stoppage of coolant flow, and the selected operating modes of the systems during testing.

6.8.1 Hydrogen System

The hydrogen system is shown schematically in Figure 6.8-1. The model side of the model/facility interface is shown; that is, all of the equipment shown in the diagram is assembled and calibrated as part of the SAM. At the inlet to the SAM system, the facility provides hydrogen at room temperature to 200°R and at 900 to 1100 psia. The exhaust from the SAM system is to the facility vent line.

The basic system consists of the valves designated PCV (pressure control valve), CRV (coolant regulating valve), FDV (fuel dump valve), and ICV (injection control valves). Operation of these valves is as follows:

PCV--This is a pressure regulator sensing the pressure in the SAM dump plenum, which is controlled at 500 to 550 psia. A drop in plenum pressure causes the PCV to open. The PCV is a ball-type valve, electrically actuated.

CRV--These valves are located at the inlet to each of the five engine flow routes. CRV's No. 1 through 4 are ball-type valves, pneumatically actuated, using solenoid control and position feedback by means of a potentiometer. CRV No. 5 is a manual needle valve. These valves are set prior to testing to provide the correct coolant flow in each of the routes for the test condition planned for the specific test. The presetting is done using room-temperature nitrogen and based on analytical and experimental predictions of flow requirements.

FDV--Two valves are used to serve the dump valve function. This is done to provide maximum flexibility in terms of bias and control. The FDV's are controlled by the temperature-control system to maintain the maximum coolant temperature from any of the flow routes below the maximum allowable for the specific operating conditions. Excess temperature in any of the flow routes causes the FDV's to open, plenum pressure to decrease, and the PCV to open to restore plenum pressure to the set range. Positioning of the FDV's is in parallel.

ICV--This valve is opened to provide for discharge of the coolant to the innerbody and outerbody fuel injectors. Initiation of valve opening is manual. The FDV's and ICV are programmed to operate in push-pull fashion to minimize perturbations to the systems during the switchover from dump to injection flow, and conversely. Following the switchover, the control system retains active control over the FDV's and opens these valves if an overtemperature condition develops. The open position of the ICV, on the other hand, is fixed at a preselected value that is determined prior to test.

Most of these valves are of a fail-safe configuration. The CRV's will open on loss of pneumatic power and will nominally hold position on loss of electrical power; the FDV's are poppet valves with pressure acting to open

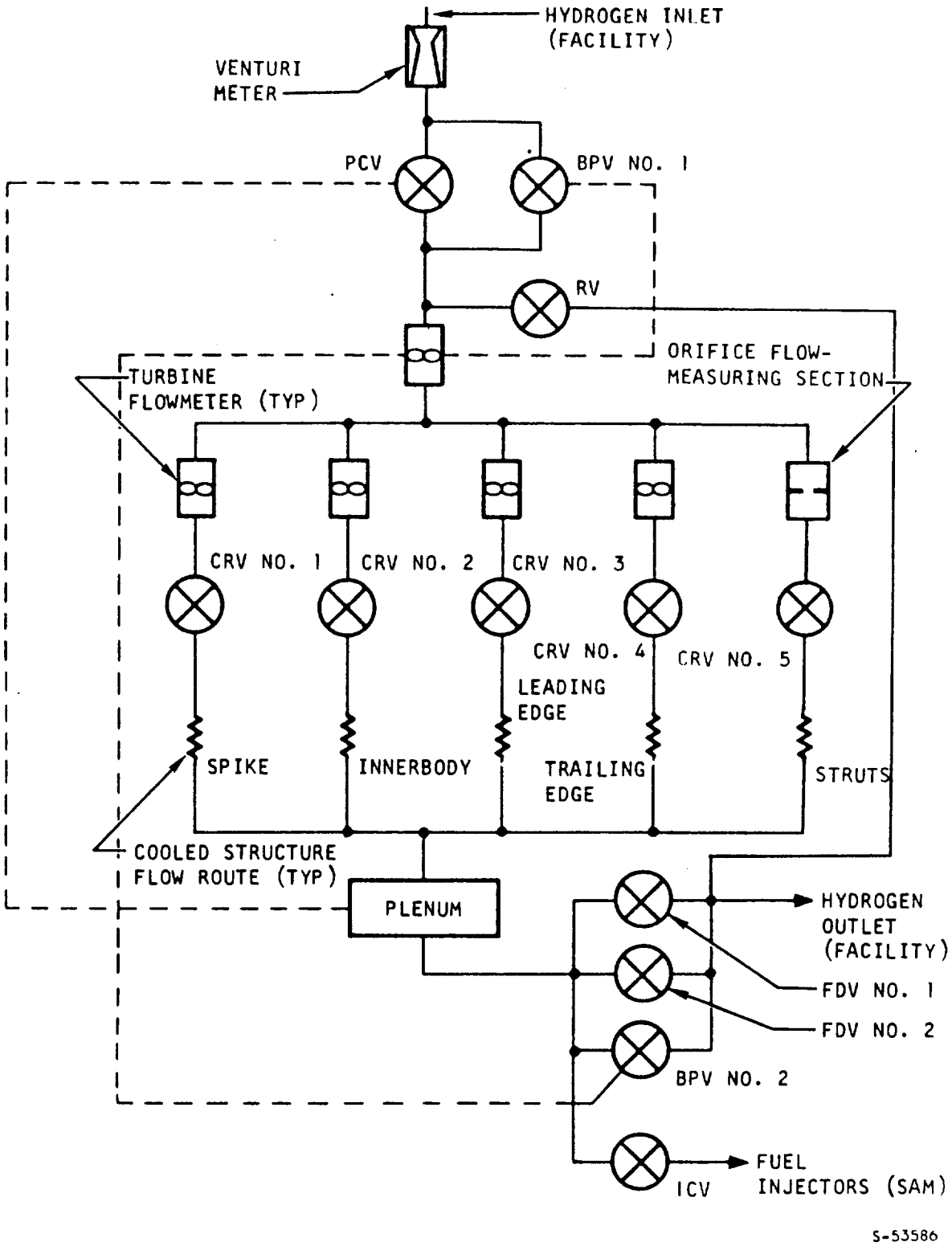

Figure 6.8-1. HRE/SAM Hydrogen System

the poppet; the electropneumatic transducer associated with the FDV's will power the valves open in the event of electrical failure in the transducer; the ICV has pressure acting in such a way as to close the valve, with the electropneumatic transducer arranged to close the valve on failure of electrical signal. In addition to the above, the system includes three failure-protection valves. These are:

> BPV 1 and BPV 2 (bypass valve)--These are solenoid operated, pneumatically driven valves which open when the system flow, as sensed by the total flowmeter, decreases to an unacceptable level. The system does not discriminate between failure of the PCV and of the FDV but will open the BPV's as though both had failed closed. At this point, the test run is considered to have been aborted.
>
> RV (relief valve)--This valve is a conventional, spring loaded relief valve used to limit upstream system pressure. Flow through this valve is directly into the vent line. Conditions which could lead to overpressure would involve wide-open failure of the PCV or wide-open failure of the FDV, which would result in a decrease in plenum pressure and opening of the PCV in an attempt to maintain plenum pressure at the set point.

Failure mode of the bypass valves is open for either electrical or pneumatic failures.

A critical consideration in the selection of all valves is that none of them must provide zero-leakage shutoff. This is particularly important for the hot valves, where the occurrence of minor leakage will not require refurbishment of the valves.

6.8.2 Water System

Figure 6.8-2 shows the water system. The facility provides a single inlet to each of the two systems. Each of the five flow routes has a manual valve at the outlet which is used to adjust flow rate to the routes. The flow rate in the individual routes is determined from a pressure-drop-versus-flow-rate calibration prior to test. This calibration also forms the basis for establishing limits on pressure differential for satisfactory operation of the system.

6.9 WIND TUNNEL TEST ADAPTERS

Wind tunnel testing of the SAM required adapters for installation of the SAM in the facility, as well as a cowl to provide a fairing and shield for the SAM outerbody. The two adapters used for these functions are the cowl/pylon and the mounting structure. Both of these components are water-cooled and generally fabricated from stainless steel.

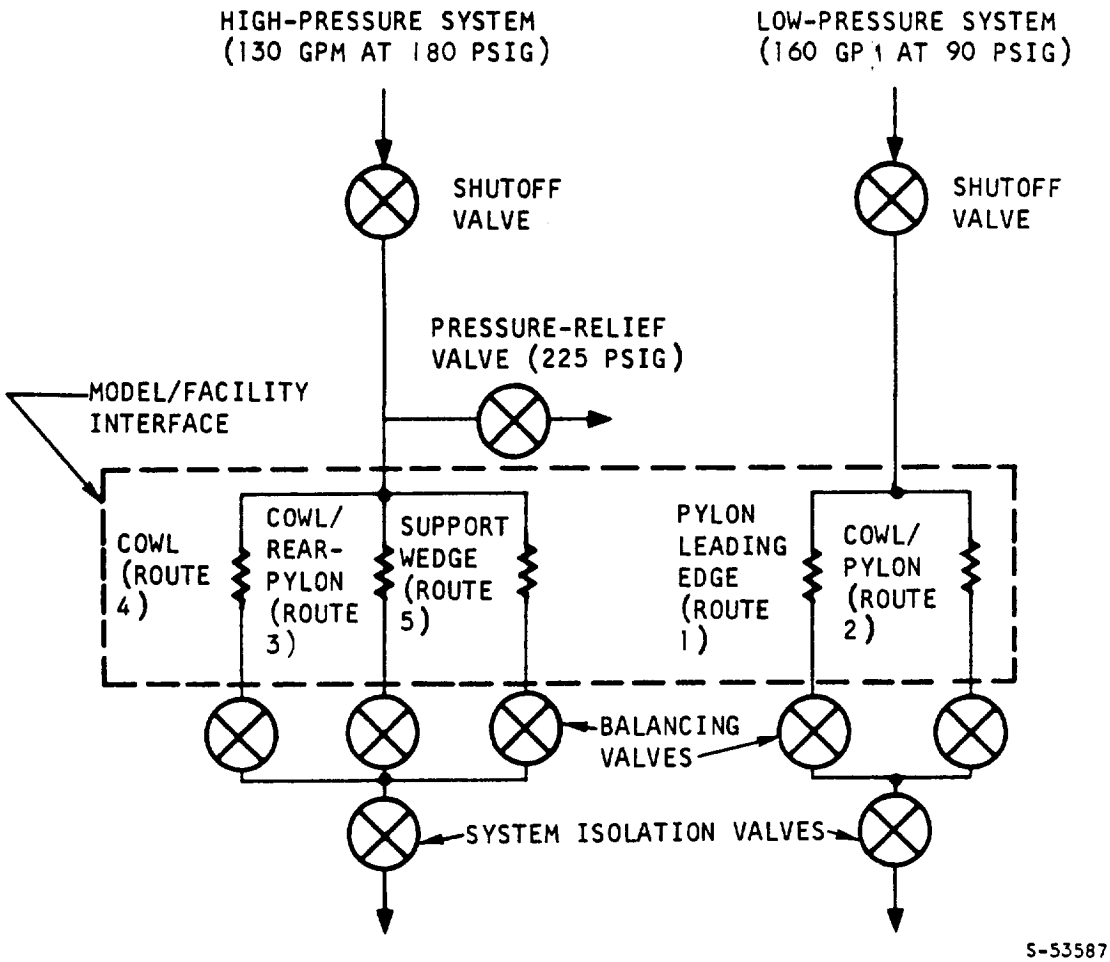

Figure 6.8-2. HRE/SAM Water Systems

6.9.1 Water-Cooled Cowl/Pylon

6.9.1.1 Design Ground Rules

The approach used to design the cowl/pylon involved the following considerations:

(a) Material of construction was to be stainless steel wherever possible, with superalloy used in selected, highly stressed areas only.

(b) Cooling was to be accomplished with water at a maximum of 200 psig of 90 psig inlet pressures depending on the particular flow route and available supply. Design proof-pressures were taken to be 1.5-times the operating inlet pressures.

(c) The cowl was to be double-shell structure provided with support pins to resist buckling loads. This approach was selected in preference to the use of fin-type structure, eliminating the need for special forming and brazing tools.

(d) Flat surfaces were to be plate-fin-type structure, with 0.090-in. hot skins and 0.12-in. cold skins.

(e) The cowl/pylon structure was to be supported from the SAM suspension frame. Interference with the free motion of the SAM was acceptable, since no thrust measurements were to be attempted.

6.9.1.2 Features

Drawing 980800 shows the cowl/pylon assembly and its components. The main components are as follows:

(a) Forward cowl panels--This assembly consists of two segments of a cone which are assembled to the SAM and main cowl by bolting to each other and to the main cowl. The joints between the forward cowl panels and main cowl and between the forward cowl panels and SAM leading edge have silicone rubber seals. The nitrogen gas used to inert the complete assembly in the wind tunnel is pressurized to a level high enough to assure outward flow of the inerting gas through the imperfect seal between the panels and the leading edge and prevent inward flow of hot gas. The forward cowl flow route is in series with the rear pylon cover.

(b) Main pylon/cowl assembly--This assembly consists of a cowl shell assembly which is welded directly to the pylon. To assemble the parts, (1) the pylon is welded as a subassembly, (2) the two cowl shells are slipped one over the other and interconnected into a subassembly by means of rosette-welded pins, and (3) the pylon is welded to the cowl shells.

(c) Rear pylon cover--This component is fabricated by welding of individual plate-fin-type flat plates. The complete, finish-machined part is bolted to the pylon of the main cowl/pylon assembly.

(d) Rear seal ring--This ring is fabricated as a separate assembly by welding and brazing, and forms a seal between the outerbody trailing edge manifold and the main cowl inner surface. It is bolted in place to the outerbody trailing edge.

All joints are provided with seals. Purpose of the seals is to limit the amount of inerting gas flow required in test. In general, minor leakage at any of these seals is not objectionable since the inerting gas will be at pressures in excess of ambient.

6.9.1.3 Assembly

The support structures and plumbing of the SAM are so arranged that the main cowl/pylon can be installed as a unit from the front of the SAM. With this accomplished, the forward cowl panels are bolted in place to close out the forward portion of the cowl. The rear pylon cover is then bolted to the main pylon from the inside. The rear seal ring is installed as the final step in assembly. In general, this approach to assembly is a consequence of the desire to not split the cowl. To permit this type of assembly, a separate forward cowl is necessary. The main cowl is terminated at an axial station with a radius sufficient to clear the SAM leading edge component.

6.9.2 Water-Cooled Support Structure

The SAM is supported on a wedge-shaped structure approximately 2 ft high. The wedge configuration was selected to minimize the effective wind tunnel blockage and was evaluated in the pilot tunnel for the full-scale facility.

6.9.2.1 Design Ground Rules

The basic configuration of the support structure, following successful pilot tunnel testing, was taken to be fixed. Subsequent layout work also showed that it was entirely adequate for the functions intended. In addition to being compatible with the facility, the following considerations apply to the design:

(a) A water-cooled structure rather than an uncooled structure was selected to minimize problems of differential expansion.

(b) It was assumed that the support structure would be preassembled to the baseplate and the SAM assembly and the water-cooled cowl/pylon assembly prior to installation in the wind tunnel test section. As a corollary, it was assumed that the final plumbing and electrical connections would be made from underneath the baseplate prior to installation in the test section.

6.9.2.2 Features

Drawing 980800 shows the support structure as part of the SAM assembly. The cooling is accomplished with a single water flow route. Water enters at the leading edge, passes through the leading edge and along the top plate and top portion of the wedge panels to the rear of the structure. From here it reenters the lower portion of the wedge panels and is exhausted from these. The significant features of the assembly are as follows:

(a) The flat wedge surface and the pylon seal plate are formed from plate-fin panels. These panels are brazed assemblies which are welded together to form the basic structural assembly. The pylon seal plate also serves as a bulkhead between the pylon and the support structure.

(b) Manifolding and load-carrying structures are welded to the basic wedge assembly.

(c) The mounting blocks which carry the SAM suspension frame are bolted to the top plate of the support structure. These blocks are preassembled to the suspension frame.

All material used in the support structure is Type 347 or 321 stainless steel. High-strength fasteners are used for tie-down of the SAM suspension frame.

6.9.2.3 Assembly

The support structure is a welded assembly of brazed panels. As indicated above, the structure and the SAM are preassembled. Precise adjustment for SAM centerline angle of attack will be provided by shimming of the mounting blocks during assembly. The bulkhead between the pylon and support structure has nominal sealing to reduce the total amount of inerting gas required.

6.10 INLET SPIKE ACTUATION SYSTEM

The actuation system flight-designed uses gaseous nitrogen blowdown to expel hydraulic oil from an in-line accumulator through a servovalve into the actuator. Modulating operation is used to control the position of the inlet spike, with position feedback to the control system by means of LVDT. Spent hydraulic oil is dumped overboard. For the SAM tests, the accumulator was removed and a closed hydraulic system connected to the actuator. This permitted continuous operation of the system.

6.10.1 Design Ground Rules

Design of the actuation system was governed by the following considerations:

(a) Purchased components (accumulator, LVDT, nitrogen pressure regulator, hydraulic servo, squib valve, and pressure switch) were to be previously qualified to military or NASA requirements or have some history of flight application and be compatible with the quality assurance provisions applied to the HRE.

(b) The design of the actuator should minimize side loading of the hydraulic piston, i.e., deflection of the structure under load was not to be transmitted to the actuator.

(c) Sliding surfaces were to use bearings or bushings rather than metal-to-metal contact.

(d) The envelope for the system was to be limited so that the control system components could be installed in the nozzle to ensure accessibility of these components.

6.10.2 Features

Drawing 981189 outlines the inlet spike actuation system. The following features are noted:

(a) Due to structural loading and envelope limitations, structural integration has been utilized where feasible. The actuator and the support structure physically connect to transmit the loads to the innerbody mounting rings. The same philosophy was used structurally to attach the nitrogen tank and accumulator for a mechanical assembly, with the nitrogen tank bolted to the innerbody.

(b) The support structure tubes have Teflon-impregnated fiberglass bearings to reduce friction loads. To eliminate the tendency of these tubes to rotate, a key is used.

(c) To provide accessibility, the nitrogen fill and bleed valve, squib valve, hydraulic fill valve, and overboard vent valve were located in the pylon.

(d) The squib valve was located upstream of the regulator to eliminate possible gaseous nitrogen leakage during standby.

(e) The actuator has a latching device to maintain the spike in the closed position when the engine is not operating. It also has snubbers to reduce the end loads as the actuator bottoms out.

(f) The actuator shaft is pinned to support structure through a universal joint to eliminate side loads.

(g) A pressure switch is provided to signal minimum pressure in the nitrogen tank required to extend the actuator and close the inlet under the worst load condition. When this occurs, the control system will command engine shutdown and full extension of the actuator.

(h) No hydraulic filter is provided due to restricted access for servicing. Filling will consist of closed-loop circulation through filters to reduce the contamination level.

(i) As a precaution against regulator wide-open failure, a downstream relief valve is incorporated in the regulator.

The material for the support structure is 4330 steel, which is readily weldable, has high strength, and is readily available. Corrosion protection will be provided by plating. The nitrogen tank is fabricated from 15-5PH steel.

6.10.3 Assembly

Teflon-impregnated fiberglass bearings are first installed in the support structure tubes as shown in the outline. The diametral step provides partial retraction before engaging the bearing surface. At this time, the actuator can be installed in the support structure. The manifold connecting the control ports of the servovalve is then positioned and mounted. The support structure and actuator are indexed to the innerbody by measurement prior to installation, so that the initial and final positions are correct relative to the aerodynamic surfaces. This assembly is then installed and bolted in the innerbody ring. The valve lines are connected to the servovalve at this time, and the accumulator is installed.

6.11 TEMPERATURE AND PRESSURE CONTROL SYSTEM

The Temperature and Pressure Control System described in this section is designed to satisfy three sets of requirements (1) it provides suitable interface logic with the facility to accommodate safe start-up, normal shut-down, and emergency shut-down of the SAM; (2) it provides a means of monitoring and adjusting the division of coolant flow (hydrogen gas) through the four flow paths; and (3) it provides automatic control of the total-flow rate of coolant in order to maintain the skin temperature of the SAM at a selected value.

6.11.1 Functional Requirements

In order to control the temperature of the SAM, the control system scans 27 different temperature sensors in five separate routes and determines which of these is the highest with respect to its set point. The system modulates the position of the fuel dump valve to keep this temperature below its safe limit.

In most of the testing of the SAM, the temperature controller will function as an overtemperature control device. An initial bias setting of the FDV will provide a pre-selected hydrogen flow somewhat below the expected nominal rate; then, as the coolant temperature rises, the FDV will modulate to increase the flow in a manner which maintains the desired operating temperatures in the controlling flow route. In the case where the coolant is being injected into the combustors, the ICV is biased to the original setting of the FDV, and again the FDV modulates to maintain the desired temperatures. The FDV has an independent bias setting which prevents it from totally closing off at any time so that valve seat chatter is avoided and, in addition, the low flow control characteristics of the system are improved. The combustion process is a secondary function in the wind tunnel tests and the amount of fuel injected is determined by the available cooling flow.

The purpose of the flow management system is to enable the operator to preset the four coolant regulator valves (CRV's). Each CRV adjusts the flow rate through the corresponding hydrogen flow branch. Total flow is a function of FDV setting only (or FDV and ICV) by virtue of the constant plenum pressure (550 psia) control. Most of this preadjustment will be done with nitrogen, rather than hydrogen, for reasons of safety and economy.

Flow rate is monitored at five points in the system. The relative flow rate (fraction of total) through each of the four coolant paths is displayed. In addition, the total-mass-flow rate through the system is measured and displayed. The monitoring scheme is described in more detail in Section 5.9.

The interface logic system must provide for safe operation of the SAM during tunnel operation, and must satisfy the following requirements:

(a) Provide a signal (switch closure) to the wind tunnel facility to permit the SAM to be lifted into the hypersonic airstream.

(b) Inhibit the opening of the fuel injection valve until a facility signal indicates that the SAM is in the airstream.

(c) Provide a signal to close the SAM inlet just prior to lowering the SAM out of the airstream during a normal shutdown sequence.

(d) Provide a signal to the wind tunnel facility to request lowering the SAM out of the airstream.

(e) Automatically initiate a shutdown sequence in the event of a low-flow alarm or a high temperature alarm. These alarms are generated by the temperature controller and the flow-monitoring system. The shutdown sequence includes signalling the spike to close, the hydrogen flow bypass valves and the FDV to open, and the ICV to close.

(f) Open all hydrogen outlet valves (FDV, ICV, BPV) on receipt of a purge command from the facility to permit purging of all hydrogen lines with gaseous nitrogen.

The flow management system is separate from the temperature controller. It must provide a visual simultaneous display of five flow rates, and must also provide a means for manually adjusting the positions of the flow dividing valves to achieve any arbitrary set of flow-rate ratios or fractions. The system must accommodate both the hydrogen flow and the nitrogen purge flow.

6.11.2 Circuits

Solid state electronic circuits are used throughout the temperature Control Console, except for some latching and switching relays. The electronic solid state circuits consist of discrete components and operational modules

mounted on printed circuit boards for ease in servicing and replacing faulty units.

6.11.2.1 Temperature Control Circuit (Figure 6.11-1)

Millivolt level signals from the thermocouple reference junction are fed into a buffer amplifier, Z1. This amplifier uses the highly stable μA 725 operational amplifier and feeds the NASA DAS, a selector switch for direct reading of any thermocouple by means of a DVM, and the auction circuit. The heart of the temperature control is the auction circuit. Each thermocouple circuit has an amplifier, Z3 (gain of 1000), which amplifies the difference between the thermocouple output, from Z1, and the relevant zone reference signal, from Z2. The zone reference amplifier, Z2, feeds all auction amplifiers corresponding to thermocouples in its zone. Input to Z2 is a ten-turn-wire potentiometer and a test-point on the output provides a monitor point for precise zone-level setting. If Z1 output is greater than Z2 output then the diode in Z3's output circuit is forward biased. However, the cathodes of all diodes for all thermocouple circuit Z3's are common so the highest Z3 output will "win" causing the diodes of all other Z3's to be back-biased. The Z3 of the winning thermocouple will be the only one that has a positive output, all others being saturated negative, and this fact is detected by the comparator, Z4. The switching point is set at -3v. to ensure fast response to a Z3 output swinging from -14v. to the "winning" level, and Z4's output drives an indicator lamp which shows that it is the controlling thermocouple. The interposing latching logic is used under high temperature alarm conditions. Besides the auction point being common to all thermocouple Z3 amplifiers it is also the input to the summing amplifier for the FDV drive and to the alarm comparators, Z5 and Z6. Temperature control is exercised over a temperature window of 375°F. If the highest temperature in the system, as indicated by the "winning" thermocouple, exceeds half this window then comparator Z5 switches causing an amber warning lamp to light. If the total window temperature is exceeded then the temperature control has reached the limit of FDV opening and the comparator Z6 switches to initiate a shutdown. A simple filter on the input prevents Z6 from switching on noise spikes. Z6 also lights a red HIGH TEMPERATURE lamp and latches to maintain the red, amber, and relevant green thermocouple lamps lighted until reset by the reset button. The remaining thermocouple indicators are inhibited to ensure that only the initiating thermocouple green lamp is latched. This is to aid post-shutdown analysis. There are 27 thermocouple circuits (one per thermocouple), five zone reference circuits (one per zone), and one high-temperature circuit. These three circuit types are shown separated by dashed lines in Figure 6.11-1.

6.11.2.2 Startup and Shutdown Control Circuit (Figure 6.11-2)

All gates used in this circuit are logical NAND gates. Each shutdown parameter is fed into a latching circuit which on receipt of a low (grounded) input, lights an alarm indicator and sends a low signal to the shutdown gate, Z6. The gates Z1 and Z2 form a simple flip-flop which remains latched until reset by a common button. The low-flow alarm (which is normally low and goes high on low flow) is inhibited until the carriage is at the center line. This additional feature is accomplished by gates Z3 and Z6. Upon receipt of any alarm signal, the output of Z6 goes high which operates a relay to control

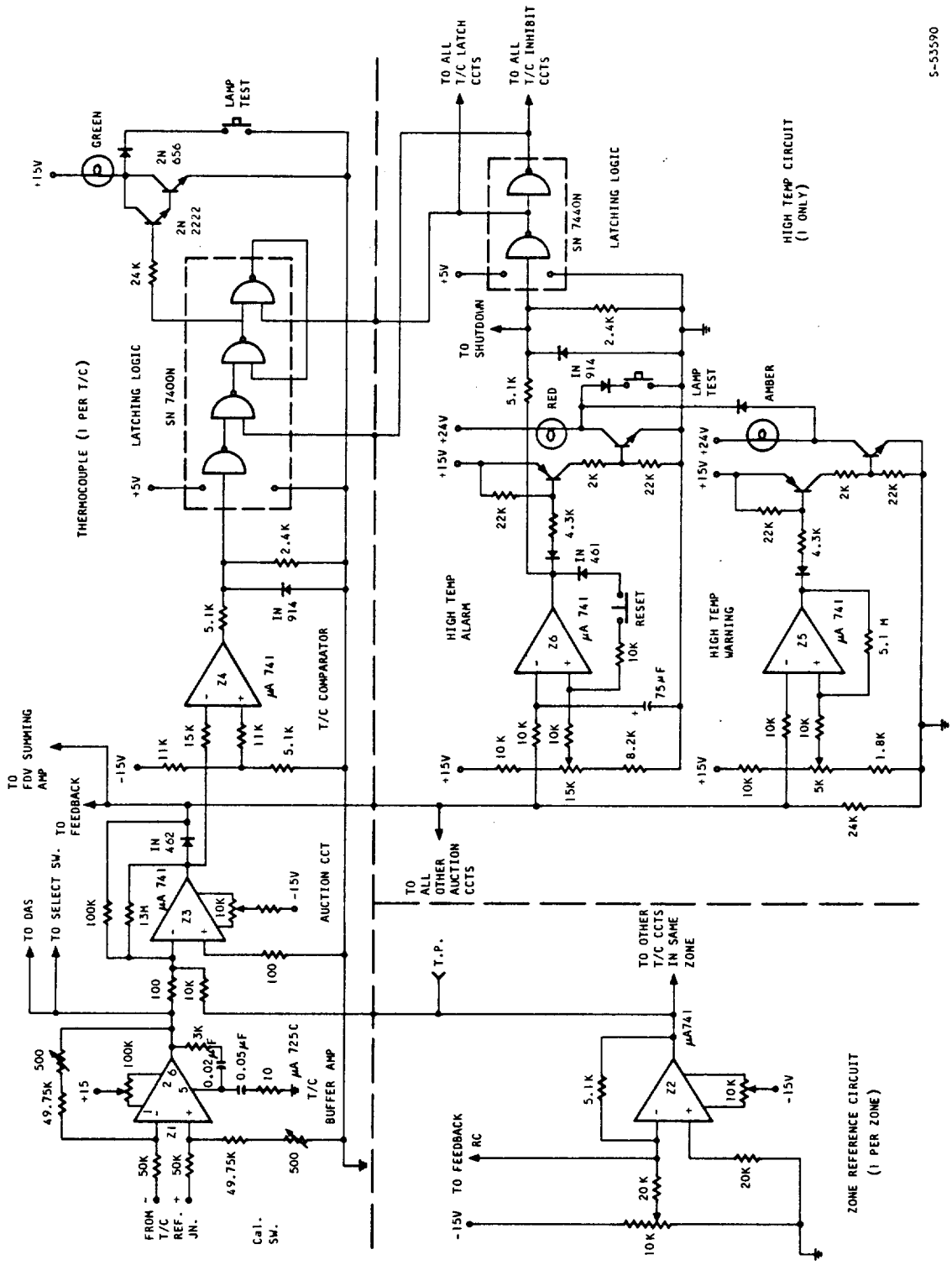

Figure 6.11-1. HRE Temperature Control

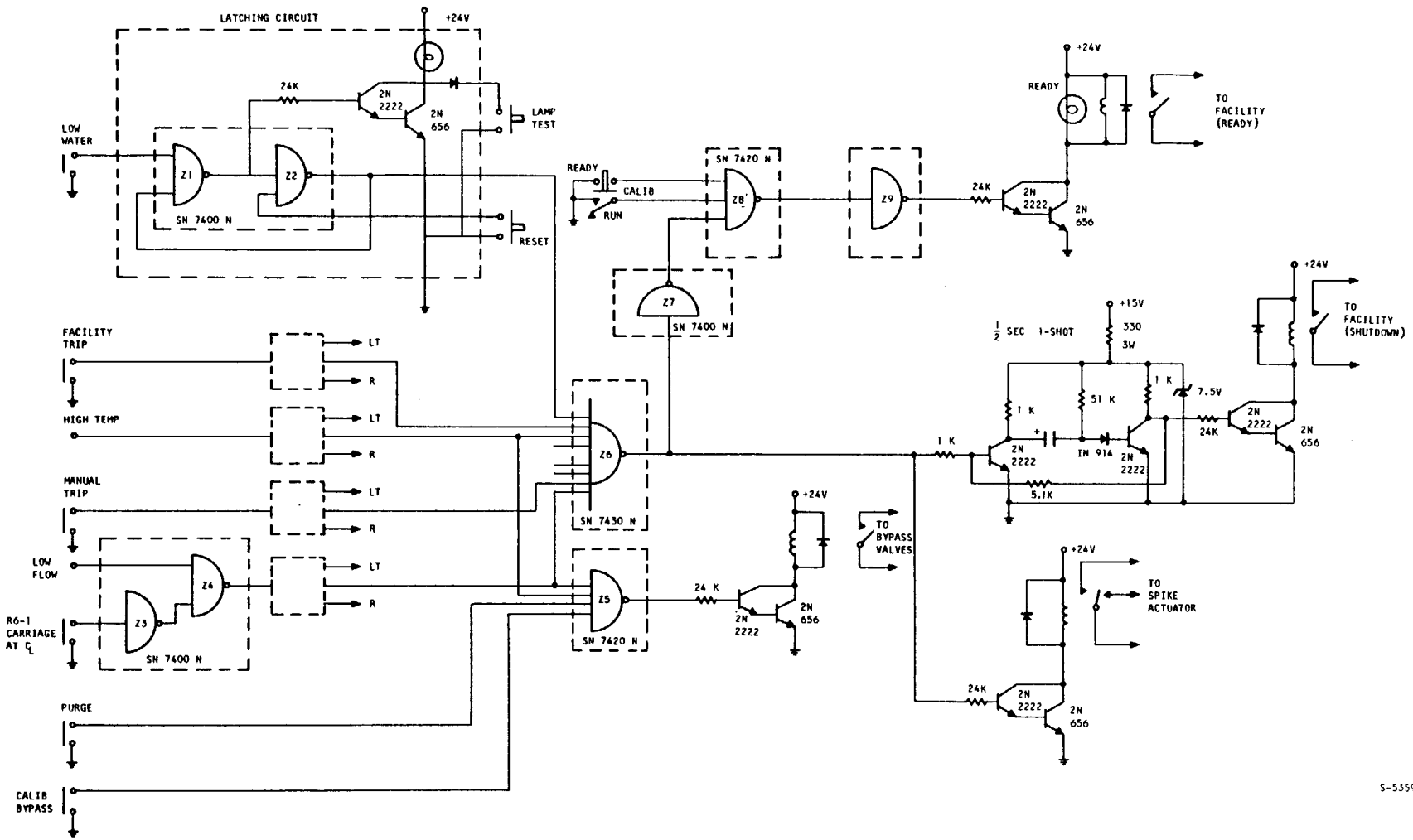

Figure 6.11-2. Startup and Shutdown Circuit

the spike actuator and also triggers a one-shot circuit which sends a momentary (1/2 sec) contact closure to the facility to request carriage withdrawal. Z5 acts as an OR gate which controls a relay that opens the bypass valves. Inputs to Z5 are low flow, high temp, purge, or calibrate control.

For startup, a "ready" signal is sent to the facility by operating a relay controlled by Z8 and Z9. All inputs to Z8 must be high to operate the relay, i.e., provided there is no shutdown condition existing (output of Z7 high) and the CALIBRATE/RUN switch is in the RUN position, then pushing the READY button will send the appropriate signal to the facility.

6.11.3 System Dynamics

An analog computer simulation of the SAM coolant system and the pressure and temperature controls was prepared for analysis of the system dynamics. The results of this analysis showed frequency response and modulation band obtainable with the pressure control valve actuator to be unsatisfactory. The design of the valve was changed to use the same low-friction ball valve with electric torque motor drive as discussed in the next paragraph.

6.11.4 Pressure Control Valve

As initially fabricated and tested, the pressure control valve consisted of a low-friction ball valve element and a pneumatic actuator. The frequency response and modulation band obtainable with this actuator were considered unacceptable based on the results of analog simulation studies. As a result, the design of the valve was changed to use the same low-friction ball valve element with electric torque motor drive. Figure 6.11-3 shows the assembly of the valve drive. The motor is a printed-circuit armature type, direct-coupled to the shaft of the ball valve. A potentiometer is coupled to the other end of the motor shaft and provides position feedback (the error signal that positions the valve is generated by comparison of the output of a strain gage pressure transducer with the set point voltage). The motor and potentiometer assembly are contained in a hermetically sealed cylinder. This cylinder was vented to sea level pressure in the wind tunnel to ensure satisfactory operation of the motor with wind tunnel static pressures in tenths of psia.

All cylindrical parts of the motor assembly are fabricated from heavy-wall aluminum tubing. The coupling connecting motor and valve is fabricated from PH13-8Mo steel, heat treated to Rockwell C43. The tongue and groove interface between this coupling and the valve allows for misalignment. A hardenable material was selected to minimize wear and, hence, backlash in actuation of the valve.

Figure 6.11-4 shows a photograph of the completed valve and drive assembly, the power amplifier, and the electronic controller.

6.12 VIBRATION MODEL

The purpose of the vibration model was to evaluate the engine structural design under conditions of dynamic loading at an early time in the program.

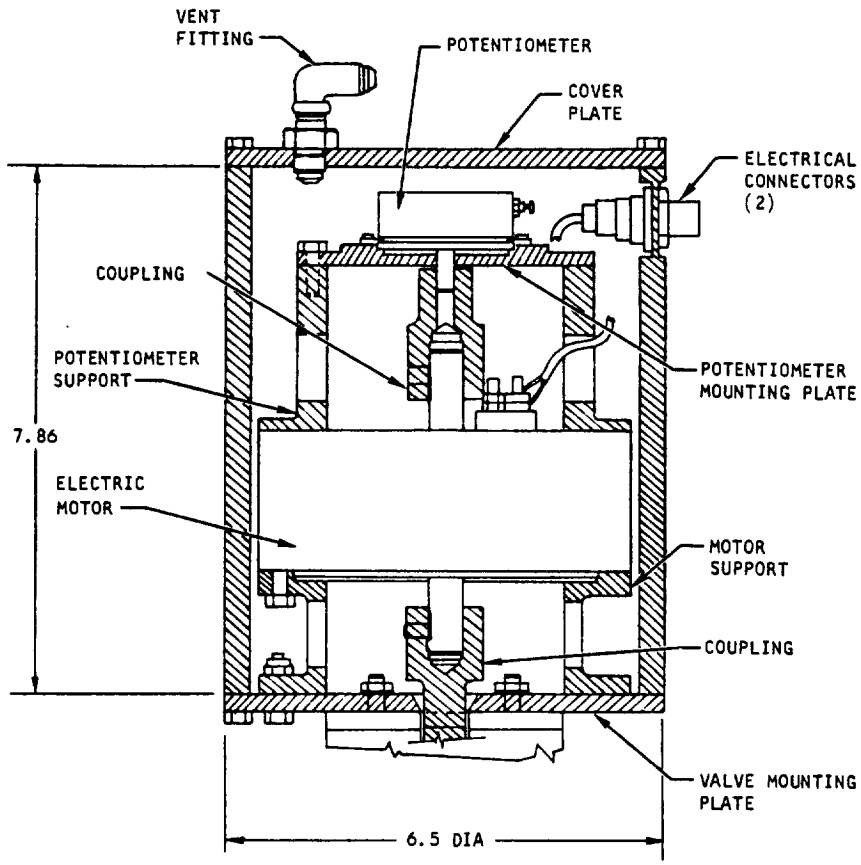

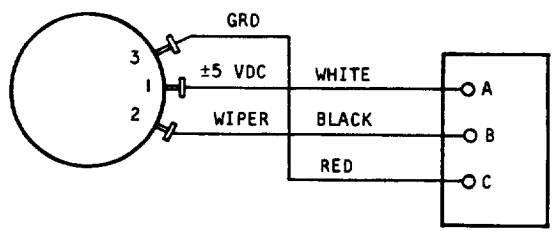

POTENTIOMETER SCHEMATIC

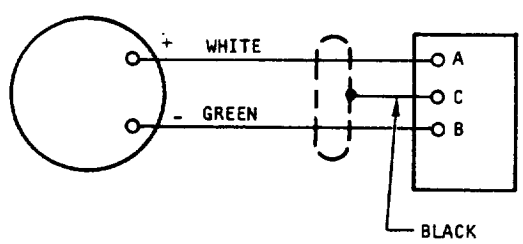

MOTOR SCHEMATIC

S-58592

Figure 6.11-3. Pressure-Control Valve Drive Assembly

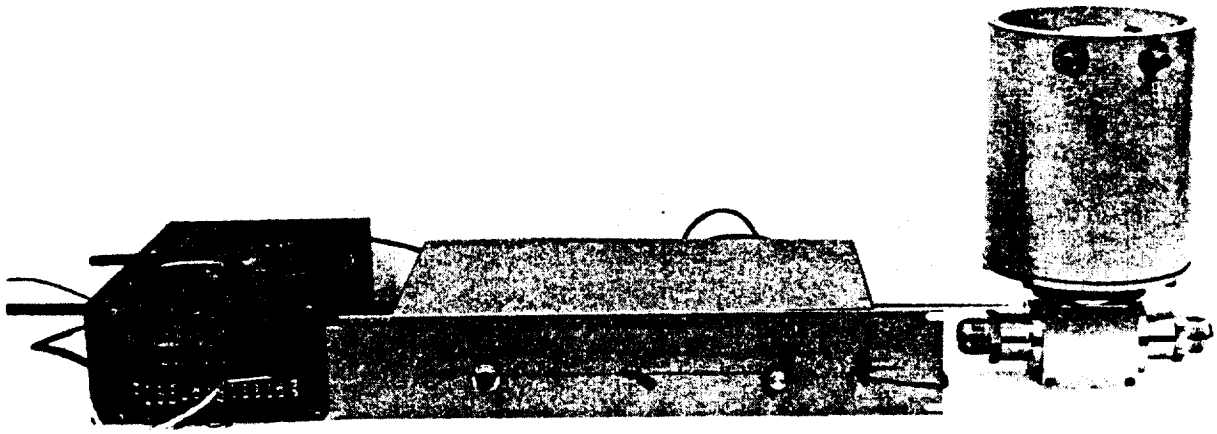

68786-1

Figure 6.11-4. HRE/SAM Pressure-Control System

Results of the tests could then have been incorporated into the design of the first flightweight engine being manufactured during that phase.

6.12.1 Design Ground Rules

The basis for design of the model to achieve the desired dynamic simulation involved the following:

(a) Duplication of component masses and centers of gravity of the component parts.

(b) Approximation of the pitching inertias and polar inertias of all shell assemblies, with pitching inertias the more critical of the two.

(c) Duplication of inlet-spike mounting cone flexibility by use of the actual part.

(d) Duplication of actuator assembly and mounting flexibility by use of the actual part.

(e) Duplication of the suspension frame (wishbone), thrust block, and rear mount flexibilities by use of the actual parts.

(f) Duplication of critically loaded manifold rings, the spike-innerbody seal and the spike bellows by use of the actual parts, to permit evaluation of the part itself as well as a simulation of effect on flexibility.

(g) Dynamic simulation of local flexibility by use of equivalent-stiffness single-sheet shells to replace the actual sandwich construction at all critical structural connections.

6.12.2 Features

With respect to Layout Drawing L-980619, the following features of the vibration model should be noted:

(a) The four manifolds between which the struts are mounted are the actual full-scale manifolds with minor modifications. These modifications include deletions of unnecessary instrumentation, and addition of tubes for circulation of hot gas. The outer shell outlet manifold, which forms the forward engine mount, is also the actual part.

(b) The inner shell and outer shell (Items 13 and 31) follow the contour of the cold surface of the full-scale components to permit installation of the manifolds. Other shells are simulated without reference to the actual component contours (nozzle, inlet spike, leading edge).

(c) The actual seal configuration is used in the nozzle-inner shell crossover manifold, Items 16 and 26. The integrity of this seal will be checked by gas pressurization during test.

(d) The fuel injection manifolds, Items 15 and 33, and the outer shell outlet manifold, Item 32, have suitable connections for gas heating to 1200°F during test. Thermocouples are placed on these manifolds as well as along adjacent skin sections.

(e) The fuel control valves are simulated by means of flat-plate masses mounted to the inner-shell injection manifold, Item 15.

Plumbing to the inlet-spike actuator was to be modified for purposes of vibration testing in such a way that the actuator could be powered from an external hydraulic pump. Actuation would be under conditions of no-external-load.

7. MANUFACTURING

Fabrication of the various assemblies required in the course of the program entailed a considerable manufacturing effort. This effort is summarized in the following sections, with emphasis on the regeneratively-cooled, flightweight engine structure. This structure constituted the major portion of the overall effort and was also the most important end-objective of this task of the program. In addition, certain items of hardware associated with the original flight test program are discussed. Work on these items was discontinued following re-orientation of the program to one involving ground testing only. Temperature and pressure control systems were fabricated for use with the SAM in the wind tunnel tests and are discussed.

7.1 FLIGHTWEIGHT SHELLS

The full-scale, flightweight engine components were placed in three development categories to facilitate identification. These categories were retained for convenience even though original distinctions and sequences were eliminated in many cases. They are:

(a) Experimental components. This designation was applied to assemblies used to develop the manufacturing techniques and in practice applied to the first completed assemblies. These assemblies were tested as required to evaluate manufacturing techniques and design features.

(b) Static test components. These assemblies were manufactured to include the experience obtained from the experimental components. They were used to evaluate pressure containment and to obtain calibrations of pressure drop and flow distribution.

(c) SAM components. These assemblies were used to manufacture the SAM for the wind tunnel tests. Plumbing and instrumentation were made compatible with the SAM requirements. In addition, minor modifications to the coolant flow routes were made to reflect test experience on flow distribution.

Each of the major shell assemblies of the HRE (inlet spike, inner shell, nozzle, leading edge, and outer shell) has, as its basic structure, a sandwich shell using plate-fin heat transfer surface brazed between face sheets. The spike is made up of three shell assemblies. Two of these are single sandwich; the third is a double sandwich consisting of three shells. The leading edge and outer shell each consist of two shell assemblies, and the nozzle and the inner shell each consist of one shell assembly. Figure 7.1-1 is illustrative

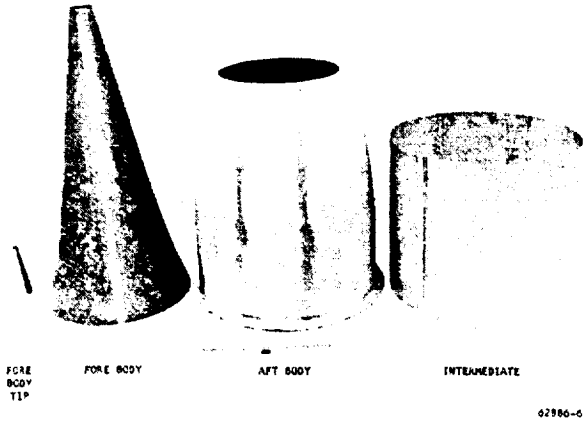

a. INLET SPIKE SHELLS

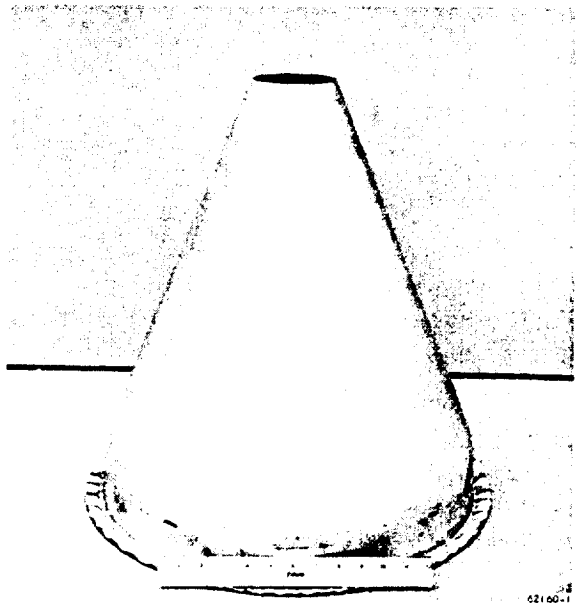

b. PREFORMED NOZZLE SHELL

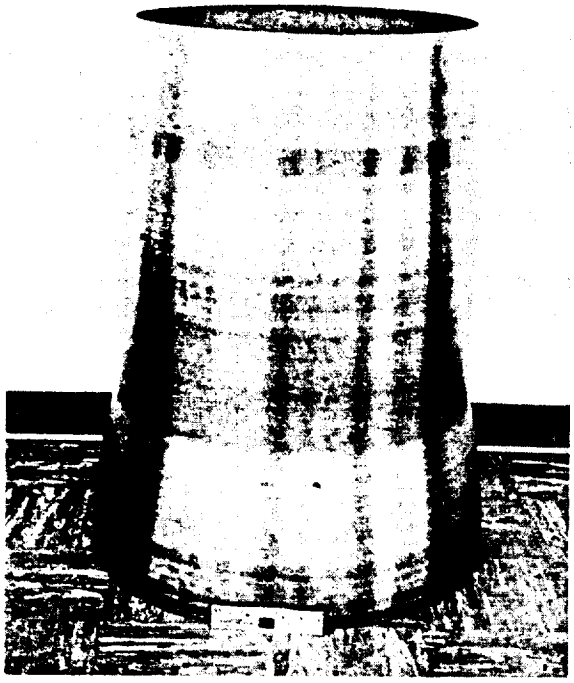

c. OUTER SHELL - COLD (OUTER) SHELL

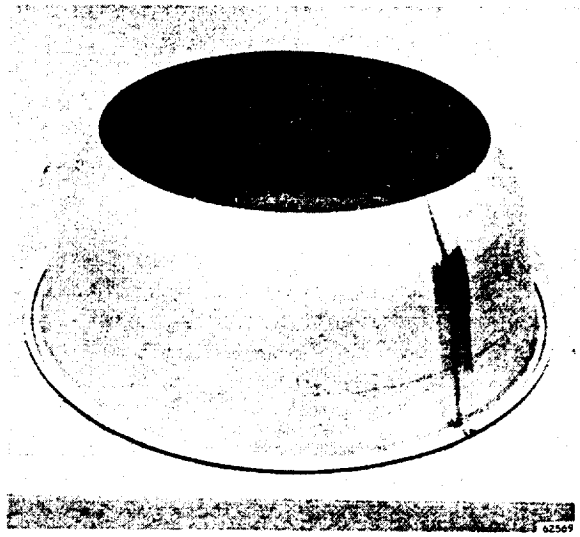

d. LEADING EDGE TYPICAL SHELL

F-14897

Figure 7.1-1. HRE Shell Assembly Shells

of the variety of sizes and shapes of shells required for the various assemblies. Manufacturing procedures, however, were similar for all assemblies. The following discussion outlines these procedures.

7.1.1 Shell Forming

The major operations involved in forming all of the shells were as follows:

(a) Blanking, forming, and welding a frustro-conical or cylindrical shell using slightly thicker material than that required for the finished part.

(b) Trimming and spinning an external flange on the large end of the cone; this flange was used for holding the part in preforming and final forming.

(c) Preforming to a size approximately 1-percent smaller in diameter than the finished dimensions.

(d) Chem-milling and polishing the shell to the final specified wall thickness.

(e) Finish-forming by the electro-hydraulic technique.

(f) Trimming to final required length.

The preforming of the shells was done on an expanding mandrel. The unformed shell was first clamped by its spun flanges over a set of segmented shoes that had been machined to the finish contour of the shell, then a center plug was hydraulically forced up between the shoes causing them to expand which, in turn, expanded the cone to its desired shape. A side effect of this forming operation was to create zones of varying thickness over the surface of the shells. To compensate for this, a localized chem-milling operation was performed to bring all zones of the shells to an equal thickness.

The sizing to final dimensions was done by electro-hydraulic forming on a Cincinnati "Electroshape" machine. In this operation, the shell was mounted inside a die cavity that had been precisely machined to the desired shell dimensions. The die ends were equipped with rubber gaskets to seal against the open ends of the shell. Details of the die assembly for forming the shells of the outer shell are shown in Figure 7.1-2. The die assembly ready for firing is shown by Figure 7.1-3. After the shell was mounted in the die and secured against the end seals, the inside of the shell was filled completely with water, and the space between the outside of the shell and the die was completely evacuated of air. When this step had been completed, a high voltage potential was built up in a capacitor bank and then discharged as a spark or across an exploding wire in the water inside the shell. The energy released by the discharge (120,000 joules maximum) forced the shell against the inside of the die. For some of the shells, a deflector was used to control the variation of pressure along the shell axis, as shown in Figure 7.1-2 for the outer shell.

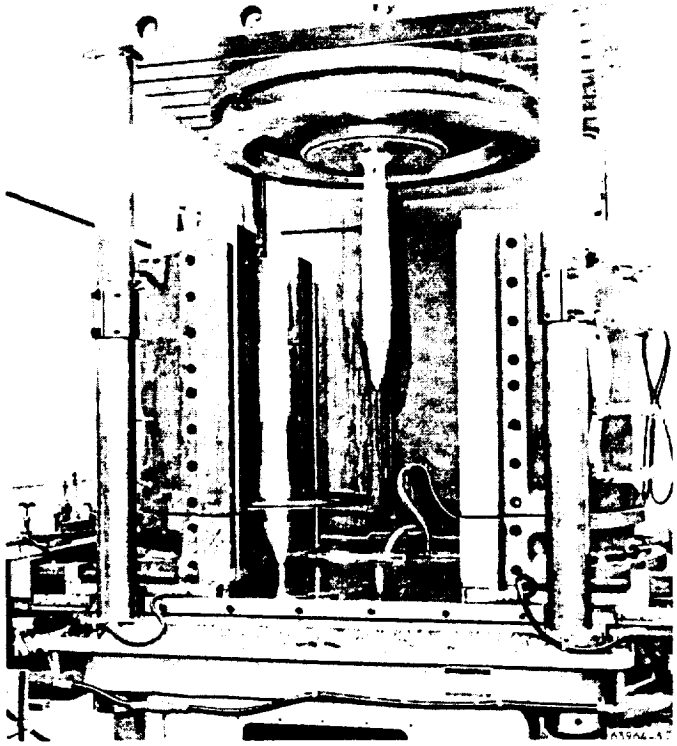

Figure 7.1-2. Outer Shell "Electroshape" Forming Die--Die Halves Separated to Show Machined Inside Contour

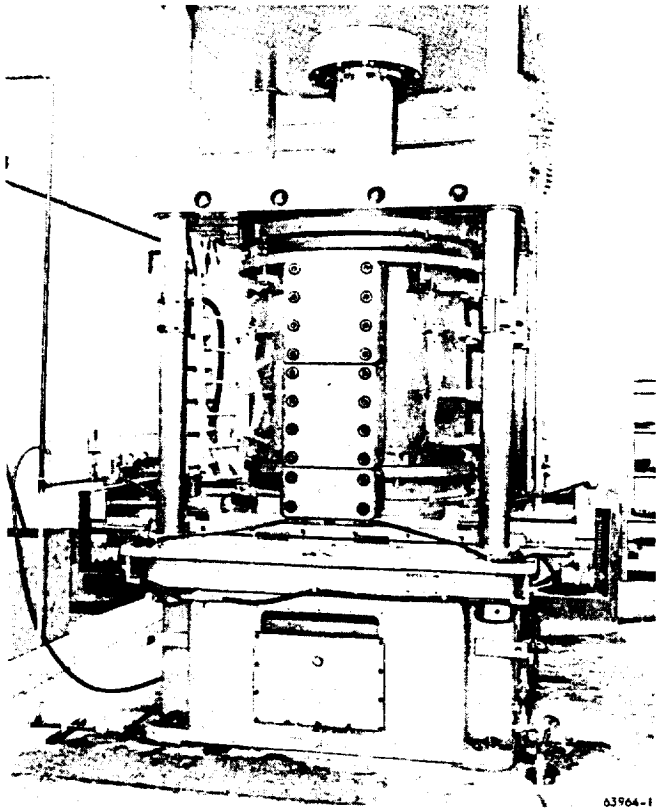

F-14898

Figure 7.1-3 Outer Shell "Electroshape" Forming Die Ready for Firing

7.1.2 Shell Brazing

All of the shell assemblies for the engine were fabricated entirely from Hastelloy X. The shell sandwiches consisted of a hot skin, 0.015-in. thick; the fins, either 0.004-in. or 0.006-in. thick; and the cold skin, either 0.015-in. or 0.060-in. thick, depending on the structural requirements. Brazing of the shell sandwiches occurred in machined graphite fixtures in an argon atmosphere. Argon was also used to force the inner of the shells into close contact with the fins, and the outer of the shells against the graphite fixture. Palniro 4 (30Au-34Pd-36Ni) was used during the first braze operation, at 2150°F, on all shell assemblies except the inner shell. The subsequent braze operations using Palniro 1 (50Au-25Pd-25Ni), Palniro 7 (70Au-8Pd-22Ni), Palniro RE (55Au-15Pd-30Ni), and Nioro (82Au-18Ni) were performed without degradation of the primary fin joints. The nominal brazing temperatures used for these alloys are, respectively: 2050°F, 1970°F, 2025°F, and 1850°F.

During the first braze operation both ends of the shell assemblies were sealed off either by the permanent headers or temporary headers that would be machined off later. After the braze operation two holes were drilled in one of the headers and capillary tubes installed; the assembly was then coated with a brittle lacquer ("StressCoat") and proof-pressure tested at 1050 psig while the surface was carefully scrutinized for evidence of elastic deformation of the shell at any unbrazed areas. This method of non-destructive testing is described more fully in Section 8 of this report. After proof-pressure testing, any machining operations required before subsequent assembly operations were performed. The appearance of a typical assembly, the inner shell assembly, during the first operation--that of stacking the foil-type braze alloy, the fins, and the shells together--is shown in Figure 7.1-4a; the inner shell assembly with the pressure inserts installed and ready for braze is shown by Figure 7.1-4b; the preparation for proof-pressure testing is illustrated by Figure 7.1-4c; and the appearance of the shell assembly after final machining operations is shown in Figure 7.1-4d.

7.2 FLIGHTWEIGHT COMPONENTS

As outlined above, fabrication of the basic sandwich shells was much the same for all of the cooled engine components. The following sections discuss peculiarities of the basic sandwich shells as related to specific components and the further operations involved in completing the assembly of the components.

7.2.1 Inlet Spike

The inlet spike is a brazed and bolted assembly consisting of three separate brazed shell assemblies, a sheet metal nose cone, fuel injector plenum, coolant outlet plenum, and support flange, all brazed together. Three inlet spike assemblies were completed during the program, with the third for use in the SAM. The latter included hydrogen bellows and instrumentation as required for the wind tunnel tests.

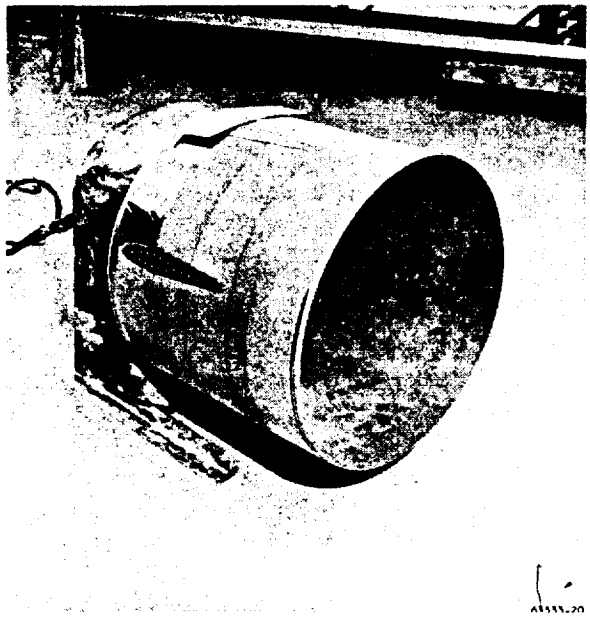

a. VIEW SHOWING COLD SHELL, BRAZE ALLOY, FINS AND DUMMY HEADERS

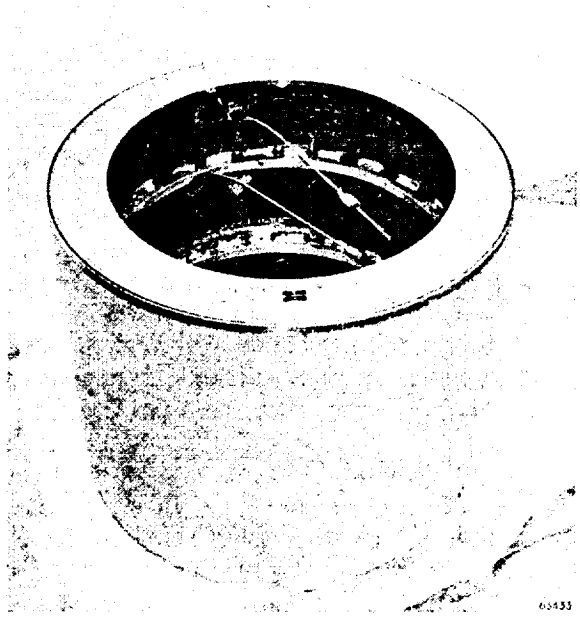

b. VIEW SHOWING PRESSURIZATION INSERT IN PLACE READY FOR BRAZE OPERATION

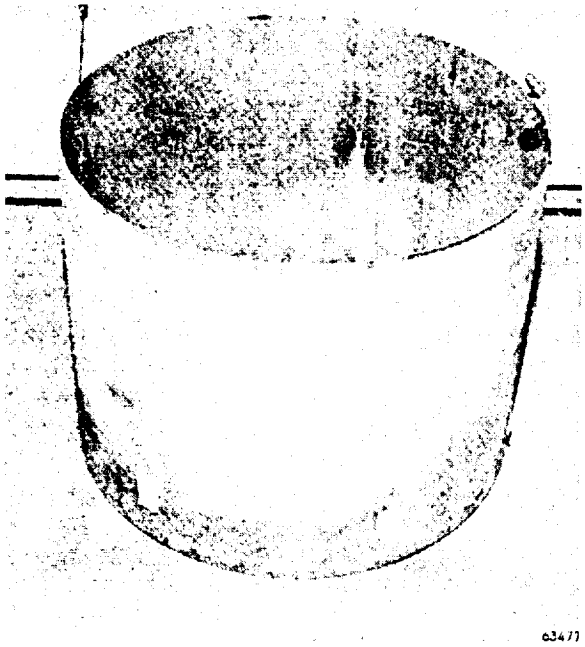

c. CAPILLARY TUBES IN PLACE READY FOR PROOF-PRESSURE TEST

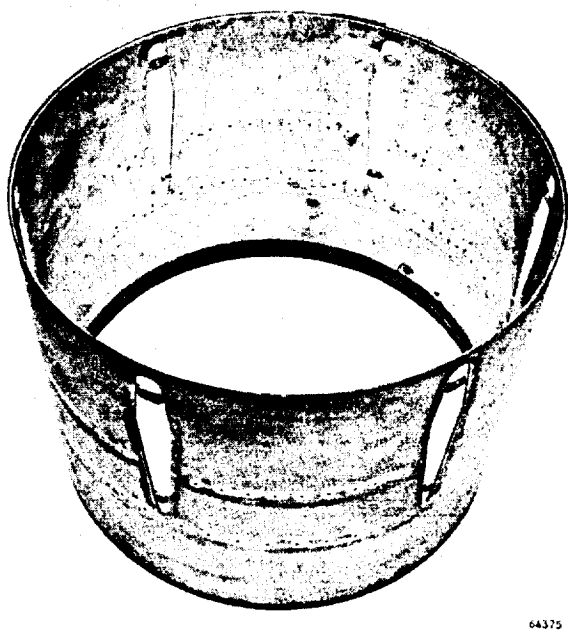

d. VIEW AFTER INSTALLATION OF INJECTOR PORTS AND MACHINING OF STRUT OPENINGS

F-14899

Figure 7.1-4. Inner Shell Assembly

7.2.1.1 Spike Brazed Assembly

The spike components, shown in Figure 7.2-1, were sequentially brazed as tabulated below:

1. Palniro 1 (2050°F)

   (a) Spike Tip

      1. Plenum and tip-coolant tube brazed to cold skin of spike tip

      2. Cold skin doublers brazed to cold skin of spike tip

   (b) Fore-Spike Assembly

      1. Pressure and temperature inserts brazed into assembly

      2. Hot and cold skin doublers brazed to the shell assembly at the forward end

2. Palniro RE (2025°F)

   (a) Spike Tip and Fore-Spike Assembly (Fore Body)

      1. Nose cone brazed to spike tip

      2. Spike tip brazed to fore-spike assembly

   (b) Aft Spike Assembly (Aft Body)

      1. Doubler at forward end brazed to cold skin

      2. Actuator mounting cone brazed to cold skin

      3. Fuel injector plenum brazed to cold skin

      4. Coolant outlet plenum brazed to cold skin

      5. Control thermocouple inserts brazed to cold skin

3. Palniro 7 (1970°F)

   Used to join fore body and aft body brazed assemblies.

4. Silver Braze BAg-8 (1550°F)

   Used to install coolant control thermocouples into inserts by induction brazing.

7.2.1.2 SAM Inlet Spike Assembly

The inlet spike assembly was completed with installation in the basic

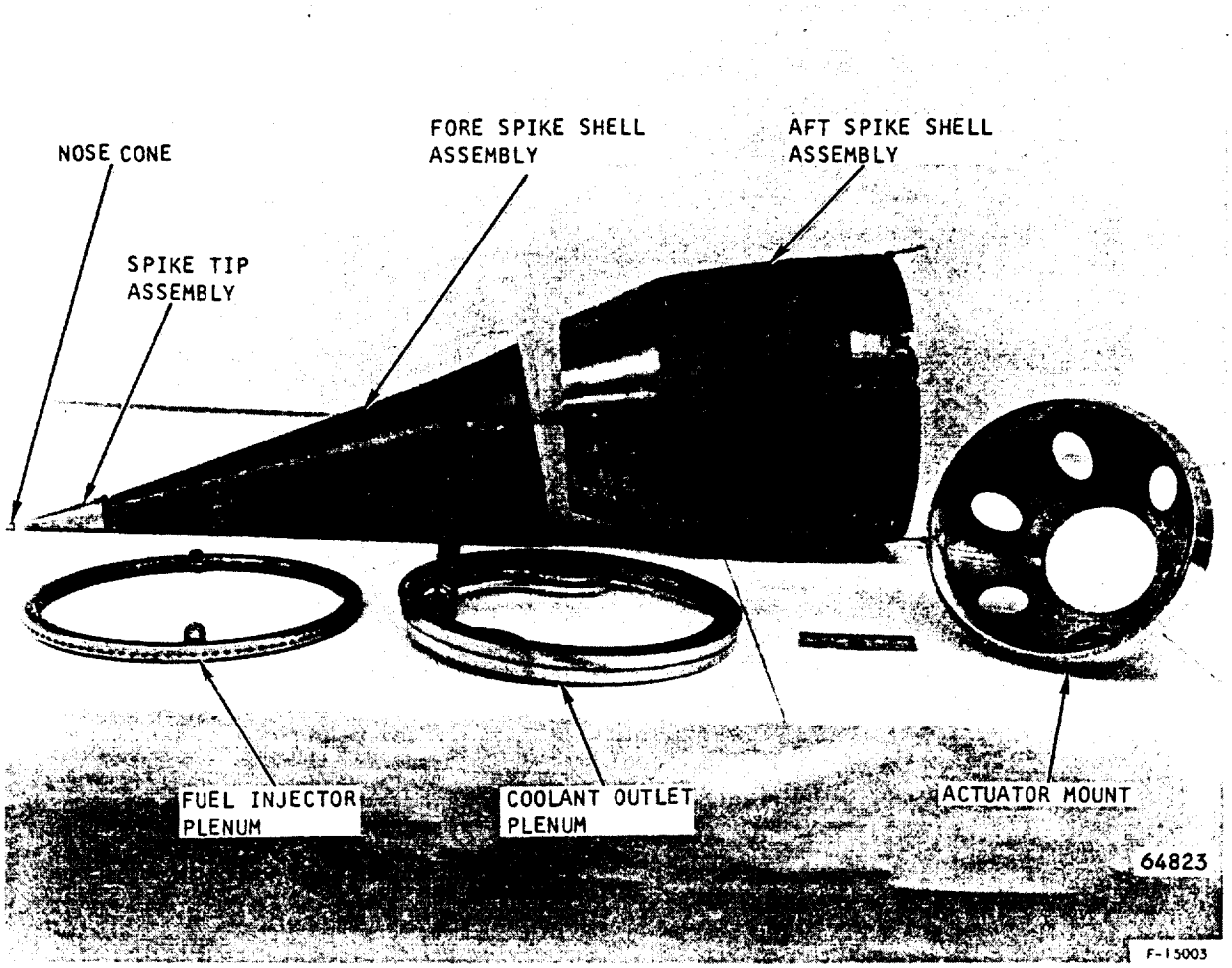

Figure 7.2-1. Major Components of Inlet Spike Brazed Assembly

spike of (1) strain gages on the actuator mounting flange, (2) of the pressure transducer package, (3) bellows assemblies, (4) accelerometers, and (5) required cabling and connector assemblies.

Photographs of the outside and inside of the spike assembly are shown in Figure 7.2-2. The thermocouple terminal bracket can be seen in the upper-left quadrant of Figure 7.2-2b, attached to the coolant inlet bellows (small diameter tube). The pressure transducer cabling was pulled through a hole in the bottom of the bracket and clamped to the side of the bracket along with the thermocouple wires. The thermocouple wires, pressure transducer cables, strain gage cables, and the accelerometer cables were laced together and placed inside of shrink-tubing to provide a common cable assembly for the transition from the inner shell assembly to the inlet spike assembly.

The aluminum housing for the pressure transducers appears in the center of the actuator mounting flange. It is supported by low frequency vibration isolators. The coolant outlet bellows and the fuel inlet bellows for the injectors appear above and below the flange. The bellows used to seal the gap between the inner shell and the spike is attached to the large-diameter flange in the photograph.

One of the two accelerometers on this assembly can be seen in Figure 7.2-2b, installed on the flange of the actuator mounting cone, in the lower-left quadrant of the photograph. This is a uniaxial accelerometer that measures acceleration along the engine axis. A uniaxial accelerometer on a rib of the mounting flange measures acceleration in the vertical direction.

The strain gages installed on the spike were located on the actuator mounting cone. Two uniaxial full-bridge installations were placed on ribs of the actuator mounting cone and two full-bridge bending-moment bridges were placed on the inside of the cone. The bending bridges were for measuring bending in the vertical and horizontal planes. All strain gage installations were covered with epoxy for water-proofing and protection from physical damage.

7.2.2 Inner Shell Assembly

This assembly, because of its straight, slightly-tapered walls, was one of the easiest to assemble. The unit consisted of the basic sandwich shell assembly, inlet and outlet coolant manifolds, injector manifolds, and the support pads for the inner-outer body struts and the spike actuator. The appearance of these details is shown in Figure 7.2-3, and the arrangement of the details to create the coolant and injector flow paths is shown in Figure 7.2-4. Three inner shell assemblies were made during the program, the final one, shown in Figure 7.2-5, being used in the SAM. The two rows of injection ports were incorporated in the first two assemblies, as shown in Figures 7.2-3 and 7.2-4, but were omitted from the SAM, as seen in Figure 7.2-5. Because of structural requirements, the injection manifolds were retained for SAM. Figure 7.1-4 shows additional details of this assembly.

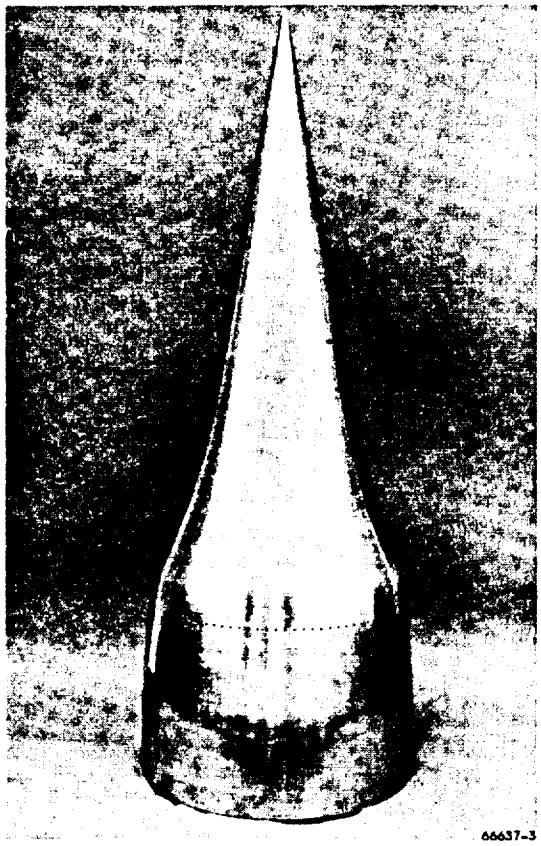

a. INLET SPIKE ASSEMBLY

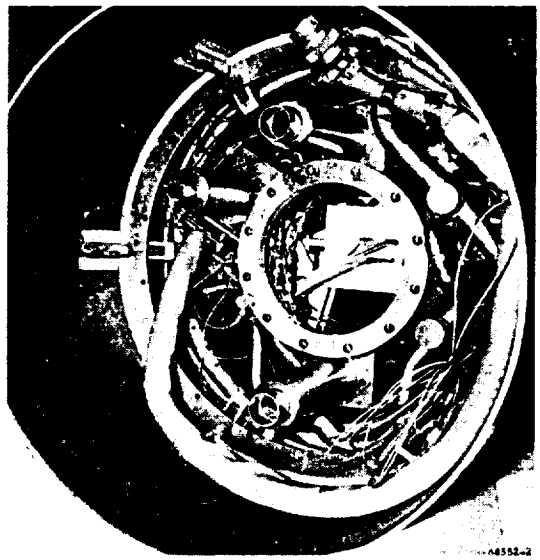

F-15000

b. VIEW INTO INSIDE OF INLET SPIKE ASSEMBLY SHOWING PRESSURE TRANSDUCER ASSEMBLY, BELLOWS ASSEMBLIES, AND ACCELEROMETERS

Figure 7.2-2. SAM Inlet Spike

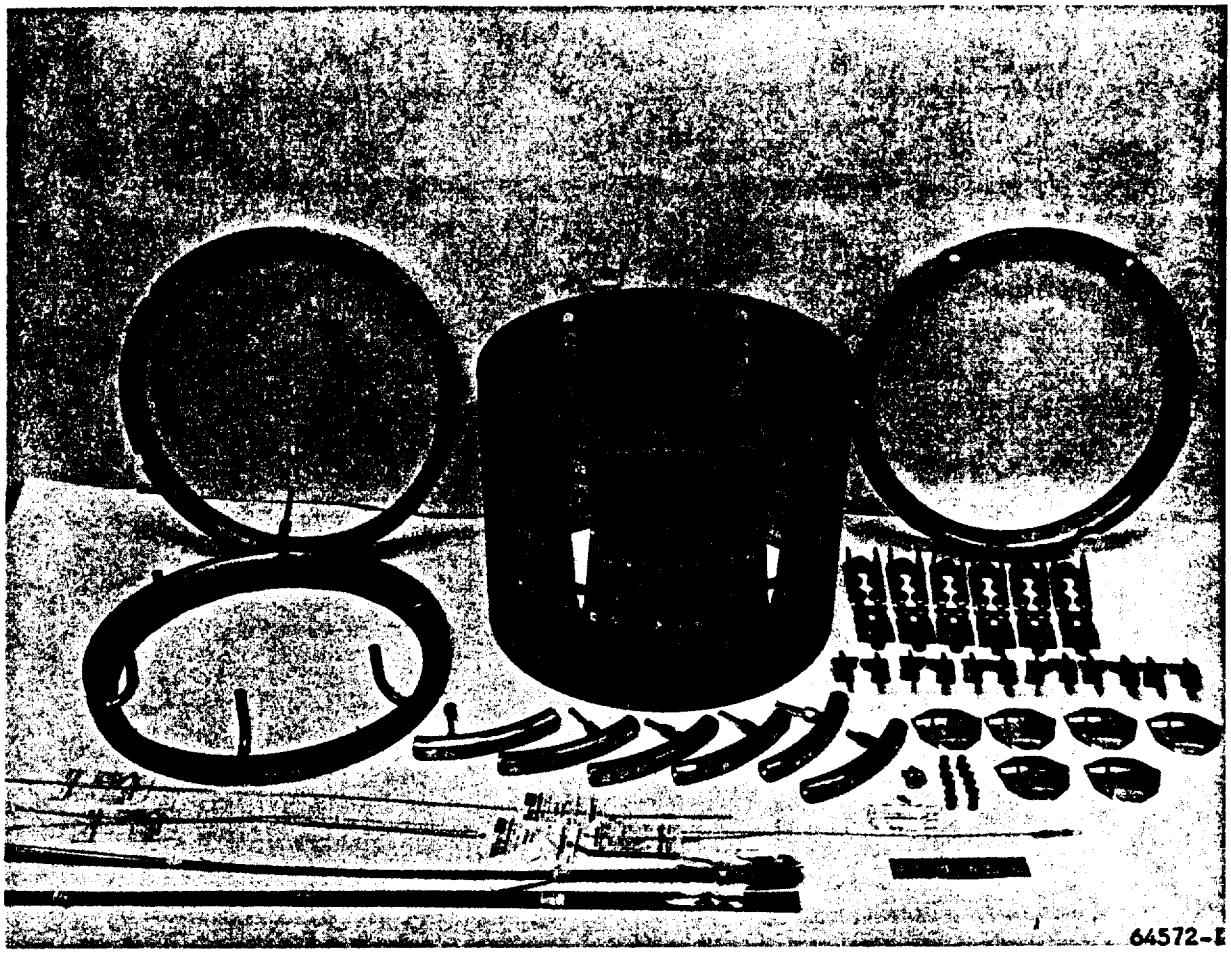

Figure 7.2-3. Inner Shell Assembly-Detail Components

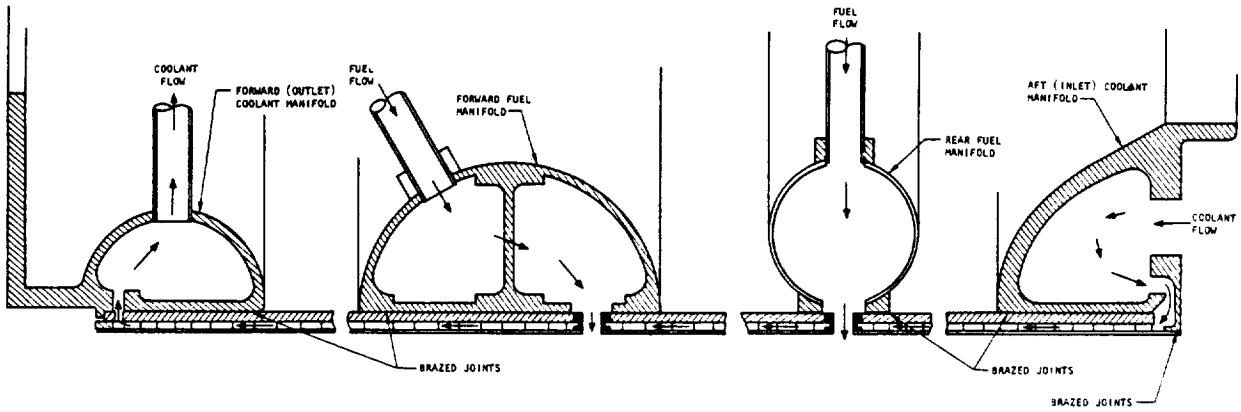

Figure 7.2-4. Inner Shell Final Assembly--Braze Joint Arrangement and Flow Paths

F-14894

Figure 7.2-5. Inner Shell Assembly - View Into Aft End Showing Actuator Mounting Pads, Strut, Mounting Pads, and Nozzle Mounting Flange

7.2.2.1 Sandwich Shell Assembly

The general fabrication details of this assembly are described in Section 7.1; however, this assembly contained the cutouts for the struts which required special attention. The cutouts, in addition to being leak-tight against the coolant pressure, had to be located within a few thousandths of an inch of true position and the contour controlled within a few thousandths of an inch tolerance. To achieve this control, tooling holes were machined in the inner (cold) shell after final sizing but before assembly. These tooling holes were first used to locate header blanks in the sandwich assembly and, after brazing, the special electro-discharge machining (EDM) electrodes were used to cut out the strut openings. The holes were preserved through the EDM operation, as can be seen in Figure 7.2-3, and used to locate the strut mounting flanges that were subsequently brazed inside the shell.

7.2.2.2 Final Assembly

The step-brazing sequence used to assemble the inner shell assembly was:

(a) 1st Cycle--Palniro 1. Fins, headers, and strut header blanks to shells. This basic sandwich shell assembly was brazed with Palniro 4; for all other components, Palniro 1 was used here because the additional braze cycle provided by Palniro 4 was not required. Structural performance is about the same for both filler alloys, while the lower braze temperature of Palniro 1 is less abusive to the parent metal.

(b) 2nd Cycle--Palniro RE. Pressure tap and thermocouple inserts to shells; fuel injectors to shells (on experimental and static test components only).

(c) 3rd Cycle--Palniro 7. Manifolds and strut and actuator mounting pads to shell.

(d) 4th Cycle--Nioro. Strut pad and manifold joint repairs.

During installation of the manifolds and plenums into the shell, Palniro 7 braze alloy was pre-placed in the joints and the parts were TIG-tack-welded in place. Flanges, pads, and gussets were also TIG-tack-welded in place. After all details had been located and tacked in place, a slurry of Palniro 7 braze alloy powder and "Nicrobraz" cement was filletted around all of the joints. The various coolant, or fuel containment braze joints in the final assembly are shown in Figure 7.2-4. The unit was brazed in vacuum at a temperature of 1970°F.

During the final machining operations, both of the end flanges were first faced, and cut to the correct diameter in a vertical lathe. The assembly was

then installed in an EDM where the actuator pads were faced, and the actuator pad bolt holes and coolant crossover holes in the aft plenum were machined. In the final setup, in a jig boring machine, the bolt holes in the flanges on both ends of the assembly were drilled and tapped.

7.2.3 Nozzle

This assembly, bolted to the aft end of the inner shell, completes the innerbody. It is a brazed and machined assembly to which are bolted a cover and baffle; an end cap is screwed in place to close out the assembly. The brazement is made up of the shell assembly, described in Section 7.1, the forward manifold, and aft cold and hot rings. The arrangement of the various details to make up this assembly is shown in Figure 7.2-6 and the overall appearance of the nozzle is shown in Figure 7.2-7. The inner cold skin and outer hot skin of the shell assembly were both 0.015-in. thick. Three complete assemblies of this component were fabricated during the program, of which the final was used on the SAM.

7.2.3.1 Shell Assembly

The shell assembly, because of its steeply conical shape, with the small diameter approximately 28 percent of the large diameter, was particularly critical of setup during the first braze cycle. The first shells were installed in the furnace for the braze cycle with the small end down. Buckling of the inner shell and blockage of a portion of the fin passages with braze alloy were experienced at the small end. Also, tensile deformation sufficient to rupture the inner skin at the small end was encountered. Two changes in setup led to successful braze cycles:

1. The fixture was inverted to permit brazing with the large end of the nozzle down. This discouraged the concentration of alloy that might cause fin plugging, and eliminated any tendency for the straight section at the large end to seize prematurely in the graphite/pocket.

2. The heating cycle was controlled and monitored to restrict the temperature differentials between the inner structure and skin to less than 75°F. This had the effect of approximately doubling the length of the heating cycle, from approximately 4 to 8.3 hr, but eliminated unacceptable differential thermal growth.

The control of the temperature of the part (and braze alloy) during the portion of the braze cycle above the solidus temperature of the alloy (2075°F) proved to be extremely critical in limiting the settling of the alloy, and fin plugging. The more rapidly the part could be heated to the liquidus (2140°F) and chilled back through the solidus, the less tendency to plug and the more uniform the braze fillets from top to bottom of the structure. This characteristic was evident in all of the fin-skin brazements made.

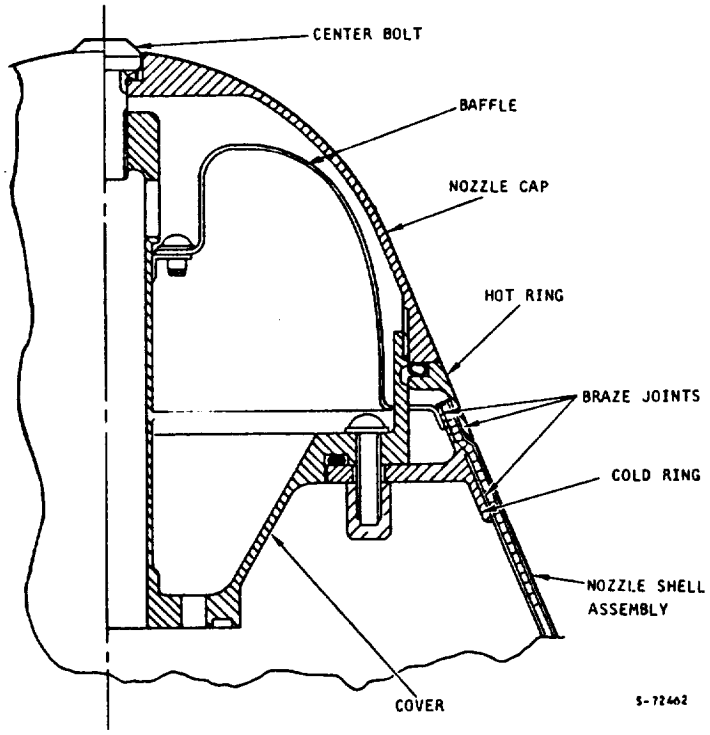

a. CONFIGURATION AT SMALL END

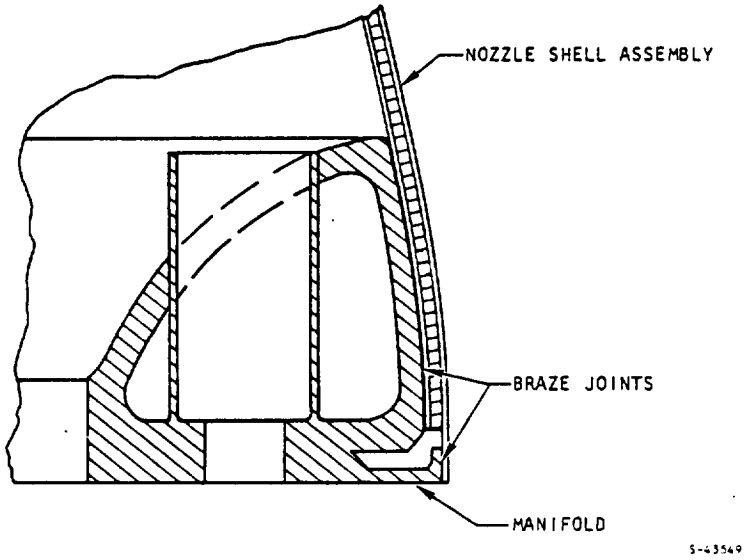

b. CONFIGURATION AT LARGE END

Figure 7.2-6 Nozzle Assembly Details

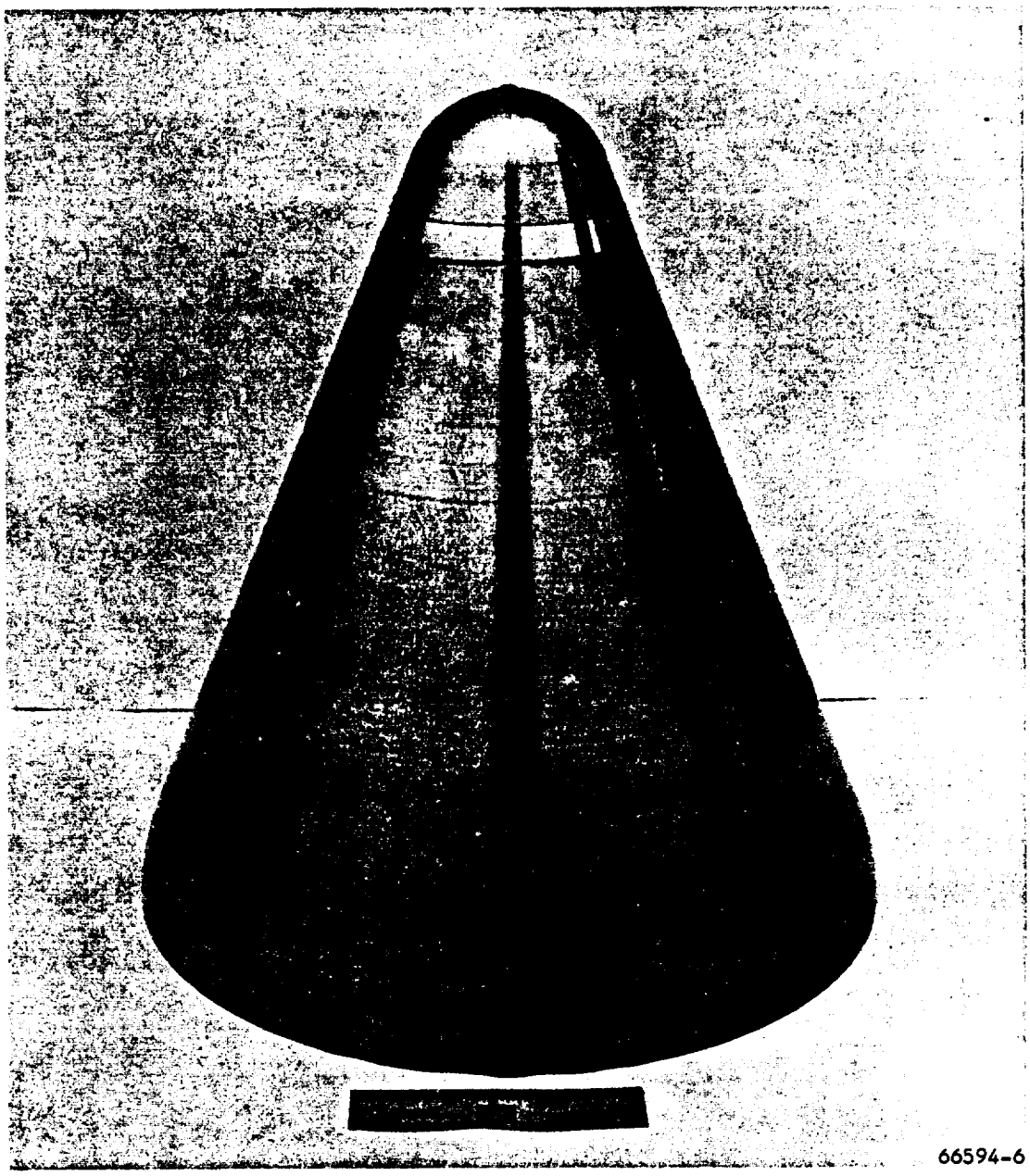

Figure 7.2-7. SAM Nozzle Assembly

7.2.3.2 Final Assembly

The braze cycles selected for joining the various subassemblies and final assembly of the nozzle were:

(a) Cycle No. 1--Palniro 4. Shells to fins; crossover manifold flange to torus.

(b) Cycle No. 2--Palniro 1. Pressure and thermocouple inserts to crossover manifold. Cap screw bosses to small-end ring.

(c) Cycle No. 3--Palniro RE. Crossover manifold, small-end rings, thermocouple inserts and pressure tube inserts to shell assembly.

(d) Cycle No. 4--Palniro 7. Pressure tubes and thermocouples to inserts in shell assembly.

Machining, facing, drilling, and tapping of both ends of the assembly were done after the final braze cycle in jig bores and vertical lathes. Teflon "Omniseals" were used at all the flange faces. The center bolt was sealed with a Harrison "K" seal.

7.2.4 Leading Edge

The leading edge assembly consists of three major subassemblies; (1) the inner (coolant outlet) manifold assembly, (2) the outer (coolant inlet) manifold assembly, and (3) the tip assembly, as shown in Figure 7.2-8. A major preoccupation in fabricating this component was control of size, particularly at the mating rings which interconnected the three subassemblies. Here, the size tolerances were held plus or minus 0.002 in. for braze fitup. Three leading edge assemblies were completed during the program, with the final one used on SAM.

7.2.4.1 Subassemblies

Details of the coolant inlet and the coolant outlet manifold assemblies are shown in Figures 7.2-9a and 7.2-9b. The basic sandwich shells responded to the normal fabrication operations described in Section 7.1. Precise control of the timing of the application of pressure during the braze cycles was required to ensure the close tolerances on the shell sizes.

The 0.015-in.-thick shell for the tip assembly was machined from a single Nickel 200 ring forging. Brazing of the fins and inner ring into the tip assembly presented a unique set of problems, dictated by the shape of the skin and close size tolerances. The braze fixture used a graphite ring to restrain the outside contour. A pressurized Hastelloy X bellows supplied the necessary pressure to the inside surface of the assembly for sizing and braze clearance. A multi-operation procedure incorporating controlled brazing conditions, resizing in the braze fixture, and a small amount of cold forming was successful

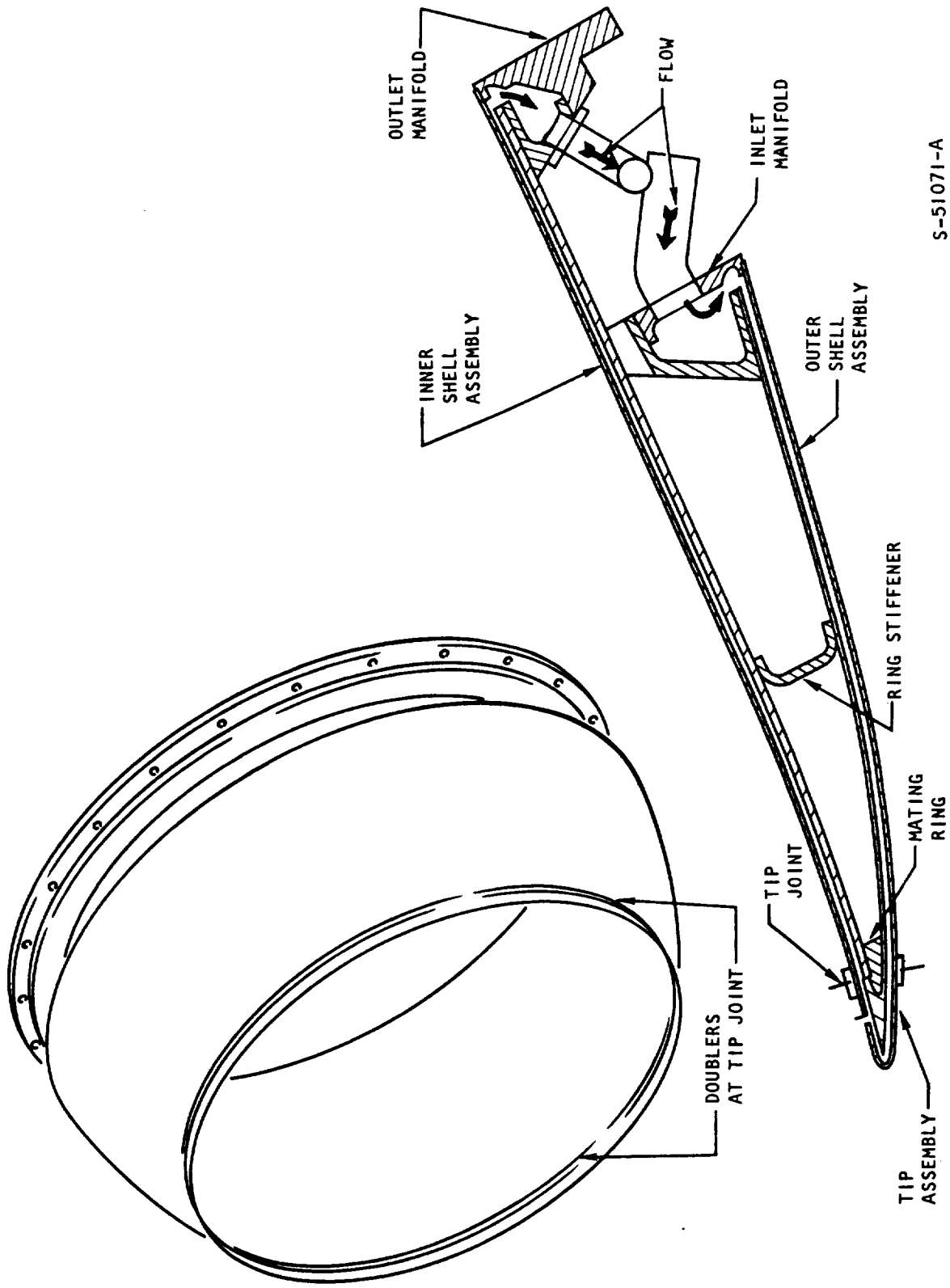

Figure 7.2-8. Leading Edge Assembly

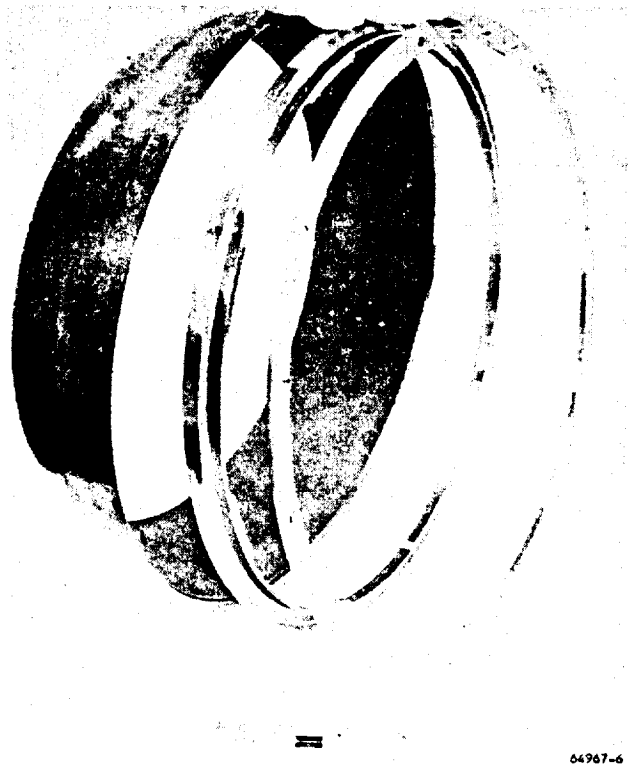

a. INLET MANIFOLD ASSEMBLY DETAILS

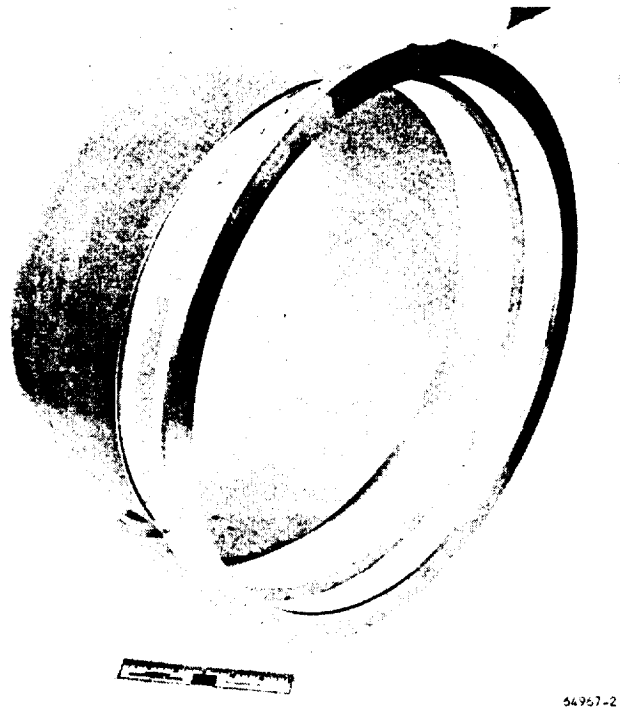

F-15001

b. OUTLET MANIFOLD ASSEMBLY DETAILS

Figure 7.2-9. Leading Edge Shell Assemblies

in producing the required size.

7.2.4.2 Assembly Sequence

Assembly of the parts occurred in the following sequence, arranged according to the basic braze cycles.

Palniro 4 (2150°F)

(a) Inner shell assembly (shells and fins),

(b) Outer shell assembly (shells and fins)

(c) Tip assembly (shell, inserts, and fins)

Each assembly was individually brazed and proof-pressure tested to 1050 psig after brazing. Pressure testing was performed with "StressCoat" on the surfaces to permit detection of unbonded areas. The tip assembly, at this point, was put aside until required for final assembly.

Palniro 1 (2050°F)

(a) Outlet manifold and instrumentation inserts to inner shell assembly, to form outlet manifold assembly.

(b) Inlet manifold and instrumentation inserts to outer shell assembly, to form inlet manifold assembly.

Each assembly was leak-tested at low pressure (100 psig) following its braze cycle.

Palniro 7 (1970°F)

This cycle joined the two manifold assemblies, the mating ring, and the stiffening ring, illustrated in Figure 7.2-10a, into the structural assembly. The joints between the mating ring and the shells were checked for leakage, at essentially zero pressure, in two ways:

(a) With the mating ring pointing down, the cavity above the ring was filled with acetone and the joints inspected for seepage.

(b) With the mating ring pointing up, the cavity below the ring was filled with helium and sniffed, using a mass spectrometer.

Nioro (1850°F)

This cycle joined the tip assembly to the structural assembly

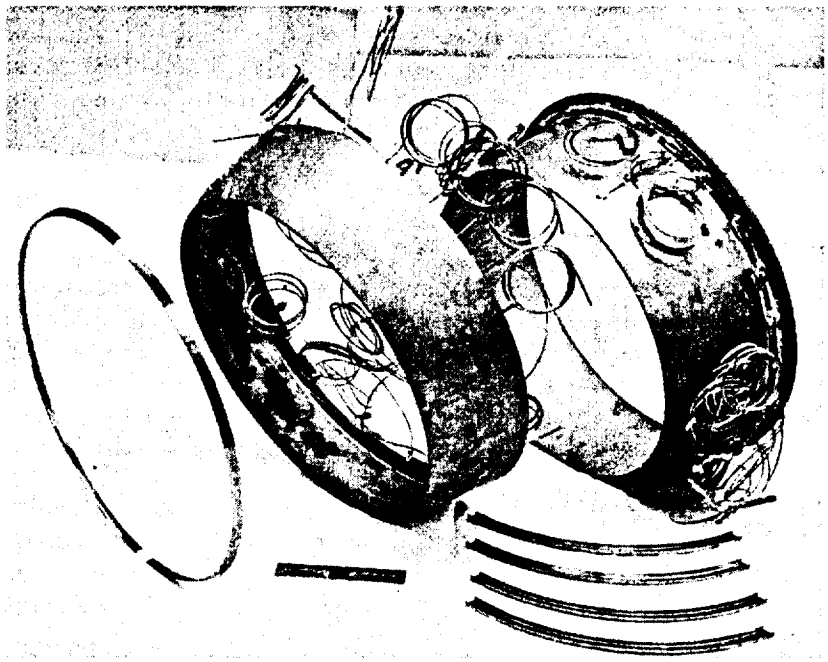

a. COMPONENTS OF LEADING EDGE STRUCTURAL ASSEMBLY (INLET AND OUTLET MANIFOLD ASSEMBLIES, MATING RING, RING STIFFENER)

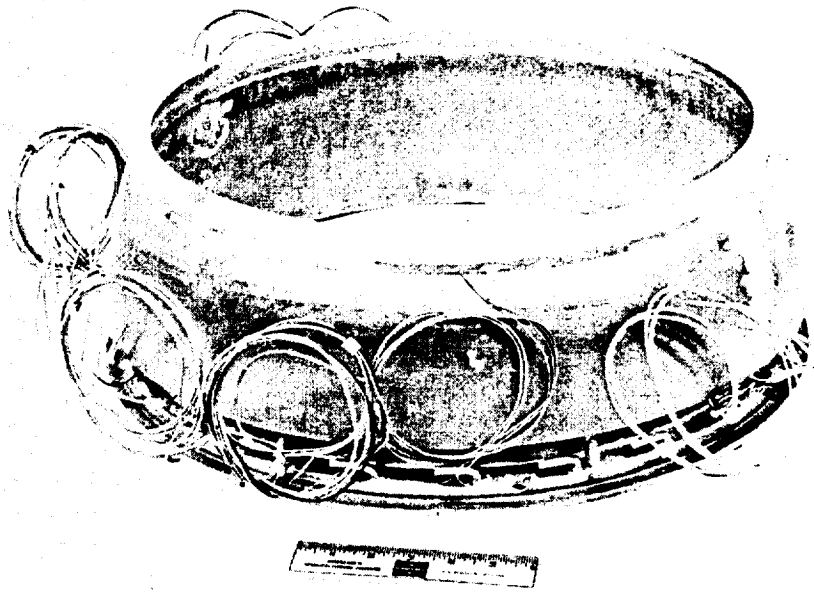

65890-2

F-15002

b. LEADING EDGE ASSEMBLY AFTER COMPLETION OF ALL BRAZING OPERATIONS

Figure 7.2-10. Leading Edge Assembly

to complete the joining operations on the leading edge assembly, illustrated in Figure 7.2-10b. Doublers were brazed across both the internal and external tip joints during this cycle. This final assembly was again proof-pressure tested to 1050 psig with "StressCoat" on the surfaces.

7.2.5 Outer Shell

In terms of the number of detail parts and joints, the outer shell is the most complex of the assemblies on the engine. In addition to two separate shell assemblies, it incorporates four toroidal ducts, three machined structural support manifolds, two machined plenum assemblies, the six flange pads for strut mounting, and the fuel injectors. These subassemblies are shown in Figure 7.2-11, which shows the completed outer shell assembly.

Fabrication of the manifolds and ducts embodied essentially the full gamut of conventional metal forming, joining, and machining techniques. The two primary support manifolds required four separate circular machined forgings each, in addition to the strut pads. Each of these manifolds was made up of a semi-toroidal ring brazed to an inner cylinder. The close fits required for these braze joints required close tolerances (±0.001 in.) and temperature control of the parts during measurement. In order to achieve the required fits with the shell, all manifolds were final-machined to dimensions taken from the shells after their last preceding braze and test operations.

The braze cycles used for the outer shell assembly were:

(a) Cycle No. 1--Palniro 4.	Main shell assembly, shells to fins Trailing edge shell assembly, shells to fins Manifold subassemblies
(b) Cycle No. 2--Palniro 1.	Main shell assembly to fuel injectors Trailing edge shell assembly to plenum
(c) Cycle No. 3--Palniro RE.	Main shell assembly to all manifolds, static pressure sensing tubes, thermocouple inserts, strut mounting pads, leading edge mounting plenum (inner), and trailing edge/main shell mating ring (inner).
(d) Cycle No. 4--Palniro 7.	Main shell to leading edge mounting plenum (outer), trailing edge cap ring, gussets, doubler, and thermocouples.

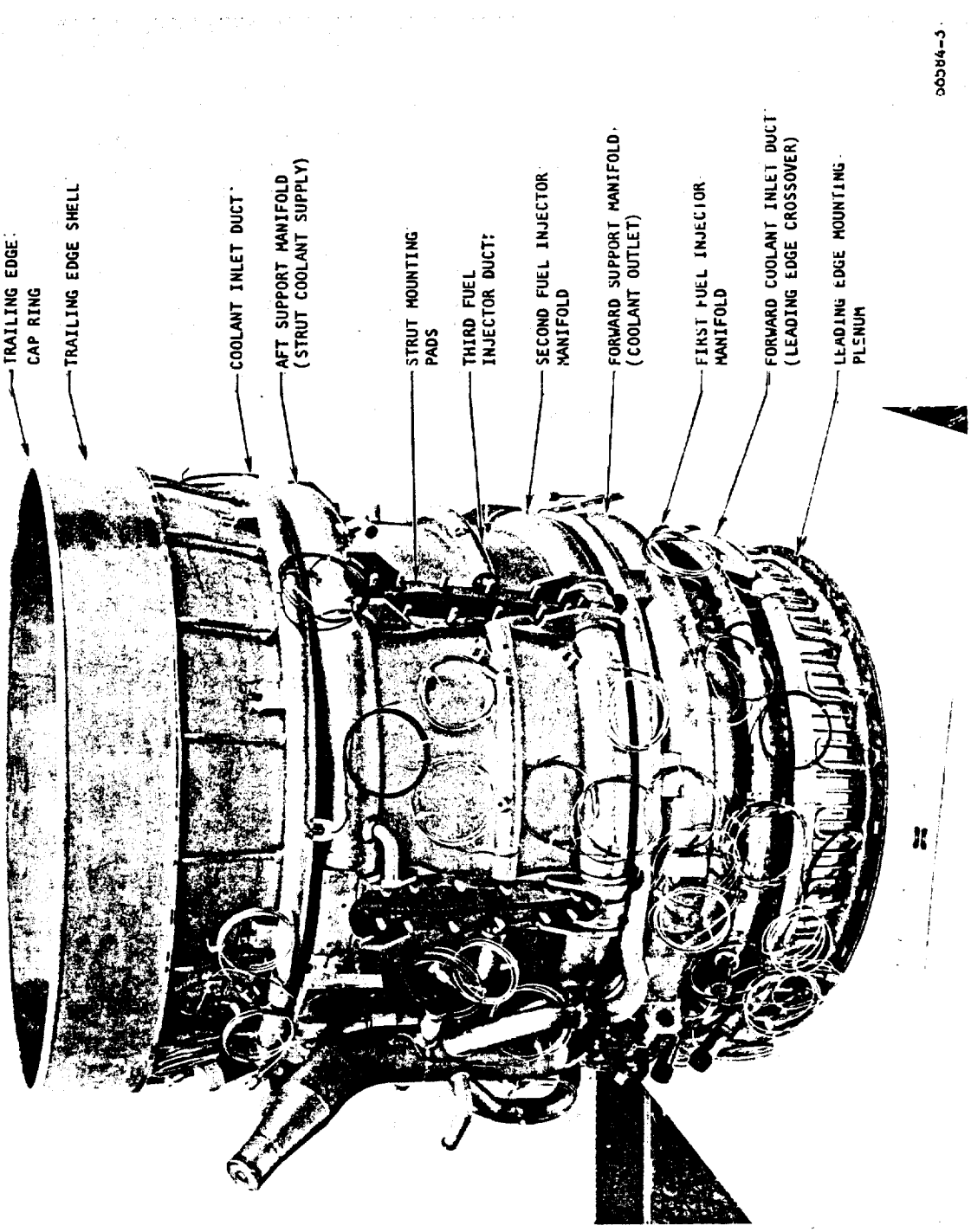

Figure 7.2-11. SAM Outer Shell Assembly

Experience during brazing of the shells showed a problem that was peculiar to fabrication of this component. The inner (hot) skin, which was welded to the pressurizing insert, is 0.015 in. thick and much weaker than the insert. The inner skin of the first assembly that was brazed buckled severely during the brazing cycle because of differential growth resulting from differences in temperature. Incorporation of a strain-absorbing bead in the joint between the inner skin and pressurizing insert, and limitation of the temperature differences between skin and insert to less than 100 deg, permitted successful brazing on the second and third shells. Fin-plugging was avoided during the first braze cycle by limiting the time that the part was in the brazing temperature range.

The third braze cycle, using Palniro RE alloy, was the crucial cycle of the outer shell sequence. In addition to the sealing requirements for all of the manifolds and plenums, there was the hazard of fin-plugging by migration of alloy through the slots around each of the strut openings. Stopoff was applied in the slots, and extra restraint was applied to maintain minimum clearance between the strut pads and shell. These measures were successful in preventing any plugging except for a minor amount in the experimental component.

7.2.6 Struts

Six struts are required to connect the innerbody to the outerbody of the engine and provide passages for all of the service lines between the inside of the innerbody and outside of the engine. The struts use 0.020-in.-high fins, formed from 0.004-in. Hastelloy X, between the 0.015-in.-thick Hastelloy X skin and the forged Hastelloy X body. Figure 7.2-12 shows the major details used in the fabrication of a typical strut.

Three braze cycles are required for strut assembly:

(a)	Cycle No. 1--Palniro 4.	Fins to skin and body
(b)	Cycle No. 2--Palniro 1.	Special fin strip into tip coolant passage
(c)	Cycle No. 3--Palniro 7 or AMS 4778.	Doublers to skin and coolant tubes to body

Because of the small fin passages, an important consideration during fabrication was prevention of plugging of the fin passages with braze alloy. An 0.001-in.-thick layer of alloy pre-placed between the fins and the body or skin did not plug fins, provided the portion of the braze cycle above the solidus temperature was controlled. However, any excess alloy that was allowed to enter the fin passages in addition to this amount caused plugging. The family of alloys used are sufficiently compatible that interalloying occurred at even the lowest braze temperatures to permit flow of alloys into the passages unless positive provisions were taken to prevent it. "Stopoff" compounds on top of previously brazed joints proved to be reasonably dependable barriers to flow of alloy through the joints.

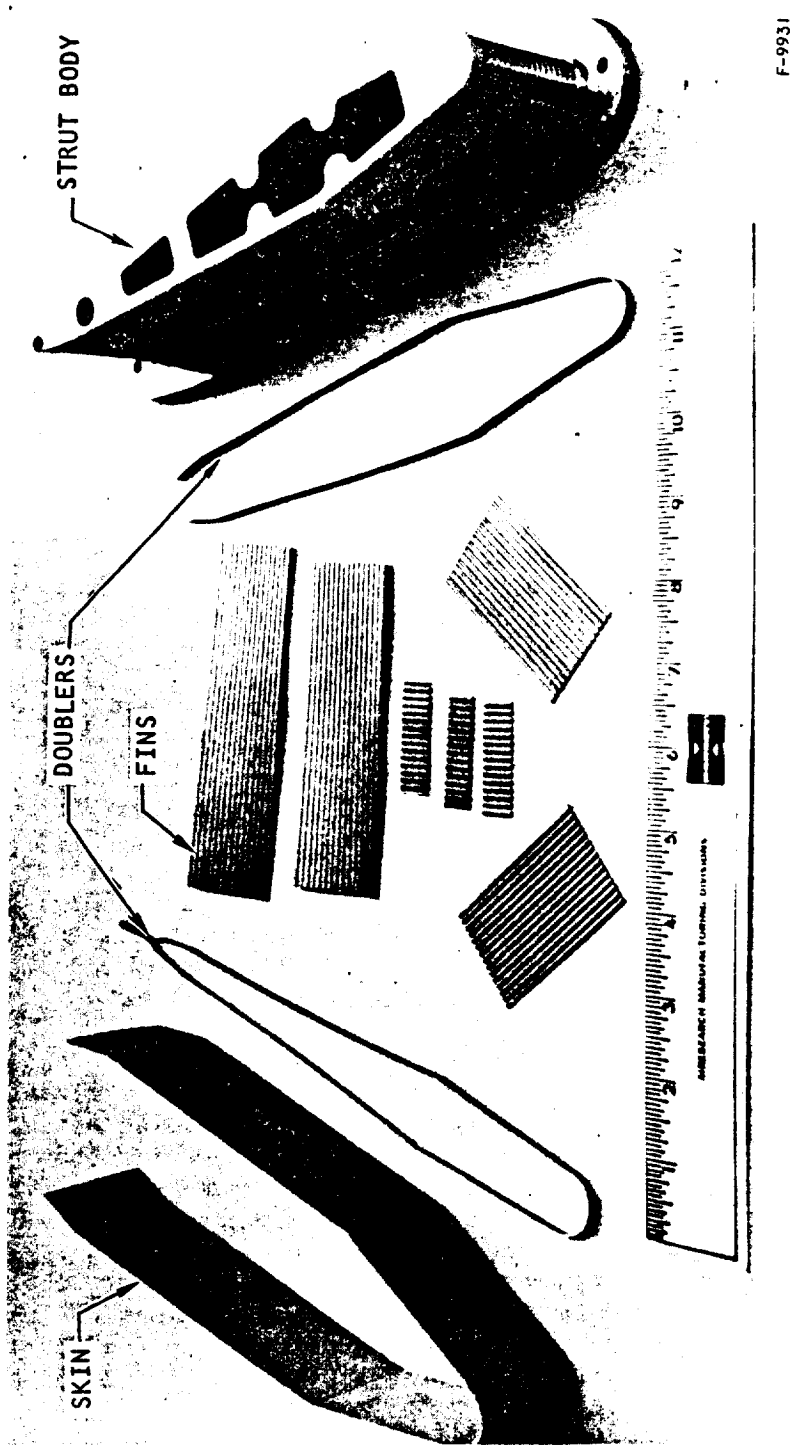

Figure 7.2-12. Struts Internal Details

A second important consideration for fabrication was the design of fixturing for use during the first braze cycle. This fixturing had to provide the contact necessary for maintenance of braze clearance in spite of inevitable tolerances in the contour of the strut bodies. It consisted of four machined graphite blocks, corresponding to the four major flat surfaces of the strut, which were pressed against the skin by means of stainless steel bellows during the braze cycle.

7.2.7 Test Summary

A summary of the tests performed on the shell assemblies is shown in Table 7.2-1. The final assemblies for the inlet spike, cowl leading edge, outer shell, nozzle, and inner shell are tabulated with their respective shell assembly(ies) for the experimental, static, and SAM units. The components and shell assemblies had no leakage or deformation unless specifically noted in the table. The shell assemblies, as tabulated, are the basic shell assemblies, i.e., shells and fins without any inserts or attachments, tested following the initial braze cycle.

Hydrostatic proof-pressure testing is distinguished from leak testing. All units were, in fact, carefully checked for leakage during hydrostatic testing. The criterion for acceptability of the SAM final components, however, was that they be bubble-tight when pressurized with nitrogen at the proof pressure and immersed in water for a period of 15 min.

7.2.8 Engine Mockup

A stainless steel and wood mockup of the flightweight, flight-designed engine was fabricated as an aid in establishing detail configurations of parts and to evaluate the packaging of the engine subsystems. Flight testing of the engine was still planned at the time. As a result, all subsystems were incorporated into the mockup. The completed assembly, shown in Figure 7.2-13, was made using the full-scale engine drawings to control all significant dimensions.

Subassemblies similar to those in the flightweight engine were used. Outerbody, innerbody, spike, nozzle, leading edge, and strut assemblies are all separate and were assembled as components. The spike/actuator and spike/innerbody were made such that spike translation through the full 5-in. stroke was possible. Also, the actuator mounts were made sufficiently strong to accept the actual actuator system. The stainless steel shells that had been fabricated to investigate forming operations were used as the mockup shells. The other components, such as manifolds, actuator, control system, and instrumentation were fabricated from wood or aluminum. Aluminum tubing was assembled to the mockup to evaluate plumbing fitup and routing. In addition, the accessibility of tubing braze joints for induction brazing was checked.

7.3 INLET SPIKE ACTUATOR

This unit supports the spike to the innerbody and provides the actuation

UNCLASSIFIED

TABLE 7.2-1

COMPONENT TEST SUMMARY

Assy		LEAK TEST*				STRESSCOAT HYDROSTATIC PROOF PRESSURE TEST**				AIR FLOW TEST
		Final Assembly	Shell Assembly 1	Shell Assembly 2	Shell Assembly 3	Final Assembly	Shell Assembly 1	Shell Assembly 2	Shell Assembly 3	Final Assembly
INLET SPIKE			SPIKE TIP	FORE SPIKE	AFT SPIKE		SPIKE TIP	FORE SPIKE	AFT SPIKE	
	SAM	1050 psig (N_2)	1050 psig (N_2)	None	None	1050 psig	None	1050 psig	1050 psig-yielding after 5 sec	Pressure drop 20% lower than predicted
	STATIC	1050 psig (water)	1050 psig (N_2)	None	None	1050 psig	None	1050 psig	1050 psig	Pressure drop 5% lower than predicted
	EXP	1050 psig (water) Leakage at coolant inlet tube to plenum	1050 psig (N_2)	None	None	600 psig-yielding at repairs on external doubler ***	None	1050 psig	1050 psig	Pressure drop 23% higher than predicted due to fin blockage
LEADING EDGE			TIP	INNER SHELL	OUTER SHELL		TIP	INNER SHELL	OUTER SHELL	
	SAM	1050 psig (N_2)	None	None	None	1050 psig	1200 psig	1800 psig	1500 psig	Pressure drop 33% lower than predicted
	STATIC	1050 psig (N_2)	None	None	None	1050 psig-no yielding with doublers brazed on tip assembly	800 psig-evidence of yielding	1800 psig	1500 psig	Pressure drop 15-20% higher than predicted
	EXP	100 psig (air) Leakage between inner and outer shell assemblies	None	None	None	1050 psig	600 psig-evidence of yielding	1800 psig	1500 psig	None
OUTER SHELL			MAIN ASSY	TRAILING EDGE			MAIN ASSY	TRAILING EDGE		
	SAM	1050 psig (N_2)	100 psig (air)	1050 psig (N_2)		1050 psig	1050 psig	1500 psig		Forward coolant circuit pressure drop 18% higher than predicted.
	STATIC	No test-unit not completed	100 psig (air)	1050 psig (N_2)		No test-unit not completed	2200 psig	1500 psig		None - unit not completed
	EXP	825 psig (water)	No test-inner skin buckled during brazing	1050 psig (N_2)		825 psig - limited by spalling of StressCoat	No test - inner skin buckled during brazing	1500 psig		Forward coolant circuit pressure drop 18% higher than predicted. Aft coolant circuit pressure drop 8% higher than predicted.
NOZZLE	EXP	1050 psig (N_2)	1050 psig (N_2)			1050 psig	1050 psig			Pressure drop 18% lower than predicted
	STATIC	1050 psig (N_2)	1050 psig (N_2)			1050 psig	1050 psig			Pressure drop 18% lower than predicted
	EXP	1050 psig (N_2)	1050 psig (N_2)			1050 psig	1050 psig			None
INNER SHELL	SAM	1050 psig (N_2)	1050 psig (N_2)			1050 psig	2200 psig			Pressure drop 16% higher than predicted
	STATIC	1050 psig (N_2)	1050 psig (N_2)			1050 psig	2200 psig			Test data not usable because of blockage
	EXP	1050 psig (N_2)	1050 psig (N_2)			1050 psig	1650 psig			None

NOTE: *Assembly leakage as noted
**Assembly yielding as noted
***Subsequently pressurized to 1700 psig to verify structure. Unit survived without rupture. Leak developed at doubler repair at 1400 psig.

UNCLASSIFIED

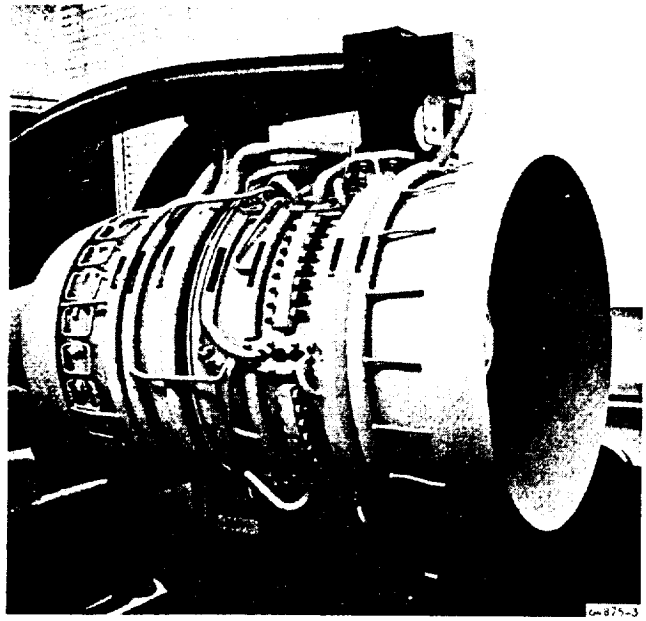

a. LEFT SIDE VIEW, NOZZLE REMOVED

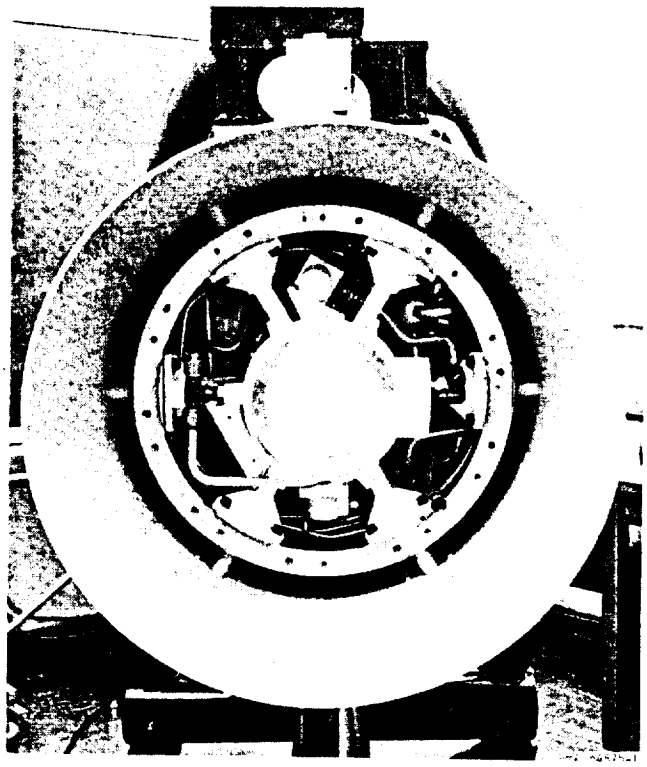

F-15211

b. VIEW LOOKING FORWARD,
NOZZLE REMOVED

Figure 7.2-13. Flightweight Engine Mockup

required to translate the spike for variation of inlet geometry. The complete assembly is shown in Figure 7.3-1. It consists of three major components. The support housing incorporates the six mounting struts and pads for attachment to the innerbody. Its inside diameter is the bearing surface for the slide assembly. Figure 7.3-2 shows both the housing and slide assemblies. The spike attaches to the flange at the end of the slide assembly. The hydraulic actuator assembly is shown in Figure 7.3-3. The large normal loads on the spike that result from asymmetric inlet unstarts are supported by two Teflon-impregnated fiberglass journal bearings, shown at the left in Figure 7.3.2b. These bearings are pressed in place on the housing and slide assemblies. Sensing of the actuator displacement is provided by a linear variable differential transformer (LVDT) shown at the bottom in Figure 7.3-3a and mounted to the assembly in Figure 7.3-3b. As originally designed for flight testing, the actuator incorporated a spherical accumulator, shown in Figure 7.3-2, as the source of high-pressure hydraulic fluid. This detail was deleted and replaced by an external hydraulic system for the SAM tests.

The support structure housing is a 4340 steel weldment. The dimensional tolerances on the struts were closely controlled to ensure a precise and rigid attachment to the innerbody of the engine. Attachment for the actuator was by a 4340 steel hub brazed into the housing. The mounting cone and cylinder for the slide assembly were rough machined before welding. The material for the slide is also 4340 steel. Bearing surfaces of both assemblies were hard-faced by chrome plating.

The actuator housing was lathe-machined from 4340 steel. Provisions were made for bolted attachment of the LVDT mounting bracket at one end of the housing and soft mounting at the other. The housing itself was heat treated to Rc 38-42, then TI-cadmium plated externally, and chrome plated internally on the piston contact area. The piston and universal joint attachment for the actuator were machined parts made by standard methods. Since both are required to absorb the aerodynamic shock loads, they were made from 17-4 PH to ensure structural integrity and proper surface condition. The snubbing springs and locking piston inside the actuator were made from stainless steel. The snubbing device was machined from 303 CRES, with an aluminum locking ring. The latching device was made from nickel bronze to absorb the impact loads during latching and unlatching. The end cap on the actuator was also made from nickel bronze to provide ease of assembly and to accommodate friction loads.

7.4 ENGINE SUSPENSION FRAME

The suspension frame was designed to provide the means for mounting the engine in flight. With minor modification, this design was directly usable in the SAM wind tunnel test application. In the tests, the frame supported the engine from below rather than above. The completed suspension frame is shown in Figure 7.4-1. The unit consisted of three components, bolted together. These are the basic frame, the deflection block that formed the forward mount, and the aft mount assembly located approximately at the center of the frame. The frame was fabricated from Inconel 718 sheet and plate, welded into box sections and heat treated. The deflection block was designed to provide, by means of strain gages, data on the axial and normal engine loads.

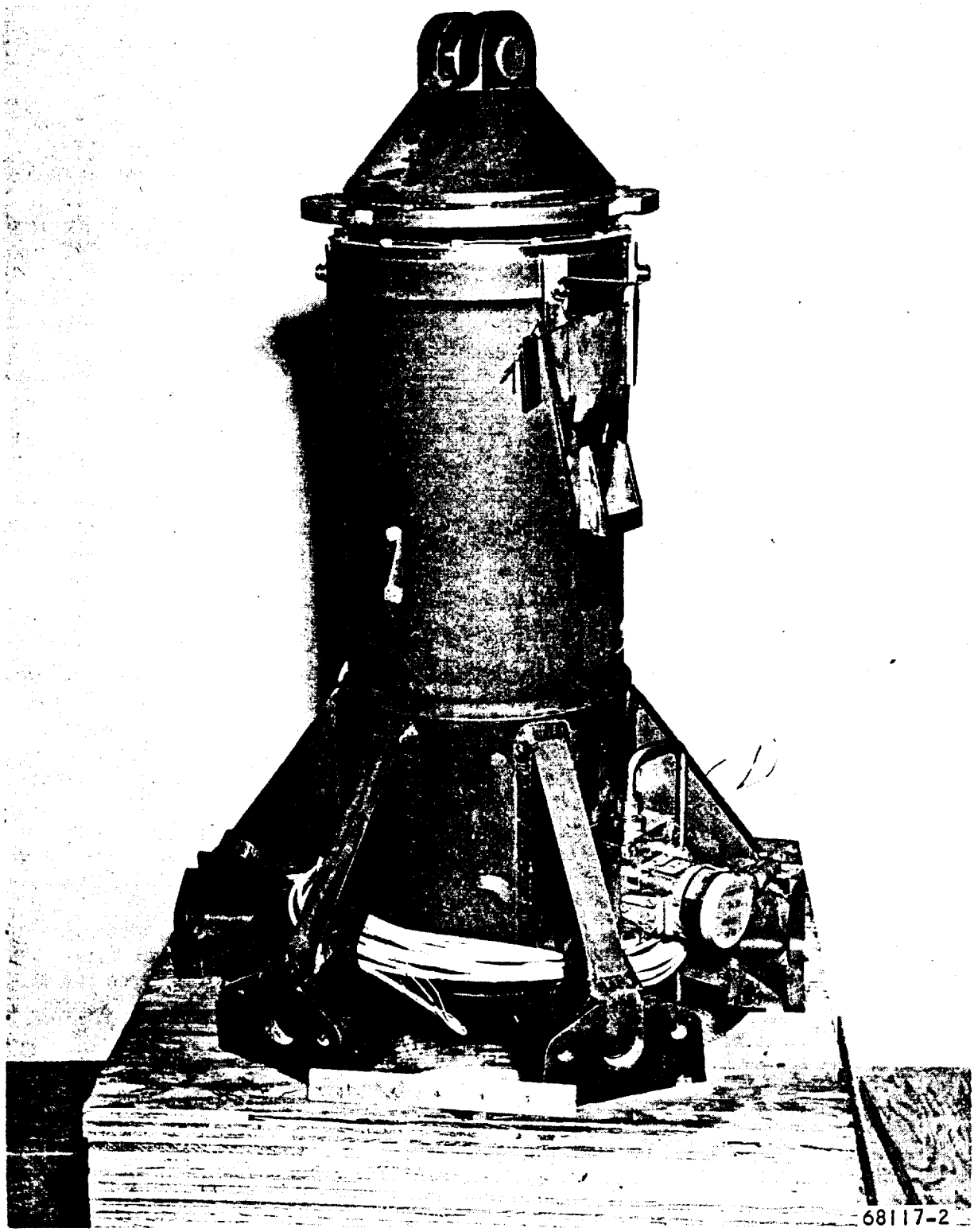

Figure 7.3.1. SAM Inlet Spike Actuator

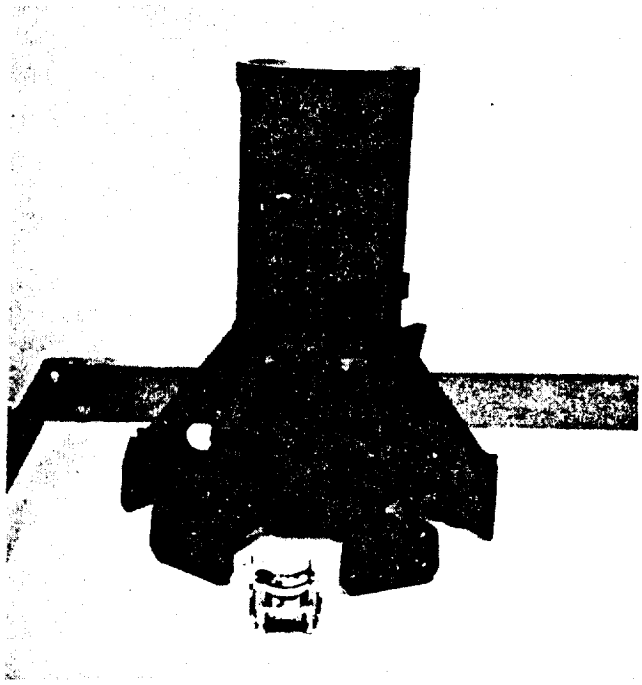

a. HOUSING ASSEMBLY AND SERVOVALVE

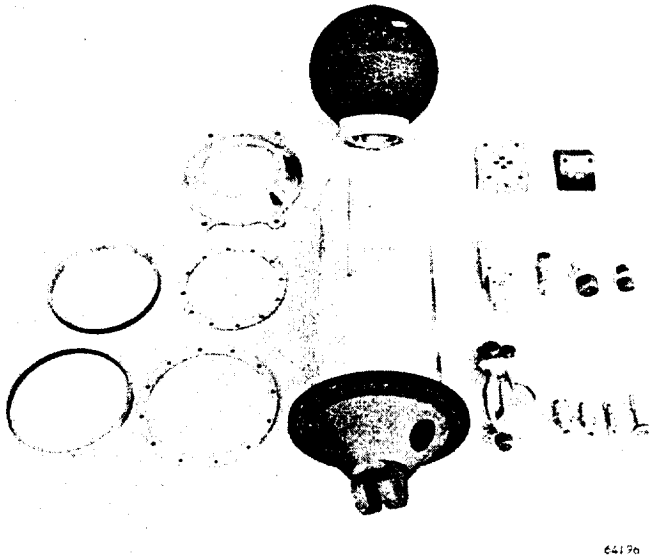

b. SLIDE ASSEMBLY AND VARIOUS ACTUATION SYSTEM COMPONENTS

F-15208

Figure 7.3-2. Support Structure

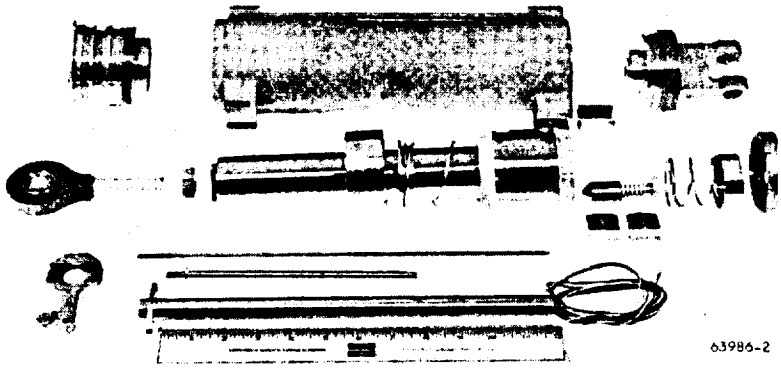

a. COMPONENTS

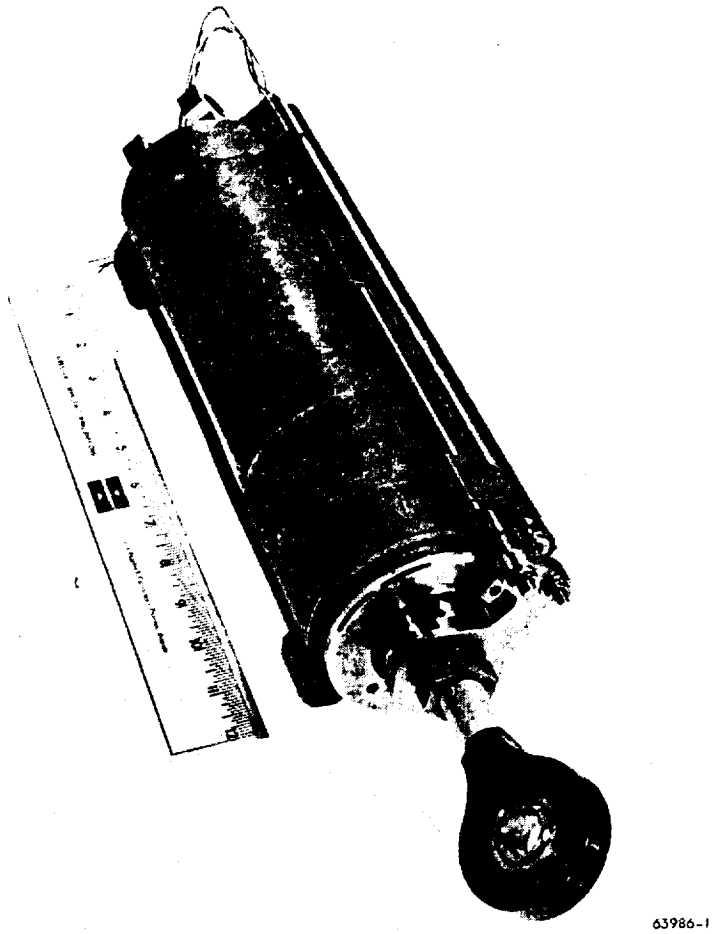

F-15210

b. ASSEMBLY

Figure 7.3-3. Hydraulic Actuator

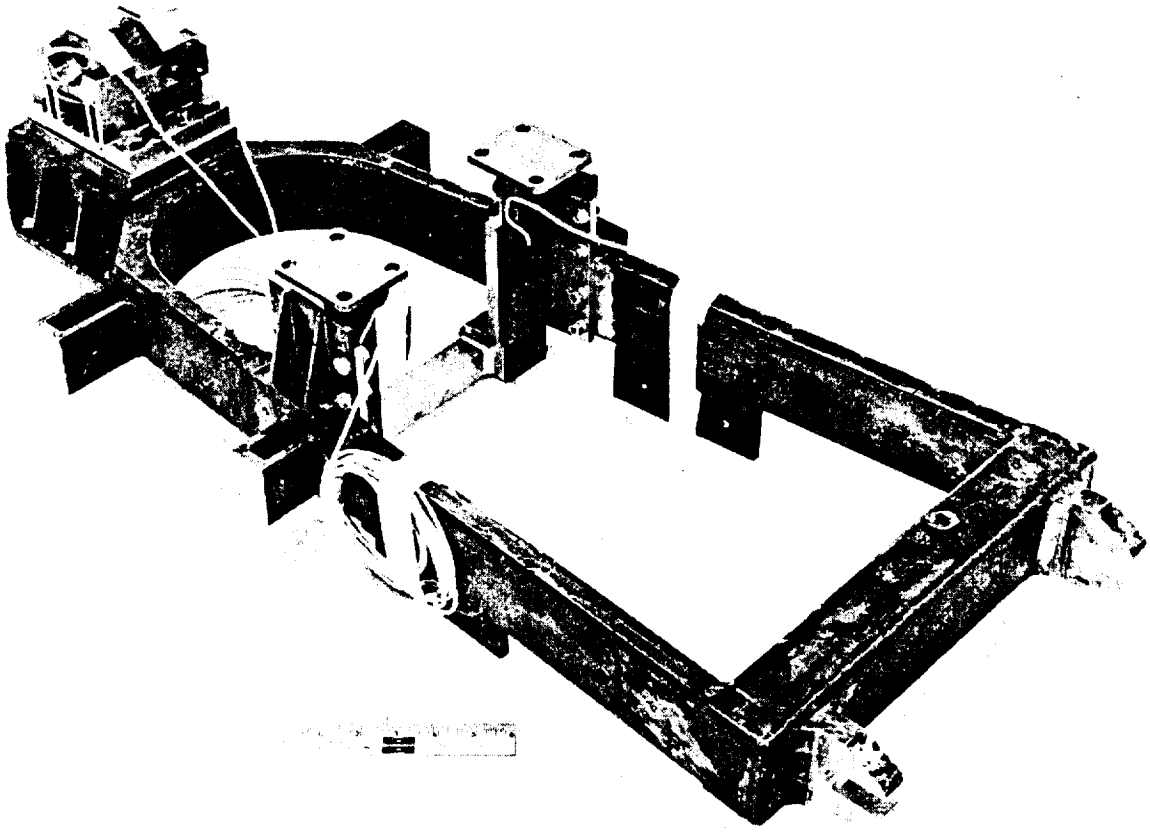

68350-2

Figure 7.4-1. SAM Suspension Frame

The aft mount assembly was made to be very flexible parallel to the axis of the engine, and instrumented with strain gages to measure vertical load components only. Two standoffs on each side of the frame were used to support the water-cooled cowl/pylon. They were drilled and tapped on assembly to assure snug fits.

7.5 WATER-COOLED WIND TUNNEL ADAPTERS

For testing of the SAM in the wind tunnel, the outerbody surfaces and the plumbing and instrumentation were protected by water-cooled adapters. A water-cooled support wedge was used to space the engine to the tunnel centerline. In total, five separate assemblies, bolted together and sealed with silicone rubber ring gaskets, were utilized: (1) the cowl/pylon; (2) the support wedge; (3) the forward cowl panels to provide sealing between the water-cooled cowl and the hydrogen-cooled outerbody leading edge; (4) the rear seal ring in the gap between the aft end of the cowl and outerbody trailing edge; and, finally, (5) the rear pylon cover which encloses the aft portion of the suspension frame. The material used for all of the water-cooled components was Type 347 stainless steel except for the pylon leading edge which was fabricated from Hastelloy X.

7.5.1 Cowl/Pylon

This component consists of five major subassemblies welded together. The main cylindrical shell weldment, shown by Figure 7.5-1a, and the frustro-conical forward end, shown by Figure 7.5-1b, form the cowl; the two flat plate sub-assemblies (not shown), and the leading edge assembly shown by Figure 7.5-1c form the pylon.

After fabrication of the details, the main cylindrical cowl and frustro-conical forward end were welded together, then a large opening was cut from this weldment to receive the pylon. The appearance of the unit at this stage of fabrication is shown by Figure 7.5-1d. The next series of operations then joined the pylon sides and leading edge to the cowl and attached the tubes and manifolds to the assembly to produce the configuration shown by Figure 7.5-2. The heavy rings and posts visible in Figures 7.5-1a, 7.5-1d, and 7.5-2 are removable fixturing used to hold the assembly round during the welding and stress-relief heat treatment operations.

After completion of all of the joining operations, the unit was stress relieved and then proof-pressure tested, using "StressCoat" for early detection of abnormal stress zones. The welded pins used to connect the inner and outer shells of the cowl were of particular concern. Percussion welding was used to bond the pins to the inner shells but had not previously been inspected under load.

7.5.2 Rear Pylon Cover

The rear pylon cover assembly is fabricated from five separate plate-fin brazed assemblies and three coolant collector manifolds.

The plate-fin assemblies were brazed with "Nicrobraz" alloy at a brazing

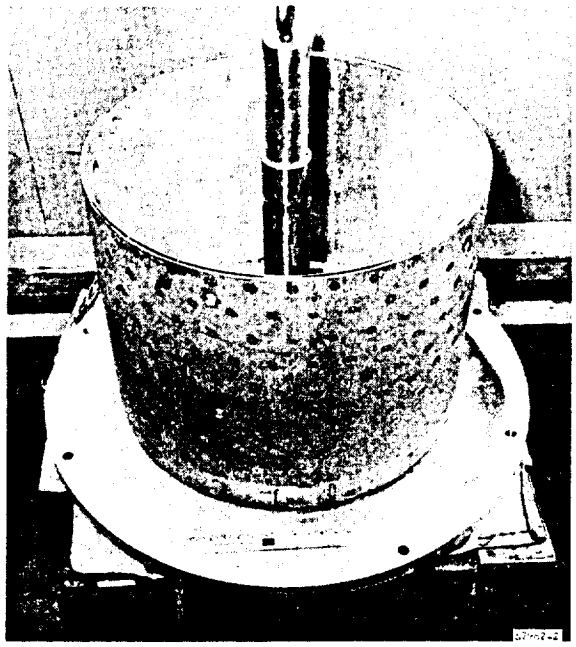

a. MAIN CYLINDRICAL SHELL

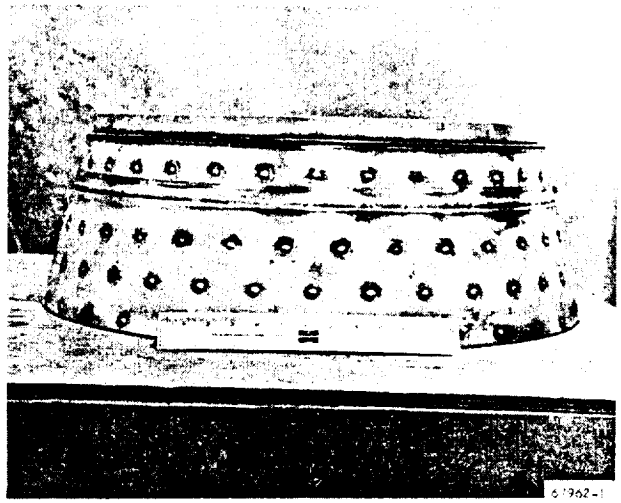

b. FRUSTRO-CONICAL FORWARD END

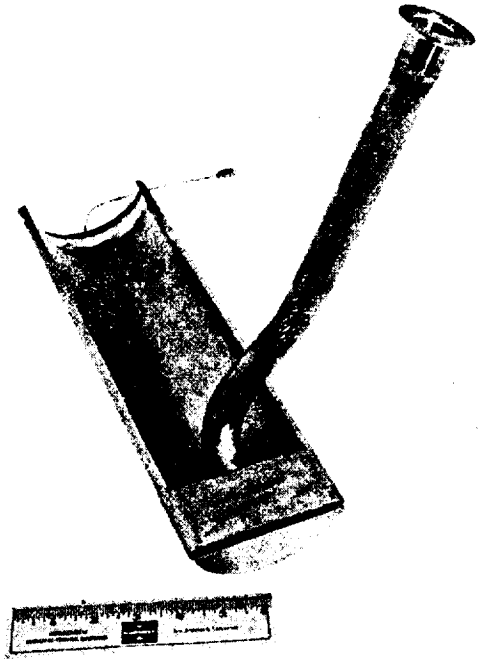

c. LEADING EDGE ASSEMBLY

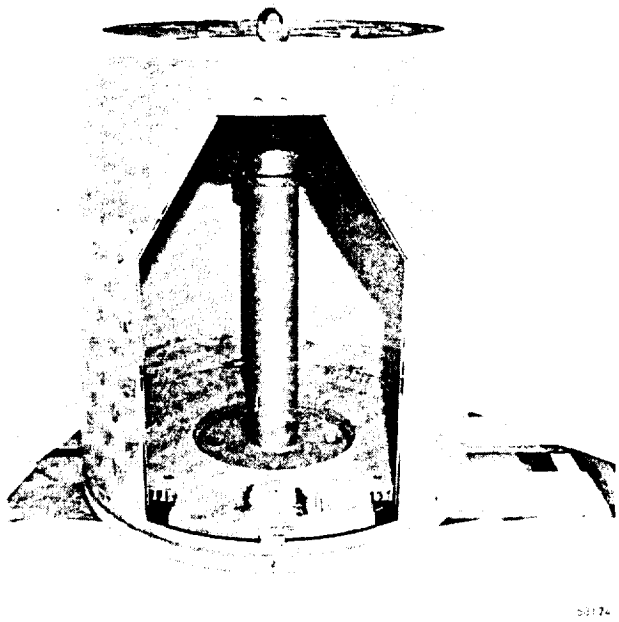

d. CYLINDRICAL WELDMENT AFTER CUTTING OF THE OPENING FOR THE PYLON

F-15212

Figure 7.5-1. Cowl/Pylon Subassemblies

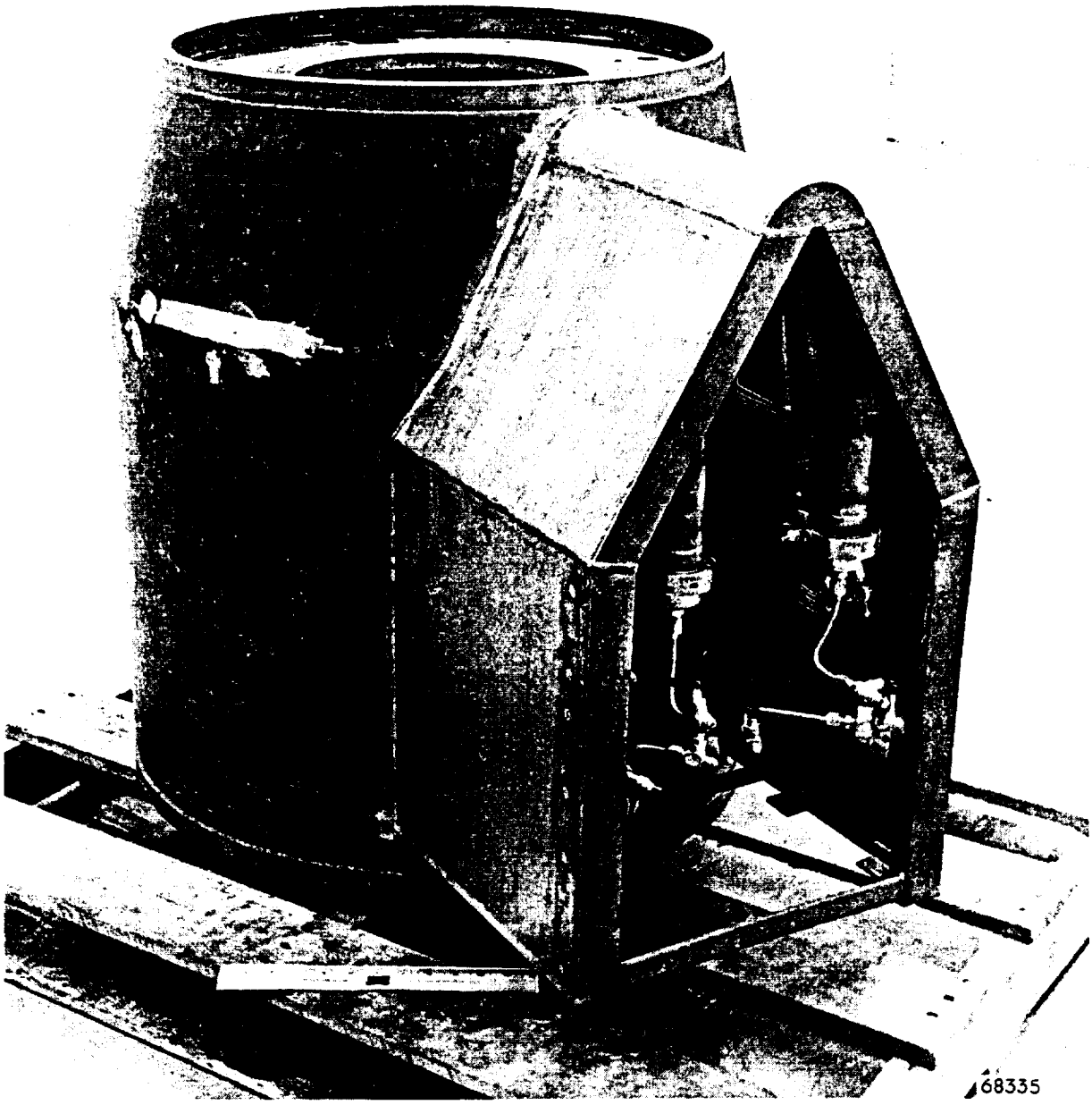

Figure 7.5-2. SAM Cowl/Pylon Assembly Ready for Proof Pressure Test

temperature of 1950 to 2000°F and were pressure tested hydrostatically to 285 psig (1.5 x operating pressure differential) prior to being machined for assembly by welding. Figures 7.5-3a and 7.5-3b show two views of the nearly finished final assembly after the front plate-fin assembly and manifolds were welded in place. The remaining operations to be performed on the assembly were stress relieving, installation of coolant outlet tubes, and final machining of the radius on the front panel assembly.

The assembly, after final machining and pressure testing, is shown in Figures 7.5-3c and 7.5-3d. Figure 7.5-3c shows the machined radius that mates with the rear seal ring; the coolant inlet tubes; and the coolant tubes that pass through the plate-fin assembly and connect to the forward cowl and rear seal. Figure 7.5-3d shows the machined manifold surfaces that seal on the O-ring in the support wedge.

7.5.3 Rear Seal Ring

The seal between the aft end of the cowl and the engine is achieved with the seal ring shown by Figure 7.5-4. The seal ring is a brazement, made up of a machined U-shape ring, cover ring, the bolt pass-through inserts, and the tubular connections. Brazing was done in a vacuum using "Nicrobraz" filler alloy.

7.5.4 Forward Cowl Panels

The transition between the hydrogen-cooled cowl leading edge of the engine and the water-cooled cowl is made by means of the forward cowl panels. The means of attachment and sealing to the engine and water-cooled cowl are shown by the sketch in Figure 7.5-5. The assembly, consisting of two halves bolted together, is also shown in the figure. The halves were fabricated from two concentric stainless steel rings welded together. The rings, because of close size and shape tolerances, were machined from forgings. After welding of the concentric rings, the two halves were produced by cutting the ring and welding on the manifold-connecting flanges.

7.5.5 Support Wedge

The completed water-cooled support wedge is shown in Figures 7.5-6a and 7.5-6b. Figure 7.5-6a shows the base of the assembly, with the water inlet on the leading edge and the water outlet fitting at the rear of the unit. The base of the support wedge assembly rests on the wind tunnel base plate and is bolted in position. Figure 7.5-6b shows the O-ring grooves used for sealing, with the cowl/pylon at the forward end of the support wedge assembly and the rear pylon cover assembly at the rear of the assembly. The bulkhead opening in the center of the assembly is for instrumentation and plumbing.

The last stages of the assembly of the support wedge are shown in Figures 7.5-6c and 7.5-6d. Figure 7.5-6c shows a view of the manifolding on the inside back panel assembly. A later stage of assembly is shown in Figure 7.5-6d, where the large forward side panels have been electron-beam welded to the bulkhead rear bottom plate and the forward bottom plate.

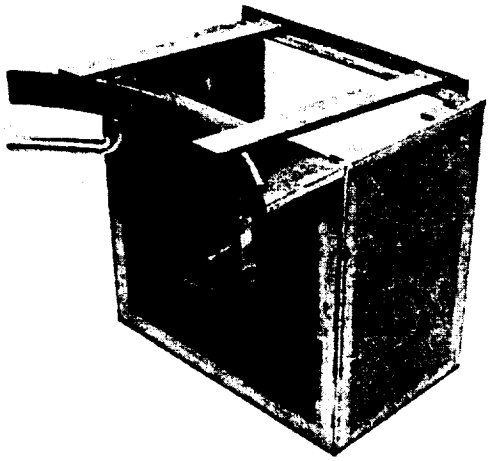

a. FRONT

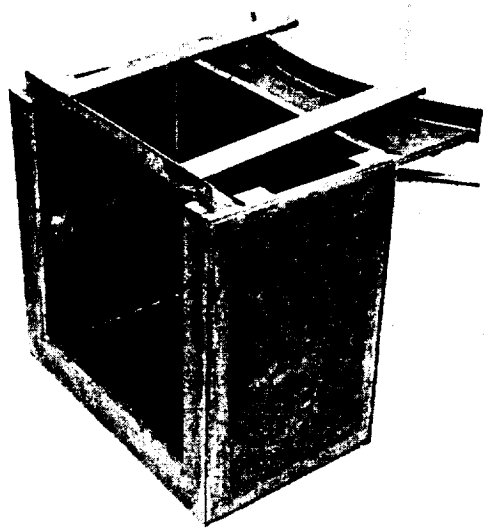

b. REAR

Note: Above views show the assembly after welding the coolant collector manifold and the front plate-fin assembly in place. Bars and angle iron are used to locate the plate-fin assembly and to minimize distortion.

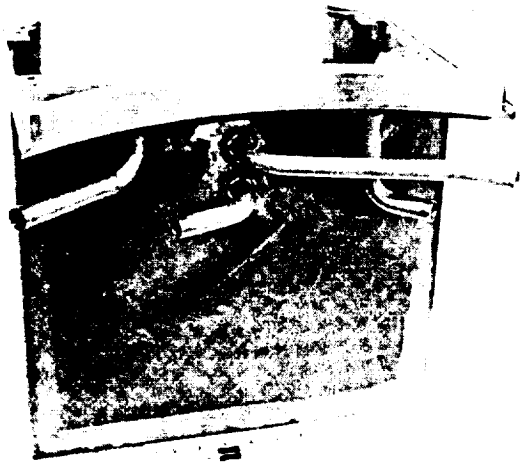

68069-1

c. REAR PYLON COVER-
EXTERNAL VIEW

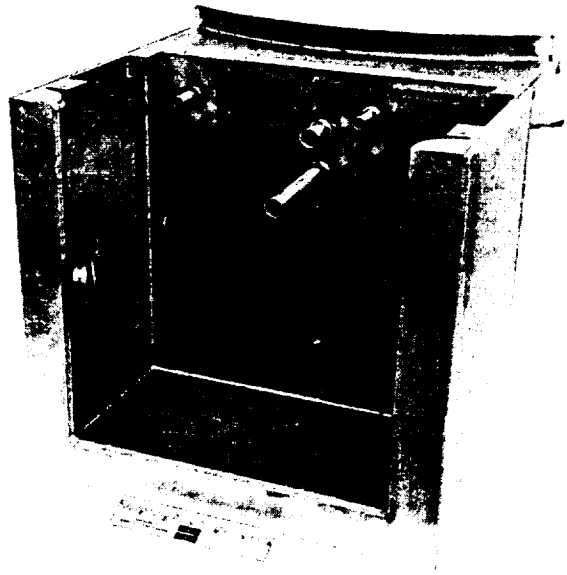

68069-2

d. REAR PYLON COVER-
INTERNAL VIEW

Figure 7.5-3. Rear Pylon Cover Assembly

F-15217

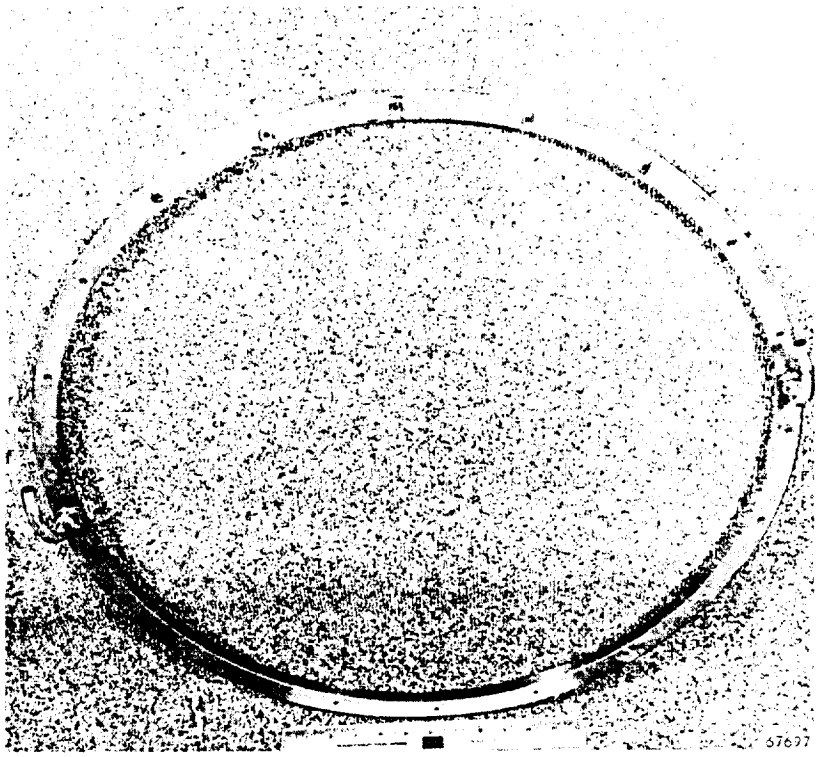

a. COMPLETED ASSEMBLY

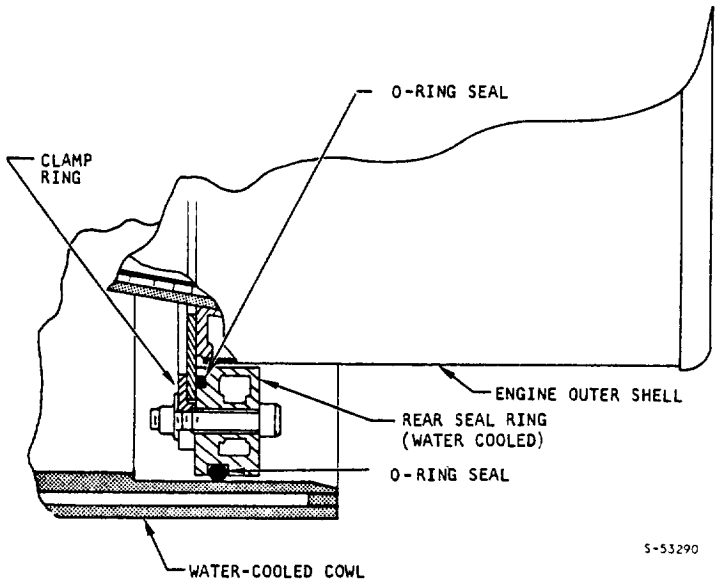

b. SCHEMATIC--REAR SEAL RING ATTACHMENT AND SEALS

F-14892

Figure 7.5-4. Water-Cooled Rear Seal Ring

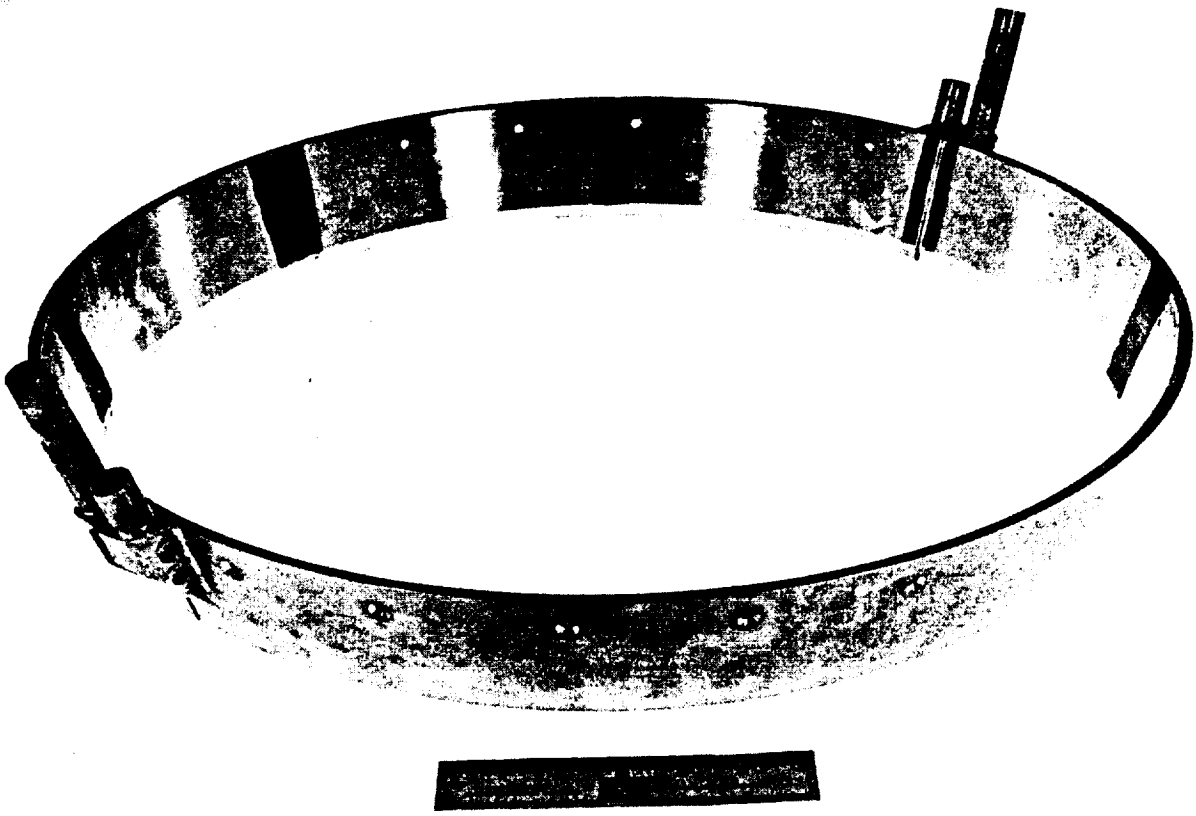

a. SCHEMATIC OF FORWARD COWL ATTACHMENT AND SEALS

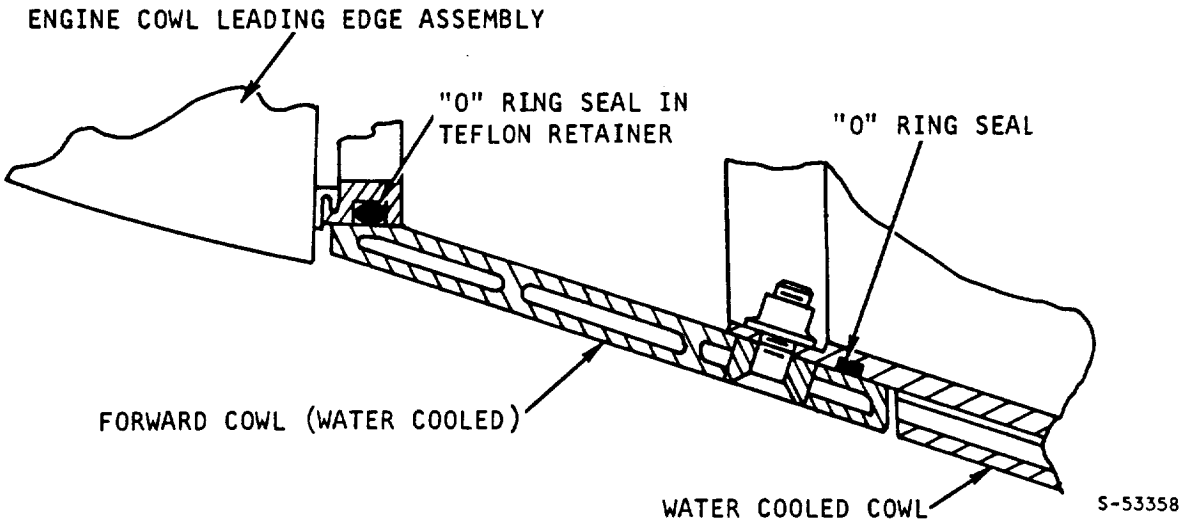

b. ASSEMBLY OF COWL HALVES

F-14893

Figure 7.5-5. Water-Cooled Forward Cowl

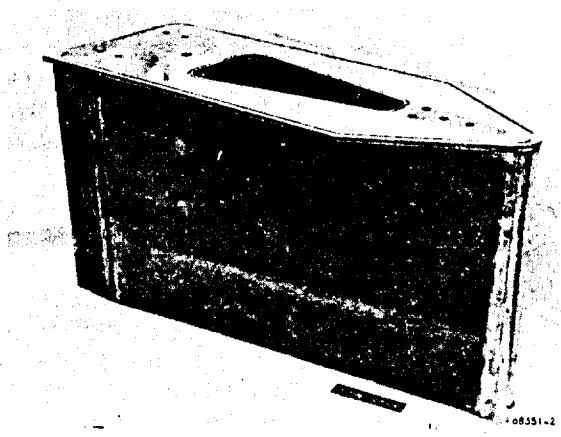

a. BOTTOM VIEW

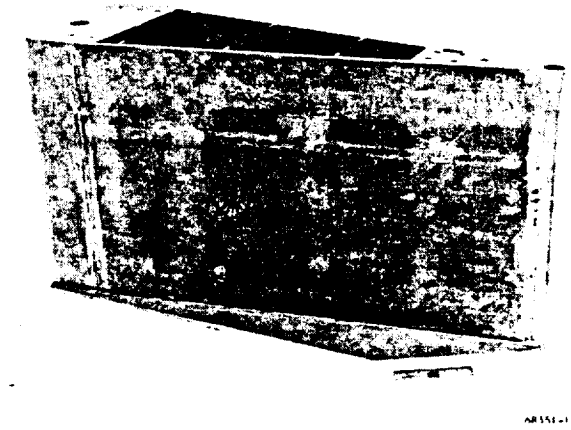

b. TOP VIEW

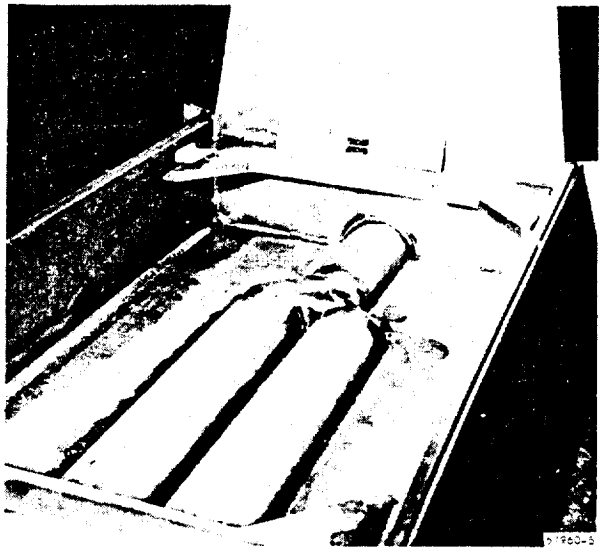

c. COOLANT MANIFOLDING USED ON THE REAR PLATE-FIN PANEL ASSEMBLY

d. SHOWN AFTER FORWARD SIDE PANELS WERE ELECTRON-BEAM WELDED TO THE BULKHEAD PLATE AND THE FRONT AND REAR BOTTOM PLATES

Figure 7.5-6. Water-Cooled Support Wedge F-15219

7.6 SAM ASSEMBLY

The Structures Assembly Model (SAM) of the HRE consists of three major sections: the engine, the water-cooled adapters and support for the engine, and, finally, the hydrogen manifold/valve assembly. Details of the fabrication of the engine and test adapters have been discussed in the previous sections of this report. The assembly and nomenclature are schematically shown in Figure 7.6-1.

7.6.1 Experimental Assemblies

Two special assemblies were made to evaluate specific areas of concern in the engine. One of these was a preliminary assembly of the centerbody involving the innerbody, spike, and actuator, to confirm the fitup and action of this portion of the engine; the other was a preliminary assembly of the entire engine to check the fitup and help establish the requirements for assembly fixturing. Both assemblies used the experimental components and a functioning inlet spike actuator, which was connected to a hand-pump-pressurized hydraulic supply. The inner shell and nozzle assemblies were joined using the special wrenches needed for this operation. The overall appearance of both experimental assemblies is shown in Figure 7.6-2.

Significant conclusions from this effort were (1) tooling and procedures used in machining of strut cutouts in the inner and outer shells were capable of producing the close tolerances necessary for satisfactory assembly of struts into the shells, and (2) tolerances obtained in the overall assembly resulted in a satisfactory closeout of spike and leading edge, with annular gap variation from 0.035 to 0.048 in. in the latched-actuator position. This gap was increased to 0.060 in. in the SAM by a change of actuator dimensions that affect latching position.

7.6.2 Engine Assembly

The assembly of the various components of the SAM, as shown in Figure 7.6-1, is restricted to a very specific sequence that permits proper alignment of components and joining of the complex plumbing. The major assembly milestones required, in the correct order, are:

(a) Alignment of inner shell assembly and outer shell, and final machining of struts

(b) Alignment of outer shell and leading edge

(c) Alignment of actuator with inner shell, and machining for dowel pins

(d) Final assembly of inner and outer shells and plumbing

(e) Installation of suspension frame, spike, and spike actuator

(f) Assembly and plumbing of leading edge

(g) Installation of nozzle

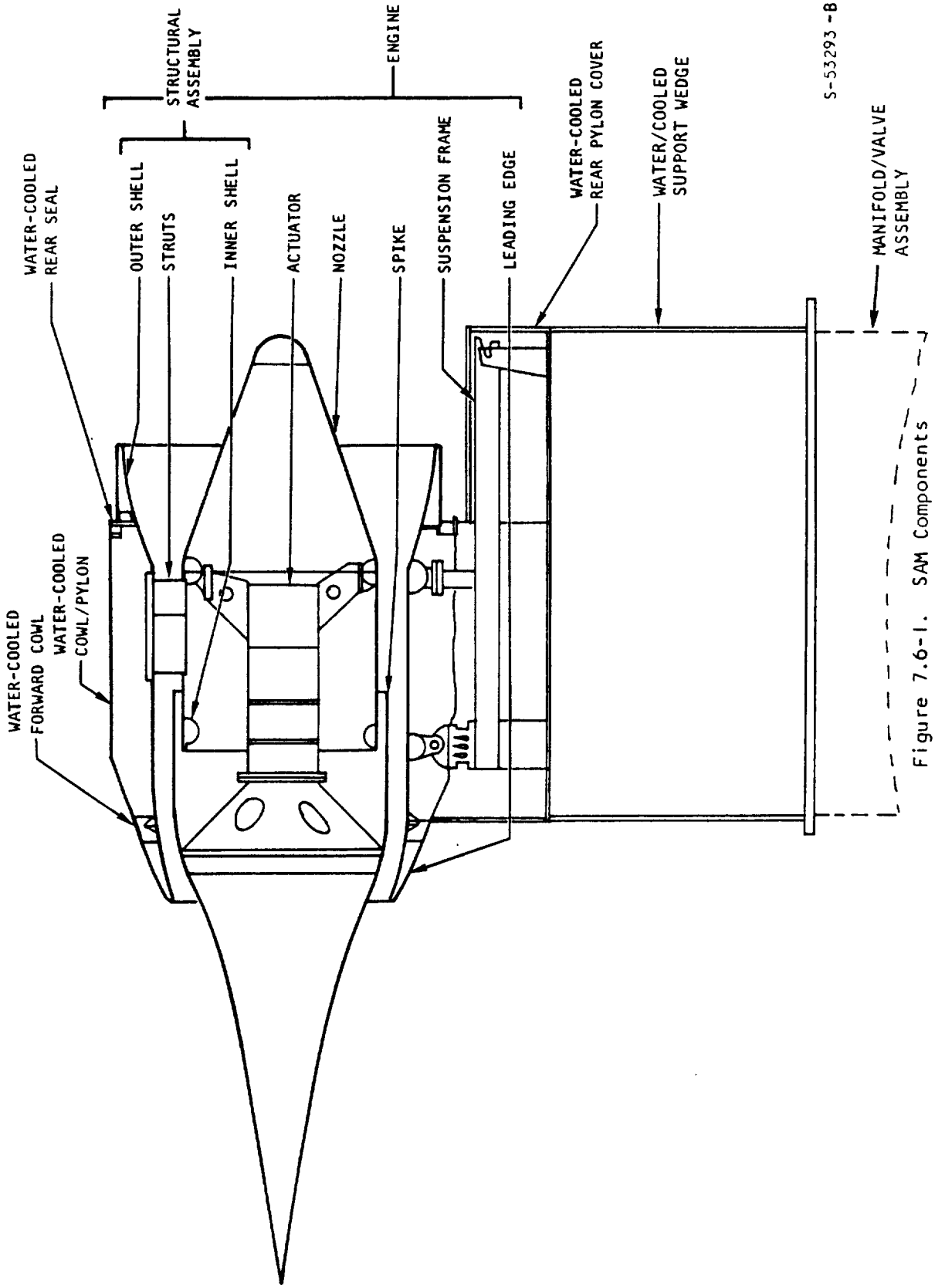

Figure 7.6-1. SAM Components

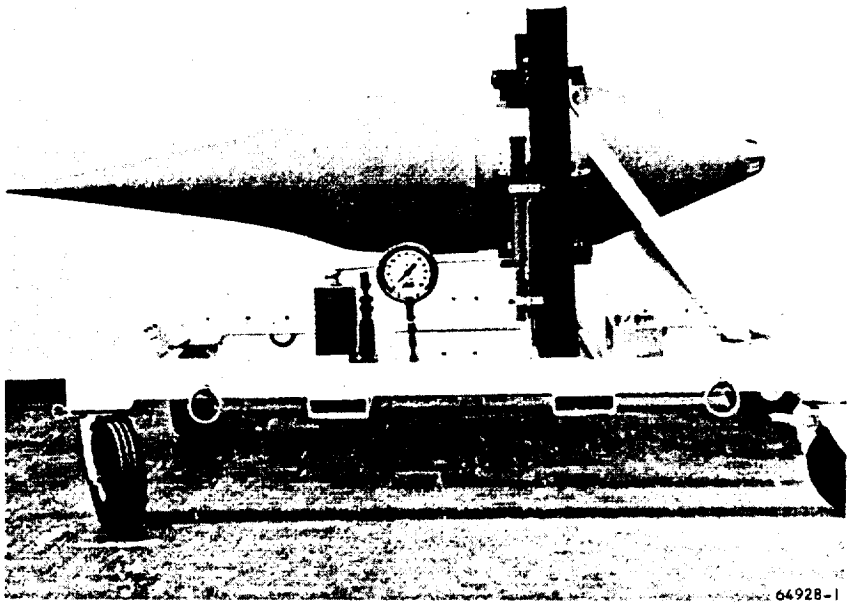

a. HRE CENTERBODY ASSEMBLY, MOUNTED ON SHIPPING CART

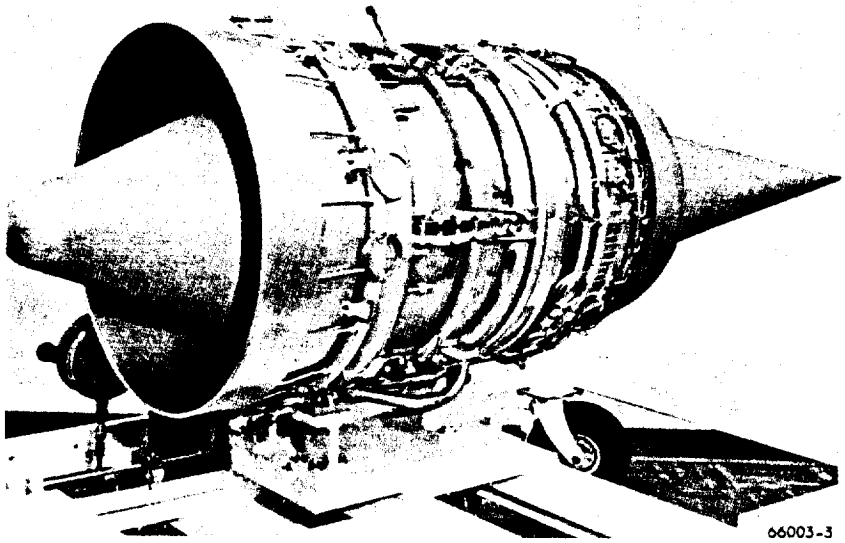

b. HRE EXPERIMENTAL ASSEMBLY-VIEW LOOKING INTO AFT END

F-15215

Figure 7.6-2. Experimental Assemblies

7.6.2.1 Inner/Outer Shell Prealignment

The clearance between the struts and the openings in the inner and outer shells must be limited (0-0.015 in.). At the same time, the axial concentricity of the inner and outer shells must be maintained within 0.010 in. total. These simultaneous relationships are obtained by providing for a prealignment of the two shells and a final machining of each of the struts in such a manner as to compensate for minor misalignment of the strut openings.

To determine the relationship of the inner and outer shells, they were first assembled in true alignment and concentricity, using undersized dummy struts. Then an adjustable pair of templates were fit simultaneously into each pair of the inner and outer openings and bolted together to duplicate the relationship of the two openings. The misalignment in the axes of the openings was then measured from the templates and recorded. This information was then used to align tracer templates relative to the axis of each strut, to control a Bridgeport Milling Machine with a tracer attachment in machining the excess material from each strut.

7.6.2.2 Leading Edge/Outer Shell Assembly

A preliminary assembly of the outer shell and leading edge section was made to ensure that the inside circumferences matched at the joint. To control the joint concentricity, the outside diameters of both the outer shell and leading edge flanges were re-machined to the same diameter and concentricity within 0.002 TIR. A ring was then fabricated to hold the outside diameters of both flanges concentric while the bolts holding the flanges together were installed and tightened.

7.6.2.3 Inner Shell/Actuator Assembly

Upon completion of the alignment activities of the inner and outer shells, the spike actuator housing was installed in the inner shell and aligned. A special locating fixture which registered on the bore of the housing and the circumference of the inner shell was used, and the spacing between each actuator mounting pad and the corresponding support pad on the inner shell was measured. Laminated shims were then installed, the assembly bolted in place, and the fixture removed. Dowel pin holes were machined radially through three of the supports to insure repeatability of the assembly.

7.6.2.4 Structural Assembly

Following the preliminary fitups described above, the final assembly of the inner and outer shells took place. In order to position the assembly most advantageously for the various fitup, installation, and induction brazing operations, a special holding framework was used, as shown by Figure 7.6-3.

The inner and outer shells were fixtured in their correct position relative to each other and the struts were then bolted in place, first to the inner shell, and then to the outer shell. After tightening of the nuts and bolts holding the struts, the concentricity of the inner shell relative to

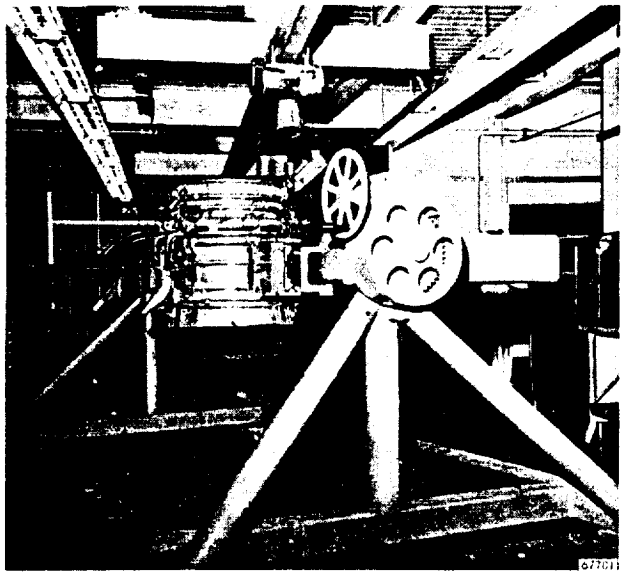

Figure 7.6-3. HRE SAM Outer Shell Assembly Mounted on Holding/Positioning Fixture

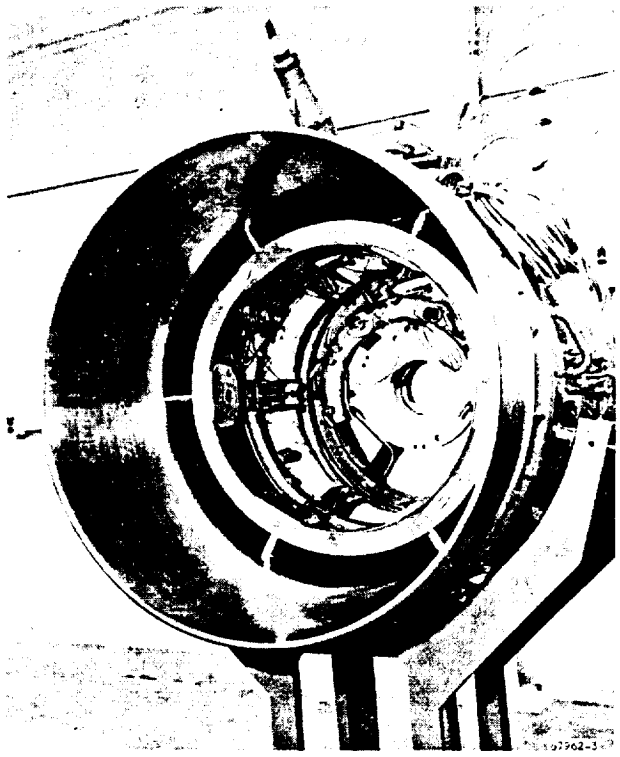

F-15214

Figure 7.6-4. SAM Structural Assembly Ready for Start of Plumbing Fitup, Showing Fuel Plenum and Its Locating Fixture

the outer was measured at each end. The centerlines of the two assemblies were found to be within 0.009 in. of each other and maximum variation in spacing between the inner and outer shell surfaces around any circumference was found to be 0.016 in. This alignment was acceptable.

The plumbing installation on this assembly consisted of over 62 tubes, elbows, and manifolds, connected by more than 140 induction-brazed sleeves or butt-welded joints. Before making the first permanent joint, all of the plumbing was assembled on a trial basis to permit establishment of the best sequence of final assembly and brazing and to insure clearance with the water-cooled cowl on the outside, and the actuator on the inside. An important portion of the plumbing is connected to the fuel plenum assembly. This assembly is attached to the actuator housing by means of a bolted bracket. To ensure correct installation, a special locating fixture was used during the trial fit and final brazing operations, as shown by Figure 7.6-4. Also shown in this illustration is the heating blanket for the unused inner shell injector manifold, which was installed prior to any of the plumbing.

To induction braze the joints inside the inner shell, all of the strut openings were sealed, both ends were covered with plexiglas, and an argon atmosphere was established inside. Manipulation of the coil was accomplished through hand holes sealed with rubber gloves. After each circuit was completed, it was leak tested at 100 psig. The tubular joints outside the shell, if accessible, were butt-welded utilizing the TIG process with either No. 349 or Hastelloy W filler rod. Induction-brazed joints outside of the shell assembly were individually bagged with plastic and filled with argon. After all of the tube joints had been sealed, the entire assembly was immersed in a tank of water and the hydrogen circuits were pressurized with gaseous nitrogen to 1050 psig.

The appearance of the structural assembly after installation of plumbing is shown by Figure 7.6-5 and a detail view into the front end is shown by Figure 7.6-6.

7.6.2.5 Installation of Suspension Frame, Spike, and Spike Actuator

Installation of the suspension frame occurred while the assembly was still mounted on the fixture, Figure 7.6-3. It consisted of attachment of the aft support pads to the engine mounts with eight bolts, and installation of the 3/4-in.-dia pin in the deflection block and brackets at the forward end. The unit was then transferred from the yoke fixture to a large, box-frame, tumble fixture, which provided more clearance and positional flexibility, and was positioned with its axis vertical, as shown by Figure 7.6-7.

A trial installation of spike, actuator, and leading edge was made first, with the packing-type seals, between the spike and inner shell, in place, to confirm concentricity of the components and make final adjustments on tube lengths and fits at the three bellows connections between the spike and inner-body. The final installation of the spike was then performed using the following sequence of operations:

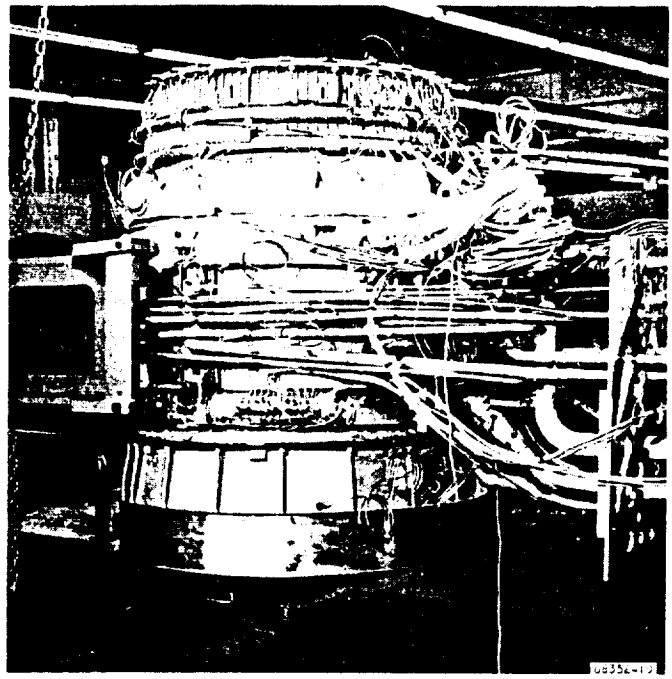

Figure 7.6-5. SAM Structural Assembly After Completion

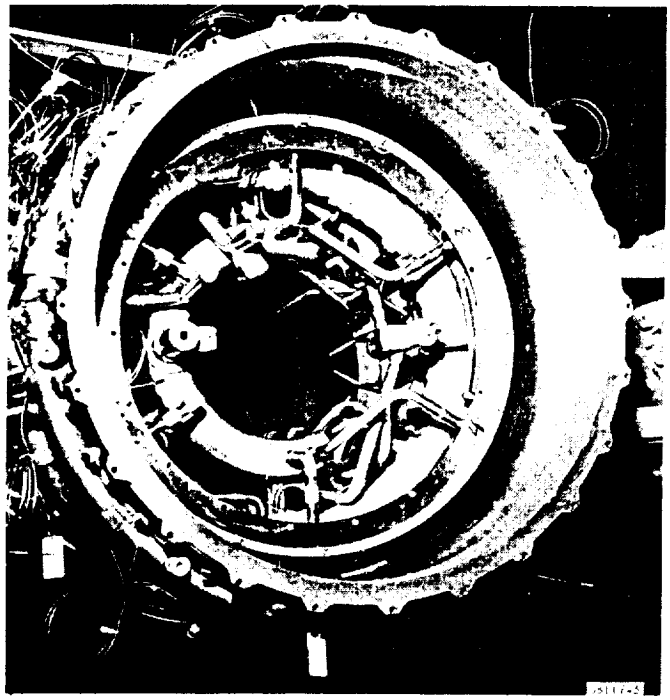

F-15216

Figure 7.6-6. SAM Structural Assembly-View Looking Into Front End

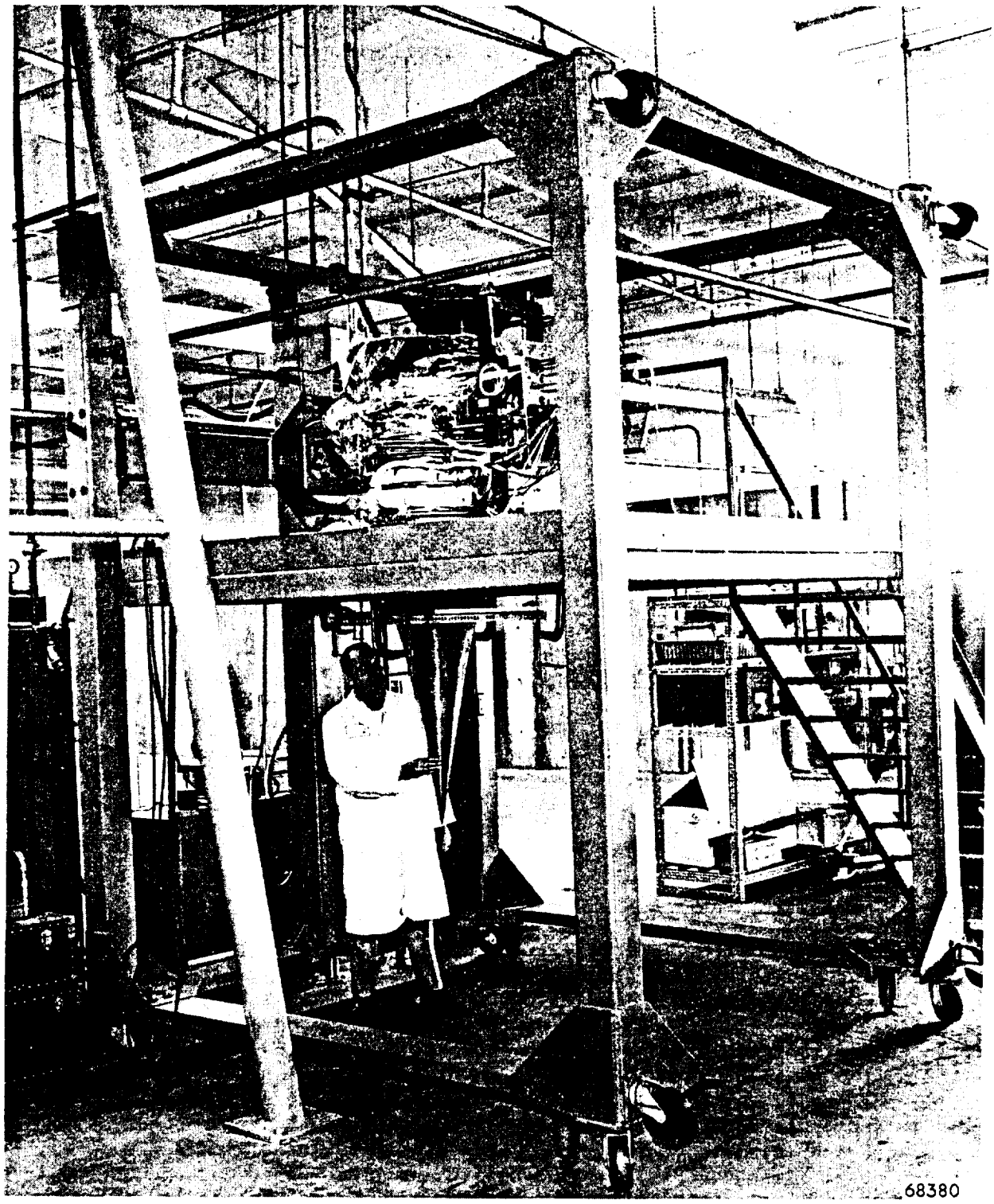

Figure 7.6-7. SAM Engine Assembly - Setup for Installation of Spike and Actuator

(a) Raising the spike into position corresponding to maximum extension of the actuator, with the large bellows used to seal the centerbody cavity clamped in a compressed position.

(b) Tightening the screws on the packing gland between spike and inner shell.

(c) Removing clamps from the large bellows and bolting its flange to the mating flange on the innerbody.

(d) Induction brazing the connections between the three hydrogen bellows in the spike and the corresponding tubes in the inner shell, and leak-testing the joints.

(e) Insulating tubes and cables.

(f) Lowering the actuator (retracted) into place and bolting to the inner shell, then extending the actuator and bolting it to the spike.

(g) Checking actuator operation and the concentricity of the spike relative to the inner shell.

The arrangement of the unit in the fixture during the above operations is as shown in Figure 7.6-7.

7.6.2.6 Installation of Leading Edge

Following installation and checkout of the spike, the fixture was rotated so as to place the engine axis horizontal for installation of the leading edge assembly. A ring was used to ensure alignment of the flanges and inner surfaces during bolting of the leading edge to the outer shell. The eight 3/8-in.-dia coolant inlet tubes and twenty-four 1/4-in.-dia coolant crossover tubes were then induction-brazed and leak-tested.

7.6.2.7 Installation of Nozzle

Before the nozzle could be bolted in place, it was necessary to install the coolant manifold which connected the six strut leading edges to the inlet (aft) end of the nozzle. Also, before bolting, the six pressure taps which sense gas pressure on the surface of the nozzle were connected to pressure transducers mounted in a housing, as shown by Figure 7.6-8. The actual attachment of the nozzle to the inner shell involved a series of operations performed while the nozzle was held in position for bolting, Figure 7.6-9. The thermocouple and pressure transducer cable assemblies were first connected, clamped in place, and insulated. Then ten "Omniseals" were installed in the pockets in the nozzle flange. Finally, the nozzle was lined up and bolted to the inner shell. Installation and bolting of the cover with its "Omniseals" followed and the baffle was screwed in place (see also Figure 7.2-6). Finally, the outer cap with its "Omniseal" was screwed on and tightened with a special spanner wrench, as shown in Figure 7.6-10. The installation of the center bolt and metallic seal completed the assembly. The coolant system was then pressurized with helium at 100 psig and a mass spectrometer "sniffer" was applied at

Figure 7.6-8. Nozzle Assembly Showing Pressure Transducer Housing

Figure 7.6-9. SAM Engine Assembly - Nozzle in Place for Connection of Cable Assemblies

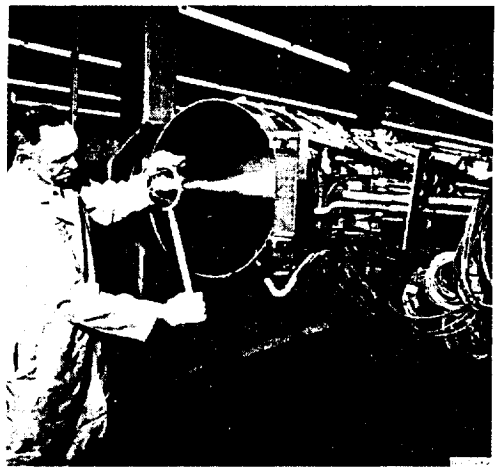

F-15406

Figure 7.6-10. SAM Engine Assembly - Installation of Cap on Nozzle

all of the seal joints to detect leakage; none was detectable.

7.6.3 Manifold/Valve Assembly

This assembly consists of the water and hydrogen supply and return lines and the hydrogen system control valves and flowmeters. A plywood mockup of the wind tunnel carriage was built to check the envelope constraining the assembly. The model base plate, mounted on the mockup, is shown in Figure 7.6-11. The completed assembly is shown in Figure 7.6-12.

Water system plumbing was fabricated from standard pipe and tubing and, generally, used mechanical joints and standard fittings. To the greatest extent possible, hydrogen plumbing was welded, with most welds dye-penetrant and radiographically inspected. Materials are all 300-series stainless steels.

To permit transport of the SAM by conventional methods, it was shipped as two sub-assemblies. One of these was the assembly of the engine and the water-cooled components, and the other the base plate and manifold/valve assembly. This required the incorporation of mechanical, union type, connections in each of the circuits coming from the engine. Furthermore, to allow for assembly and disassembly of the two major subassemblies in the field, it was necessary to locate all of these connections within the confines of the cutout in the base plate, visible in Figure 7.6-11.

7.6.4 Final Assembly

The major assembly milestones required to complete the SAM were:

(a) Installation of bulkhead

(b) Installation of cowl/pylon

(c) Assembly of support wedge

(d) Fitup and connection to manifolding/valve assembly

The installation of the bulkhead required a series of relatively major operations. The first group, performed with the engine axis horizontal, tubes pointing downward, accomplished the emplacement of the bulkhead assembly, the routing of all of the pressure connection tubes (approximately 70) through the correct holes in the bulkhead, and the induction brazing of extension tubes to each of these. Also, all of the cable assemblies (thermocouple, pressure transducer, accelerometer, and strain gage) were routed through their allotted holes in the bulkhead and secured. After these operations were completed, the assembly was installed on a stand as shown in Figure 7.6-13a for additional operations. The water tubes for connection to the cowl/pylon were put through the bulkhead for the first time at this point, then the cowl/pylon was slipped into place around the outerbody using a special yoke for support, as shown in Figure 7.6-13b. The water pipes through the bulkhead were connected to the pylon, the cowl body was centered relative to the outerbody, and four bolt holes were drilled, reamed, and countersunk in the pylon and matching pads on

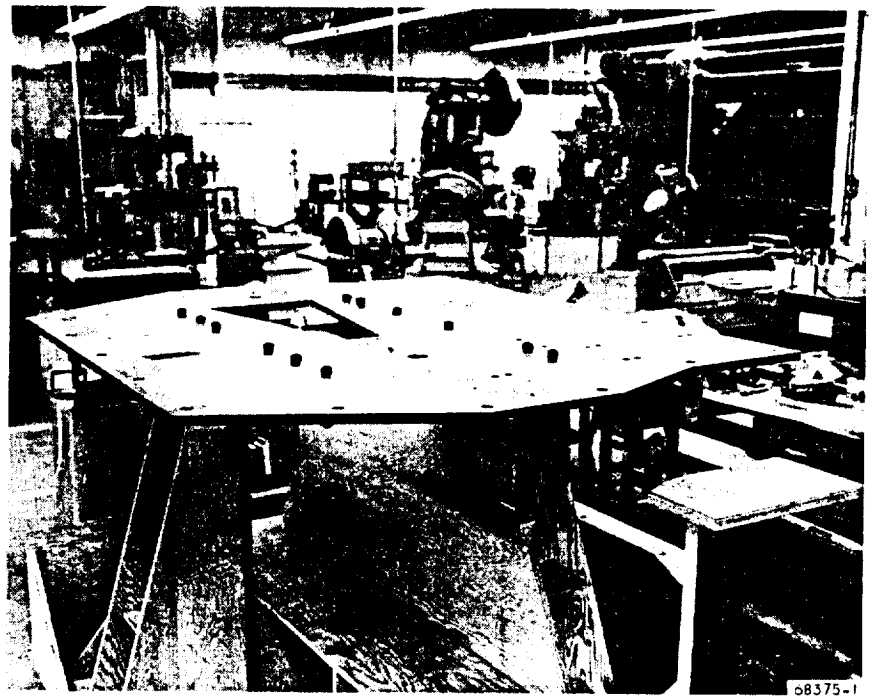

Figure 7.6-11. Base Plate Mounted on the Plywood Elevator Carriage Mockup

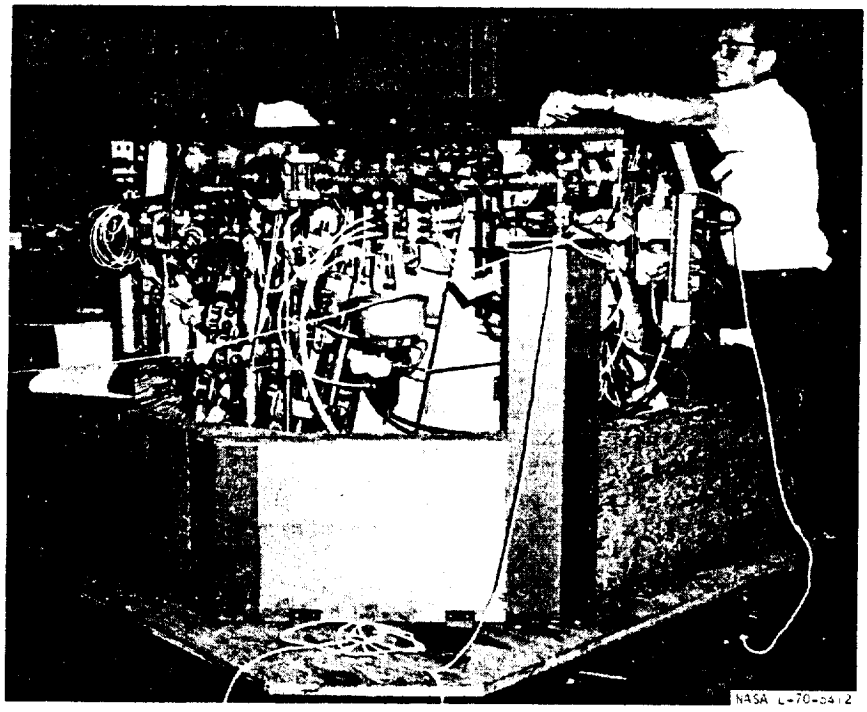

F-15237

Figure 7.6-12. Completed Manifold/Valve Assembly on Mockup of Elevator Carriage

the suspension frame assembly. After this operation, the cowl/pylon was removed and the bellows used to seal the tubes to the bulkhead were welded to the tubes.

The unit was next re-mounted on the stand and the outerbody was insulated with a blanket of "Refrasil" approximately 1/4 in. thick and an outer membrane of silicone-impregnated fiberglas cloth. Then the cowl/pylon, the aft sealing ring, and forward cowl panels were permanently installed with their silicone O-rings in place. The aft pylon cover, with its seals, was then installed, and all of the water connections to the cowl/pylon, forward cowl panels, and aft seal ring were secured.

The next group of operations consisted of the fitup and connection of all of the tubes between the engine and manifold/valve assembly. First, the suspension yoke was attached to the cowl/pylon assembly and a table-type fixture of the same height as the support wedge was bolted to the bottom of the unit. The matching tubes on the engine and manifold assembly were all trimmed to the correct length. The engine was then lowered onto the manifold assembly, as shown in Figure 7.6-13c, where all tubes were fitted and any misalignments corrected. Suitable extensions, with the proper end fittings brazed or welded in place, were joined to the lines at this time. After this operation, all of the joints were leak-tested; those in the hydrogen circuits at 700 psig and those in the water circuits at 100 psig.

The final group of operations covered the mechanical assembly of the remaining components. The locating jig under the cowl/pylon was removed and the unit was lowered onto the support wedge, Figure 7.6-13d, and bolted into place. The general appearance of the completed SAM unit is shown by Figure 7.6-14.

7.6.5 Handling Cart

For shipment, the assembly of the engine and the water-cooled test adapters was disassembled from the base plate and manifolding and enclosed in a specially built cart that could be rolled on casters or hoisted by specially located eyebolts. Figure 7.6-15 shows a drawing of the cart. The yoke shown in Figure 7.6-13 was used to hoist the engine, as indicated in Figure 7.6-15. Prior to installation or removal of the SAM, the aft cross beams can be removed. In this way, the height for hoisting is minimized. Once the protective enclosure for the plumbing and wiring clears the wedge support beams (about 18 in.), the SAM can be extracted toward the rear. Guides are provided for the aluminum cover to prevent inadvertent swinging. Spanner bars for use in the hoisting are part of the handling cart. All structural members of the cart are cold-rolled steel. Panelling is aluminum and removable by means of quarter-turn fasteners.

The manifold/valve assembly was shipped still mounted to the plywood mockup. It was removed from the mockup after reassembly of the engine to the base plate at the wind tunnel.

7.7 VIBRATION MODEL

The purpose of this model was to provide an inexpensive dynamic model of

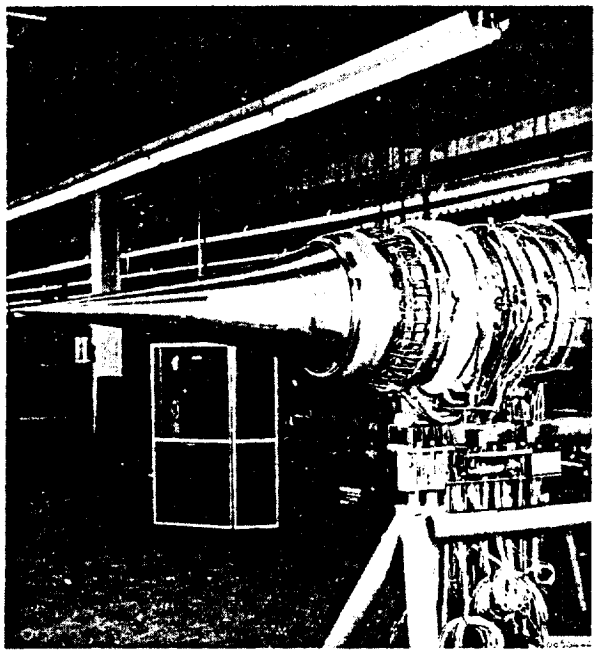

a. MOUNTED ON STAND FOR BULKHEAD INSTALLATION OPERATIONS

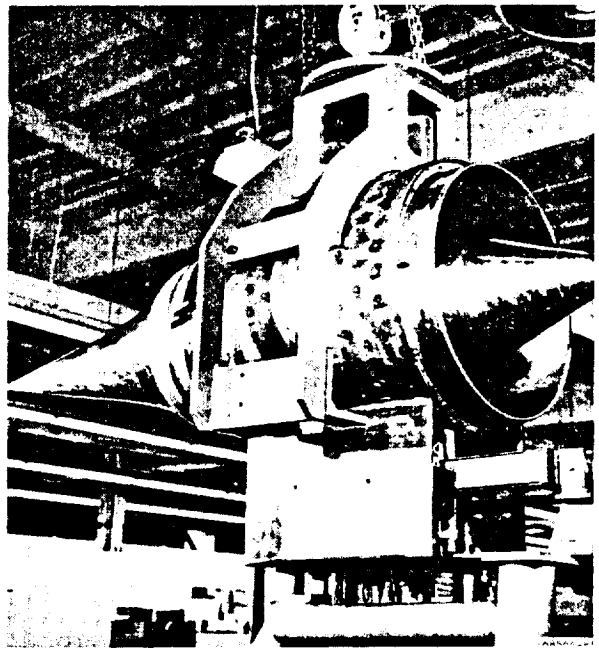

b. SETUP FOR FITUP OF COWL/PYLON TO ENGINE, AND MACHINING OF BOLT HOLES INTO SUSPENSION FRAME ASSEMBLY

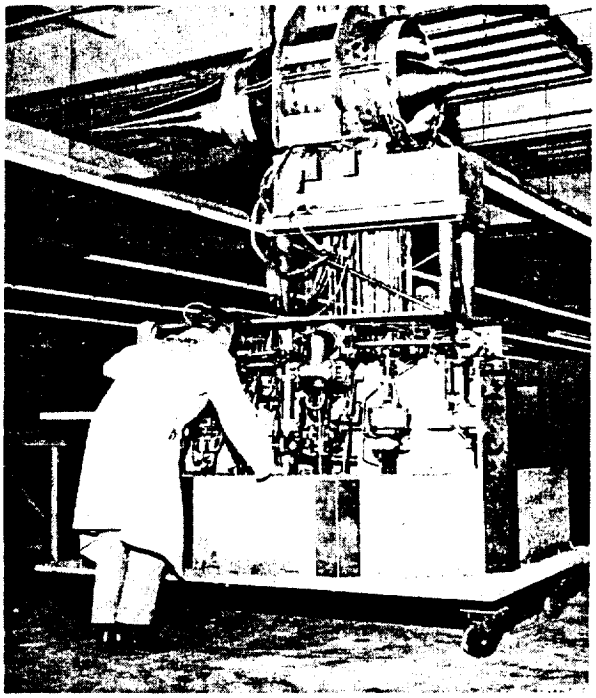

c. SETUP FOR FITUP OF CONNECTING TUBES BETWEEN ENGINE AND MANIFOLD ASSEMBLY

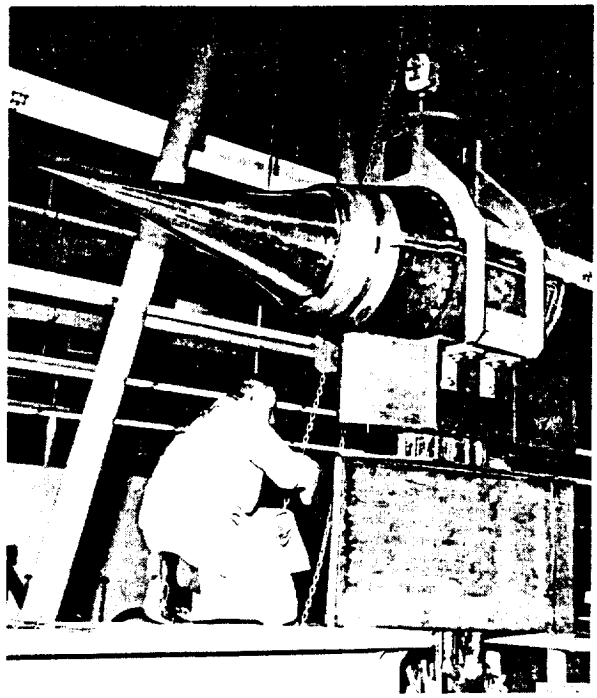

d. INSTALLATION ON SUPPORT WEDGE AFTER BRAZING OF CONNECTING TUBES

F-15218

Figure 7.6-13. SAM Engine Final Assembly Operations

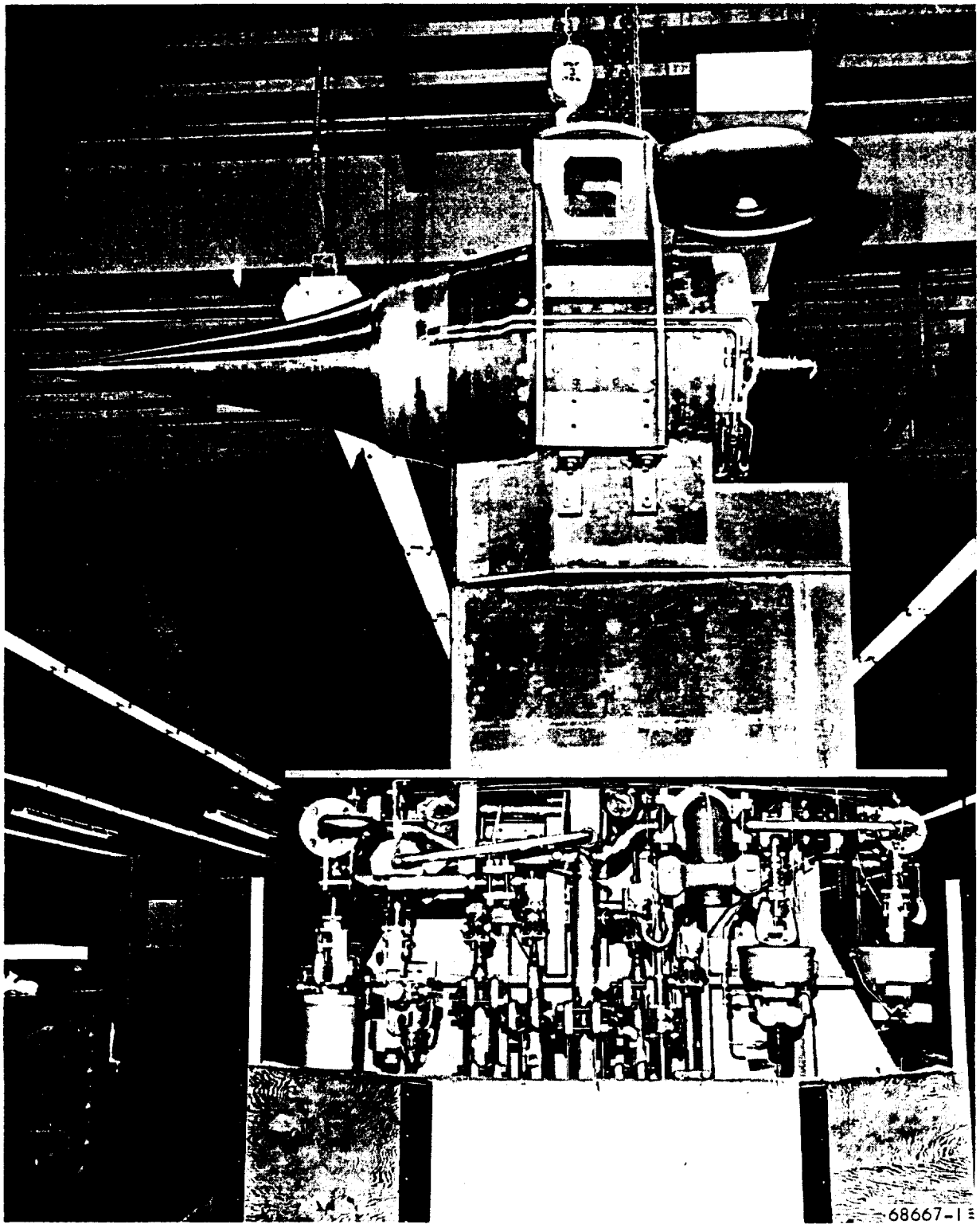

Figure 7.6-14. SAM Engine and Water-Cooled Structures Mounted on Manifold/Valve Assembly

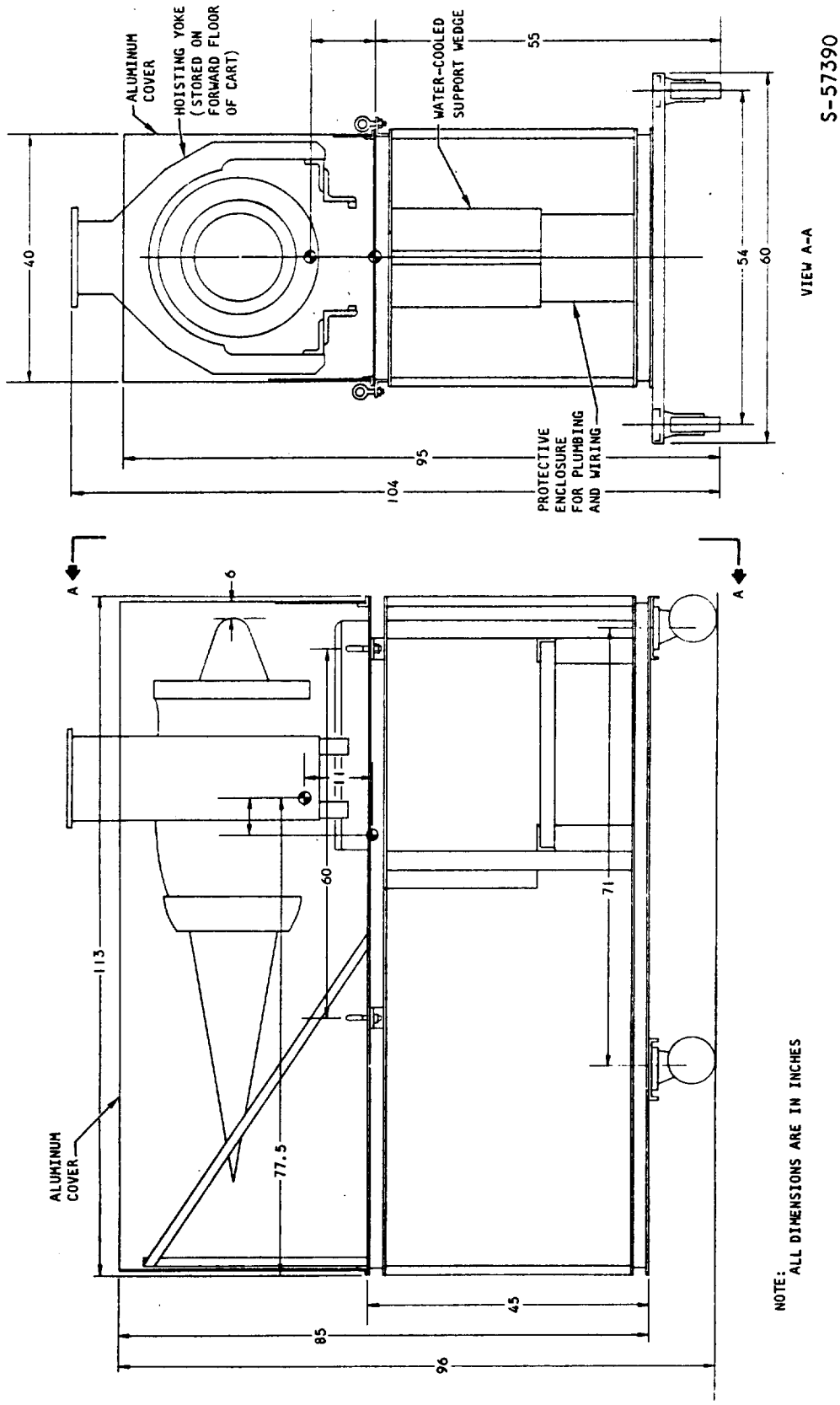

Figure 7.6-15. SAM Handling Cart

the HRE early in the program. Work on fabrication of the model was stopped following deletion of flight testing from the program. Detailed parts and subassemblies were placed in storage or used to furnish hardware to the cooled components used in the SAM.

The struts, actuator assembly, and suspension frame were usable in the SAM, as were the innerbody crossover manifold and outerbody support manifolds. All other components were simulated. The regeneratively-cooled shells were modeled with single-wall instead of sandwich construction. In some cases, the configurations used produced the required dynamic similarity but differed in shape from the original to facilitate manufacture. The main shell assemblies are shown in Figure 7.7-1 and show the modeling used in several cases.

7.8 SHELL ASSEMBLY FLOW TEST ADAPTERS

Although three major assemblies were designed (the innerbody (and spike) adapter, the leading edge adapter, and the outer shell adapter), fabrication had not been started on the outer shell adapter when work in this area was stopped. These adapters were for subsonic flow testing of the regeneratively-cooled shells. The requirement for this testing and, hence, the adapters, was deleted at the time the flight testing was deleted from the program.

7.8.1 Innerbody (Spike)

The design of the adapter for mounting the innerbody was made to permit its utilization, with minor modifications, to test the spike. SAE 1020 Steel was used for the major water-cooled structures, to capitalize on its better thermal conductivity compared to stainless steel. The heavy-wall sections permitted extensive use of welded joints and torch brazing. Figure 7.8-1 shows the major subassemblies of the adapter and Figure 7.8-2 shows the appearance of the assembled adapter, tack welded prior to final welding. The round cover plate in Figure 7.8-1 was fabricated as a brazement.

7.8.2 Leading Edge

This unit incorporated heavy flanged spool assemblies and flat brazements similar to those for the innerbody adapter. The frustro-conical shells for the water-cooled walls are shown in Figure 7.8-3. The slots visible in Figure 7.8-3 provided access for welding of the spacers that connected the inner and outer shells of the double-wall assemblies.

7.9 TEMPERATURE CONTROL SYSTEM

The temperature-control system comprises (1) a control panel built in three sections, (2) a panel for monitoring temperatures, (3) a temperature-control module, (4) a flow-computing module, and (5) a master power panel. Photographs of these panels and modules are shown in Figures 7.9-1 through 7.9-7.

The three sections of the control panel are shown in Figure 7.9-1. The upper section contains the flow-indicating meters, the low-flow alarm level

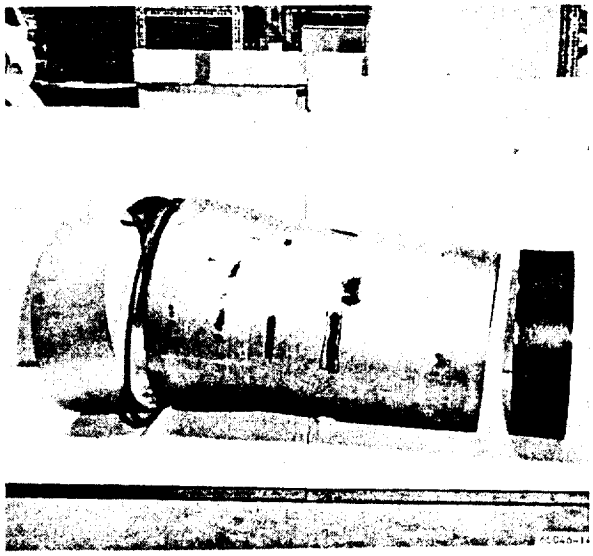

a. OUTERBODY (OUTER SHELL, LEADING EDGE SEGMENT, AND TRAILING EDGE SHELL)

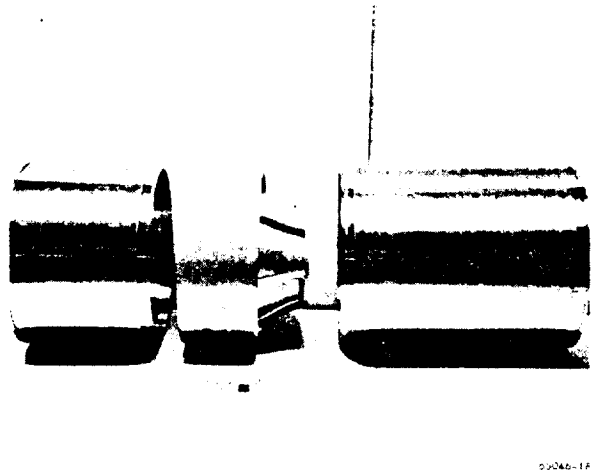

b. SPIKE ASSEMBLY

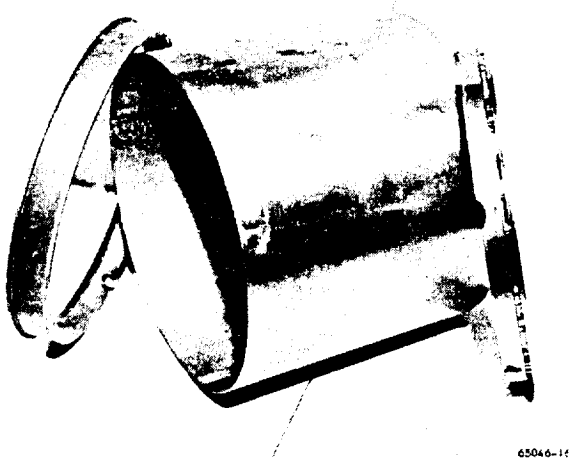

c. INNER SHELL ASSEMBLY (INNER SHELL, AFT CROSSOVER MANIFOLD, AND FORWARD INJECTOR MANIFOLD)

d. NOZZLE ASSEMBLY

F-15213

Figure 7.7-1. Vibration Model Components

Figure 7.8-1. Innerbody (Spike) Flow Test Adapter Subassemblies

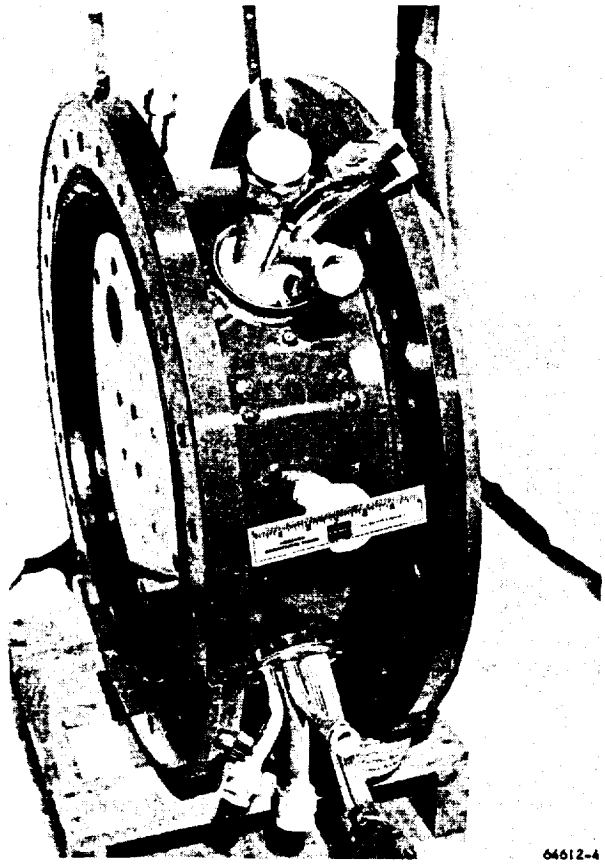

Figure 7.8-2. Innerbody (Spike) Flow Test Adapter, Tack-Welded Assembly - Left Side View

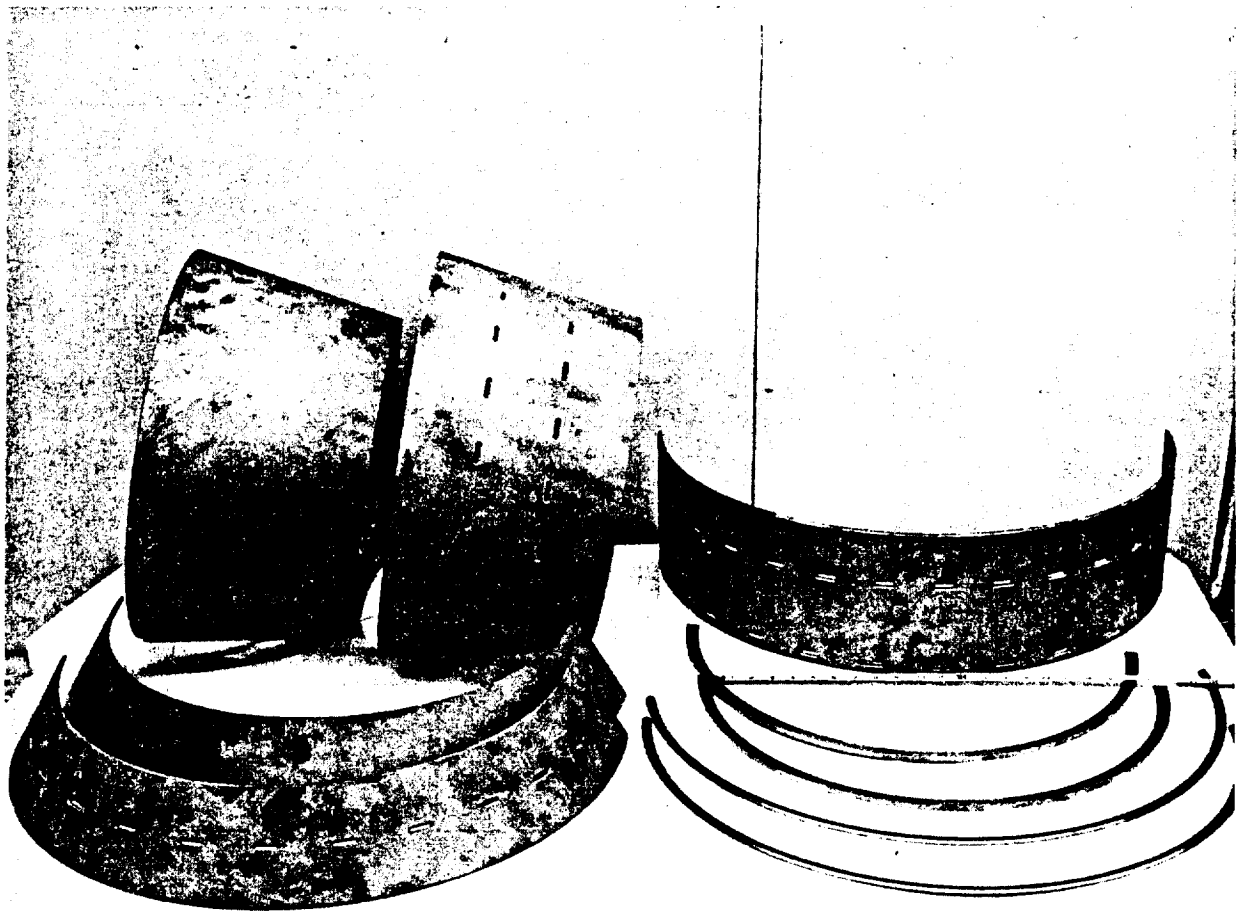

64476-3

Figure 7.8-3. Details for Outer Shroud and Plug Assembly, Leading Edge Flow Test Adapter

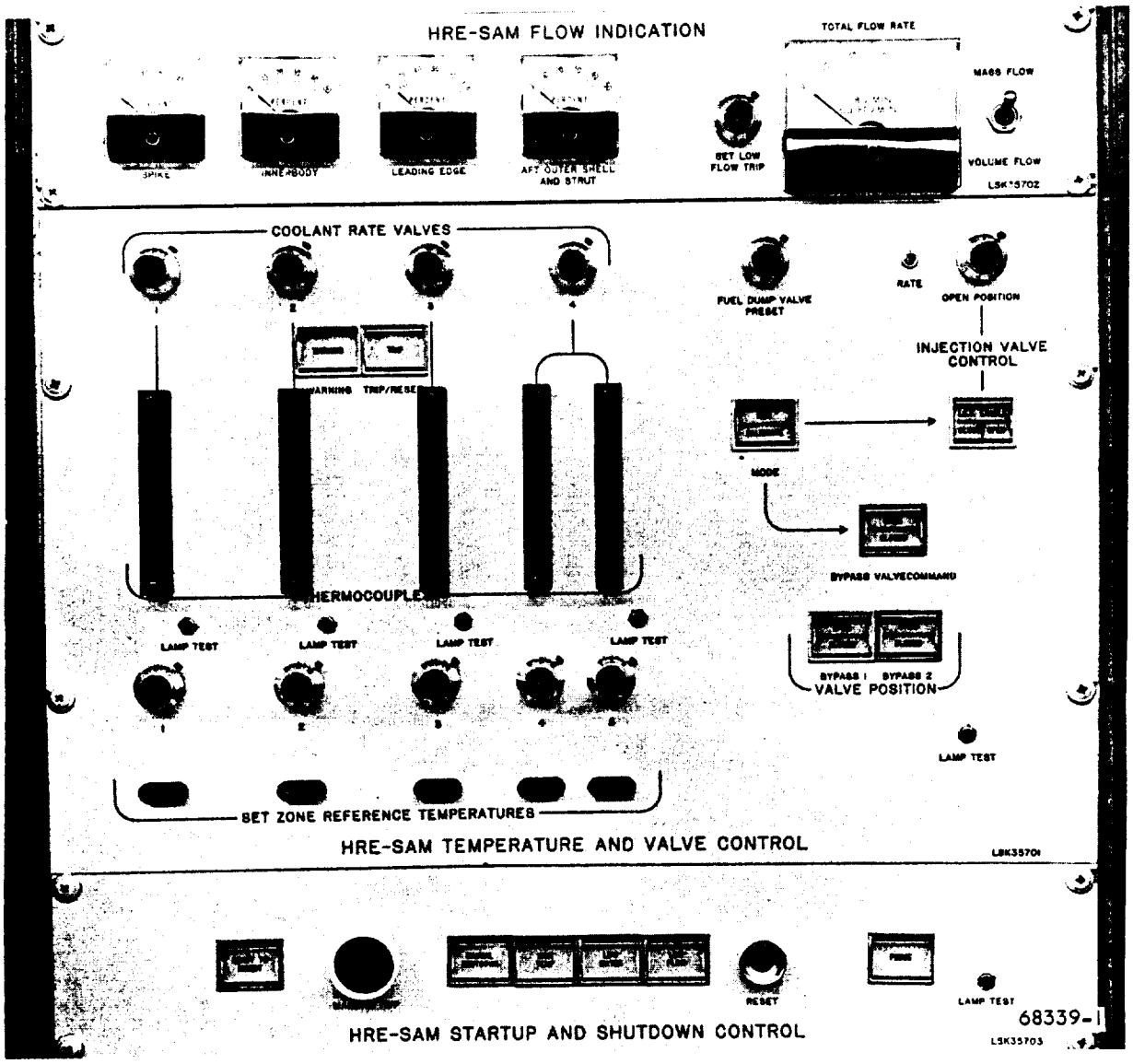

Figure 7.9-1. Temperature Control System Control Panel

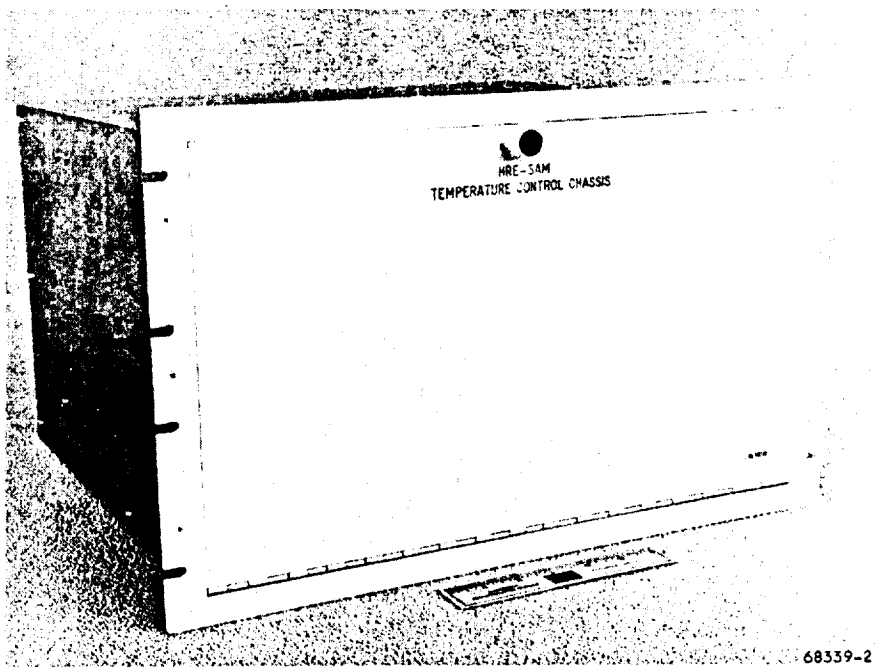

Figure 7.9-2. Temperature Control Chassis, Front View

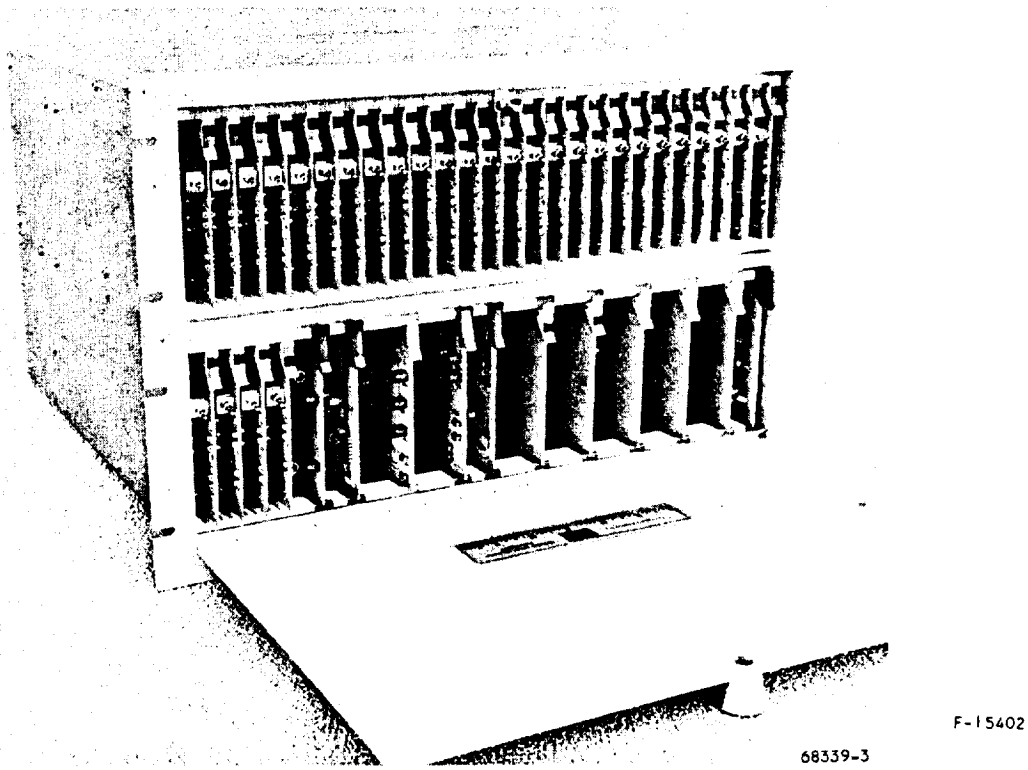

Figure 7.9-3. Temperature Control Chassis, Front Panel Open to Expose Circuit Boards

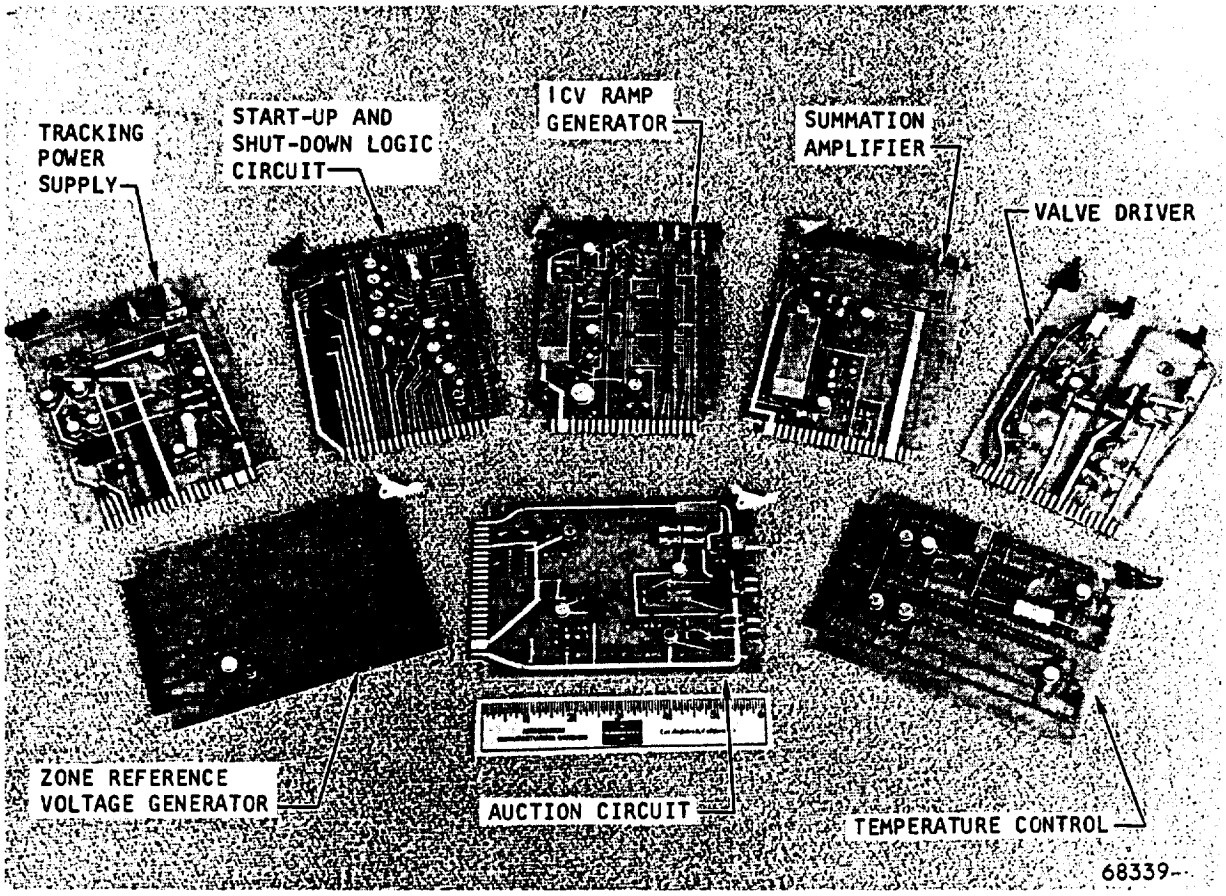

F-11696

Figure 7.9-4. Printed Circuit Board Types in Temperature Control Chassis

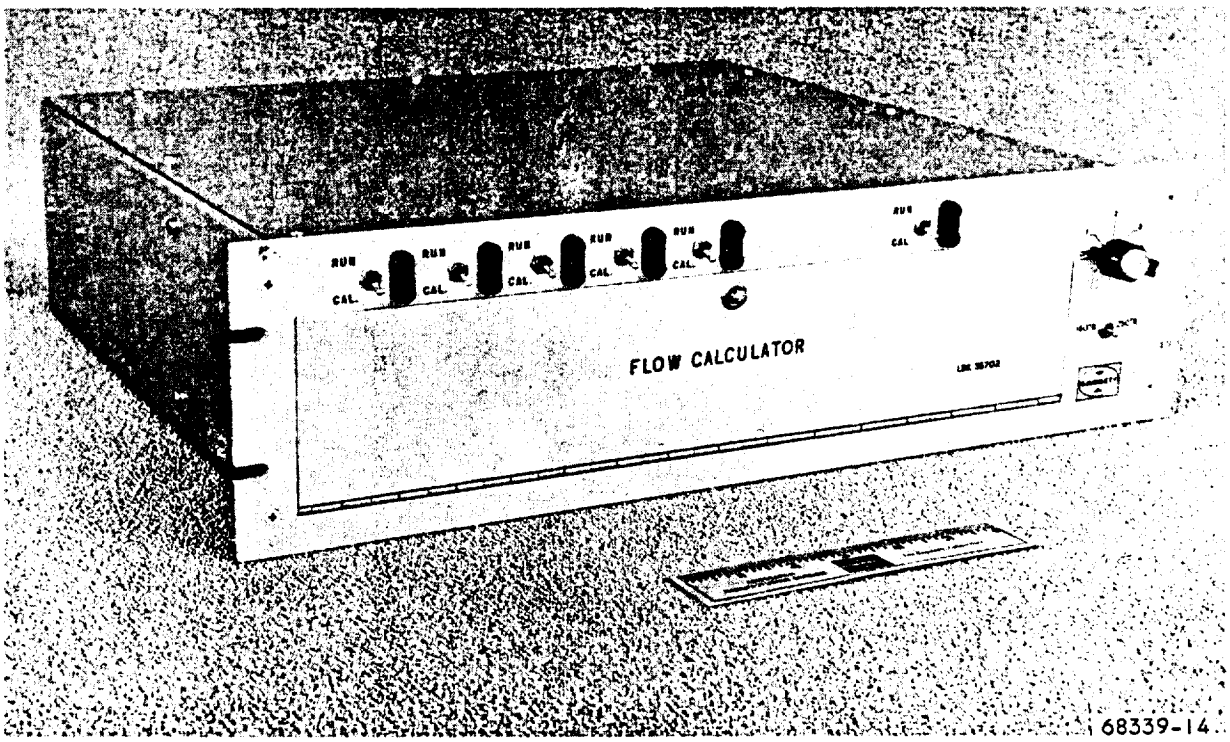

Figure 7.9-5. Flow Calculator Chassis, Front View

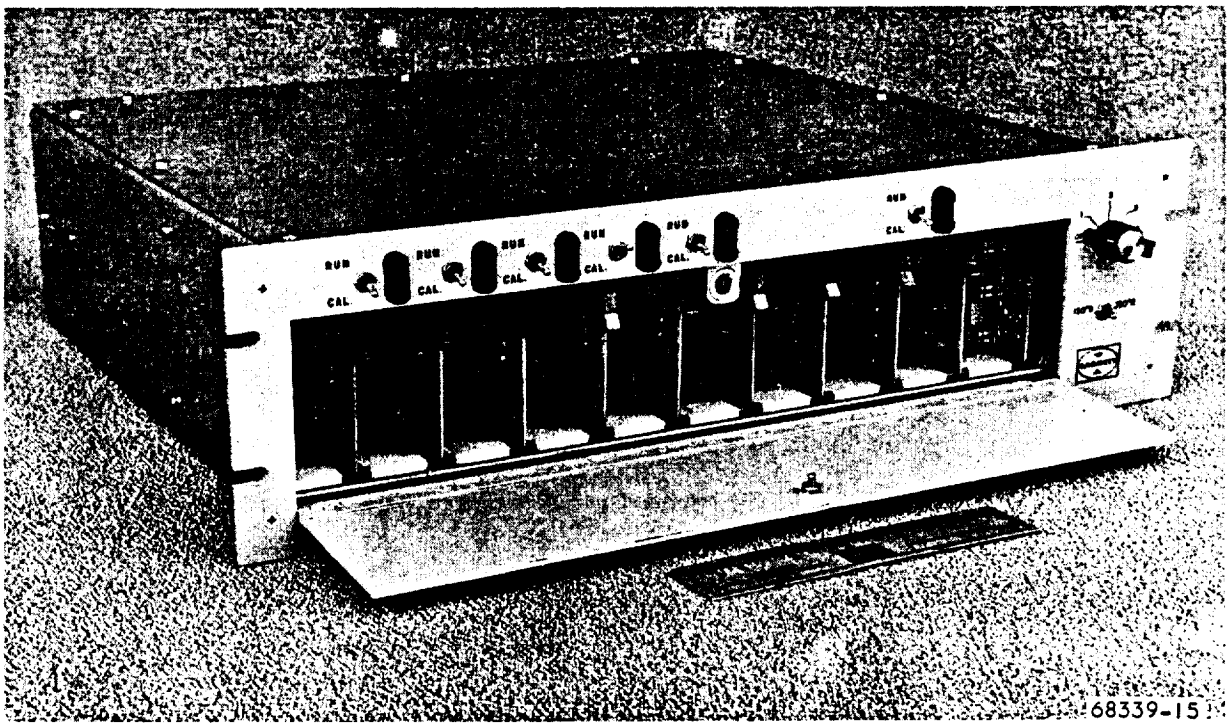

F-15404

Figure 7.9-6. Flow Calculator Chassis, Front Panel Open to Expose Circuit Boards

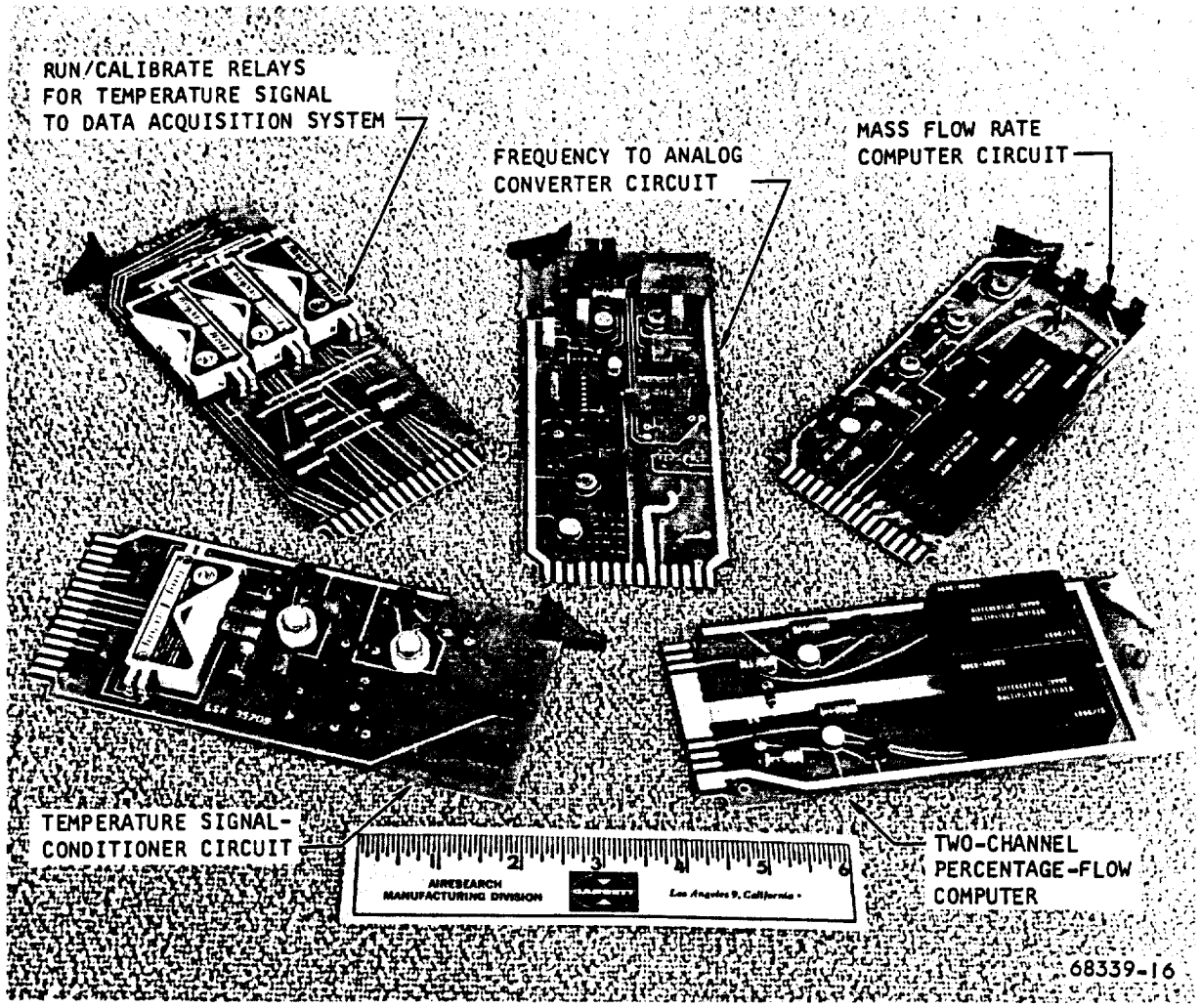

F-11697

Figure 7.9-7. Printed Circuit Board Types in Flow Calculator Chassis

adjustment, and the selector switch for mass-or volume-flow-rate indication on the total-flow panel meter. The middle section contains the four control knobs for operating the CRV's over-temperature warning; and alarm indicators and Reset switch, control channel indicator lights, ICV operating switch, Run-Calibrate switch, by-pass valve indicators and switch and zone-reference temperature voltages. The lower section contains the Shutdown and Reset switches, alarm indicators, purge annunciator, and Facility-Ready switch.

The temperature control circuits are mounted in a chassis, shown in Figures 7.9-2 and 7.9-3. Figure 7.9-2 shows the chassis with the front panel closed. Figure 7.9-3 shows the same chassis with the front panel open to show the mounting arrangement of the circuit boards. The eight types of printed circuit board used in the chassis are shown in Figure 7.9-4.

The flow calculator circuits are housed in a separate chassis, shown in Figures 7.9-5 and 7.9-6. As before, the two views show the front panel closed and open, respectively. The five types of circuit boards are shown in Figure 7.9-7.

Group 4

Downgraded at 3 year intervals;
declassified after 12 years
DOD DIR 5200.10

This material contains information affecting the national defense of the United States within the meaning of the espionage laws, Title 18, U.S.C., Sections 793 and 794, the transmission or revelation of which in any manner to an unauthorized person is prohibited by law.

8. TESTING

8.1 STRUTS

This section outlines the procedures and results of tests conducted on full-scale struts of the Hypersonic Research Engine. The tests were designed to determine (1) thermal performance and thermal fatigue resistance of the strut, (2) thermal performance and thermal fatigue resistance of the support panels which simulate the engine structural shells in the vicinity of the struts, and (3) coolant flow distribution.

8.1.1 Purpose and Scope

Design of the struts was dictated by the severe thermal operating conditions in the combustion chamber and by their basic function of carrying centerbody structural loads to the outer shell while keeping spike deflections within acceptable limits. A leading edge radius of 80 mils was used to limit drag. Because of the resulting large leading edge heat flux, large temperature differentials exist between the strut stagnation line outer surface and the average metal temperature of the strut. Thermal cycle fatigue data as well as creep rupture test data are required to provide assurance of adequate engine life. Meaningful thermal cycle fatigue data can best be obtained if the actual flight engine parts are used as test specimens in usage conditions. All struts tested were essentially identical in design, except in a few specimens where a fin was brazed in the leading edge cooling passage. The strut top and bottom support panels, which are constructed and cooled to represent a segment of the engine shells in the vicinity of the struts, were tested in combination with the struts. A total of four struts, three top support panels, and three bottom support panels were tested in hydrogen/oxygen/air combustion products up to a total gas temperature of 5300°R.

8.1.2 Description of Test Specimens

8.1.2.1 Strut Configurations

All of the struts tested were similar in design and were full scale in size. The strut is made of Hastelloy X. It has an 0.08-in. leading edge radius, a 0.3-in. trailing edge radius, and is 8.6 in. long. Its initial half-angle is 13 deg, with a maximum chord thickness of 1.8 in. Its height is 2.1 in. excluding the flange. The sidewall exposed to aerodynamic heating is 1.4 in. between support panels, and is cooled by hydrogen flow in plain rectangular fins beneath the 0.015-in. skin. The fins are 0.004 in. thick and 0.020 in. high, with 20 fins per in. normal to the flow path. The leading edge coolant passage is a 0.131-in.-dia hole. Two configurations of the flow circuits for the sidewall and leading edge coolant were tested as shown in

Figure 8.1-1a. Configuration No. 1 utilized a single inlet tube, and a brazed-in obstruction in the shorter path to equalize pressure drop and flow distribution; configuration No. 2 featured two separate inlet tubes, and a partition between the two inlets to the strut passages to permit measuring pressure drop in each passage and flow distribution. The hot skin and fins are brazed to the strut body in the primary brazing cycle. In subsequent brazing cycles, the doubler, coolant inlet and outlet tubes, and in some assemblies, a leading edge cooling fin were brazed in place.

8.1.2.2 Support Panel Configurations

The support panels were plate-fin configurations and were fabricated to simulate the inner and outer shell assemblies in the area of the strut cutouts.

The coolant flows into a manifold at one end of each panel and is distributed in the manifold before flowing through the fins to the outlet manifolds where it is collected and discharged.

Instrumentation for measuring hot gas pressure and hot wall temperature was brazed into the panel. Thermocouples for measuring cold wall temperature were spot-tacked onto the panel surface. In some cases temperature-indicating paint was sprayed onto the cold wall surfaces to obtain a temperature profile.

Three support panel configurations were tested. The configuration No. 1 support panels had no provision to adjust for the maldistribution of the coolant due to the strut cutouts. The coolant holes between the inlet and outlet manifolds and the fins were of a constant diameter across the width of the support panel. The configuration No. 2 top and bottom support panels had flow distribution adjustment between the inlet and outlet manifolds and the fins by the use of three different hole diameters across the panel width. The configuration No. 3 top and bottom support panels had the final engine coolant passage configuration used in the inner and outer shell assemblies. The coolant holes between the inlet and outlet manifolds and the fins vary, in order to provide the required flow distribution in the panel. An unfinned channel between the fins and the strut cutout provides the necessary cooling around the cutout. The configuration No. 3 panel is shown in Figure 8.1-1b.

8.1.3 Test Setup

The strut test specimens were tested in a 1.4 by 6-in. Mach 2 tunnel in which the flow was high-enthalpy gas produced by hydrogen, air, and oxygen combustion. Atmospheric air was introduced into the burner. Oxygen was injected into the air stream upstream of the hydrogen injection. The mixture was ignited and burned in a burner section and expanded through an adapter, the C-D nozzle, and the test section, and exhausted into atmosphere. The adapter was needed to match the burner diameter to the C-D nozzle inlet which has a 4 by 6-in. cross section.

The basic burner was 72-3/8 in. long with a 13-1/4-in. ID and a water-cooling jacket around the outside. An electrical igniter was located in the burner, and the air flowed past the bluff body. When oxygen was required, it was injected into the air upstream of the bluff body.

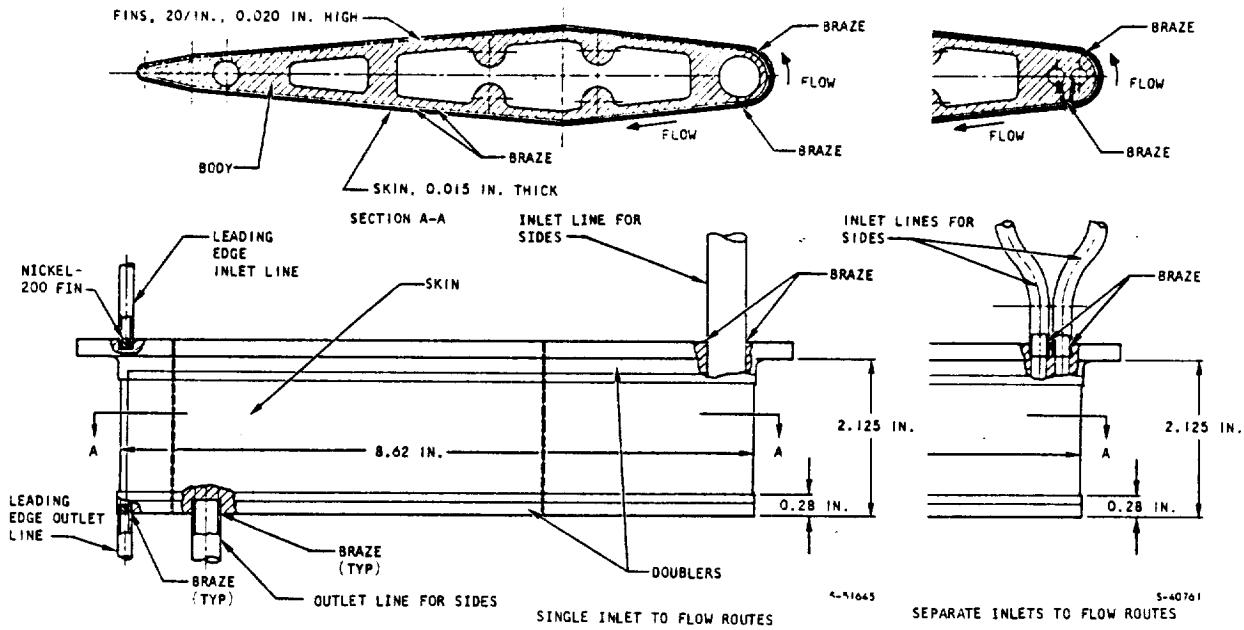

a. STRUT CONFIGURATIONS

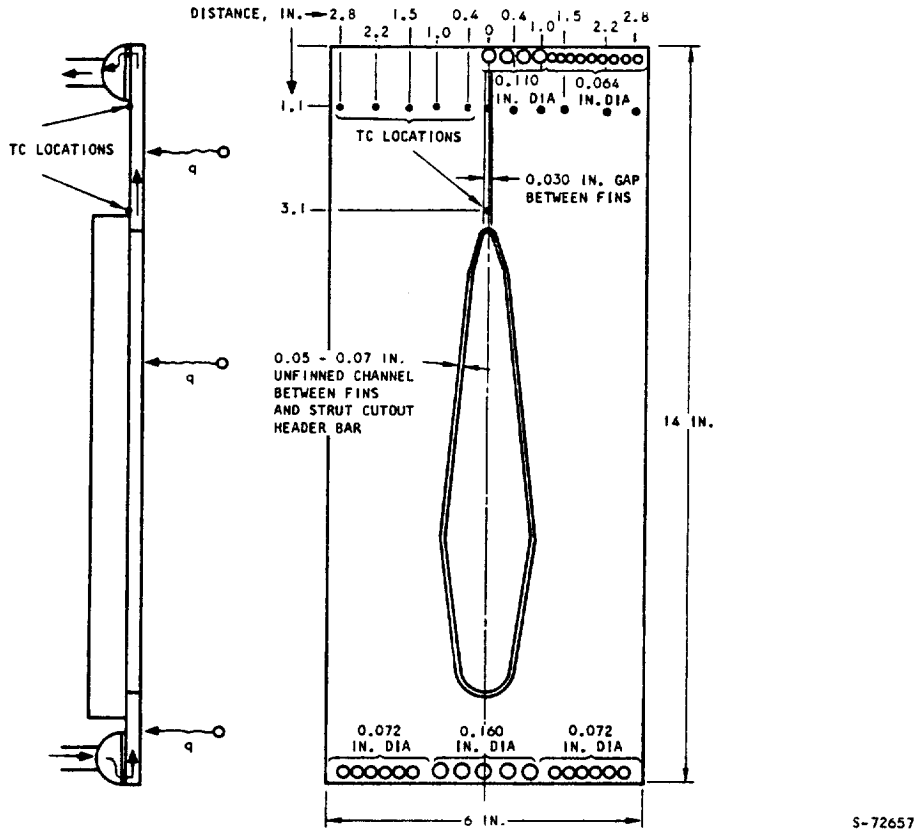

b. CONFIGURATION NO.3 PANEL SCHEMATIC AND FLOW DISTRIBUTION INSTRUMENTATION

Figure 8.1-1 Strut Test Specimens

Water-cooled adapter sections were used between the 13-1/4-in.-dia burner and the inlet of the water-cooled nozzle, and between the nozzle outlet and the strut test section.

The test section was downstream of the Mach 2.3 nozzle and consisted of top and bottom support panels and a strut assembly. The strut was bolted between the top and bottom support panels. Gaseous hydrogen was supplied to the top and bottom support panels at ambient temperature and 500 psia, to the strut-side wall coolant circuit at ambient temperature and 700 psia, and the leading edge coolant circuit at 160° to 200°R and 700 psia. Inlet pressures were regulated.

The gaseous hydrogen supplied to the burner and to the test section for coolant was stored in a cascade at 1900 psig. The cascade was pumped up from a liquid hydrogen storage system. Pumping occurred automatically when the gaseous hydrogen pressure reached 1600 psig. The pumping rate was generally below the test flow rates so that cascade pressure decayed gradually during the tests. The hydrogen was supplied directly to the test cell with the exception of the leading edge coolant, which was passed through a liquid nitrogen heat exchanger before being supplied to the test assembly.

The test measurements fell into four groups relating to (1) the hot gas, (2) the coolants, (3) wall temperature, and (4) hydrogen composition.

The ortho-para composition of the leading edge coolant hydrogen was analyzed with a gas chromatograph. The gas chromatograph was a Perkin-Elmer vapor fractometer with a 4-ft molecular sieve column and a 4-ft silica-gel column. A hydrogen sample was taken downstream of the strut leading edge cooling circuit and then passed through the gas chromatograph. The electrical output of the gas chromatograph was recorded on a continuous-reading single-channel recorder.

8.1.4 Test Procedures

The test was conducted with a fixed C-D nozzle tunnel exhausting to atmosphere. The test section Mach number varies slightly, depending on combustion products composition. For clean air, the test section Mach number is 2.3. The overall test program involved three parts, (1) calibration, (2) performance test, and (3) thermal cycle test. The calibration was performed to evaluate (1) the effective flow area of the leading edge passage at the downstream thermocouple station to permit correction of test readings, and (2) the leading edge back-side conduction effects.

For the performance test, all flows were held steady for a period of 3 min or longer. The steady-state tests covered conditions ranging from 1260° to 5300°R in total temperature and 1.3 to 8.8 million-per-ft unit-Reynolds number. The burner pressure ranged between 160 and 300 psia.

For the thermal cycling test, the burner oxygen, hydrogen, and airflow rates were varied during a cycle to produce a nominal temperature range from near room temperature to 4000°R. The corresponding burner pressures were at

nominal 100 and 275 psia respectively. The peak-heating periods last approximately 60 sec. During the cycling test all coolant controls were held steady. Due to change in temperature, however, the leading edge coolant-flow rate varied appreciably.

Leading edge coolant flow was calibrated for SN 6, configuration No. 1, and SN 2, configuration No. 2 struts. During one period of the calibration all flows were off except the leading edge coolant. The net flow area of the leading edge coolant passage at the downstream thermocouple station was determined from this condition. Since the flow was nearly adiabatic, the flow throttling effects could also be determined. In another calibration period, only the strut sidewall and leading edge coolants were turned on. The sidewall coolant was at room temperature, and the leading edge coolant was at 200°R nominal. Heat exchanging between these two coolants provided a check on the analytical conduction model.

The test section total temperature was not measured during each run, but was read from a chart which gives temperature as a function of the hydrogen-to-oxidant weight ratio. Total enthalpy at the test section inlet is assumed to be the combustion enthalpy less the heat loss to the cooling jacket. The total temperature is not sensitive to pressure for temperatures below 3000°F and is only slightly pressure-dependent for temperatures between 3000° and 4000°F.

8.1.5 Test Results

A total of 41 runs of steady-state tests and 219 thermal cycles was completed. A complete summary of the strut and support panel test conditions is given in Table 8.1-1. The strut leading edge heat transfer results are summarized in Figure 8.1-2a which presents the ratio of the measured average heat flux to the theoretical heat flux which is assumed to be one-half of the Fay-Riddell stagnation line heat flux as a function of Reynolds number and K-factor. The heat-flux ratio has an average value of 1.8, which implies that the area-average flux is approximately 90 percent of the peak heat flux. The high heating is thought to be caused by the thick boundary layer and turbulence in the tunnel flows. Due to upstream turbulence, the stagnation zone heat transfer rate increased by a factor, K, which applies uniformly over the curved portion of the leading edge. Based on this concept, the theoretical heat flux distributions for K = 1 to K = 3.5 are shown in Figure 8.1-2c. The relation between the average heat flux (area average under each curve in Figure 8.1-2c) and K is shown as Figure 8.1-2b from which the K-factor for each run is determined. Average heat flux was based on test heat addition to leading edge coolant and the external area of the leading edge.

During runs 30 to 35, the SN 6 strut was coated with low-melting-temperature strips. Since the external heat transfer coefficient decreases monotonically from the stagnation line, the strut surface temperature also would vary. The strips would melt and be blown away where the surface temperature exceeds their melting temperature, Thus, the edges of the unmelted strips after the test represent the surface isotherm line at the melting temperatures of the

UNCLASSIFIED

TABLE 8.1-1

STRUT TEST CONDITIONS

Strut No.	Run No.	Support Panel		Coolant Test Conditions			Hot Gas Test Conditions			Leading Edge Surface Roughness AA, μin.	Gap-Strut Doubler to Top Support Panel, in.	Gap-Strut Doubler to Bottom Support Panel, in.	Type of Test	Remarks
		Top	Bottom	Leading Edge (6)	Side Walls (6)	Support Panels (6)	Temp, °R	Pressure, psia	Flow, lb/sec					
Configuration 1 SN 2	A-18A	Configuration 1	Configuration 1	Water 2.3-2.8 gpm 200 psig 60°F	Water 2.5-4.3 gpm 200 psig 60°F	Water 18-24 gpm 200 psig 60°F	1500-5300	180-300	3.9-12.9	Not available	0.005-0.030	0.002-0.020	Facility checkout and calibration	No data analyzed prior to run 12.
	19-21			Hydrogen 0.022-0.036 lb/sec	Hydrogen 0.024 lb/sec	Hydrogen 0.100 lb/sec	3600-5000	211-315	5.1-6.9	250-500 (after)	0.005-0.030	0.002-0.015	Performance	Leading edge cracked due to accidental loss of coolant.
Configuration 1 SN 6	22-27	Configuration 2	Configuration 2	Hydrogen 0.034-0.059 lb/sec	Hydrogen 0.025-0.030 lb/sec	Hydrogen 0.097-0.121 lb/sec	2500-4500	250-300	4.3-9.2	Not available 100-150 (after)	0.005-0.036	0.010-0.050	Performance	
None	28-29	None	None	-	-	-	2000-2500	150-200	6-7.5	-	-	-	-	Burner checkout
Configuration 1 SN 6	30-35	Configuration 2	Configuration 2	Hydrogen 0.020-0.57 lb/sec	Hydrogen 0.020 lb/sec	Hydrogen 0.062 lb/sec	2500-3100	160-240	6.2-8.4	100-150 (after	0.005-0.044	0.010-0.037	Performance	Low melting point alloys and thermocouples on leading edge
	35A Thermal Cycles 1-11			Hydrogen 0.046-0.050 lb/sec	Hydrogen 0.024 lb/sec	Hydrogen 0.060-0.062 lb/sec	500-3600	76-283	6.6-11	175-400 (after)	0.005-0.044	0.010-0.037	Thermal cycle	
	36-37	Configuration 3		Hydrogen 0.057 lb/sec	Hydrogen 0.030 lb/sec	Hydrogen 0.070 lb/sec	1260	170	7.1	175-400 (after)	0.002-0.013 (5)	0.003-0.006 (5)	Performance	Run 37-Data is no good
	38-54 Thermal Cycles 12-73			Hydrogen 0.041-0.048 lb/sec	Hydrogen 0.024-0.027 lb/sec	Hydrogen 0.070-0.074 lb/sec	500-4000	83-268	6.4-7.6	-	-	-	Thermal cycle	
	55			Hydrogen 0.03-0.05 lb/sec	None	None	None	None	None	Too rough for profilimeter stylus	-	-	Leading edge calibration	
Configuration 1 SN 5 (4) (5)	56-68 Thermal Cycles 1-102	Configuration 1	Configuration 3	Hydrogen 0.028-0.032 lb/sec	Hydrogen 0.026-0.029 lb/sec	Water 11-15 gpm	500-4000	80-264	6.6-10	60-80 (before) 100-250 (after)	0.005-0.020 (5)	0.003-0.021 (5)	Thermal cycle	(a) Spalling of 5 mil 80% C_2-C_3 + 20% NiCr coating after cycle 48. (b) Leading edge outlet tube 50% plugged
Configuration 2 SN 2 (4) (5)	69-80 Thermal Cycles 1-44	Configuration 3		Hydrogen 0.048-0.052 lb/sec	Hydrogen 0.026-0.029 lb/sec	Hydrogen 0.077-0.098 lb/sec	500-4000	81-262	6.6-8.0	50-85 (before)	0.004-0.012 (5)	0.003-0.009 (5)	Thermal cycle	
	81			Hydrogen 0.031 lb/sec	Hydrogen 0.026 lb/sec	Hydrogen 0.080 lb/sec	2900	200	6.6	50-80 (after)	-	-	Performance	

NOTES:
1. Panel has no correction for flow distribution in inlet and outlet manifolds.
2. Panel has flow distribution holes in the inlet and outlet coolant manifolds.
3. Panel has strut cut-out fin gap and flow distribution holes in the inlet and outlet coolant manifolds.
4. Nickel-200 (0.031-in. thick) fin in leading edge coolant circuit.
5. Doublers brazed on struts to minimize strut-to-support panel gap.
6. The following nominal inlet pressures were used for the hydrogen cooled runs: leading edge, 700 psia; side walls, 700 psia; and support panels, 500 psia.

L-51721

UNCLASSIFIED

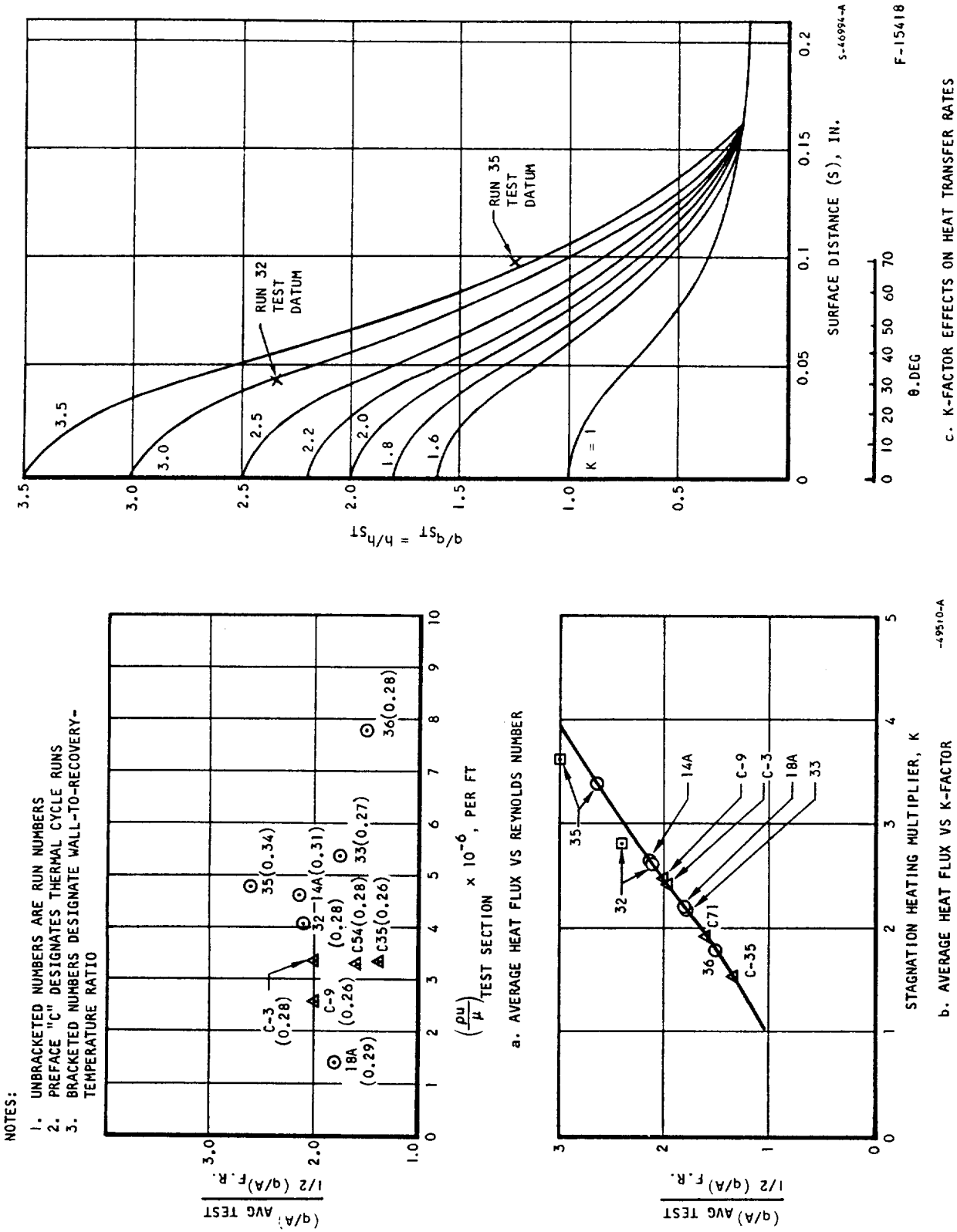

Figure 8.1-2. Strut Leading Edge Heat Transfer Results

strips. Since the strut leading edge internal cooling coefficient is known fairly accurately, the added knowledge of the external surface temperature permits the determination of heat flux. The cadmium strip melted at 610°F, and receded back to θ = 30 deg after run 32. The zinc strip melted at 787°F and receded to θ = 70 deg after run 35. Based on these temperatures, the heat transfer coefficient determined at θ = 30 deg from run 32, was 2.3-times larger than the stagnation line value predicted by the Fay and Riddell theory; and the coefficient at θ = 70 deg for run 35, was 1.25-times larger than the theoretical stagnation line value.

A considerable reduction of the stagnation line wall temperature was achieved by adding a fin to the leading edge cooling passage. For a hot gas total temperature of 3800°F, the stagnation line temperature for the configuration No. 2, SN 2 strut with a fin was 1700°R, as compared to 2040°R for the SN 6 strut without a fin. The thermal fatigue life of the strut leading edge was demonstrated most conclusively on the SN 5 strut when one of the two flow passages (one on each side of the fin) was plugged during fabrication. Analysis of the SN 5 strut test data reveals that a maximum Hastelloy X metal temperature of 2600°R was reached during the test.

8.1.5.1 Thermal Cycling Test Results

Thermal cycling tests were conducted for struts SN 2 (configuration No. 2); SN 5; and SN 6 to 42, 102, and 73 cycles, respectively. The nominal hot gas conditions for peak heating were 250 psia and 4000°R total temperature. The strut sides and leading edge heat loads for thermal cycling runs had a range of ±10 percent and ±15 percent, respectively from the nominal values. The peak leading edge temperatures for the three struts are nominally 1800°R, 2100°R, and 2600°R for struts SN 2, SN 5, and SN 6. For strut SN 5, the peak temperature of 2600°R occurs approximately 30 degrees off the stagnation line.

8.1.5.2 Strut-Side Flow Distribution

The strut-side wall is cooled with hydrogen gas entering near the trailing edge. The coolant flows forward in two branches -- the leading edge side and the trailing edge side. The strut-side wall flow characteristics were determined for configurations No. 1 and 2. Flow distribution (percentage of flow split to the leading and trailing edge strut sides) for configuration No. 1 strut (SN 2) was estimated from structural temperature measurements during hot-tunnel operation. Configuration No. 2 flow split was determined from individual measurements for isothermal airflow to each of the strut sides.

Configuration No. 1 strut has a single inlet to the strut sides and uses pressure drop to aportion flow. Results indicate that the percentage of flow split to the leading edge side is 41 percent, while the trailing edge side receives 59 percent. The design objective is 55 percent and 45 percent, respectively. Temperatures used in the estimate were obtained from four thermocouples tacked to the inner strut structure at two locations along the strut length on both sides.

Configuration No. 2 strut differs from the first configuration in having the sides of the inlet separated. Separate inlet tubes were used for test; however, in the actual installation, a single inlet tube will be used. The objectives of these tests were twofold: (1) to experimentally verify the design flow-rate split to each of the revised strut-sides coolant passages, and (2) to calibrate the strut-sides pressure drops predicted with hydrogen to design.

Air test results indicate that overall $\rho\Delta P$ for configuration No. 2 struts at the Mach 6.5L design point flow rate (1.86 lb/min of H_2 per strut) is 25.5 lb/ft^3-psi for SN 2 and 28.5 lb/ft^3-psi for SN 3. The design point $\rho\Delta P$ requirement is 32.3 lb/ft^3-psi and requires the use of orifice restrictions in the lines to assure proper flow withdrawal from the outer shell. The percent flow-rate split to the leading and trailing edge strut sides respectively is approximately 50-50 for both SN 2 and SN 3. The design objective flow-rate split is 55-45.

8.1.5.3 Creep Rupture Test Results

Flat panel tests, reported in Section 8.3, indicated that the 20-fins-per-in., 0.004-in.-thick plain rectangular fins used in the struts should achieve a fin-strength efficiency of 0.350 to 0.400 for creep rupture and 0.500 for short time burst. A total of four strut assemblies were subjected to creep rupture tests to evaluate the containment strength of the finished components. The maximum fin design operating conditions were 700 psi internal pressure and 1200°F maximum fin temperature. The tests were carried out at 1300°F to provide an overtemperature margin of 100°F.

The structural design basis for all fins in the engine is a safety factor of not less than 1.5 for creep rupture strength. The following published strength data were used to evaluate fin strength performance at 1300°F.

$$\sigma_{ult} = 74{,}000 \text{ psi}; \quad \sigma_{10\text{-hr creep rupture}} = 43{,}000 \text{ psi}$$

For the 20-fin-per-in., 0.004-in.-thick fin, nominal fin stress due to internal pressure is $\sigma_{fin} = 11.5\ p$. For 1050 psi pressure (= 1.5 x 700), the nominal fin stress is 12,100 psi.

The test specimens were tested with incrementally increased pressures. The load history for the first specimen was 650 psi for 16 hr, 750 psi for 10 hr, 850 psi for 10 hr, 950 for 10 hr, and rapidly increased pressure until burst at 1650 psi. This specimen survived 46 hr of sustained pressure without creep rupture, 36 hr of which were at pressures in excess of the 700 psi design operating pressure. The burst rupture initiated near the aft end of the strut at the end of the fins. Inspection of the failed part showed that a braze void had occurred at this location. Beyond the void area, the failure was entirely within the fin parent material. This strut did not achieve its full potential fin strength capability because of the braze void. In spite of this defect it did achieve adequate strength to meet the design goals.

The second strut was tested at 700 psi for 10 hr, 1050 psi for 10 hr, 1350 psi for 9 hr, and burst at 2850 psi. The elapsed time of 10 hr at 1050 psi by itself demonstrated compliance with the 1.5 safety factor on stress rupture. Calculations were carried out to assess fin-strength efficiency values for creep rupture and for short-time burst. These were:

η_{fin} = 0.35 for creep rupture

η_{fin} = 0.45 for short-time burst

These results were definitely in line with the anticipated values of 0.40 for creep and 0.50 for burst. This test strut is shown in Figure 8.1-3. Failure initiated at the aft end of the struts at the end of the fins. There were no braze voids, and failure was in the fin parent metal.

The loading history for the third specimen was 1050 psi for 10 hr and then 1500 psi for 5 hr. The pressure was then to be increased in 100-psi increments at one-minute intervals until burst. The feeder tube failed at 1600 psi. After the tube was repaired, the component was rapidly repressurized to 1600 psi, and then the pressure was increased as indicated above until rupture occurred at 2100 psi. From inspection of the test specimen, it was determined that the rupture occured in the fin parent metal and that there were no braze voids.

At 1050 psi, the nominal fin stress is 12,100 psi, while at 1500 psi internal pressure, fin stress is 17,250 psi. If rupture had occured precisely at the end of the 15-hr of cumulative creep-loading, the fin-strength efficiency for the test would have been 0.370. This is actually a lower-bound estimate, since the unit was subjected to additional creep before rupturing at 2100 psi. The fact that the burst pressure of 2100 psi was not significantly higher than the 1500 psi (which was held for 5 hr) indicates that the failure was essentially due to creep-rupture, rather than short-time burst.

The loading history for the fourth specimen was 1050 psi for 10 hr followed by 1500 psi for 5 hr. The unit was then subjected to increased pressure in 100-psi increments at one-minute intervals to 2300 psi, at which time the feeder tube developed excessive leakage. Upon repairing the tube, the unit was rapidly pressurized to 1600 psi, and then the pressure was incremently increased until rupture occurred at 2020 psi. By again assuming that the unit creep-ruptured after the 15 hr of sustained loading, the fin-strength-efficiency factor would have been 0.370. The actual failure of this unit was also due to creep rupture. This is substantiated by the fact that the unit eventually ruptured at 2020 psi after previously having been exposed to 2300 psi.

8.1.5.4 Low-Cycle Fatigue Results

The requisite temperature data needed to perform the low-cycle thermal fatigue calculations are summarized in the tabular information shown on Figure 8.1-4. The temperature rise along the strut length is linear, and

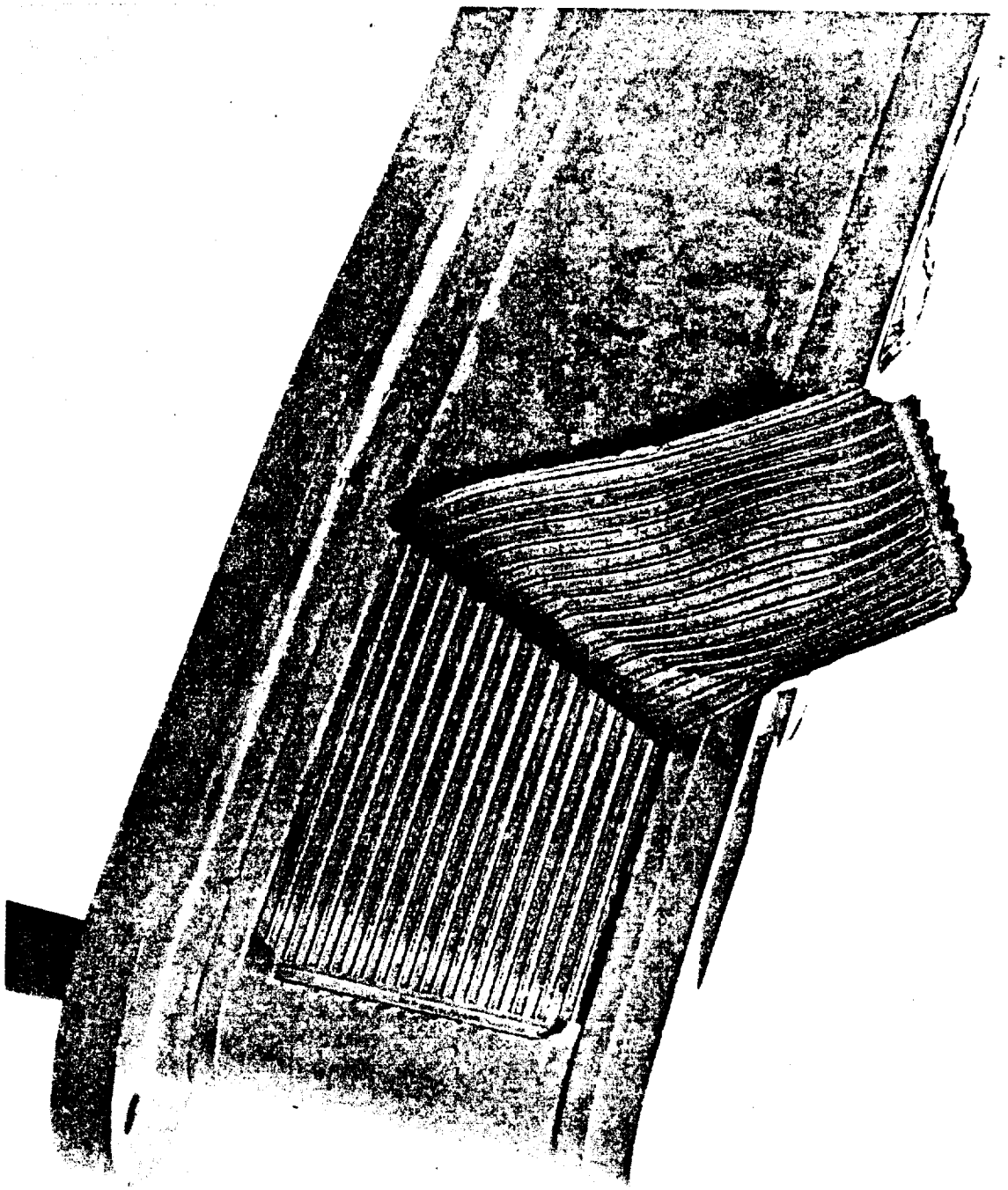

63573

Figure 8.1-3. Strut Assembly After Rupture Test

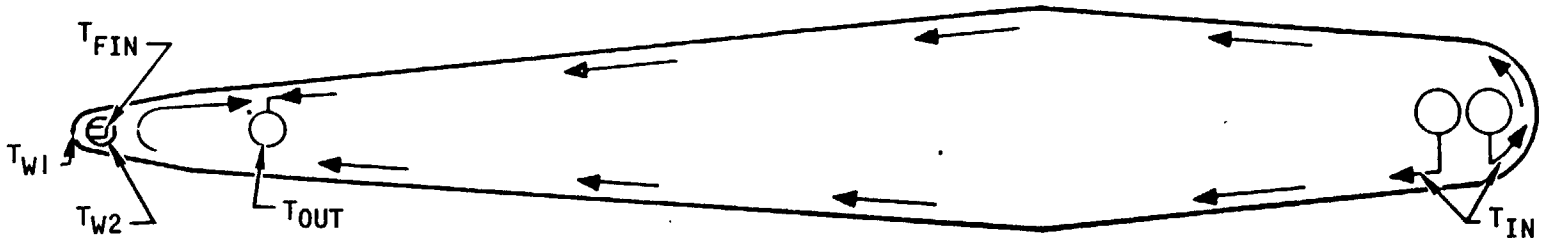

	TEMPERATURES, °R				
	T_{IN}	T_{OUT}	T_{W1}	T_{W2}	T_{FIN}
TEST SPECIMEN SN 2 (Config. 2)	550	900	1850	1300	200
TEST SPECIMEN SN 5 (Config. 1)	550	900	2600	2100	200
TEST SPECIMEN SN 6 (Config. 1)	550	900	2150	1800	NO FIN
TEST CONDITION SAM	540	1430	1700	1250	200
M = 8 FLIGHT	445	1170	2625	1400	200

S-51054

Figure 8.1-4 . Strut Thermal Fatigue Temperatures

the strut body will operate at local coolant temperature. Since this temperature rise is gradual and linear, the strut body will be essentially free of thermal stresses, and the differential expansion of the hot surface producing thermal fatigue will be the local difference between the hot surface and the strut body.

In the area of the leading edge, differential expansion was computed by comparing the local outside wall stagnation temperature, the inside wall temperature at the stagnation line, and the coolant fin temperature to the coolant outlet temperature. The numerical data on Figure 8.1-4 pertains to the thermal cycle testing on specimens SN 2, SN 5, and SN 6, to the SAM test conditions, and finally to the Mach 8 flight conditions. A thermal fatigue analysis was carried out for each of these cases. The fatigue performance was based upon parent metal Hastelloy X data obtained by AiResearch on the Regeneratively Cooled Panels program (Contract No. NAS1-5002) and from Nickel-200 data reported in AiResearch Report No. AP-68-4617 during the HRE program.

8.1.5.4.1 SN 2 Cycle Life

The maximum differential expansion from the strut outlet reference temperature is at the leading edge stagnation line. The differential temperature was

$$\Delta T = 1390^{\circ}F - 400^{\circ}F = 950^{\circ}F$$

The differential expansion due to these two temperature levels was $\alpha\Delta T = 0.0088$ in./in. The plastic-strain range corresponding to this total strain amplitude was $\Delta\varepsilon_{pl} = 0.0044$ in./in. From the Hastelloy X low-cycle fatigue information, the predicted cycle life would be N = 1650 cycles.

The mean metal temperature at the stagnation line was 1115°F, and the pressure-containment stress with 700 psi coolant was

$$\sigma = \frac{p\ r_m}{t} = \frac{(700)(0.0725)}{(0.015)} = 3350 \text{ psi}$$

At this temperature and stress intensity, creep was not a factor at all. This unit survived a total of 44 actual test cycles without failure.

8.1.5.4.2 SN 5 Cycle Life

This test unit was constructed with a blocked cooling package on one side of the leading edge internal cooling fins. Because of this blockage, the test unit was subjected to extremely severe thermal cycles, and because of this, an excellent measure of cycle life capability was obtained. This test unit survived 102 thermal cycles without failure at these conditions with an average time at maximum temperature of approximately 2 min per cycle.

The elapsed time at maximum temperature was approximately 3.5 hr during this test. Based upon a mean metal temperature at the stagnation line of $(2150^{\circ}F + 1800^{\circ}F)/2 = 1825^{\circ}F$, the creep rupture life would have been 50 hr. The creep rupture life fraction was 3.5/50 + 0.7.

The total applied differential temperature between the strut body at the coolant outlet edge was

$$\Delta T = 2150^{\circ}F - 440^{\circ}F = 1710^{\circ}F$$

The differential thermal expansion was 0.0169 in./in., and the resulting plastic-strain range was $\Delta\epsilon_p = 0.0125$ in./in. From Hastelloy X fatigue data, the low-cycle fatigue life without considering creep was N = 175 cycles. With creep effects included, this would have been

$$N = 175\ (1 - 0.07) = 163 \text{ cycles}$$

8.1.5.4.3 SN 6 Cycle Life

The mean metal temperature at the stagnation line was 1500°F, and the creep rupture life due to pressure containment would have been in excess of 10,000 hr. The total elapsed time of 2.5 hr at maximum temperature, therefore, contributed a negligible amount of creep damage. This unit survived 62 cycles at the above conditions and another 25 cycles at varying conditions without failure.

The maximum temperature differential during each of the above test cycles occurred at the leading edge stagnation line, and was

$$\Delta T = 1700^{\circ}F - 400^{\circ}F = 1260^{\circ}F$$

This produced a differential thermal expansion of 0.0120 in./in., and a corresponding plastic-strain range of $\Delta\epsilon_p = 0.0076$ in./in. Based upon 1540°F low-cycle fatigue data, the predicted cycle life was 650 cycles.

8.1.5.4.4 SAM Test Conditions

The temperatures for the SAM test unit were shown in Figure 8.1-4. The peak ΔT occurs at the leading edge cooling fin. The temperature differences at the leading edge stagnation line are small when compared to the coolant outlet temperature, and the maximum structural ΔT takes place at the cooling fin. The differential temperature was

$$\Delta T = 1700^{\circ}R - 200^{\circ}R = 1500^{\circ}R$$

The fin is constructed from Nickel-200, and the applied thermal expansion differential is 0.0144 in./in. Utilizing Nickel-200 stress/strain data and Nickel-200 fatigue test results, the applied plastic strain range was 0.0124 in./in. with a predicted life of 1100 cycles.

8.1.5.4.5 Mach 8 Flight Cycle Life

The Mach 8 flight thermal conditions were also shown on Figure 8.1-4. The cycle thermal conditions would be quite similar to those encountered in the SN 5 test unit. The maximum temperature predicted at the leading edge outside stagnation line is virtually identical to the SN 5 outside wall temperature. The inside wall temperature would be considerably lower, while the coolant outlet temperature would be somewhat higher than the SN 5 test conditions. In summary, the Mach 8 flight thermal fatigue conditions are somewhat more moderate than those which occurred during the testing of SN 5.

The average wall temperature at the stagnation line would be approximately 1540°F, which would produce a stress rupture life of 1000 hr due to the pressure containment of coolant at 700 psi internal pressure. The required engine design life of 10 hr would correspond to a creep rupture damage fraction of 0.01.

The differential temperature between the strut leading edge outside stagnation line and the coolant outlet would be

$$\Delta T = 2165^{\circ}F - 710^{\circ}F = 1455^{\circ}F$$

This would produce a thermal differential expansion of 0.0150 in./in., and a plastic strain range of 0.0106 in./in. Based upon 1540°F thermal fatigue data, the predicted life would be N = 380 cycles without regard to creep. Accounting for the creep rupture life fraction damage of 0.01, the predicted life at Mach 8 flight would be

$$N = 380\ (1 - 0.01) = 376 \text{ cycles.}$$

8.1.5.5 Support Panel Heat Transfer

Heat transfer information was obtained from support panel heat transfer test data during runs 16 through 25. For runs 19 through 24, the coolant was hydrogen at room temperature flowing concurrently with respect to the hot gas. For run 25, the coolant was hydrogen at room temperature counter-current to the hot gas. The direction of coolant flow produces significantly different heat transfer models. When the coolant flow is in the direction of hot gas, the wall temperature has a tendency to stabilize the boundary layer and suppress flow separation. The test results indicate that the separation zone caused by the strut leading edge shock wave is small--at the most, the separation zone extended to a distance of 1 in. off the centerline. This conclusion is based on the fact that the wall temperatures vary slowly with length. For run 25, the panel coolant flowed counter-current to the hot gas, and the wall temperature upstream of the strut exceeded 1000°R. The test results indicate that for run 25 the shock-induced boundary layer separation extended farther than 1 in. off the strut centerline. The thermocouple temperature rises and falls in good agreement with the theoretical value for flow separation and reattachment.

Application of the above data on flow separation and reattachment to the flight engine design must consider that there was no fuel injection upstream of the strut during these tests. Fuel injection will cause considerable disturbance in flow and, in the event the flow becomes separated and reattached, the subsequent flow will have a thinner boundary layer. In such a case, the flow separation zone in the vicinity of the strut will be small even though the predicted wall temperature will be on the order of 1500°R.

8.1.5.6 Support Panel Flow Distribution

Thermal cycle tests of the full-scale SN 2, configuration No. 2, strut were performed using a configuration No. 3 top support panel and a configuration No. 3 bottom support panel. Hydrogen and cold wall (structural) temperatures were used to calculate coolant flow distribution in these panels. For the configuration No. 3 top panel the hydrogen coolant mass flux in line with the strut cutout is up to 2-times average. Coolant mass flux not in line with the strut cutout is as low as 52 percent of panel average. This flow maldistribution created panel overheating near panel edges. The design objective was a uniform coolant rate distribution across the 6-in. panel width. Coolant flow distribution for the configuration No. 3 bottom panel is better than the top panel. The maximum coolant mass flux was 1.25-times panel average and occurred 0.4 in. from bottom panel centerline. The minimum coolant mass flux was 80 percent of panel average and occurred near the panel edge. The coolant maldistribution for both panels was traced from X-ray photographs to braze alloy blockage in the finned passage and misalignment of the slot between fins at the inlet.

8.1.5.7 Strut-Slot Heating

The strut flange and support panels received high heating from the flow of hot gas through the strut-support panel slot during performance and thermal cycling tests of strut SN 6, through cycle 11. Configuration No. 2 top and bottom support panels were used. Strut flange temperatures up to 1260°R were measured. A slightly higher surface temperature of 1400°R was indicated by the thermocouple in the support panel slot. The high slot heating is believed to result from the 0.01- to 0.025-in.-wide gap between the socket and the side of the strut.

Hastelloy X doublers were brazed around the strut periphery adjacent to each of the two support panels to reduce the slot width to a nominal 0.005 in. This width appears to be a practical minimum for fabrication. Test results for cycles 14 through 16 with doublers brazed on strut sides decreased the strut flange temperature by approximately 150°F from test results with no brazed doublers; i.e., 1260°R.

8.1.6 Data Analysis and Discussion

One of the objectives of the tests was to determine the strut leading edge heat transfer rates. Except for test runs 32 and 35 of strut SN 6, for which the surface temperatures were indicated by the melting of the solder

strips, no leading edge surface temperature was measured. Even with the coolant heat loads available, the heat transfer coefficient is not directly calculable without the wall temperature. In order to determine the wall temperature, both the internal flow heat transfer coefficient and the experimental heat loads must be utilized. Furthermore, to calculate the external heat transfer coefficient, the external flow field about the strut must be known. The flow field about the strut leading edge is complicated due to shock boundary layer interaction, for a two-dimensional wedge is equal to several boundary layer thicknesses, depending on the magnitude of the peak pressure. For a duct, the oblique shock wave generated by the boundary-layer thickening on one wall could cause the boundary layer flow on the opposite wall to separate also. The result is a shock train several duct-diameters long. This long separation flow model is confirmed by contaminants deposited on the support panels. The complex flow field which defies analytical treatment is a class of protuberance flow. The general treatment of protuberance flow is to correlate the experimental data with the theoretical stagnation line heat transfer value. (Reference 8.1-1). The strut experimental heat flux of 2- to 3-times that of the theoretical value suggests other flow phenomenon beside the protuberance flow. A possible major effect could be the presence of relatively high level of freestream turbulence in the tunnel due to upstream burning of hydrogen. The stream turbulence is known to have a significant influence on the stagnation zone heat transfer because the vorticity is magnified in a decelerating stream. This action carries the high energy fluid close to the wall surface. Freestream turbulence between 4 and 10 percent can produce a stagnation zone heating 2- or 3-times that of the heat flux calculated by the theory of Fay-Riddell (Reference 8.1-2 and 8.1-3). The increased strut heating, therefore, can be accounted for entirely be the freestream turbulence effects. It appears, then, that the real mechanism responsible for the protuberance heating is also caused by the deceleration of the turbulent eddies within the boundary layer upstream of the protuberance. The complex shock system upstream of the protuberance can produce very high heating due to shock intersection and shock wave impinging. This, however, does not contradict the test results, since the area affected by shock impingement is very small and the overall heat load contributed by shock impingement is insignificant. The significance in assuming that freestream turbulence is the major mechanism responsible for the heat flux increase is two-fold. One is to permit the use of Lees' distribution with confidence since the K-factor is nearly constant over the curved portion of the leading edge. Another is to increase the reliability in applying the test data for the flight engine design once the turbulence level in the flight engine combustion chamber is known.

These test data are presented as the ratio of the average leading edge heat flux to one-half of the theoretical stagnation line value which is

$$\left(\frac{q}{A}\right)_{FR} = \frac{0.54}{Pr\ 0.6}\left(\frac{\rho_W \mu_W}{\rho_T \mu_T}\right)^{0.1} \sqrt{\rho_T \mu_T \frac{du}{dx}\left(H_T - H_W\right)}$$

where $\frac{du}{dx} = \frac{1}{R_N}\sqrt{\frac{2g(P_T - P_\infty)}{\rho_T}}$, and the subscript "T" designates the total conditions behind the bow shock.

The average leading edge heat flux is defined as the heat absorbed by the leading edge coolant, less the heat conducting and end effects, divided by the external surface area, which is 0.00408 ft^2.

8.1.7 Conclusions

The tests achieved the desired objectives. Specifically, information was obtained on the lower limits of strut thermal cycle life, support panels flow distribution and thermal cycle life, and the thermal performance of the struts and panels.

8.1.7.1 Creep Rupture and Low-Cycle Fatigue

8.1.7.1.1 Creep Rupture

Test work on plate-fin specimens with 20R-.004 offset fins demonstrated a fin-strength efficiency of approximately 0.400. Since the above figure for the struts of 0.370 makes no allowance for the creep effects at pressures above 1500 psi, the actual performance of the strut assemblies was somewhat better than 0.370 and the results come into good agreement with the plate-fin tests.

The elapsed time of 10 hr at 1050 psi, by itself, demonstrated compliance with the design goal of a 1.5-safety factor on stress rupture. By using the fin-strength factor of 0.370 and the Hastelloy X 10-hr rupture stress of 43,000 psi, the estimated 10-hr pressure capability of the strut is:

$$p = (0.370)\ (43{,}000)/11.5 = 1385 \text{ psi}$$

Hence the margin of safety above 1050 psi is:

$$M.S. = \frac{1385}{1050} - 1 = 0.32$$

It is concluded that the strut is assuredly adequate for the containment requirements.

A short term test of a strut at room temperature yielded a burst pressure of 5500 psi. Rupture initiated in the fin gap at the inlet manifold. This is again a completely satisfactory result for pressure containment.

8.1.7.1.2 Low-Cycle Fatigue

The test conditions on all three strut specimens, SN 2, configuration No. 2; and SN 5 and SN 6, configuration No. 1, were more severe than those that will be encountered during the SAM test program. The most informative test sequence occurred with SN 5, where the test conditions were somewhat in excess of the predicted Mach 8 flight conditions. The successful achievement

of 102 test cycles without failure compares favorably with the predicted life of 163 cycles for these conditions. More importantly, since the Mach 8 flight considerations should produce slightly lower thermal expansion and average metal temperature at the stagnation line than the SN 5 conditions, the SN 5 test is a good demonstration of strut adequacy for 100 operating cycles and 10 hr operating time. The configuration No. 3 top and bottom panels successfully completed 106 and 41 thermal cycles, respectively. Both strut (finned leading edge) and configuration No. 3 panel designs are considered adequate for use in SAM and have been incorporated as tested.

8.1.7.2 Flow Distribution

Good flow distribution was achieved for the bottom panel configuration No. 3. Mass flux variation was limited to +25 and -20 percent with respect to the overall panel average. Without the manufacturing discrepancies that were present in the test specimen, the design flow distribution is expected.

Of the two strut sidewall cooling designs, configuration No. 2 (Figure 8.1-1) performed well and was adopted for use in the engine. This design split the trailing edge side. The ideal flow distribution is 55 percent to the leading edge side and 45 percent to the trailing edge side. For the selected design, the predicted mis-match is 140°R at the coolant outlet temperature which is a tolerable structural ΔT. The measured coolant pressure drop was 30 percent less than the design allowable pressure drop.

8.1.7.3 Thermal Performance

The test results revealed that the leading edge cooling design of SN 6 configuration No. 1 strut to be inadequate, primarily because the hot gas heat transfer coefficient was 2- and 3-times higher than the normal theoretical stagnation line value. Strut SN 2, configuration No. 2, which incorporated a fin in the cooling passage, showed reduced leading edge stagnation zone wall temperature and was selected for the engine design. The expected peak strut leading edge temperature for the $M_\infty = 8$, 88,000-ft condition is 2625°R, without a fin.

The test also revealed that the slot between the strut doubler and the panel socket must be carefully controlled in order to reduce the strut flange temperature and the panel socket temperature. For a gap size of 0.005 in., the predicted peak socket metal temperature is 1570°R which is within the limits of the design.

The thermal performance of the strut and panels could be satisfactorily analyzed for the conditions of the tests. Calculation of leading edge heating required (1) calculation of the stagnation line heat transfer with the Fay-Riddell equation and application of Lees' theories over the curved portion of the leading edge, and (2) multiplication of the final results by a factor (K), which varied from 1.5 to 3.6 in the tests. The factor (K) is considered to be unique to the test facility used, and in particular, to the tunnel free-stream turbulence as related to the air-oxygen supply turbulence and to the burner characteristics. Knowledge of this factor is essential to estimation of leading edge metal temperatures and, hence, low-cycle fatigue conditions.

8.2 LEADING EDGE STRAIGHT SECTION

This section outlines the procedures and results of tests on Hypersonic Research Engine (HRE) leading edge straight section test specimens to determine (1) thermal performance, (2) thermal cycling performance, and (3) coolant flow distribution.

8.2.1 Purpose and Scope

In order to reduce drag and insure inlet starting over a wide range of Mach numbers in the HRE, a cowl leading edge radius of 0.030 in. was selected as a practical minimum for cooling purposes. Larger radii are aerodynamically marginal for low-Mach-number starting with the inlet configuration now being used. Uncooled surfaces were rejected early in the leading edge design because (1) radiation equilibrium temperatures are at or above the melting temperatures of superalloys at flight Mach numbers of 6 or greater, and (2) the problems of thermal fatigue, attachment to cooled-structure, and oxidation resistance for 100-cycle and 10-hour design life would have made the use of refractory materials unacceptably developmental. The hydrogen-cooled leading edge selected for the design used 0.015-in.-thick Nickel-200 or Hastelloy X tips.

The physical characteristics which control the structural and cooling design of the cowl leading edge are closely related. Low cycle thermal fatigue limits the maximum temperature difference between leading edge stagnation line and adjacent structure. Creep-rupture strength limits maximum temperatures at high coolant pressures needed to obtain adequate cooling. In turn, high coolant pressures are necessary because flow passages must be small to provide high mass fluxes and/or small turning radii for high coolant heat transfer coefficients. The design of a leading edge that is compatible with these structural cooling considerations was evaluated in a test program using two candidate designs.

The objectives of the test program were threefold:

(a) To evaluate the thermal performance of two candidate leading edge tip coolant configurations.

(b) To evaluate the low thermal cycle fatigue and creep rupture performance of the two leading edge coolant configurations.

(c) To evaluate the coolant flow distribution with room temperature air under isothermal conditions and with hydrogen coolant under heat transfer conditions.

8.2.2 Description of Test Specimens

The leading edge straight section test specimens are directly applicable to the flight engine axisymmetric outerbody leading edge. The use of a straight section, instead of a compound-curved section, greatly simplifies the fabrication and testing. The two types of specimens used in the test program, designated configuration No. 1 and configuration No. 2, were previously shown

in Figure 5.5-6. Both types have the same overall dimensions of an 8-in. span, a 4-in., chord and a 26-deg wedge angle. The 8-in. length is approximately equal to 1/7 of the outerbody circumference at the leading edge tip. The features that distinguish the two types of specimens are described below.

8.2.2.1 Configuration No. 1

Configuration No. 1 test specimens had leading edge tip-coolant flows perpendicular to the specimen stagnation line through a 154-deg turn. The tip-coolant also provides coolant to the sides of the specimen. All face sheets, fins, and structure are Hastelloy X. The tip, which is fabricated separately from the sides, has 20 R-.020-.004 plain rectangular fins brazed to the 1/2-in.-length arrowhead piece, and the 0.015-in. V-shaped surface sheet. The side subassemblies consist of 20R-.075-.100(0)-0.006 rectangular offset fins brazed between two 0.015-in.-thick sheets. The sides are brazed to the tip at the arrowhead piece and two outer skin joint covers. Coolant enters and exits from the specimen side fins through manifolds located at the base of the 26-deg wedge (see Figure 5.5-7). The manifolding was selected to simulate the manifolding in the flight engine.

8.2.2.2 Configuration No. 2

Configuration No. 2 test specimens had leading edge tip coolant flows parallel to the stagnation line and separate from the sides coolant flow. The construction details are similar to the configuration No. 1 specimen except at the leading edge tip, where the construction detail shown in Figure 5.5-5 is used. All material is Hastelloy X except the tip outer sheet where Nickel-200 is used. Coolant in specimen sides bypassed the leading edge tip area by flowing through 10 slots (0.035 x 0.70 in.) along the 8-in. specimen length just in back of the tip.

8.2.3 Test Setup

8.2.3.1 Hot Gas Heating Thermal Performance

Hot gas thermal performance testing was conducted in a wind tunnel on two of the configuration No. 1 leading edge straight section test specimens. The test setup was schematically shown previously in Figure 5.5-8.

Subsonic air, heated by a hydrogen/oxygen combustor to temperatures between 2500° and 4000°F, was flowed over the test unit at rates between 2 lb/sec and 6.5 lb/sec. The test unit was cooled with gaseous hydrogen at inlet temperatures between 200° and 520°F, at inlet pressures between 400 psia and 700 psia, and at flow rates between 0.02 lb/sec and 0.12 lb/sec.

8.2.3.2 Radiant Heating Thermal Performance and Cycling

The radiant heating test setup is shown schematically in Figure 8.2-1. The radiant heat source is a single-element quartz lamp and elliptical-reflector combination which concentrates the 360-deg radiation about the lamp

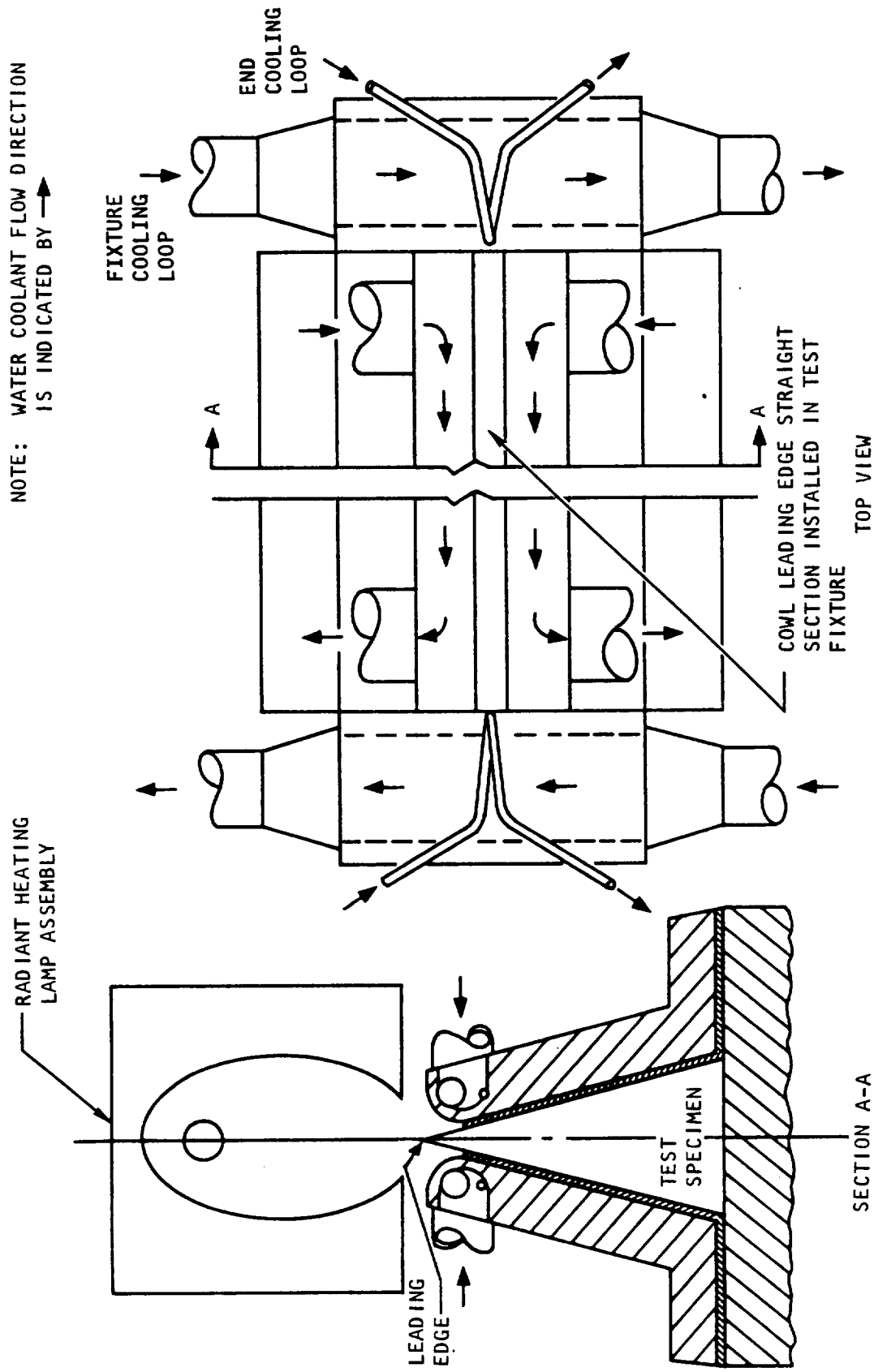

Figure 8.2-1. Leading Edge Straight Section, Radiant Heating Test Fixture Schematic

axis into a discrete focus 0.06- to 0.09-in. wide over the axial length of the lamp. The lamp was electrically controlled to maintain discrete power settings up to 6.5 kw. The lamp assembly was water-cooled, and the coolant ΔT, flow rate, and input electrical power were measured.

The sides of the test specimen were protected by a water-cooled aluminum fixture, which leaves only the leading edge stagnation area exposed. Cooling of the test specimens during test was accomplished with either ambient temperature air or water at 700 psia. The flow rates of the air and water were adjusted to yield the desired temperature differences between the external surfaces of the stagnation line and the internal structure.

The configuration No. 2 specimens were used for leading edge tip thermal performance testing and then for thermal cycle testing in the radiant heating test setup. The configuration No. 1 specimens were used for thermal performance testing only. Water was used as the coolant during preliminary checkout tests for configuration No. 2 specimens, and air was used as the coolant for both configurations thereafter.

8.2.3.3 Coolant Flow Distribution

Flow distribution tests were conducted on configuration No. 1. Tests were conducted using hydrogen coolant with heat transfer, and also isothermal air. Tests with hydrogen were conducted simultaneously with hot gas thermal performance tests. The important features of both test setups relative to flow distribution are measurement of total flow, inlet and outlet pressures and temperatures, and inlet and outlet manifold pressure distributions. In the isothermal air tests, six pressure taps were used in each manifold; in the hydrogen tests, three pressure taps were used in each manifold. The significant parameter of maximum-to-minimum flow ratio could be deduced from all sets of data, as the maximum and minimum manifold pressures were monitored continuously.

8.2.4 Test Procedures

8.2.4.1 Thermal Performance Tests

For configuration No. 1, the coolant fluid approaches perpendicular to the leading edge and then makes a sharp 154-deg turn. The sharp turn at the tip causes the flow to separate and makes knowledge of the effective flow uncertain. Thus, experimental evaluation of the stagnation region cooling design was necessary. A configuration No. 1 specimen made of Hastelloy X was subjected to a simulated flight-heating environment consisting of subsonic air, heated by a hydrogen/oxygen combustor, flowing over the test section. The test section was cooled with gaseous hydrogen. Hydrogen heat transfer coefficients on the inside surface of the stagnation region, and metal temperatures on the sides of the test specimen were calculated from experimental measurements and conditions. Configuration No. 2, which has leading edge coolant flow parallel to the stagnation line in a key-shaped passage, was subjected to a heating environment consisting of a radiant heat source (single-element quartz lamp and elliptical reflector) impinging on a discrete 0.06- to 0.09-in. width along the 8-in. length of the specimen stagnation line. The test section was

cooled with room temperature inlet air. Air heat transfer coefficients on the inside surface of the stagnation line were calculated from experimental measurements and conditions. Configuration No. 2 is also made of Hastelloy X but has a 0.015-in.-thick Nickel-200 outer shell at the leading edge tip.

Although two stagnation-line cooling configurations were tested, configuration No. 1 had the greatest uncertainty in coolant heat transfer coefficient prediction. For configuration No. 2, with hydrogen flow parallel to the leading edge in a tube of complex cross section, the coolant heat transfer coefficient could be predicted with greater confidence.

8.2.4.2 Thermal Cycling Tests

The same radiant heat source that was used for thermal performance tests of the configuration No. 2 specimen was used for thermal cycling tests. With air-cooling in both configurations, radiant heat was applied to the leading edge tip so that the leading edge temperature was increased from room temperature to between 1400° and 1800°F and back to room temperature in a 5-min cycle. This cyclic heating pattern was continued until the specimens failed. Evaluation was based on examination of photomacrographs and photomicrographs of the crack locations.

8.2.4.3 Coolant Flow Distribution Tests

The inlet and outlet manifolding is similar to that on the flightweight engine. Several static pressure taps were located along the inlet and outlet manifolds of the 8-in.-long specimen. The ratio of the local core-flow rate to the average core-flow rate along the length of the specimen was calculated from the measured pressure data.

8.2.5 Test Results

8.2.5.1 Hot Gas Heating Thermal Performance Tests

From the hot gas data for configuration No. 1, the internal cooling coefficient at the leading edge tip in terms of Nusselt number vs Reynolds number was calculated, based on stagnation line heat flux and the measured stagnation surface temperatures. The conversion of thermocouple readings to stagnation surface temperatures was based on a three-dimensional conduction model in the vicinity of the thermocouple junction. The leading edge heat flux was calculated by the theory of Reference 5.5-1 with the velocity gradient based on potential flow theory. Based on the data of Kestin (Reference 8.1-2), the heating coefficient was increased by 10 percent to account for turbulence. The experimentally determined coolant heat transfer coefficients at the stagnation line are equal to about four-times the heat transfer coefficient in the adjacent plain-fin passage at the design Reynold number of 30,000, as shown in Figure 8.2-2. A value of 1.94-times the straight-pipe coefficient at a Reynolds number of 30,000 was used for coolant analysis of the original flight engine leading edge. This increase in coolant coefficient is in fair agreement with the empirical relation of Reference 5.5-2 which predicts the heat transfer coefficient for multiple jets impinging on the inner surface of simulated turbine blade leading edges.

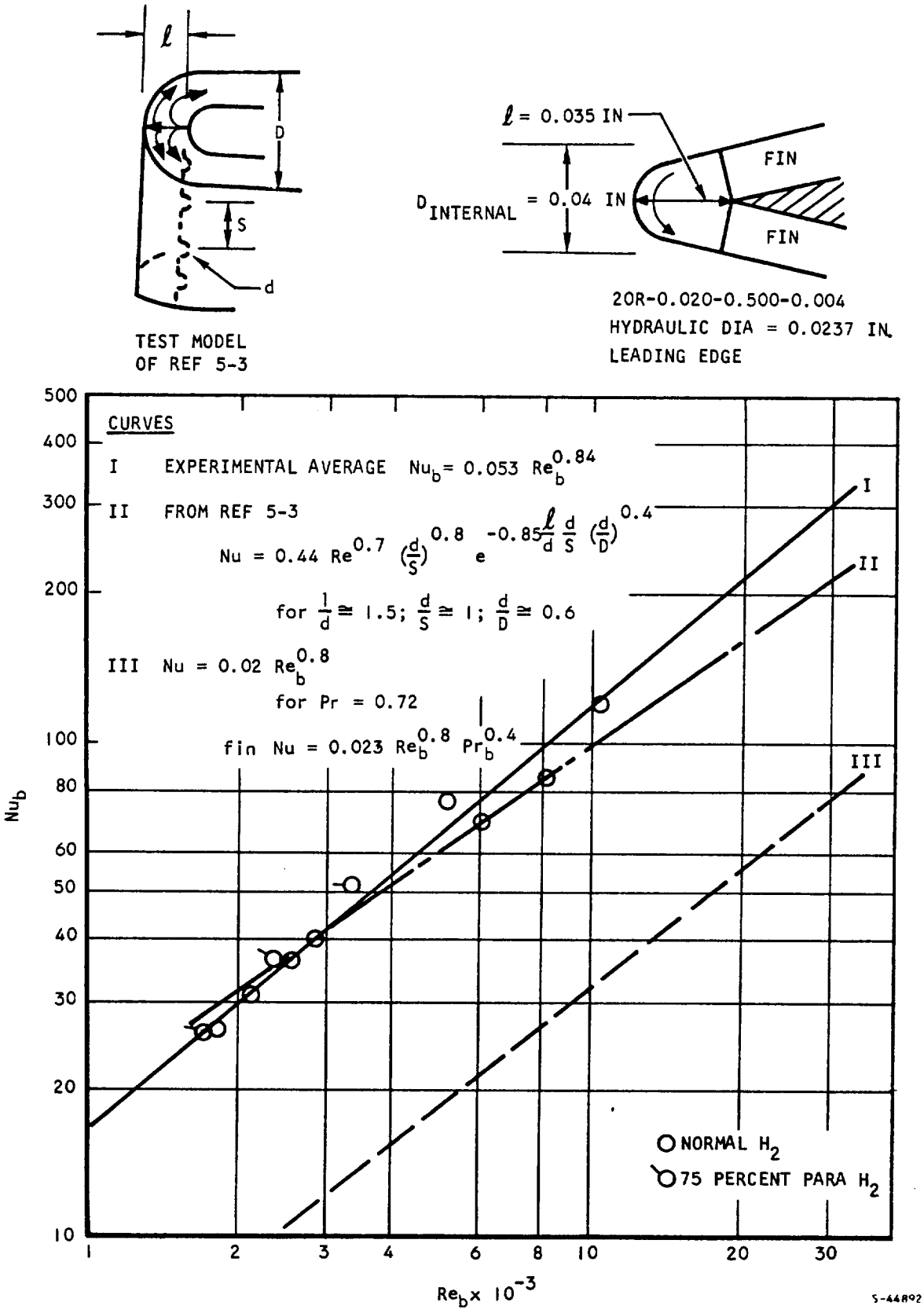

Figure 8.2-2. Cowl Leading Edge Internal Cooling Nusselt Number

8.2.5.2 Radiant Heating Thermal Performance Tests

On the radiant heating thermal performance tests, conducted on configuration No. 2 specimens, the internal cooling coefficient in the leading edge tip passage was calculated in terms of Stanton number vs Reynolds number from a heat balance on the air in the leading edge passage, and measured-metal temperatures in the stagnation region. The radiant heat input was assumed to occur in the 180-deg arc centered on the stagnation line. The remainder of the coolant passage was assumed to act as a fin which rejected heat to the air in the leading edge passage, and to the water-cooled aluminum test fixture. There was no airflow in the side fin passages just in back of the parallel-flow leading edge passage. Good agreement in coolant heat transfer was obtained between the average of the test data and the standard pipe-flow relation for plain rectangular tubes, when a suitable adjustment is made for unsymmetrical heating as shown in Figure 8.2-3.

8.2.5.3 Thermal Cycling Tests

Radiant heating thermal cycling tests conducted on configuration No. 1 specimens using room temperature inlet air coolant in the sides and perpendicular-flow leading edge tip passage; those conducted on configuration No. 2 specimens used room temperature inlet air coolant in the parallel-flow leading edge tip passage only. Radiant heat was applied to the leading edge tip so that the tip temperature was increased from room temperature to between 1400° and 1800°F and back to room temperature in a 5-min cycle. This cyclic heating pattern was continued until the specimens failed. Evaluation was based on examination of photomacrographs and photomicrographs of the crack locations. Configuration No. 1 specimens (Hastelloy X tip) failed at 110 and 200 cycles. Configuration No. 2 specimens (Nickel-200 tip) failed in the range of 40 to 260 cycles. Failure was defined as a large increase in pressure decay from an initial pressure of 700 psia during a 1-min period with the test unit isolated from the rest of the system.

8.2.5.3.1 Test Data

Thermal cycle test data is illustrated in Figure 8.2-4 where typical thermal cycles for two Hastelloy X units (SN's 4 and 5), and three Nickel-200 units (SN's 1, 2, and 5) are shown. The plotted cycle for Hastelloy X units SN 4 and SN 5, and also for the nickel unit SN 1 was just before failure as noted. Failure was defined as a large increase in pressure decay from an initial pressure of 700 psia during a 1-min period. The range of maximum temperatures during all cycles, and the average maximum temperature during all cycles is noted for each unit. Generally, the cracks occurred at the location of a thermocouple where heat input was maximum and where a local strain concentration occurs. In the Nickel-200 units SN 1 and SN 5, this was not the case. The crack in SN 1 occurred in a hotter zone about one inch away from the thermocouple plotted. The dashed line indicates the average maximum at this crack of about 1630°F. Nickel-200 unit SN 5 survived 260 cycles, and the maximum temperature for various groups of cycles is listed in Figure 8.2-4 (the test was terminated after 280 cycles).

$$St_{LE} = \frac{h}{GC_p} = \frac{(Q_{LE}/Q_{TOT})(WC_p)(T_2 - T_1)A_F}{A_{LE}(T_{LE} - 0.5T_1 - 0.5T_2)(WC_p)}$$

$$St_{LE} = \frac{(Q_{LE}/Q_{TOT})(T_2 - T_1)(6.2 \times 10^{-3})}{4.36 \times 10^{-3}(T_{LE} - 0.5T_1 - 0.5T_2)}$$

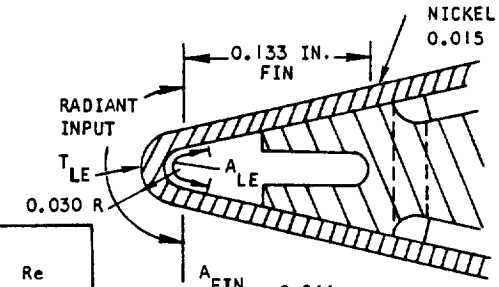

h_{AVG} BTU/SEC-°R-FT²	$\frac{Q_{LE}}{Q_{TOT}}$	$\frac{(q/A)_{LE}}{(q/A)_{AVG}} = \frac{T_{LE} - 0.5T_1 - 0.5T_2}{T_{WAVG} - 0.5T_1 - 0.5T_2}$	Re
0.02	0.288	1.12	7,500
0.04	0.316	1.24	18,000
0.08	0.367	1.44	45,000
0.16	0.444	1.73	110,000

$$\frac{A_{FIN}}{A} = 0.866$$

$$\frac{A_{LE}}{A} = 0.256$$

$$A = 0.00191 \text{ FT}^2$$

$$h_{AVG} = \frac{0.019\ WC_p}{(Re)^{0.2}(Pr)^{2/3}(T_{WAVG}/(0.5\ T_1 + 0.5T_2)^{0.37}}$$

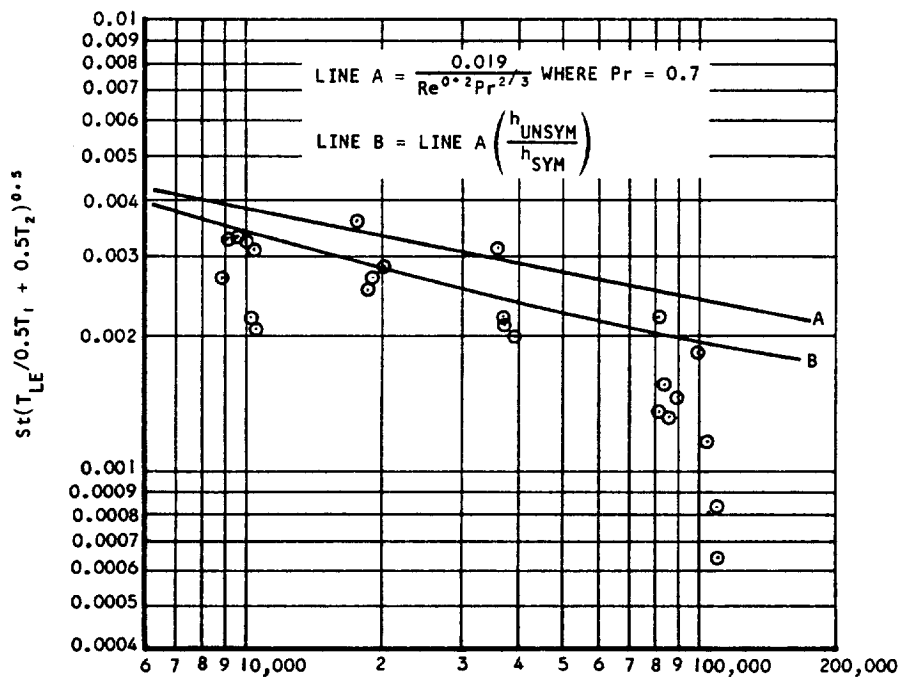

5-49816

Figure 8.2-3. Cooling of Leading Edge With Parallel Flow

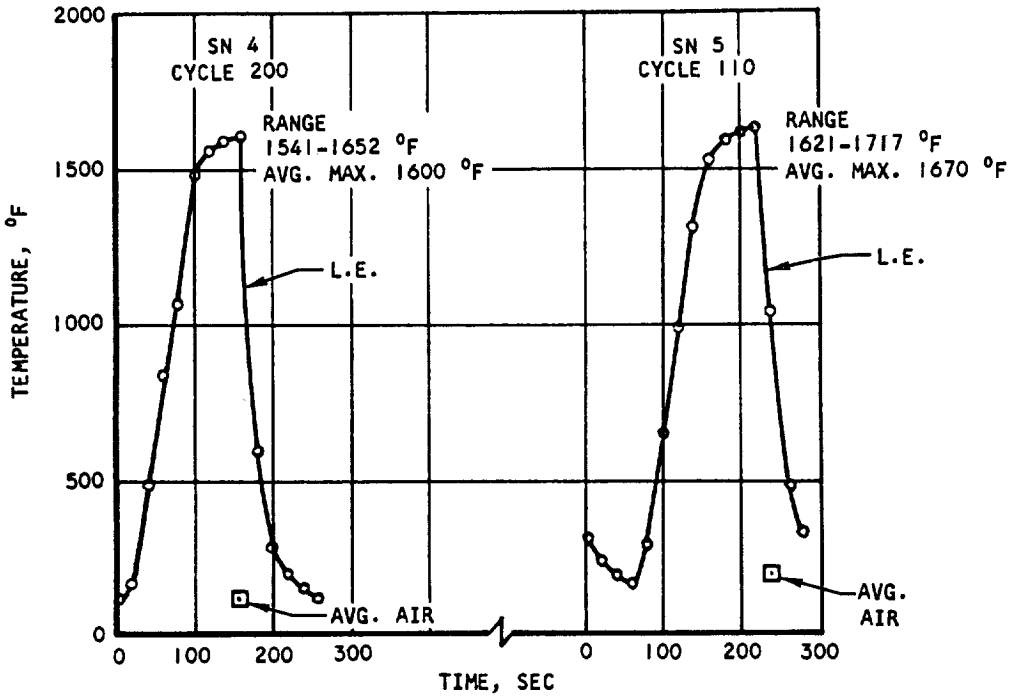

a. HASTELLOY X PERPENDICULAR FLOW (CONFIGURATION NO. 1)

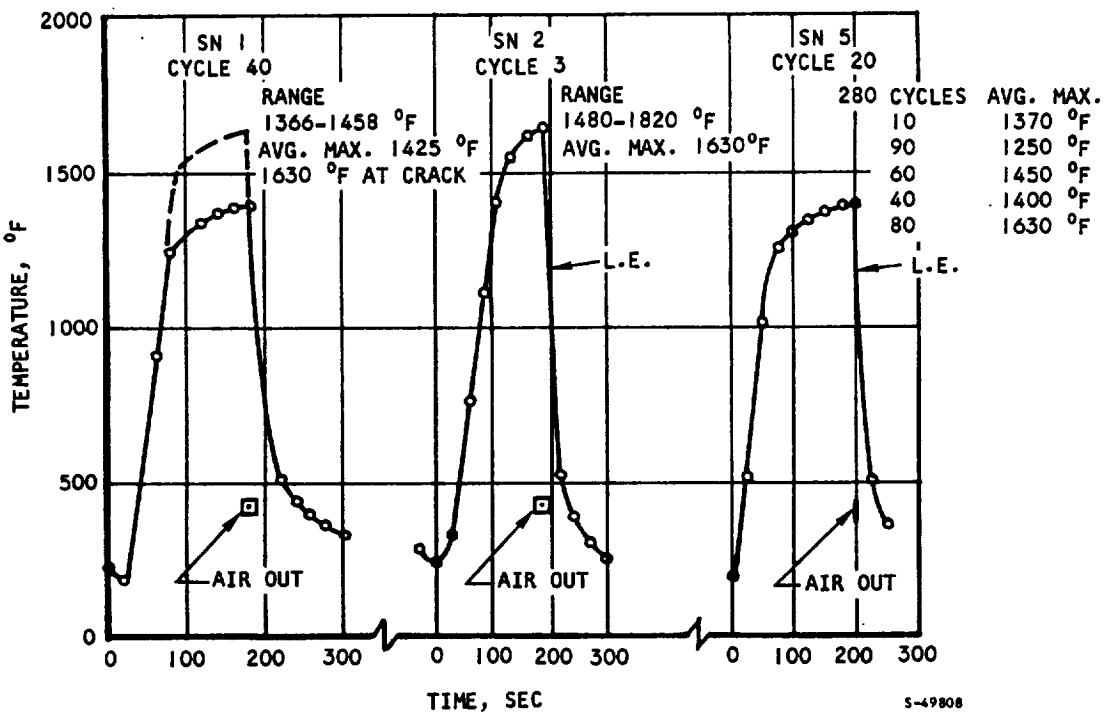

b. NICKEL-200 PARALLEL FLOW (CONFIGURATION NO. 2)

Figure 8.2-4. Leading Edge Thermal Cycles

The two Hastelloy X specimens were thermally cycled to approximately 1600° to 1700°F maximum metal temperatures. Because the Hastelloy X creep strength is quite high at this temperature, cumulative creep strain was a relatively small cause of cracking, and low-cycle fatigue due to plastic cycling was substantially the reason for failure. Specimen SN 5 was sectioned for metallurgical investigation after the testing. The failure crack was at the very tip of the leading edge, parallel to the coolant flow direction, and an excellent example of low cycle fatigue failure. The failure crack was transgranular rather than intergranular as in the Nickel-200 specimens, further evidence that the failure was due to plastic cycling.

The three Nickel-200 specimens were closely studied after the tests were concluded. Specimen SN 2 was tested first, and this unit was subjected to extensive creep damage as a result of test cycles up to 1800°F with 700 psi coolant pressure. This specimen developed a bulged region extending from the tip back to the brazed joint between the Nickel-200 tip and Hastelloy X basic structure. The brazed joint was separated slightly due to incomplete brazing and apparently opened up, but did not crack. Cracks in the Nickel-200 tip were intergranular, typical for failure at high temperatures where grain boundaries are weaker than grains. The Nickel-200 grain size was large (about 0.010-in. grains) due to brazing at 2150°F.

The second Nickel-200 specimen to be tested was SN 5. Thermal cycling tests to a nominal 1400°F maximum tip temperature and 700 psig pressure produced failure after 260 to 270 cycles and in approximately 8-1/2 hr cumulative creep time. Almost all of the cracks that were developed were of the creep-type appearance on the side of the tip.

The third and last Nickel-200 specimen to be tested was SN 1. After approximately 40 thermal cycles, several leaks developed in two areas on the tip. Both cracks appeared to be basically due to creep. This unit had been subjected to 1435° to 1450°F for 15 min at 700 psig for thermocouple calibration testing. This may have been a factor leading to failure in fewer thermal test cycles than for SN 5 (40 cycles vs 260 cycles) at similar test conditions. Scatter in Nickel-200 material properties at this test temperature also could have accounted for the significant difference in cycles-to-failure.

8.2.5.3.2 Stress Analysis Summary

The data reduction for the three configuration No. 2 Nickel-200 test specimens required the utilization of fatigue test results on solid nickel bars and plate-fin test bars that have been performed during the course of this program. The test results of the two configuration No. 1 Hastelloy X leading edge test units were analyzed by employing test data from a low-cycle fatigue experimental program carried out under NASA Contract No. NAS1-5002. Table 8.2-1 illustrates the data reduction used to calculate damage fractions.

For the three configuration No. 2 Nickel-200 specimens, the coolant flow passes through the leading edge only and is parallel to the leading edge. Coolant does not flow through the portion of the test piece away from the leading edge, but this region is shielded from heating by an external, water-cooled shroud. The bulk of the structure, therefore, essentially remains at

TABLE 8.2-1

CONFIGURATION NO. 2, SN 5 DATA REDUCTION

(a) THERMAL CONDITIONS

Cycle No.	Total No. of Test Cycles	Highest Cycle Temp, °F	Lowest Cycle Temp, °F	Test Cycle ΔT, °F
0-10	10	1370	300	1070
11-100	90	1250	300	950
101-160	60	1450	300	1150
161-200	40	1400	300	1100
201-260	60	1630	300	1330

(b) CREEP AND FATIGUE DAMAGE SUMMARY

Cycle No.	Estimated Creep Life at Highest Temp, hr	Thermal Expansion Range, $\alpha\Delta T$	Plastic Strain Range, ϵp	Low Cycle Fatigue Life	Fatigue Damage Fraction	Creep Damage Fraction
0-10	800	0.0097	0.0090	800	0.0125	0.0004
11-100	>1000	0.0085	0.0078	1000	0.0900	0.0
101-160	175	0.0105	0.0096	700	0.0860	0.114
161-200	500	0.0100	0.0092	750	0.0530	0.013
201-260	5	0.0126	0.0116	567	0.1058	0.400
TOTAL LIFE FRACTION DAMAGE					0.347	0.527

Σ FATIGUE + CREEP = 0.87

room temperature during the course of the test. As a result, the locally heated stagnation area of the leading edge test piece will be fully constrained from free thermal expansion. The fact that heavy end-plates are employed in the test piece further restricts the heated leading edge from free expansion.

The two configuration No. 1 Hastelloy X test pieces utilize a coolant-flow direction perpendicular to the leading edge stagnation line. The coolant is introduced along one lengthwise edge at the rear of the test unit and exhausts along the other lengthwise edge. The major part of the test piece away from the stagnation line area will be at an average temperature between the coolant inlet and outlet temperatures. Similar to the configuration No. 2 nickel leading edge test specimens, this bulk of material does not change in temperature appreciably during the thermal cycling and it will prevent any free thermal expansion of the heated stagnation area.

8.2.5.3.2.1 Hastelloy X Results

First Test, SN 5--This unit survived 100 cycles of thermal fatigue testing, with estimated maximum cycle temperatures ranging from 1620° to 1717°F and an average maximum of 1670°F. With an average cooling air temperature of 200°F, the average value of thermal expansion cyclic range was an $\alpha\Delta T$ of 0.0140 in./in. Based on the tests of solid Hastelloy X test specimens, the fatigue life with this applied total strain range was estimated as 190 cycles.

The test pressure of 700 psi caused a containment stress of approximately 1000 psi. Based upon a Hastelloy X stress rupture life at this temperature of well in excess of 1000 hr, the creep damage fraction was not of any consequence. The test panel work was performed on Hastelloy X bars in the as-received condition. The material in the leading edge test piece had been exposed to brazing temperature and alloying. These effects could well have accounted for the reduced test life as compared to the computed life.

Second Test, SN 4--This unit was subjected to a total of 200 thermal fatigue cycles, with a maximum cycle temperature ranging from 1541° to 1652°F, and an average maximum value of approximately 1600°F. As in SN 5, the effects of creep damage were negligible. The lowered maximum temperature would have led to a computed life of 200 cycles, or a figure that is in excellent agreement with the previous solid-bar fatigue test work.

8.2.5.3.2.2 Nickel-200 Results

First Test, SN 2--This unit was cooled with ambient air at 700 psia pressure in order to approximate operating pressures, and therefore, actual containment conditions. The flow rate was adjusted to produce the desired test temperature differences between the most highly heated metal area at the stagnation line and the remainder of the total structure. Prior to the initiation of the thermal-cycling sequence,

the unit was subjected to a number of performance cycles. Since these cycles contributed to both thermal fatigue and creep rupture damage of the test piece, this data has been included in the test data reduction of life performance. A total of 25 such cycles occurred.

Of the 25 performance runs carried out, peak stagnation line temperatures ranged from 250° to 1820°F and cyclic ΔT's ranged from 130° to 1610°F. The test unit was held at these temperatures for 10 min during each cycle. During seven cycles, the maximum metal temperature was less than 1000°F and the ΔT's were less than 770°F. The cumulative creep and low cycle fatigue damage fractions were found to be negligible for these cycles. Of the remaining 18 cycles, the maximum metal temperature fell within the range from 1480° to 1630°F, with ΔT's ranging from 1260° to 1410°F in 13 of the cycles. The estimated creep damage fraction for these 13 cycles was less than 0.200, while the cyclic fatigue damage fraction was less than 0.025. In the remaining five cycles, the peak temperatures were 1675°F, 1690°F, 1710°F, 1785°F, and 1825°F respectively. The ΔT's ranged from 1450° to 1610°F. The low-cycle fatigue damage fraction was less than 0.010 for these five cycles, but the creep damage fraction was approximately 0.895. The cumulative sum of the damages from these 25 test cycles was actually in excess of 1.0, which means that the test unit failure was largely attributed to this sequence of tests with the bulk of the damage being due to creep effects.

Following the performance runs, ten additional checkout cycles were imposed upon the test unit of approximately two minutes duration, each with a maximum metal temperature of 1550°F and a cyclic ΔT of 1330°F. The combined creep and cycle fatigue damage fraction was computed to be approximately 0.06 for these cycles.

Finally, the unit was subjected to a total of 40 rapid thermal fatigue cycles. The maximum metal temperature in these cycles was 1550° to 1600°F and the test time at peak temperature was one minute. Actual unit failure at the time of increased leakage occurred after 20 cycles. The accumulated creep damage fraction was 0.042 and the low cycle fatigue damage fraction was 0.035 for these 20 cycles. Hence, these cycles contributed a damage fraction of less than 0.080 towards the failure life of the test unit.

The high metal temperatures during the performance runs were responsible for the relatively short cycle life of the test unit. Once creep was taken into account, as indicated above, the correlation between life of the leading edge unit and the analysis results cited are in good agreement.

Second Test, SN 5--The cycles run and the details of the low cycle fatigue and creep calculations are displayed in Table 8.2-1. The test had no unusual features.

Third Test, SN 1--Data analysis for this unit directly follows that for the SN 5 unit, except for the lower life.

8.2.5.4 Coolant Flow Distribution Tests

Flow distribution tests were conducted on two configuration No. 1 specimens using isothermal air and hydrogen with heat transfer. Extrapolation of test results to full-scale leading edge geometry and hydrogen conditions indicated an acceptable range of maximum-to-minimum flow ratio of 1.01 to 1.03.

The test results are summarized in Figure 8.2-5 for air in SN 4 and SN 5, and hydrogen in SN 4. The flow will be uniform (max W/min W = 1) for core ΔP/overall ΔP = 1.0 and inlet manifold ΔP/core ΔP = 0. The air data for SN's 4 and 5 are in good agreement, showing repeatable test unit geometry and use of the test setup. The three hydrogen data points for SN 4 are averages of five points each. The data scatter was large because three local hydrogen pressures were measured separately in each manifold whereas, for air tests, the difference between one reference manifold pressure and the other five were measured in each manifold. Good agreement (as expected) was obtained between hydrogen and air tests because the tests are all in the Reynolds number regime above 1400, based on the 20R-0.075.100-0.004 Hastelloy X fin hydraulic radius of 0.01396 in. and most of the pressure drop is due to turns and area changes.

8.2.6 Conclusions

Two leading edge straight section configurations were designed and tested to determine the feasibility for flight engine leading edge cooling, coolant flow distribution, and low-cycle thermal fatigue and creep rupture performance. Based on test results, the following conclusions were drawn.

8.2.6.1 Thermal Performance

The cooling coefficient for coolant flow perpendicular to leading edge stagnation line (configuration No. 1) is 3.9-times that for a straight duct at the Mach 8 local design Reynolds number of 30,000. This is twice the value of 1.94-times the straight-duct coefficient at a Reynolds number of 30,000 used for the original flight engine leading edge cooling analysis.

The cooling coefficient for coolant flow parallel to the leading edge stagnation line (configuration No. 2) is in reasonable agreement with predicted coefficients for plain rectangular tubes when a suitable adjustment is made for unsymmetrical heating.

8.2.6.2 Thermal Cycling

Once the creep effects of high temperature are distinguished in Nickel-200 tests, it is evident that even for the same ΔT magnitude, the fatigue life of Nickel-200 is better than that obtainable with Hastelloy X for this leading edge application. For the Nickel-200 configuration, the Mach 8 operating conditions would lead to the following temperatures:

Temp at L.E. Stagnation Line = 1620°R (1160°F)

Coolant Temp = 160°R (-300°F)

$\alpha\Delta T$ = 0.01160

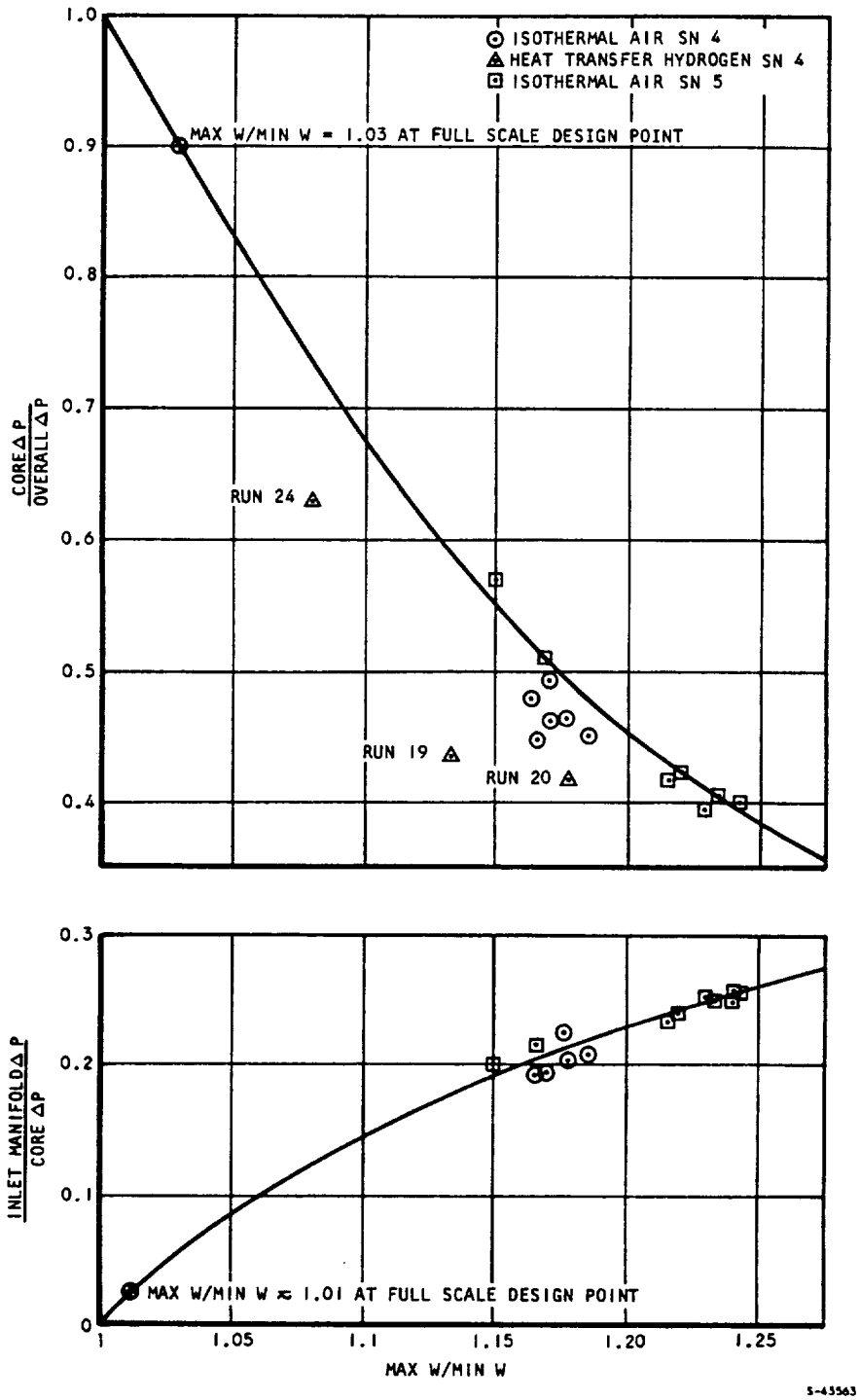

Figure 8.2-5. Leading Edge Straight Section Flow Ratio

Thermal fatigue failure, based upon the Nickel-200 data, would occur after approximately 690 cycles of operation. Creep effects would have a moderate influence on total life. Containment of 700 psi coolant at 1160°F would cause creep rupture of the leading edge in 60 hr. By using the total damage fraction analysis, the creep life fraction of 10 hr of sustained usage would exhaust a damage fraction of 0.167, leaving a life fraction of 0.833 for low-cycle fatigue. This would produce a reduction from 690 to 575 cycles.

This prediction is consistent with the test results for SN 5, which indicated a cycle life in excess of 550 cycles for similar ΔT's, but higher temperatures and somewhat longer time exposure to containment (18 hr). Also, it can be concluded that the Hastelloy X unit showed a lower cycle life (110 to 200 cycles), and the Nickel-200 is the better design choice for this application in terms of low-cycle fatigue life.

8.2.6.3 Coolant Flow Distribution

The conclusion of flow distribution tests performed on configuration No. 1 leading edge straight sections are:

(a) The flow is always highest at the end of the core farthest from the inlet because the inlet manifold static pressure increases with distance from the inlet port, and the outlet manifold static pressure is almost uniform.

(b) Hydrogen and air data, as well as data for different units of the same geometry, are in good agreement.

(c) Extrapolation of test results to full-scale leading edge geometry and hydrogen-conditions indicates an acceptable range of maximum-to-minimum flow ratio of about 1.01 to 1.03

8.3 FLAT PANELS

Flat panels were used to evaluate the effects of braze alloy foil thickness, brazing cycle time, and fin material thickness on the structural strength of the cooled structure. Their use permitted close control of all variables in order to accurately evaluate specific variables affecting the strength of the cooled structure.

The design of the panels was modified slightly to adapt them to the specific types of tests performed. The sections below describe the specimens, various tests performed, and conclusions drawn from them.

8.3.1 Burst and Stress Rupture

8.3.1.1 Specimens

The detail parts for a typical flat panel specimen for burst or creep rupture testing are shown in Figure 8.3-1. This 2 in. by 3 in. panel, with

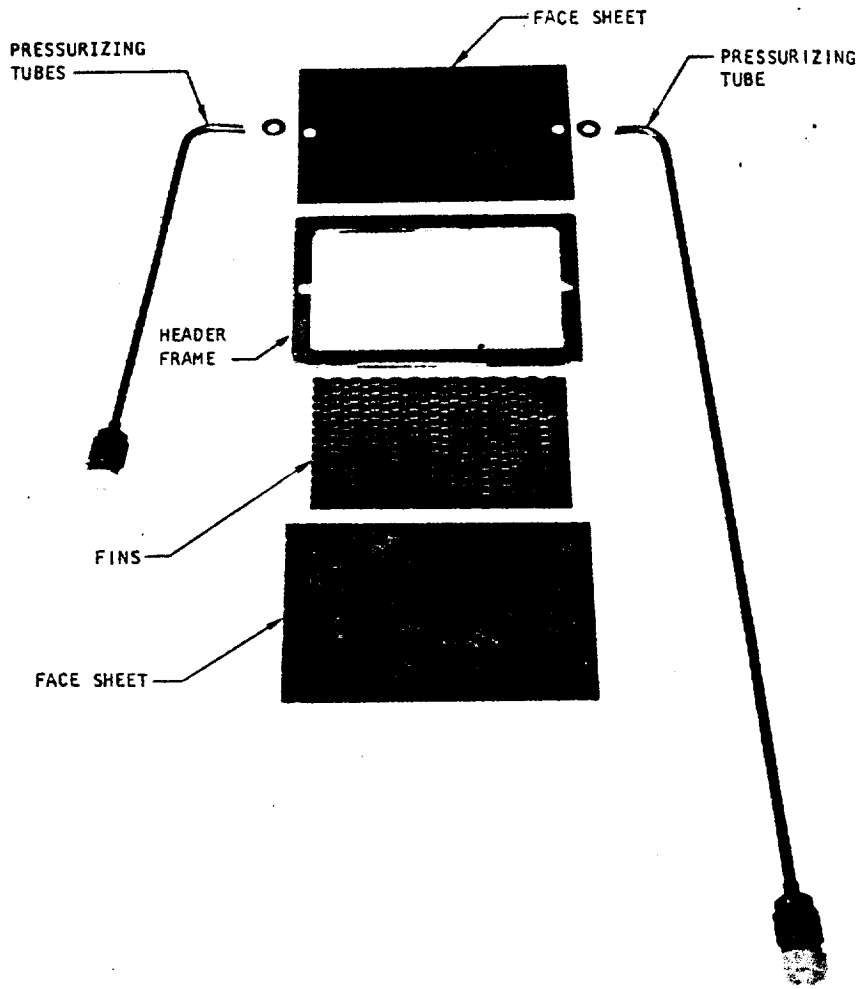

Figure 8.3-1. Detail Components of Basic Static Test Flat Panel

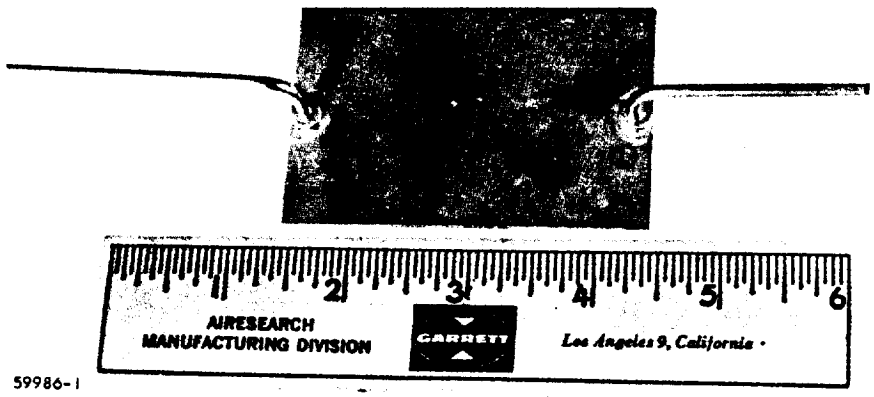

Figure 8.3-2. Basic Flat Panel Configuration

a series of various fin configurations, braze alloy thicknesses, and face sheet materials was fabricated to produce specimens as shown by Figure 8.3-2. Modifications of this panel incorporating local inserts to simulate pressure taps, thermocouples, and fuel injectors were fabricated to look like Figure 8.3-3. In addition, a modification of the panel, illustrated by Figure 8.3-4, was fabricated to permit evaluation of the continuous fin gap required under exhaust manifolds.

The manufacturing sequence was the same for all panels, first brazing the assembly of face sheets, headers and fins with Palniro 4 or Palniro 1, followed by a proof-pressure test; then machining the assembly to accommodate addition of inserts or special manifolds, and brazing of these with a lower melting point alloy, Palniro 7 or Palniro 1.

8.3.1.2 Test Setup and Procedure

Test panels were instrumented to measure panel temperature and pressure and installed in one of the Marshall muffle furnaces shown in Figure 8.3-5 for elevated temperature burst tests, or in a water tank for ambient temperature tests. Pressure was applied and slowly and continuously increased until failure by rupture or deformation occurred.

Panel instrumentation and test setup for the creep rupture tests were the same as used for the short term burst elevated temperature tests. Test panels were installed in the furnace, the temperature was then raised to bring the test specimen to specified temperature in approximately one-half hour, specified pressure was then applied, and both temperature and pressure held at specified values until failure occurred.

8.3.1.3 Test Results - Basic Panels

The following variables were evaluated during the flat panel burst and creep rupture program.

Braze alloy thickness - 0.0005, 0.001, and 0.0013 in.

Fin thickness - 0.001, 0.004, and 0.006 in.

Time at brazing temperature - 5, 10, and 20 min.

Table 8.3-1 summarizes the significant test conditions, and the calculated average fin efficiency factor exhibited during the tests. This factor is the ratio of the stress in the fins (burst or rupture pressure divided by the unit fin cross-section area) and the published ultimate tensile stress or rupture stress corresponding to the time and temperature of the test.

The results indicate that a fin efficiency factor of 0.33 on creep rupture strength and 0.50 on short-time ultimate strength is reasonable for the Hastelloy X fins.

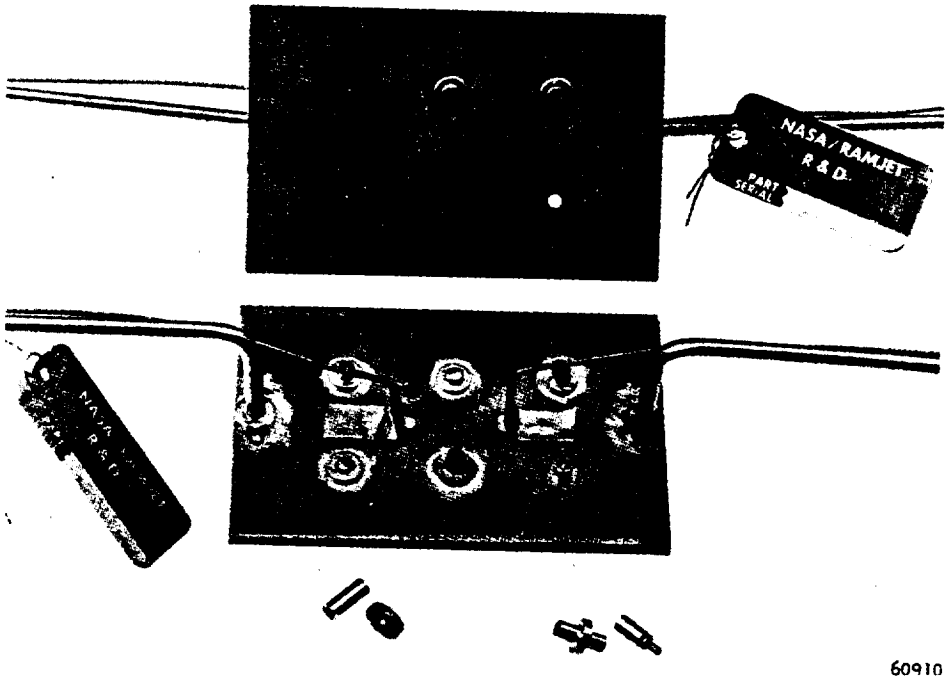

Figure 8.3-3. Static Test Local Joint Flat Panel

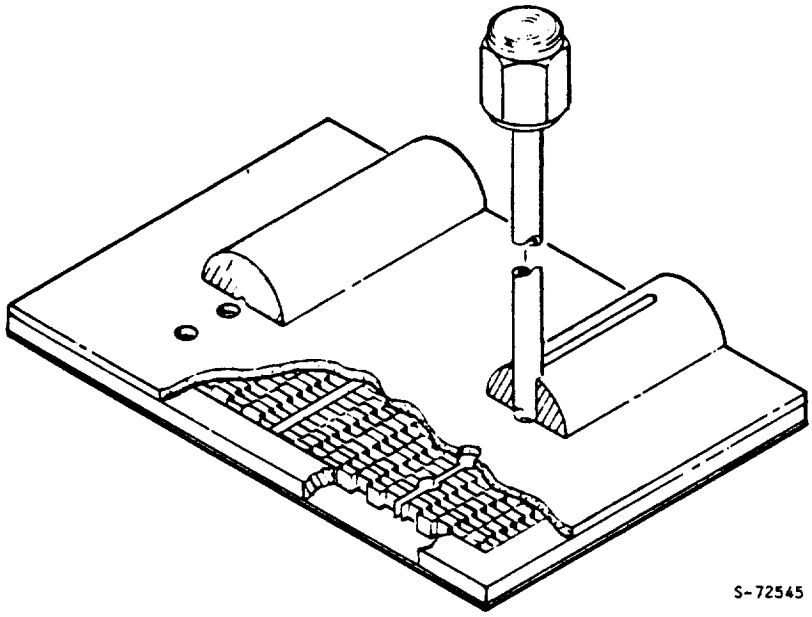

Figure 8.3-4. Coolant Exhaust Continuous-Gap Flat Panel

F-15282

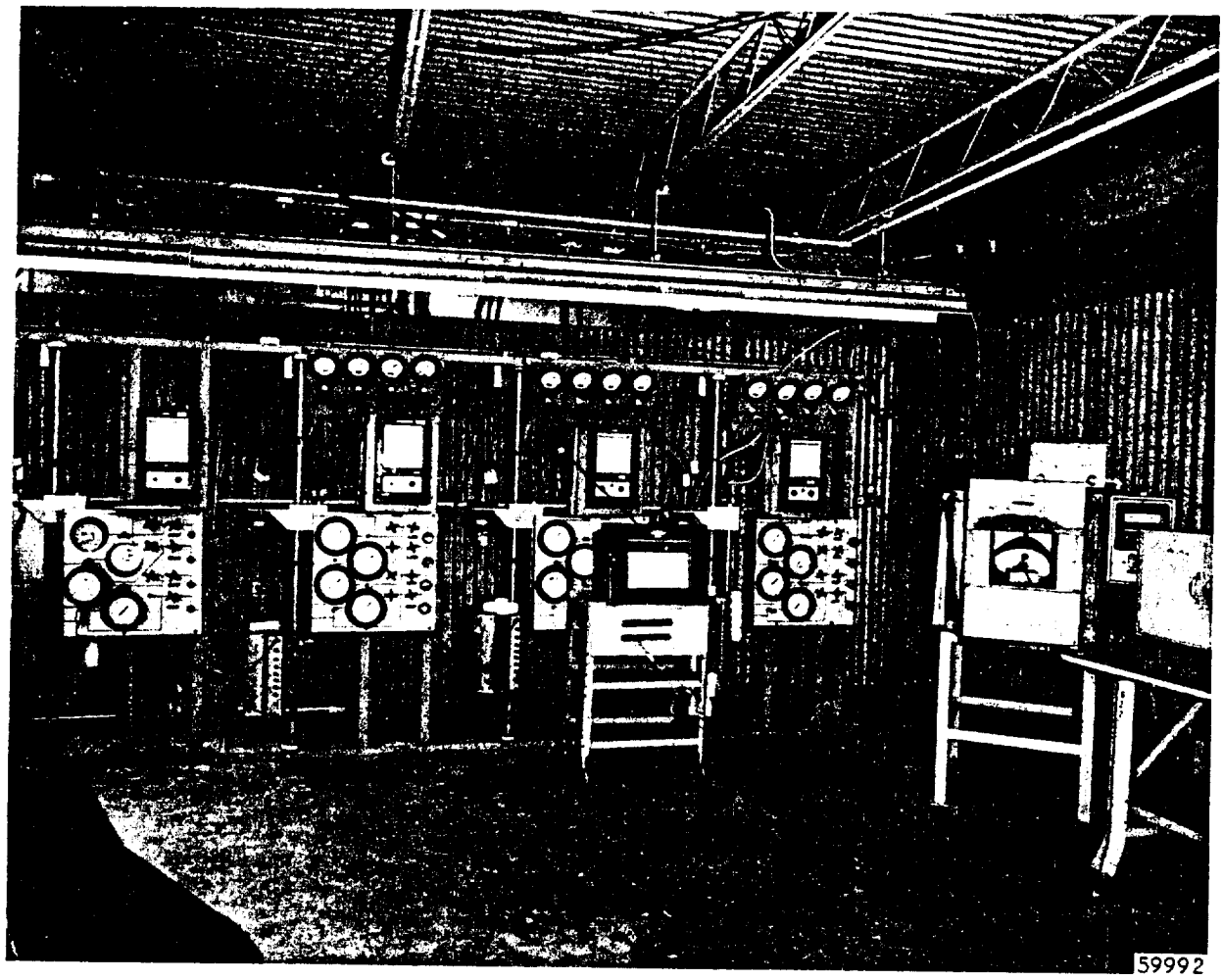

Figure 8.3-5. Regenerative-Cooled Panels High Temperature Test Facility

TABLE 8.3-1

HRE FLAT PANELS TEST SUMMARY

I. Burst Tests

Fin Configuration	Braze Alloy Thickness, in.	Cond. Time at Temp, min.	Test Temp, °F	Burst Pressure Range, psig	No. of Tests	Fin Efficiency Factor
34R-.025-.050-.002	0.001	5	1500	3250-3650	2	0.91
	0.001	20	1500	2125	1	0.56
	0.0005	20	1500	1400	1	0.37
	0.0005	5	1500	2475-2575	2	0.68
20R-.075-.100-.004	0.001	5	1600	2375-2680	2	0.80
	0.001	20	1600	1675-2075	2	0.59
16R-.153-.100-.006	0.001	5	1600	2125	1	0.55
	0.001	5	RT	7300-7400	2	0.61
	0.001	5	1200	3600-3750	3	0.41
	0.001	20	1600	1610-1700	3	0.43
	0.001	10	1600	1475-1575	3	0.39
*28R-.050-.100-.006	0.0013	5	RT	1800-2200	2	0.087

II. Creep Rupture Tests

Fin Configuration	Braze Alloy Thickness, in.	Cond. Time at Temp, min.	Test Temp, °F	Creep Rupture		No. of Tests	Fin Efficiency Factor
				Pressure Range, psi	Time Range hr:min		
34R-.025-.050-.002	0.001	5	1500	750-850	4:41 - 6:24	2	0.47
	0.0005	5	1500	700-750	10:36 - 6:46	2	0.46
20R-.075-.100-.004	0.001	5	1600	650-780	5:14 - 3:21	3	0.45
	0.001	20	1600	500-600	2:46 - 4:26	3	0.36
16R-.153-.100-.006	0.001	20	1600	550-700	10:46 - 1:00 approx.	3	0.34
	0.001	10	1600	550-700	10:00 - 5:17	4	0.35
20R-.050-.100-.006	0.0013	5	1600	700-800	17:12 - 14:06	3	0.42
28R-.050-.100-.006	0.0013	5	1600	950-1050	18:0 - 10:42	3	0.37
*28R-.050-.100-.006	0.0013	5	1500	1000	12:0 - 0:18	4	0.20

S-72520

*Nickel-200 Face Sheets

8.3.1.4 Test Results - Local Joint Flat Panels

Seven local joint flat panel specimens were tested. Four of the assemblies contained 0.002-in.-thick fins and three were fabricated with 0.004-in.-thick fins. All of the units incorporated eight inserts representing four different diameters and geometric configurations. (Ref. Figure 8.3-3.)

Table 8.3-2 lists the details of the test specimens, conditions and results including fin-efficiency factor. Except for 1 repaired unit that failed at the insert-plate braze joint, all the specimens failed through the fins, away from the insert joints at pressures reflecting fin efficiency factors well in excess of the established design criteria.

8.3.1.5 Test Results - Continuous Fin Gap Flat Panel

Two specimens fabricated as shown by Figure 8.3-4 with a gap between the 20R-.100-.050-.006 fins of 0.055 in. were creep-rupture tested. Conditions and results are tabulated below.

Unit	Temperature, °F	Pressure, psig	Time to Rupture hr
1	1600	650	5.66
2	1550	600	25.25

Post-test observation indicated that both specimens failed in the fin-joint areas, parting at the braze joints rather than through the fins.

The above data reduces to provide an allowable pressure at the operating design conditions of 540 psi which provides a margin of safety of 0.23 for the design.

8.3.2 Pressure Cycle and Axial Loading

The configuration at the nozzle-inner shell joint represents unique structural loadings. Consequently, a special flat-panel-type test specimen was fabricated to simulate this portion of the structure and was tested under cyclic pressure loads as well as axial tension.

8.3.2.1 Specimen

The details involved in the assembly are illustrated in Figure 8.3-6a and the completed subassemblies are shown in Figure 8.3-6b. The manifold sections were joined by TIG welding, the fins were brazed to the face sheets with Palniro 4 braze alloy, and the final assembly braze operations were performed using Palniro 1 braze alloy.

TABLE 8.3-2

LOCAL JOINT FLAT PANEL TEST RESULTS

SN	Fin Description	Temperature, °F	Burst Pressure, psi	Test Pressure, psi	Hr to Rupture	Calculated Stress at Pressure, psi	Published Strength, psi	Efficiency, f_{burst}	Efficiency, f_{creep}
1	20R-.075-.004	1600		600	8.33	6,900	14,700		0.470
2		1600	3020			34,700	36,500	0.950	
4		1600		600	3.30	6,900	17,200		0.400
1	34R-.025-.002	1600		600	5.08	8,220	16,000		0.514
2		1600	1980			27,100	36,500	0.743	
3		1600	2500			34,200	36,500	0.938	
4		1600		600	0.52*	8,220	24,400		0.296

NOTE: 0.001 in. Palniro 4 Fin Braze Alloy (5 min braze cycle) and Palniro 1 Insert Braze Alloy

*Repaired unit

S-72661

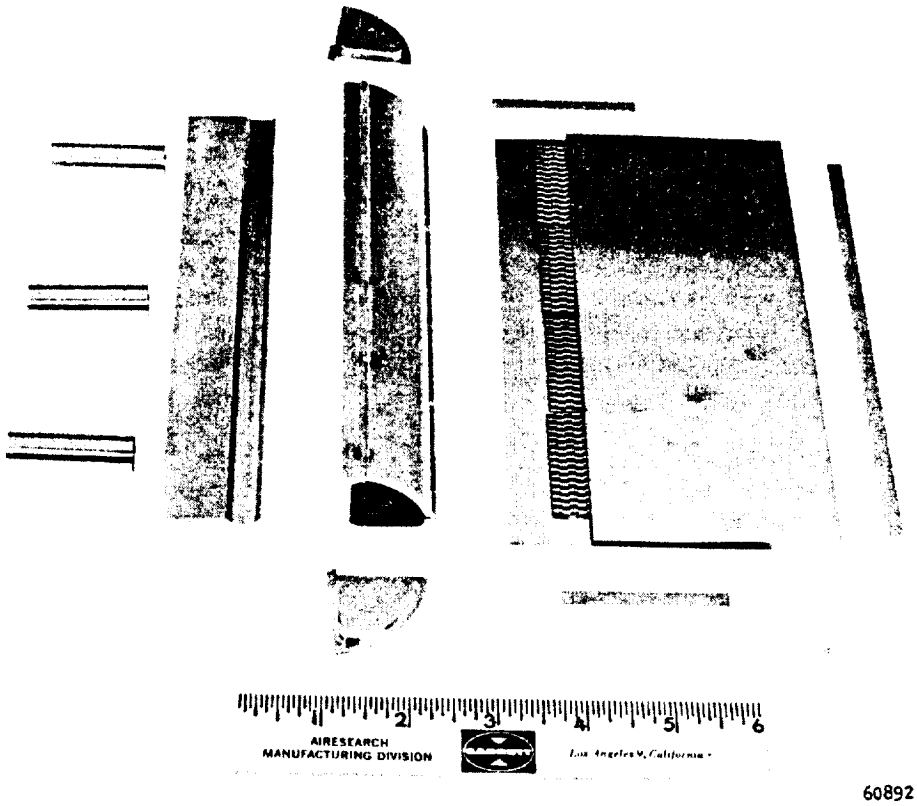

a. DETAIL COMPONENTS

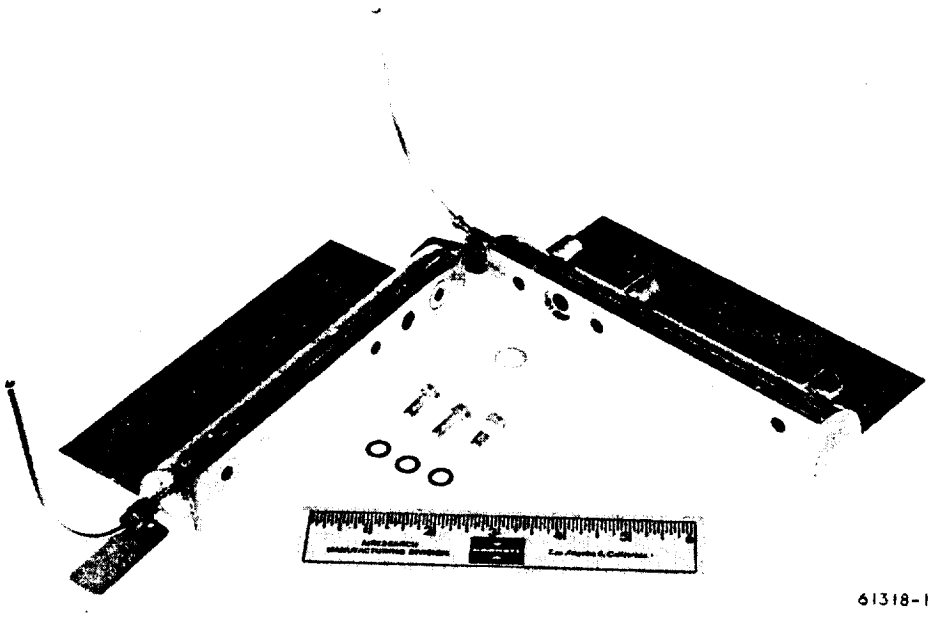

b. PANELS, UNASSEMBLED

F-15276

Figure 8.3-6. Inner Shell-Nozzle Joint Flat Panels

8.3.2.2 Test

Two tests were performed on the assembly. The first, performed on two specimens, was a cyclic pressure test to failure, the second performed on a thin portion cut from the original, was an axial pull test.

The setup for the pressure cycle test consisted of a dual cylinder, pressure cycle rig. The dual cylinder was connected to timers, solenoid valves, and pressure regulators arranged to provide cycling of pressure at controlled rates and values. A cycle of 6-sec total duration, consisting of a 1-sec dwell at maximum and minimum pressure was used for the test. During the course of testing, constant surveillance was maintained for signs of change in the specimen.

The results of the internal pressure test for the two test specimens, indicate a pressure capability of the nozzle-to-inner body detachable joint of about 3600 psig for 1000 cycles as compared to a desired design value of 1000 cycles at the 1050-psig proof pressure for actual hardware.

The pressure cycle test was conducted on an accelerated fatigue testing basis. Testing was performed by cycling from zero to a maximum internal pressure, p_{max}, and back to zero, with p_{max} increased in 25-percent increments until rupture occurred. The factor of 1.25 was selected based on the desire to increase specimen damage (or reduce life) by a factor of 10 for each incremental pressure level increase.

Testing of the first specimen indicated that its strength was higher than expected. 1000 cycles were conducted at 3180 psig rather than the intended 100 cycles performed on the preceding levels above 1050 psig. After completing 1000 cycles to 3180 psig, the specimen ruptured after 88 cycles at 4000 psig.

Based on the results of the first specimen, the initial pressure for the second specimen was increased to 2050 psig. The specimen survived this, plus 100 cycles at 2560 psig, 100 cycles at 3200 psig and finally 716 cycles at 4000 psig before failure.

The second test, an axial pull test, was conducted to determine the braze strength at the joint of the sandwich structure with the collector ring. The direction of applied load is shown in Figure 8.3-7a, and the critical joint is at (C). The load path along the sandwich through the rings and bolts and back to the sandwich on the opposite side was intended to cause a bending moment at (C) that would tend to separate the collector and sandwich. Application of the load as shown in the figure does not produce the desired moment at (C) because of a counter moment produced by bearing of the manifolds at (B). The specimen, therefore, was tested in the configuration shown in Figure 8.3-7b. A single specimen was loaded in the manner shown, and yielding of the sandwich panel occurred. The braze joint between the sandwich and the manifold cracked on one-half of the specimen but did not separate. Figure 8.3-7c shows a photo of the specimen after testing.

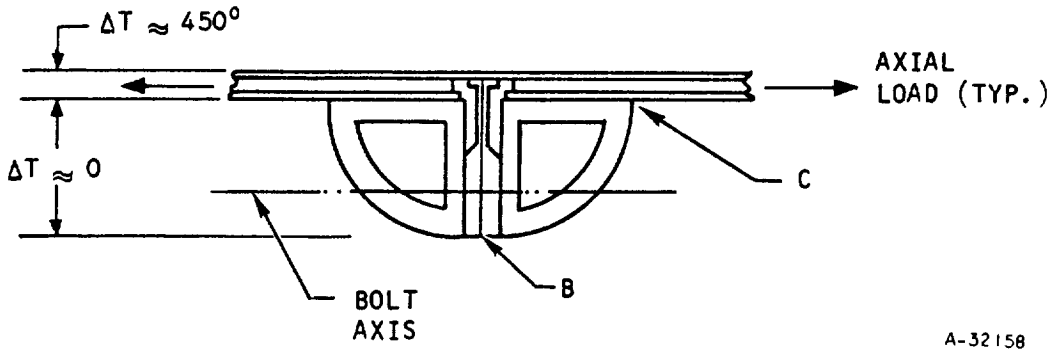

a. CROSS SECTION OF TEST SPECIMEN

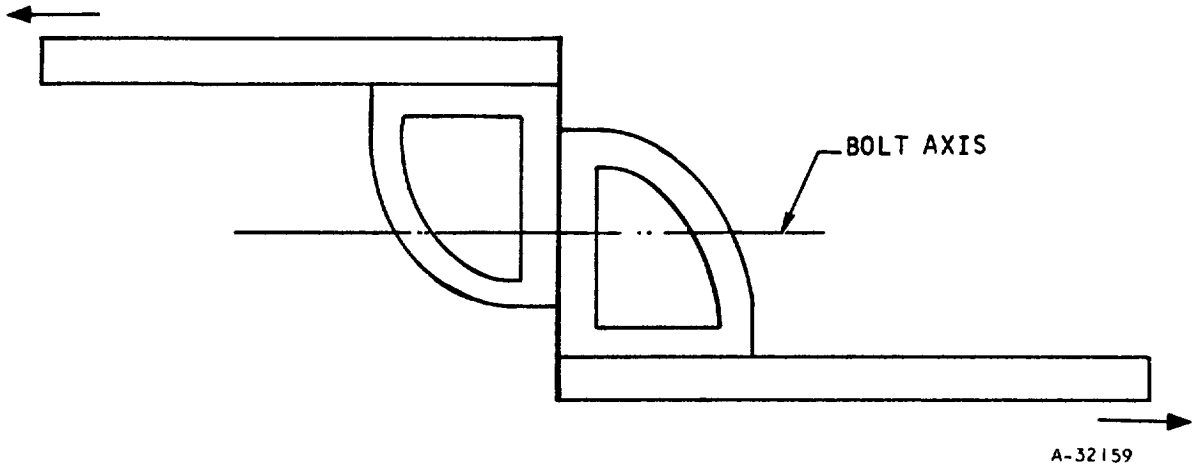

b. REVISED LOAD SCHEME

c. TEST SPECIMEN AFTER PULL TEST

F-15277

Figure 8.3-7. Flat Plate Collector Manifold Pull Test

8.3.2.3 Conclusions

The following conclusions were drawn from the test results and data:

1. An infinite cycle life is predicted for the actual hardware at the 1050-psig proof pressure assuming only internal pressure is applied. A 1000-cycle life can be expected for an internal pressure of 3600 psig.

2. The ring-to-plate fin sandwich joint strength exceeds the plate-fin sandwich strength is bending. The internal pressure tests indicate that the joint area is conservatively designed for this loading. In the actual application, additional loads due to inertia, and thermal and nozzle blow-off loads may be superimposed in the internal pressure loading. The additional loads are generally small compared to the internal pressure requirements, and some reduction in ring thickness is considered to be possible.

3. Metallic "K" seal performance during the tests was satisfactory.

8.3.3 Thermal Fatigue

The main objective of the flat panel thermal fatigue tests was to obtain low-cycle fatigue performance of the plate-fin structures under cyclic thermal differential loadings. This data supplemented results obtained from mechanical bending tests of plate-fin structures, Reference 8.3-1. Manufacturing techniques, particularly pertaining to joining techniques, were also verified.

8.3.3.1 Test Specimens

The test specimens illustrated in Figure 8.3-8a were of three-layer plate-fin sandwich construction from Hastelloy X. The lower two layers were 0.060 in. thick, and they were separated by 0.075-in.-high rectangular offset fins. The top layer was 0.015 in. thick and it was spaced from the middle plate by 0.075-in.-high rectangular offset fins.

The top layer of fins was enclosed by header bars along all four edges, and it was pressurized by a feeder tube during the tests. Header bars were used along both lengthwise edges of the bottom layer of fins, and cylindrical manifolds were attached at each end. The specimen configuration with the thermocouple wiring and terminal boards is illustrated in Figure 8.3-8a. The detail components for the specimens are shown in Figure 8.3-8b. Fabrication was performed using two braze cycles and by employing conventional shop techniques. In the first cycle, using Palniro 4 filler alloy (2170°F braze temperature), the three plates, the two layers of fins, and all of the header bars were joined. The second braze cycle used Palniro 1 filler alloy (2070°F braze temperature), and the cylindrical manifolds were attached in this operation. A total of twelve specimens were tested. Particulars and remarks pertaining to the specimens are presented in Table 8.3-3.

8.3.3.2 Test Setup

The test setup is shown in Figure 8.3-9. It included (1) a quartz lamp heat source to heat the top surface, (2) an argon gas supply to pressure the

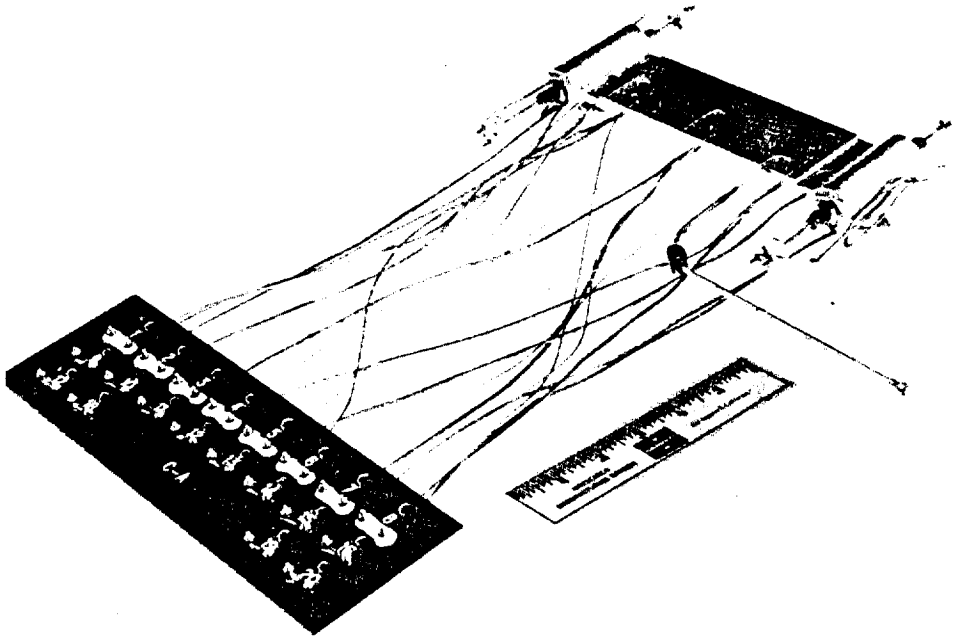

60780-1

a. SPECIMEN CONFIGURATION WITH THERMOCOUPLE WIRING AND THERMAL BOARD

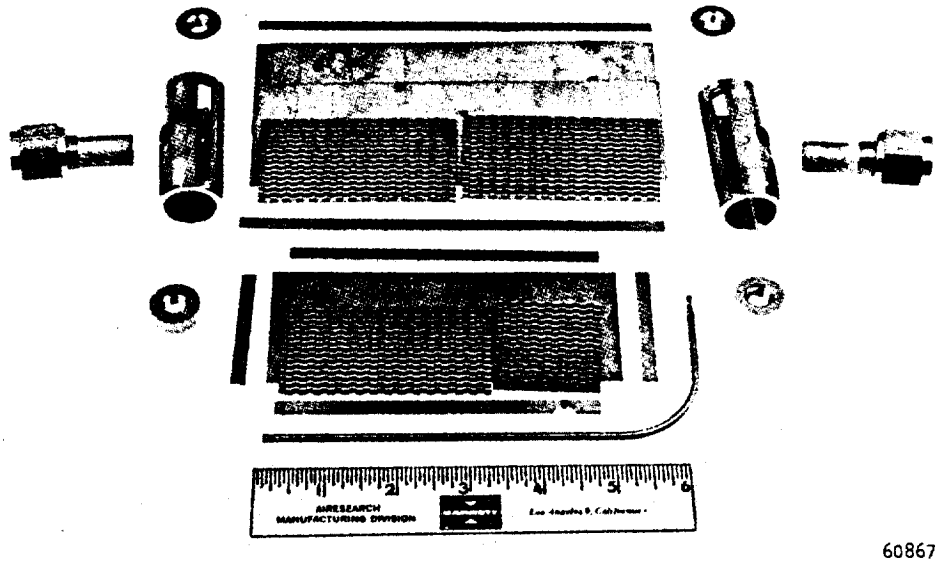

60867-1

b. DETAIL COMPONENTS OF THERMAL FATIGUE PANEL

F-15275

Figure 8.3-8. Flat Panel Thermal Fatigue Test Specimen

UNCLASSIFIED

TABLE 8.3-3

THERMAL FATIGUE TEST SPECIMEN PARTICULARS

Specimen No.	Fin Braze Alloy	Alloy Thickness	Remarks
1	Palniro 4	0.001	Approx. .008 in. space between fin sections
2	Palniro 4	0.001	Approx. .030 in. space between fin sections
3	Palniro 4	0.001	.010 fin gaps plus 4 inserts to simulate instrumentation
4	Palniro 1	0.001	Same as No. 3
5	Palniro 4	0.001	Same as No. 1
6	Palniro 4	0.001	Same as No. 1
9	Palniro 4	0.0013	Four fin joints; less than 0.010 between fin sections
10	Palniro 4	0.0013	Same as No. 4
12	Palniro 1	0.0013	Same as No. 9 except for braze alloy
13	Palniro 1	0.0013	Same as No. 12
14	Palniro 4	0.0013	Two fin gaps 0.050 wide reinforced by doublers
15	Palniro 4	0.0013	Same as No. 14

NOTE: Thermocouples were attached to all three plates at several locations to monitor temperatures during testing

UNCLASSIFIED

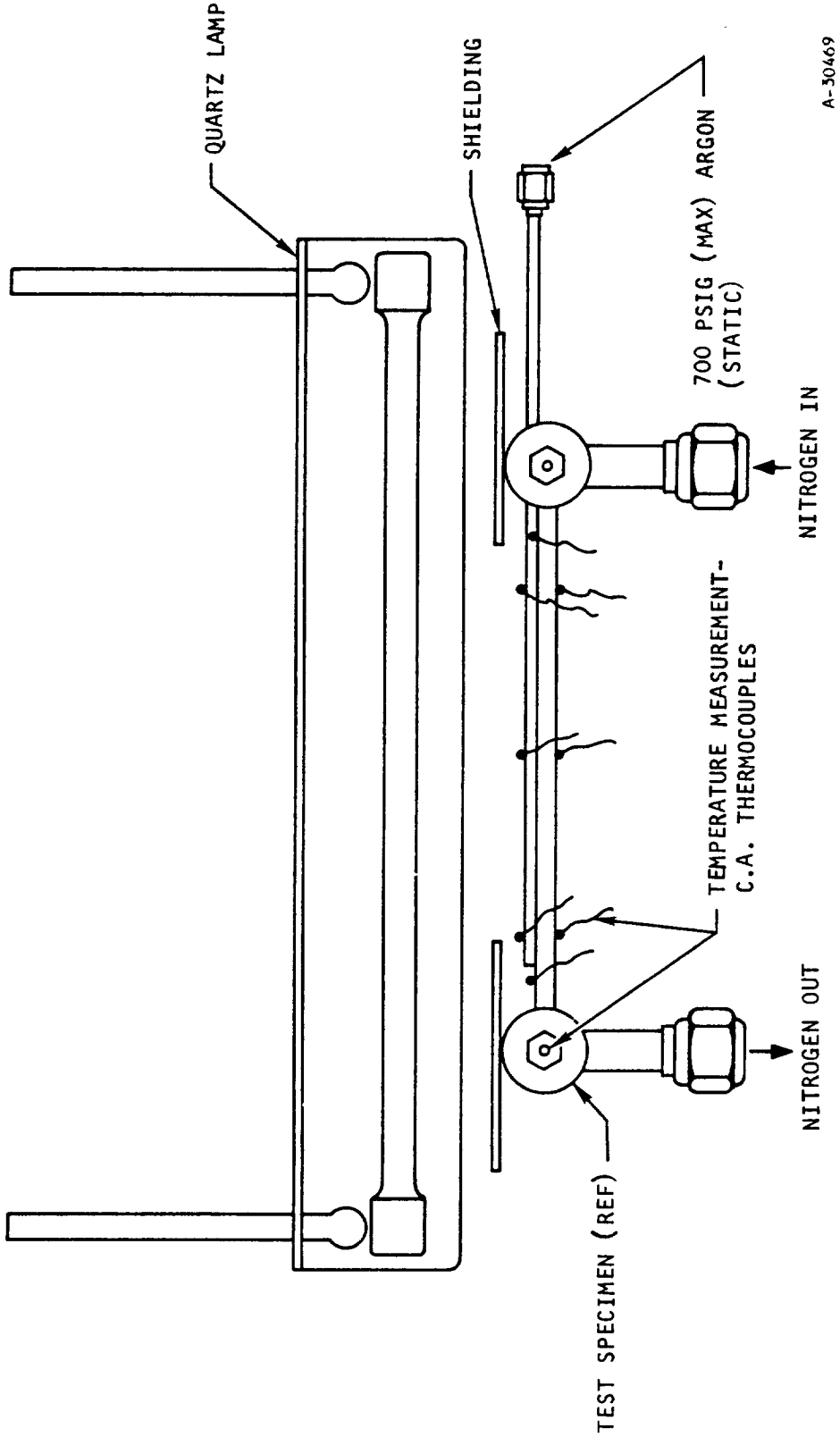

Figure 8.3-9. Flat Panel Thermal Cycle Test Setup

top layer of fins, (3) a heated nitrogen supply for regulated flow through the structural fin layer, (4) controls, and (5) recording instrumentation to collect the test data. During the initial tests, the proper argon pressure level for the top fin layer was determined, as were the nitrogen flow rates for the structural fins. The quartz lamp power settings and cycle timing were also established to obtain different temperature levels in the three layers of the test specimens.

The first six test specimens were used to determine the various setup conditions. The cycles-to-fail in these first six tests were widely scattered, and it was concluded that the braze alloy thickness had to be increased from 0.001 in. to 0.0013 in. to obtain more reliable braze joints. Consistent and valid results were obtained with the last six specimens.

8.3.3.3 Test Data Reduction and Results

The early test runs were used to calibrate the various thermcouple readings to monitor metal temperatures. It was necessary to consider the metal temperatures in all three layers to evaluate plastic strain in the top surface.

An elastic-plastic analysis of the three-layered structure was performed to determine, first, the total strain, and second, the plastic strain per cycle in the upper surface. The total strain was applied biaxially. If the loading were uniaxial, the plastic strain amplitude would be computed as follows:

$$\epsilon_p = \epsilon_{total} - \frac{\sigma_c}{E_c} - \frac{\sigma_h}{E_h}$$

For these tests, the heated surface alternated between 1500°F and 475°F. The Rambeg-Osgood expressions for stress versus plastic strain at these temperatures are:

$$\text{at } 475^\circ\text{F}, \ \sigma = 177{,}000 \ \epsilon_p^{0.215}$$

$$\text{at } 1500^\circ\text{F}, \ \sigma = 52{,}500 \ \epsilon_p^{0.115}$$

These expressions were used to generate the stress-strain curves. For each specific value of ϵ_p, the elastic strain components at the hot and cold temperatures were computed, and a plot of ϵ_p versus ϵ_{total} was generated.

For equi-biaxial loading, the expressions were modified to account for the biaxial deformations and constraints. This was accomplished by using the elastic and plastic multiaxial stress-strain relationships and by applying the expressions given above for uniaxial stress vs strain. A curve for effective plastic strain vs total strain range was obtained.

A typical plate-fin cross section is shown below.

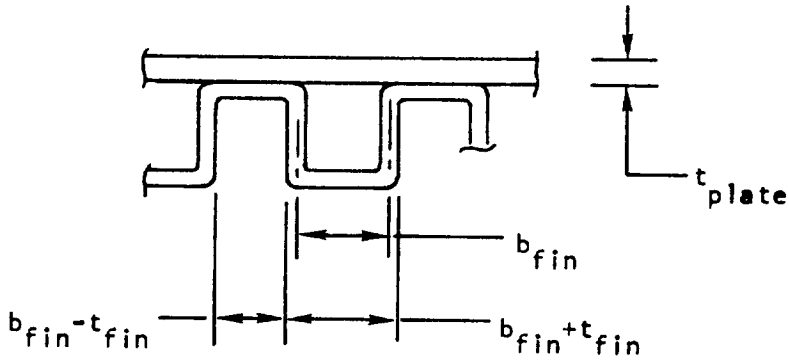

For this structure the ratio of total span to unreinforced span is:

$$K = \frac{2\ b_{fin}}{b_{fin} - t_{fin}}$$

With 20 fins/in. and a fin thickness of 0.004 in., the value for K is 2.18. Since braze filleting further reduced the unsupported span, a plasticity concentration factor of 2.5 was used for fatigue analysis. Strain concentration for the lengthwise deformations was assumed to also be 2.5. Cycles-to-failure was computed from the low-cycle fatigue formula

$$N = \left(\frac{C}{K\ \epsilon_p}\right)^2$$

The ductility coefficient based upon RA of 20 percent is C = 0.25. Using this numerical value of C and 2.5 for K, the fatigue formula became

$$N = \left(\frac{0.100}{\epsilon_p}\right)^2$$

The thermal cycle test results for specimens 9, 10, 12, 13, 14, and 15 are given on Table 8.3-4. The table shows the metal temperatures in all three plate layers, the test cycles applied to produce failure, the applied thermal differential expansion range plastic strain per cycle, calculated life fraction, and comparable engine ΔT.

TABLE 8.3-4

THERMAL CYCLE TEST RESULTS

Specimen Number	Type	Test Temperatures, °F			Test Cycles	Applied Thermal Range	Plastic Strain/ Cycle	Calc. Cycles To Fail	Life Fraction	Comparable Engine ΔT
		T_{upper}	T_{center}	T_{lower}						
9	Palniro 4 Braze Alloy	1440	570	420	200	0.00630	0.00655	234	1.03	665
		1460	310	220	14	0.00898	0.001120	81		
10		1475	540	490	149	0.00735	0.00830	145	1.03	775
12	Palniro 1 Braze Alloy	1485	590	465	165	0.00660	0.00710	199	0.83	700
		1520	555	450	200	0.00758	0.00870	136	0.95	800
13		1500	435	340	47	0.00836	0.01010	98		890
14	Doubler Sheets on Hot Surface	1470	420	330	112	0.00818	0.00970	106	1.05	870
15		1480	400	400	140	0.00906	0.01140	77	1.82	975

For ΔT = 800°F, Calculated Life = 136 Cycles

As a last step in data correlation the total plastic strain range was computed as a function of ΔT for the HRE shell structure. This is a two-layered sandwich construction, in contrast with the three-layered test specimen configuration. The thermal expansion difference due to the ΔT between the engine hot surface and the cooler structural layer was computed, and from this the constrained thermal expansion applied to the hot surface was calculated. It is this quantity that is related to the constrained thermal expansion in the test specimens. The test results were then plotted as cycles-to-fail versus engine ΔT in Figure 8.3-10. It can be noted that there are eight data points as compared to six specimen tests. The two-level tests performed on SN 9 and SN 13 provided the two extra points. The data points shown in Figure 8.3-10 were obtained by multiplying the computed cycles-to-failure for each test point by the life fraction for each test and plotting these results against engine ΔT. Note that for a single-level test, this is identical to plotting actual test cycles-to-failure versus comparable engine ΔT. A single curve is shown which is a plot of calculated life versus engine ΔT. This plot shows that for $\Delta T = 800^{\circ}F$, the calculated engine life is 136 cycles.

8.3.3.4 Conclusions

The tests show that the fatigue performance of the engine hot sheet is approximately the same for the three different specimen types that were tested. It is concluded that Palniro 4 and Palniro I are both acceptable braze alloys. Engine structures with sizeable fin gaps, as will occur where there are manifolds, can be reinforced by the use of local doubler strips with no measurable loss in thermal fatigue performance.

From Figure 8.3-10, it can be seen that except for a single test point, the line for cycles-to-fail versus engine ΔT is at or below the test results. This line is, therefore, representative of HRE anticipated performance. It shows an engine life of 136 cycles for an $800^{\circ}F$ ΔT, or conversely, a ΔT capability of $875^{\circ}F$ for a 100-cycle life.

8.3.4 Flow Distribution

The objective of these tests was to obtain a qualitative indication of how panel temperature is affected by local flow interruptions caused by various diameter and cross-section geometry of inserts.

8.3.4.1 Specimens

Three types of flat panel test specimens were used; one, incorporating an uninterrupted flow path, used to confirm uniform flow distribution through the panels, and the other two incorporating various inserts in the stream. Figure 8.3-11a shows the typical details common to the three specimens. These were assembled, brazed, and welded together to form a configuration as shown by Figure 8.3-11b, except without inserts. After proof-pressure testing the assembly to confirm the integrity of the structure, holes were machined into the assemblies by E.D.M. process and inserts brazed in place as shown in Figure 8.3-11b. Just prior to testing, thermocouples and pressures taps were incorporated to produce a test specimen such as illustrated in Figure 8.3-11c.

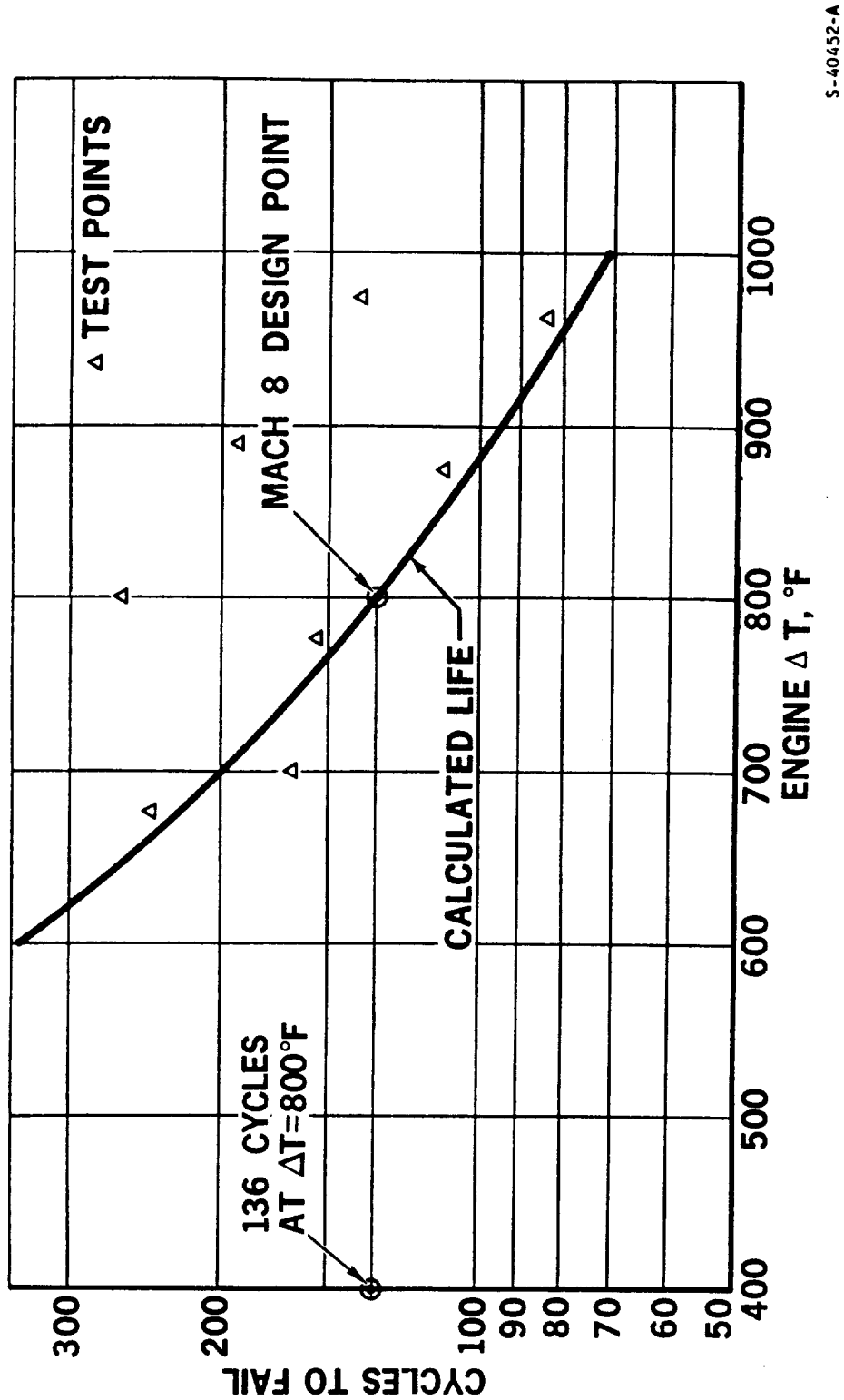

Figure 8.3-10. Thermal Fatigue Test Results

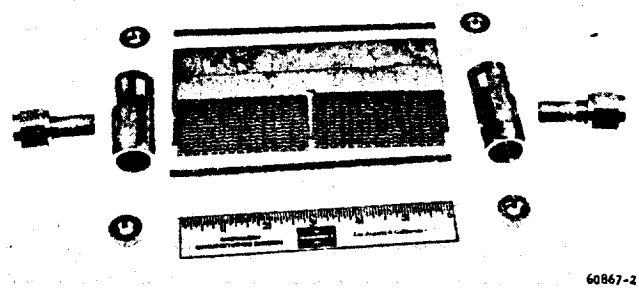

a. DETAIL COMPONENTS - TEMPERATURE DISTRIBUTION FLAT PANEL

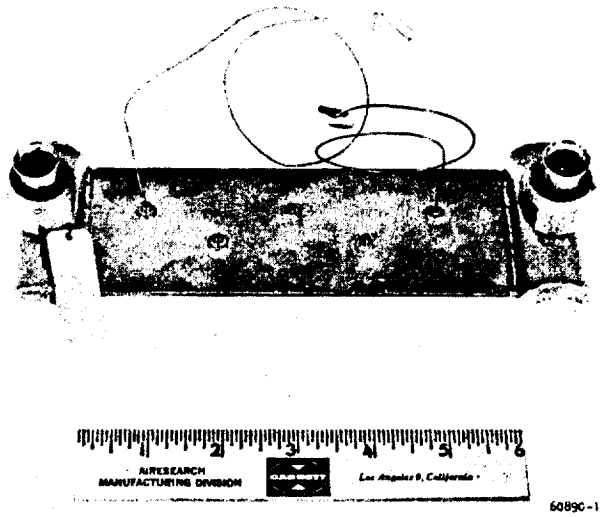

b. LOCAL JOINT FLAT PANEL FOR TEMPERATURE DISTRIBUTION TEST (BACK FACE)

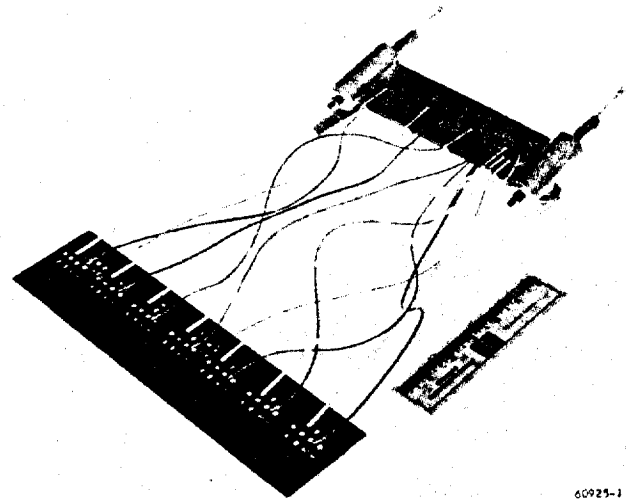

F-15263

c. FLAT PANEL FLOW TEST SPECIMEN

Figure 8.3-11. Flow Distribution Test Specimens

Both solid inserts; i.e, inserts that filled the machined holes in the fin passages, and those undercut to provide coolant flow around the body were incorporated in the test panels as shown schematically in Figure 8.3-12.

8.3.4.2 Test Setup and Procedure

The tests on these panels were run in the same setup as used for the thermal fatigue tests previously shown in Figure 8.3-9. The quartz lamp output and nitrogen flow were adjusted to produce the desired values of surface metal temperatures (1000^0-1500^0F) and steady state parameters; flow and temperature were measured. In addition, temperature-indicating paint was used to provide comprehensive data on temperature variations on the surface.

8.3.4.3 Test Results and Conclusions

Six test runs were made on the basic panels at flow rates from 0.95 to 2.21 lb/min and quartz lamp heat fluxes from 17.9 to 39.8 Btu/sec-ft^2. The data generated confirmed that flow was uniform in the panel and provided limited verification of the analytical techniques used to generate the coolant heat transfer data.

The insert panels were subjected to the same heat fluxes and flow-rate ranges as the basic panels. Temperature readings from both surface-mounted thermocouples and temperature-indicating paint provided evaluation data. Figure 8.3-13 shows a typical paint pattern resulting from the testing. Based on the data and heat transfer calculation, the following conclusions were drawn.

(a) Solid cylindrical inserts do not permit satisfactory flow and wall temperature distributions for the HRE cooling jackets.

(b) Undercut inserts with flow-to-frontal-area ratios above 0.29 permit satisfactory flow and wall temperature distributions for the HRE cooling jackets.

(c) Undercut inserts with flow-to-frontal-area ratios of 0.29 at transverse-to-flow spacing of three diameters or more do not cause pressure drops above those for passages with fin only.

(d) Satisfactory insert geometries for the HRE cooling jackets are (1) fuel injector insert diameter of 0.250 in. and A_f/A_{fr} of 0.24, based on extrapolation of the test data; and (2) pressure tap and thermocouple insert diameter of 0.200 in. and A_f/A_{fr} of 0.39.

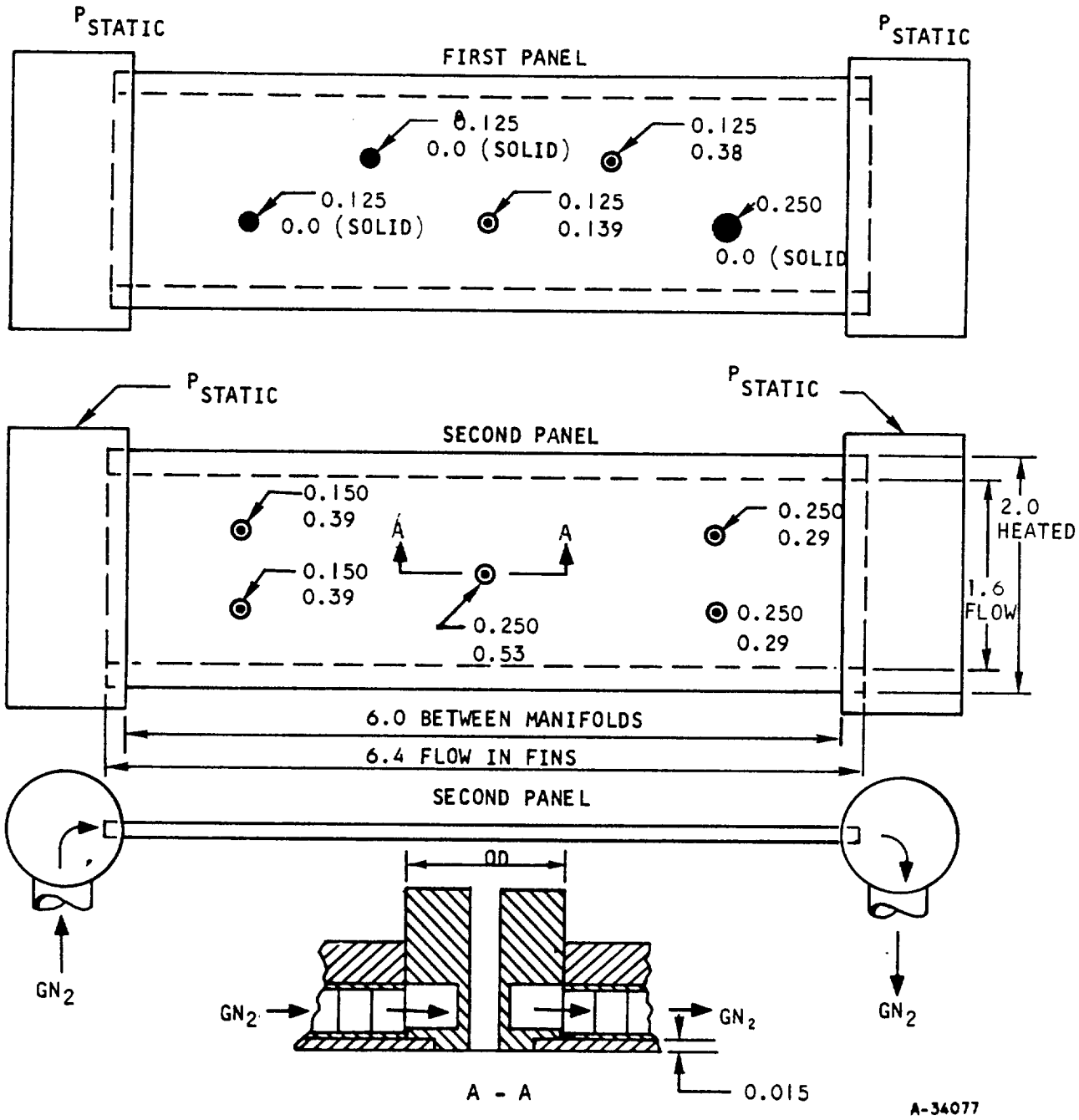

NOTE: 1. TEST VALUES FOR OUTSIDE DIAMETER AND RATIO OF FLOW TO FRONTAL AREA A_f/A_{fr} ARE INDICATED BESIDE EACH INSERT

2. FIN 2°R-0.075-0.100-0.004 HASTELLOY X

3. BOTH WALLS HASTELLOY X AND 0.015 IN. THICK

4. DIMENSIONS ARE IN INCHES

Figure 8.3-12. Insert Flow Test Panel Schematic

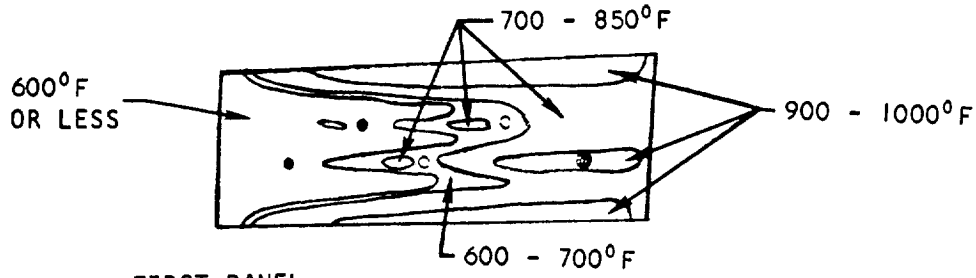

FIRST PANEL

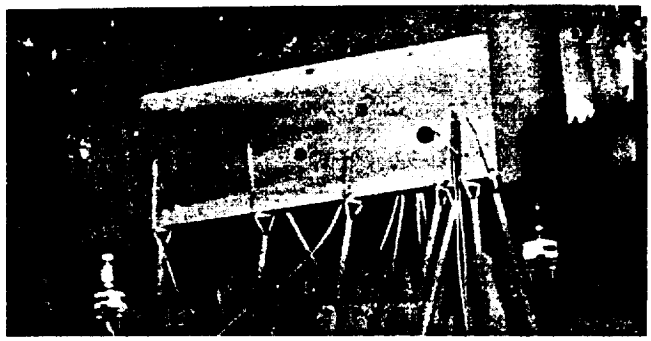

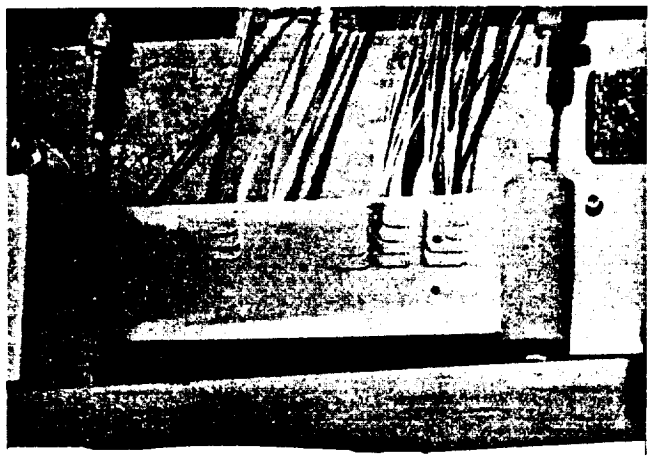

SECOND PANEL

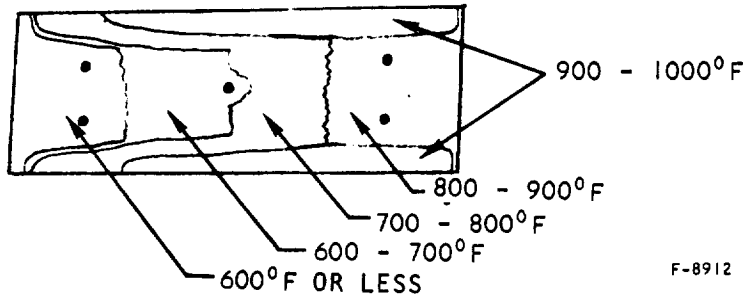

Figure 8.3-13. Temperature-Indicating Paint for First and Second Insert Panels After Run A

8.3.5 Nondestructive Testing

An investigation was conducted of the various techniques of nondestructive testing to evaluate the brazing quality of plate-fin shell assemblies using plate-fin flat panel test specimens that had been fabricated with intentional localized braze voids. The panels were fabricated from 0.015-in. Hastelloy X plates with 20R-.075-.100-.004 Hastelloy X fins brazed with Palniro 4 braze alloy. The voids consisted of five single unbrazed (stopped off) fin segments, five groups of two adjacent unbrazed fin segments, and five groups of four adjacent unbrazed fin segments.

The nondestructive techniques that were investigated included:

Ultrasonic "C" scan

Liquid crystals

Infrared radiography

X-Ray radiography

"Stresscoat"

8.3.5.1 Ultrasonic "C" Scan

This procedure produces a "picture" by gating the transducers to pick up any reflections of the initial transmitted sound wave when a sudden change in density occurs (metal to air) at the depth where the braze joint is located. The picture was graphic and easily interpreted as long as near-perfect normality was maintained between specimen and equipment. When scanning curved surfaces, focus (and resolution) was difficult to maintain.

8.3.5.2 Liquid Crystals

A survey of the existing technology of liquid crystals was made in order to ascertain the feasibility of its application as a nondestructive testing technique for brazed plate-fin assemblies. The survey showed that the liquid crystals were not recommended for the following reasons:

(a) The use of a closely controlled heating source is required.

(b) The interpretation of the color pattern is often not clearcut in small areas such as the size of one fin (approximately 0.050 by 0.100 in.).

(c) The high conductivity of the metal would tend to mask the effect of a small braze void.

8.3.5.3 Infrared Radiography

This technique incorporates the application of a rapid localized heating in conjunction with a rapid infrared radiometry sensing and recording technique. Both infrared area-scanning and infrared line-scanning were attempted on panel specimens. The area-scanning image was unable to detect the single fin segment void and the line scan, which appeared as a graph, required specialized interpretation as to its significance.

8.3.5.4 X-Ray

Extensive experience and equipment were available for X-ray radiography and excellent figures of the panels were produced which detected the voids clearly, as shown by Figure 8.3-14. The disadvantage of the technique is its lack of ability to differentiate depth and, in common with the other techniques (except Stresscoat), its lack of indication of strength of the assembly.

8.3.5.5 Stresscoat

This technique utilizes a coating of opaque,carefully controlled brittleness paint that is sprayed on the surface of concern. Any tensile movement in the surface is reflected as minute cracks in the paint. The cracks can be detected immediately by careful examination and proper illumination of the surface, and can be made more visible by subsequent surface treatment of the paint.

The excellent resolution of the technique is illustrated in Figure 8.3-15. The cracks (over single-fin segment voids) in SN 1 panel first occurred at a pressure of 800 psig, which corresponds to a bending stress in the skin of approximately 14,000 psi. The cracks over the dual-fin segment voids in panel SN 3 first occurred at a pressure of 450 psig and over the quadruple-fin segment voids in panel SN 5 at 275 psig.

8.3.5.6 Conclusion

To assure sound fin passages, a dual process testing procedure was adopted. Immediately after the first braze cycle the surfaces were 100 percent X-ray photographed and examined for plugged fins or braze voids. Then the assemblies were covered with Stresscoat and proof-pressure tested. The pressure level at which cracks first appeared and the nature of propagation during subsequent higher pressure levels provided excellent indication of the nature of the voids. The X-ray surveillance was conducted after each braze cycle, but Stresscoat proof-pressure testing was not repeated until after the final braze cycle on the assemblies.

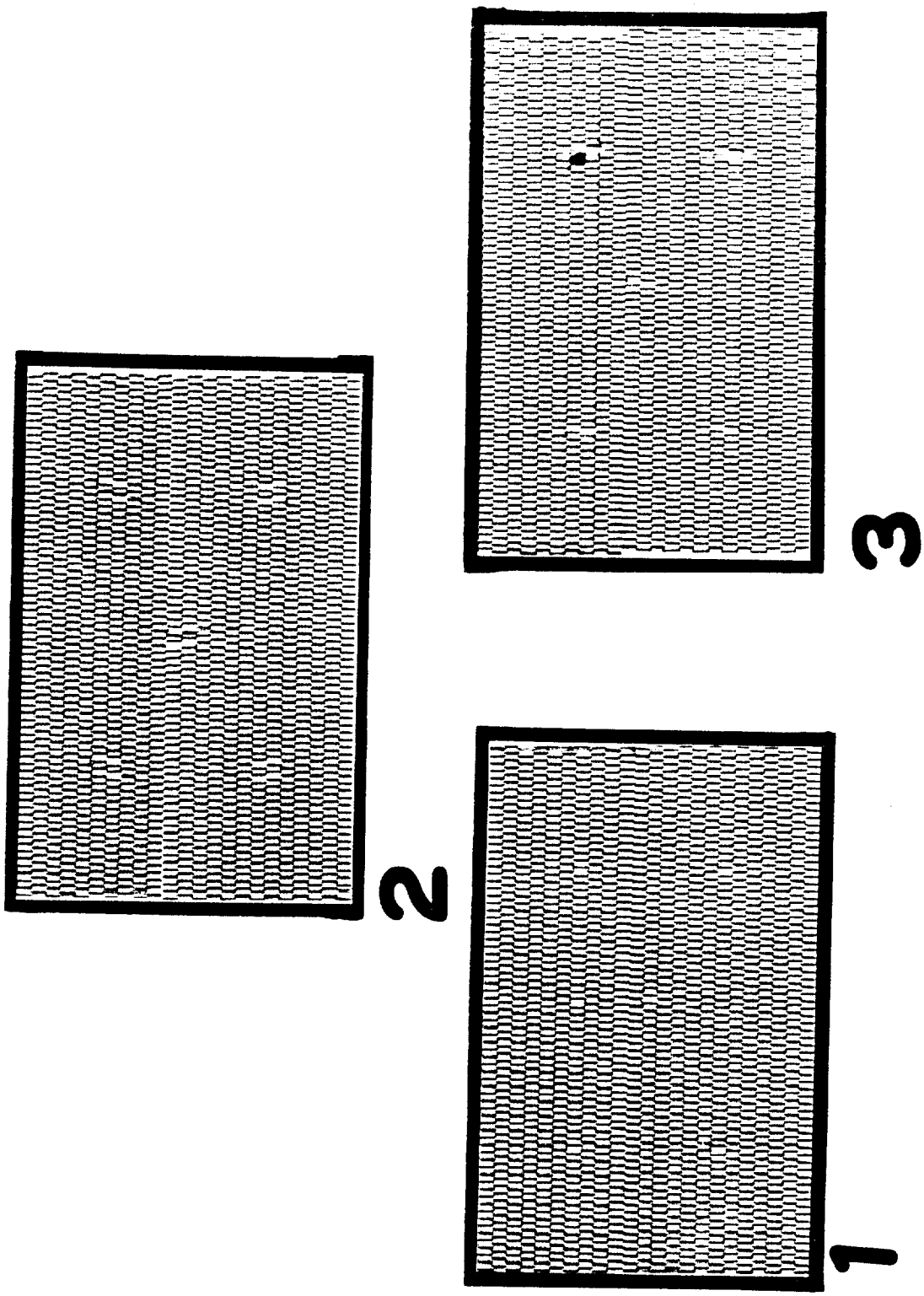

Figure 8.3-14. X-rays of Plate-Fin Braze Void Panels, Nondestructive Testing Techniques

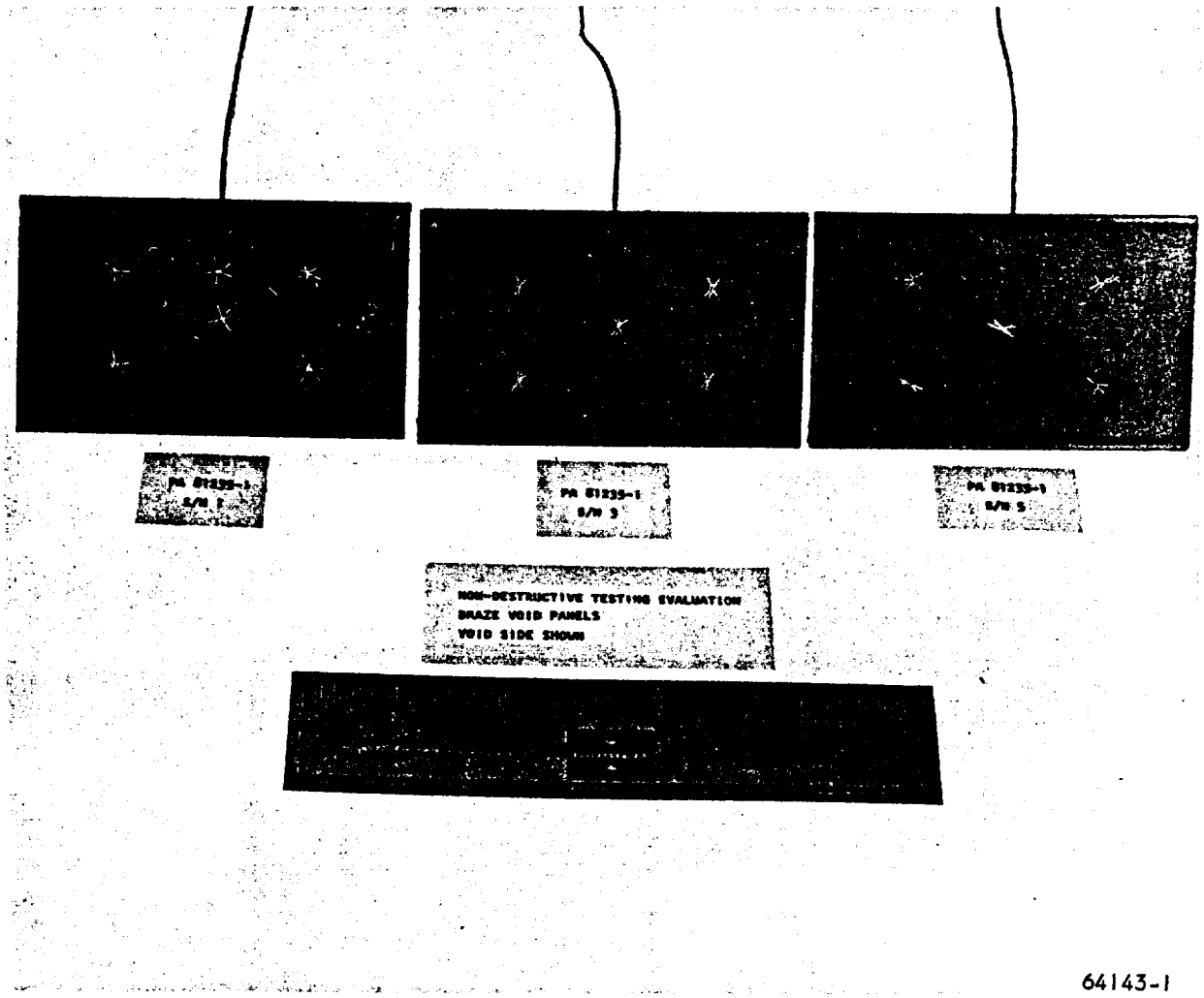

Figure 8.3-15. Nondestructive Testing Evaluation - Braze Void Panels (Void Side) "StressCoat" Coated

8.4 INLET SPIKE ACTUATION SYSTEM

This section outlines the procedures and results of the tests performed on two prototype systems of the HRE inlet spike actuator and control system (ISACS).

The initial pneumatic system concept was superseded by the hydraulic system discussed herein when design progress indicated significantly increased aerodynamic spike loads.

8.4.1 Test Setup

The test fixture is a floor-mounted, horizontal support structure to hold the actuation system by its mounting pads in the normal operating position. This fixture has, as an integral part of its construction, two hydraulic cylinders to provide the axial and lateral (normal to axial) forces. The load sensors (strain gages) are cylinder-mounted on both cylinders, with an inertial mass simulating the mass of the spike. The piston end of the actuator is secured to this mass by its normal means of attachment. The structural rigidity of the test fixture is sufficient to confine all coupling effects to the support assembly under maximum axial and lateral force conditions.

The command signal to the test assembly actuators is provided by a T-48 computer. The computer receives a position signal from the test fixture position transducer and provides the command function to both closed-loop servo-actuator systems (axial and lateral). The force signal loop is preprogrammed so that the proper functions can be selected by a single-switch position.

The recording instrumentation is arranged in a rack-mounted console adjacent to the fixture and consists of multipoint temperature recording and a CEC oscillograph. Electrical and electronic equipment is rack and panel-mounted and located convenient to the test fixture. Auxiliary test systems required to complete the setup are as follows:

(a) Vacuum pump to evacuate and fill the system with oil

(b) Hydraulic power and oil recovery systems

(c) Oil filtration system

The test setup is shown schematically in Figure 8.4-1. The functional arrangement of the test setup control instrumentation is shown in Figure 8.4-2. Figure 8.4-3 shows ISACS installed in the test fixture.

The environmental temperature enclosure for the ISACS test specimen provides controlled temperature from -20° to 160°F.

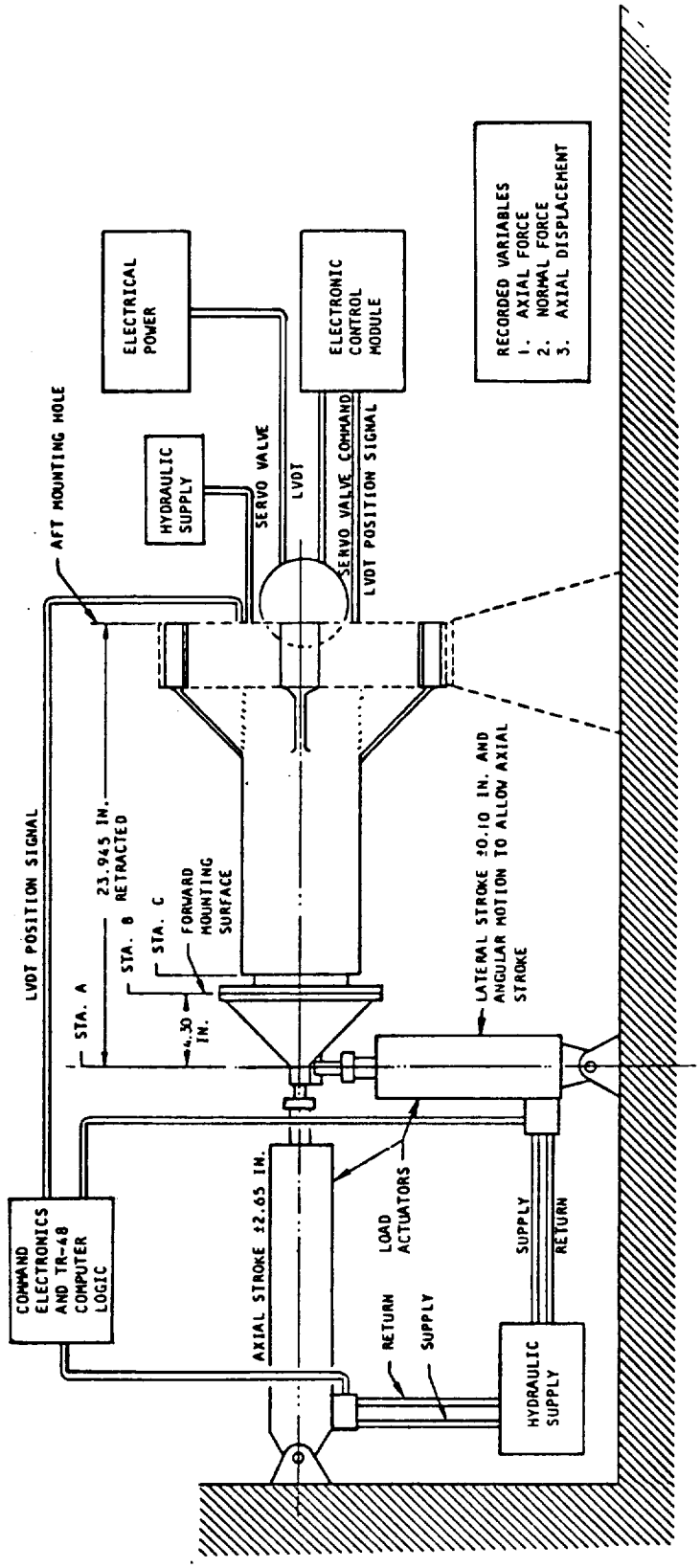

S-40447-A

Figure 8.4-1. Spike Actuation System Test Schematic

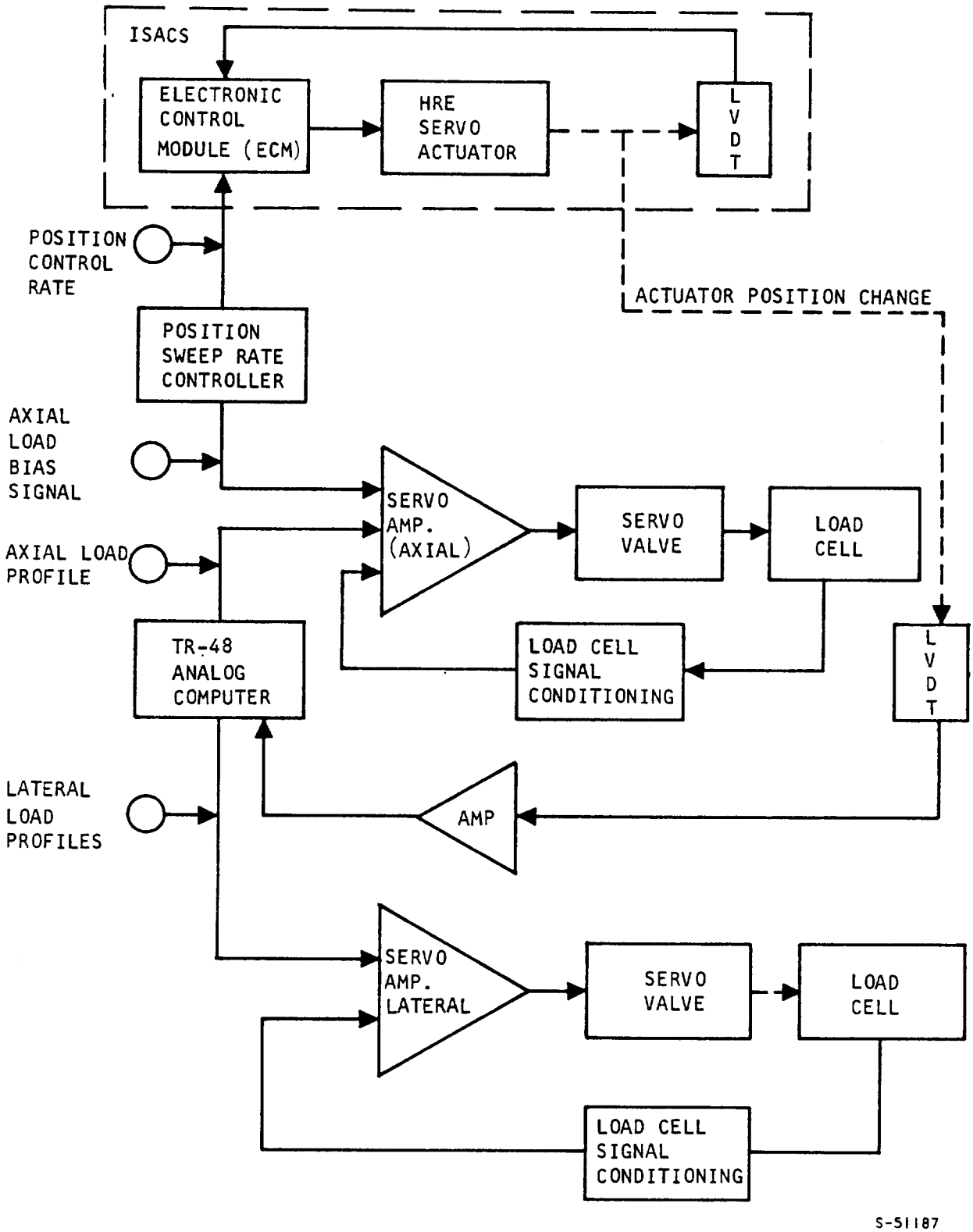

Figure 8.4-2. Functional Block Diagram of ISACS Test Setup

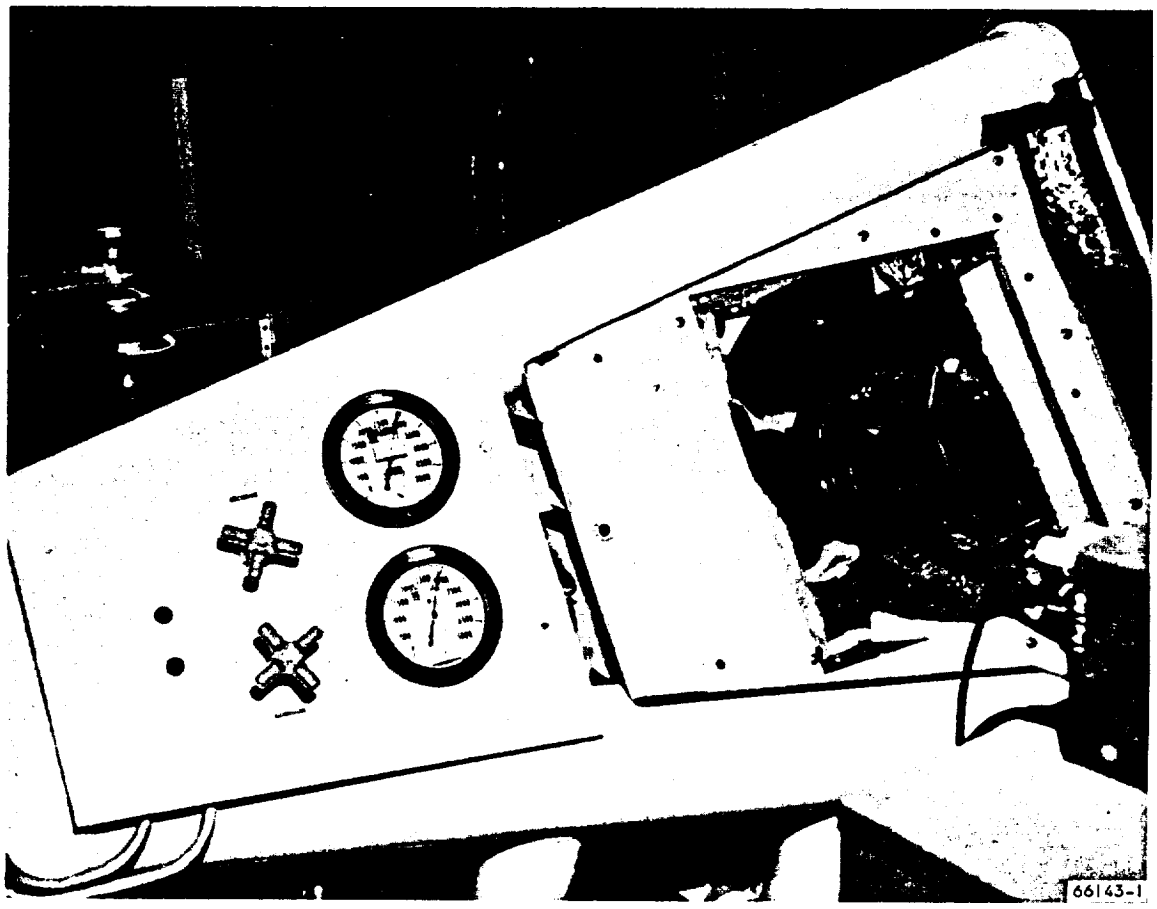

Figure 8.4-3. ISACS Installed in Test Fixture

8.4.2 Test Procedure

Two prototype ISACS units were utilized for the development tests with the objective of establishing design capability to meet the work statement. Inlet spike actuator and control system, PN 981190-2-1 was subjected to the tests outlined in para. 8.4.2.2.1, 8.4.2.2.2, and 8.4.2.2.3. PN 981190-1-1 was subjected to the tests outlined in para. 8.4.2.2.1; steps (a) and (c) of para. 8.4.2.2.2; and para. 8.4.2.2.4. An additional test was performed to determine the ISACS displacement response resulting from actuator step commands from 0.020 to 0.50 in.

8.4.2.1 Test Assembly Checkout Procedure

An interim actuator was used as the test specimen while the test assembly was checked out in accordance with the following procedure:

(a) The interim test actuator was installed in the test fixture in an open-loop manner to receive extending and retracting commands. The force-displacement profile was monitored on an X-Y plotter. All force-displacement profiles were preprogrammed on the TR-48 analog computer.

(b) From the extended position the actuator was commanded to fully retract, utilizing a load profile on the TR-48 computer. The force displacement profile on the load actuator was monitored and the necessary adjustments made to obtain the desired profile.

(c) The actuator was commanded to fully extend. The force-displacement profile was monitored. The necessary adjustments to obtain the desired profile on the load actuator were made.

(d) Step (b) was repeated with two different load profiles.

(e) Step (c) was repeated with two more load profiles.

8.4.2.2 Development Test Procedure

8.4.2.2.1 Inlet Spike Actuator System Hydraulic Test

These tests were performed under no-load test conditions and without pressurized GN_2 for the purpose of verifying design performance characteristics.

(a) The actuator was connected as shown in Figure 8.4-4. The hydraulic system was filled with MIL-H-5606 filtered oil, and the actuator piston was cycled between the extended and retracted position until all air was removed from the hydraulic system.

(b) The actuator locking mechanism test was set up and the pressure at control port 2 was increased until the actuator lock released. This was repeated several times to determine average release pressure values. Axial external loads on the locking mechanism were imposed by pressurizing the test assembly axial load actuator to 700 psid.

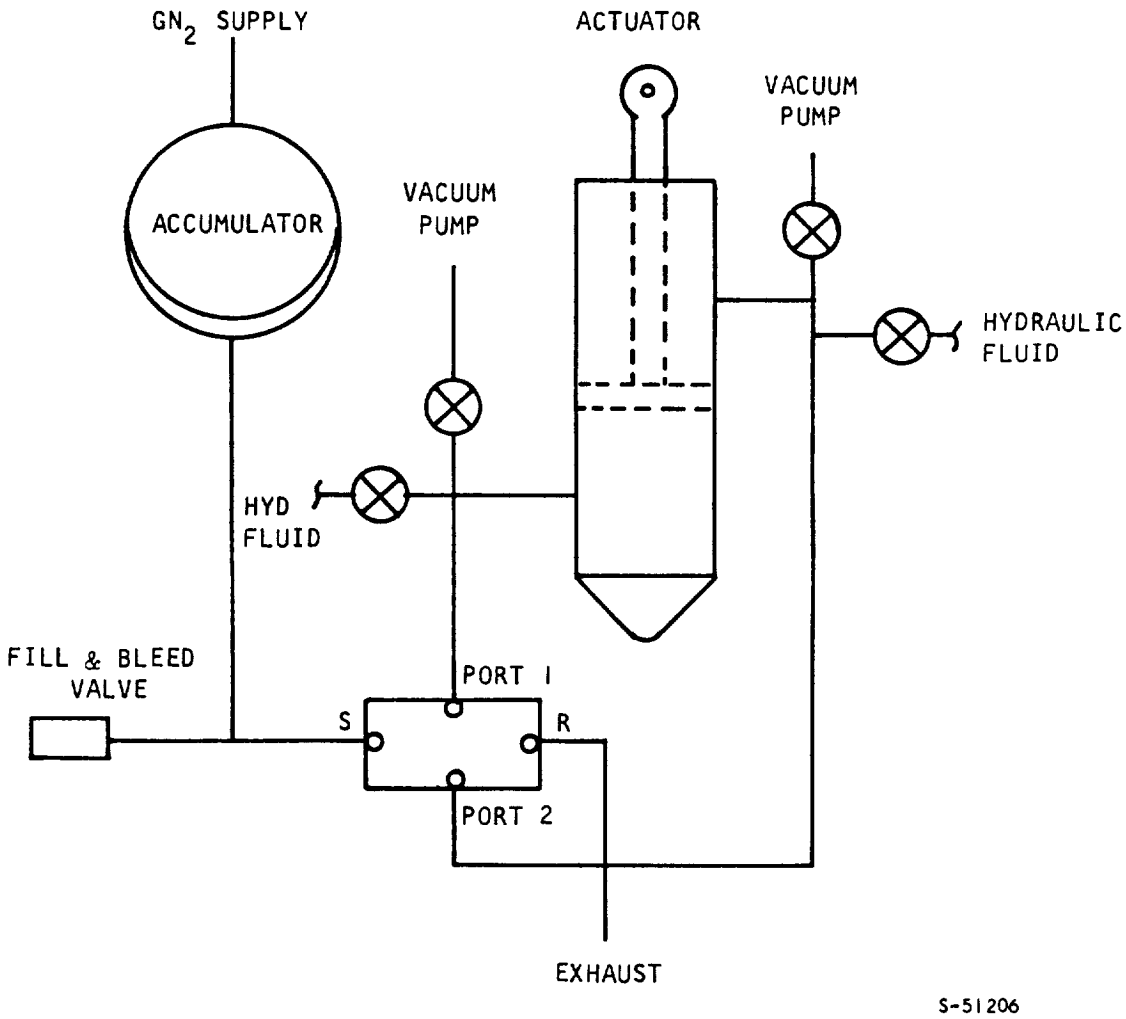

Figure 8.4-4. Schematic of ISACS Test Setup

(c) Actuator friction values were measured with the test specimen setup as in step (b). The piston differential pressure was gradually increased and measured at the minimum value sufficient to sustain piston movement. The actuator piston differential pressure was then increased to obtain a positioning rate of 5 in./sec.

(d) Calibration of the LVDT was accomplished by comparing linear actuator piston positions, measured with an 0.001 in. dial indicator, with the LVDT signal output value. Measurements were made at 0.5-in. increments from fully retracted to fully extended piston positions. Compensating adjustments of the ECM were made as required.

8.4.2.2.2 Inlet Spike Actuator System Calibration Test

These tests were performed following the tests described above. The test specimen was installed in accordance with Figure 8.4-4 with the exception that the 6000 psig GN_2 supply was not used. The hydraulic accumulator was charged with oil and pressurized to 500 psig with GN_2. The tests were performed at ambient and elevated temperature as noted in each instance. Applicable transient data was oscillograph recorded.

(a) Positioning accuracy tests were performed at ambient temperatures. Measurements were made at 0.5-in. increments between 2 in. and 5 in. from the extended position under no-load conditions. The measurements were repeated with an axial load of 10,000 lb.

(b) Stresscoat patterns were obtained during imposed axial loads to 15,500 lb and lateral loads to 16,800 lb. Lateral structural deflection was measured at several stations. Longitudinal deflection of the mounting pads was measured under the above load conditions.

(c) Load responses were recorded, under ambient temperature conditions, while extending and retracting commands were made to the ISACS for each of the load profiles previously established.

(d) Elevated temperature tests were performed with a thermal enclosure around the ISACS. Following a preliminary soak period of 4 hr, 160°F specimen temperatures were maintained while the testing described in steps (a) and (c) was conducted.

8.4.2.2.3 Inlet Spike Actuator Control System Endurance Test

The endurance test consisted of extending and retracting the actuator for a maximum of 200 cycles while at 160°F and under the test conditions noted in the following steps. The test setup was in accordance with Figure 8.4-4.

(a) Fifty test cycles were completed with axial loads imposed while extending and retracting.

(b) Fifty test cycles were completed under the maximum lateral load conditions while retracting and extending.

(c) Fifty test cycles were repeated under the test conditions of step (a).

(d) Fifty test cycles were repeated under the test conditions of step (b).

(e) Post-endurance calibration tests were performed at ambient temperature and in accordance with steps (a) and (c) of para. 8.4.2.2.2.

8.4.2.2.4 Frequency Response Characteristics

An audio oscillator was connected to the electronic control module and the peak-to-peak displacement amplitude was adjusted to less than ±0.1 in. at 1 Hz. The frequency was gradually increased to determine the amplitude as a function of frequency. This test was performed first with the actuator unloaded and then with a static load of 10,000 lb.

8.4.3 Summary of Test Results

When the test results are compared with the requirements of the work statement, the following points are significant.

(a) The load profiles show the ISACS capable of controlling maximum load changes during gross displacement changes at a rate of 5 in./sec. During flight, the load changes are expected to be within 60 to 600 μsec. The test assembly load changes occurred within 40 msec. This does not appear significant since the actuator is a positive displacement device and will absorb sudden loads without appreciable change in displacement.

(b) Considering the initial philosophy of having the on-board flight electronics compensate for predictable errors of the calibrated ISACS, the positioning accuracy is essentially a matter of correcting for the displacement variation due to load changes with possible minor effects from temperature conditions. With this approach, the positioning accuracy of a complete flight system would be well within the design value of $\pm 58(10)^{-3}$ in. In the present configuration, the ISACS is used in the AIM and SAM wind tunnel tests without flight electronics. The acceptable stroke range for $M_\infty = 8$ is from 0.0 to 1.1 in. and 3.9 to 5.0 in. for no-load conditions; 0.0 to 1.4 in. and 3.6 to 5.0 in. for 10,000-lb load conditions. The $M_\infty = 6$ acceptable stroke range is approximately 0.5 in. greater.

(c) The natural frequency of the ISACS was determined analytically and experimentally to be about 10 Hz or less and highly damped. No response was experienced during the frequency response test to 45 Hz. This appears to be sufficiently removed from the critical frequency range of 15 to 17 Hz mentioned in the work statement.

(d) The mechanical locking mechanism will meet the axial design load requirement of 8200 lb with no structural damage.

(e) Structural wear and deformation were evident on actuator locking latch at the end of the endurance test of PN 981190-2-1; however the testing of these components exceeded the design criteria of 200 endurance load cycles, since 195 load cycles were accomplished prior to the endurance test.

(f) The hydraulic servovalve PN 981160, used on the endurance unit, was returned to the supplier for failure analysis. The valve was tested and performance was acceptable except for dynamic response. The test showed a minor instability at 28 to 38 Hz, which agreed with the data. This discrepancy was found to be the result of operating the servovalve electrically without hydraulic pressure in the system.

(g) The lateral load tests, before and after endurance testing, indicated structural yielding of the Fabroid journal bearings was approximately seven-times greater than analytically predicted. However, during the most severe spike position, the clearance between the spike and cowl lip were found to be adequate. The StressCoat tests results indicated a very low stress level in the housing.

Results of the tests performed on the two prototype units, PN 981190-1-1 and PN 981190-2-1 indicate satisfactory performance in all areas except in a limited range of positioning accuracy and minor actuator structural degradation that occurred during the endurance test.

8.4.4 Conclusions

Test results of the two prototype flight configuration ISACS show the hydraulic design concept to be acceptable. The system performance is satisfactory for the test conditions including an elevated temperature environment of 160°F. The present design is capable of 100 cycles of endurance-type testing without attention to mechanical detail.

The natural frequency, determined analytically and experimentally, is 10 Hz with highly damped characteristics. This is adequate with respect to the critical frequency range of 15 to 17 Hz which is specified in the work statement.

For use in the structural assembled model, the actuator system will require some compensation in the position feedback circuit to maintain the desired positioning accuracy over the full displacement range.

8.5 COOLANT HYDROGEN BELLOWS

8.5.1 Test Units

Two coolant bellows assemblies of the designs used in the SAM were cycle-tested until failure. The first unit (tested at room temperature), was the spike coolant inlet bellows, PN 980232-1, SN 002. This bellows assembly is shown in Figure 8.5-1. The second bellows configuration tested was PN 980231-1, SN 003. Two of these units are used in the SAM, one for the purpose of carrying the hot spike outlet hydrogen into the innerbody, and the second is used to supply hot hydrogen fuel to the spike injector manifold. These bellows operate at elevated temperature, and the cycling test, accordingly, was conducted in an atmosphere furnace at 1000°F.

Both bellows assemblies were designed with the convolutions heat treated in the fully extended position. The assemblies were also designed to apply external pressure to the convolutions in order to prevent them from squirming at operating pressure. The convolution arrangement within the bellows assembly is depicted in Figure 8.5-1.

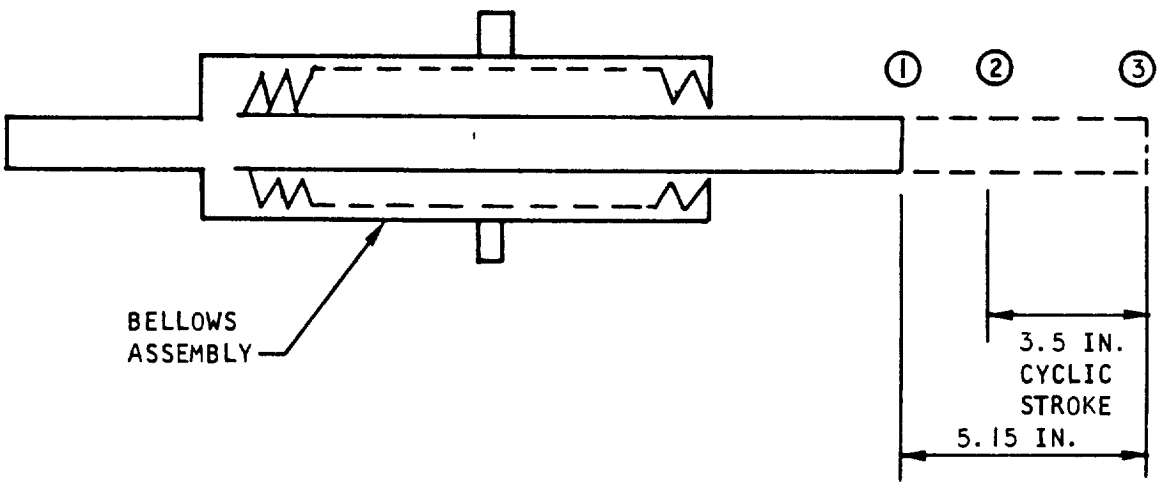

BELLOWS POSITIONS

1. AS DELIVERED; CORRESPONDS TO MAXIMUM SPIKE RETRACTION
2. SPIKE IN MACH 6 OPERATING POSITION
3. INLET CLOSED; CORRESPONDS TO MAXIMUM SPIKE EXTENSION

S-57650

Figure 8.5-1. SAM Bellows Details

8.5.2 Test Description

Both bellows were tested in the cyclic test fixture shown on Figure 8.5-2. In each test the bellows assembly was first extended to position 2 as depicted in Figure 8.5-1. The bellows was then repetitively stroked between positions 2 and 3 per Figure 8.5-1. With the bellows assembly in position 3, the convolutions were compressed to very nearly the solid height of the convolution stackup.

The bellows was cycled by a hydraulic actuator that was connected to a double-acting hydraulic pump, thereby enabling the actuator to drive the bellows assembly in either direction. The bellows assembly was capped at both ends, and connected to a high pressure nitroger cylinder. With the unit in position 2 , Figure 8.5-1, the assembly was pressurized to 700 psig and then isolated from the gas source by a shutoff valve. The pressure within the bellows decreased from 700 psia to approximately 600 psia when it was stroked to position 3 during test. At intervals of 50 cycles, cycling was stopped and the assembly checked for pressure decay during a two-minute period. Observable pressure decay was used as an indication of failure.

The nitrogen pressure source and the hydraulic pump are shown in Figure 8.5-3. The cyclic test fixture can be seen inside the spring steel burst-chamber.

8.5.3 Test Results

8.5.3.1 Cold Bellows, PN 980232-1, SN 002

The unit successfully completed the design objective of 500 cycles. It was decided to operate for another 500 cycles under identical conditions. The bellows audibly ruptured at the 985th cycle, accompanied by a rapid decrease in nitrogen pressure.

8.5.3.2 Hot Bellows, PN 980231-1, SN 003

The test procedure was identical to that employed for the cold bellows, except that a furnace was used to heat the unit to a nominal 1000°F (the temperature along the length of the unit ranged from 980°F at one end to 1100°F at the other end). The unit completed 503 cycles of operation without failure. At this point the stroke was increased from 3.5 in. to 4.5 in. The unit operated for an additional ten cycles, at which time a leak was detected.

8.6 COMPONENT PRESSURE DROP AND FLOW DISTRUBUTION

The following sections summarize the isothermal air pressure drop and flow distribution tests performed on the SAM components. These tests cooroborated the design predictions in Section 5.1.3 and provided the data required to pre-select the SAM test conditions.

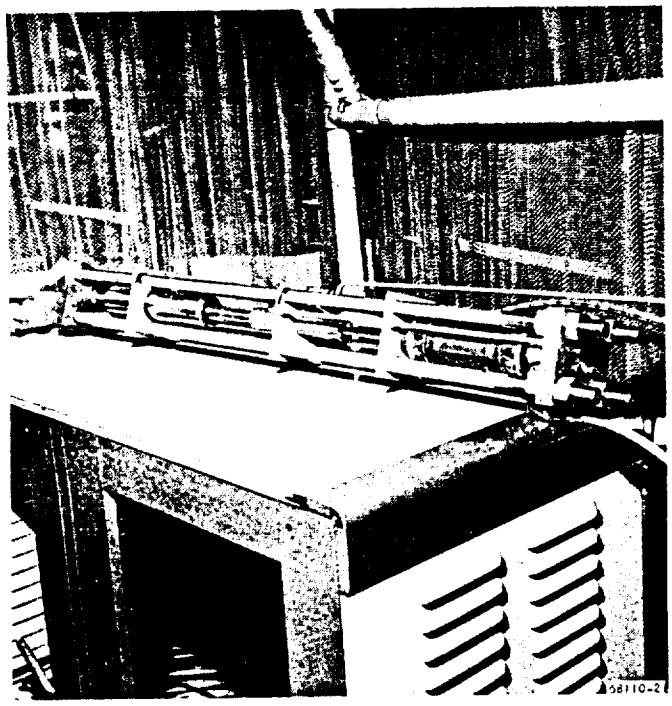

Figure 8.5-2. Coolant Inlet Bellows Assembly Installed in Cycle Test Fixture

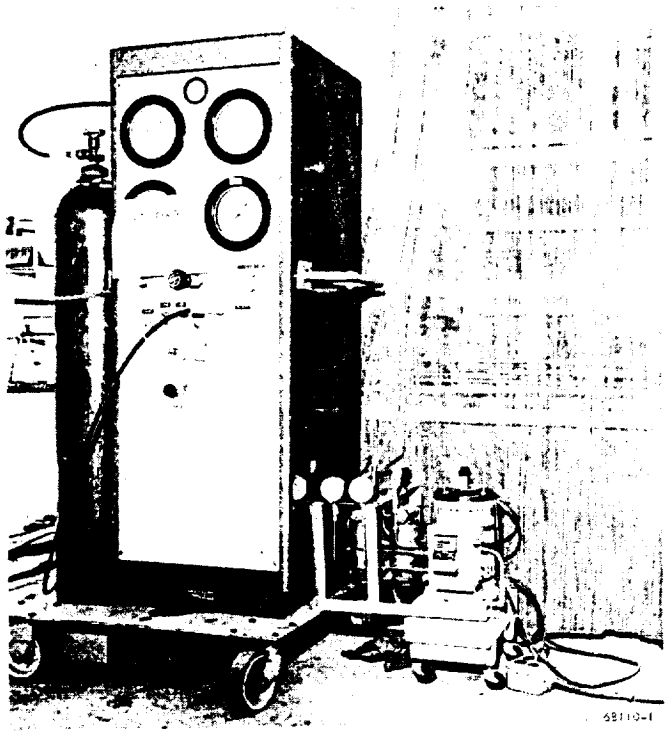

F-15207

Figure 8.5-3. Nitrogen Source and Hydraulic Pump Shown Outside of Burst Chamber Used for Bellows Cycle Testing

8.6.1 Spike

Pressure drop results from tests using room temperature air in the SN 2 and SAM spike coolant passages are presented in Figure 8.6-1 as the product of static pressure drop and average density versus airflow rate. The predicted hydrogen flow rate at Mach 6.5 local, 88,000 ft-altitude flight conditions is included for comparison. Results indicate that the test pressure drop for the SAM spike assembly is 20 percent lower than predicted and 14 percent lower than test data for the SN 2 spike assembly.

Two pressure taps placed 84 deg apart in the SAM spike outlet manifold indicated a manifold static pressure differential that was within 15 percent of predictions for uniform flow distribution. This is expected to produce an acceptable local flow rate increase of not more than 0.5 percent above average at 1300°F and 590 psia hydrogen outlet manifold conditions.

8.6.2 Innerbody

Pressure-drop tests using room temperature air in the coolant passages of two nozzle assemblies and one inner shell assembly were performed. One nozzle assembly (SN 2) was individually tested with air exhausting to ambient pressure through the bolted flange/manifold orifices. Another nozzle assembly (SN 3, SAM) was attached to an inner shell assembly (SN 3, SAM) and tested with air, exhausting to ambient pressure through the six inner shell outlet tubes. Pressure-drop results are presented in Figures 8.6-2a and 8.6-2b, as the product of static pressure drop and density at average temperature and pressure, versus airflow rate. Predicted results for hydrogen flow are included for comparison.

The overall innerbody test pressure drops for both nozzles are approximately equal and about 9 percent lower than predicted, primarily because test pressure drops in the inlet tube and nozzle cap, nozzle cap orifices, bolted flange/manifold orifices, and inner shell outlet tubes were from 31 to 52 percent lower than predicted. These overpredictions, however, were offset by underpredictions of test pressure drop in the nozzle fins by 42 percent, and in the inner shell fins by 16 percent.

8.6.3 Leading Edge

Pressure drop and flow distribution tests using room temperature air in the coolant passages of the SN 2 and SN 3 (SAM) leading edge assemblies have been performed. Airflow entered the inlet manifold through eight flexible hoses and exhausted to ambient pressure through the 24 crossover tubes. Test results are presented in Figure 8.6-3 as the product of static pressure drop and average density, versus airflow rate. The predicted value of hydrogen flow at Mach 6.5 local, 88,000-ft-altitude flight condition is included for comparison.

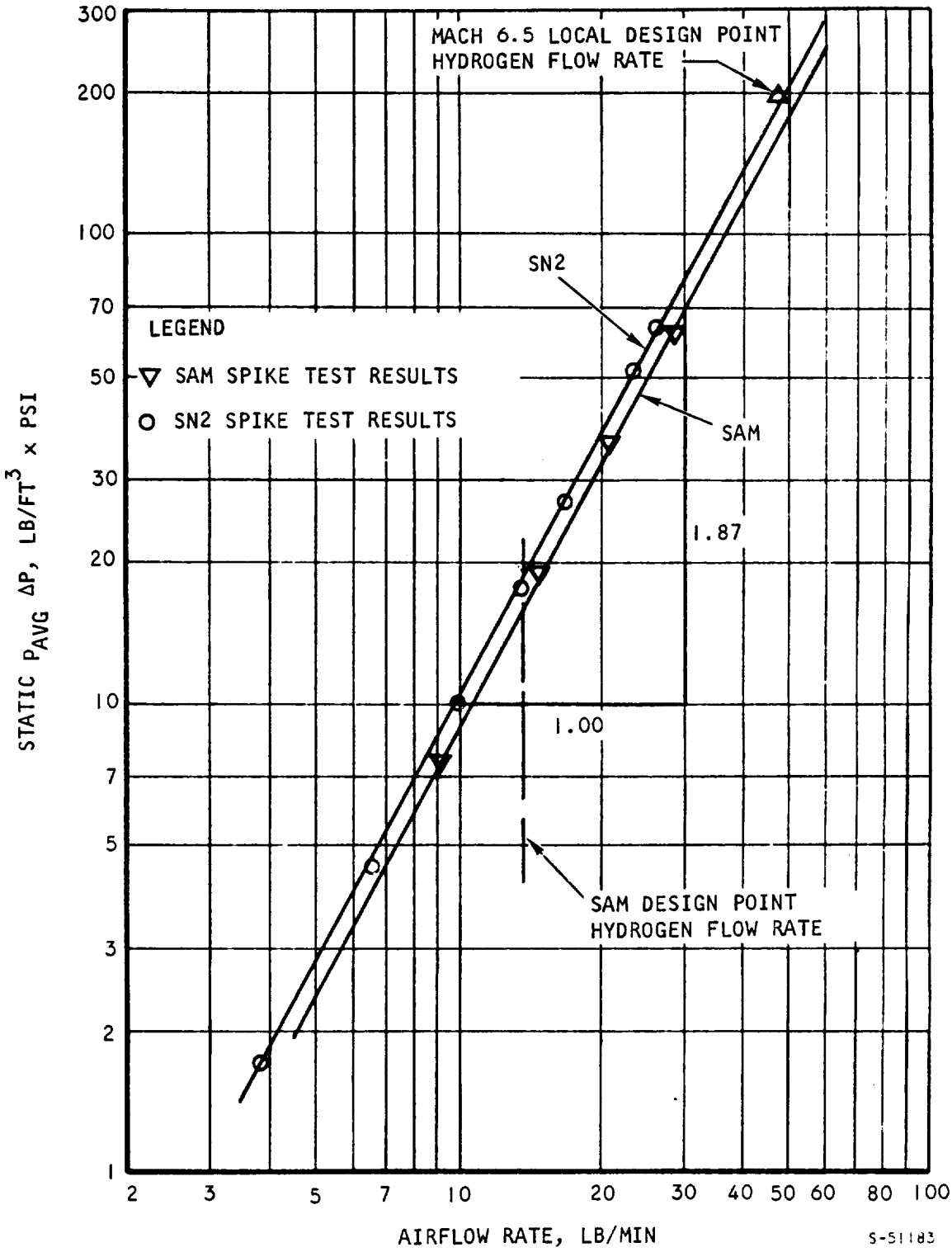

Figure 8.6-1. SAM Spike Air-Pressure-Drop Test Results

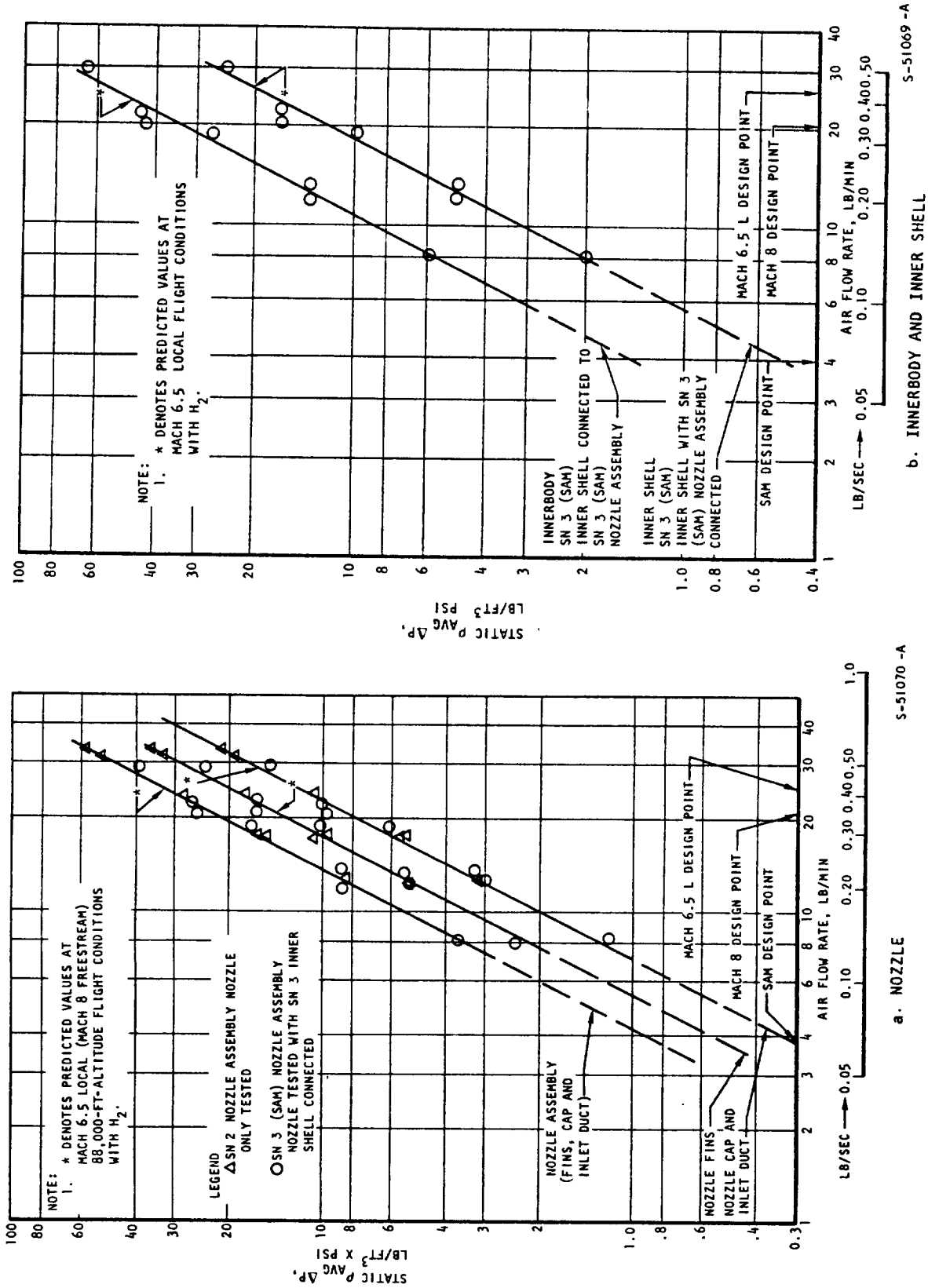

F-15280

Figure 8.6-2. Nozzle, Innerbody, and Inner Shell Air-Pressure-Drop Test Results

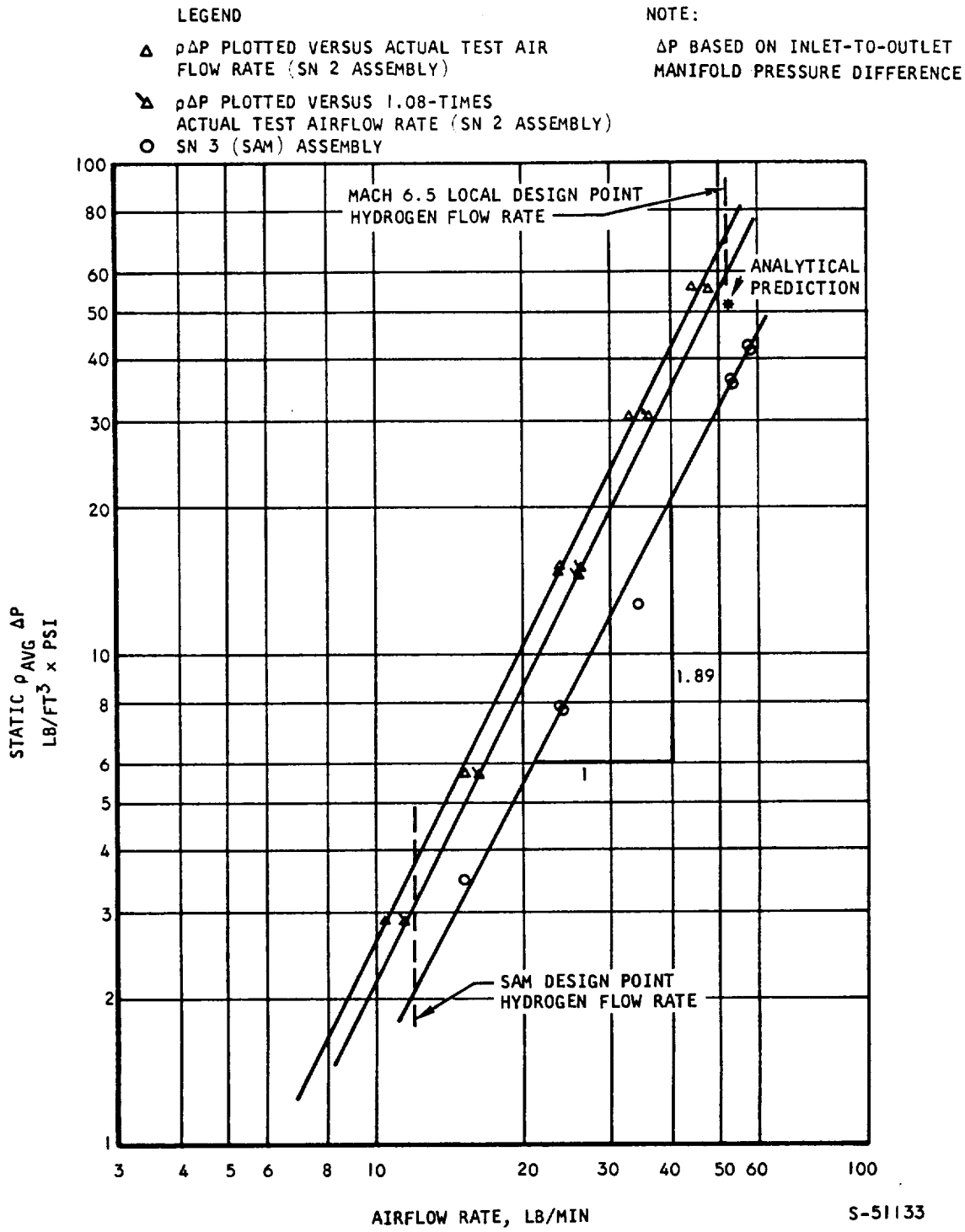

Figure 8.6-3. Leading Edge Air-Pressure Drop Test Results

Results indicate that the test-pressure drop (inlet manifold to outlet manifold) for the SN 2 assembly, as tested, is approximately 40 percent higher than predicted; however, when the test data is corrected to account for the presence of blocked-finned passages, the pressure drop is about 15 to 20 percent above prediction. The test pressure drop for the SN 3 (SAM) assembly is 33 percent lower than prediction.

Several static pressure taps were installed in the inlet and outlet manifolds of the SN 2 assembly in an attempt to measure coolant-passage flow distribution. However, the presence of braze-alloy blockages in the finned passages obscured the outlet manifold pressure distribution and the resulting fin-passage flow distribution. Flow distribution tests on the SN 3 (SAM) assembly were performed by indirectly measuring the outlet manifold pressure distribution. Results indicate that the ratio of local-maximum to local-mininum flow rate is an acceptable 1.033. The corresponding predicted value is 1.016.

8.6.4 Outer Shell

Pressure drop and flow distribution tests, using room temperature air in the coolant passages of outer shell assemblies, have been performed. Two outer shell assemblies were tested. For the first assembly, SN 1, air pressure drop and flow distribution tests were performed on both the forward and aft outer shell coolant flow passages, with and without simulated strut sides coolant flow. For the second assembly SN 2 (SAM), air pressure drop tests were performed on the aft outer shell coolant flow passages only, with and without simulated strut-sides coolant flow.

Pressure-drop results from the aft outer shell coolant passages of both assemblies are very close and practically indistinguishable within the band of data scatter obtained. When compared to the Mach 6.5 local prediction, aft outer shell test data is 8 percent higher. Pressure-drop results for the forward outer shell coolant passages of the SN 1 assembly are 18 percent higher than predicted. Simulating strut sides coolant flow appeared to have no effect on the pressure drop results of the aft outer shell. A simulated strut-sides flow rate of from 17.3 to 21.4 percent of the aft outer shell inlet flow rate was maintained for 15 test runs on the two outer shell assemblies. The flight engine design requires 20 percent for adequate strut sides cooling. The SN 1 forward outer shell coolant maldistribution, W_{max}/W_{min}, is 1.005, as calculated from manifold pressure distributions. The ratio of coolant flow, maximum to minimum, for the aft outer shell is less than 1.005. Both of these are acceptable.

Pressure drop data reduced to the product of static pressure drop and density at average temperature and pressure versus airflow rate are presented in Figure 8.6.4a for the forward outer shell coolant passages (SN 1 assembly only), and in Figure 8.6.4b for the aft outer shell coolant passages (both assemblies). Predicted results for hydrogen coolant at Mach 6.5 local, 88,000-ft-altitude flight conditions are included for comparison in these figures.

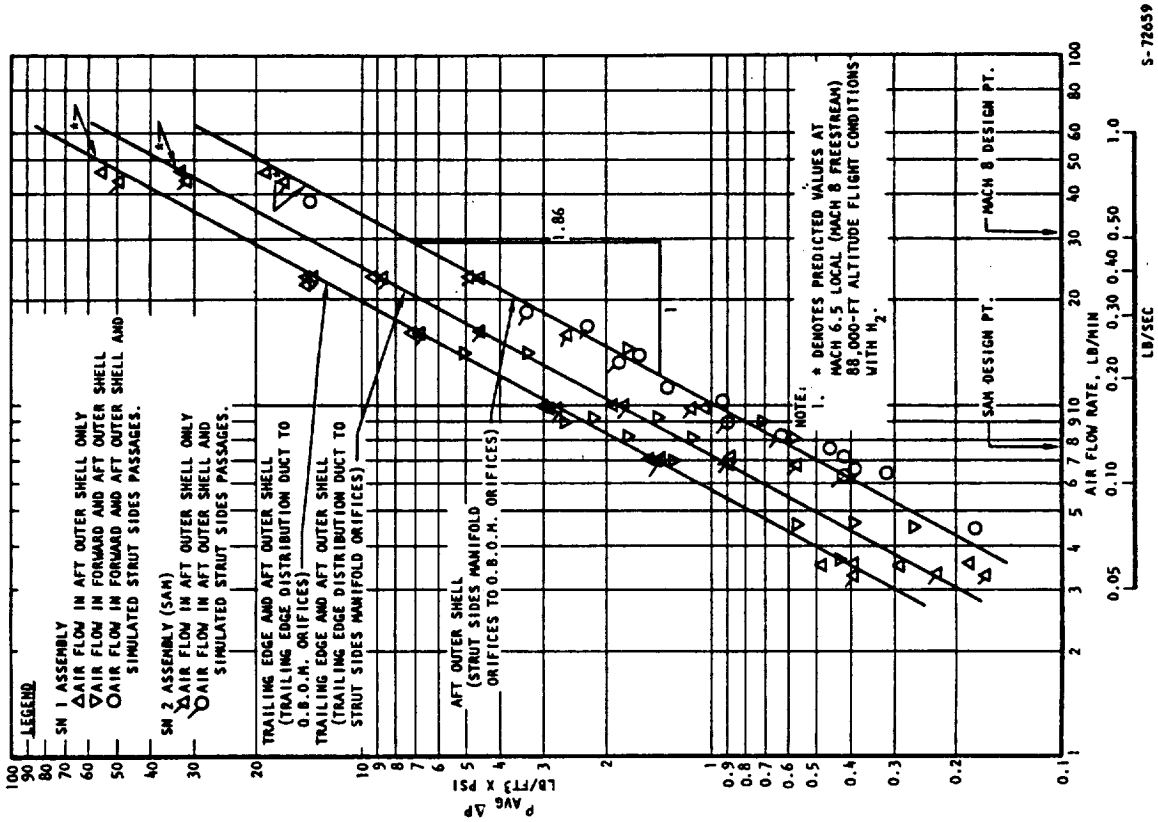

b. SN1 AND SN2 AFT OUTER SHELL

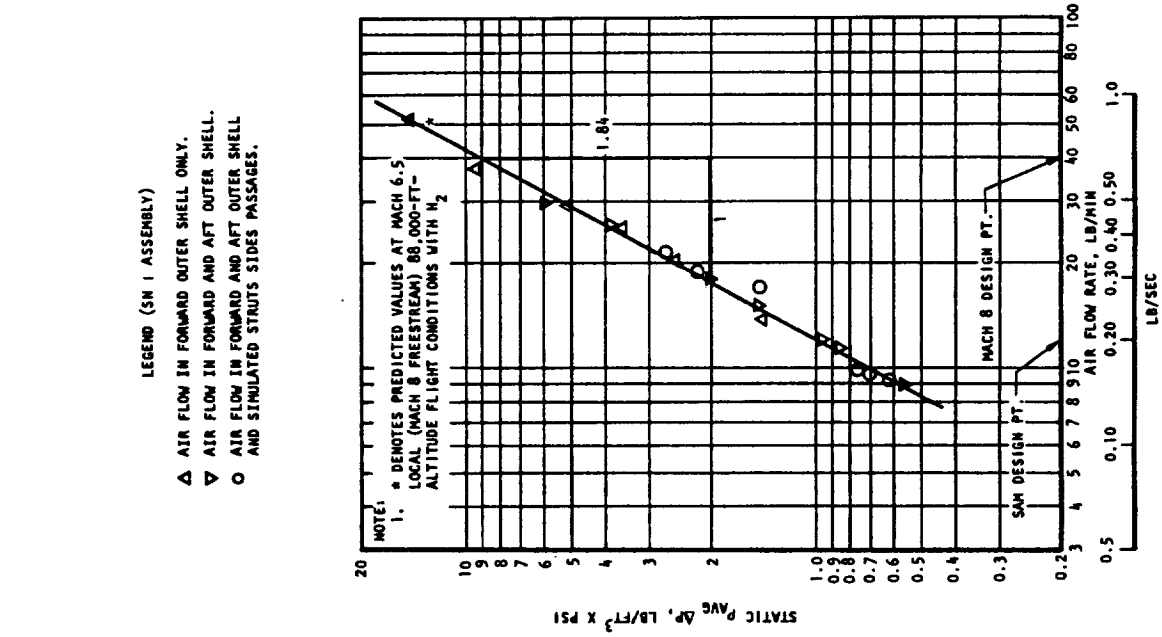

a. SN1 FORWARD OUTER SHELL

Figure. 8.6-4 Outer Shell Air-Pressure-Drop-Test Results

8.6.5 Strut Sides

Pressure-drop tests using room temperature air in the side coolant passages of the struts have been performed. These struts have a single 1/2-in.-dia inlet tube providing coolant to the strut sides. Results are presented in Figure 8.6-5 as the product of static pressure drop and density at average temperature and pressure vs airflow rate. The engine system requirement is included for comparison in Figure 8.6-5. The engine system requirement is determined from the available pressure drop from the outer shell to the fuel plenum and the required hydrogen flow rate and does not represent the pressure-drop characteristic of any air-tested strut. Because the pressure-drop characteristics for the tested struts are lower than the requirement, the strut-sides coolant-passages circuit will be orificed so that the effective strut-sides pressure-drop characteristic will match the requirement. In the data reduction, a velocity head based on the 0.312-in.-inside diameter outlet tube was subtracted from the overall pressure drop to account for the dump loss to atmospheric pressure.

8.7 SAM FLOW CALIBRATION

The purpose of these tests was to perform leakage, calibration, and check-out tests of the SAM prior to delivery to the 8-ft high temperature structures tunnel (HTST) at NASA-Langley. These tests consisted of the following:

(a) Pressure drop versus water flow rate in each of the five water flow routes

(b) Calibration of differential pressure switches in each of the five water flow routes

(c) Overall pressure drop versus airflow rate in each of the four hydrogen flow routes, for different valve settings. Pressure drops in the regeneratively cooled shells were previously obtained and reported on a component basis.

(d) Overall pressure drop versus airflow rate in the fuel injection circuit, for different valve settings. The flow characteristic without external plumbing was previously obtained and reported.

(e) Checkout of the TCS when integrated with the SAM, including the flow measuring subsystem, the abort and interlock functions, and the valve control functions.

(f) Nitrogen purge gas flow versus inlet pressure

For tests (c) and (d), pressure transducers installed in the SAM were used for many of the measurements. These transducers were ranged for the higher hydrogen pressures planned for wind tunnel use. This caused inaccuracies during air tests because of the relatively low pressures used.

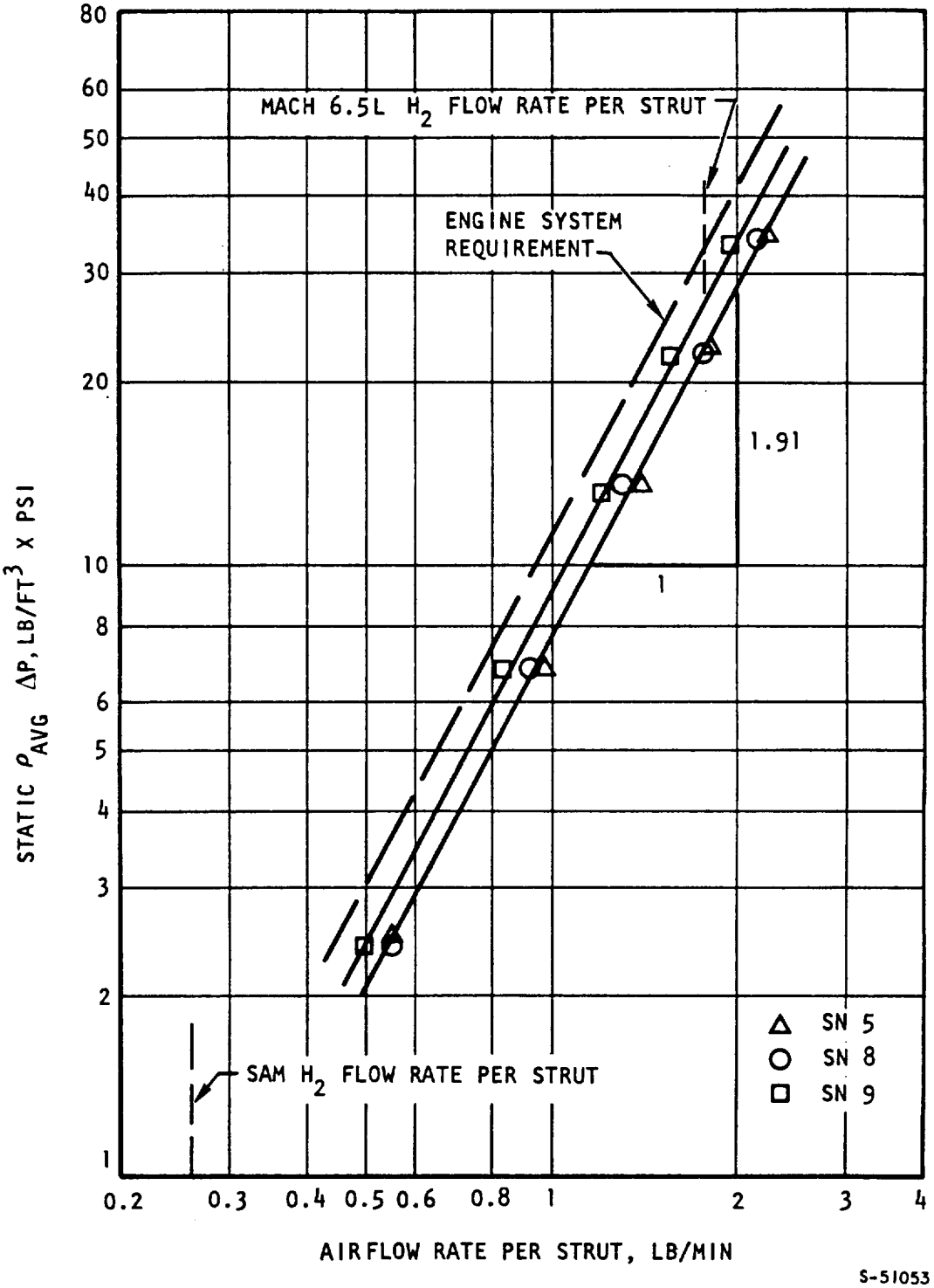

Figure 8-6-5. Strut Sides Air-Pressure-Drop Test Results

The complete assembly, tested in the laboratory, consisted of the following items:

(a) Engine assembly

(b) Manifold assembly. This assembly was assembled to the engine assembly for testing.

(c) Temperature control system (TCS)

8.7.1 Hydrogen Coolant System

An isothermal air flow test was performed on the hydrogen coolant system. The fuel dump valves and the coolant regulating valves were controlled by the controls located in the TCS console. The SAM was tested with all its actual plumbing in the final configuration, as used in the wind tunnel. The procedure for establishing the coolant flow rate was to set the pressure downstream of the pressure control valve (PCV) with the coolant regulating valves (CRV's) in the fully open position. One fuel dump valve (FDV 2) was used as the running valve, with the other fuel dump valve (FDV 1) electrically positioned in the fully closed position. The FDV 2 was opened to obtain the desired flow rate by adjusting the potentiometer setting on the TCS console. The coolant regulating valves were adjusted to obtain the flow split as follows in each coolant circuit:

Cooling Circuit	Flow, Percent
Spike	41.2
Innerbody	9.3
Leading edge	29.0
Trailing edge	17.8
Strut	2.7

Data was recorded at five levels of airflow ranging from 46.2 lb/min to 14.4 lb/min at a system inlet pressure of approximately 270 psig, and at three settings of the CRV's with flow splits maintained the same.

Results of the isothermal airflow tests are summarized below. Figure 8.7-1 presents the average density-pressure drop product ($\rho\Delta P$) for the spike. Included is the curve obtained from component tests performed on the spike (Section 8.6.1). Acceptable agreement is noted (pressures were measured with built-in 1000 psi transducers, giving a possible error in ΔP of ± 7 psi). Pressure drops were checked for two other flow routes (innerbody and leading edge) and are adequately within the range of prediction when the accuracy of the pressure measurements were considered. For most test runs the innerbody and leading edge pressure drops were approximately equal to or less than the instrument and reading accuracy of the pressure gages (± 2 psi). Similarly

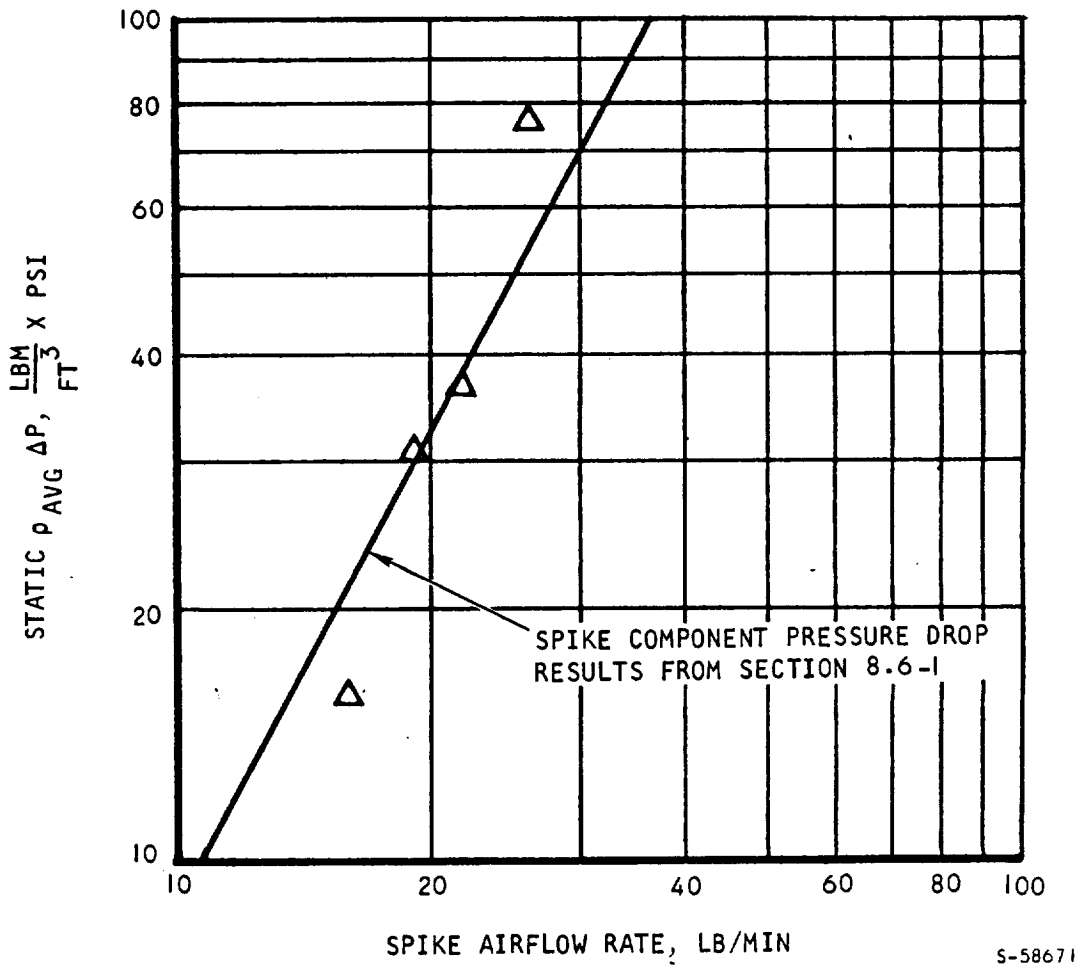

Figure 8.7-1. SAM Spike Air-Pressure-Drop Test Results

small pressure drops are predicted in the two innerbody, leading edge, outer shell, and strut routes during hydrogen testing. Differential pressure transducers will be used in several of these routes during wind tunnel tests to improve data accuracy.

The total flow rate through the SAM as measured by the turbine flowmeter (Cox Model GM-32, SN 13664) was compared with the flow measured by a 4 by 2 in. flange tap orifice upstream of the SAM. The standard deviation error is ±1.2 percent for the thirteen test points sampled. The largest error (3 percent) occurred at 18.6 lb/min. Mass flow rate through the flowmeters was calculated by multiplying the volume flow rate (as determined by the frequency reading of the flowmeters) by the air density at the flowmeters.

Static pressure taps were located adjacent to each of the flowmeters (spike, innerbody, leading edge, outer shell, and total) and the strut-sides flow-measuring orifice. For all flow test runs, these six pressures were sufficiently close to each other that a random error analysis was performed. The standard deviation between these six pressures for all test runs was ±2.2 psi at an average pressure level of 270 psig or ±0.8 percent. Thus, any one of these pressures can be used to calculate any of the flows with a deviation of up to ±0.8 percent. This deviation was accepted for SAM data reduction since pressures adjacent to the innerbody and trailing edge flowmeters were not measured during SAM testing.

The total engine flow rate percentage to each of the five flow routes is plotted versus total engine flow rate, in Figure 8.7-2. The CRV potentiometer settings were fixed for the range of total engine flow rates shown and were set to give the design percentages for N_2 calibration indicated in Figure 8.7-2. With the CRV positions fixed, the FDV position was changed from run to run to vary the total engine flow rate. The maximum flow deviations between the flow rates shown are 1.9 percent (of total engine flow) for the spike, 2.5 for the innerbody, 1.7 for the leading edge, 0.7 for the trailing edge, and 0.5 for the strut sides. The flow percentages were set using flow percentage gauges that are accurate to ±2 percent of total engine flow. These settings were not refined from run to run and gave flow percentages that were as much as 2-1/2 percent away from the design setting for N_2 calibration. Additional adjustment of the CRV settings (particularly the spike) would have reduced these differences.

8.7.2 Injection System Test

An isothermal airflow test was performed on the injection system circuit. Airflow rates varying from 46.21 lb/min to 14.4 lb/min were used to calibrate the fuel injection circuit. The flow rates in the coolant routes were maintained the same as in the coolant circuit tests. For the fuel injection tests, the desired flow rate was established by flowing air through the coolant circuit and FDV and then making the transition from the coolant circuit to the injector circuit by means of the TCS (i.e., close FDV and open injection control valve (ICV)).

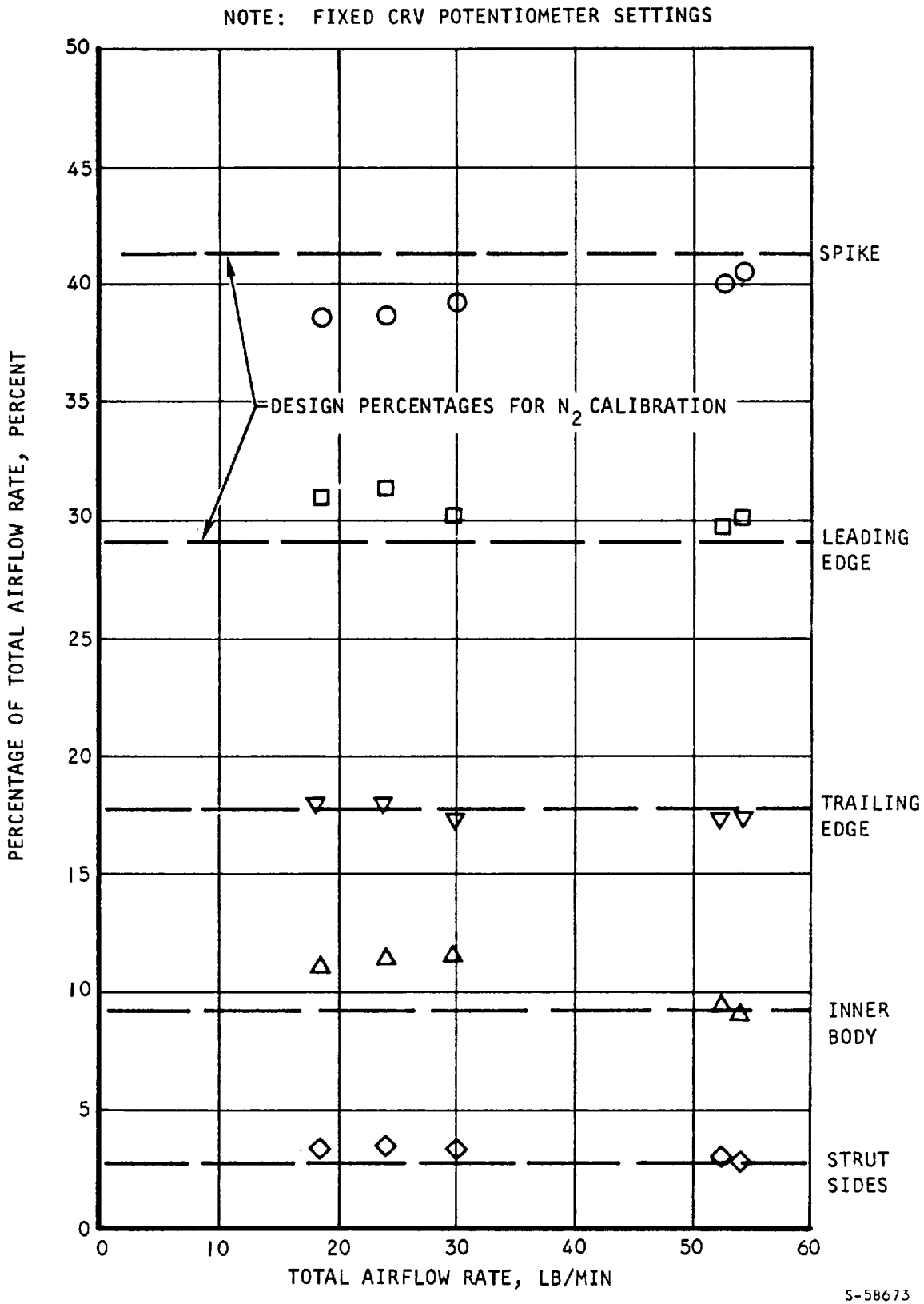

Figure 8.7-2. Coolant Route Flow Rate Percentages

To maintain coolant system pressures (120 to 300 psia) and airflow rates (15 to 60 lb/min) equal to those using the FDV only, the transition to the injection system required that the injector control valve (ICV) be positioned at small openings. These small openings choked the flow through the ICV and created pressure ratios across the spike and outer shell injectors that were just equal to or less than the critical choking ratio. Flow through the spike and outer shell injectors was estimated from the recorded pressures in the injector manifolds and the injector calibration discharge coefficients. However, the sum of the estimated injection flow rates differed from the total airflow rate (as measured by the orifice upstream of the SAM) by 3 to 100 percent. These differences were caused by pressure gauge and pressure transducer inaccuracies at pressure levels from 20 to 30 psia. For injector flow rates that agreed fairly well with the total flow rate (3 to 6 percent), it is estimated that approximately 54 to 62 percent of the total engine flow was routed through the spike injectors, while the remainder was routed through the outer shell injectors. The design objective was a 50-50 split between spike and outer shell injectors.

8.7.3 Temperature Control System

The TCS functions and operating modes were checked out during the course of the isothermal airflow testing.

The external purge command from the facility was simulated to verify that the BPV's, FDV's, and the ICV opened upon command and returned to their previous settings when the signal was removed.

The ICV permissive signal from the facility was simulated to ensure that the ICV valve would open only when the enabling signal from the facility, showing that the engine was at the tunnel centerline, was sent to the TCS panel.

The low-hydrogen, flow-abort system was checked by first presetting the potentiometer on the low-flow switching mechanism and establishing a flow rate in the coolant circuit. A step change was then imposed on FDV area. As the valve closed and the coolant flow was reduced, the two solenoid-controlled BPV's opened. System inlet pressures, the dump plenum pressure, and system flow rates were continuously recorded. From the dynamic recordings, an undershoot in total flow of approximately 25 percent was observed relative to the preset trip values in the low-flow switch. This was consistent at all flow rates tried. For slow changes in flow, the trip flows match the calibration values. Actual settings during test were based on an intermediate trip flow to provide protection during step change and also avoid unnecessary aborts.

The FDV to ICV transition was dynamically checked both with and without the PCV valve functioning. Again, only the one FDV valve was used, with the upstream FDV closed electrically. The transition was not satisfactory without the pressure control system functioning. Results are considered satisfactory, i.e., the total system flow rate is maintained near constant (about 6 percent excursion from steady state) during transition.

The pressure control system and fuel dump valve interaction was determined by applying a step change to the FDV electropneumatic transducer. This was accomplished by electrically switching from the use of one FDV valve to both valves open to the same setting. Valve area change is at the maximum possible rate. With a pressure control system damping factor of 0.1, performance was satisfactory.

8.7.4 Water Systems Flow Versus Pressure Drop

Pressure drop tests were performed on the five water-cooled routes of the SAM. Test pressure drops of flow routes 1 and 2 (low pressure system) are 41 and 18 percent lower than predictions, respectively, at the design point flow rates. Pressure drops of routes 3, 4, and 5 (high pressure system) are 25, 51, and 5 percent higher than predicted values. The predicted pressure drops and flow rates were reported in Section 5.8.

8.7.5 Differential Pressure Switches

As a result of differences in test pressure drops from predicted values reported above, the differential pressure switch settings and operating pressures of all routes, and the flow rates of routes 3 and 4 were modified from those reported in Section 5.8. The pressure switch settings and resulting flow conditions based on water test data and the initial settings and conditions for SAM testing are presented in Table 8.7-1. The lower (than predicted) operating flow rates in routes 3 and 4 were accepted so that the inlet pressure on the high pressure system can be common for routes 3, 4, and 5. It is noted that the predicted water flow rates were based on maximum tunnel heating conditions. As the SAM tunnel heating conditions were increased from test to test, the water routes (and, in particular routes 3 and 4) were checked for overheating. No indications of overheating were noted in any of the flow routes.

8.7.6 Nitrogen Purge Systems

Tests were performed to measure the airflow through the two circuits that have nitrogen purge flow during wind tunnel test. One circuit leads into the innerbody cavity and exhausts by means of leakage at the various O-ring seals between the outerbody and cowl/pylon, and between the cowl/pylon and the support wedge. The second circuit leads into and out of the second-stage injector manifold in the inner shell assembly to provide a purge flow for hydrogen leakage into this manifold from one of the strut pads. Exhaust was to sea level ambient in the tests.

The results were used to set purge flows during tunnel tests. Cavity purge pressure was limited to 12 psi differential relative to tunnel free-stream static pressure. Manifold inlet pressure was approximately 120 psi. These pressure levels assured outflow of purge gas at all tunnel and coolant operating conditions.

TABLE 8.7-1

WATER TEST RESULTS AND MODIFIED CONDITIONS FOR SAM TESTING

	Parameter	Route 1	Route 2	Route 3	Route 4	Route 5
Test results at design flow rate	Design flow rate, gpm	37	125	43	15	70
	Test pressure drop, psi	45 (70)*	62 (80)*	210 (160)*	220 (140)*	170 (160)*
	Trip flow rate, gpm	31	108	40	13	63
	Trip pressure drop, psi	33	47	165	170	139
	Reset pressure drop, psi	43	57	185	190	159
Initial setting and conditions for SAM testing	Operating flow rate, gpm	37	125	42	13	70
	Operating press.drop, psi	45	62	175	170	170
	Trip flow rate, gpm	31	108	39	12	63
	Trip pressure drop, psi	33	47	150	145	139
	Reset press. drop, psi	43	57	170	165	159
	Operating inlet pressure, psig	90	90	190	190	190
	Operating outlet pressure, psig	45	28	15	20	20

*Indicates predicted pressure drop

8.8 SAM WIND TUNNEL TESTING

This section describes the wind tunnel testing performed on the Structures Assembly Model (SAM), in the 8-ft High Temperature Structures Tunnel (HTST) at the NASA-Langley Research Center, Hampton, Virginia. The data obtained from the tests was analysed to determine the aerodynamic heating conditions, the cooling performance of the structure, and the applied structural loads. The results of these analyses are presented in Section 8.8.5. Where appropriate, comparison of the test results with the predicted performance of the cooled structure is made. A total of 47 wind tunnel runs involving 60 loading cycles was performed. The accumulated time in the wind tunnel stream was 30.7 min. Reference 8.8-1 is the SAM test report and provides additional details of test results, data reduction, and conclusions.

8.8.1 Purpose and Scope

The general approach to the SAM tests, as reflected in the specific test conditions, was based on not exceeding the basic HRE structural design capability. This capability is considered to be as follows:

Cross section, ΔT	=	800°F (cooled shells)
Hot surface, T	=	1600°F (maximum steady-state)
Hot surface, T	=	1700°F (maximum transient)
Cold structure, T	=	1140°F (maximum)
Design life	=	10 hr at the above condition
Cycle life	=	100 cycles at the above condition
Coolant pressure	=	700 psia

At the same time, however, parameters were adjusted in such a way as to produce significant loading in the structure. Reflecting actual operating conditions, for example, cross-section ΔT's as high as 1400°F were imposed, offsetting hot surface temperatures that were lower than design maximum.

The specific objectives of the program fall into two broad categories involving heat transfer and structural performance. The main objectives of the test program relative to heat transfer were to demonstrate the adequacy of the cooling system design, to verify the analytic procedures used, and to compare the test results with analytic predictions. Specific heat transfer test objectives can be divided into three main areas, (1) aerodynamic heating, (2) cooling performance, and (3) transient response.

The principal objectives of the test program, as related to structures, were to evaluate structural loading due to aerodynamic effects, structural capability to withstand the applied loads, thermal fatigue performance of the engine, and internal pressure-containment capability.

8.8.2 Description of SAM

The test item as furnished to the test facility, consisted of the SAM and its associated manifolding and valves, and of support equipment necessary to control the SAM subsystems. The configurations of the various components and subsystems are discussed below.

8.8.2.1 Flight-Designed Cooled Structure

The basic configuration of the SAM is shown in AiResearch Drawing 980800, Sheets 1 and 2 (attached at end of this report). Sheet 2 shows the external water and hydrogen manifolding for the SAM and defines the SAM/wind-tunnel interfaces. The SAM and its manifolding systems were delivered as separate items and assembled at the facility. Instrumentation and electrical lines on the assembly were terminated at connectors compatible with the facility interface.

Figure 8.8-1 shows the SAM hydrogen system schematically. This system is modified slightly from the flight engine schematic discussed in Section 5.1 in that the strut-sides hydrogen coolant is supplied from the main inlet manifold. In the flight engine design, the strut-sides hydrogen was tapped from the aft support manifold on the trailing edge flow route. All of the plumbing and valves shown in Figure 8.8-1 form a part of the SAM, as shown on either sheet of Drawing 980800. The system has a single inlet connection and a single outlet connection. At the inlet to the SAM system, the facility provides hydrogen at ambient or at 160°R, and at 900 to 1100 psia. The exhaust from the SAM system is to the facility vent line.

The basic system consists of the valves, designated PCV (pressure control valve), CRV (coolant regulating valve), FDV (fuel dump valve), and ICV (injection control valves). In addition to the basic system valves, the system included three failure-protection valves, designated BPV1 and BPV2 (bypass valves) and RV (relief valve). Failure mode of the bypass valves is the open position for either electrical or pneumatic failures.

8.8.2.2 Water Systems

The facility provides a single inlet to each cowl, pylon,and mounting structure water cooling of the two systems (high pressure and low pressure). Each of the five flow routes has a manual valve at the outlet which is used to adjust flow rate through the routes. The flow rate in each individual route is determined from a pressure-drop-versus-flow-rate calibration prior to test.

8.8.2.3 Support Equipment

The support equipment required for testing of the model includes the temperature-control system, the pressure-control system, and the inlet spike actuation-control system.

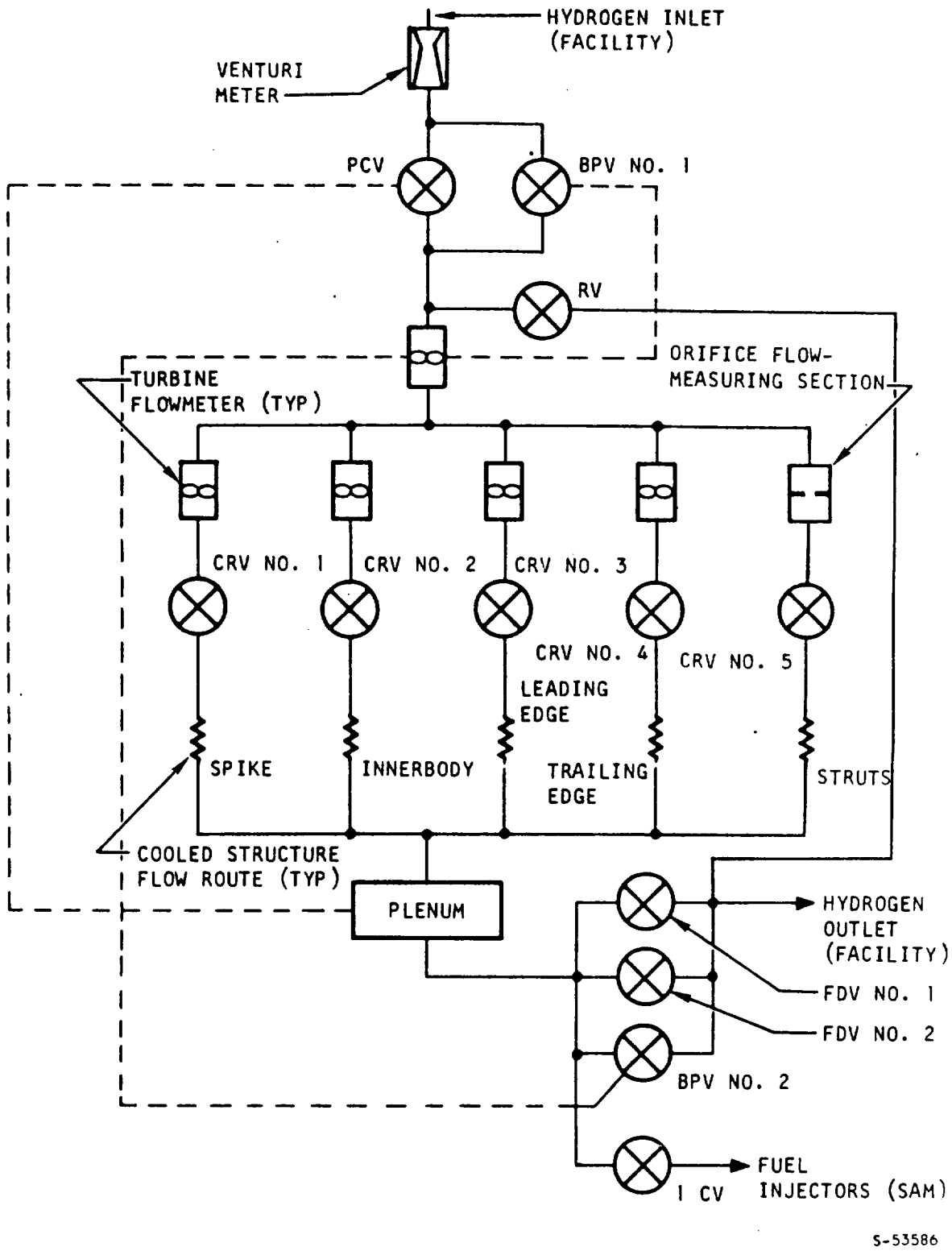

Figure 8.8-1. HRE/SAM Hydrogen System

8.8.2.4 Instrumentation

Much of the instrumentation (hydrogen thermocouples, hot skin thermocouples, and static pressure taps) associated with the basic flight-weight components is installed as part of the manufacturing process. This portion of the instrumentation was defined at a very early stage. Accelerometers, strain gages, and cold-wall thermocouples were installed as required, as were thermocouples and pressure taps in the hydrogen lines.

The instrumentation of the coolant water systems was aimed at permitting verification of operating conditions (flow rates, pressure drop, and water temperatures). Performance data (aerodynamic heating and metal temperatures) on the water-cooled cowl/pylon and support wedge were not obtained, in keeping with the test objectives. A summary of the SAM test instrumentation is shown on Table 8.8-1. The assignment of instrumentation to specific recording devices reflects availability as follows:

Data Acquisition System	Channels
Beckman B-210	99
SEL	90
Total	189
Less facility requirements	20
Total available	169
FM tape	26
CEC recorders	60

The Beckman B-210 has a 2-Hz response and the SEL has a 20-Hz response. This response difference was not a primary consideration and, in general, the two systems were used interchangeably. In assigning measurements of aerodynamic static pressure, preference was given to the Beckman System because the SEL might have produced unwanted hash. To minimize manual handling of data, the DAS and FM tape were considered primary devices. CEC recording channels were used to record strains and accelerations in parallel with the FM tapes, as well as for post-run playback, as indicated in the tables (two records were obtained in this way as a convenience). Additional CEC channels were used to monitor parameters for the various system valves.

Monitoring of data on the Beckman B-210 occurs on a bargraph (98 channels) or on a Sanborn recorder (8 channels). The number of monitored quantities was minimized. Run times were relatively short; consequently, the capability for reaction was limited, and monitoring was confined to the critical parameters. Reliance was generally placed on the temperature-control system to ensure failsafe operation of the model. Monitoring of data on the strip chart recorders

TABLE 8.8-1

SAM TEST INSTRUMENTATION SUMMARY

Description	Installed Channels	Recording Channels Per Test						Monitoring Channels Per Test	
		Test Group 1		Test Group 2					
		B-210	SEL	B-210	SEL	CEC	FM	B-210	Strip Chart
H_2 Pressure	28	3	13	3	19	1		4	
H_2 ΔP	6		6		6				
Hot Gas Pressure	71	60		45		1		1	
H_2O Pressure	7								7
H_2O ΔP	2								2
N_2 Cavity Pressure	1	1		1				1	
H_2 Thermocouple	51	4	30	4	37			4	
H_2 Resistance Thermometer	5		3		3				
Metal Thermocouple	57	21	17	35	18	1			3
H_2O Thermocouple	8								8
Frequency	5		5		5				
Actuator	2	1		1		1		1	
Strain	12						12		
Acceleration	13						13		
Totals	268	80	74	89	88	4	25	11	20
Total 4-Wire	134	65	22	50	28	3	12	7	9
Total 2-Wire	134	15	52	39	60	1	13	4	11

served to purposes: (1) pretest setup of coolant water flows, and (2) recording of water flows and pressures during test to verify adequacy of operation and permit failure analysis as required.

Test groups are noted in Table 8.8-1 for data recording purposes. Each group reflects a single run or group of runs during which a specific number of parameters were recorded. The changeover from one test group to the other was accomplished with electrical patch boards. Test Group 1 constitutes runs during which aerodynamic data (pressures) were measured. Test Group 2 was aimed at obtaining thermal performance data (temperatures) at the cost of aerodynamic data. Strain gages and accelerometers were recorded during all runs, since(1) they did not infringe on available DAS channels, and (2) these data would be of particular interest during abnormal tunnel or model operation. The differences in instrumentation hookups between Test Groups 1 and 2 are reflected in Table 8.8-1.

8.8.3 Test Setup

8.8.3.1 Wind Tunnel Facility

The basic 8-ft High Temperature Structures Tunnel (HTST) was modified to permit testing of the hydrogen-cooled SAM. The hot gas system constitutes the basic facility. A hydrogen system was added to this facility.

8.8.3.1.1 Hot Gas System

The 8-ft HTST is a blowdown facility, shown schematically in Figure 8.8-2. Methane is burned with air in the combustor and discharged into the test section through the supersonic nozzle. The nominal Mach number in the test section is 7; the nozzle diameter is 8 ft. An air-driven ejector is used in the diffuser. Tunnel run times are a function of total conditions in the combustor and of the air requirements in the ejector. During the SAM tests, the total pressures in the combustor ranged from 920 to 3370 psia, and the total temperatures in the combustor ranged from 2500° to 3500°R. For the low pressure runs, run times (i.e., SAM in the stream) were in the range of 40 to 50 sec; the run times reach a maximum near 2200 psia. At this condition, a run duration of 116 sec was achieved. At maximum tunnel conditions (3300 psia), run times were between 35 and 40 sec.

The SAM was installed on an elevator with a travel of 7 ft. The elevator inserted the model into the gas stream at the beginning of the test in 1.4 sec; at the conclusion of the run, the elevator retracted the model from the gas stream. Insertion and retraction occured with the tunnel flow established at supersonic conditions. In this way, shock loadings on the SAM associated with tunnel starting and flow breakdown were avoided.

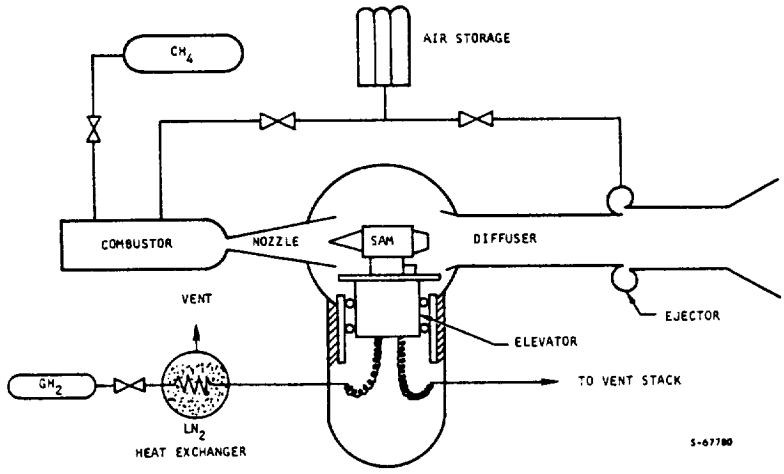

Figure 8.8-2. NASA-Langley 8-Foot High Temperature Structures Tunnel - SAM Tests

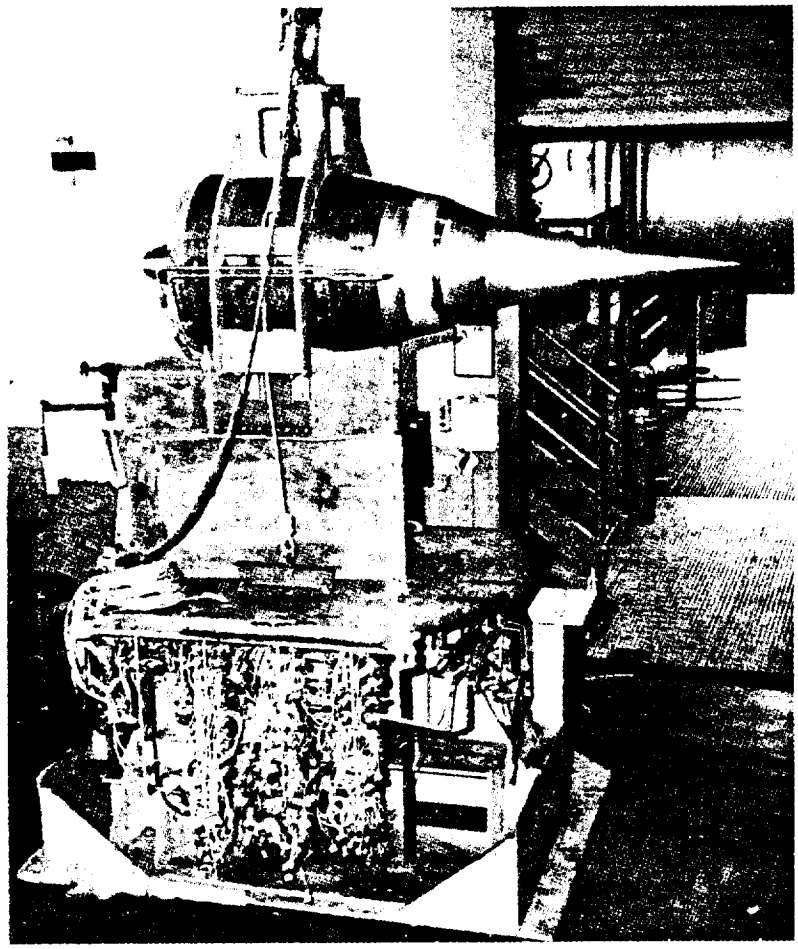

F-15260

Figure 8.8-3. SAM at Wind Tunnel, on Mockup of Elevator Carriage

8.8.3.1.2 Hydrogen System

The hydrogen used in the tests was obtained by the blowdown of bottle cascades. The nominal flow capability of the system was 1.25 lb per sec at 1000 psia SAM inlet pressure. The flow was plumbed through a liquid nitrogen heat exchanger to provide the cooling for runs requiring cryogenic hydrogen. This heat exchanger was capable of furnishing hydrogen at approximately 160°R and 1 lb per sec. It was possible to achieve essentially steady-state outlet temperatures from the heat exchanger in most of the runs. For runs at tunnel conditions not requiring cryogenic hydrogen, the liquid nitrogen heat exchanger was drained. Ambient temperature hydrogen was used to facilitate control for runs requiring relatively low hydrogen flow rates. The hot hydrogen exhausted from the model was ducted to five vent stacks for direct discharge to the atmosphere. Gaseous nitrogen purges were provided at the beginning and at the end of the test runs.

The hydrogen system was interlocked with the other tunnel system in such a way that hydrogen flow could only be initiated after supersonic flow was established in the test section. This was a safety precaution to prevent accumulation of hydrogen in the test section.

8.8.3.1.3 Water Systems

Two separate water systems were available to supply the five water flow routes in the SAM test adapters. They were continuous-operating and were turned on prior to start of tunnel flow, and turned off after tunnel flow had stopped.

The low pressure system, supplying Routes 1 and 2, operated at 163 gpm and 96 psig inlet pressure. This essentially corresponded to the design flow rates and inlet pressure. The high pressure system supplied 118 gpm at an inlet pressure of 205 psig. This compared to a design flow rate of 130 gpm at 180 psig. This system supplied Routes 3, 4, and 5. Visual inspection of the test adapters showed that the flow rates obtained were entirely adequate, i.e., there was no evidence of overheating. No effort was made to modify the system (reduce back pressure) to obtain design values.

8.8.3.2 SAM Installation

A photo of the SAM at the wind tunnel, prior to installation in the wind tunnel test section, is shown in Figure 8.8.3. The assembly is mounted on a mockup of the elevator carriage. The tight fits involved in the installation were checked in this way. The particular view in the figure also shows the array of pressure transducers as mounted to the SAM baseplate. To minimize vibratory inputs to the transducers, they were all mounted in rubber cushions. Rubber dampers were used at the frame mounting points.

Figures 8.8-4 and 8.8-5 show the SAM installed in the test section at zero angle of attack, with the elevator in the raised, or running position. Attachment to the elevator carriage was by a series of bolts on either side of the support wedge. Figure 8.8-5 shows cameras installed in protective

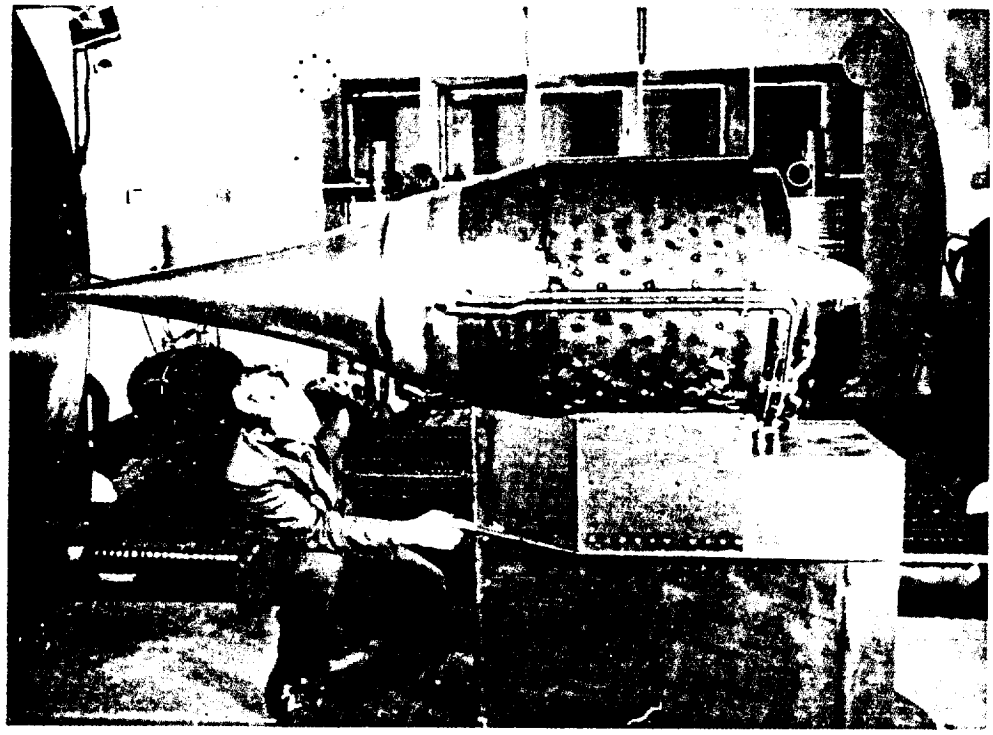

Figure 8.8-4. SAM Installed in Wind Tunnel Test Section - Side View

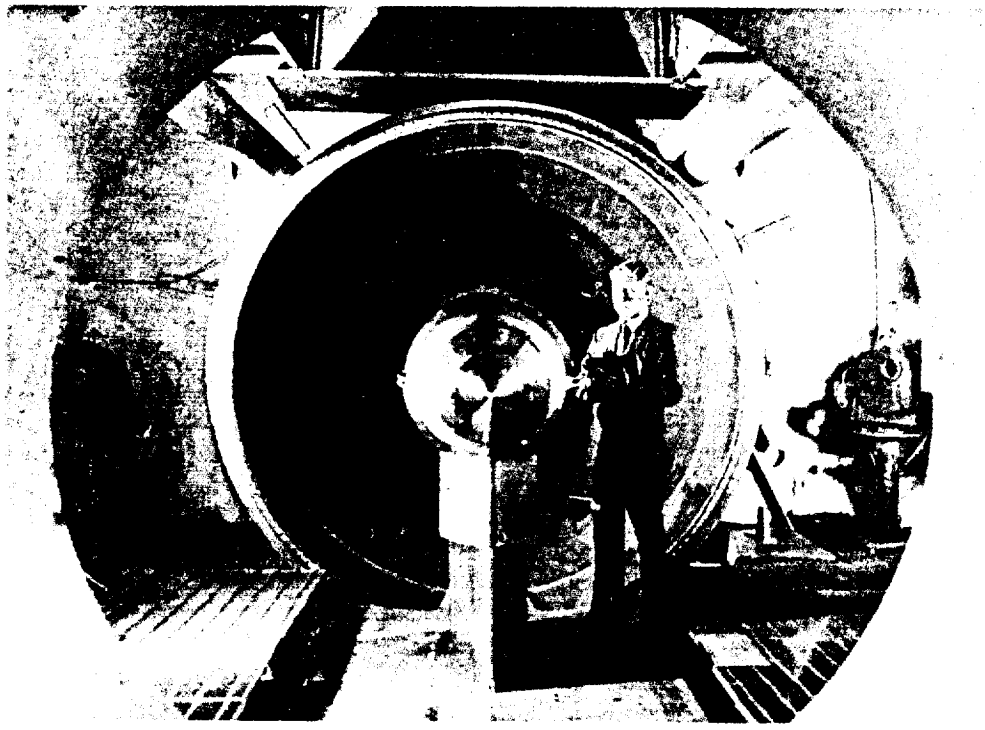

Figure 8.8-5. SAM Installed in Wind Tunnel Test Section - Front View

F-15259

housings on either side of the diffuser inlet; one of the forward cameras is visible in Figure 8.8-4. Up to eight cameras were used during a test run. Schlieren photography was made by means of a setup mounted outside of the test section and operating through the windows shown in Figure 8.8-4.

The final sections of plumbing were fitted with the model in place. In this way, a relatively strain-free installation was obtained. In addition, the lines on the SAM side of the interface were solidly anchored to avoid introduction of leads into the SAM plumbing during operation. Hydrogen connections were limited to a single inlet and outlet. Each of the water systems had a single inlet. To allow adjustment of flow splits among the routes, however, each of the outlets from the five water flow routes was separately plumbed into a manual valve.

8.8.4 Test Procedures

This section outlines the sequencing of various test operations, inspections performed before and after tests, and the integration of the SAM and the wind tunnel operations. The numerous detail checks performed on both the wind tunnel and SAM systems prior to and between tests are not discussed. All systems were elaborately interlocked to prevent damage to both the facility and the SAM as a result of malfunction of components or subsystems.

8.8.4.1 Wind Tunnel Systems

The limiting wind tunnel function was air storage. Frequency and length of the test runs were determined by the air-storage pressure.

With all systems ready prior to a test, the hydrogen system was purged with nitrogen gas. After this, the airflow was started and the pilot burner lit. With everything satisfactory, the main burner was lit. At this point the hydrogen flow to the model was started. The SAM could now be inserted at the discretion of the model controller. Only minor adjustments to the wind tunnel systems were generally required in the course of a run.

When the available air supply was depleted to within approximately 95 percent of the setpoint pressure, the model was retracted on a verbal command. Hydrogen flow through the model was stopped as soon as the model hit the bottom of the test section pod. On some runs, this interlock was manually overridden to permit controlled cooldown of the model or two insertions during a single run.

8.8.4.2 SAM Systems

The following are highlights of the procedures used to operate the SAM systems before, during, and after tests. All operations were performed against checklists.

8.8.4.2.1 Pretest

The most significant pretest activities involved setup and calibration of various control functions. These included the following:

(a) Presetting of the coolant regulating valves to give the flow split desired for the upcoming test conditions. This was done with nitrogen at approximately 100 psi.

(b) Adjustments of the control temperature set points for each of the flow routes.

(c) Calibration of spike position vs LVDT output.

(d) Verification of water flows in each of the five water flow routes on the basis of pressure drops in the flow routes.

(e) Instrumentation zeros and spans.

8.8.4.2.2 Test

Functions of the model operator during the test were limited because of the generally short run times. Figure 8.8-6 shows a typical test cycle involving two insertions and retractions during the run for the purpose of thermally cycling the SAM. During the performance runs, the intermediate retraction of the SAM from the wind tunnel gas streams was omitted.

8.8.4.2.3 Post test

Following a test, the SAM was visually inspected for areas of high heating and for foreign object damage. Leak tests were run on both a pressure-decay basis and using soap solution. Selected data was played back on the SEL system, on paper tape. Using this data, run conditions could be reviewed and adjusted prior to the next run.

8.8.5 Test Results

A total of 47 thermal performance and cycling test runs were performed for the SAM test program (Test 41, Run 5, through Test 41, Run 53; the SAM was not inserted into the gas stream for Test 41, Run 30). The runs were divided into two test groups: the first group, designated as Test 41, emphasized the collection of aerodynamic and thermal performance data. The second group, designated as Test 42, was aimed at the accumulation of thermal-structural data. Twenty-seven runs were performed in this latter test group, twenty-three of them using hydrogen injection. Instrumentation hookups for the two test groups differed to reflect the test emphasis. The SAM was subjected to 60 thermal/structural loading cycles with an accumulated time in the hot gas stream of 30.7 min (1843 sec). Individual run times were from 6 to 115 sec.

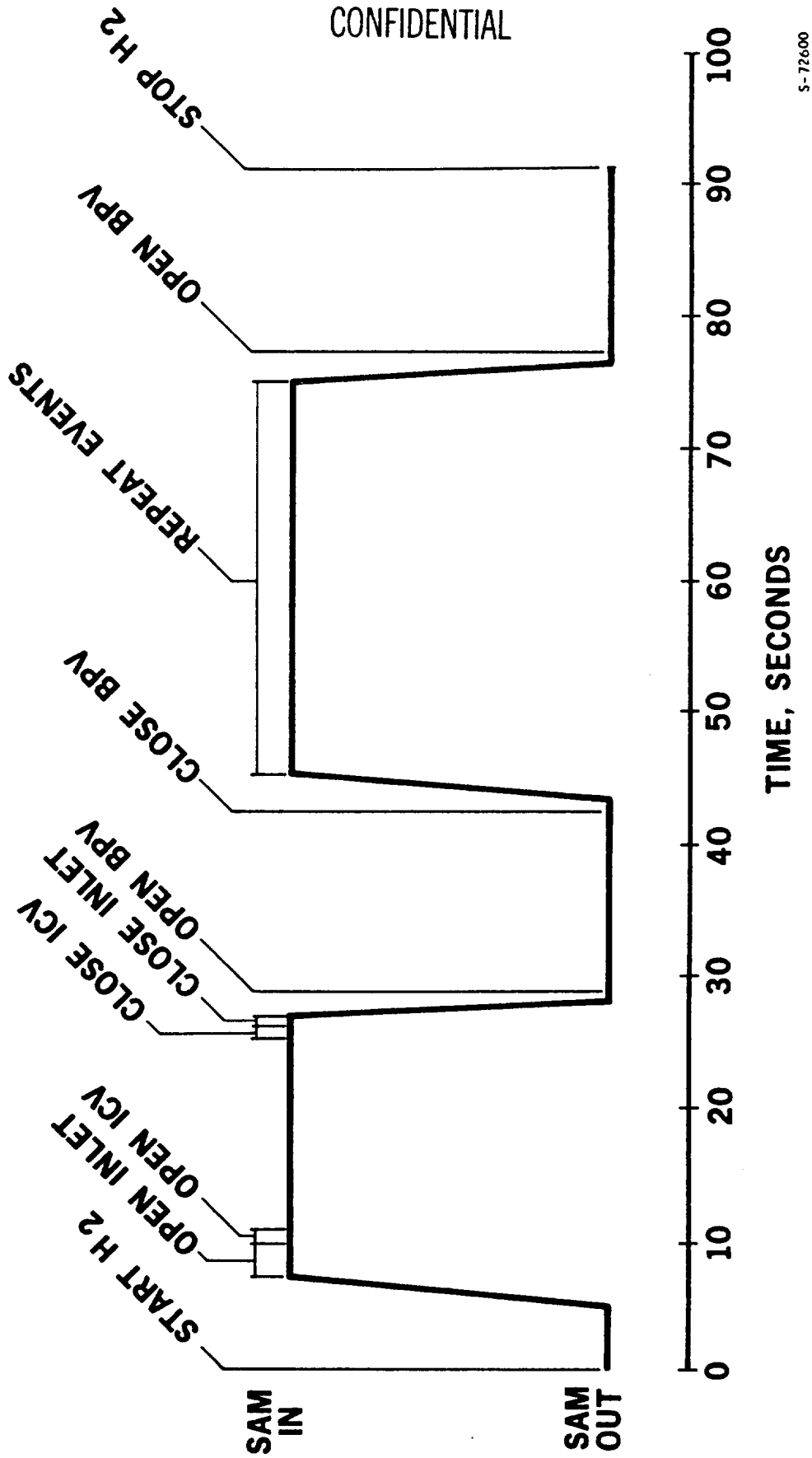

Figure 8.8-6. Wind Tunnel Test Cycle

8.8.5.1 Test Run Summary

A summary of the test conditions and operating parameters is presented in Table 8.8-2, in chronological sequence. Corresponding AiResearch run numbers are included in this table. Tunnel reservoir total pressures and temperatures ranged from 920 to 3370 psia and 2500° to 3500°R, respectively. These reservoir conditions produced test section Mach numbers from 6.3 to 6.8 and total pressures from 300 to 2300 psia. Engine times in the gas stream were from 6 to 115 sec.

Most test runs were performed with a spike retraction (from the fully closed, latched position) of approximately 2.9 in. This retraction gave a spike-shock position outside the leading edge lip. For the remainder of the runs, the spike retractions were from 1.70 to 4.34 in. This range of spike positions gave inlet mass flow ratios from 0.78 to 1.0. The shock-on-lip spike retraction was approximately 3.9 in. at 1380 psia, 2700°R tunnel reservoir total conditions. Operation with spike shock-on-lip was attempted at 1380, 2290, and 3300 psia reservoir total pressures.

The engine was cooled with room temperature inlet hydrogen for the first 34 runs (through Test 42, Run 43) where tunnel reservoir pressures were up to 2200 psia. For the remainder of runs, cryogenic hydrogen (approximately 160°R) was used to cool the engine (reservoir pressures of 2200 psia and above). Of the 47 test runs, 23 were performed with partial or full coolant-jacket hydrogen flow injected into the hot gas stream.

Most of the thermal cycling runs (Test 42, Runs 17 to 38) were achieved by inserting the engine into the tunnel gas stream twice during a test run, with an intermediate withdrawal into the tunnel pod. Three thermal cycles were performed for Test 42, Run 21. Three angle-of-attack runs (Test 41, Runs 51, 52, and 53) were performed at the maximum reservoir pressure of 3370 psia, with the engine centerline pitched 3-deg downward. All other runs were at zero angle of attack.

In addition to the test conditions and operating parameters, Table 8.8-2 contains the significant data affecting thermal fatigue of the hot skin at the outerbody outlet manifold, Station 51.4 in. The summed ΔT's represent the absolute sum of positive and negative ΔT's of the hot skin with respect to the manifold. Δ is the differential growth, and the damage fraction is the fraction of the estimated cycle life expended at the conditions listed. At the conclusion of the tests, 49 percent of the cycle life available in the structure at this location is estimated to have been expended in the course of the tests.

8.8.5.2 Aerodynamic Heating

8.8.5.2.1 Summary of Results

One of the SAM test objectives was to verify or update the methods previously used to predict design flight heat loads and fluxes (Mach 8 freestream and local, 88,000-ft altitude, zero-deg angle of attack). Test heat loads and

CONFIDENTIAL

TABLE 8.8-2

SUMMARY OF HRE SAM STRUCTURAL AND COOLING TESTS (U)

LRC			AiResearch Run No.	Tunnel Total		Time in Tunnel, sec	Spike Retraction, in.	H_2 Injection	Nom. Venturi H_2 Flow Rate, lb/sec	Max Outlet H_2 Temp, T101, °R	Max H_2 Heat Load, Btu/sec	Outerbody Outlet Manifold					Remarks
Test No.	Run No.	Cycle No.		Pressure, psia	Temp, °R							ΣΔT, °R	Max Hot Wall Temp, °R	Δ(∝ΔT)	Damage Fraction	Accum. Damage	
41	5	1	2	975	2600	46	2.34	No	0.38	1025	650	660	1260	0.00535	0.0013	0.0013	
41	7	1	2	960	2600	32	2.30	No	0.19	1210	497	680	1680	0.00620	0.0031	0.0044	Automatic shutdown due to SAM over-temperature.
41	12	1	3	950	2500	13	2.88	No	0.29	850	337	661	1110	0.00520	0.0010	0.0054	
41	13	1	3	920	2500	42	2.89	No	0.23	1160	508	845	1370	0.00710	0.0041	0.0085	Foreign object damage (FOD) in 13 areas of leading edge.
41	16	1	5	1300	2600	42	2.89	No	0.35	1180	770	805	1360	0.00674	0.0034	0.0129	
41	17	1	5	1290	2700	49	2.89	No	0.35	1220	820	840	1420	0.00700	0.0040	0.0169	
41	20	1	7	1540	2700	45	2.86	No	0.31 - 0.44	1291	911	1122	1565	0.00952	0.0114	0.0283	Dent and leak at leading edge stagnation line due to FOD.
42	3	1	4	950	2600	39	2.85	Yes	0.24 - 0.33	1210	480	819	1380	0.00680	0.0035	0.0318	
42	11	1	6	1275	2700	44	2.89	Yes	0.25 - 0.47	1290	830	1207	1555	0.01020	0.0138	0.0456	0.045 x 0.065-in. hole in side of leading edge tip due to FOD.
42	12	1	8	1510	2800	41	2.89	Yes	0.25 - 0.40	1310	1100	1035	1510	0.00875	0.0086	0.0542	
41	26	1	30	2200	3100	16	1.70	No	0.31 - 0.47	1205	770	1215	1675	0.01037	0.0158	0.0700	Automatic shutdown caused by electrical noise.
41	27	1	30, 31	2200	3000	40	0.0	No	0.34 - 0.41	682	190	---	---	---	0	0.0700	No spike retraction. Control error. 0.010-in. dia hole in side of leading edge.
41	28	1	30, 31	2200	3000	22/8	2.33/2.87	No	0.37 - 0.51	1350	1380	1265	1550	0.01055	0.0151	0.0851	Two spike positions. Automatic shutdown due to methane alarm. Leak at nozzle-inner shell port seals; replaced these.
41	29	1	9	1380	2700	50	2.86	No	0.20 - 0.50	1310	690	1215	1570	0.01027	0.0142	0.0993	Leak at aft end of strut No. 5.
42	14	1	8	1530	2700	52	2.89	Yes	0.25 - 0.35	1410	800	1300	1637	0.01093	0.0177	0.1170	
42	16	1	10	1375	2700	7/6/6	0.0	No	0.38 - 0.42	680	---	130	708	---	0	0.1170	Four model insertions. No spike retraction. Determine minimum ejector pressure.
42	17	1	10	1360	2700	68	2.89	Yes	0.16 - 0.35	1320	690	1050	1384	0.00813	0.0079	0.1249	
42	19	1	11	1380	2700	21	2.89	Yes	0.24 - 0.31	1100	480	770	1390	0.00648	0.0030	0.1279	Leak at nozzle-inner shell port seals; replaced these with rubber O-rings.

CONFIDENTIAL

TABLE 8.8-2 (Continued) (U)

LRC			AiResearch Run No.	Tunnel Total			Spike Retraction, in.	H_2 Injection	Nom. Venturi H_2 Flow Rate, lb/sec	Max Outlet H_2 Temp, T101, °R	Max H_2 Heat Load, Btu/sec	Outerbody Outlet Manifold					Remarks
Test No.	Run No.	Cycle No.		Pressure, psia	Temp, °R	Time in Tunnel, sec						$\Sigma\Delta T$, °R	Max Hot Wall Temp, °R	$\Delta(\propto\Delta T)$	Damage Fraction	Accum. Damage	
42	38	1	24	1370	2700	18	2.90	Yes	0.13-0.44	1210	450	970	1599	0.00830	0.0081	0.2857	
42	38	2	24	1370	2700	31	2.89	Yes	0.15-0.30	1340	630	955	1550	0.00814	0.0066	0.2923	
42	41	1	25	1380	2700	8	3.68	No	0.21	830	210	620	1083	0.00488	0.0007	0.2930	Shock-on-lip calibration. No Schlieren obtained.
42	41	2	25	1380	2700	9	4.00	No	0.21	930	270	656	1182	0.00537	0.0012	0.2942	
42	41	3	25	1380	2700	8	4.34	No	0.21	940	300	650	1186	0.00524	0.0011	0.2953	
42	42	1	25	1390	2700	8	3.56	No	0.23	750	85	530	1054	0.00420	0.0003	0.2956	Shock-on-lip calibration. Hole and leak in leading edge due to foreign object damage.
42	42	2	25	1390	2700	8	3.86	No	0.21	970	200	743	1304	0.00761	0.0048	0.3004	Automatic shutdown due to faulty SAM thermocouple.
42	43	1	26	1370	2700	62	3.85	No	0.21-0.30	1190	630	1078	1414	0.00883	0.0084	0.3088	Shock-on-lip. Spike coolant outlet bellows leak. Replaced nozzle seals; adjusted nozzle fit.
41	30	1	---	---	---	---	---	---	0.50-1.0	---	---	4.60	RT	0.00343	0.0001	0.3089	Cryogenic H_2 calibration run.
41	37	1	27	2835	3300	57	2.90	No	0.60-0.94	1170	2775	1224	1435	0.00999	0.0119	0.3208	
41	38	1	32	3330	3500	18	2.91	No	0.75-0.87	1240	3200	1410	1561	0.01159	0.0195	0.3403	Shutdown due to high tunnel nozzle throat temp
41	39	1	33	3320	3400	32	2.89	No	0.62-0.77	1330	2840	1390	1535	0.01140	0.0183	0.3586	
42	44	1	34	2220	3000	34	2.89	Yes	0.15-0.45	1360	1500	1452	1675	0.01215	0.0240	0.3826	
42	45	1	34	2250	3000	115	2.89	Yes	0.30-0.67	1180	2050	1128	1511	0.00950	0.0109	0.3935	Tunnel flow breakdown during SAM refraction.
42	46	1	28	3330	3400	36	2.90	Yes	0.60-0.90	1260	3030	1326	1458	0.01084	0.0154	0.4089	Hole and leak in leading edge due to foreign object damage.
42	47	1	35	3350	3200	31	2.90	Yes	0.58-0.80	1415	2350	1327	1570	0.01093	0.0168	0.4258	
41	40	1	29	2290	3000	64	3.43	No	0.23-0.54	1280	1910	1373	1544	0.01127	0.0178	0.4436	Shock-on-lip. Automatic shutdown due to SAM overtemperature (trailing edge route).
41	42	1	37	3300	3200	40	3.12	No	0.57-0.85	1290	2620	1297	1488	0.01059	0.0145	0.4581	Shock-on-lip.

CONFIDENTIAL

TABLE 8.8.2 (Continued) (U)

LRC			AiResearch Run No.	Tunnel Total		Time in Tunnel, sec	Spike Retraction, in.	H_2 Injection	Nom. Venturi H_2 Flow Rate, lb/sec	Max Outlet H_2 Temp, T101, °R	Max H_2 Heat Load, Btu/sec	Outerbody Outlet Manifold					Remarks
Test No.	Run No.	Cycle No.		Pressure, psia	Temp, °R							$\Sigma\Delta T$, °R	Max Hot Wall Temp, °R	$\Delta(\alpha\Delta T)$	Damage Fraction	Accum. Damage	
42	19	2	11	1380	2700	22	2.89	Yes	0.24 - 0.31	1200	560	715	1430	0.00627	0.0028	0.1307	
42	21	1	12	1380	2800	14	2.90	Yes	0.18 - 0.27	1080	300	1017	1500	0.00856	0.0080	0.1387	
42	21	2	12	1380	2800	14	2.89	Yes	0.18 - 0.27	1120	410	723	1364	0.00605	0.0022	0.1409	
42	21	3	12	1380	2800	15	2.89	Yes	0.18 - 0.27	1130	380	735	1378	0.00612	0.0024	0.1433	
42	22	1	13	1370	2700	19	2.89	Yes	0.25 - 0.43	1220	380	945	1636	0.00817	0.0077	0.1510	
42	22	2	13	1370	2700	20	2.88	Yes	0.20-0.22	1280	540	610	1506	0.00528	0.0015	0.1525	
42	24	1	14	1370	2700	24	2.89	Yes	0.19 - 0.22	1080	460	1010	1480	0.00842	0.0075	0.1600	Automatic shutdown due to methane alarm after one cycle.
42	25	1	15	1380	2700	14	2.90	Yes	0.13 - 0.18	1080	460	1020	1500	0.00850	0.0078	0.1678	Leak at forward end of strut No. 5
42	25	2	15	1380	2700	13	2.89	Yes	0.14 - 0.17	1090	270	820	1370	0.00682	0.0036	0.1714	
42	28	1	16	1370	2700	18	2.89	Yes	0.19 - 0.33	1216	450	1139	1576	0.00965	0.0120	0.1834	
42	28	2	16	1370	2700	15	2.89	Yes	0.16 - 0.21	1260	420	724	1490	0.00620	0.0027	0.1861	
42	29	1	17	1380	2700	19	2.89	Yes	0.20 - 0.30	1220	400	1122	1563	0.00940	0.0110	0.1971	
42	29	2	17	1380	2700	17	2.88	Yes	0.16 - 0.20	1290	410	810	1518	0.00720	0.0042	0.2013	
42	30	1	18	1380	2700	31	2.89	Yes	0.15 - 0.23	1320	510	1147	1560	0.00955	0.0115	0.2128	Leak at forward end of strut No. 2.
42	31	1	19	1380	2750	22	2.90	Yes	0.18 - 0.21	1160	360	935	1452	0.00760	0.0053	0.2181	
42	31	2	19	1380	2750	34	2.90	Yes	0.16 - 0.20	1320	400	841	1516	0.00710	0.0045	0.2236	
42	32	1	20	1380	2700	19	2.89	Yes	0.08 - 0.20	1150	360	1064	1498	0.00877	0.0086	0.2322	Leak at forward end of strut No. 3.
42	32	2	20	1380	2700	31	2.89	Yes	0.08 - 0.20	1310	450	870	1547	0.00636	0.0031	0.2353	
42	33	1	21	1380	2700	20	2.89	Yes	0.09 - 0.21	1150	400	905	1429	0.00713	0.0043	0.2396	
42	33	2	21	1380	2700	31	2.90	Yes	0.09 - 0.21	1310	460	921	1536	0.00768	0.0058	0.2454	
42	34	1	22	1390	2700	67	2.90	No	0.19 - 0.41	1300	720	1388	1573	0.01155	0.0198	0.2652	
42	36	1	23	1390	2700	59	2.89	Yes	0.14 - 0.23	1360	660	1183	1570	0.00980	0.0124	0.2776	Leak at aft end of inner shell.
41	51	1		3370	2700	12	4.24	No	0.47	1250	2300	1140	1489	0.00926	0.0100	0.4670	Automatic shutdown due to methane alarm. Large dent in spike, with small leak.
41	52	1		3350	2700	6	4.24	No	0.56	1225	-	1112	1658	0.00956	0.0122	0.4792	Automatic shutdown due to SAM over-temperature. Low flow in L.E. and T.E. routes.
41	53	1		3370	2900	19	4.22	No	0.56	1350	2600	1199	1351	0.00989	0.0108	0.4900	Bolt damage at outerbody flange; leading edge separated from outer shell by 0.2 in. and held in place by connecting tubes. No new hydrogen leaks.

CONFIDENTIAL

average heat fluxes were obtained from measurement of the heat input to the hydrogen coolant in the flow routes at steady state. Analytic heat loads and fluxes were obtained from measured tunnel freestream conditions, SAM hot gas surface pressure and temperature distributions, and the design prediction methods. Test and analytic average heat fluxes agree within ±20 percent over most surfaces of the engine.

Hot coolant hydrogen from the outlet of the SAM flow routes was injected into the captured hot gas stream for most of Test 42 runs. The effect of hydrogen injection was detected as higher hot gas static pressures downstream of the injectors than for runs (Test 41) without injection. The effect of injection was not detected in the hydrogen heat loads or measured surface temperatures on the aft flow routes.

Locally highly heated areas were detected from posttest observations of surface metal discolorations. The highly heated zones were traced to shock wave-boundary layer interactions. The heating rates relative to unaffected adjacent areas were estimated from a layout of the aerodynamic flow field.

8.8.5.2.2 Test Data

8.8.5.2.2.1 Tunnel Conditions

Heat loads on the spike flow route and the total SAM are shown in Figure 8.8-7 as a function of tunnel reservoir total pressure. These heat loads are maximum loads during thermal performance runs as measured from the hydrogen coolant heat absorption. The range of tunnel reservoir total pressure was from 900 psia to 3330 psia for the tests shown. Tunnel total temperature increased from 2500° to 3400°R with increasing tunnel total pressure in the following manner:

Total Pressure, psia	Total Temperature, °R
900	2500
1400	2700
2200	3000
3300	3400

Circular data points represent test runs with room temperature inlet hydrogen; triangular data points represent test runs with cryogenic inlet hydrogen (150° to 200°R). Room temperature inlet hydrogen was used for tunnel total pressures up to 2200 psia, and cryogenic hydrogen was used at and above 2200 psia. Though the inlet lines were sized for cryogenic hydrogen, room temperature inlet hydrogen was permissible from the standpoint of inlet line pressure drop below 2200 psia because the lower flow rates required at or below 2200 psia (0.15 to 0.50 lb/sec model total) more than offset the threefold reduction in hydrogen density. Cryogenic inlet hydrogen flow rates of up to 0.90 lb/sec were used for test runs up to 3330 psia tunnel total pressure.

S-67774

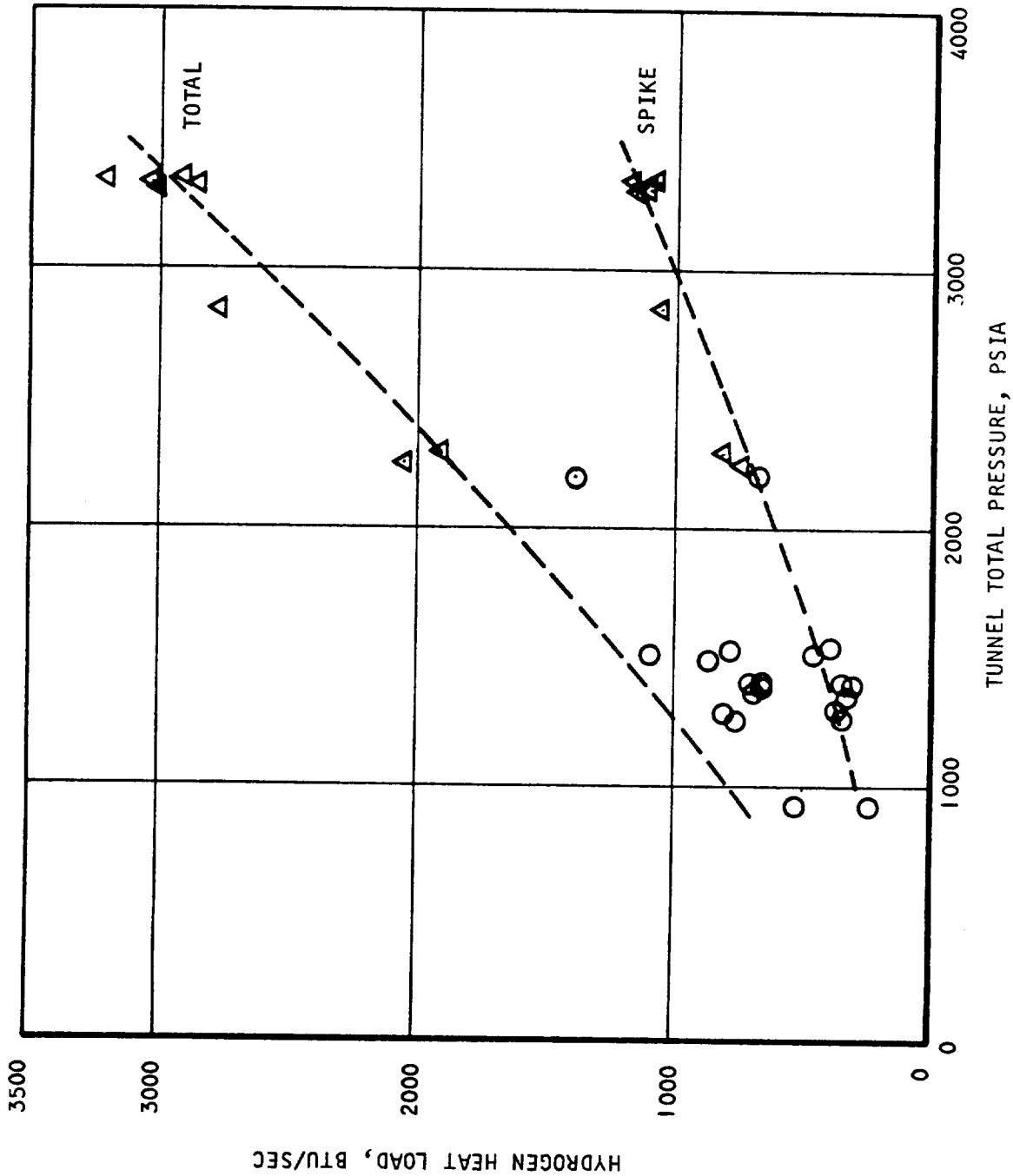

Figure 8.8-7. Test Hydrogen Heat Loads (U)

The dashed lines represent steady-state analytical predictions of spike and total heat loads. These predictions were based on a detailed analysis at 3300 psia tunnel reservoir total pressure. Predictions at lower pressures were calculated by ratioing the detailed prediction by the total-pressure ratio (to the eight-tenths power) and the total-to-average wall-temperature-difference ratio.

Agreement between the data and prediction is good (±20 percent or less) for the spike at all total pressures, and for the total model at pressures of 2200 psia and above. At total pressures at and below 2200 psia with room temperature inlet hydrogen, the total heat loads are consistently lower than the prediction by as much as 43 percent. These lower-than-predicted test loads result from non-attainment of steady-state thermal conditions on the aft routes (innerbody, trailing edge, strut sides) during exposure times of up to 68 sec to the hot gas. The spike and leading edge flow routes reached steady state (as determined by hydrogen coolant outlet temperatures) in 10 to 30 sec for all thermal performance runs. At the higher coolant flow rates used with tunnel reservoir total pressures above 2200°R, steady state on the aft routes was achieved in 40 sec or less.

8.8.5.2.2.2 Heat Load Distribution

Flow route heat loads and average heat fluxes were based on test hydrogen flow rates and inlet and outlet hydrogen temperatures at steady state. At intermediate locations along the flow routes, cold wall thermocouple measurements were used interchangeably with hydrogen temperatures. Enthalpy differences, derived from hydrogen (or cold wall) temperatures, were multiplied by hydrogen flow rate to obtain heat load. The enthalpy-temperature curve for normal hydrogen is shown in Figure 8.8-8. This curve applies to all test runs, since the hydrogen for the cryogenic runs was obtained from ambient temperature storage and no ortho-para conversion is expected for the conditions encountered.

A tabulation of the heat loads and average heat fluxes for Test 41, Run 39 is presented in Table 8.8-3. This test run was performed at the tunnel reservoir total conditions of 3320 psia and 3400°R. The spike retraction was 2.89 in. relative to the fully extended position; the coolant hydrogen inlet temperature was approximately 150°R; and all outlet coolant was exhausted out the vent line (no hydrogen injection). The run time in the tunnel was 32 sec and the flow rate and temperature data indicated in Table 8.8-3 are averages over the last 10 sec prior to engine withdrawal from the tunnel. All flow routes were at approximately steady-state thermal conditions during this period.

The total engine heat load is 2956 Btu/sec and compares with a pretest analytical prediction of 2890 Btu/sec for approximately the same tunnel reservoir total conditions (3300 psia, 3600°R). The heat loads on the external surfaces of the leading and trailing edge flow routes in Table 8.8-3 are estimated values. There are no hydrogen thermocouples directly at the leading and trailing edges, so discrete heat load values on these external surfaces could not be obtained. The heat flux distribution on the external leading edge was estimated by calculating the local heat fluxes at 2.30 in. and 4.35 in. aft of the leading edge tip based on hot and cold wall thermocouple pairs T1, T3, and T2, T4, respectively. A flat-plate heat flux distribution passing through the

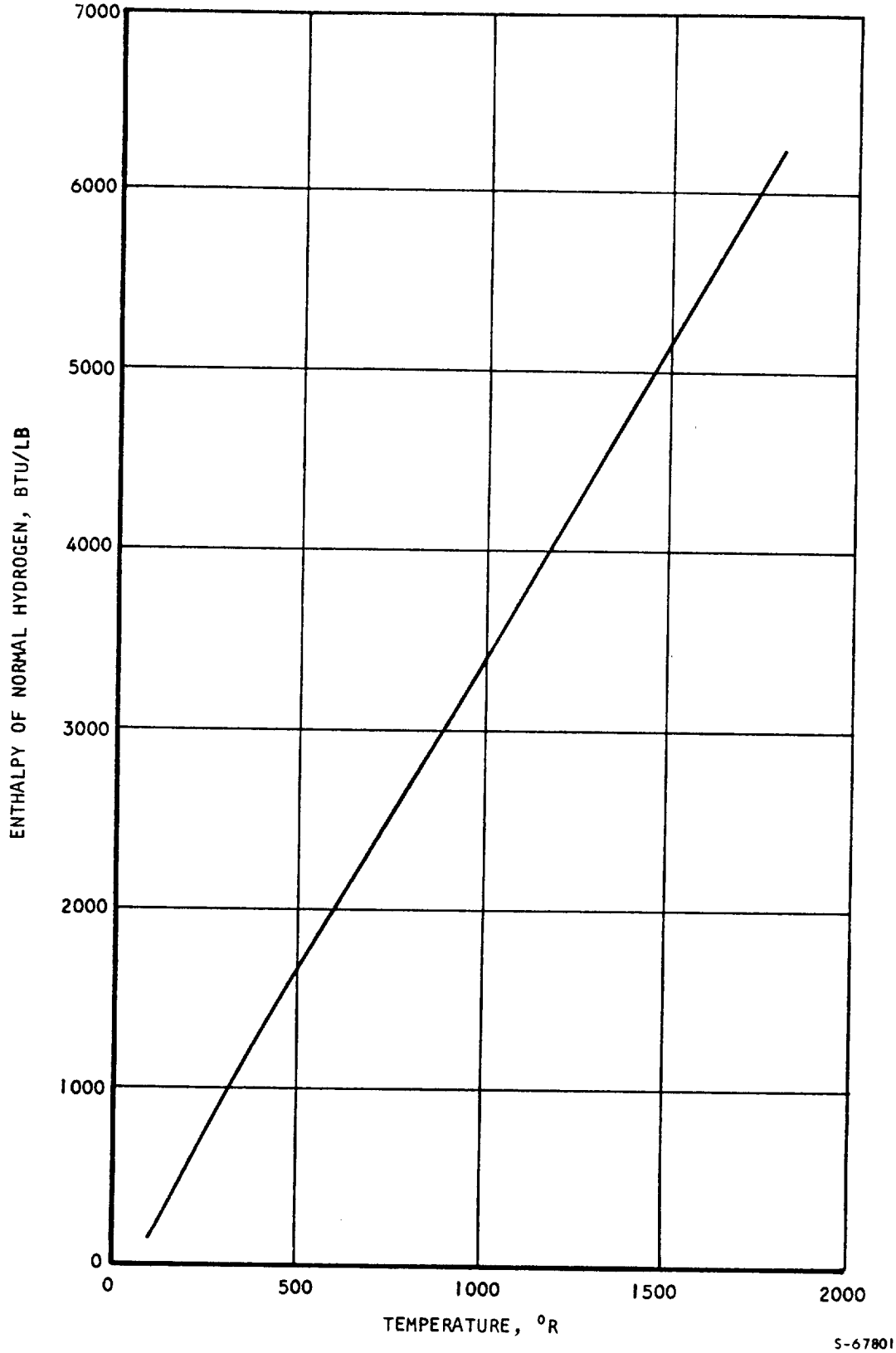

Figure 8.8-8. Enthalpy of Normal Hydrogen

CONFIDENTIAL

TABLE 8.8-3

HYDROGEN HEAT LOAD DISTRIBUTION FOR TEST 41, RUN 39 (U)

Flow Route	Axial Location X_1, in. (ref. coord)	Axial Location X_2, in. (ref. coord)	H_2 Flow Rate, lb/sec	H_2 Temp at X_1, °R	H_2 Temp at X_2, °R	H_2 Heat Load X_1 to X_2, Btu/sec	Surface Area X_1 to X_2, ft²	Avg Heat Flux X_1 to X_2, Btu/sec-ft²
Spike	Inlet	35.70	0.279	154	388	251	5.10	49.2
↓	35.70	44.30	↓	388	821	430	3.30	130.3
	44.30	55.76		821	1237	408	4.87	83.8
Innerbody	55.76	65.60	0.078	1160	555	166	4.80	34.6
↓	65.60	75.60	↓	544	316	68	3.50	19.42
	75.60	Inlet		316	212	31	2.00	15.5
Leading Edge	Inlet (external surface)	LE Tip	0.269	151	343**	200*	1.30	168.4
↓	LE Tip	43.45	↓	343	921	546	3.15	173.0
	43.45	46.00		921	1065	136	1.13	120.2
	46.00	50.40		1065	1212	140	1.97	71.0
Outerbody Outlet Manifold (OBOM)	50.40	54.13		1212 (1255***)	1140	88	1.70	51.7
Trailing Edge	54.13	TE Tip	0.166	1140	210	389	10.75	36.2
↓	TE Tip (external surface)	Inlet	↓	210**	148	27*	2.11	12.8
Strut Sides	Inlet	Outlet	0.0163	154	1116	58	0.87	60.0
Strut Leading Edges	Inlet	Outlet	(0.078)	154	212	18	0.0213	845.0
Totals			0.754	154 (inlet temp to engine)	1240 (average	2956	46.67	63.4

Test 41 Run 33
3320 psia, 3400°R reservoir total conditions
2.89 in. spike retraction
No H_2 injection

NOTES
* Estimated heat load, see text
** Calculated from estimated heat load
*** H_2 temp in OBOM, equals average of T77 and T78

CONFIDENTIAL

two calculated heat flux points was extrapolated up to the leading edge tip. The analytical value above was used as the external trailing edge heat load in Table 8.8-3 since there is no hot gas pressure or thermocouple instrumentation in this region. These external surface heat load estimates do not affect the total engine heat load since the inlet and outlet hydrogen temperatures of all routes are experimentally measured. These estimates do, however, affect the heat load distribution within the leading and trailing edge flow routes.

8.8.5.2.2.3 Effect of Hydrogen Injection

Some or all of the outlet coolant hydrogen from the engine flow routes was injected into the captured hot gas stream for most of Test 42 runs. The injection ports are located at Station 43.00 on the spike and at Station 43.84 (ref. coord.) on the forward outer shell. The purpose of injection was to thermally cycle the structure in the vicinity of the injection ports, since the injected hydrogen temperature was expected to be several hundred degrees higher than the local coolant temperature. The effects of the hydrogen injection were detected in the hot gas surface pressure measurements downstream of the injectors. It is unlikely that overall combustion occurred, since the hydrogen heat loads on the aft routes were no higher than without hydrogen injection.

Hot gas surface pressure measurements (expressed in terms of a pressure coefficient) are presented in Figure 8.8-9 for a test run with hydrogen injection (Test 42, Run 46) and a test run without hydrogen injection (Test 41, Run 39). Both test runs were at the maximum tested tunnel reservoir total conditions of 3320 psia and 3400°R. The spike retraction was 2.89 in. relative to the fully latched position. The circular data points are centerbody measurements and triangular data points are outerbody (internal surface) pressure measurements. Flagged data points indicate pressure measurements of the hydrogen injection test run. The injection rate was 0.35 lb/sec relative to a captured methane combustion products (equivalence ratio of 0.74) flow rate of 28.9 lb/sec. The curve is the analytical prediction without hydrogen injection.

Static pressure measurements with injection are generally higher than without injection, particularly near the injector locations, as indicated in Figure 8.8-9; however, the increase in static pressures near the injectors with hydrogen injection falls within the data scatter of equivalent static pressure increases recorded during 2/3-scale inlet model testing with helium injection. Similar static pressure results were obtained when two test runs at 1380 psia, 2700°R tunnel reservoir total conditions were compared (Test 42, Run 34 without hydrogen injection, and Test 42, Run 36 with hydrogen injection). At these tunnel conditions, the freestream oxygen content of the methane combustion products (equivalence ratio of 0.45) is higher than for the comparison in Figure 8.8-9 but the total temperature is lower.

Heat loads on the trailing edge flow route were calculated for Test 42, Run 34 (without hydrogen injection) and Run 36 (with hydrogen injection). Since the trailing edge flow route (as well as the strut sides and innerbody flow routes) did not reach thermal steady-state conditions after test run times of 67 and 59 sec, respectively, the heat-sink rate into the flow route structure was added to the hydrogen heat load to obtain an estimate of the aerodynamic heat load. The average trailing edge structural temperatures and

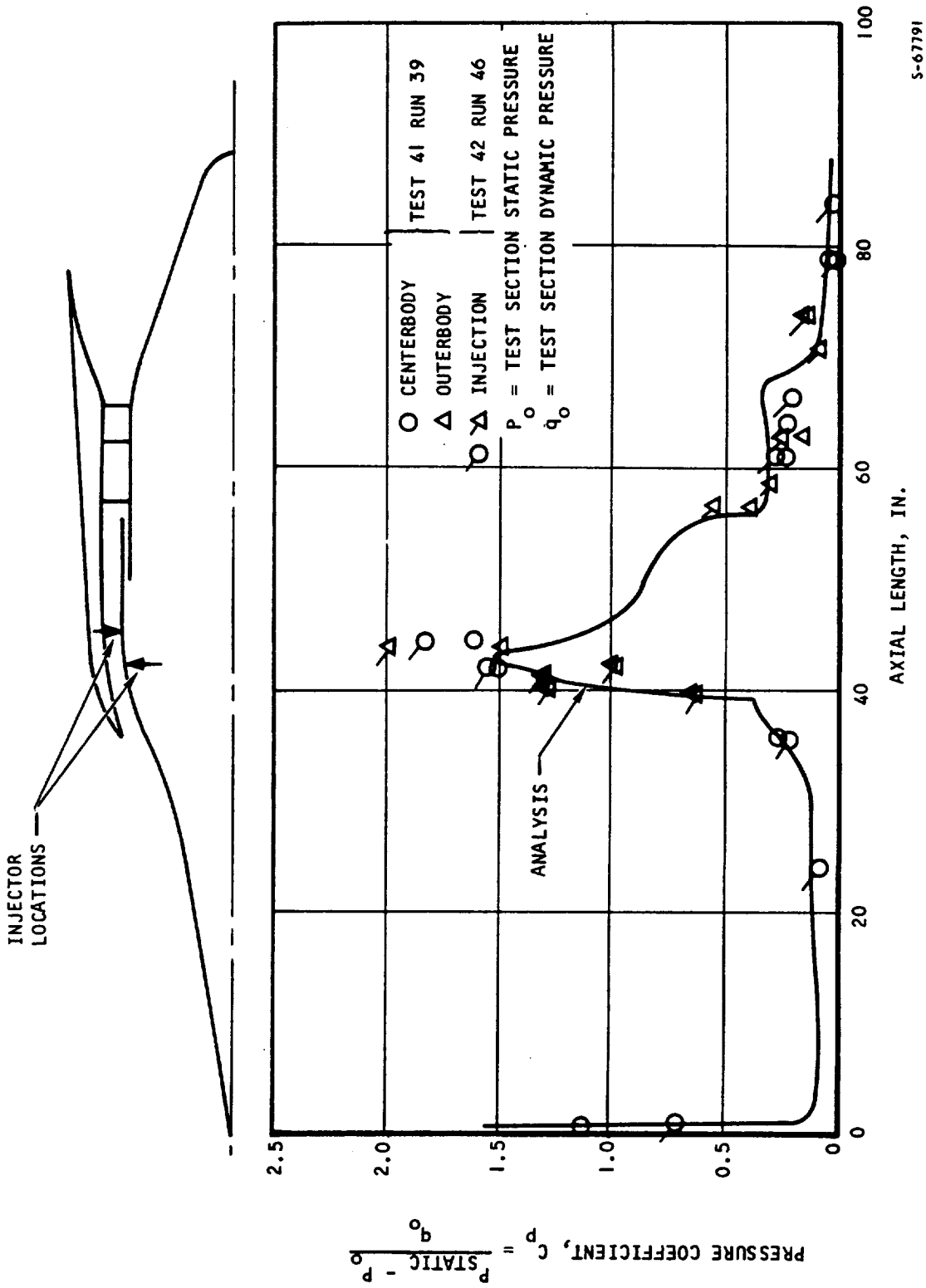

Figure 8.8-9. Aerodynamic Static Pressure Distributions (U)

hydrogen heat loads for both test runs are shown in Figure 8.8-10. The data acquisition time periods shown are the last 32 and 22 sec of Runs 34 and 36, respectively, prior to test shutdown. The average structural temperature is formed by the arithmetic average of thermocouple readings T88, T93, and T100, at reference coordinate axial Stations 54.13, 62.30, and 70.10, respectively. For both runs, the rate of structural temperature increases and the hydrogen heat loads are approximately equal over the time periods shown. A summary of the hot gas and coolant conditions and the parameters that contributed to the aerodynamic heat load estimate for both runs is shown in Table 8.8-4. The estimated aerodynamic heat load without hydrogen injection (Run 34) is 45.0 Btu/sec, and 42.5 Btu/sec with hydrogen injection (Run 36). The 6-percent difference between these heat loads is within the estimated ±11.2-percent band of uncertainty in trailing edge heat load.

8.8.5.3 Cooling Performance

8.8.5.3.1 Summary of Results

The basic objective of the SAM test program was to verify the design of the hydrogen-cooled engine structure in a severe wind tunnel environment. Since the engine design is dependent on the cooling system, a specific objective was to evaluate the cooling performance. The steady-state cooling performance was evaluated by comparing measurements of hot wall, cold wall and hydrogen temperatures in the engine coolant routes with results of heat transfer analyses for the specific test measurement conditions.

The coolant-side data analyses gave hot and cold wall temperatures at each axial location based on average circumferential conditions. When the test hot and cold wall temperature measurements were adjusted for circumferential heating and coolant flow maldistribution, test and data analysis values agreed within 50°R. For this comparison, the hot wall insert-thermocouple data was corrected to account for the insert thermocouple bead location in relation to the hot wall outer surface.

During the thermal cycle tests, the engine structure was subjected to a thermal environment (combination of hot wall temperatures and hot wall-to-structure temperature differences) as severe as the predicted Mach 8 flight conditions. This was accomplished by undercooling the coolant flow routes. Hot wall temperature results presented later in this Section were evaluated from (1) a comparison of surface discolorations with Hastelloy X specimens that had been subjected to a known time-at-temperature history, and (2) data analysis based on measured flow route conditions. Hot wall-to-structure temperature differences were calculated by transient heat transfer analysis in the areas of surface discoloration. The discolorations indicate that temperatures as high as 1860°R occurred on the nozzle or about 1000°R higher locally than the Mach 8 prediction. This locally high temperature produced a hot wall-to-structure ΔT of 1000°R compared to a maximum predicted Mach 8 ΔT of 950°R on the leading edge. At the outerbody outlet manifold, ΔT's as high as 1400°R were measured at lower hot skin temperatures.

The density-adjusted pressure drop was calculated for most of the engine flow routes from measured hydrogen flow rates and inlet and outlet pressures

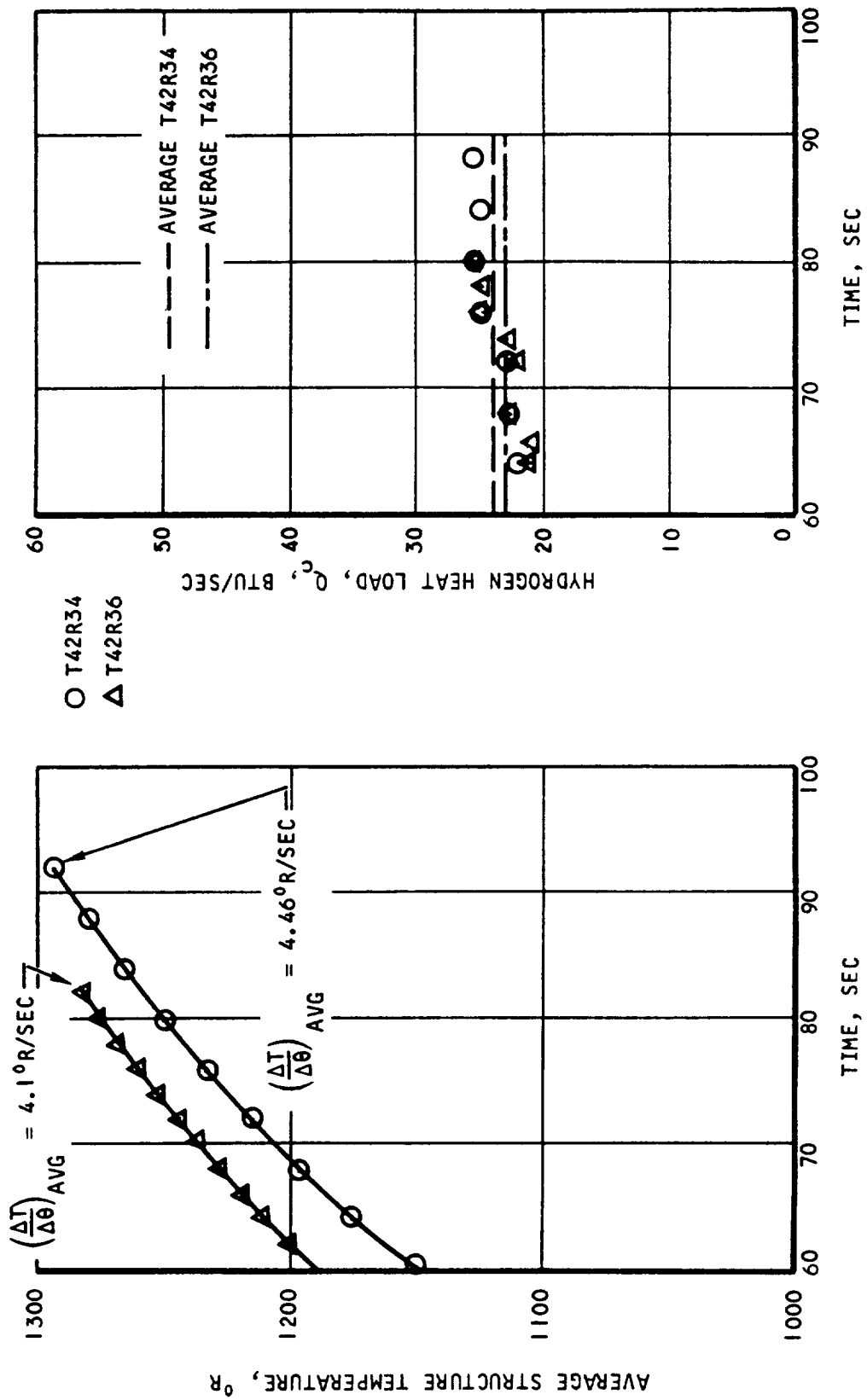

Figure 8.8-10. Trailing Edge Average Structure Temperature and Hydrogen Heat Load (U)

TABLE 8.8-4

TRAILING EDGE FLOW ROUTE HEAT LOADS (TEST 42)* (U)

		Run 34	Run 36
Spike retraction from latched position, in.		2.90	2.89
Captured hot gas flow rate,	lb/sec	12.4	12.5
$W_{H_2 TOTAL}$,	lb/sec	0.257 ±0.016	0.223 ±0.009
$W_{H_2 TRAILING\ EDGE}$,	lb/sec	0.0089 ±0.0005	0.0087 ±0.0004
$W_{H_2 INJECTION}$,	lb/sec	None	0.143 ±0.005
$\left(\Delta T_m/\Delta\theta\right)_{AVG}$,	°R/sec	4.46	4.10
$M \times C_m \times \left(\frac{\Delta T_m}{\Delta\theta}\right)_{AVG} = Q_{SINK}$,	Btu/sec	21.1	19.4
$W_{H_2} \times C_P \times (\Delta T_{H_2}) = Q_c$,	Btu/sec	23.9	23.1
Q_{AERO},	Btu/sec	45.0	42.5

*Nominal tunnel reservoir total conditions, 1380 psia, 2700°R

$$Q_{AERO} = Q_c + Q_{SINK}$$

$$= W_{H_2} \times C_P \times (\Delta T_{H_2}) + MC_m \left(\frac{\Delta T_m}{\Delta\theta}\right)_{AVG}$$

where M = estimated trailing edge structural mass = 45 lb

C_m = metal specific heat = 0.105 Btu/lb-°R

C_P = hydrogen specific heat = 3.5 Btu/lb-°R

and temperatures. Results to be presented later in this Section are compared with isothermal air results. The comparison of the hydrogen results with the air results is only fair because the measured pressure drops were of similar magnitude to the measurement uncertainty of the individual inlet and outlet pressure measurements. The coolant maldistribution, W_{MAX}/W_{MIN}, in the engine flow routes was estimated as high as 1.10 on the spike. These estimates were based on coolant control-thermocouple measurements around the flow route circumference. The maximum coolant maldistribution based on inlet and outlet manifold pressure distributions during air tests was 1.033 on the leading edge route.

8.8.5.3.2 Test Data

The steady-state cooling performance evaluation was based on the measurements and test conditions of Test 41, Run 39 (3320 psia, 3400°R tunnel reservoir total conditions). This test run was at the maximum tunnel heating conditions for the test program and was one of the few test runs where thermal steady-state conditions were reached simultaneously on all flow routes. The hydrogen inlet temperature was approximately 160°R. The maximum hot wall temperatures and hot wall-to-structure temperature differences occurred during the thermal cycle test runs where the engine flow routes, particularly the aft routes, were undercooled. These runs (Test 42, Run 14 to Test 42, Run 38) were performed at 1380 psia, 2700°R nominal tunnel reservoir total conditions, and the engine was inserted and withdrawn from the tunnel test section up to three times per test run.

The data for the flow route pressure-drop results were obtained from test runs at several tunnel total pressures, hydrogen flows, and both cryogenic (160°R) and room temperature (520°R) inlet hydrogen. Flow distribution results were obtained from Test 41, Run 39 data. Data from Test 42, Run 45 (2250 psia, 3000°R tunnel reservoir total conditions) were also used because steady-state conditions were well established for this 115-sec run, and more structural and hydrogen temperature channels were recorded than during Test 41 runs. The 3-deg angle-of-attack tests (Test 41, Runs 51, 52, and 53 at 3350 psia, 2700°R tunnel reservoir total conditions) demonstrated the asymmetric heating effect as measured by the coolant control thermocouples.

8.8.5.4 Transient Operation

8.8.5.4.1 Summary of Results

The transient behavior of the engine flow routes was investigated by analytical methods and the results were correlated with experimental SAM data. Basically, the results indicate that the time required for the hydrogen outlet temperature to reach steady state (when subjected to a step-change in hot gas heating such as at engine starting) is inversely proportional to the flow route hydrogen flow rate. The estimated time for the engine flow routes to reach steady state at the Mach 8 flight condition is 8 sec as measured from spike retraction and lightoff.

Undercooling of the flow routes produces higher than acceptable hot wall

temperatures and results in higher hot wall-to-structure ΔT's during transient heatup than at steady state. Undercooling is defined as a hydrogen flow rate less than would be required to maintain structural temperatures at or below 1600°R at steady state. For flight application, then, the design hydrogen rates should be established at the onset of spike retraction and lightoff.

8.8.5.4.2 Test Data

Analytical transient results were correlated with flow route outlet temperatures for Test 41, Run 39. Since steady state was established on all flow routes for this run, both the end points of the analytical correlation (steady-state hydrogen outlet temperatures) and the transient portion of the test could be verified from the test data. Data from Test 41, Runs 26 and 28 (2200 psia, 3000°R tunnel reservoir total conditions with room temperature inlet hydrogen) provided a basis for the data analysis for the transient behavior of hot wall temperature and hot wall-to-structural temperature differences. Metal discolorations on the nozzle and inner and outer shells were first observed during these tests and were produced by the combined effect of locally high hot gas heating and flow route undercooling.

8.8.5.5 Thermal Fatigue

8.8.5.5.1 Summary of Results

8.8.5.5.1.1 Test Objectives

The primary test objective for thermal fatigue was to impose controlled thermal duty cycles that could be closely monitored during the test program. This allowed direct evaluation of the fatigue damage in each test cycle. It also provided data from the early runs to establish coolant flow rates, test cycle timing, and sequencing, to effect the desired cumulative fatigue loading during subsequent test runs. A specific test goal was to simulate the severity of the $Mach_\infty = 8$ design conditions in as many areas as possible.

Thermal transient analysis was carried out for the various critical areas in the engine. This analysis provided data for temperature-time histories in the struts, the outerbody outlet manifold, strut and cowl leading edges, and several other large manifolds. The maximum thermal fatigue damage for the intended test sequence was determined to be in the strut sides, with a calculated damage fraction of 0.428. The cumulative damage in the hot skin adjoining the outerbody outlet manifold (OBOM) was nearly the same. These were found to be the two most critical areas in the engine.

A number of thermocouples had been placed on the OBOM and on the hot skin at or near the OBOM. Although several thermocouples were installed within the strut bodies, the extremely low fins on the strut walls made it impractical to install thermocouples on the hot skins that would have provided reliable transient temperature data for the hot skins.

A further test objective was to discover problem areas not considered in the design phase. One such problem-area example would be regions of intensified heating due to shock interactions. Other possibilities would be inadequate

cooling in local areas where there were interruptions in fin continuity.

An important objective of the SAM tests was the evaluation of design approaches used for the cooled structure. The construction and testing of a complete structural prototype permits the effect of the interactions between components under severe thermal loading to be evaluated in terms of structural capability and survival.

8.8.5.5.1.2 Engine Critical Areas

Several of the most critical thermal fatigue areas are shown in Figure 8.8.-11. The first area depicted is the hot skin adjoining the outerbody outlet manifold (OBOM). The coolant is at its highest temperature, and this produces the hottest structural metal temperature in the outerbody. It is a region of high heat flux, and the hot skin temperature achieves its peak value at this location. Large temperature differences occur between the manifold and the hot skin as a result of startup and shutdown transients.

The strut sides, the strut sockets, and the strut leading edges are all critical areas. The design of the strut cooling passages on the strut sides involved the use of small (0.020-in. high) plain fins; the strut body is relatively massive to carry structural loads. Large thermal differentials occur here during the tunnel testing due to transients, and produce significant thermal fatigue damage. The strut leading edge is subjected to stagnation-line heating which leads to large ΔT from the strut body temperature. The strut sockets are mechanically heavily loaded and restrained between heavy stiffening rings. In turn, they constrain the inner and outer shells. Hot gas flow between the strut and the sockets results in high local temperatures that can cause significant thermal loading on the joints in these areas.

Shock interaction effects lead to local areas of high heat fluxes and occur in several places. One such area is the nozzle. This again creates zones of high skin temperature and high ΔT values, with resulting thermal fatigue damage.

The cowl leading edge is a region of high stagnation-line heating. The small leading edge radius of 0.030 in. results in a difficult cooling design problem. Large differential temperatures between the leading edge stagnation line and the cooler prime engine structure are produced at this location.

It was not possible to simulate or duplicate $M_\infty = 8$ differential temperatures in all of these areas during the wind tunnel tests. Because of the massiveness of the outerbody manifold, the hot-skin-to-cooled-structure ΔT could be produced most easily in this portion of the engine during the wind tunnel tests. Heat fluxes on the strut leading edge and cowl leading edge, and hence, thermal fatigue damage, were expected to be lower during the wind tunnel tests than at $M_\infty = 8$ operating conditions.

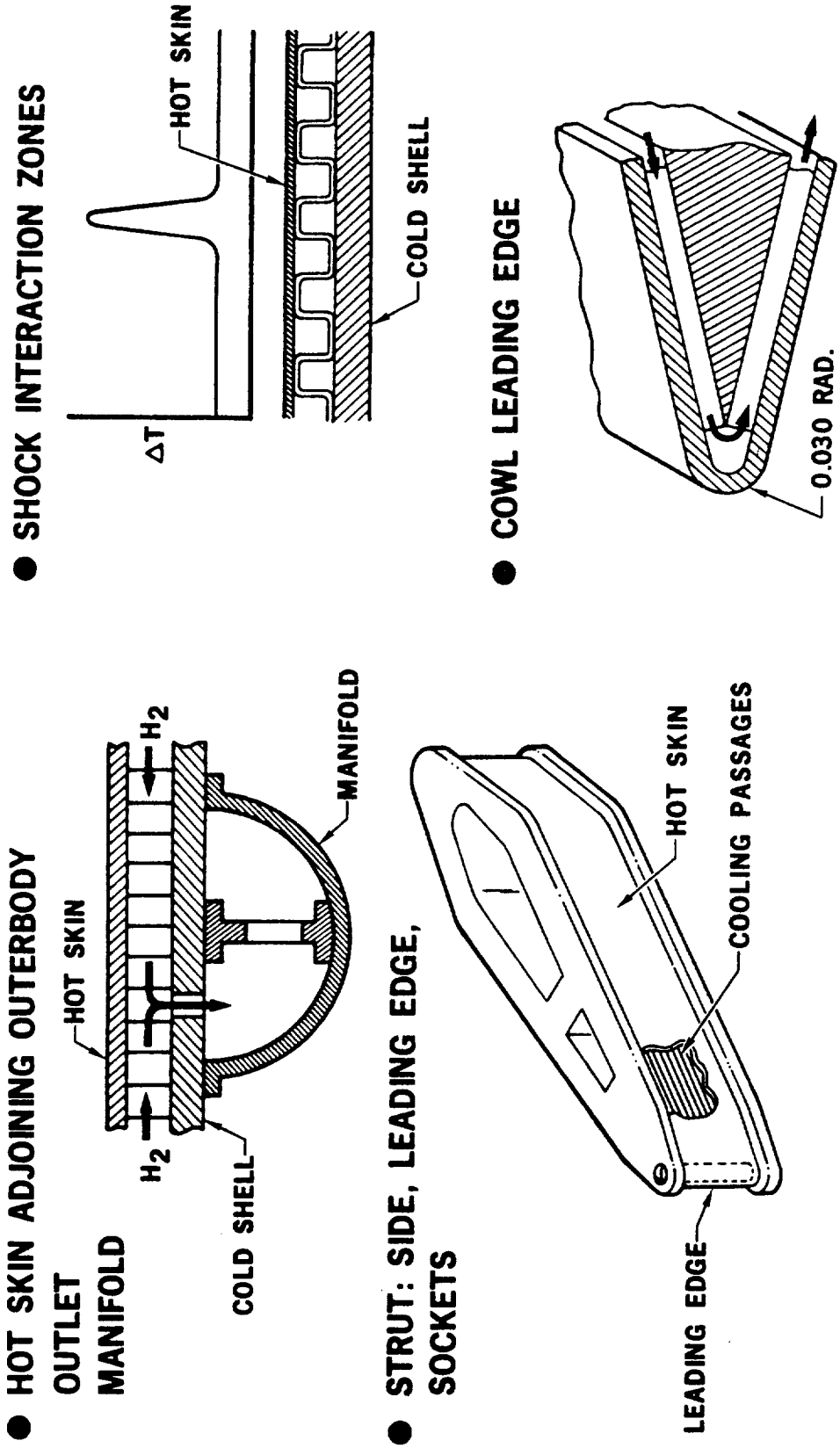

Figure 8.8-11. Thermal Fatigue Critical Areas

8.8.5.5.1.3 Outerbody Outlet Manifold Thermal Fatigue

The maximum shell ΔT at design conditions occurs at this location on the engine. As indicated above, thermal transient analysis showed that this would also be a critical area during the SAM wind tunnel tests. By adjustment in cycle timing, this was made the governing test region for thermal fatigue. It has also been noted that several thermocouples are installed on the OBOM and hot skin at or near the most critical area. The desired ΔT transients were obtained by timing of insertion and retraction sequences of the SAM engine during the test runs, and adjustment of coolant flow rates.

Figure 8.8-12 shows a cross section of the OBOM and adjoining hot skin.

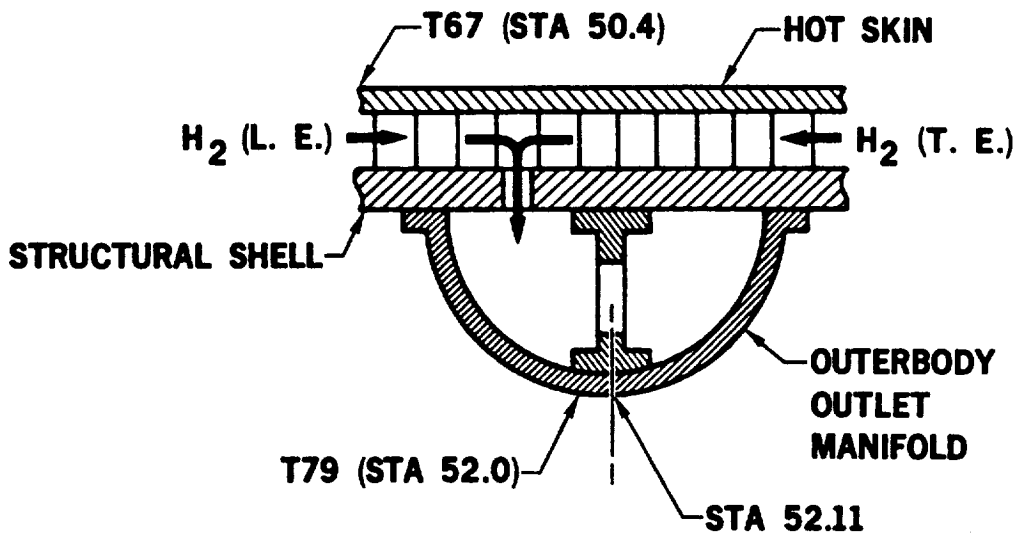

Figure 8.8-12. Outerbody Outlet Manifold Cross Section

Analysis of thermal data showed that thermocouple T67 (located at Station 50.4) readings provided a direct measure of the maximum hot skin temperature at the coolant outlet at Station 51.40. Similarly, T79, which was mounted at Station 52.00 on the OBOM, provided a direct reading equal to the effective average cold structural temperature at Station 52.11. Accordingly, the differential reading, T67-T79, provided a direct time history recording for the applicable ΔT. With these various data, it was a relatively straightforward procedure to compute maximum differential expansion, maximum hot skin temperature during each thermal fatigue cycle, and thermal fatigue damage fraction during each cycle.

8.8.5.5.1.4 Summary of Results

Table 8.8-5 presents a summary of the 58 thermal fatigue cycles applied to the engine at the OBOM. This table includes data from all of the applicable runs, in which the last three tests were carried out with the engine at an angle of attack of 3 deg to the tunnel centerline. Two cycles during

CONFIDENTIAL

TABLE 8.8-5

THERMAL FATIGUE SUMMARY (OBOM) (U)

Tunnel Total Conditions		No. of Thermal Fatigue Cycles**	Time in Stream, Under Thermal Load, sec**	Avg. Cycle Temperatures		Damage Fraction, Percent
psia	^{o}R			T_{max}, ^{o}R	ΔT, ^{o}R	
950	2600	5	172	1360	733	1.30
1300	2700	3	135	1445	950	2.12
1380	2700	33	829	1446	906	20.50
1500	2700	3	138	1571	1152	3.77
2200	3000	5	259	1591	1287	8.36
2800	3300	1	57	1435	1224	1.19
3300	3400	5	157	1522	1350	8.46
3350	2800	3*	37	1493	1150	2.30
TOTALS		58	1784 (28.7 min.)	———		49.0

*Model was at 3° angle of attack for these runs.
**Total cycles = 60, total time = 30.7 min

CONFIDENTIAL

which the spike was not retracted (Test 41, Run 27 and Test 42, Run 16) are not counted.

The summary information is tabulated for the varying tunnel conditions employed during the test program. The chart shows that maximum temperature and ΔT generally increased as the tunnel conditions were intensified. The increased temperature conditions do not exactly increase in proportion to tunnel conditions, since coolant flow rates and time of the model in the tunnel stream also have an effect on the maximum metal temperatures and ΔT magnitudes.

The model accumulated a total of slightly under thirty minutes in the tunnel stream. The cumulative damage fraction was 49.0 percent, a slightly higher value than the projected damage fraction of 43.8 percent on the strut, from the analysis carried out prior to the wind tunnel tests. The damage fraction of 49.0 percent corresponds to 67 thermal duty cycles at $M_\infty = 8$ design conditions. There was no visible evidence of thermal fatigue damage, i.e., cracking and leakage, anywhere on the engine surface at this time. In general, the tests have shown no basic weakness in the structural design concept for the HRE, from the standpoint of thermal fatigue.

8.8.5.5.2 Test Data

8.8.5.5.2.1 Thermocouple Data Interpretation

For purposes of data reduction, the metal thermocouples T67 and T79 were used to calculate the maximum hot wall temperature and maximum hot wall-to-structure difference at the outerbody outlet manifold. T67 is a hot wall insert thermocouple located at axial Station 50.4 (ref. coord.). This location is one inch upstream of the leading edge flow route outlet where the maximum hot wall temperature was expected to occur. To determine this maximum hot wall temperature, insert thermocouples T67 and T61 at axial Station 46.0 were corrected as per the procedure in Appendix A. The corrected temperatures were linearly extrapolated to the flow route outlet at axial Station 51.40. Though the trailing edge flow route also terminates at this location, the equivalent hot wall temperature extrapolation from trailing edge insert thermocouples was not included because these insert thermocouples showed temperatures which were much lower for almost all test runs. From an inspection of several leading edge insert thermocouple extrapolations, it was observed that the result was from 10° to 30°R lower than the uncorrected T67 thermocouple reading. For simplicity, then, the recorded value of T67 less 20°R was used as the hot wall temperature during the heatup portion of each test run. During the cooldown portion of the test cycle (intermediate or final withdrawal into the engine pod), the recorded value of T67 alone was used because, without hot gas heating, the insert and hot wall temperatures are almost equal to each other and axial temperature gradients are small.

Thermocouple T79 was used as the average structural temperature of the outerbody outlet manifold, and is located at the tip of the manifold (farthest away from the fins). Thermocouple T76 is also located on the manifold, but near the 0.060-in.-thick cold wall of the hydrogen fin passage. For most tests

T76 was no more than 50°R higher than T79 and was less than 30°R higher than T79 at the time of maximum temperature difference. At most, this would reduce the hot wall-to-structure temperature difference by 15°R if the average of T76 and T79 were used. It is noted that T76 and T79 are located at 45 deg (CWLA). This angular location was expected to have the fastest manifold temperature response since the highest manifold hydrogen flow rate occurs here near the tubes leading to the piggyback manifold. Because no other manifold temperatures were recorded, the interpretation of the average manifold temperature was biased toward the slower-responding and measured structural temperature near the outlet tubes, i.e., T79.

8.8.5.5.2.2 Metal Temperature-Time History

Figure 8.8-13 shows the metal temperature-time history for a typical test cycle for the outerbody outlet manifold. The data are for Test 42, Run 38, which involved two insertions and retractions of the model into and out of the wind tunnel stream.

Room temperature hydrogen was used in the test run. At the start of the test, the entire structure was approximately at RT. Immediately after insertion into the hot gas stream, the hot skin temperature increased rapidly; the cold structure responded quite slowly. The maximum ΔT of 944°F occurred just prior to model retraction, and the peak hot skin metal temperature of 1599°R occurred precisely at the time of retraction. After model retraction, the hot skin cooled down rapidly while the cold structure temperature continued to rise slowly. The hot skin passed below the cold structure temperature, resulting in a ΔT reversal.

Upon reinsertion of the model into the stream, the hot skin once again increased in temperature. The cold structure temperature at this time was substantially above room temperature. A relatively long time in the stream was employed for this cycle. The maximum positive ΔT of 529°F took place well before model retraction, and this positive ΔT was much lower than in the first cycle. At the time of the second retraction, the cold structure was hotter than at the first model retraction (approximately 1200°R vs 900°R). Upon retraction from the tunnel, the hot skin rapidly cooled to RT, and the cold structure cooled more slowly. A ΔT reversal of 426°F was produced in the second thermal cycle. Total ΔT for the first cycle was 970°F; for the second cycle it was 975°F.

8.8.5.5.2.3 Temperature Data

The pertinent temperature data for all of the test runs has been provided in Table 8.8-2. This table provides the total ΔT, i.e., the sum of the positive and negative ΔT's, the maximum metal temperature, the total differential expansion, and the fatigue damage for each full thermal fatigue cycle.

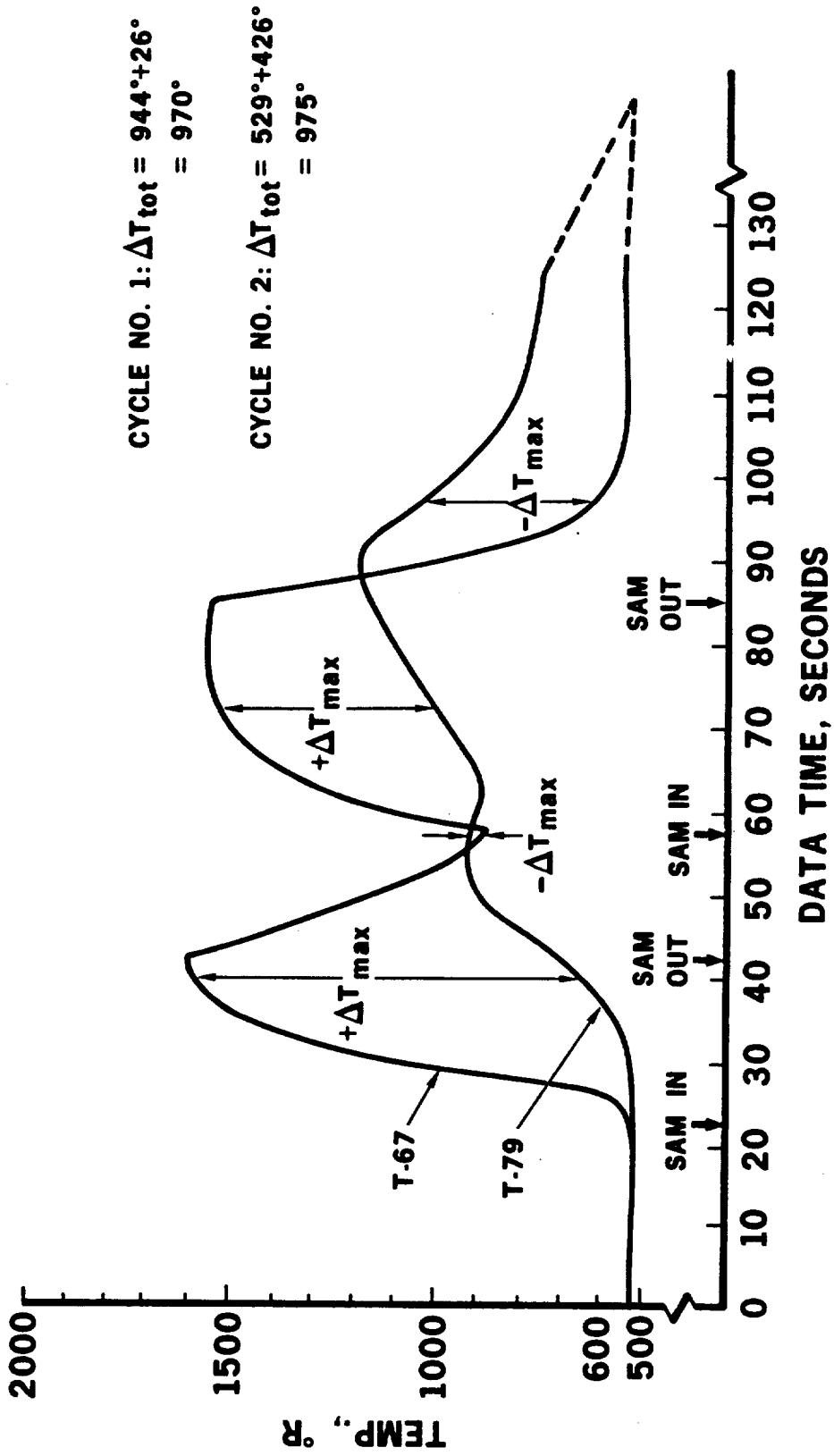

Figure 8.8-13. Typical Cycle Metal-Temperature History (U)

8.8.5.6 Structural Performance

The engine structure was designed to be compatible with all the loads occurring during the operation of the X-15A-2 aircraft. In addition to the gust and maneuver loads acting on the aircraft, it was designed to withstand the large internal loads due to inlet unstart. Symmetrical and asymmetrical inlet unstart loads and the vibration qualification loads governed the design of most parts of the engine. The design loads were described in Section 5.2.1.

The peak tunnel operating condition during the SAM tests produced a dynamic pressure of 2010 psf (M = 7.06) during Test 41, Run 38. This exceeded the maximum dynamic pressure of 1770 psf that was originally planned for the testing, but was still well within the structural capability in terms of total applied design loads.

The structural load data was monitored and recorded utilizing the output from 12 strain gages and four uniaxial and three triaxial accelerometers. The strain gages were installed at locations (Figure 8.8-14a) where the temperatures were sufficiently low to assure accurate functioning of these devices. Foil gages were used to form full-strain bridges to increase sensitivity and to provide temperature compensation.

Strain bridges S1 through S7 were tested and calibrated after installation inside the engine. The other gages were tested after installation on the particular part and prior to engine installation.

All test data were recorded on FM tape. The data were then digitized, then printed out as stress, strain, and force and/or moment versus time. Instantaneous values of the data were printed out at 0.05-sec intervals.

In order to be able to study the dynamic behavior of the engine structure, a total of seven accelerometers were installed on the structure, as shown in Figure 8.8-14b. Of the seven, four were uniaxial and three were triaxial.

Each accelerometer was assembled to a Kistler impedance converter, and the combined units were calibrated prior to installation into the engine. Maximum peak output voltage from each accelerometer was predicted upon a maximum of 20-g peak acceleration at each accelerometer. The data from all 13 channels were recorded on one FM tape having a frequency response from 5 to 10,000 Hz at a tape speed of 30 ips. The test data were tabulated at every 0.01 sec in terms of instantaneous "g" units. Further processing of the test data produced acceleration plots; power spectra and histogram plots; and printout, computed maximum, minimum, and mean values of the accelerations utilizing the NASA-Langley Time Series Analysis Program. The data from the various channels were intended to provide information regarding resonant frequencies, mode shapes, and potential resonant amplifications.

8.8.5.6.1 External Reactions

The SAM was supported in the wind tunnel with the support frame and the pylon facing down. Four strain gage bridges (S12, S13, S16, and S17) measured the external reaction components. The schematics of the support, the measured

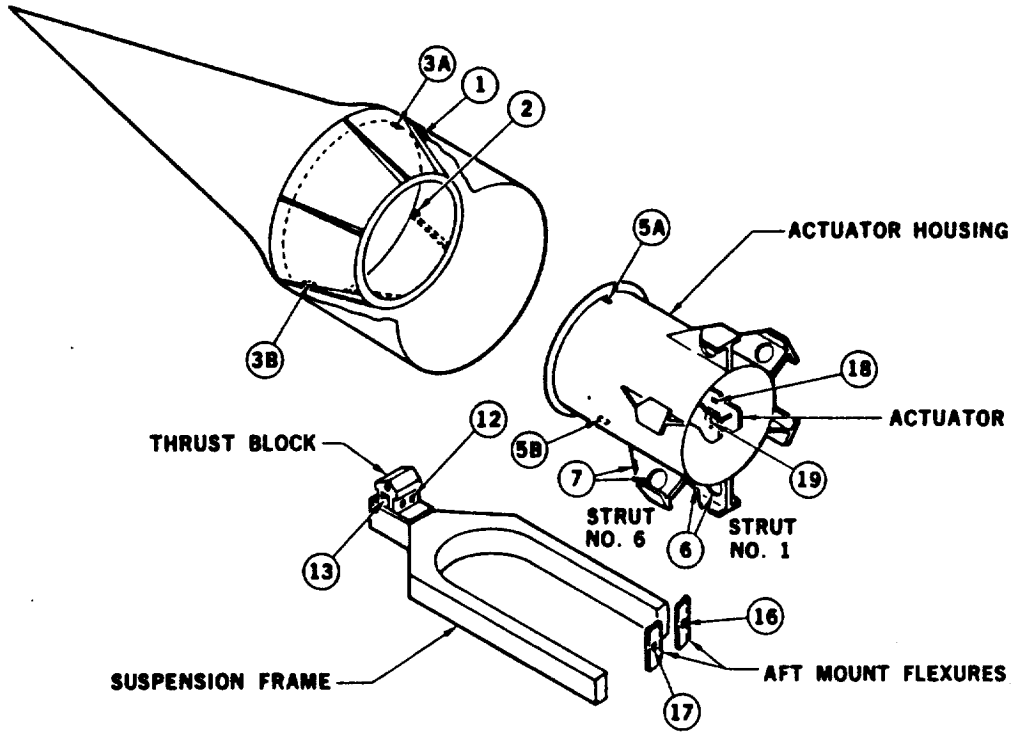

a. STRAIN GAGE LOCATIONS

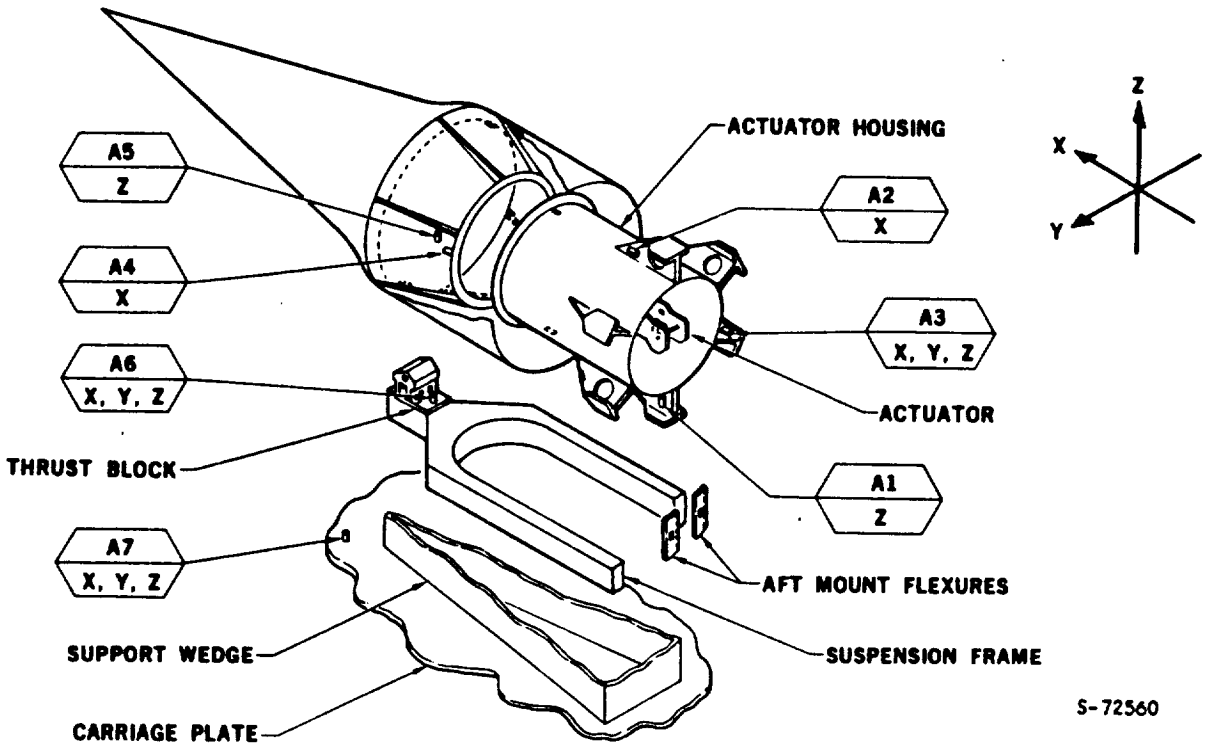

b. ACCELEROMETER LOCATIONS

Figure 8.8-14. Strain Gage and Accelerometer Locations

reaction components, and the resultant load are shown in Figure 8.8-15. It was assumed that the resultant of the external loads intersected the centerline of the engine.

The mounting of the SAM is a modified version of the HRE mounting which was designed to attach the engine to the X-15A-2 aircraft and was described in Section 5.5.8. A simplified isometric drawing of the mounting frame, and tabulation of the maximum mounting loads is shown in Figure 8.8-16.

Data from the following runs was analyzed to determine applied structural loads, steady-state stresses, and dynamic loads.

Test 41 (No hydrogen injection)	Test 42 (Hydrogen injection)
Run 7	Run 3
13	14
20	16
26	17
28	19
37	45
40	46
42	47
53	

Maximum axial (R_{XF}), vertical (R_{ZF}) reactions measured at the front support, and maximum and minimum vertical reactions measured at the aft supports during the studied runs are included in Table 8.8-6. These values did not occur simultaneously.

8.8.5.6.2 Spike-Actuator Loads

The inlet spike, a long (55.16 in.) and light shell structure, is attached to the forward flange of the actuator. The actuator provides the means of stroking the spike over a distance of 5 in. and also provides the structural support for the spike as shown in Figure 8.8-17. The front end of the actuator attaches to the sliding cylinder of the support structure by means of a pinned, self-aligning, spherical bearing. In turn, this bearing is attached to the actuator piston. At the aft end, the actuator cylinder is attached to the structural housing with a universal connection to eliminate side loads. The bearings between the inner and outer structural cylinders are made of bonded Fabroid (a woven fabric of fiberglass and Teflon). The deformation and dynamic behavior of this complex structure were important to the engine design. To provide for verification of design and monitoring, a total of eight strain gage bridges were installed on the spike, the actuator housing, and on the actuator attachment. Two identical bridges, S18 and S19, were intended to measure the net load (P_{18}) at the aft end of the actuator. Only S18 data recordings were utilized because S19 became inoperative during the first runs.

8.8.5.6.2.1 Actuator Load vs Time

The most significant loads were expected to occur during model insertion,

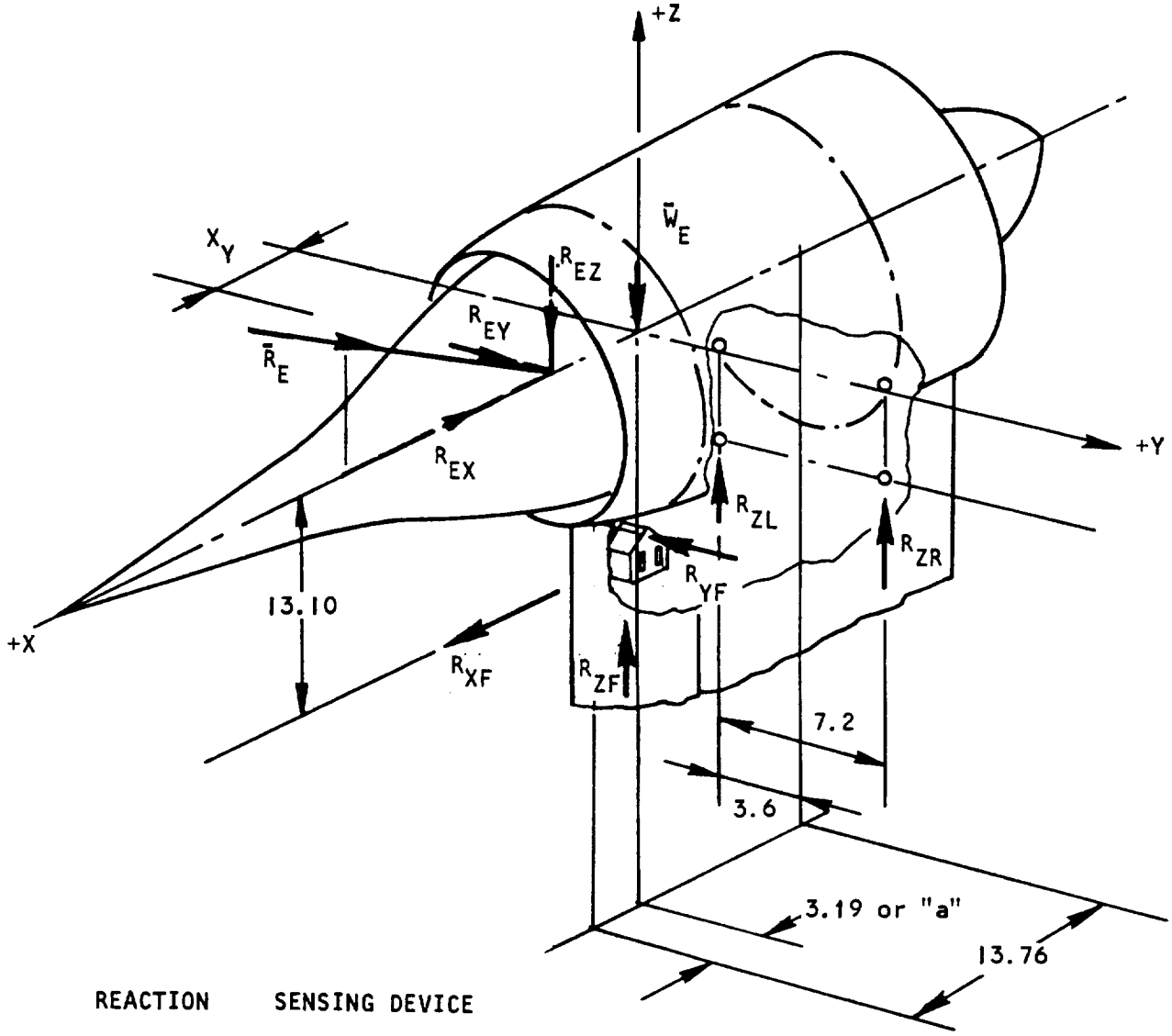

REACTION	SENSING DEVICE
$\bar{R}_{XF}$	S13
$\bar{R}_{ZF}$	S12
$\bar{R}_{ZL}$	S16
$\bar{R}_{ZR}$	S17

S-70132

Figure 8.8-15. SAM External Reactions

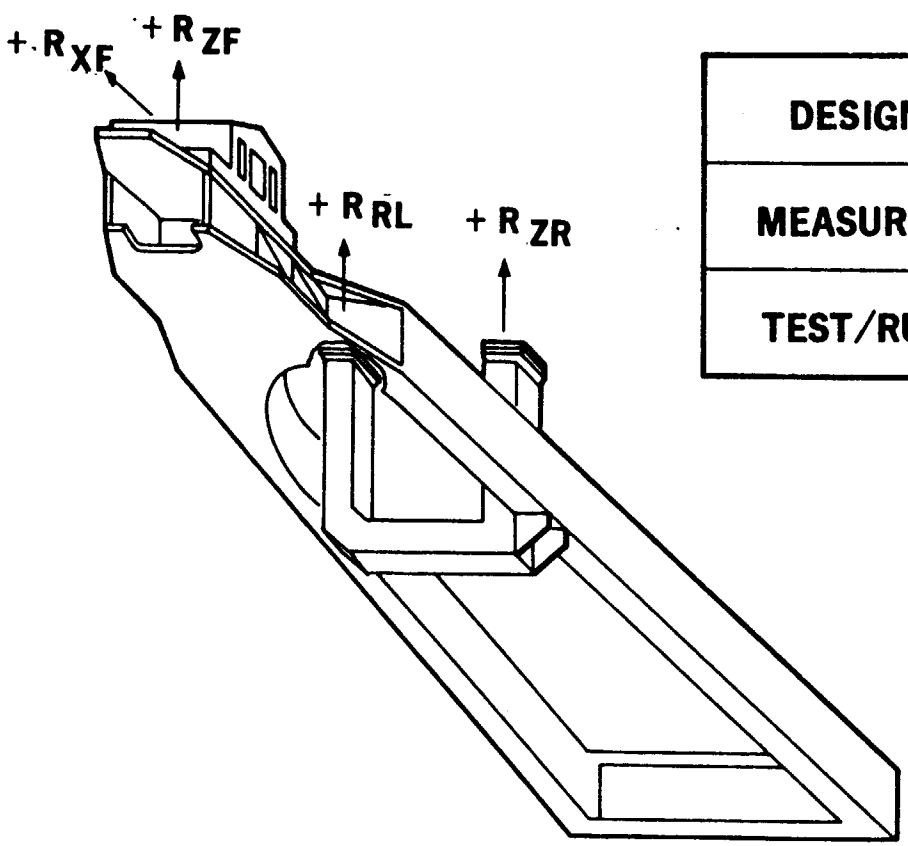

MAXIMUM LOADS, POUNDS

	R_{XF}	R_{ZF}	R_{RL}	R_{ZR}
DESIGN	-14100	-13100	-6065	-6065
MEASURED	-5611	-4906	-717	-2315
TEST/RUN	42/46	42/45	42/45	42/45

S-70127

Figure 8.8-16. Mounting Frame and Measured Maximum Reactions (U)

TABLE 8.8-6

SAM EXTERNAL REACTIONS

Minimum Flexure (Aft) Reactions							Maximum Flexure (Aft) Reactions					
Test	Run	Time, sec	P_{XF} ← (S13)	P_{ZF} ↑ (S12)	P_{ZR} ↑ / P_{ZL} ↑	$2P_{ZR}$ / $2P_{ZL}$	Time, sec	P_{XF} ← (S13)	P_{ZF} ↑ (S12)	P_{ZR} ↑ / P_{ZL} ↑	$2P_{ZR}$ / $2P_{ZL}$	Strain Gage No.
41	7	37.5	1005	569	195	390	65.89	2448	959	542	1084	16
	7	37.55	1005	401	420	840	69.84	2464	1042	757	1514	17
	13	41.64	909	356	171	342	38.99	481	478	267	534	16
	13	41.69	930	337	367	734	41.64	909	356	468	936	17
	20	45.19	679	421	-84	-168	86.39	844	1421	399	798	16
	20	45.14	519	163	455	910	86.44	650	1101	883	1766	17
	26	41.99	2786	750	233	466	49.74	1635	1029	404	808	16
	26	42.29	2798	860	765	1530	49.49	1588	1206	958	1916	17
	28	29.89	1221	85	-73	-146	63.49	1639	855	565	1130	16
	28	29.54	1179	62	502	1004	64.54	1298	1004	1139	2278	17
	37	31.29	3379	1235	-77	-154	86.79	375	2405	307	614	16
	37	29.94	2741	1118	1238	2476	88.99	1631	1794	1946	3880	17
	38	26.34	3164	1114	-8	-16	47.84	216	1386	308	616	16
	38	27.44	4013	1268	1456	2912	47.49	1388	975	1923	3846	17
	40	23.69	2004	922	3	6	86.14	549	2847	494	988	16
	40	24.34	2301	1028	1469	2918	86.39	984	2616	2007	4014	17
	42	23.59	2678	1064	-212	-424	63.64	403	2525	240	480	16
	42	23.69	2742	1163	1070	2140	63.59	323	2591	1703	3406	17
42	3	26.15	517	203	3	6	69.14	1127	918	368	736	16
	3	25.85	454	215	461	922	71.14	1139	946	778	1556	17
	14	81.28	1469	1749	369	738	80.78	1651	1322	466	932	16
	14	83.48	631	1638	1026	2052	79.68	1563	1789	1417	2834	17
	16	93.39	461	420	-461	-922	93.24	1666	1004	131	262	16
	16	49.39	906	124	414	828	93.34	615	957	1423	2846	17
	17	31.94	1343	258	5	10	102.64	1138	1954	597	1194	16
	17	31.49	1132	251	613	1226	101.64	1483	1836	1294	2588	17
	19	29.59	1117	279	-215	-430	49.79	2278	743	183	366	16
	19	29.64	1140	265	405	810	50.94	1449	1081	838	1676	17
	45	25.24	1914	875	-236	-472	140.19	610	4096	717	1434	16
	45	25.99	2243	1007	1307	2614	140.19	610	4096	2315	4630	17
	46	27.24	3557	1268	-284	-568	61.89	1577	1744	222	444	16
	46	26.04	1149	3004	1117	2234	60.69	170	2075	1747	3494	17
	47	25.49	1301	3541	-253	-506	24.69	2999	1254	-256	-512	16
	47	25.59	1354	3424	1104	2208	55.64	1067	1784	1712	3424	17

Front Support - Maximum Axial Reactions

Test	Run	R_{XF} ←	R_{ZF} ↑	R_{ZR} ↑	R_A ↑	t, sec	$\lvert R_{XF} \rvert_{max}$
41	7	2055	876	738	1476	69.79	2123
	13	1298	401	435	870	48.24	1319
	20	1583	1101	819	1638	86.04	1680
	26	2980	860	804	1608	43.49	3129
	28	2355	218	602	1204	33.89	2744
	37	2726	1183	1321	2642	31.34	5072
	40	2213	1226	1532	3064	26.49	4716
	42	2583	1408	1241	2482	25.04	4432
	53	4493	3085	1176	2352	47.19	5251
42	3	1399	378	471	942	31.2	1434
	14	281	1393	1111	2222	81.08	1248
	16	1743	213	460	920	54.89	2673
	17	1930	538	730	1460	36.69	2023
	19	1990	607	770	1540	50.14	2001
	45	2052	1047	1332	2664	28.24	3951
	46	2984	1288	1209	2418	27.39	5611
	47	1788	1479	1598	3196	53.89	3763

S-72686

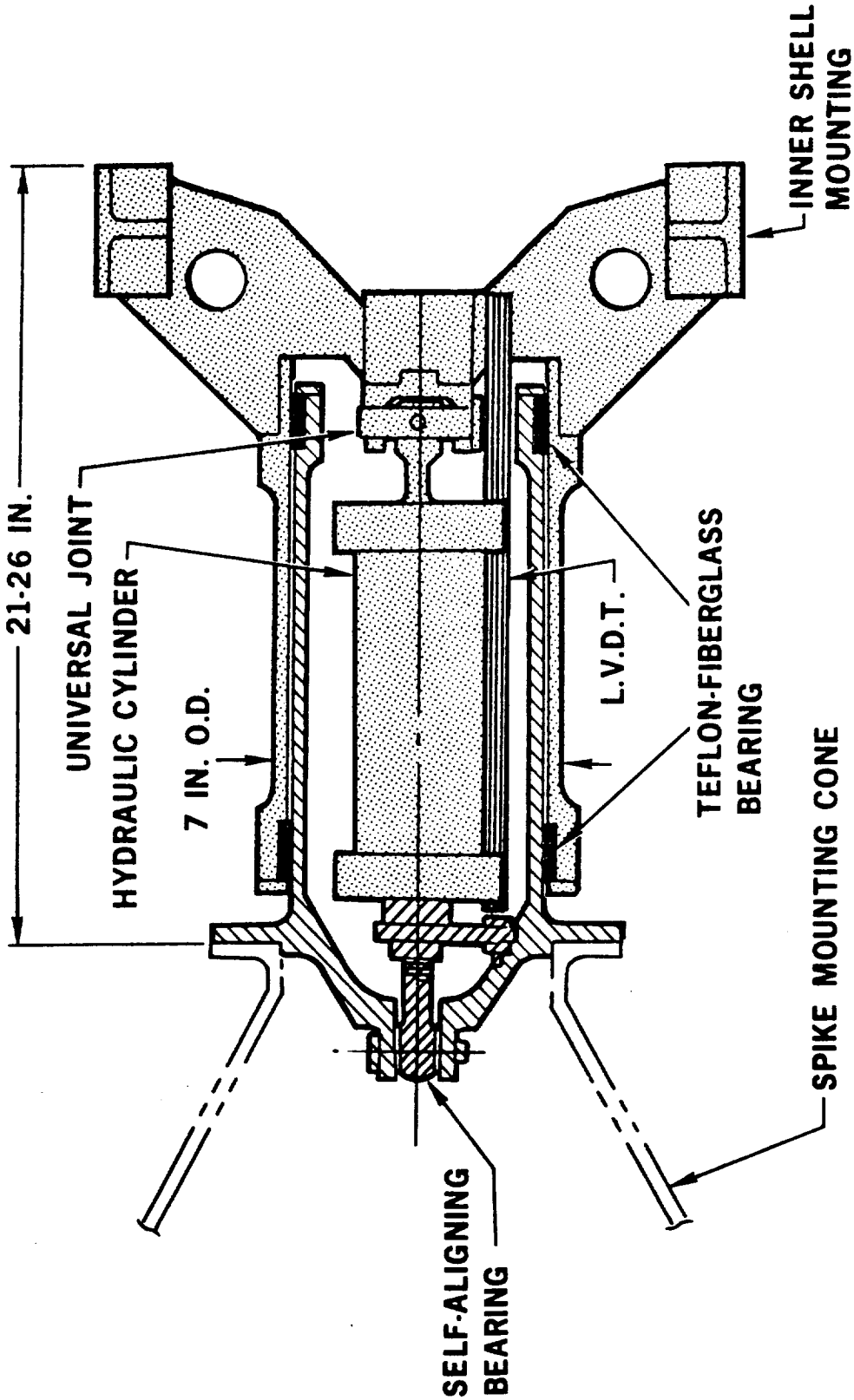

Figure 8.8-17. Inlet Spike Actuator

spike retraction, and spike extension. A typical force-time history measured at the aft end of the actuator is shown in Figure 8.8-18. The steady-state condition between spike retraction and extension is not shown, as indicated by the discontinuity of the time scale on the diagram.

The following forces are marked in this figure and tabulated in Table 8.8-7.

Load before model inserted into tunnel	P_1
Load before spike is retracted	P_2
Load after spike is retracted 0.25 to 0.35 in.	P_3
Maximum load during spike retraction	P_4
Average load between spike retraction and extension	P_5
Minimum load during spike extension	P_6
Load after spike is extended	P_7
Load after model ejected from tunnel	P_8

The pattern of the load variation was quite uniform throughout each test and similar to Figure 8.8-18.

8.8.5.6.2.2 Load Variations Due to Spike Position

The load measured at the aft end of the actuator as the spike was retracted or extended is tabulated in Table 8.8-8. Because the extension of the spike was much faster than the retraction, fewer data points were recorded during the 0.05-sec intervals used for data printout.

The governing load condition for the actuator design was the symmetrical inlet unstart case. This design condition and the corresponding load envelope measured during the test are shown in Figure 8.8-19. The loads recorded during the test are considerably less than the design loads, which were based upon a symmetrical unstart condition. No inlet unstart occurred for any of the tests.

8.8.5.6.3 Steady-State Stresses

The recorded strain gage signal was converted into digital form and the corresponding stress was calculated and printed out directly. Strain gage placement was limited by the accessibility of the structure and the operating temperature of the metal. It was known in advance that stresses during normal tunnel and SAM operation would be substantially lower than the design values for the flight environment. All gages selected were, nevertheless, based on the higher stresses and loads in order to ensure adequate data under conditions of abnormal operation. Some strain gages were mounted on very stiff members (actuator legs) where deflection criteria limited the original design, and the design stresses were very low.

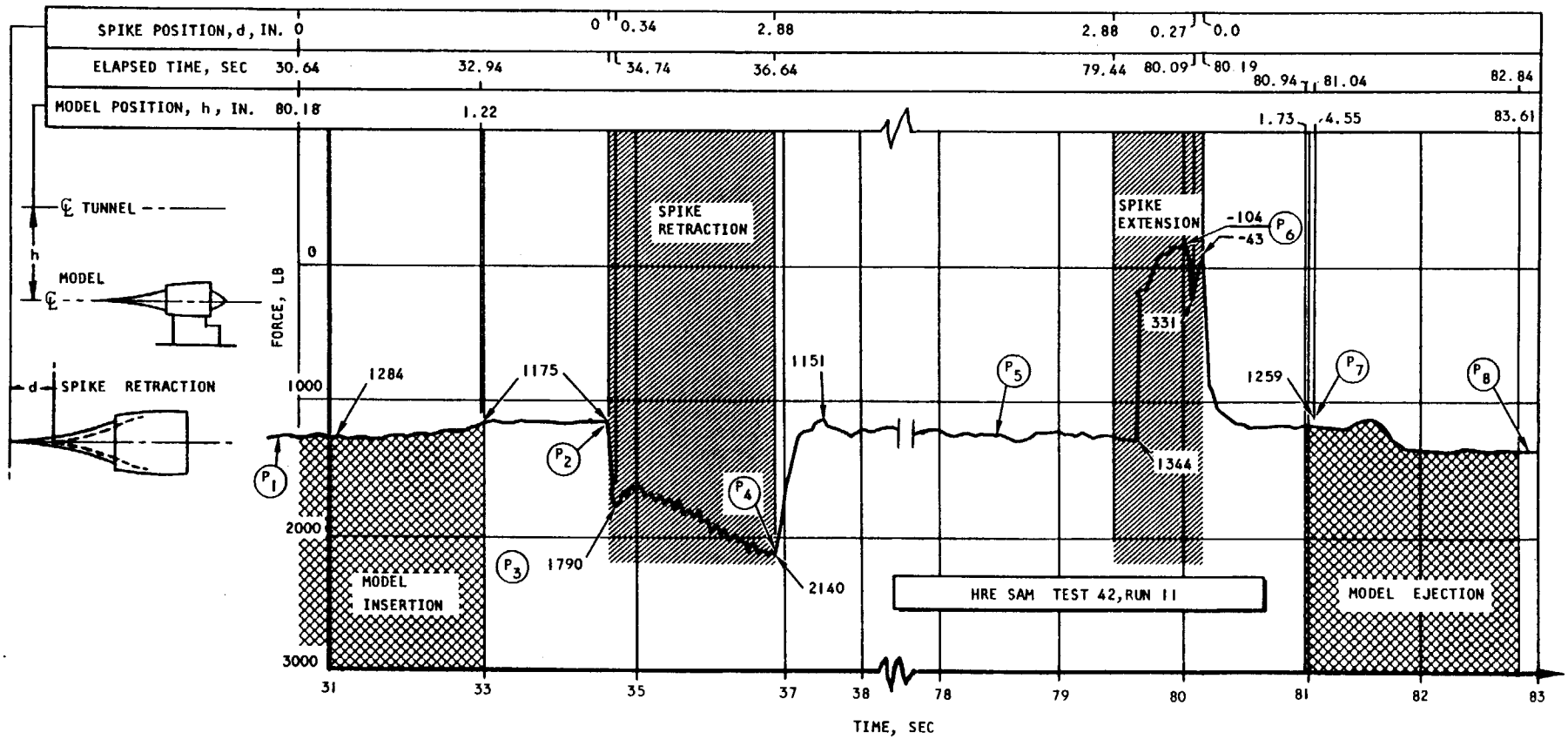

Figure 8.8-18. Force at Aft End of Actuator (U)

TABLE 8.8-7

FORCE AT AFT END OF ACTUATOR (U)

Test	Run	P_1	P_2	P_3	P_4	P_5	P_6	P_7	P_8
41	7	1212	1233	1607	1855	1133	-165	1223	1122
	13	1102	1102	1837	2188	1532	106	1204	1147
	20	1795	1635	2186	2484	1738	372	1738	1876
	26	1965	1603	2231	2219	1235	-111	1314	1265
	28	1821	1507	2111	2353	1700	249	1337	1724
	37	1746	1380	1981	2194	1298	19	1107	1640
	38	1622	1173	1878	2049	1109	-162	970	1526
42	3	1321	1321	2223	2617	1691	257	1633	1205
	14	← Not Applicable →				1235	-250	1377	1389
	16	1488	1470	← No Spike Extension →					
	17	1504	1409	2074	2478	1765	268	1647	1837
	19	1692	1681	2286	2725	1835	399	1776	1989
	45	1663	1024	1620	1961	1524	556	1066	-

TABLE 8.8-8

VARIATION OF ACTUATOR LOADS DURING SPIKE MOVEMENTS

Test	Run	Maximum Spike Retraction	Spike Movement, in.						
			0.0	0.25	0.5	0.75	1.0	1.5	2.0
41	7 →	2.80	1223	1225	1528	1528	1596	1697	1787
	← 7				1020		1178		
	13	2.89	1102	1837	1780	1780	1850	1916	2018
	13				140		350		1543
	20	2.86	1612	2186	2071	2071	2094	2197	2254
	20		1738		521		636	888	1749
	26	1.70	1615	1809	2074	2014	2074	2183	-
	26		1289	10	988		1181	1217	-
	28	2.87	1482	1773	1990	1978	2063	2075	2268
	28		1337	273			539	696	1750
	37	2.92	1330	1981	1831	1810	1799	1767	1874
	37			19	104		254	478	1320
	38	2.92	1194	1171	1686	1643	1643	1611	1686
	38		1034	19	141	77	30	1034	853
42	3	2.89	1344	2154	2108	2177	2258	2351	2374
	3		1633	257	317	384	477	604	1680
	14	2.89	Model was elevated into tunnel with spike retracted						
	14		1377	250		61		163	1447
	17	2.90	1409	2015	1967	2098	2146	2241	
	17		1670	292			684	1742	
	19	2.92	1692	2286	2238	2262	2369	2452	
	19		1692	482		636	767	1823	
	45	2.90	1024	1620	1535	1514	1492	1663	
	45			619		949	1471	1524	

NOTE: Numbers in upper row of each run represent loads during spike retraction. Numbers in the next lower row are loads during spike extension.

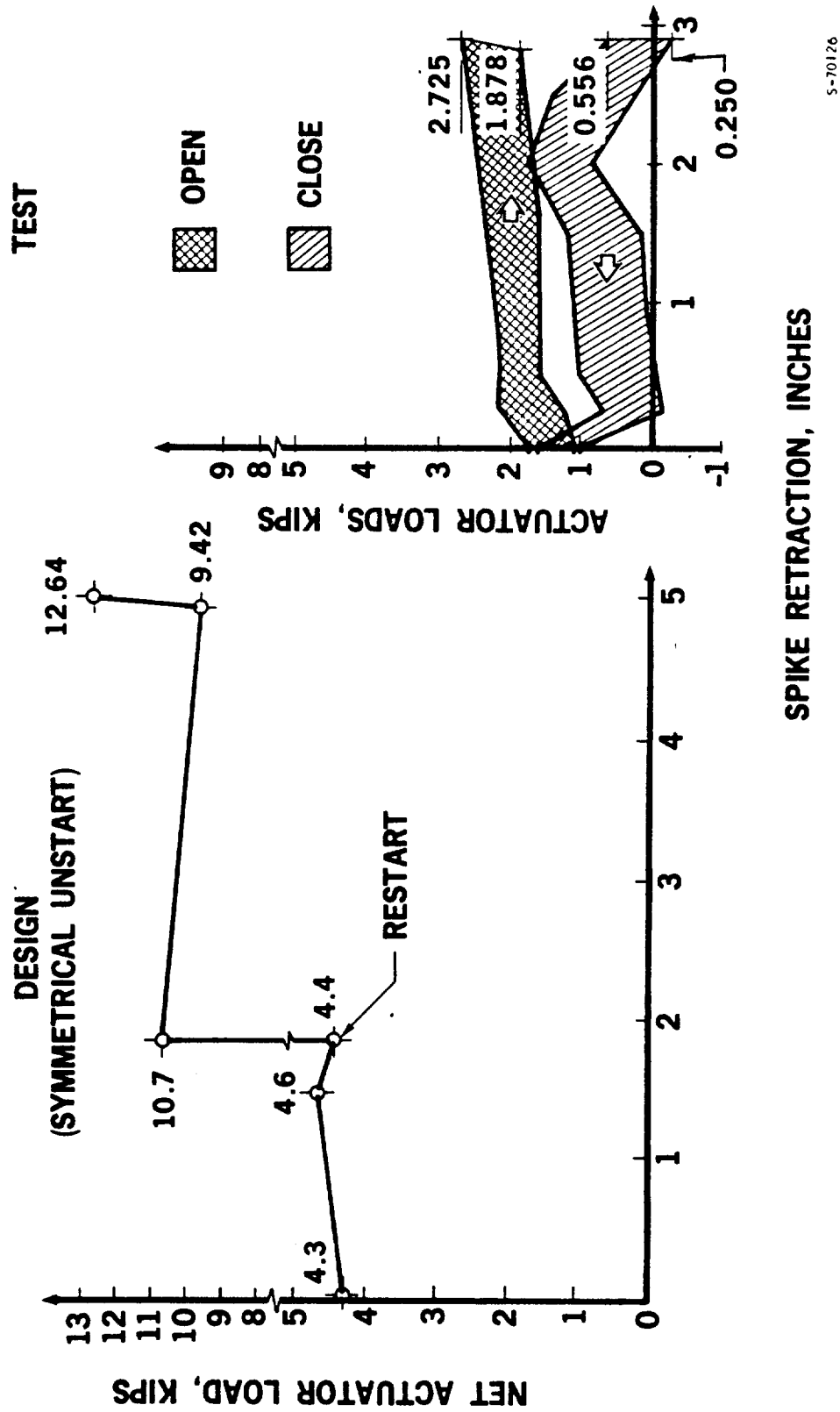

Figure 8.8-19. Actuator Loads vs Spike Movement (U)

Maximum stresses were expected due to inlet unstart, which did not occur during the tests. A tunnel flow breakdown occurred as the SAM was being retracted during Test 42, Run 45, and resulted in higher than normal load for these conditions. Figure 8.8-16 also shows the effect of this flow breakdown. Maximum stress recorded on each strain gage, the test, and run when it occurred is shown in Table 8.8-9. The tensile yield strength of the materials at 600°F is shown for reference.

TABLE 8.8-9

MAXIMUM STRESSES (U)

Strain Gage No.	Maximum Stress, psi	When Occurred		Material	Tensile Yield Strength at 600°F, psi
		Test	Run		
1	8,698	41	53	Hastelloy X	36,000
2	11,466	41	53	Hastelloy X	36,000
3	1,168	41	5	Hastelloy X	36,000
5	2,235	42	45	4330 steel	147,000
6	2,528	41	53	4330 steel	147,000
7	1,086	42	45	4330 steel	147,000
12	3,534	42	45	17-4 PH	139,000
13	20,503	41	53	17-4 PH	139,000
16	6,892	41	53	Inconel 718	139,000
17	14,758	42	45	Inconel 718	139,000
18	7,524	42	19	4330 steel	147,000
19	16,112	41	5	4330 steel	147,000

8.8.5.6.4 Dynamic Loads

The following nine runs were selected for the study of accelerometer data:

Test 41, Run 7	Test 42, Run 3
13	14
17	16
26	17
28	

No useful data was obtained after Test 42, Run 43, apparently due to a coolant leak from the spike outlet bellows which rendered most accelerometers inoperative.

The maximum negative and positive instantaneous "g" levels of the runs studied are shown in Table 8.8-10. The selection of the runs was based on increasing total tunnel pressure level. The maximum "g" values shown in the table represent extremely short duration peaks in the data. With the exception of a single data point, these responses were all below the design response limit.

TABLE 8.8-10

MAXIMUM INSTANTANEOUS ACCELERATIONS (U)

Axis	Gage	Maximum g		Design
Z	A7	19.04	-12.60	↑
	A6	4.00	- 3.75	
	A3	8.23	- 4.19	
	A1	4.46	- 4.01	
	A5	11.30	-26.50	
X	A7	14.61	-16.67	Input: 3.0 g
	A6	2.20	- 6.66	Response 20 g
	A2	13.7	- 3.02	
	A3	5.45	- 5.08	
	A4	7.67	- 3.33	
Y	A7	7.89	-9.69	↓
	A6	5.89	-5.29	
	A3	8.32	-3.45	

Acceleration-time plots of the above-mentioned runs were prepared for the periods of the tests when significant changes of model position or geometry

were made. These plots represent wide-band random vibration. The most important parameters representing such vibration are the power density spectra and the magnitude-probability distribution. The power density spectra is a presentation of the dynamic excitation, indicating the distribution of vibration energy throughout the frequency range. For wide-band random vibration the vibration energy is distributed throughout the entire frequency range, and the power density is a continuous spectrum of frequency. Sharp peaks at discrete frequencies indicate that the vibration is composed of discrete frequency vibrations superimposed upon random vibration. Such combined spectrum is representative of random environmental vibration excitation that includes the effects of structural resonances contributed by structural members in the load transmission path.

The NASA-Langley "Time Series Analysis Program" used the histogram technique for the estimation of probability densities. If the shape of the probability-density function of the data is not known, then the use of the histogram technique gives this shape, and from this a smooth probability distribution can be generated. Additional parameters for checking the form of the probability function and accuracy were calculated by the methods described in the Operation Manual of the above-mentioned NASA-Langley Program.

8.8.5.6.4.1 Forcing Functions

It was known well before the beginning of the tests that a 27- to 30-Hz vibration existed due to the tunnel combustor operation. Review of the data revealed no structural resonance either to this frequency or multiples of this frequency. No other sinusoidal forcing function was detected during testing.

8.8.5.6.4.2 Acceleration Levels

Acceleration-time history plots were the basic dynamic data recorded during testing and used as a basis for data reduction. Accelerometer A7X is attached to the model support carriage and it showed higher instantaneous accelerations than A4X, which is attached to the spike cone. The instantaneous acceleration levels were quite low throughout the recorded tests. More meaningful information of the vibration level is shown on the power spectra and the magnitude-probability distribution, the histogram. Test 42, Run 19, accelerometer time history, power spectra, and histogram are shown in Figure 8.8-20 to show the relation between these functions. The acceleration-time history again indicates quite low instantaneous accelerations representing a wide-band random function. The power spectra shows a high peak at 3 Hz for most tests, including this one. This peak is the result of a peculiarity in computing and has no significance. Data plots of the other runs also indicated low vibration levels; therefore, only the rms magnitudes, mean values, and features indicating the probability distribution in an abbreviated form were tabulated.

The total rms magnitude of a wide-band random vibration F(t) is given by:

$$\sqrt{\frac{1}{T}\int_{0}^{T}\left[F(t)\right]^{2}\,dT}$$

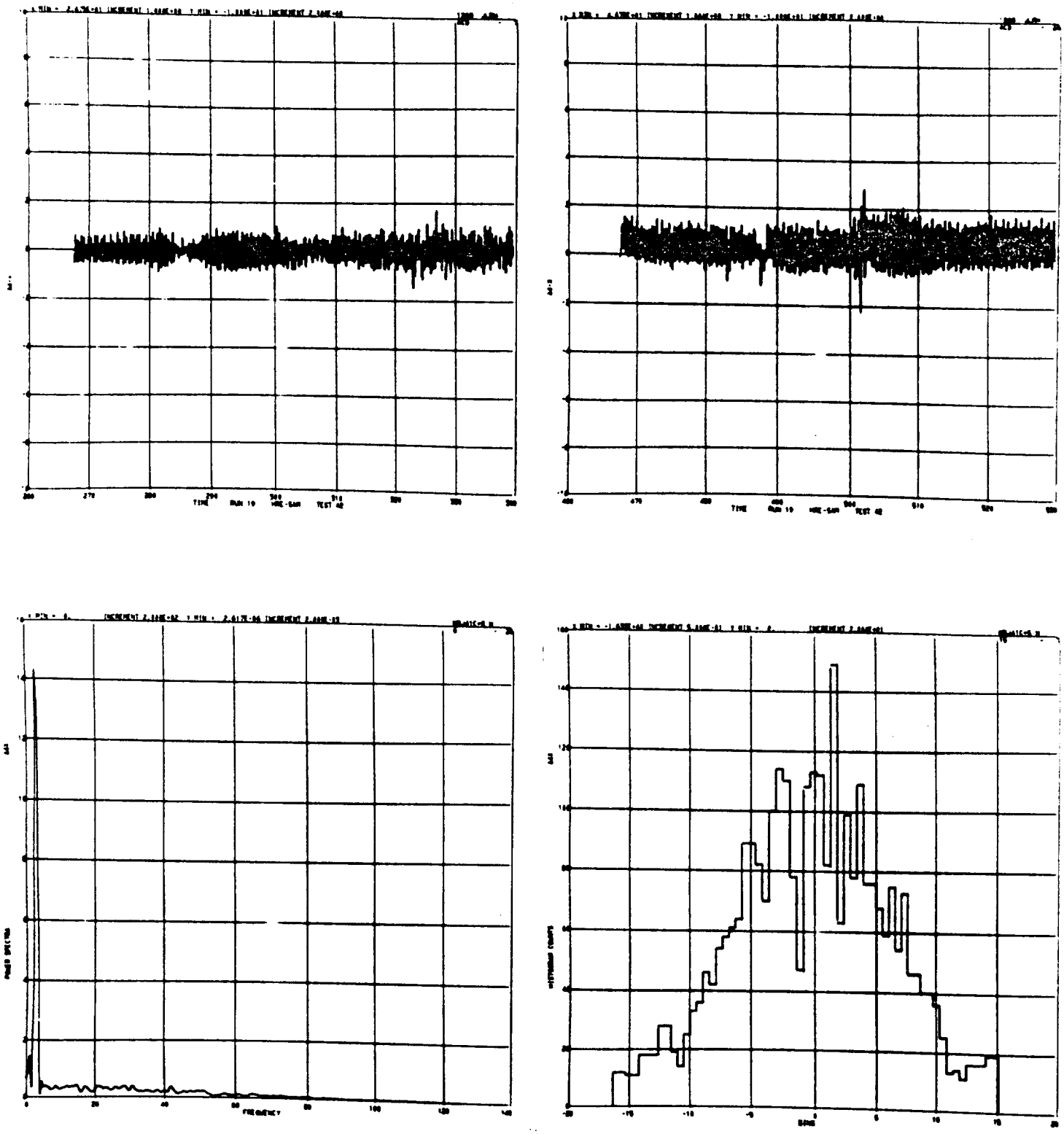

Figure 8.8-20. SAM Test 42, Run 19 A4X Accelerometer Data (U)

When dealing with the statistical properties of random vibration, the rms magnitude F_{rms} is called the standard deviation, defined

$$\text{as } J = \sqrt{\frac{1}{N-1} \sum_{c=1}^{N} (x_i - \bar{X})^2}$$

A tabulation of the standard deviation for the nine runs studied as shown in Table 8.8-11. Of the 117 values shown in this table, only 29 are above 1.0 g; the maximum being 5.48 g.

8.8.5.6.4.3 Responses

Several components of the engines are quite rigid elements. The vibration analysis indicated that the lowest natural frequency of the most flexible assembly--the spike-actuator/strut unit--is about 140 Hz, a fairly high frequency. It was felt that this assembly would be the only component that would be excited at its own natural frequency. The dynamic response of the engine as a unit would essentially be that of a rigid body.

To verify the behavior of the structure and correlate the acceleration level between various parts, instantaneous acceleration readings in the X, Y, and Z directions were plotted, and the X-directional acceleration-time history is shown in Figure 8.8-21. The time interval selected was with the model in the tunnel, but the spike not yet retracted. In the X- (fore- and aft-) direction, the three accelerometers which are attached to the actuator and the spike (A2X, A3X, A4X) show the highest acceleration level. Substantially lower instantaneous acceleration levels were recorded on the thrust block (A6X) and the carriage plate (A7X). In the Y-direction, very low acceleration was measured inside the engine (A3Y). This was somewhat amplified at the thrust block level (A6Y) and a considerably lower acceleration level was recorded at the carriage plate. Z-directional (vertical) acceleration displays similar behavior to that in the X-direction.

Studies of other time periods--elevation of model into the tunnel, spike retraction and extension, and lowering of the model--revealed similar patterns, indicating that substantial structural damping exists. This conclusion is further supported by the instantaneous maximum and rms accelerations.

8.8.6 Conclusions

The primary objective of the SAM wind tunnel tests was to evaluate the flight-designed, regeneratively-cooled structure of the HRE in a realistic environment. This has been accomplished. It was possible, in particular, to subject the structure to severe thermal loading. The cooled structure performed well, both in terms of its design requirements and in terms of its ability to survive under the imposed loads. Test results presented in this report show performance that is generally in good agreement with design predictions. From the structures point of view, the results indicate that the

CONFIDENTIAL

TABLE 8.8-11

SAM TEST STANDARD DEVIATIONS OF NINE RUNS (U)

Test	Run	A6X	A6Y	A6Z	A7X	A7Y	A7Z	A4X	A5Z	A1Z	A2X	A3X	A3Y	A3Z
44	7	1.5356	1.0326	0.8430	1.5618	0.7437	2.0671	2.8289	5.4800	1.0315	3.3853	1.1423	33.6192	2.3574
	13	1.0631	0.9895	0.7450	0.5083	0.3579	0.7394	1.7781	2.9068	0.6896	2.2354	0.7706	0.1121	1.4545
	17	0.2798	0.1860	0.1831	2.6848	2.7319	5.2222	0.5136	1.4997	0.2009	0.6085	0.2402	0.0156	0.5304
	26	0.6167	0.3857	0.3298	0.6901	0.1929	0.5997	0.7712	2.3645	0.4366	0.8168	0.4612	0.0097	0.6168
	28	0.5806	0.2872	0.3334	0.5207	0.1844	0.6638	0.9007	0.4953	0.4055	1.0725	0.4144	0.0229	0.9443
42	3	0.2247	0.1579	0.1300	1.6089	0.5180	1.1636	0.4411	0.5307	0.1677	0.5261	0.1814	0.0061	0.4446
	14	0.5873	0.3483	0.4528	1.3446	0.2418	0.6467	0.8065	1.1597	0.4867	0.9511	0.4941	0.0121	0.8102
	16	0.5837	0.7170	0.7385	3.8275	0.4172	0.5527	0.3571	0.3654	0.4080	0.3827	0.5585	2.0325	0.4733
	17	0.4523	0.3426	0.3647	0.3778	0.1178	0.4661	0.7064	3.0885	0.3245	0.7895	0.3723	0.0162	0.6680

Invalid Data-Defective Accelerometer

$$\sigma = \sqrt{\frac{1}{N-1}\sum_{i=1}^{N}\left(x_i - \bar{x}\right)^2}$$

CONFIDENTIAL

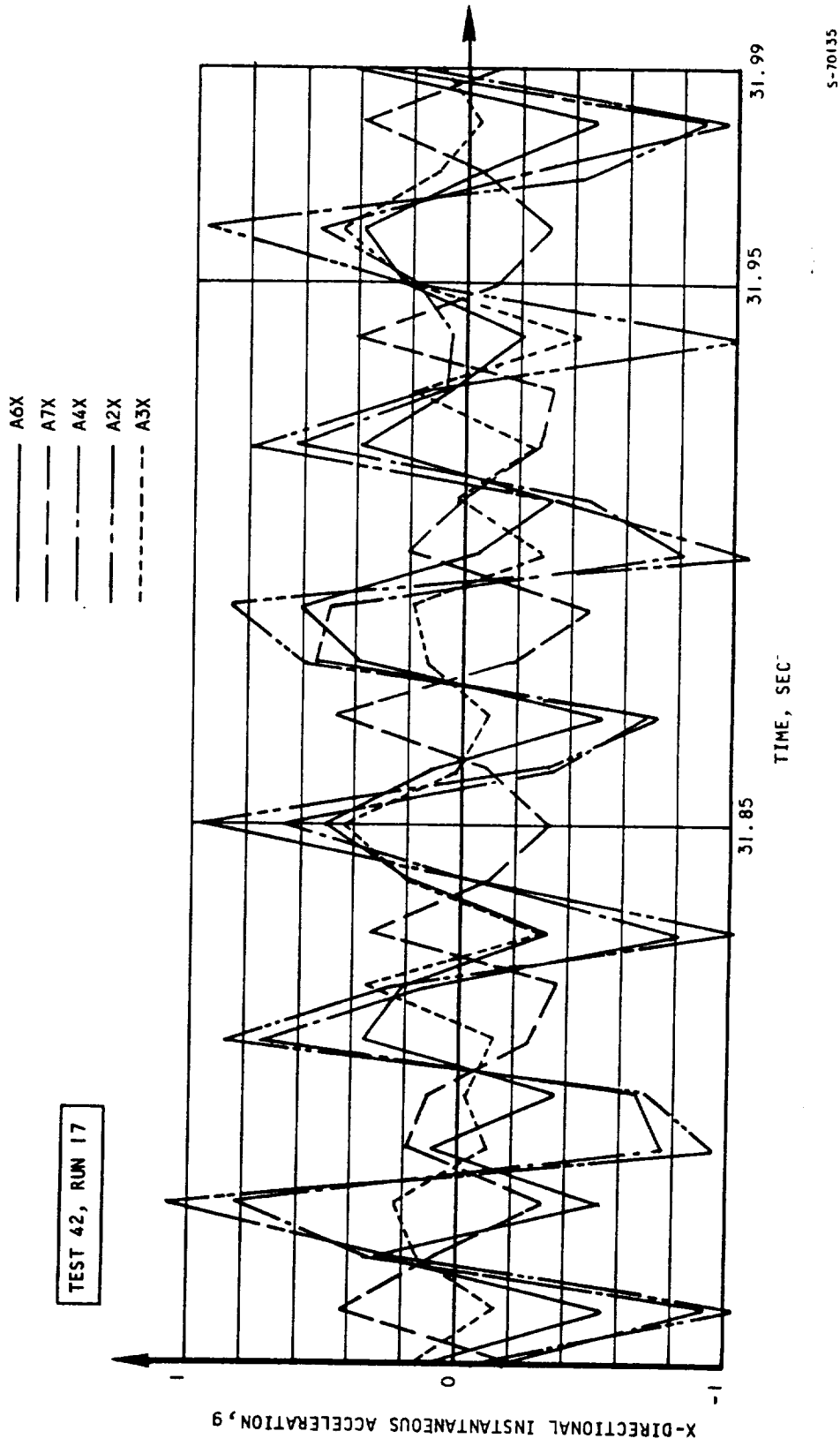

Figure 8.8-21. Instantaneous Acceleration, X-Direction (U)

basic design concepts and approaches used in the HRE are valid. The cooled structure proved to be rugged and capable of sustaining considerable abuse without degradation of performance. Some specific results are summarized below.

8.8.6.1 Thermal Performance

Heat transfer data reduction and analyses were directed toward (1) correlation of test hydrogen heat loads with heat loads and fluxes calculated from the measured aerodynamic test conditions and the flight design analytical methods; (2) evaluation of the steady-state cooling performance in terms of metal temperatures, temperature differences, hydrogen coolant usage, pressure drop, and flow distribution; and (3) evaluation of the transient response of the engine in terms of hydrogen coolant, metal temperatures, and metal temperature differences.

8.8.6.1.1 Aerodynamic Heating

The flight design heat transfer calculation method (flat-plate method with Eckert's reference enthalpy technique for hot gas property evaluation), when used in conjunction with the test pressure distribution and the one-dimensional flow solution, predicted heat fluxes to within ±20 percent over most surfaces of the engine. Based on this good agreement, the heat load level of 10,800 Btu/sec and hydrogen coolant requirement of 2.19 lb/sec (at 100°R inlet) predicted for Mach 8 flight conditions is realistic.

The correlation of heat loads did not include the effect of combustion. Although outlet hydrogen coolant was injected into the captured hot gas stream, no hydrogen combustion was expected in the methane/air combustion products and none was detected in test heat loads.

Localized heating occurred in the engine combustor and nozzle sections during testing. When interpreted in terms of local aerodynamic conditions, the relative intensity of the local heating during flight will be less than encountered during testing. Hydrogen coolant increases are not expected to be required for cooling of these areas of localized heating.

8.8.6.1.2 Cooling Performance

Steady-state hot wall temperatures were maintained at or below acceptable design limits at the most severe tunnel heating conditions. Though test heat flux levels were lower than defined for Mach 8 design flight conditions, good agreement (±50°R) was achieved between test hot wall temperatures and temperatures predicted for the hot wall at these lower heat flux levels. During the thermal cycle tests, the engine structure was subjected to a thermal environment (hot wall temperatures and hot wall-to-structure temperature differences) as severe as the predicted Mach 8 flight conditions. This was accomplished by undercooling the hydrogen flow routes. Undercooling produced a nozzle temperature that was about 1000°R locally higher than the Mach 8 prediction and a hot wall-to-structure ΔT of 1000°R. The maximum plate-fin panel ΔT at Mach 8 flight conditions is 950°R on the leading edge. In the area of the outerbody outlet manifold, ΔT's ranged to 1400°R. The SAM satisfactorily survived these conditions. Cooling performance of the leading edge

during the test program was also satisfactory. There was no evidence of overheating even though foreign object damage created dents and hydrogen leakage holes in the hot surface.

Test results of flow route density-adjusted pressure drop were in fair agreement with isothermal air calibration test results. Scatter is ascribed to test measurement uncertainties rather than to differences in hydrogen and air test conditions. The coolant maldistribution, W_{MAX}/W_{MIN}, in the engine flow routes was estimated as high as 1.10 on the spike, as measured by temperature distributions obtained from coolant control thermocouples. This caused no apparent problems in the tests. The maximum coolant maldistributions based on inlet and outlet manifold pressure distributions during isothermal air calibration tests was 1.033 on the leading edge route.

8.8.6.1.3 Transient Operation

The transient behavior of the engine flow routes was investigated by analytical methods and the results were correlated with experimental data. Basically, the time required for the hydrogen outlet temperature to reach steady state (when subjected to a step change in hot gas heating) is inversely proportional to the hydrogen flow rate. The estimated time for all engine flow routes to reach steady state at the Mach 8 flight conditions is 8 sec if the design flow rates are established at startup (onset of spike retraction and lightoff).

In addition to producing higher-than design hot wall temperatures, undercooling the flow routes (hydrogen flows less than operational requirements) will produce higher hot wall-to-structure ΔT's during transient heating than at steady state. To avoid larger-than-steady-state ΔT's at the Mach 8 flight conditions, the design hydrogen flow rates must again be established at the onset of spike retraction and lightoff.

8.8.6.2 Thermal Fatigue

At the Mach 8 design point, the design life of the engine was computed to be 136 cycles. The engine design objective was to produce a design life of 100 operating cycles at these conditions, which was based upon a maximum hot skin metal temperature of 1600°F and a ΔT of 800°F between the hot skin and the prime structure. The SAM test program exposed the engine to 58 thermal cycles of varying temperature differentials and maximum hot skin metal temperatures, resulting in a computed fatigue damage fraction of 49.0 percent in the area of the outerbody outlet manifold. This damage fraction corresponds to 0.49 x 136 = 67 engine operating cycles at the Mach 8 design point.

Upon completion of the test program, the engine showed no visible evidence of thermal fatigue damage, i.e., cracking or leakage anywhere on the hot skin. Local distortion occurred on the nozzle due to local shock interaction effects and undercooling but this did not lead to failure in the hot skin. Calculations for thermal fatigue damage were also carried out for the hot skin at the flange joint connecting the leading edge to the outerbody. The accumulated damage for the five runs used in the analysis was some 30 percent lower than at the OBOM

station for the same runs and is, generally, expected to have been less than at the OBOM.

The earlier work on mechanical bend tests and thermal cycle tests clearly demonstrated that thermal fatigue was a major problem area in the design of the HRE. The SAM test program demonstrated that the selection of Hastelloy X and the Palniro braze alloys was a sound one for the design.

8.8.6.3 Applied Loads

The test results indicate that the static and dynamic loads were below the design level. This resulted from much lower inertia load and vibration levels during tunnel testing. In addition, no inlet unstarts, which form a significant part of the internal design loads, were encountered in the tests. The structure was able to satisfactorily carry all of the applied test loads.

The only forcing function known in advance--a 27- to 30-Hz vibration due to tunnel combustor operation--created no resonance in the structure. Instead of amplification, substantial structural damping was experienced during the SAM tests. Vibration data reduction results show that the calculated natural frequencies were not excited, presumably due to lack of forcing function in that frequency. The low level wide-band random vibration recorded during the test had no resemblance to a Gaussian distribution.

8.8.6.4 Structural Performance

Damage sustained in various areas of the cooled structure indicates no problems so far as the basic design is concerned. A leak in the spike coolant outlet bellows and bolt damage at the outerbody flange, however, require review of the design in these areas. Solution of the spike-bellows problem is possible in a direct way by reducing bellows stroke/length. The outerbody flange damage appears to have had several causes. The design can be upgraded with the addition of high-strength bolting. This will insure that the performance of this area is compatible with that of the rest of the structure. When the tests were terminated due to the damage at the outerbody flange area, the cooled structure was still capable of performing at its design conditions.

REFERENCES

5.1-1 Engineering Staff, Hypersonic Research Engine Project - Phase IIA, Structures and Cooling Development, Sixth Interim Technical Data Report, Data Item 55-7.06, AiResearch Report No. AP-68-4173, 31 August 1968. (NASA No. NASA-CR-66994).

5.1-2 Preliminary Design Report, AiResearch Report No. AP-66-0168-2, Vol. II, Appendix A (CONFIDENTIAL). (NASA No. NASA-CR-66225).

5.5-1 Fay, J. A., and F. R. Riddell, "Theory of Stagnation Point Heat Transfer in Dissociated Air," Journal of the Aeronautical Sciences, Volume 25, No. 2, February 1958.

5.5-2 Chupp, R. E., H. E. Helms, P. W. McFadden, and T. R. Brown, "Evaluation of Internal Heat Transfer Coefficients for Impingement Cooled Turbine Airfoils," AIAA 4th Propulsion Joint Specialist Conference Paper No. 68-564, June 1968.

5.5-3 Edney, Barry E., "Effects of Shock Impingement on Heat Transfer Around Blunt Bodies," AIAA Journal, Vol. 6, No. 1, January 1968.

8.1-1 Burbank, Paige B., Robert A. Newlander, and Ida K. Colling, "Heat-Transfer and Measurements on a Flat-Plate Surface and Heat-Transfer Measurement on Attached Protuberances in a Supersonic Turbulent Boundary Layer at Mach Number of 2.65, 3.51, and 4.44," NASA TND-1372, 1962.

8.1-2 Kestin, J. "The Effects of Freestream Turbulence on Heat Transfer," Advances in Heat Transfer, Chapter 1, by Thomas F. Irvine, Jr., and James P. Hartnett, Academic Press, 1966.

8.1-3 Weeks, Thomas M. "Influence of Freestream Turbulence on Hypersonic Stagnation Zone Heating," AFFDL-TR-67-195, Air Force System Command, Wright-Patterson Air Force Base, Ohio, May, 1968.

8.3-1 Richard, C. E., et al., Low-Cycle Fatigue Evaluation for Regeneratively Cooled Panels, AiResearch Report No. 68-4313 (NASA No. NASA-CR-1652).

8.8-1 Engineering Staff, Hypersonic Research Engine Project - Phase IIA, Structures Assembly Model (SAM) Test Report (U), Data Item 63.05, AiResearch Report No. AP-71-7702, 22 Sept. 1971, CONFIDENTIAL.

UNCLASSIFIED

UNCLASSIFIED

NOZZLE
HRE

70210 L 930604

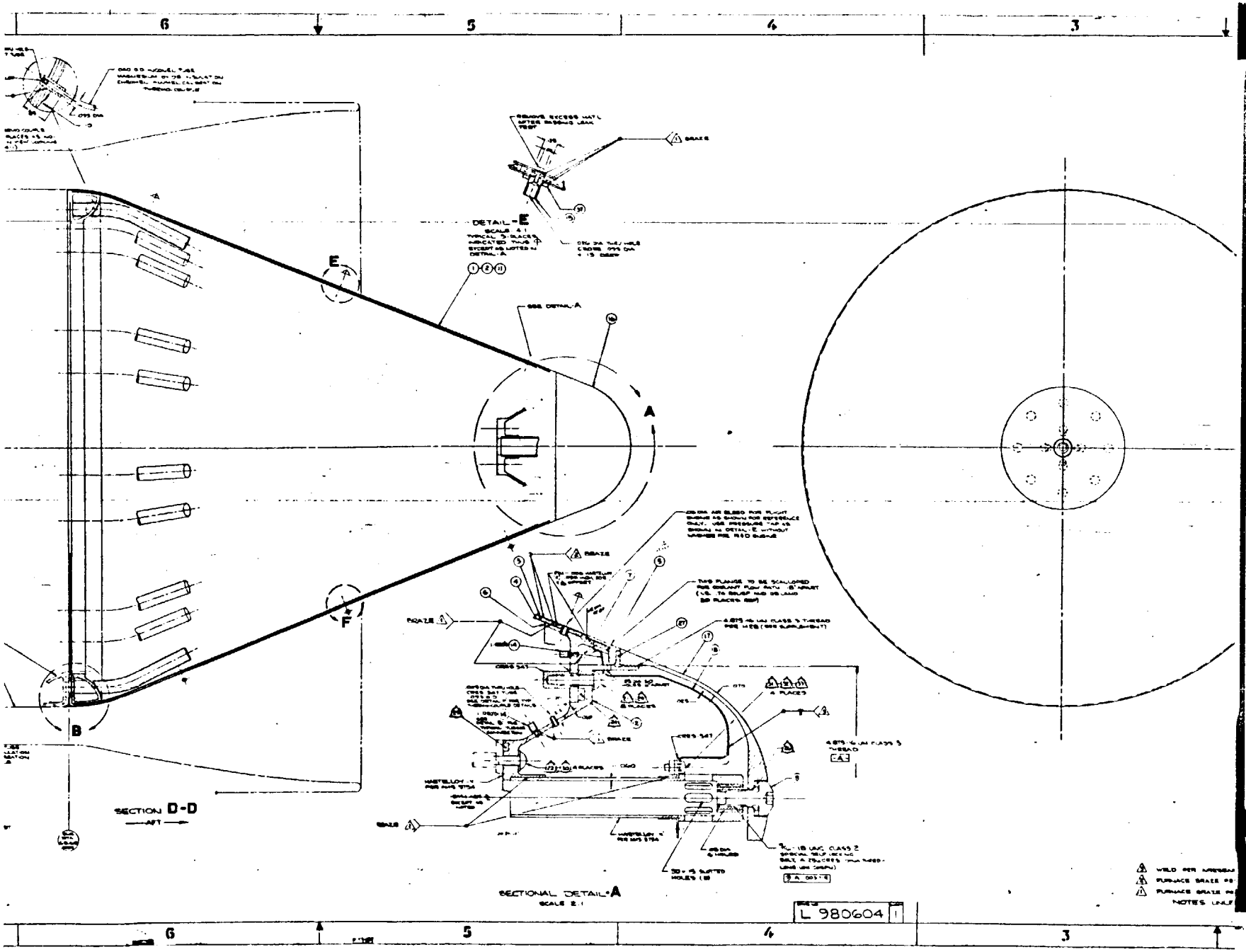
6
5
4
3
DETAIL "E"
SECTION D-D
AFT
SECTIONAL DETAIL "A"
SCALE 2:1
L 980604

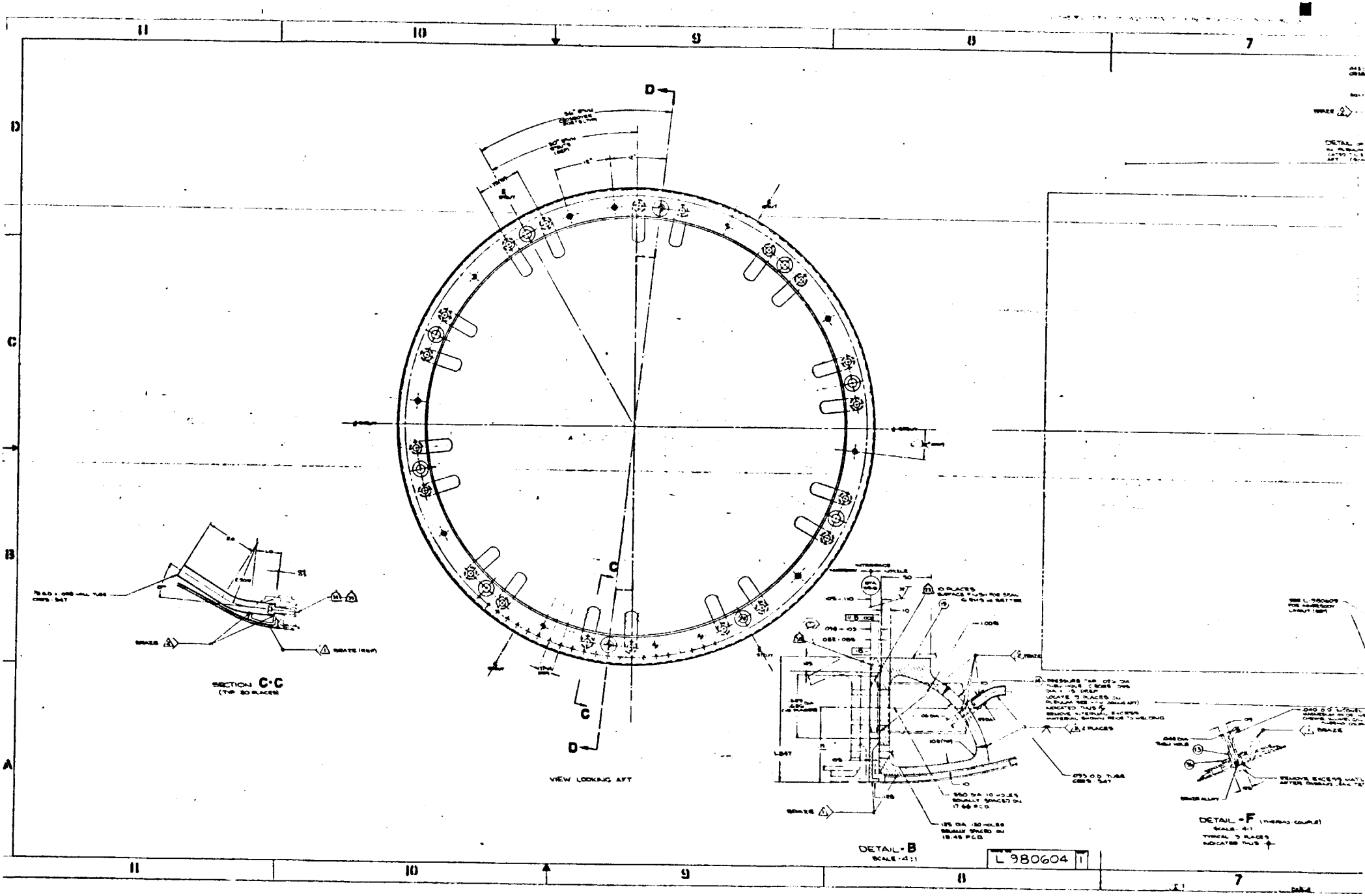
SECTION C-C
(TYP 30 PLACES)
VIEW LOOKING AFT
DETAIL - B
SCALE - 4:1
DETAIL - F
L 980604

UNCLASSIFIED

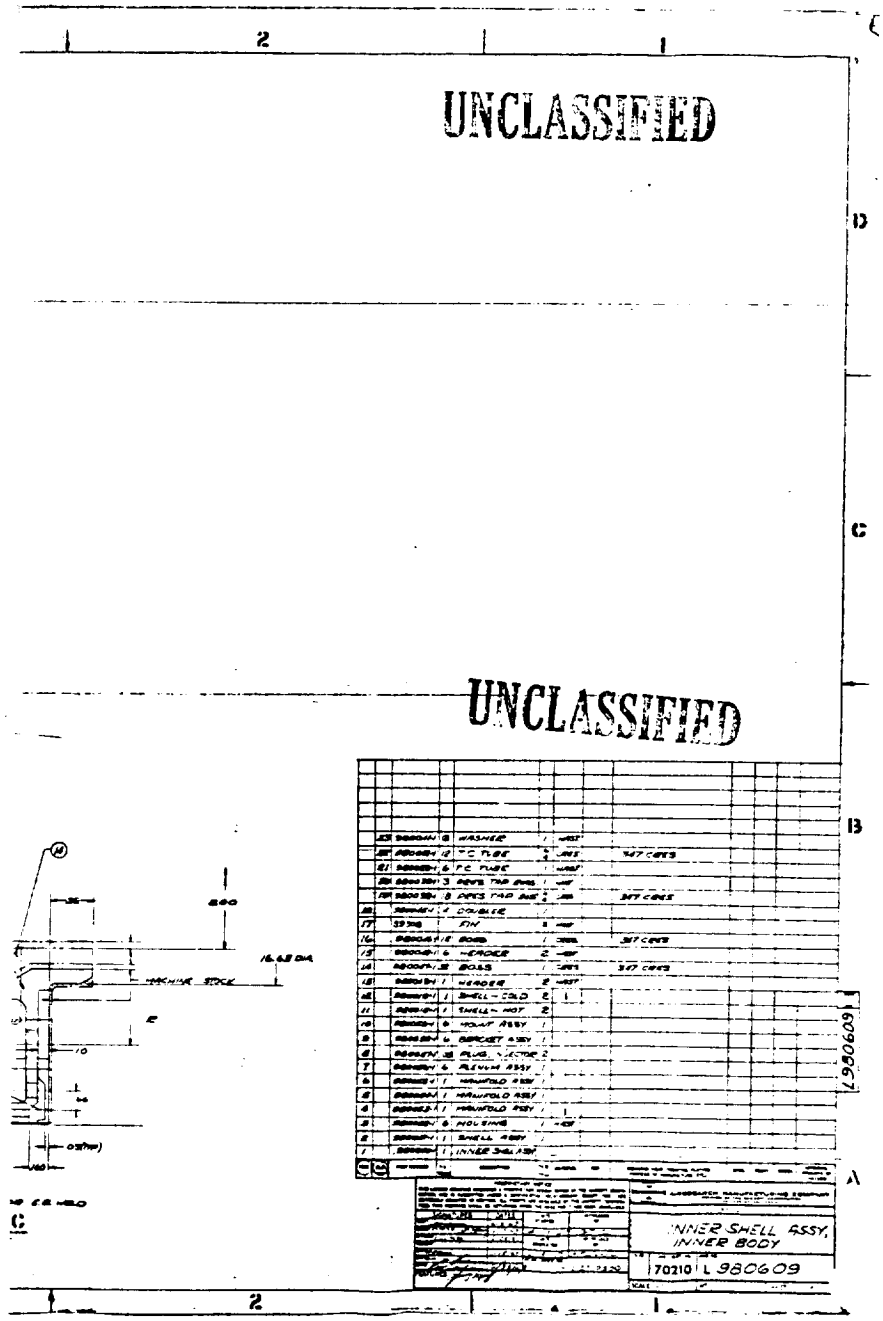

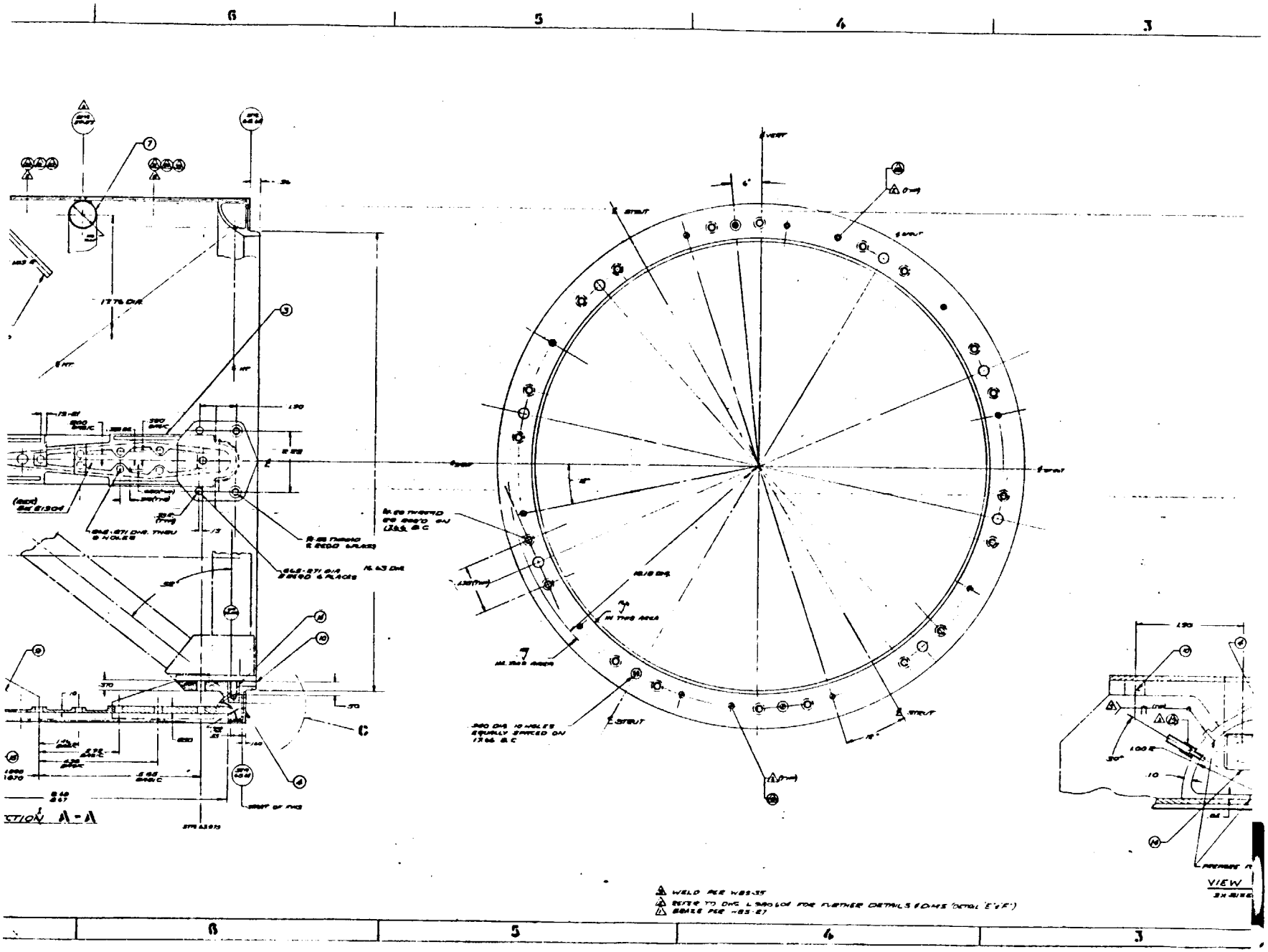
6
5
4
3
17.76 DIA
16.63 DIA
STRUT
VIEW
WELD PER WBS-35
BRAZE PER WBS-27

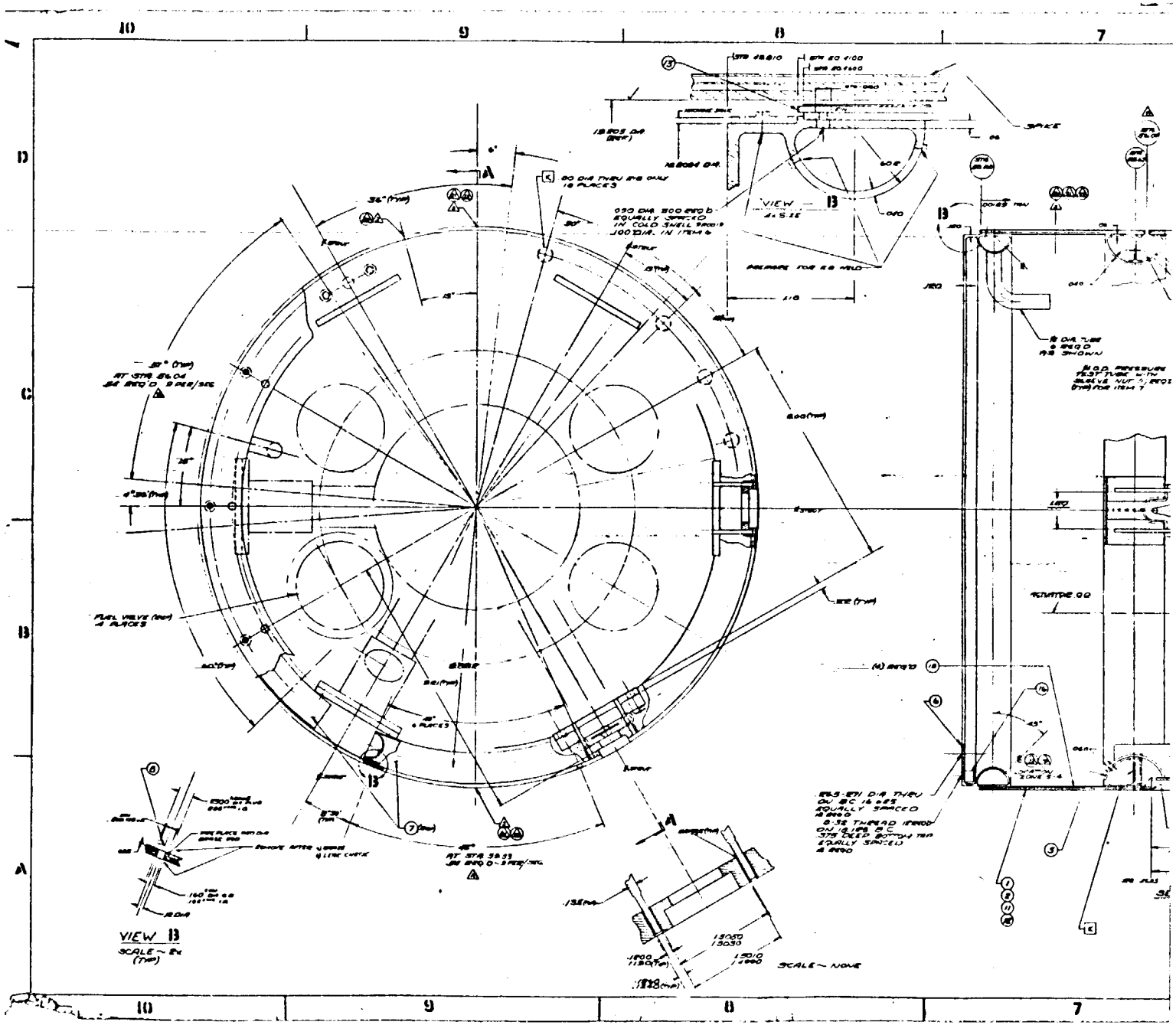
VIEW B
SCALE ~ NONE
SCALE ~ NONE

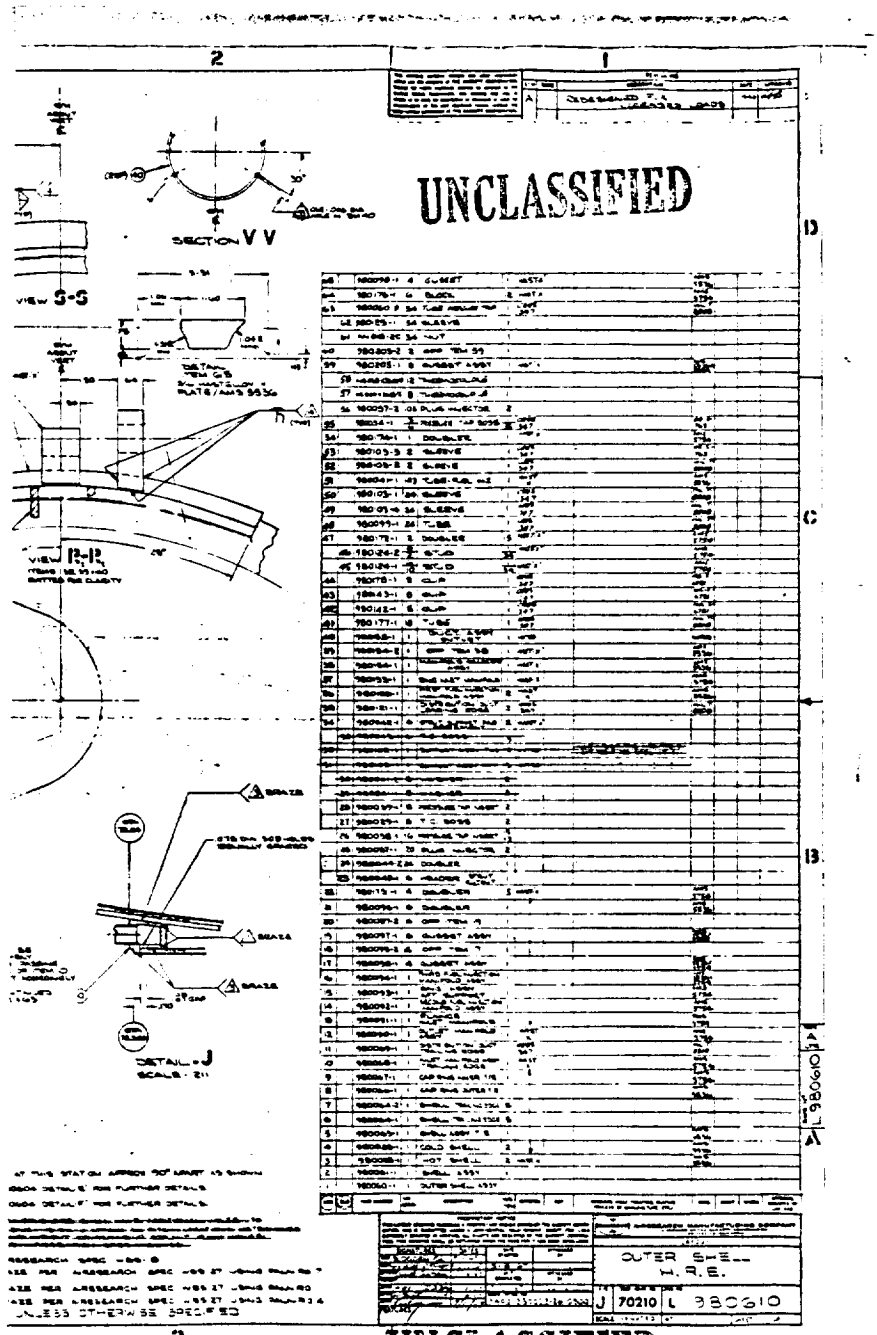
UNCLASSIFIED
SECTION V V
VIEW S-S
DETAIL J
OUTER SHELL
H.R.E.
J 70210 L 980610
UNCLASSIFIED

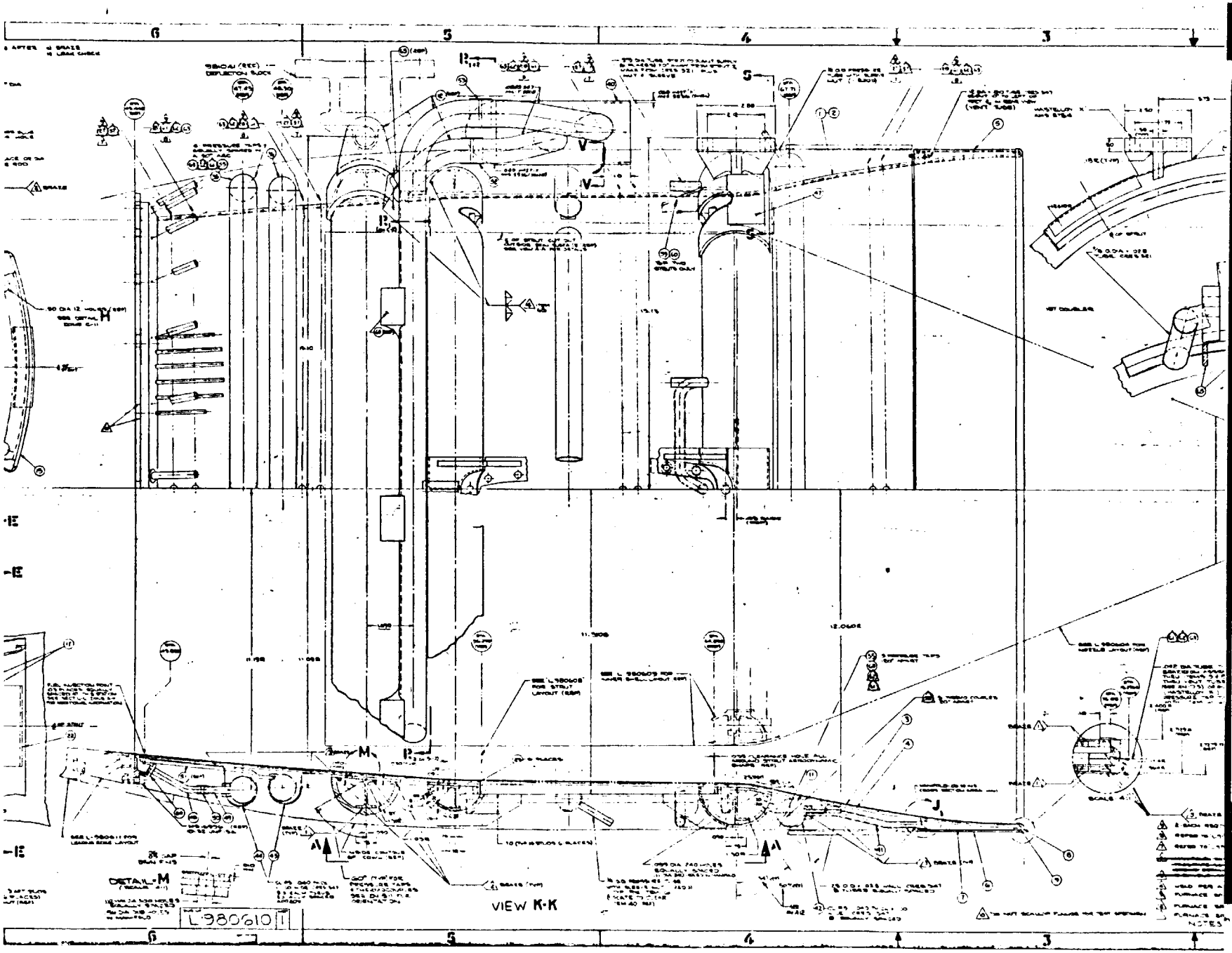
DETAIL-M
VIEW K-K
L-980610

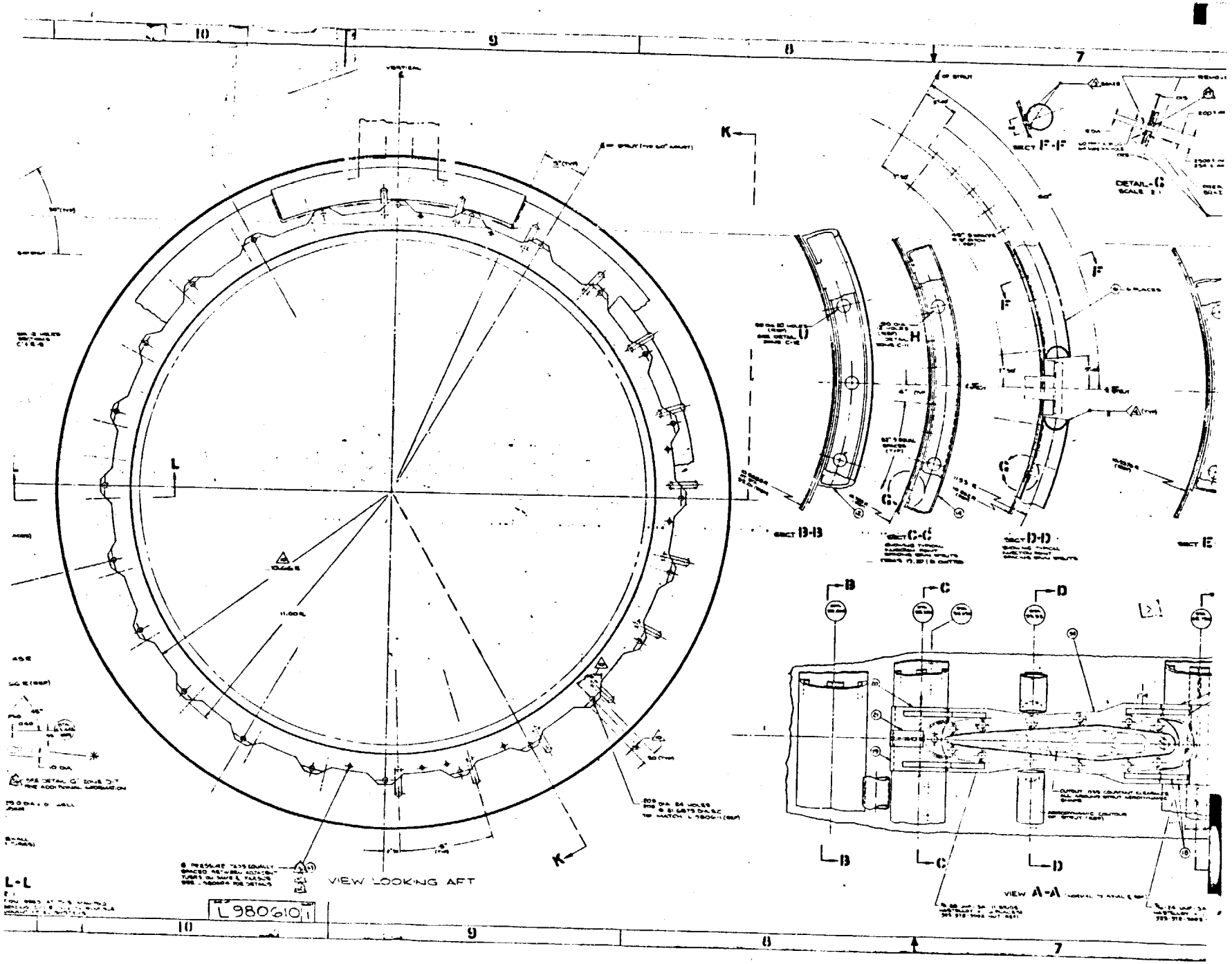
L-L
VIEW LOOKING AFT
SECT B-B
SECT C-C
SECT D-D
SECT E
SECT F-F
DETAIL-G
VIEW A-A
L980610

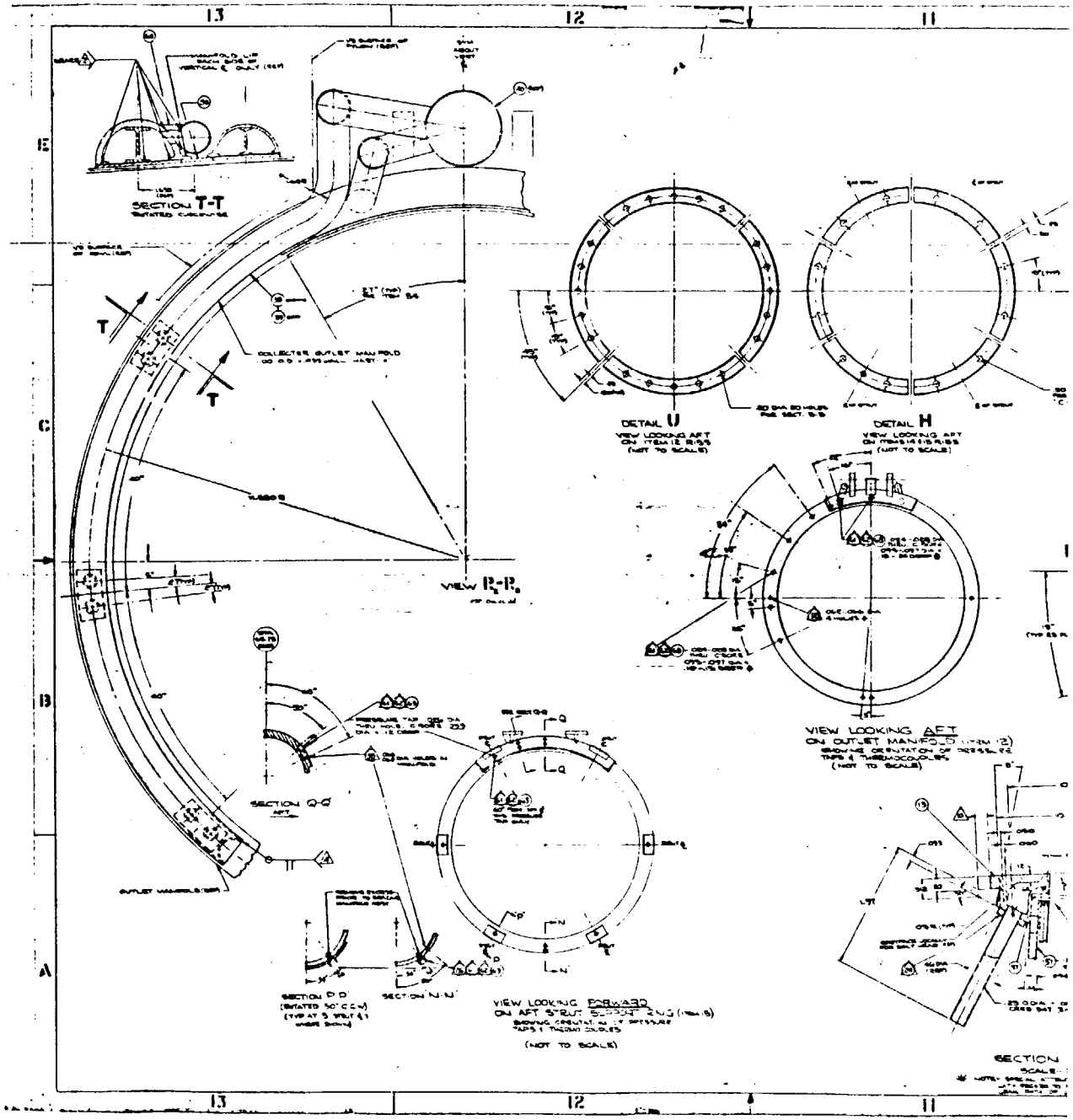
SECTION T-T
DETAIL U
VIEW LOOKING AFT
(NOT TO SCALE)
DETAIL H
VIEW LOOKING AFT
(NOT TO SCALE)
VIEW R-R
VIEW LOOKING AFT
ON OUTLET MANIFOLD
(NOT TO SCALE)
SECTION Q-Q
SECTION P-P
SECTION N-N
VIEW LOOKING FORWARD
(NOT TO SCALE)
SECTION

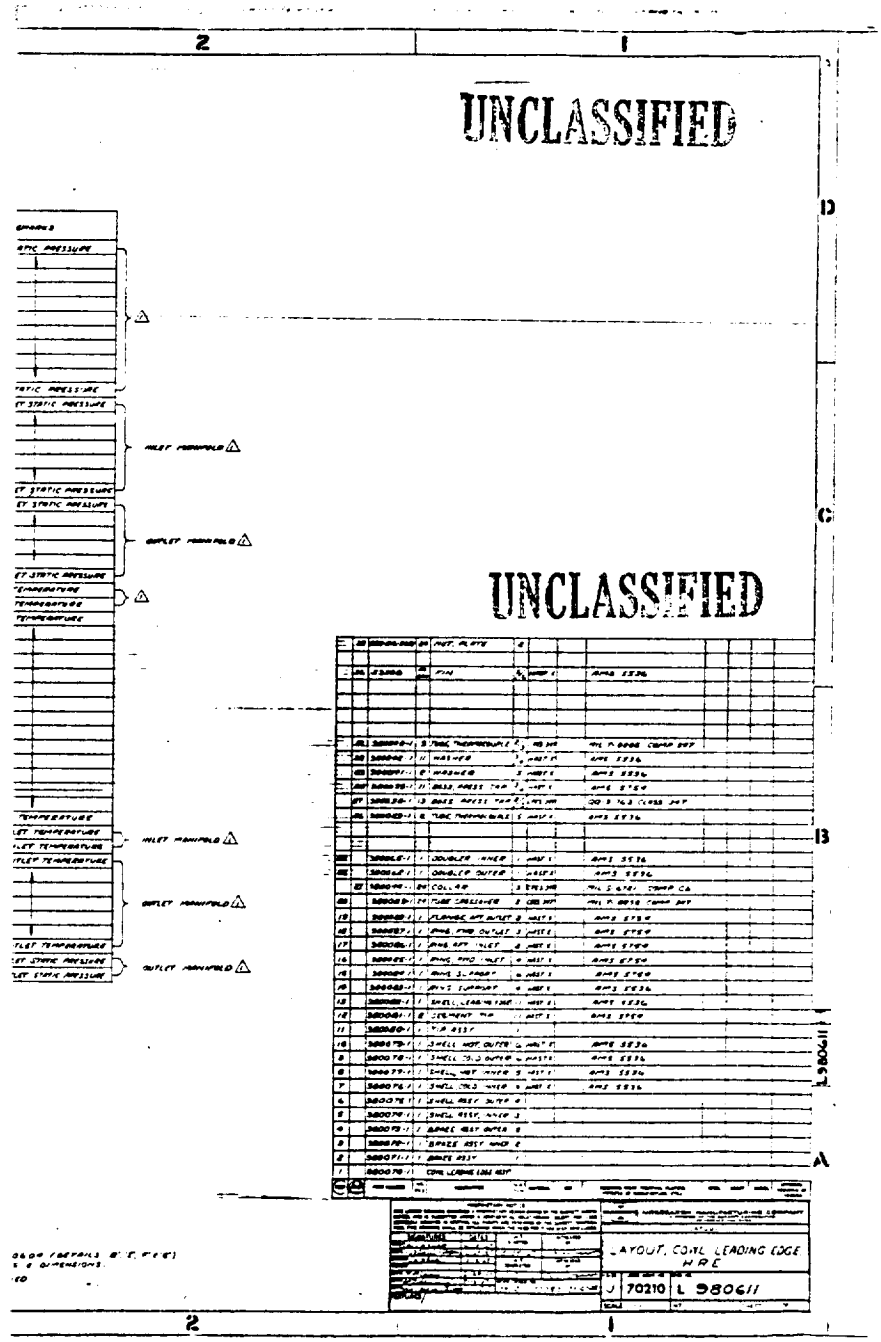
UNCLASSIFIED
UNCLASSIFIED
INLET MANIFOLD
OUTLET MANIFOLD
INLET MANIFOLD
OUTLET MANIFOLD
OUTLET MANIFOLD
LAYOUT, COWL LEADING EDGE
HRE
70210
L 980611

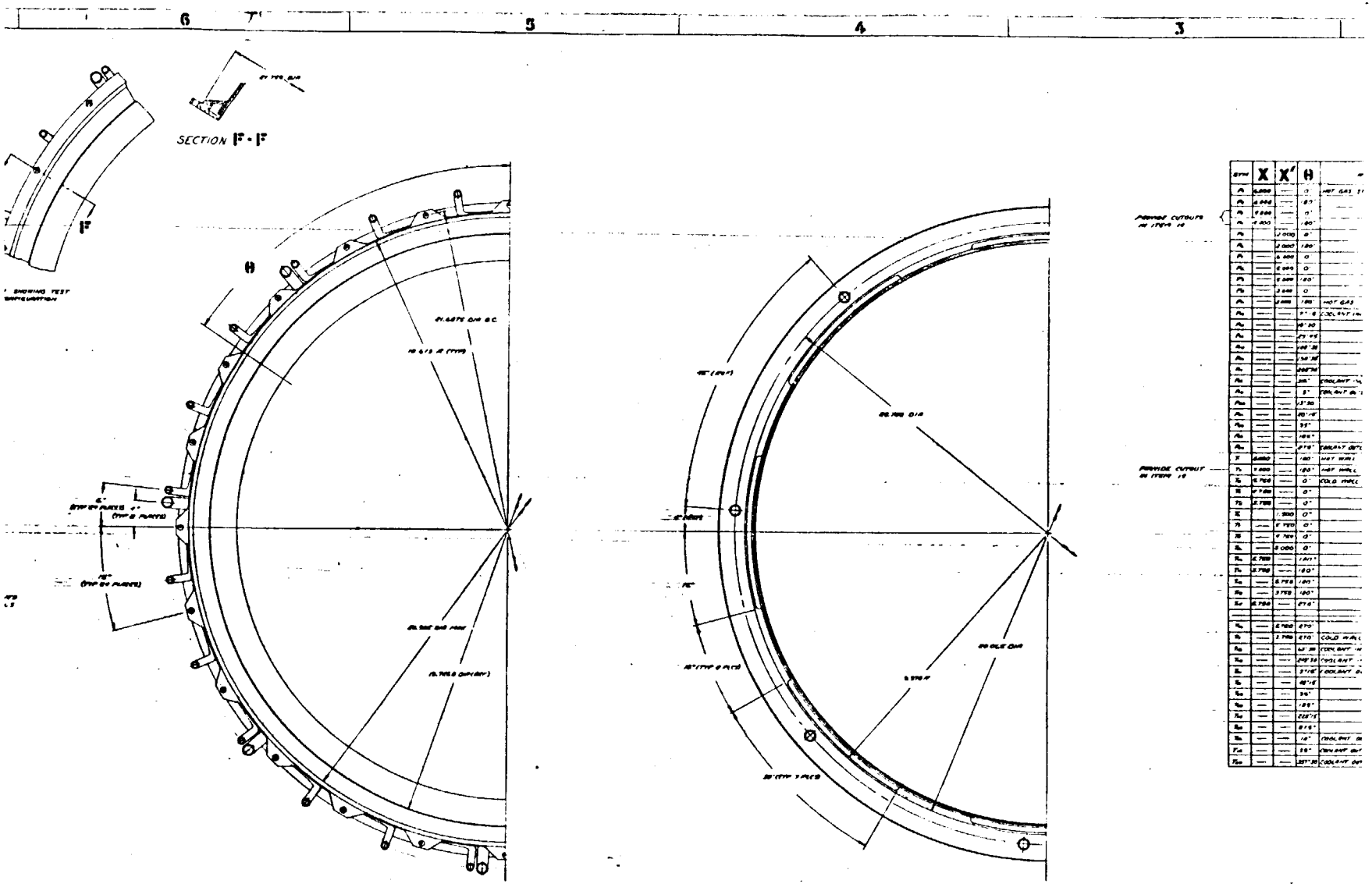
SECTION F-F
SECTION B-B
PROVIDE CUTOUTS
PROVIDE CUTOUT

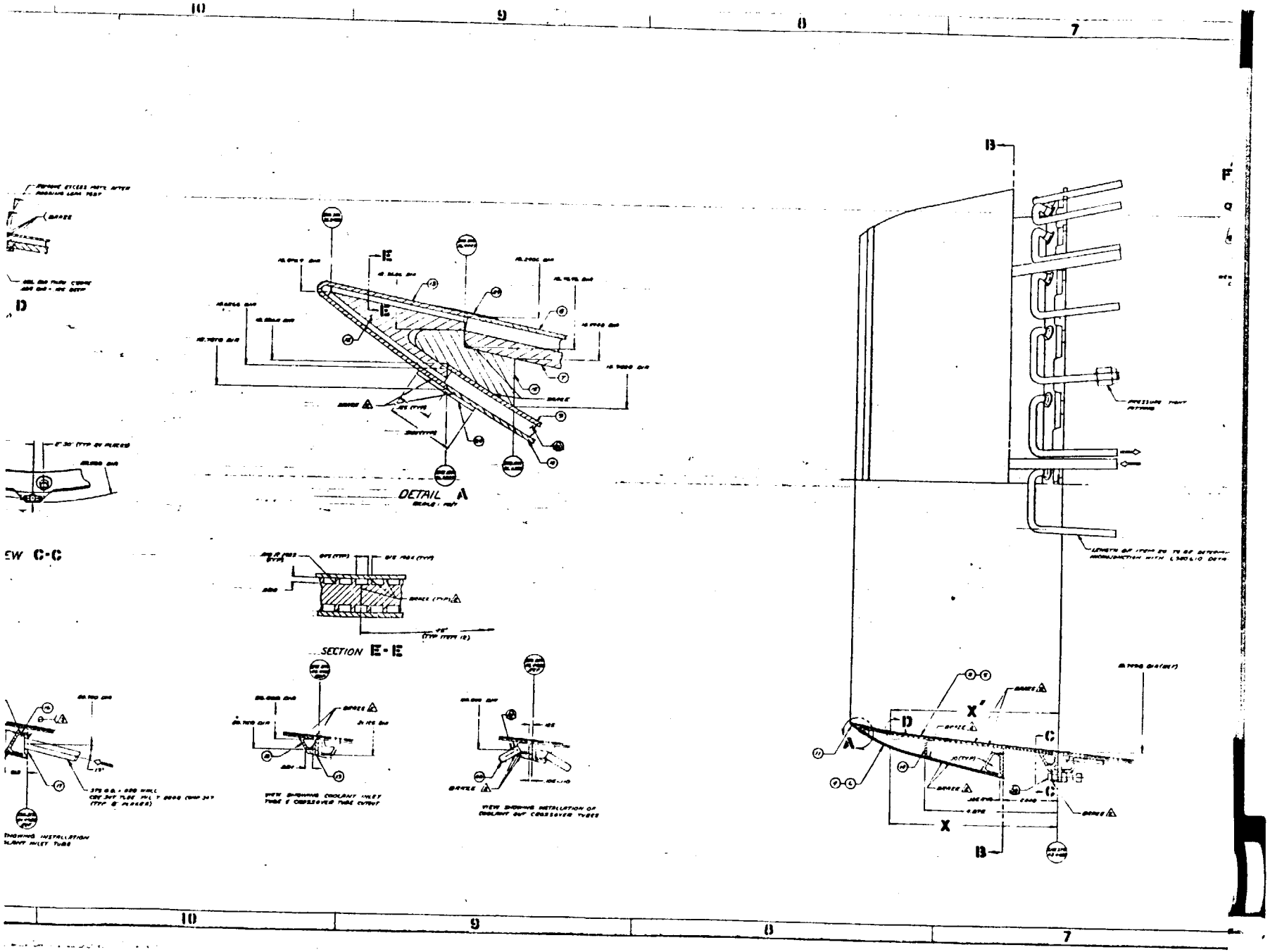

10
9
8
7
DETAIL A
SECTION E-E
EW C-C
D
E
B
A
C
X
X'

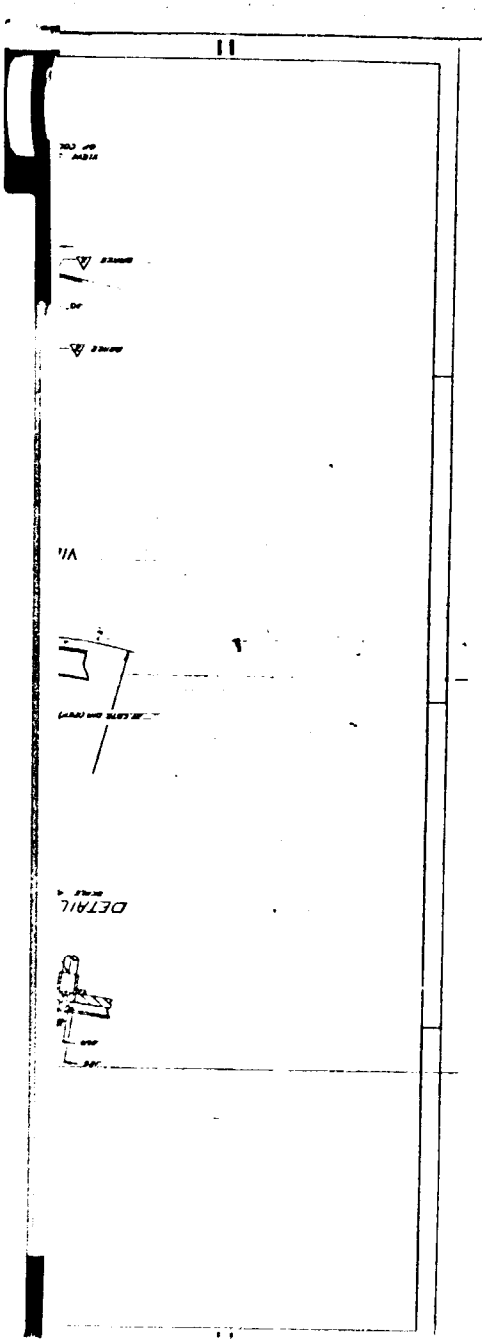

D

1

UNCLASSIFIED

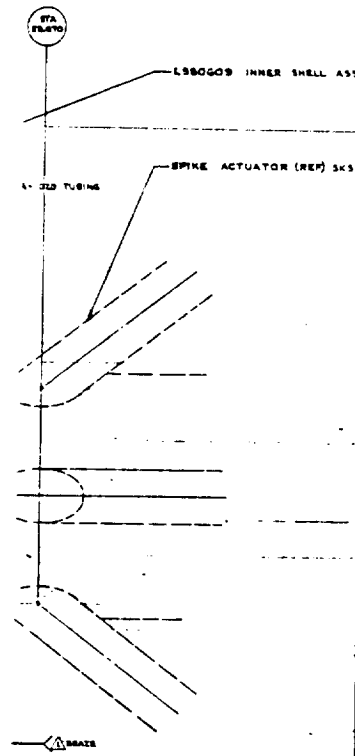

	980 9309	PIN (.080 - .090)	3	MAT'L	AMS 5536
	980 9309	PIN (.15 - .20)	2	MAT'L	AMS 5536
	28 980101	1 INSERT MSTL THERMOCOUPLE			
	27 980100	6 INSERT MSTL PRESSURE TAP			
	26 980123	10 INSERT MSTL PRESSURE TAP			
	25 980122	6 INSERT MSTL THERMOCOUPLE			
24	980579-1	91 PLUG, INJECTOR	3	MAT'L	AMS 5754
23	980117-3	1 DOUBLER	3	MAT'L	AMS 5536
22	980108-1	1 DOUBLER	1	MAT'L	AMS 5536
21	980017-1	1 SHELL, INTERMED COLD	3	MAT'L	AMS 5536
20	980016-1	1 SHELL, INTERMEDIATE	3	MAT'L	AMS 5536
19	980015-1	1 SHELL, AFT COLD	3	MAT'L	AMS 5536
18	980014-1	1 SHELL, AFT HOT	3	MAT'L	AMS 5536
17	980013-1	1 SHELL, FWD COLD	2	MAT'L	AMS 5536
16	980012-1	1 SHELL, FWD HOT	2	MAT'L	AMS 5536
15	980106-1	1 DOUBLER	1	MAT'L	AMS 5536
14	980105-1	1 DOUBLER	1	MAT'L	AMS 5536
13	980107-1	1 DOUBLER	1	MAT'L	AMS 5536
12	980103-1	1 DOUBLER	1	MAT'L	AMS 5536
11	980108-1	1 FITTING	4	MAT'L	AMS 5754
10	980104-1	1 HEADER	3	MAT'L	AMS 5754
9	980109-1	1 TUBE ASSY	4	CRES	MIL-T-8808
8	980119-1	1 FLANGE ASSY	1	CRES	MIL-S-4121
7	980116-1	1 MANIFOLD ASSY	1	MAT'L	AMS 5754
6	980115-1	1 MANIFOLD ASSY	1	MAT'L	AMS 5754
5	980114-1	2 BELLOWS ASSY	1	MAT'L	AMS 5536
4	980113-1	1 SPIKE TIP ASSY	1	MAT'L	AMS 5754
3	980112-1	1 SPIKE ASSY BRAZED W/			
2	980111-1	1 SPIKE ASSY BRAZED W/			
1	980110-1	1 SPIKE ASSY			

PER INSTRUCTIONS OF DEPT 50
UNLESS OTHERWISE SPECIFIED

SPIKE,
HRE

J 70210 L 980612

L980612

UNCLASSIFIED

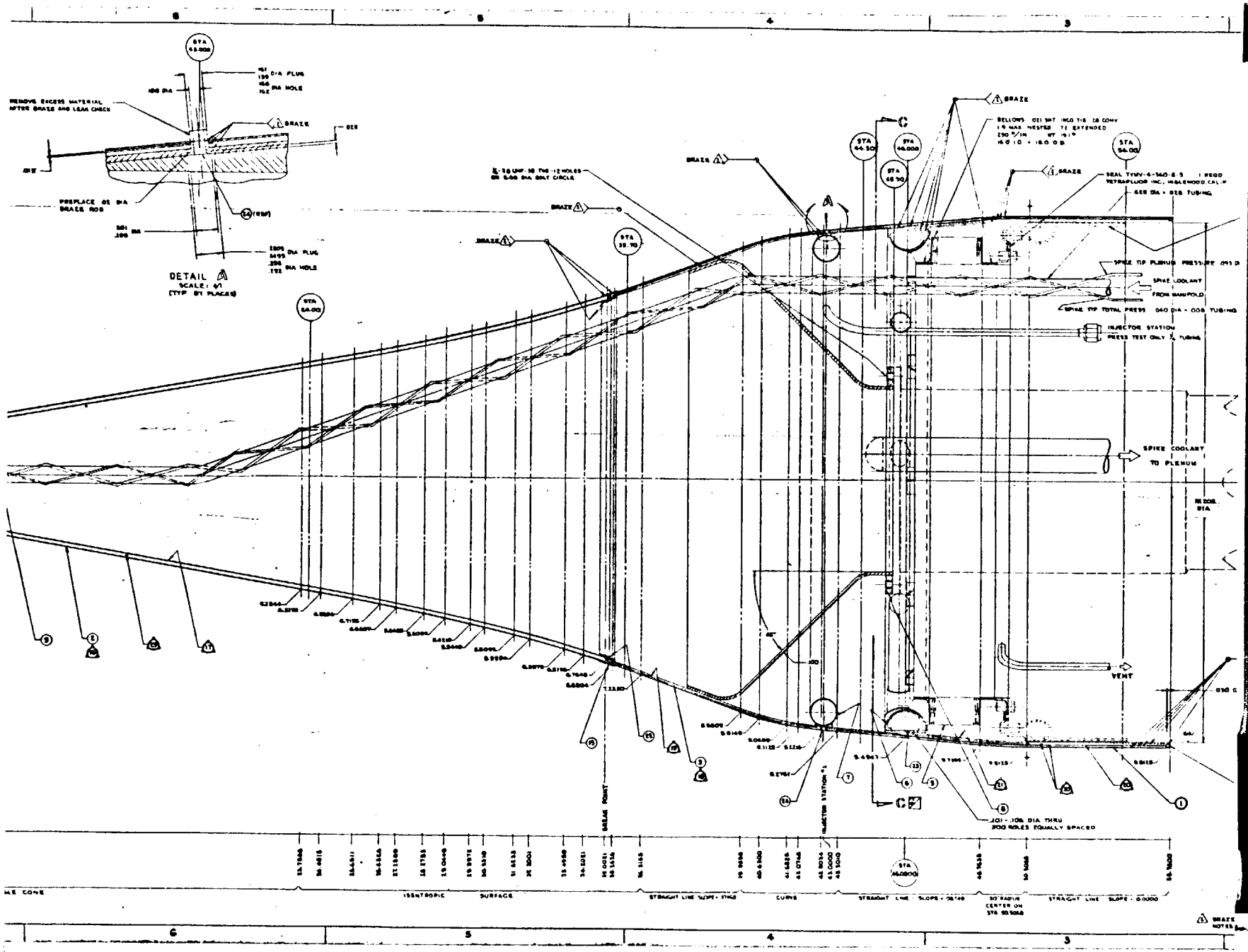

DETAIL A
SCALE: 4/1
(TYP BY PLACES)
REMOVE EXCESS MATERIAL AFTER BRAZE AND LEAK CHECK
PREPLACE .02 DIA BRAZE ROD
BRAZE
BELLOWS .021 SHT INCO 718 28 CONV
SEAL TYNY-4-560-8-5 1 REQD
TETRAFLUOR INC, INGLEWOOD, CALIF
SPIKE TIP PLENUM PRESSURE
SPIKE COOLANT FROM MANIFOLD
SPIKE TIP TOTAL PRESS .040 DIA - .008 TUBING
INJECTOR STATION
PRESS TEST ONLY 1/4 TUBING
SPIKE COOLANT TO PLENUM
VENT
BREAK POINT
INJECTOR STATION #1
.101 - .106 DIA THRU
200 HOLES EQUALLY SPACED
ISENTROPIC SURFACE
STRAIGHT LINE SLOPE = .3748
CURVE
STRAIGHT LINE SLOPE = .08748
30" RADIUS CENTER ON STA 50.5068
STRAIGHT LINE SLOPE = 0.0000
BRAZE NOTES

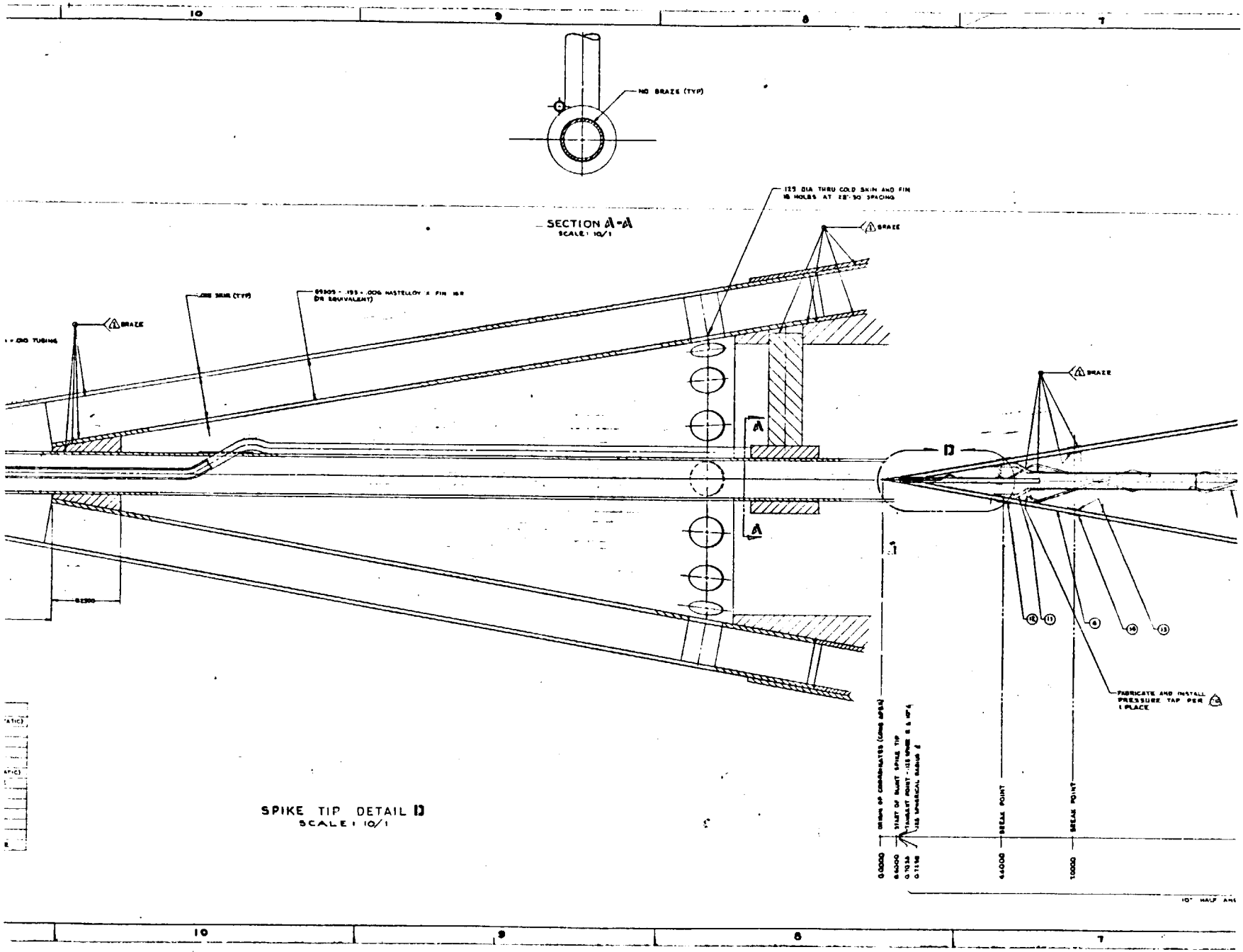

NO BRAZE (TYP)
SECTION A-A
SCALE: 10/1
.125 DIA THRU COLD SKIN AND FIN
16 HOLES AT 28°-30' SPACING
BRAZE
.010 SKIN (TYP)
.010 TUBING
A
D
FABRICATE AND INSTALL PRESSURE TAP PER 1 PLACE
SPIKE TIP DETAIL D
SCALE: 10/1
BREAK POINT
BREAK POINT
0.0000
0.6000
0.7036
0.7250
0.4000
1.0000
10° HALF ANG

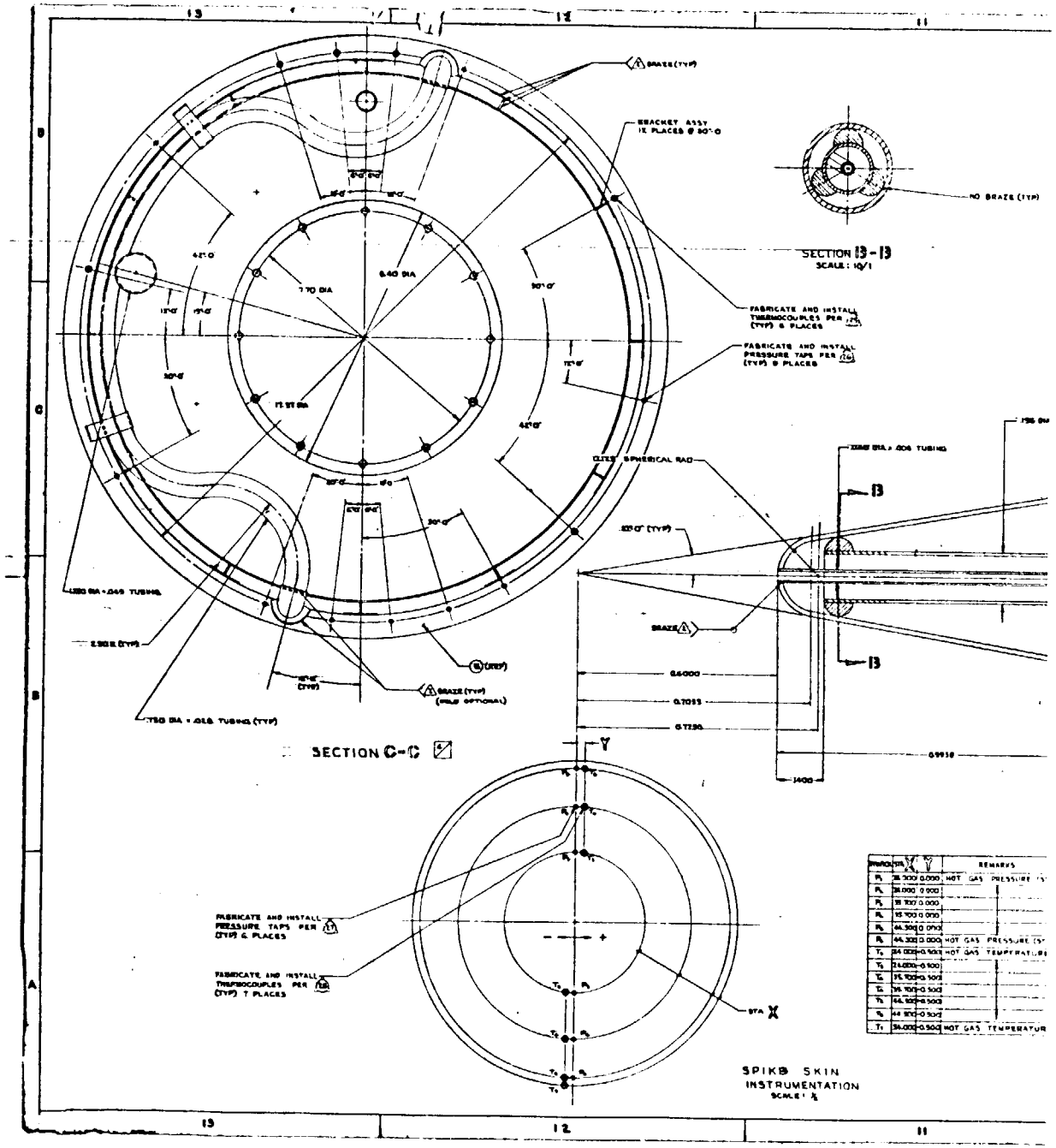

SECTION B-B
SCALE: 10/1
NO BRAZE (TYP)
BRACKET ASSY
FABRICATE AND INSTALL THERMOCOUPLES PER (TYP) 6 PLACES
FABRICATE AND INSTALL PRESSURE TAPS PER (TYP) 8 PLACES
SPHERICAL RAD
SECTION C-C
FABRICATE AND INSTALL PRESSURE TAPS PER (TYP) 6 PLACES
FABRICATE AND INSTALL THERMOCOUPLES PER (TYP) 7 PLACES
STA X
SPIKE SKIN INSTRUMENTATION
SCALE: 1/2
REMARKS
HOT GAS PRESSURE
HOT GAS TEMPERATURE

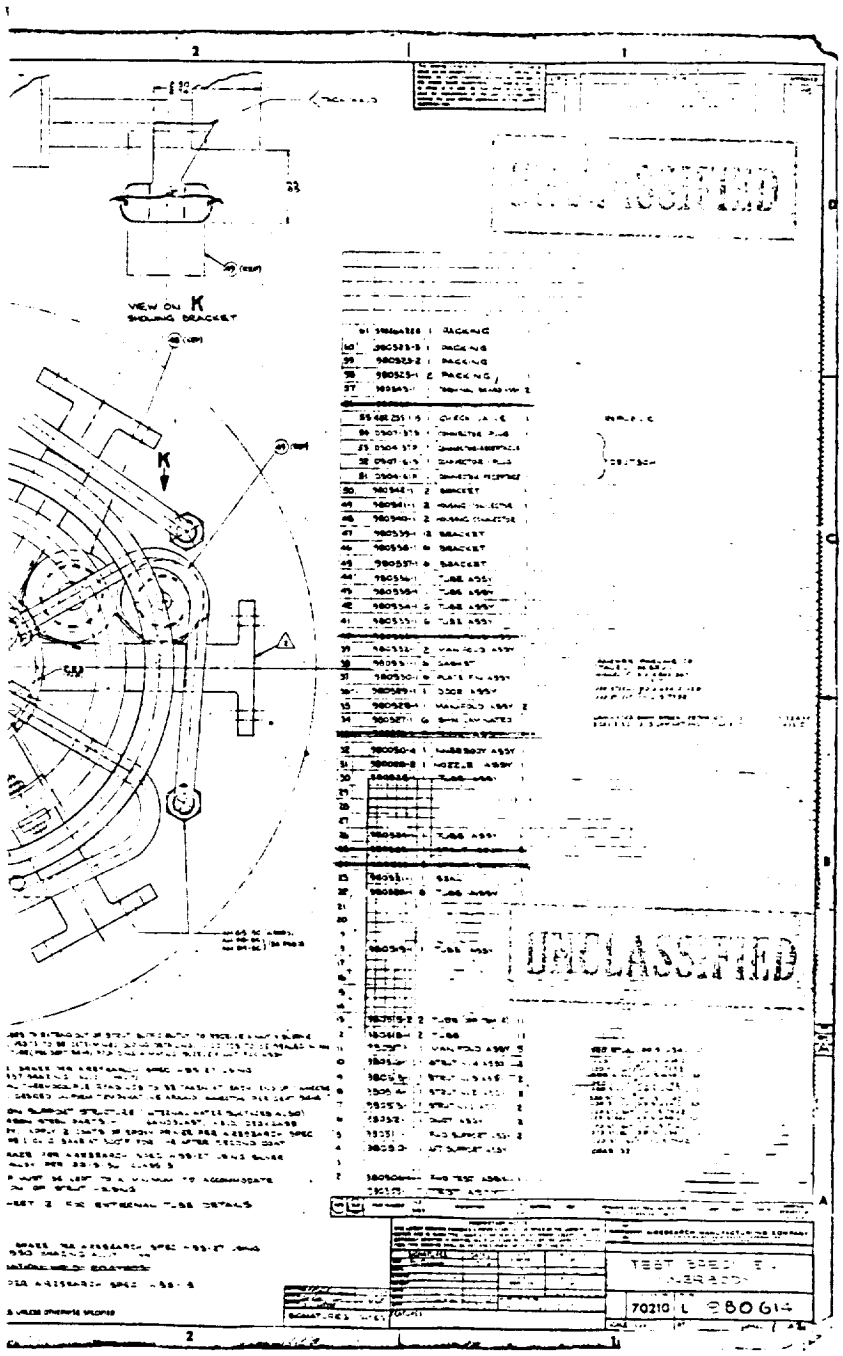
VIEW ON K
SWING BRACKET
K
UNCLASSIFIED
UNCLASSIFIED
TEST SPECIMEN
70210 L 980614

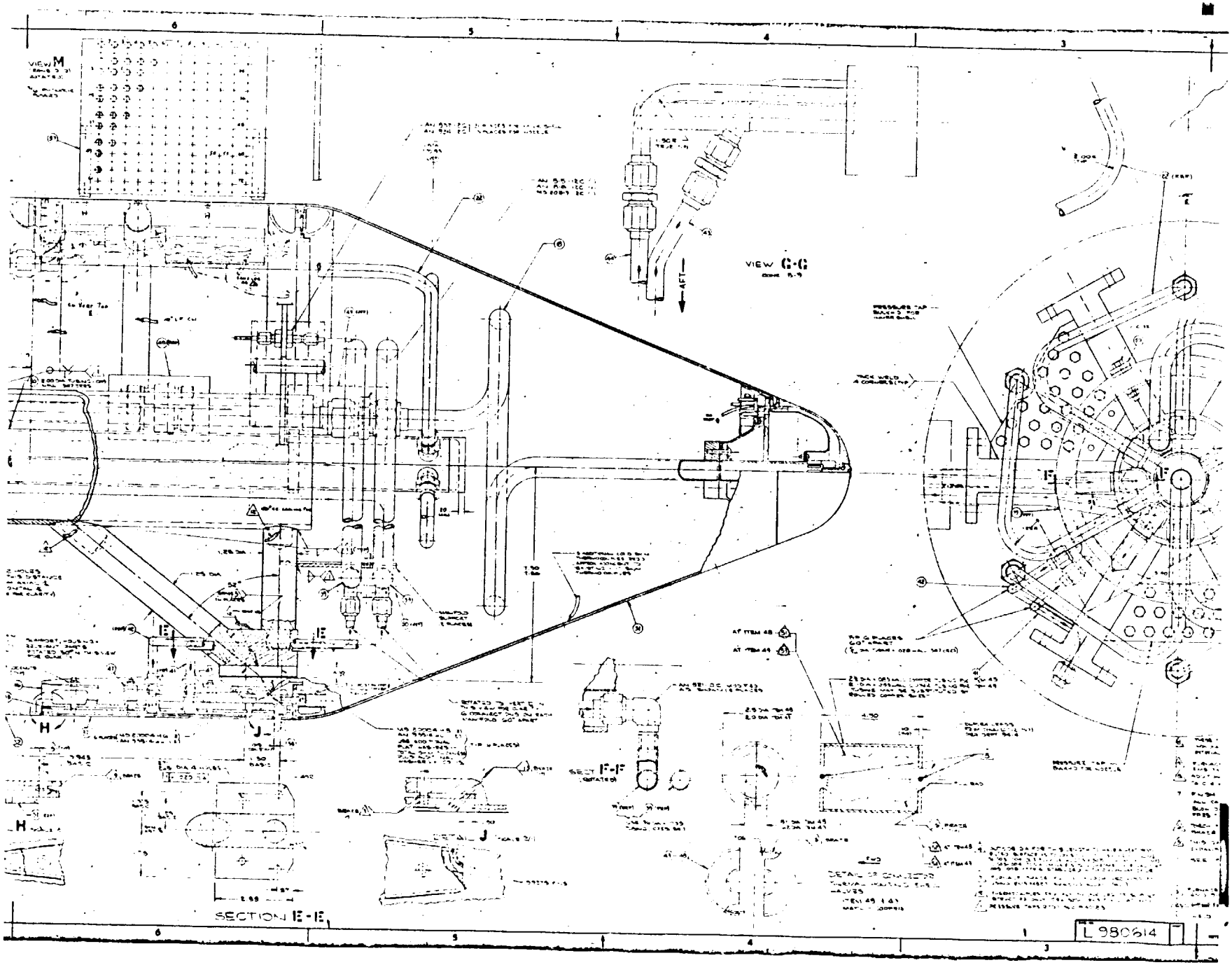
VIEW M
VIEW G-G
AFT
SECTION E-E
SECT F-F
L 980814

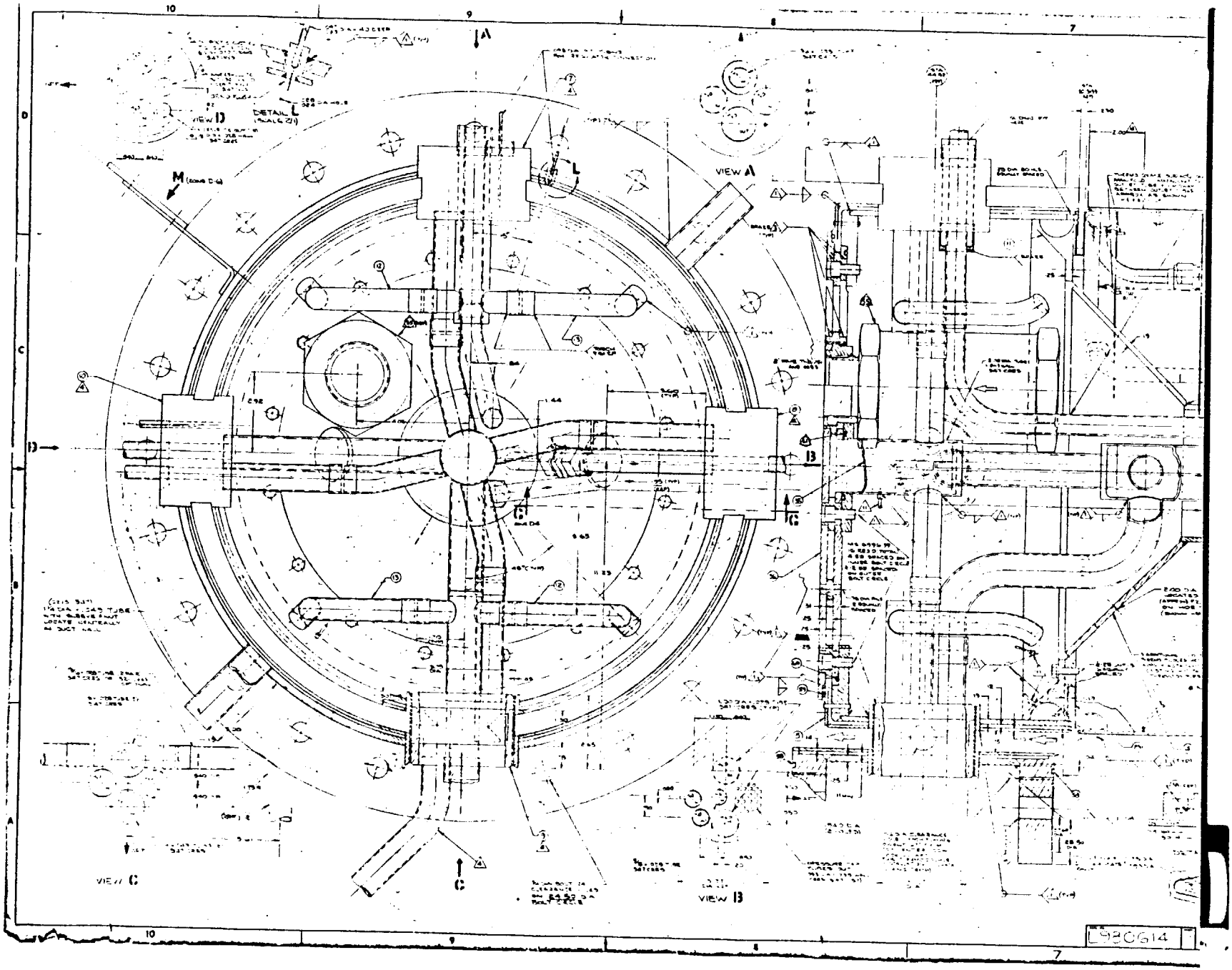
VIEW D
DETAIL L
VIEW A
VIEW C
VIEW B
L980614

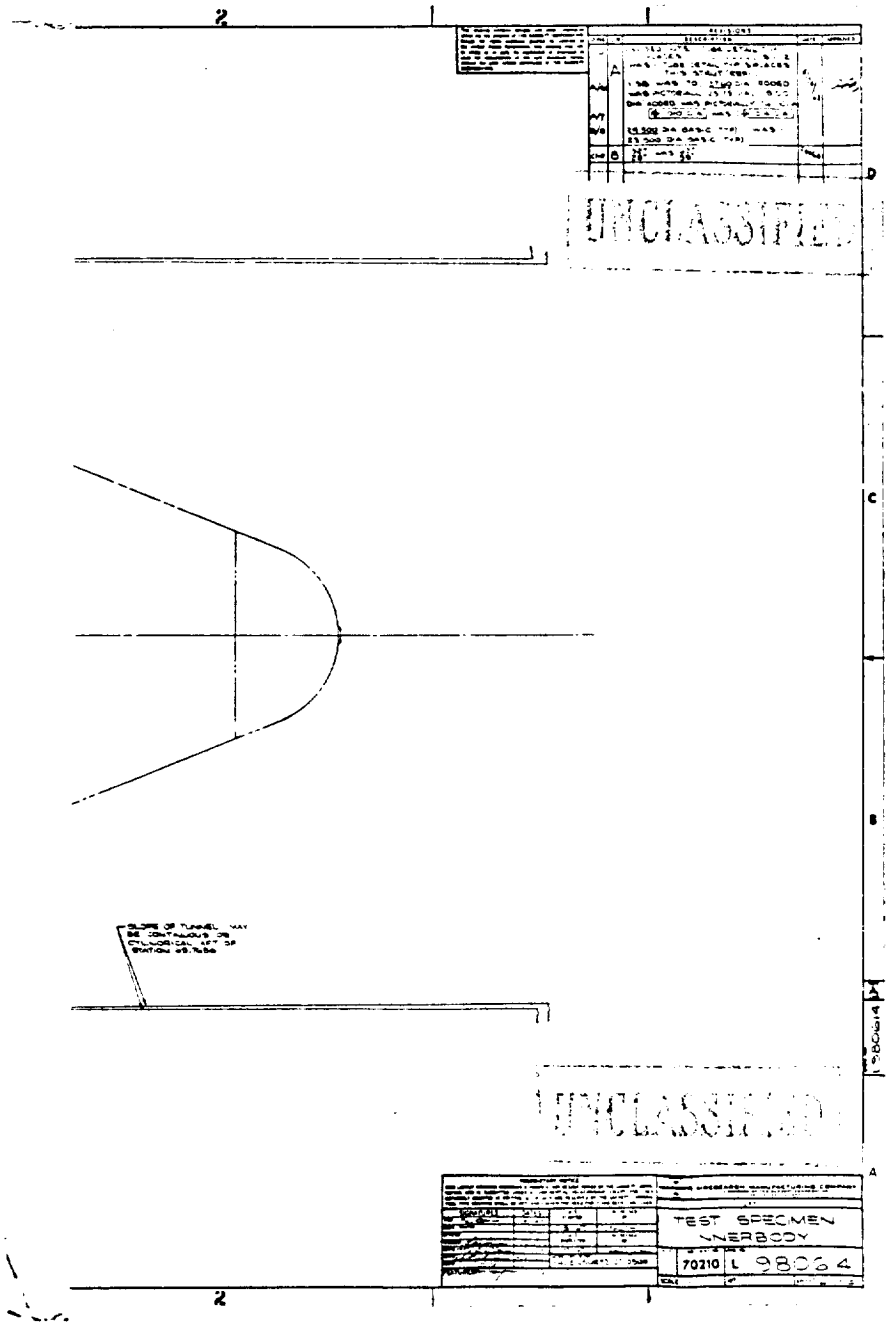
UNCLASSIFIED
UNCLASSIFIED
TEST SPECIMEN
INNERBODY
70210
L
98064

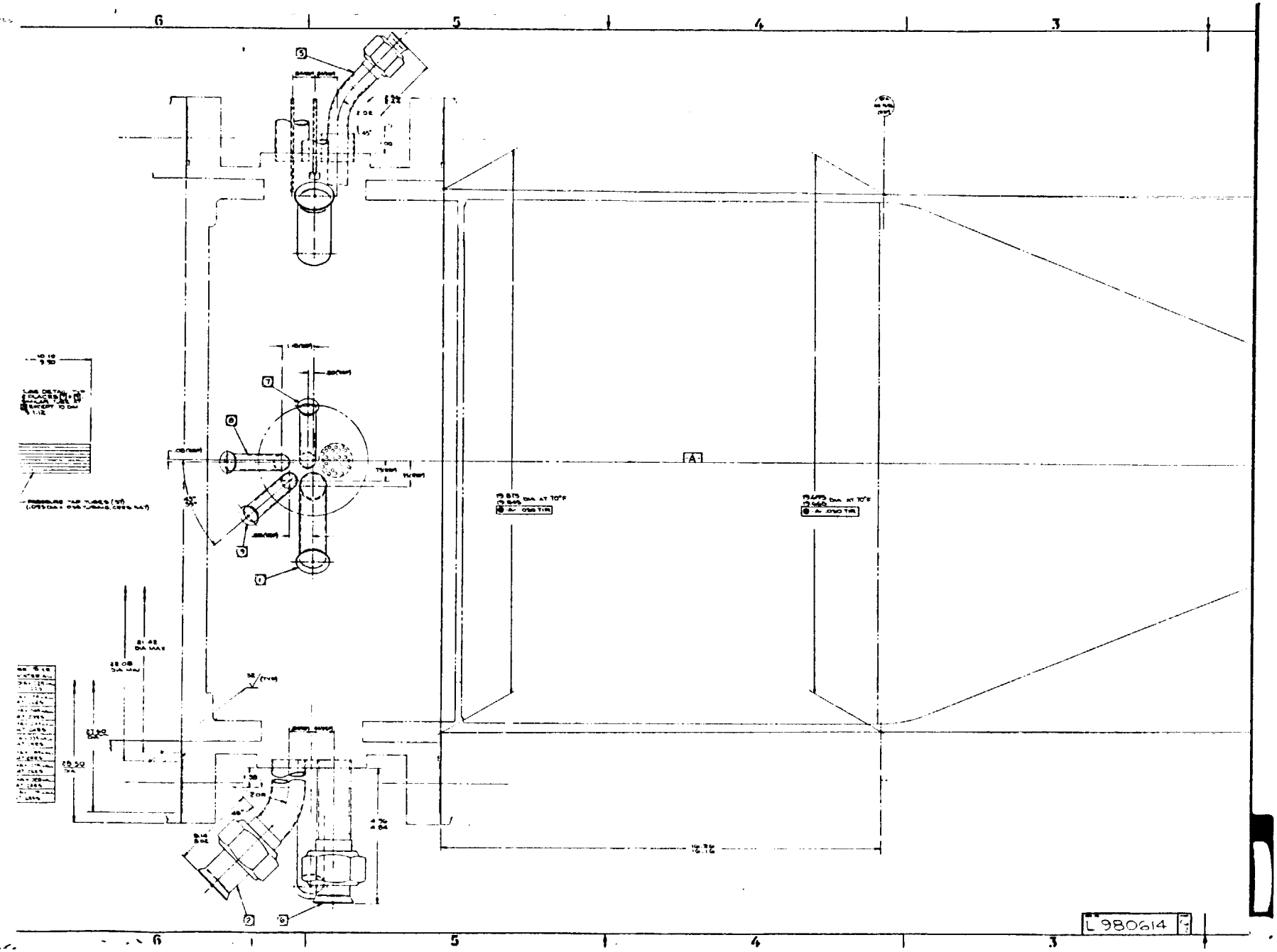
6
5
4
3
A
L 980614

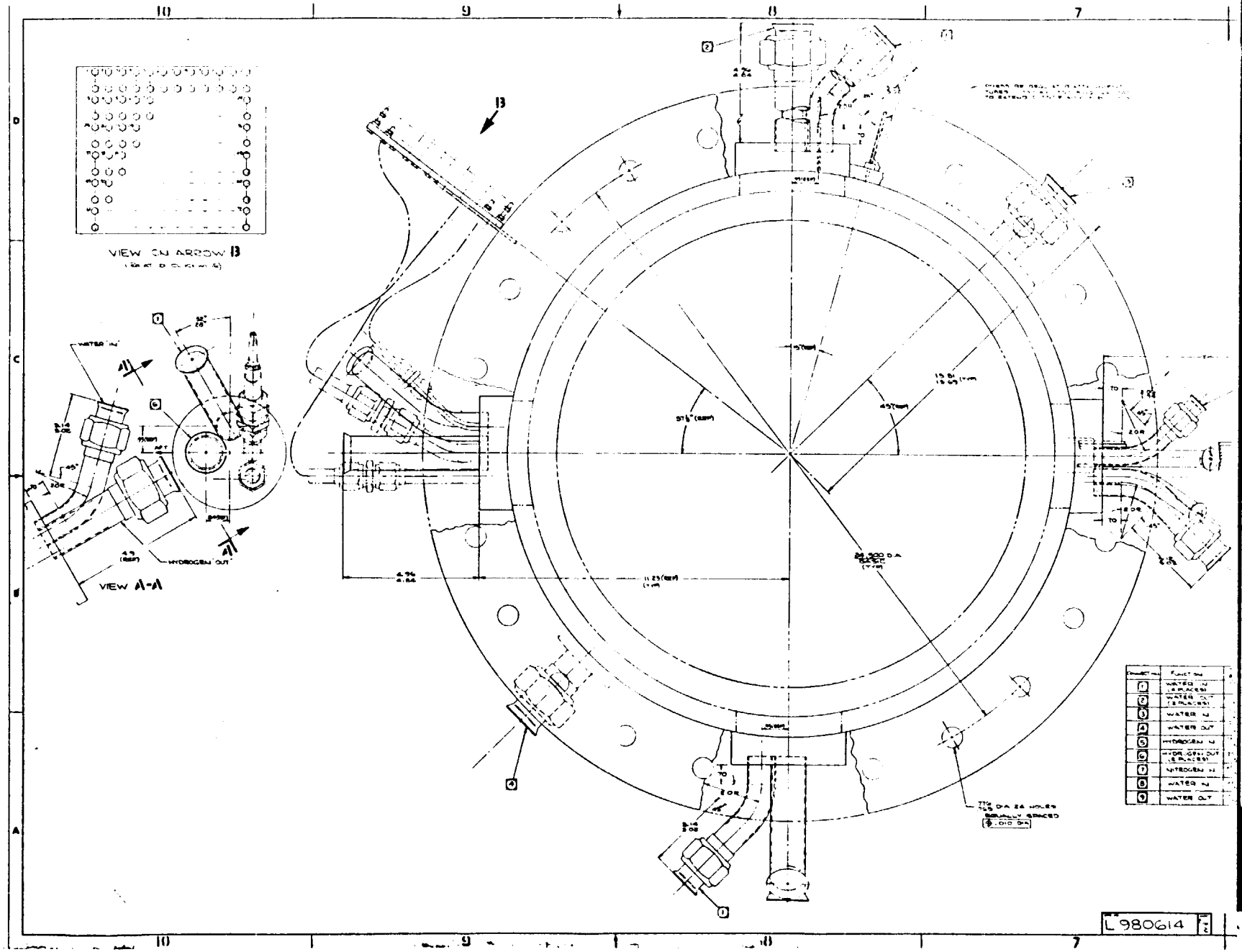
VIEW ON ARROW B
VIEW A-A
WATER IN
HYDROGEN OUT
24.500 D.A. BASIC (TYP)
11.25 (REF) (TYP)
4.96
4.84
15.81
15.69 (TYP)
45° (REF)
57½° (REF)
.776 .765 DIA 24 HOLES EQUALLY SPACED
.010 DIA
CONNECTION
FUNCTION
1 WATER IN (4 PLACES)
2 WATER OUT (2 PLACES)
3 WATER IN
4 WATER OUT
5 HYDROGEN IN
6 HYDROGEN OUT (2 PLACES)
7 NITROGEN IN
8 WATER IN
9 WATER OUT
L 980614

UNCLASSIFIED

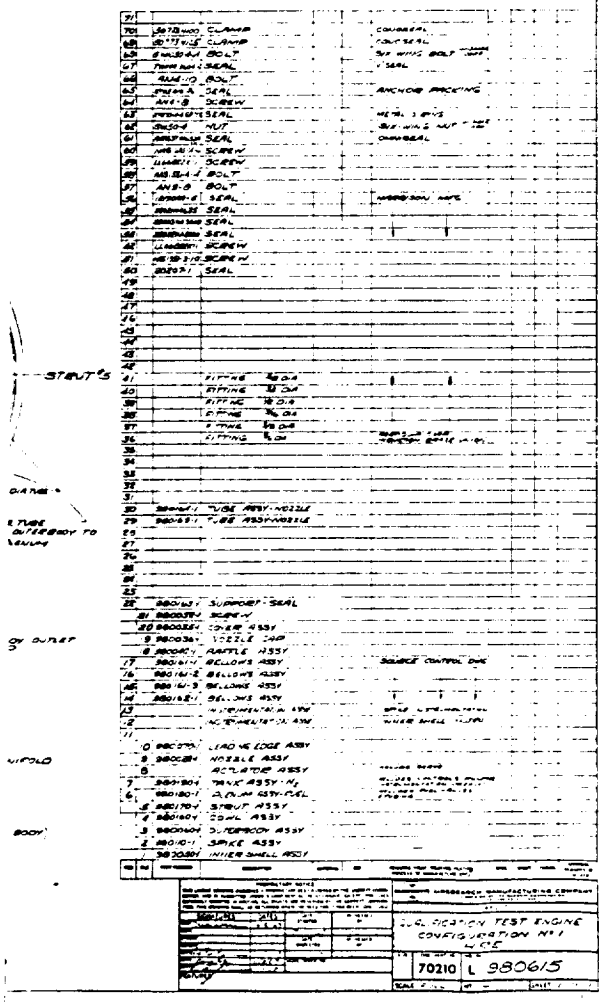

UNCLASSIFIED

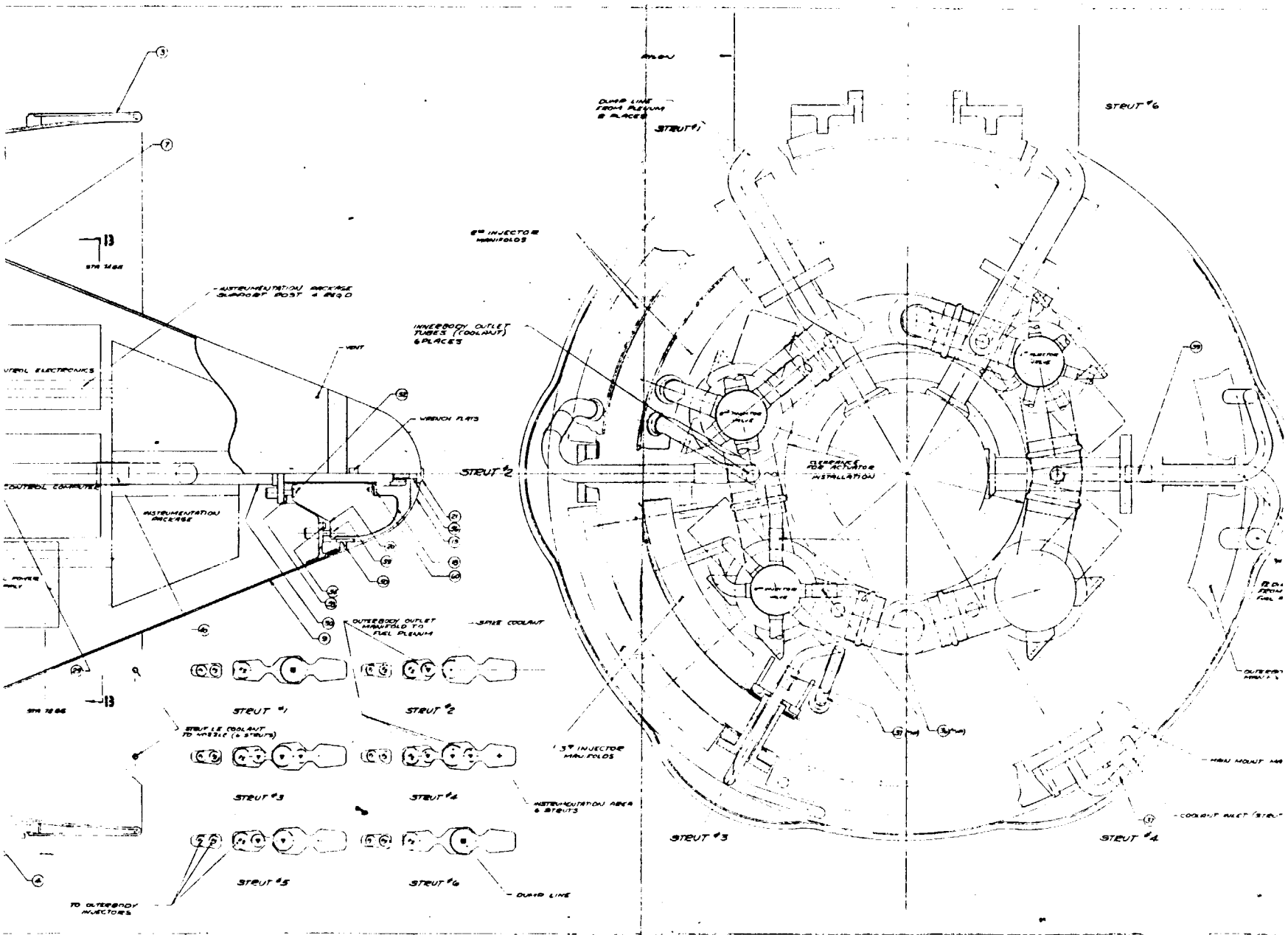

STRUT #1
STRUT #2
STRUT #3
STRUT #4
STRUT #5
STRUT #6
INSTRUMENTATION PACKAGE SUPPORT POST 4 REQ'D
INNERBODY OUTLET TUBES (COOLANT) 6 PLACES
WRENCH FLATS
VENT
CONTROL COMPUTER
INSTRUMENTATION PACKAGE
OUTERBODY OUTLET MANIFOLD TO FUEL PLENUM
SPIKE COOLANT
STRUT LE COOLANT TO NOZZLE (6 STRUTS)
INSTRUMENTATION AREA 6 STRUTS
DUMP LINE
TO OUTERBODY INJECTORS
DUMP LINE FROM PLENUM 8 PLACES
CLEARANCE FOR ACTUATOR INSTALLATION
MAIN MOUNT
COOLANT INLET

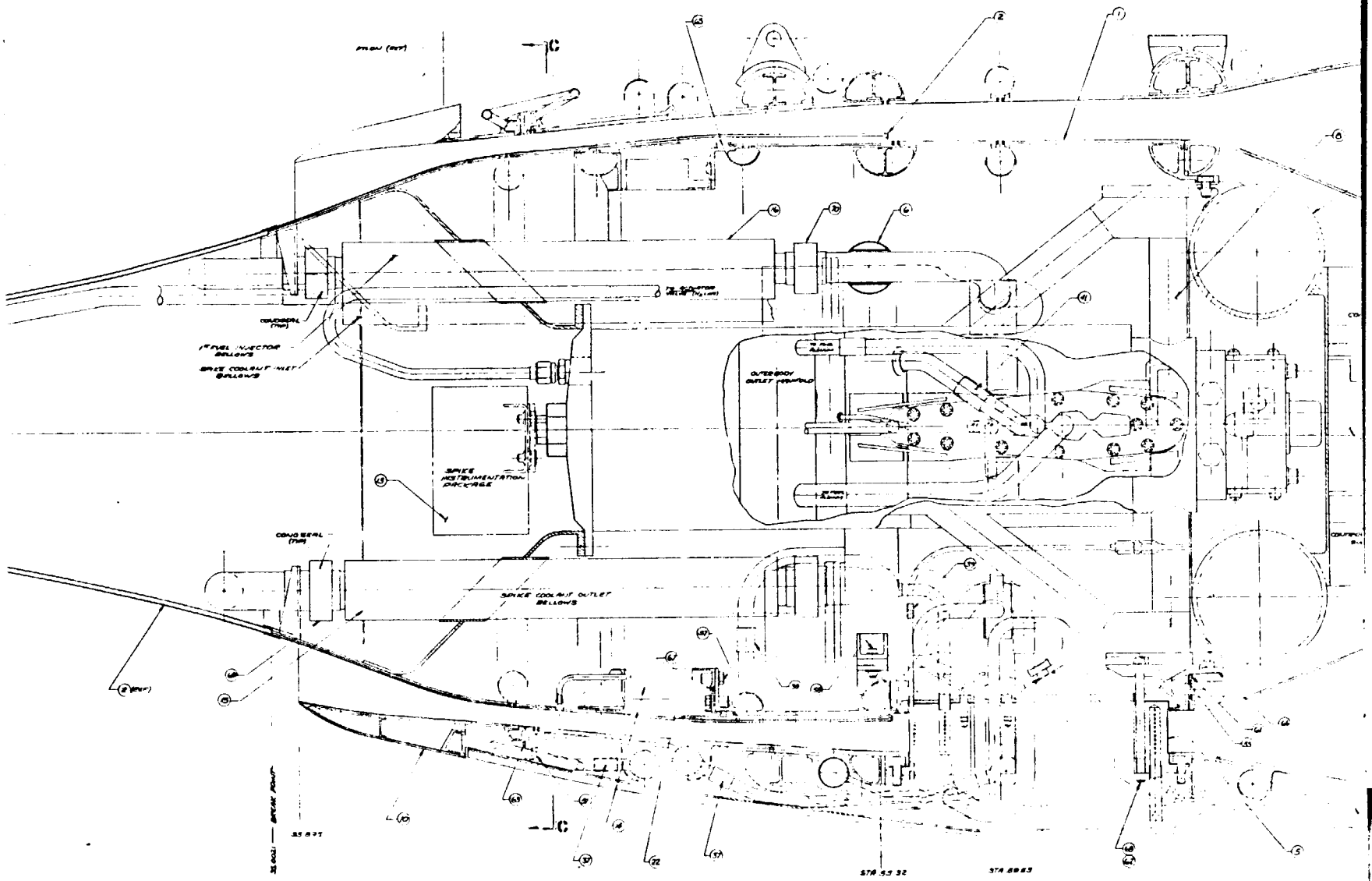

PYLON (REF)
CONOSEAL (TYP)
1st FUEL INJECTOR BELLOWS
SPIKE COOLANT INLET BELLOWS
SPIKE INSTRUMENTATION PACKAGE
OUTERBODY OUTLET MANIFOLD
SPIKE COOLANT OUTLET BELLOWS
STA 55.32
STA 89.63

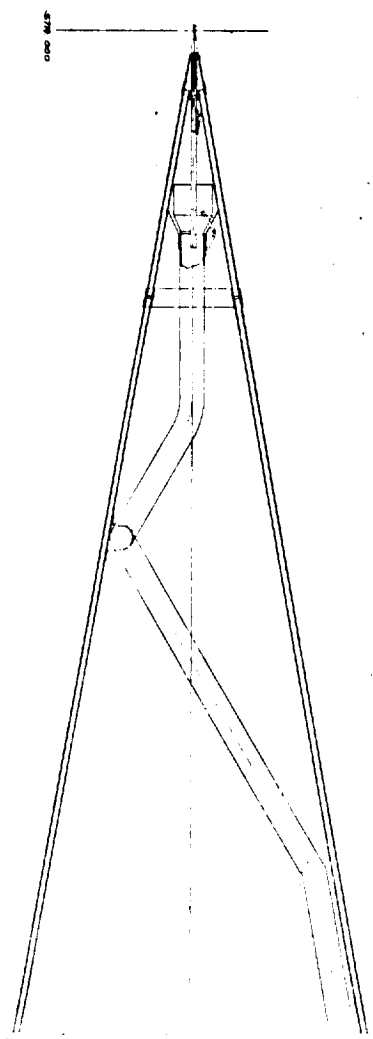

UNCLASSIFIED

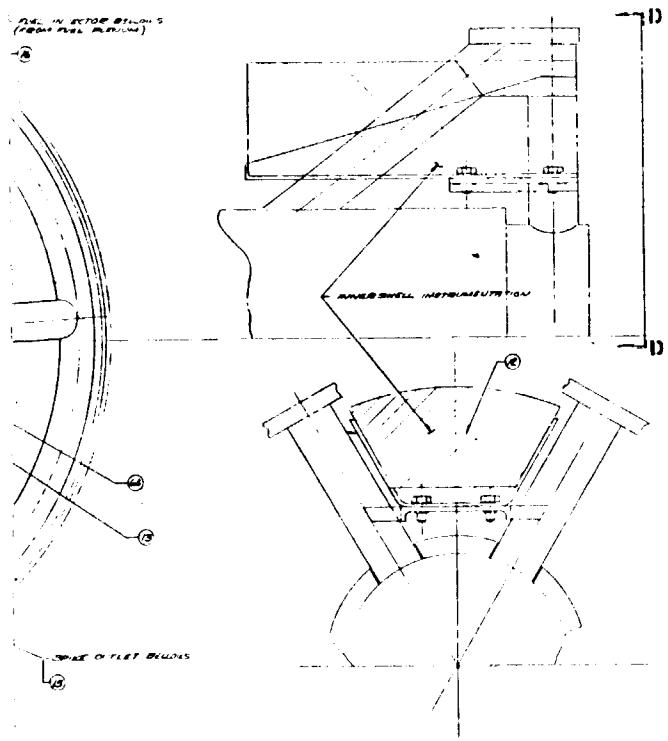

AMERICAN MANUFACTURING COMPANY

LAYOUT

QUALIFICATION TEST ENGINE CONFIGURATION No 1 HRE

70210	L 980615

UNCLASSIFIED

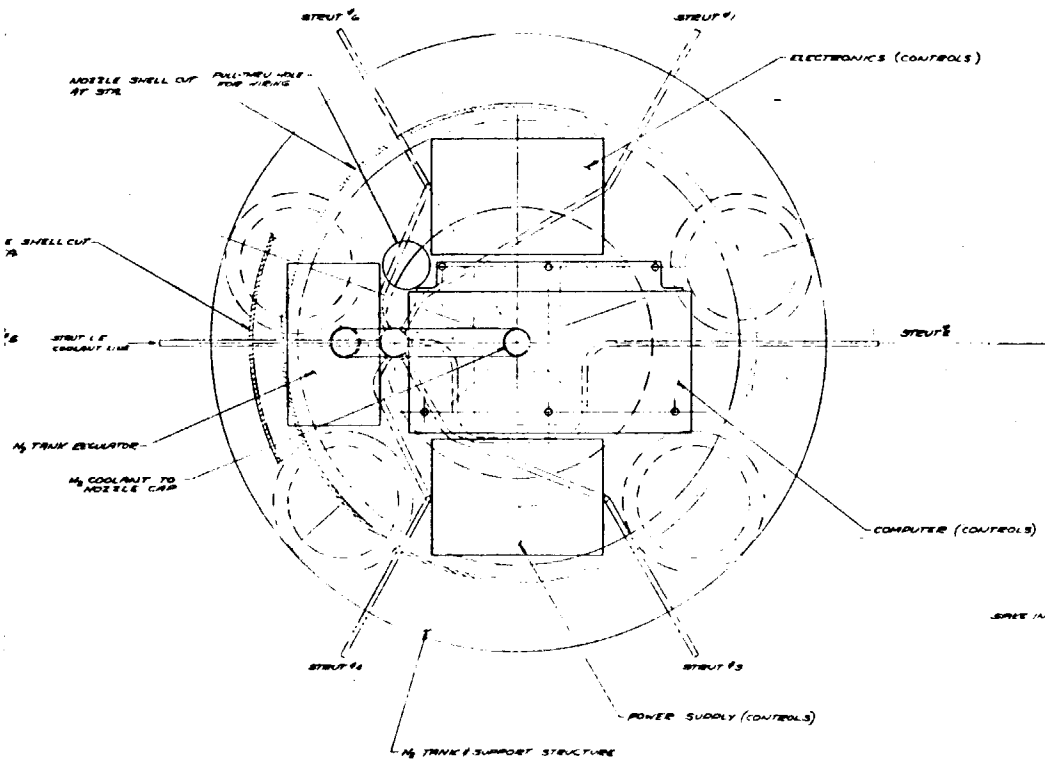

SECTION B-B

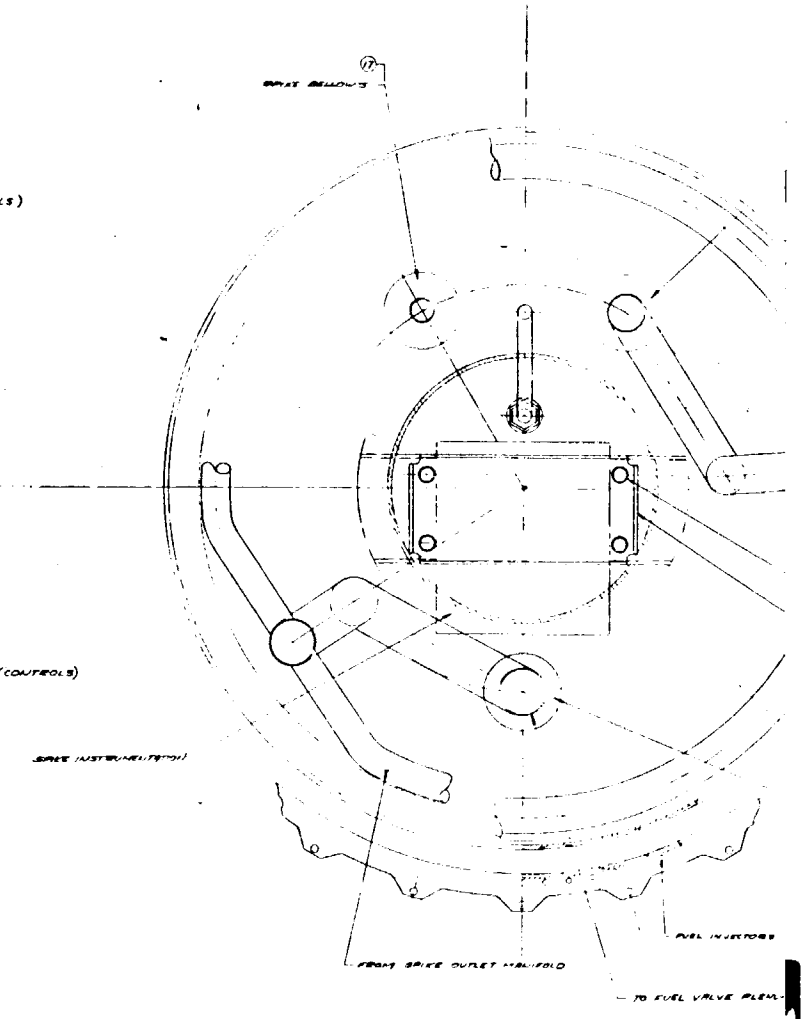

SECTION C-C

UNCLASSIFIED

UNCLASSIFIED

	19	482 [illegible]	1	CHECK VALVE	REPUBLIC 15 PSI SPRING
18		0507-575	1	CONNECTOR PLUG	DEUTSCH
	17	0508-37P	1	CONNECTOR RECEPTACLE	DEUTSCH
16		0507-615	1	CONNECTOR PLUG	DEUTSCH
	15	0504-61P	1	CONNECTOR RECEPTACLE	DEUTSCH
	14	980541-1	1	HOUSING CONNECTOR	
	13	980540-1	1	HOUSING CONNECTOR	
12		980125-2	1	SLEEVE	
	11	980125-1	37	SLEEVE	
10		980549-1	1	SILVERED PRESS [illegible]	[illegible]
9		980548-1	1	BRACKET CONN	[illegible]
8		980547-1	1	SEAL	
7		980546-1	1	SUPPORT ASSY	[illegible]
6		980545-1	1	TUBE ASSY	[illegible]
5		980544-1	1	TUBE ASSY	[illegible]
	4	980529-1	1	DOOR ASSY	[illegible]
3		980508-1	1	END TEST ASSY	
	2	980110-1	1	SPIKE ASSY	
1		980507-1	1	TEST ASSY VALVE	

1 AIRESEARCH SPEC WBS-27
[illegible] PER ASTM B 260 BAL 4
CONNECTED DIRECTLY TO STRUT ASSY
[illegible] TEST ASSY [illegible] ALTERING [illegible]
[illegible] APPROX AT SHOWN
[illegible] READINGS TO BE TAKEN AT EACH END OF CONNECTORS
[illegible] TEMPERATURE AROUND CONNECTOR PER CERT 94 4
[illegible] SPEC WBS 18
[illegible] SPECIFIED

AIRESEARCH MANUFACTURING COMPANY

TEST [illegible]

1	70210	L 980617

L980617

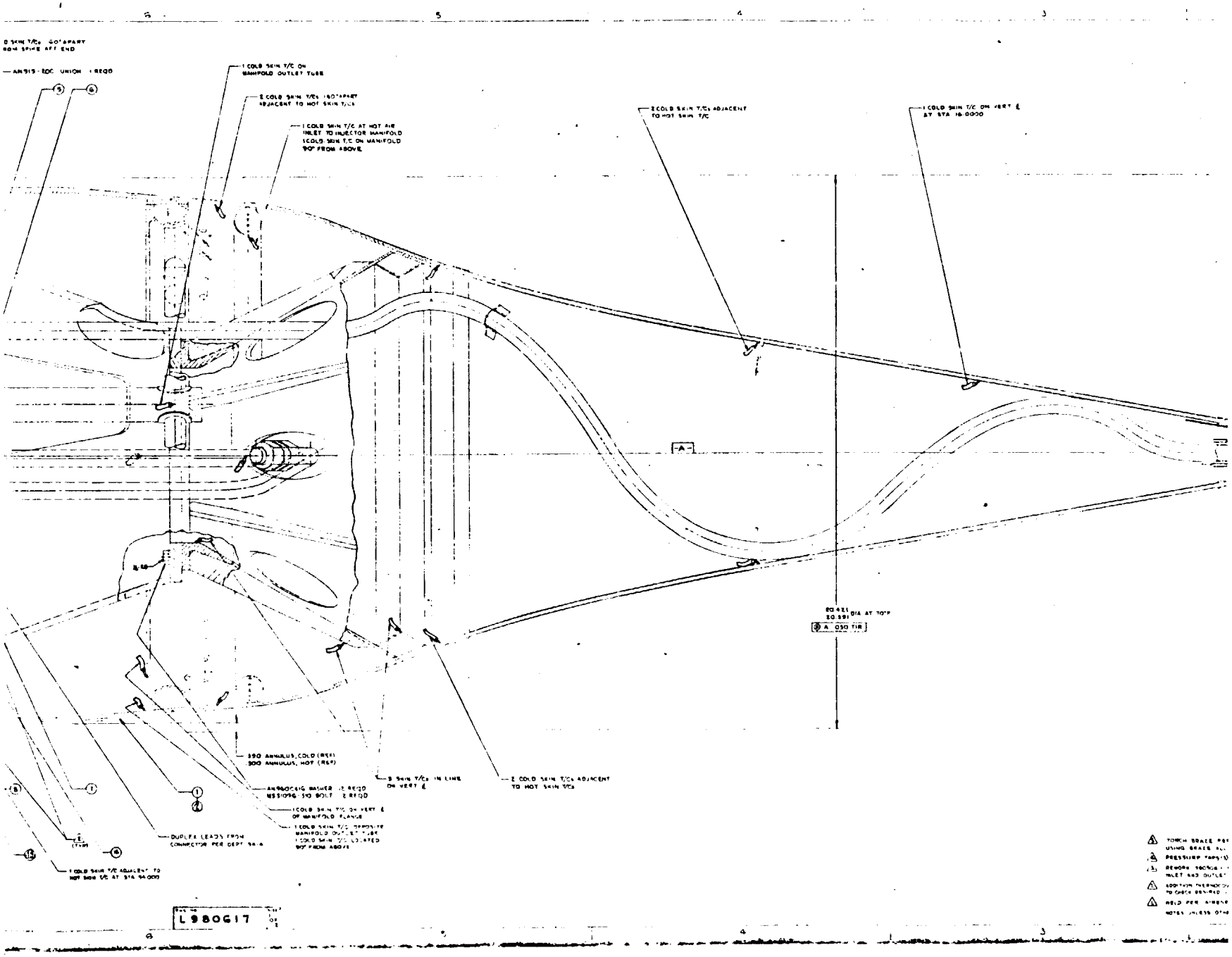
AN915-10C UNION 1 REQD
1 COLD SKIN T/C ON MANIFOLD OUTLET TUBE
2 COLD SKIN T/Cs 180° APART ADJACENT TO HOT SKIN T/Cs
1 COLD SKIN T/C AT HOT AIR INLET TO INJECTOR MANIFOLD
1 COLD SKIN T/C ON MANIFOLD 90° FROM ABOVE
2 COLD SKIN T/Cs ADJACENT TO HOT SKIN T/C
1 COLD SKIN T/C ON VERT ℄ AT STA 16.0000
A
DIA AT 70°F
A .030 TIR
390 ANNULUS, COLD (REF)
300 ANNULUS, HOT (REF)
3 SKIN T/Cs IN LINE ON VERT ℄
2 COLD SKIN T/Cs ADJACENT TO HOT SKIN T/Cs
1 COLD SKIN T/C ON VERT ℄ OF MANIFOLD FLANGE
DUPLEX LEADS FROM CONNECTOR PER DEPT 94-A
1 COLD SKIN T/C ADJACENT TO HOT SKIN T/C AT STA 94.000
L980617

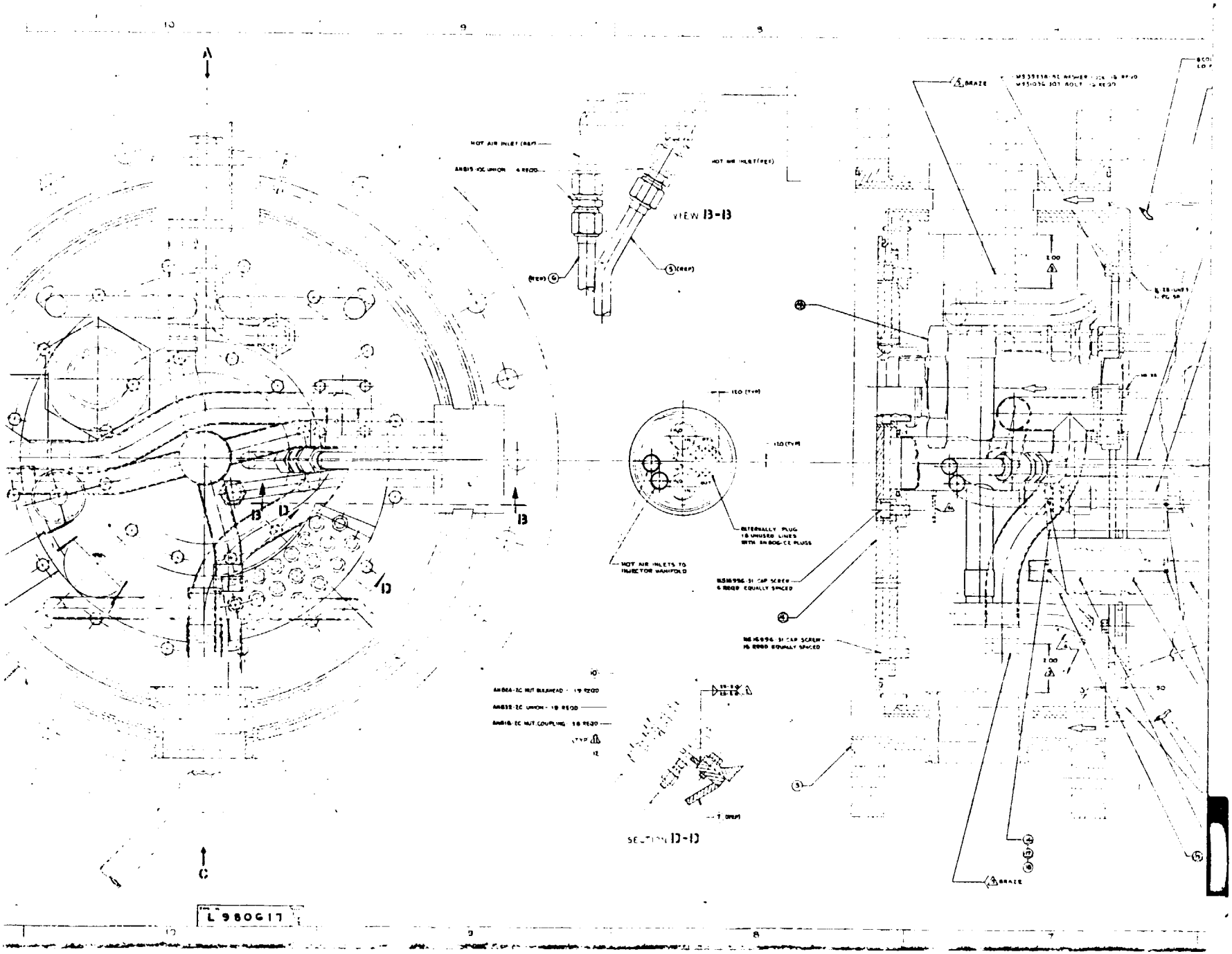

VIEW B-B
SECTION D-D
HOT AIR INLET (REF)
HOT AIR INLET (REF)
AN815-10C UNION 4 REQD
(REF) 6
5 (REF)
120 (TYP)
120 (TYP)
INTERNALLY PLUG 18 UNUSED LINES WITH AN806-C2 PLUGS
HOT AIR INLETS TO INJECTOR MANIFOLD
MS16996-31 CAP SCREW 6 REQD EQUALLY SPACED
MS16996-31 CAP SCREW 16 REQD EQUALLY SPACED
AN824-2C NUT BULKHEAD - 19 REQD
AN832-2C UNION - 19 REQD
AN818-2C NUT COUPLING 18 REQD
TYP
12
7 (REF)
BRAZE
2.00
2.00
90
A
B
C
D
L 980617

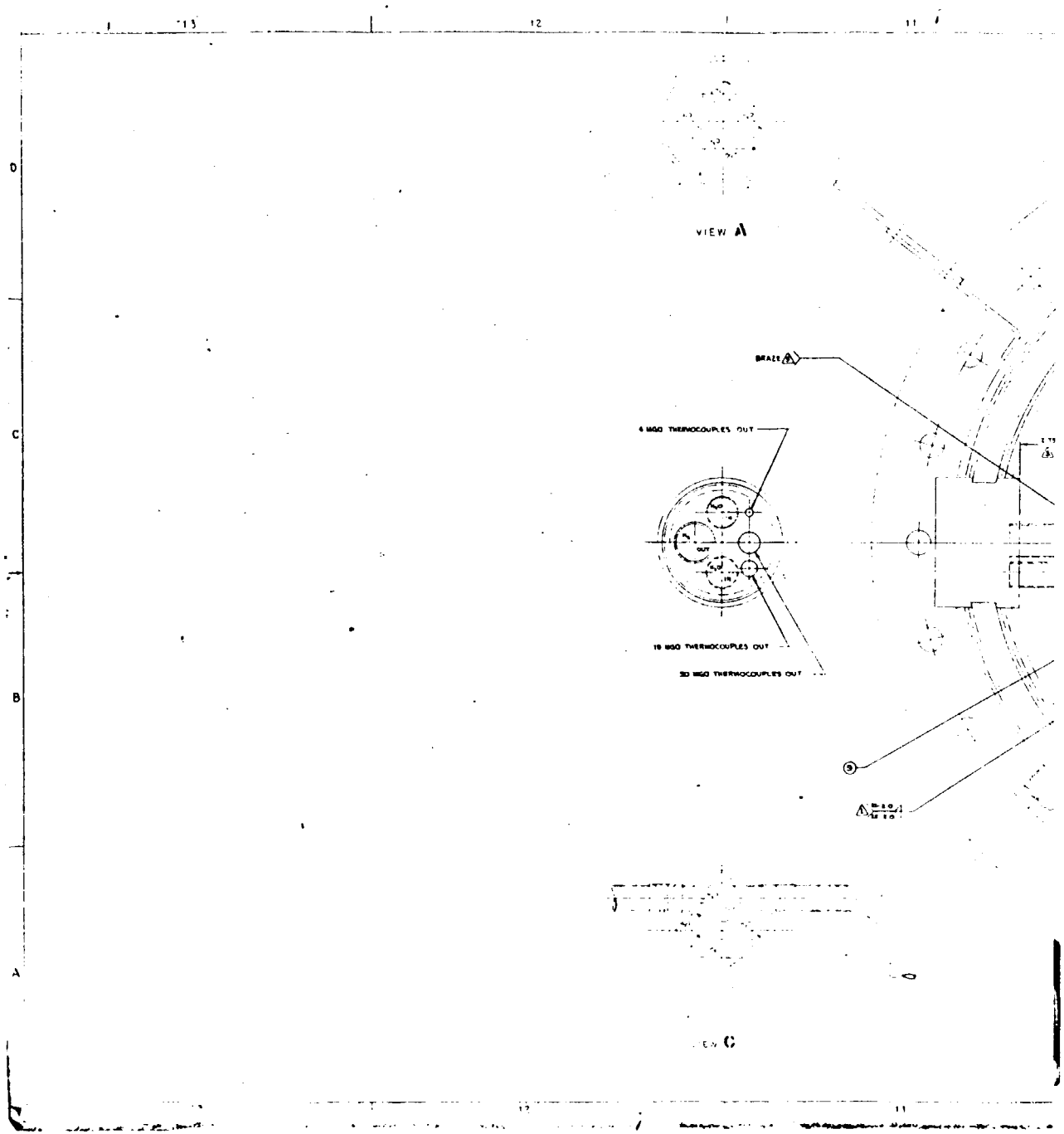
VIEW A
BRAZE
4 MGO THERMOCOUPLES OUT
19 MGO THERMOCOUPLES OUT
30 MGO THERMOCOUPLES OUT
VIEW C

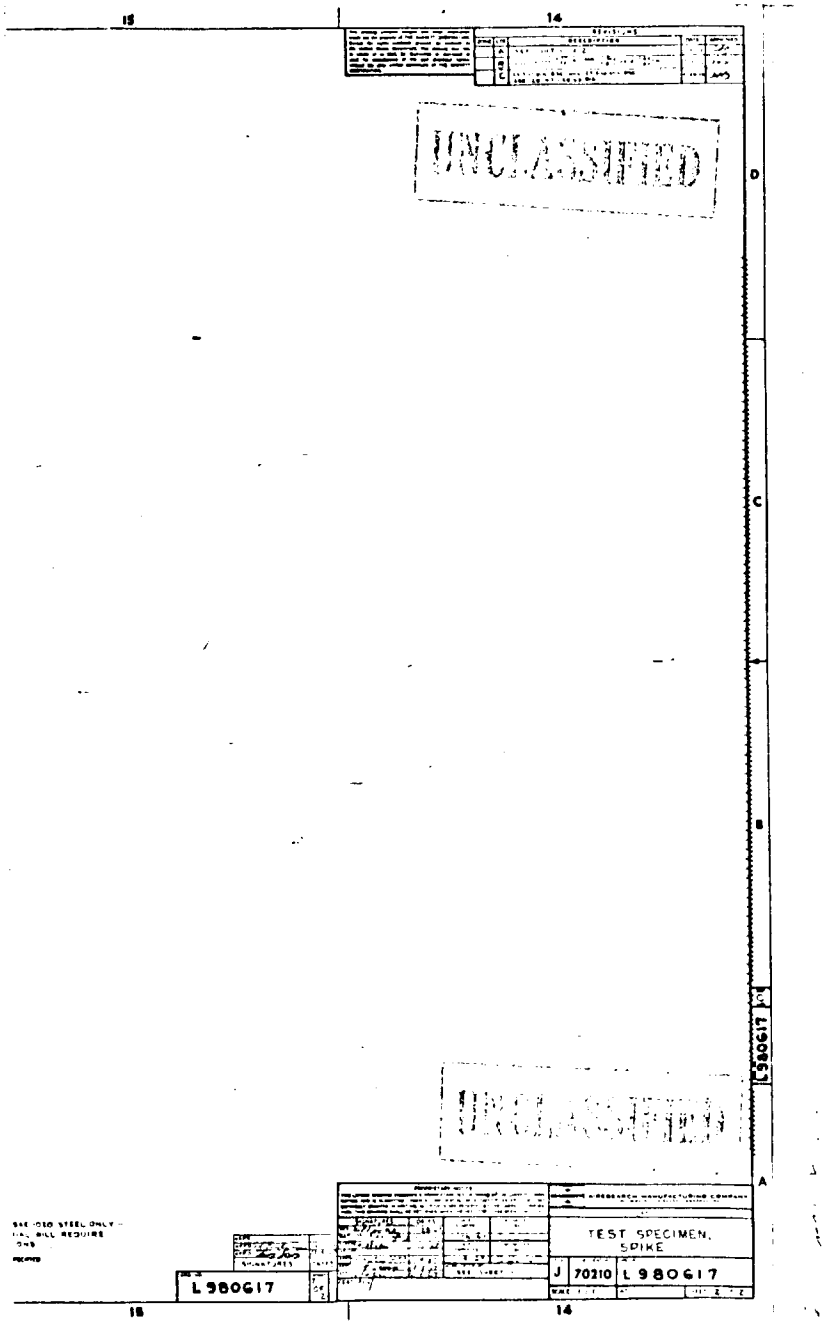
UNCLASSIFIED
UNCLASSIFIED
TEST SPECIMEN,
SPIKE
J 70210 L 980617
L 980617
L 980617

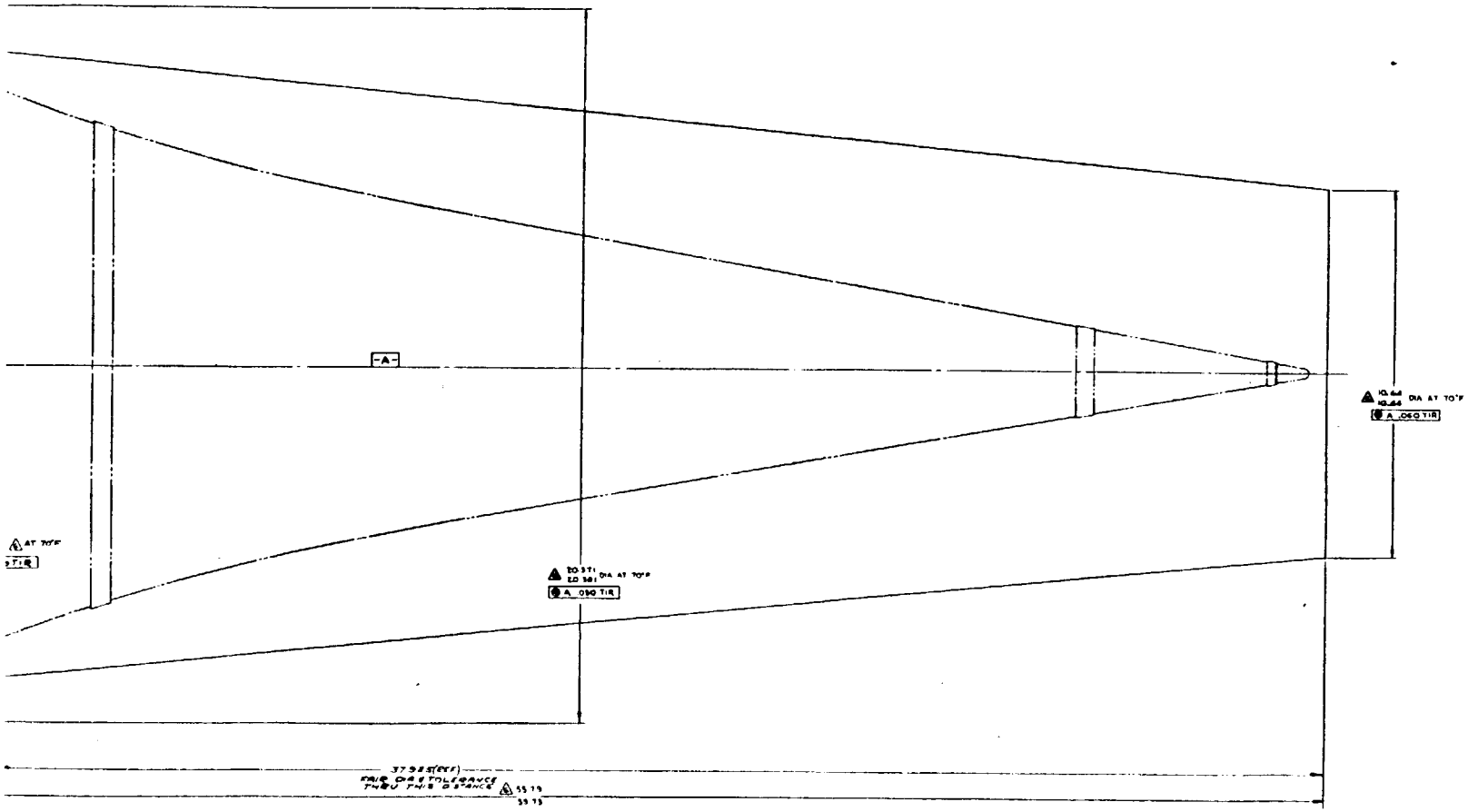

DIMENSIONS SHOWN FOR
SUBSTITUTION OF MATE
ALTERATION OF DIMEN

L980617

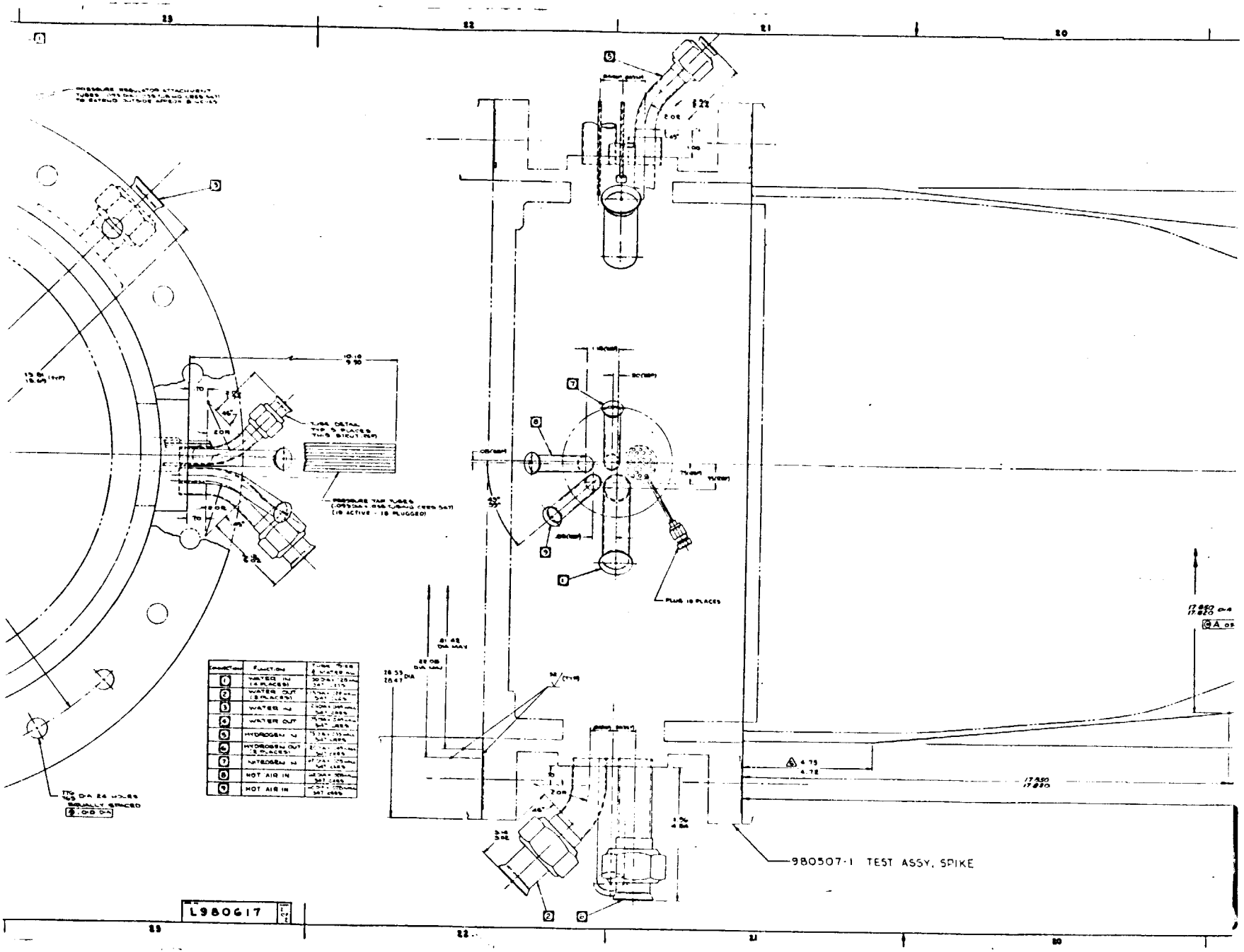

980507-1 TEST ASSY, SPIKE
L980617
PLUG 10 PLACES
TUBE DETAIL
PRESSURE TAP TUBES

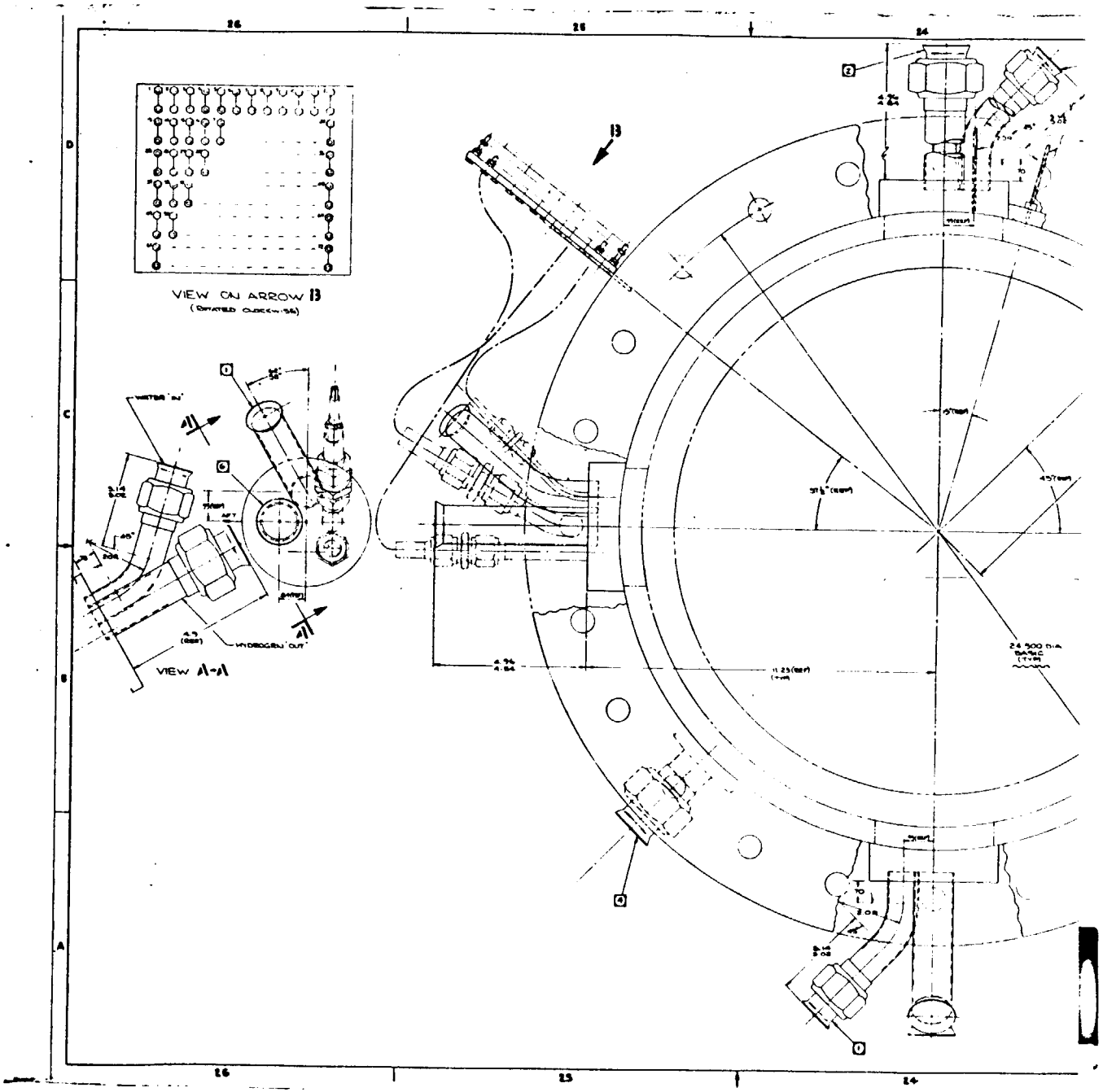
VIEW ON ARROW B
(ROTATED CLOCKWISE)
VIEW A-A
WATER 'IN'
HYDROGEN 'OUT'
24.500 DIA BASIC (TYP)
11.25 (REF) (TYP)
4.96
4.84
26
25
24
D
C
B
A

UNCLASSIFIED

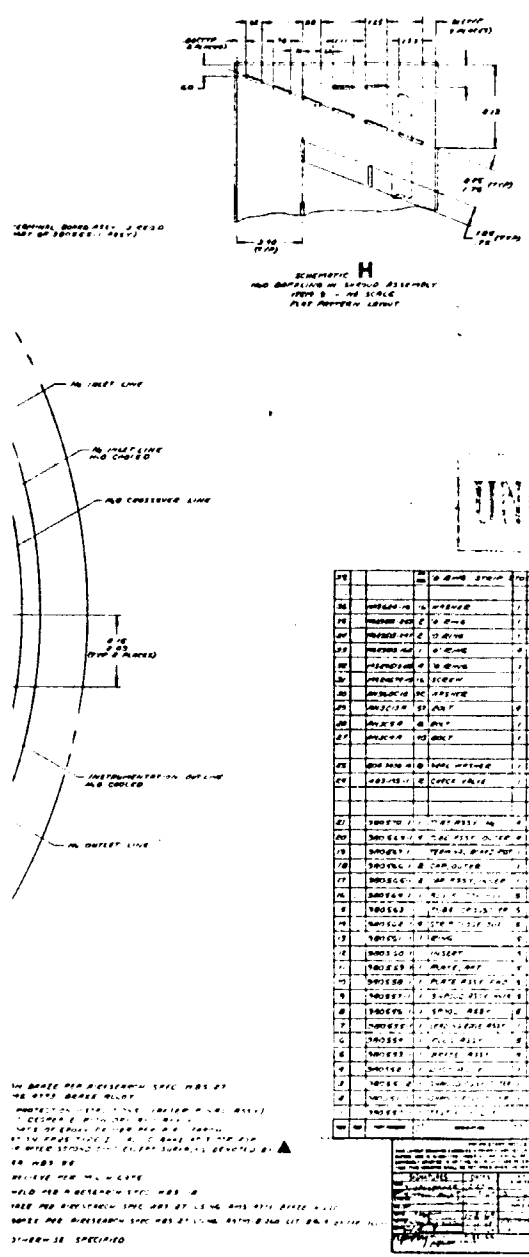

UNCLASSIFIED

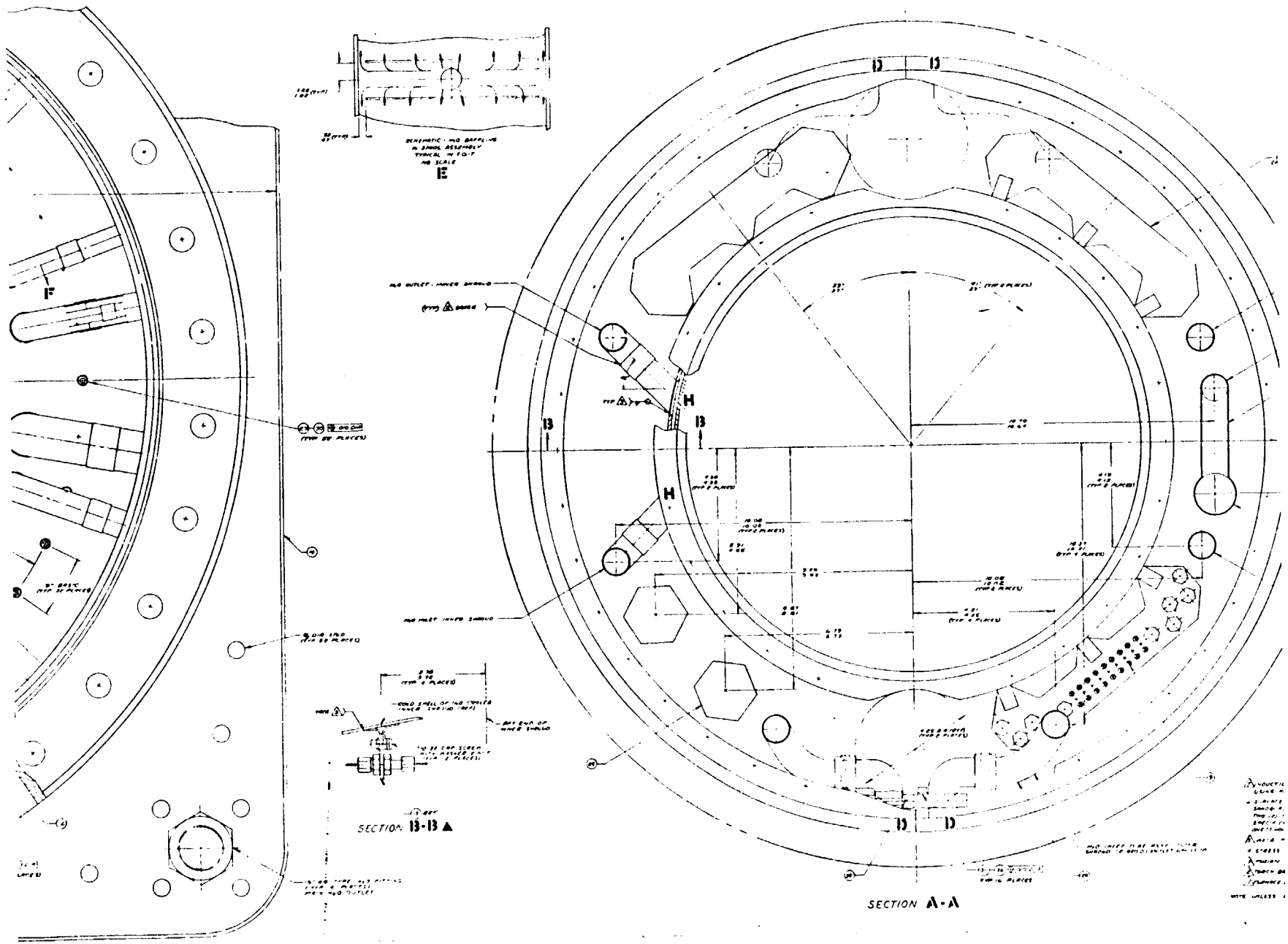
SECTION B-B
SECTION A-A
E
F
H
B
D

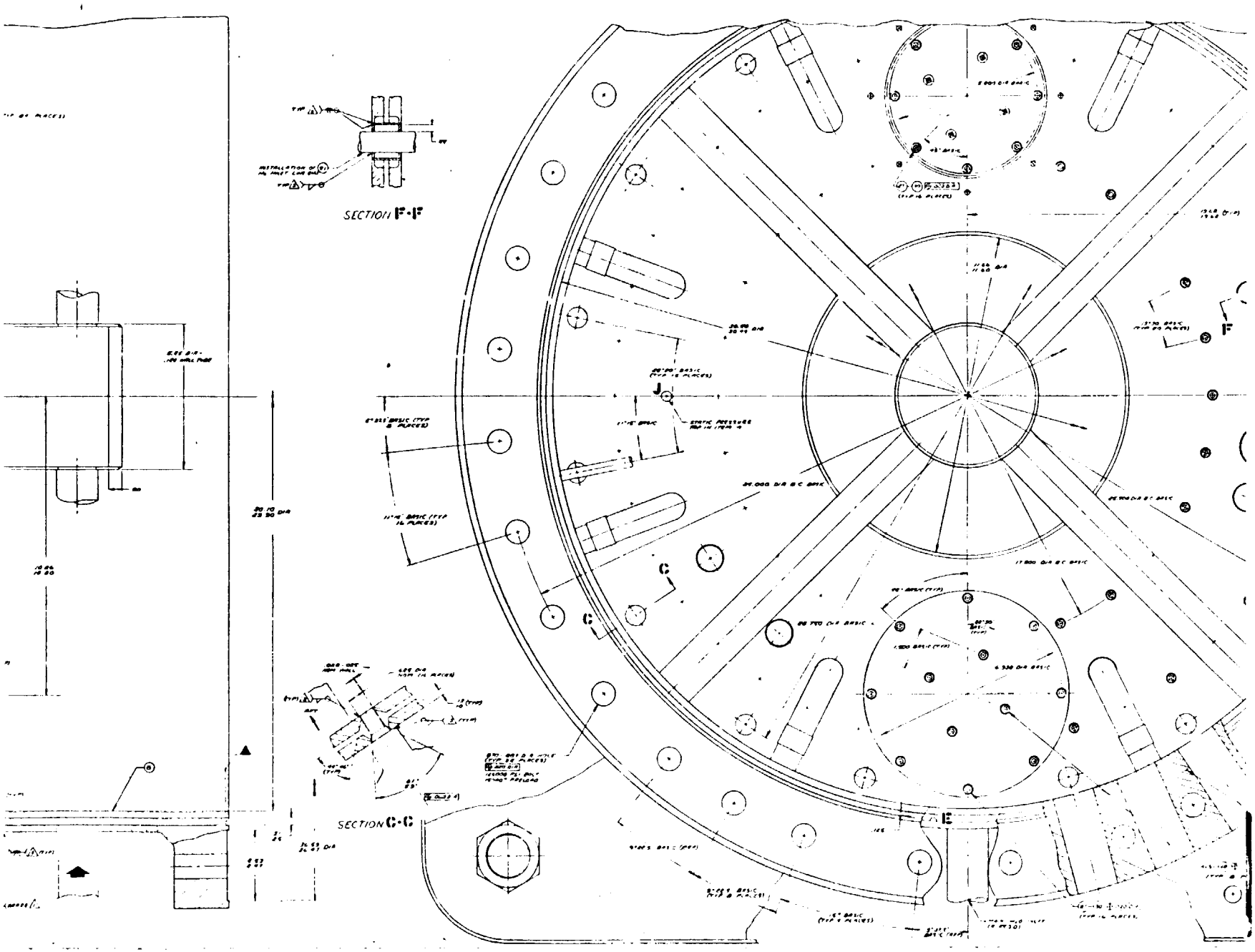
SECTION F-F
SECTION C-C
STATIC PRESSURE

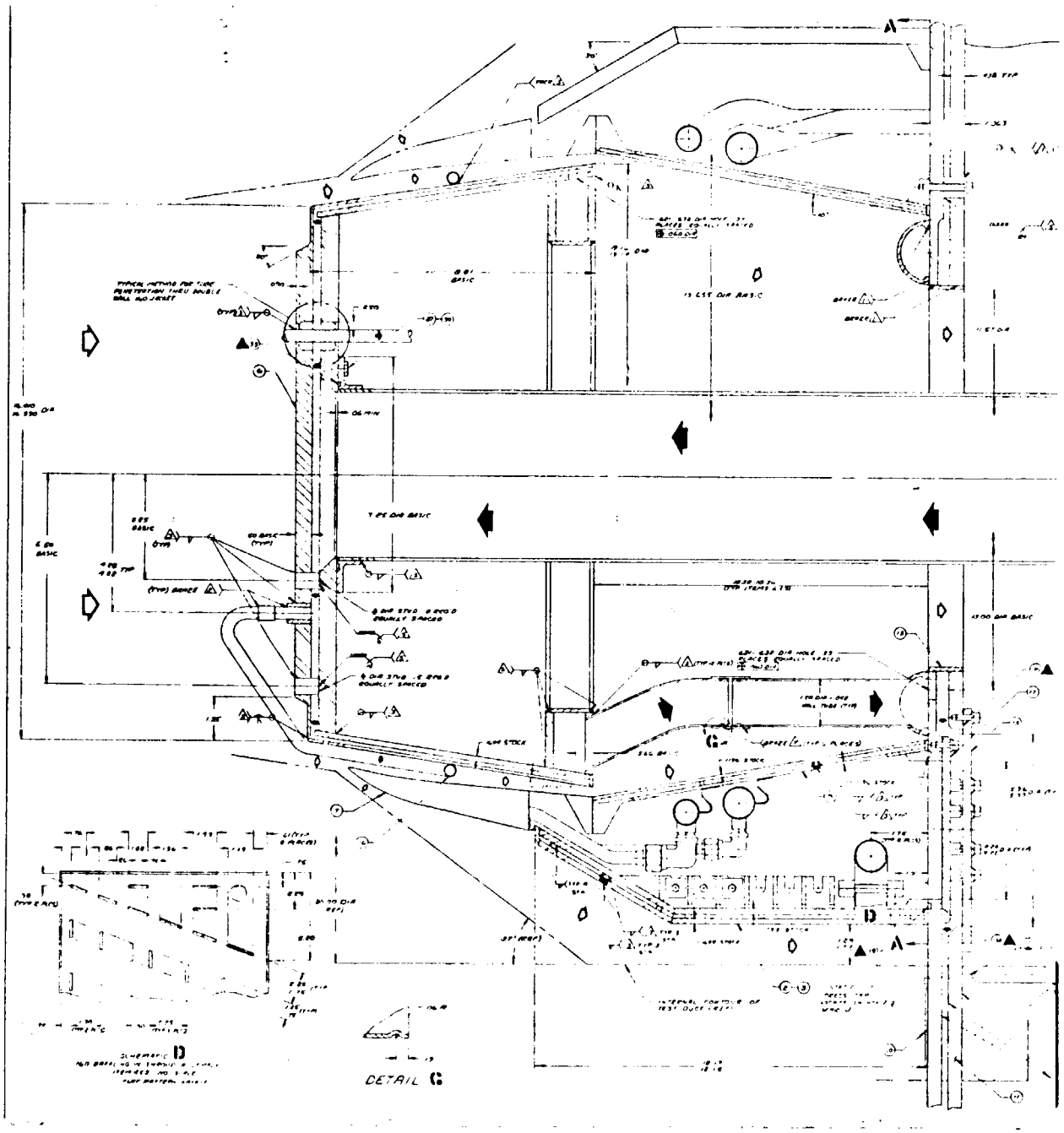
DETAIL G

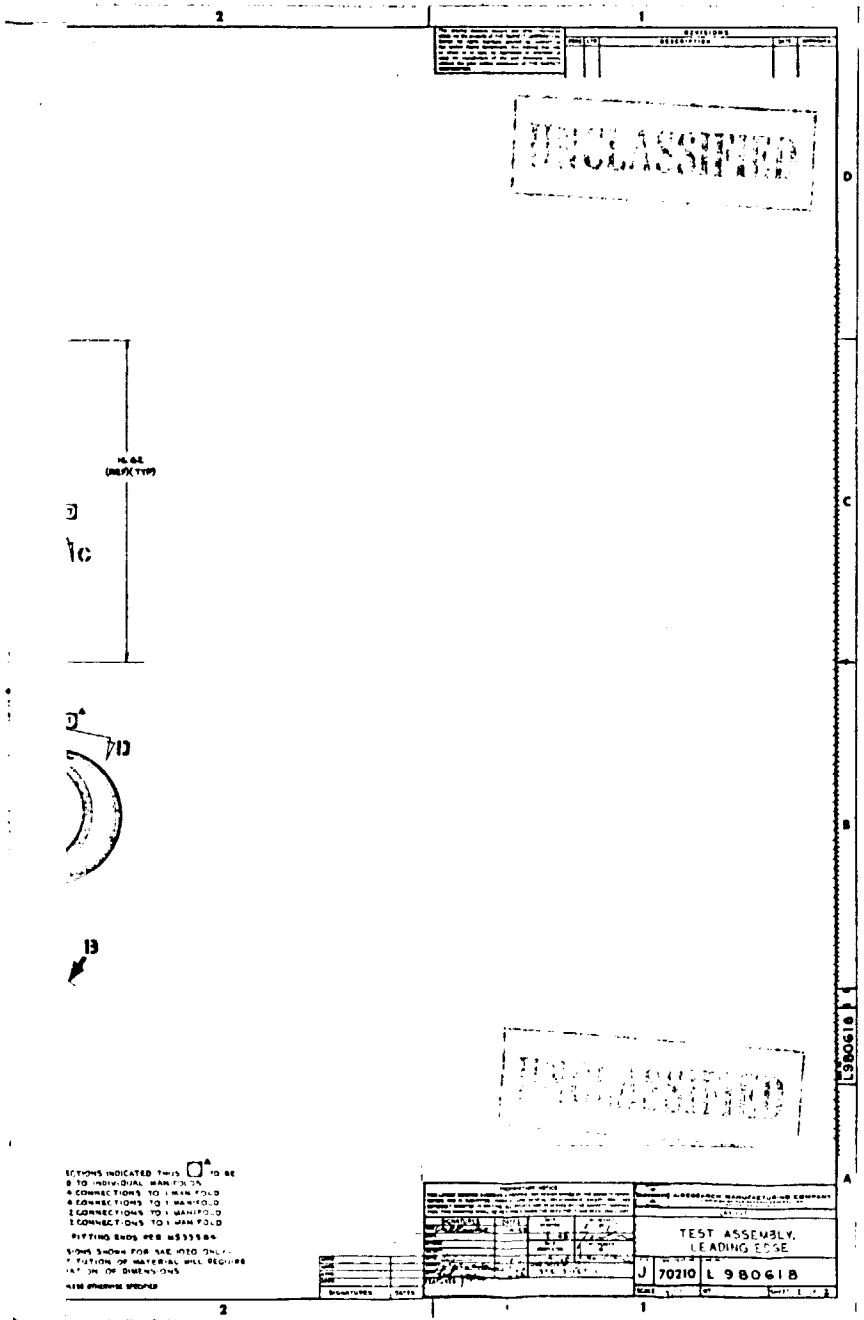
UNCLASSIFIED
UNCLASSIFIED
TEST ASSEMBLY,
LEADING EDGE
J 70210 L 980618
L980618

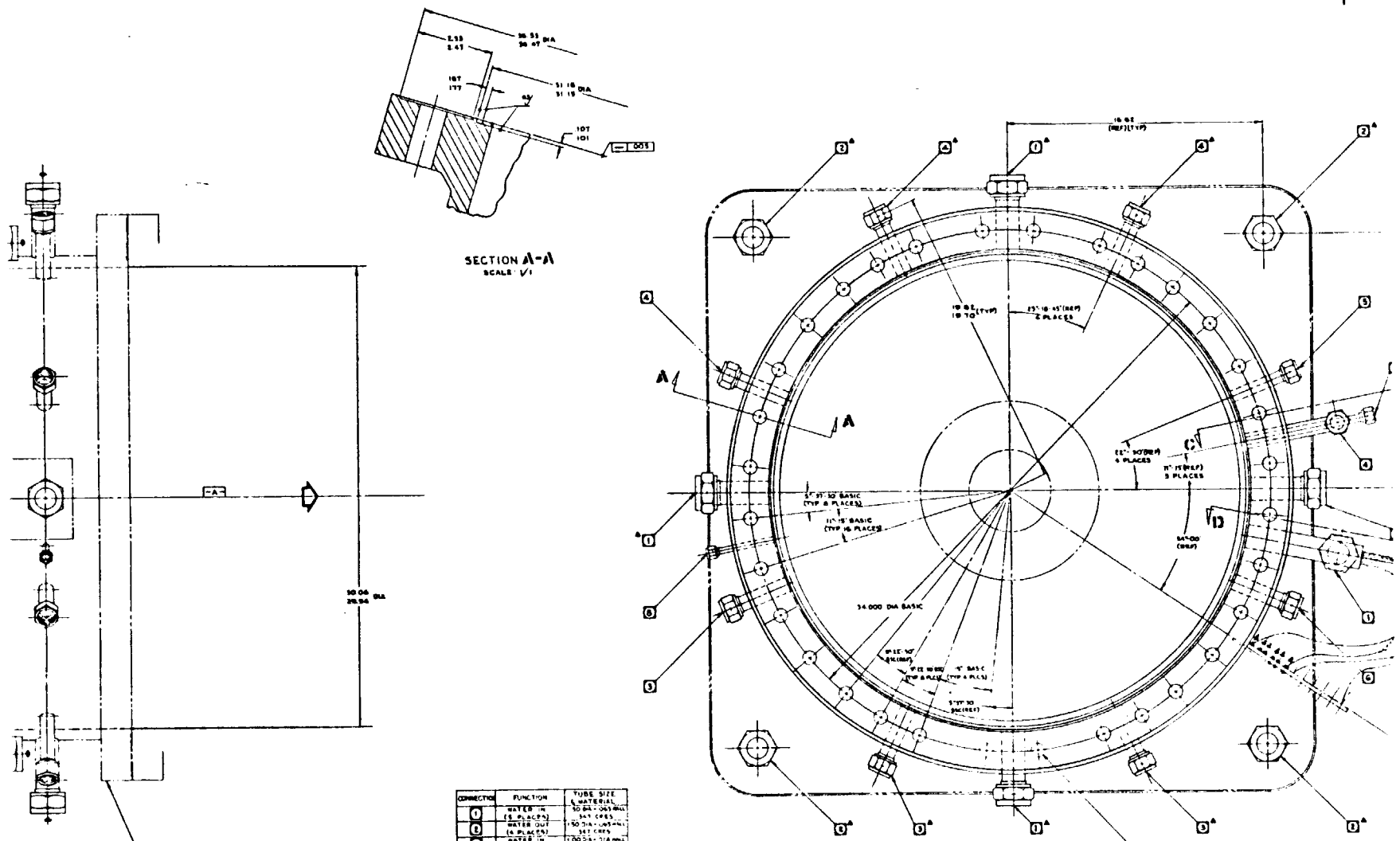

CONNECTION	FUNCTION	TUBE SIZE & MATERIAL
1	WATER IN (5 PLACES)	.50 DIA - .065 WALL 347 CRES
2	WATER OUT (4 PLACES)	1.50 DIA - .065 WALL 347 CRES
3	WATER IN (5 PLACES)	1.00 DIA - .114 WALL 347 CRES
4	WATER OUT (4 PLACES)	1.00 DIA - .014 WALL 347 CRES
5	HYDROGEN IN	.75 DIA - .095 WALL 347 CRES
6	HYDROGEN OUT	1.00 DIA - .095 WALL 347 CRES
7	NITROGEN IN	.50 DIA - .035 WALL 347 CRES
8	WATER OUT	.375 DIA - .035 WALL 347 CRES

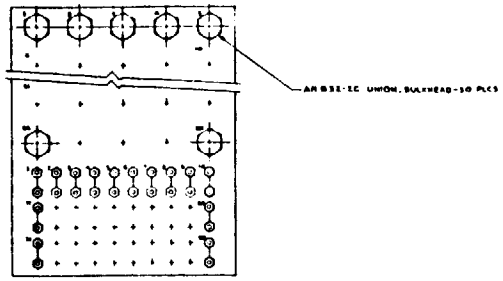

INSTRUMENTATION TERMINAL BOARD
VIEW ON ARROW B
SCALE: 1/1

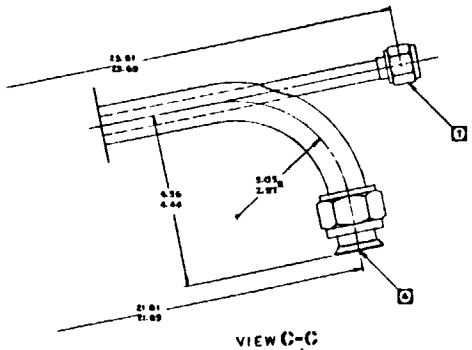

VIEW C-C
SCALE 1/1

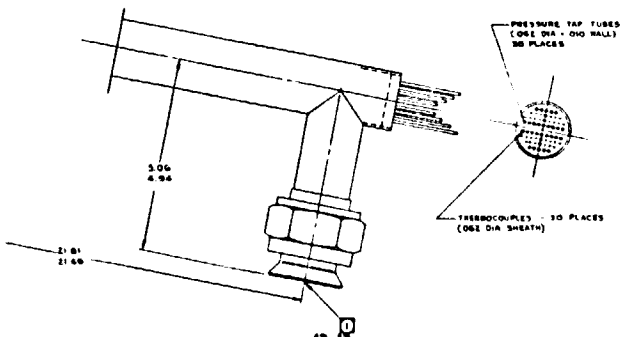

VIEW D-D
SCALE 1/1

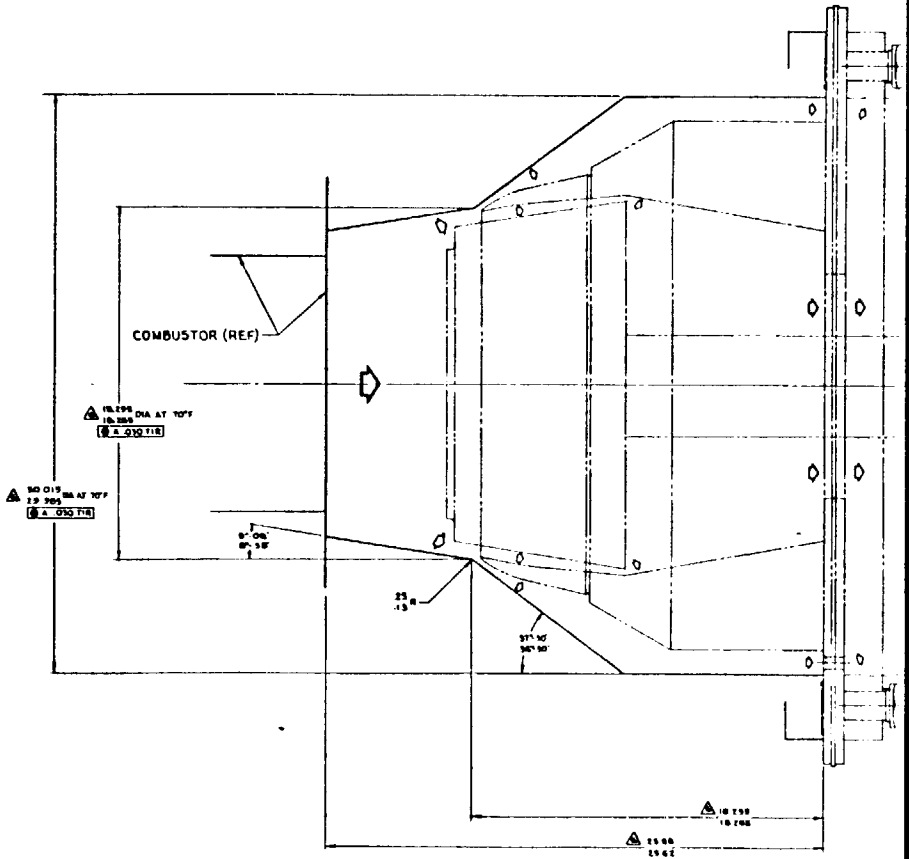

L980618

UNCLASSIFIED

UNCLASSIFIED

TABLE I - ACCELEROMETER LOCATIONS

SYM	X	Y	Z	ITEM ON WHICH TO BE MOUNTED	ORIENTATION	TYPE
A	0.750	0.000	7.720	SPIKE	X, Y, Z	TRIAXIAL
A	18.000	0.000	7.414		Y	UNIAXIAL
A	23.250	0.000	7.500		Z	UNIAXIAL
A	23.250	0.000	7.500	SPIKE	Y	UNIAXIAL
A	[illegible]	0.000	[illegible]	ACTUATOR	Y	UNIAXIAL
A	28.000	0.000	[illegible]		Z	UNIAXIAL
A	28.000	0.000	[illegible]		Y	UNIAXIAL
A	37.000	0.000	[illegible]	ACTUATOR	X, Y, Z	TRIAXIAL
A	[illegible]	0.000	3.530	INVERTOR	X, Y, Z	TRIAXIAL
A	51.000	4.130	0.006	EQUIP PLATE	X, Y, Z	TRIAXIAL
A	62.000	0.000	5.825	NOZZLE PLUG	Y	UNIAXIAL
A	62.050	0.000	5.825	NOZZLE PLUG	Z	UNIAXIAL
A	[illegible]	0.000	5.825	NOZZLE PLUG	Y	UNIAXIAL
A	[illegible]	0.000	4.930	OUTER SHELL	X, Y, Z	TRIAXIAL
A	[illegible]	0.000	11.000	OUTER SHELL	X, Y, Z	TRIAXIAL
A	[illegible]	0.000	11.000	OUTER SHELL	Y	UNIAXIAL
A	25.010	0.000	—	SHAKE TABLE	X, Y, Z	TRIAXIAL
A	[illegible]	4.000	—	SHAKE TABLE	X, Y, Z	TRIAXIAL

TABLE II - STRAIN GAUGE LOCATIONS

SYM	X	Y	Z	ITEM ON WHICH TO BE MOUNTED	DIRECTION OF READING
S	16.750	0.000	4.500	GUSSET OF ACTUATOR MOUNT	X
S	16.750	[illegible]	[illegible]	GUSSET OF ACTUATOR MOUNT	X
S	19.000	—	—	TOP OF ACTUATOR SUPPORT	X, Z
S	19.004	—	3.000	TOP OF ACTUATOR SUPPORT	X, Y
S	19.000	—	—	BOTTOM OF ACTUATOR SUPPORT	X, Z
S	19.000	—	3.000	BOTTOM OF ACTUATOR SUPPORT	X, Y
S	[illegible]	[illegible]	[illegible]	ON ITEM [illegible] DOUBLER	TANGENTIAL
S	[illegible]	8.300	0.000	ON ITEM [illegible] DOUBLER	TANGENTIAL
S	[illegible]	[illegible]	[illegible]	ON ITEM [illegible] DOUBLER	TANGENTIAL
S	37.875	[illegible]	[illegible]	ON ITEM [illegible] MANIFOLD	TANGENTIAL
S	37.875	8.300	0.000	ON ITEM [illegible] MANIFOLD	TANGENTIAL
S	37.875	[illegible]	[illegible]	ON ITEM [illegible] MANIFOLD	TANGENTIAL
S	[illegible]	[illegible]	[illegible]	[illegible] OF STRUT [illegible]	Y, Z
S	[illegible]	[illegible]	0.300	[illegible]	Y
S	[illegible]	[illegible]	[illegible]	[illegible]	Y, Z
S	14.000	[illegible]	[illegible]	[illegible]	X
S	14.000	9.300	[illegible]	[illegible]	X
S	14.000	[illegible]	[illegible]	[illegible]	X
S	14.000	[illegible]	[illegible]	[illegible]	X
S	14.000	11.300	0.000	[illegible] BODY OF STRUT [illegible]	X

TABLE II [illegible]

SYM	X
S	[illegible]
S	36.590
S	36.590
S	[illegible]
S	[illegible]
S	[illegible]
S	[illegible]
S	37.750
S	37.750
S	[illegible]
S	[illegible]
S	[illegible]
S	[illegible]
S	[illegible]
S	[illegible]
S	[illegible]
S	[illegible]
S	[illegible]
S	[illegible]
S	[illegible]
S	—
S	—
S	[illegible]
S	[illegible]

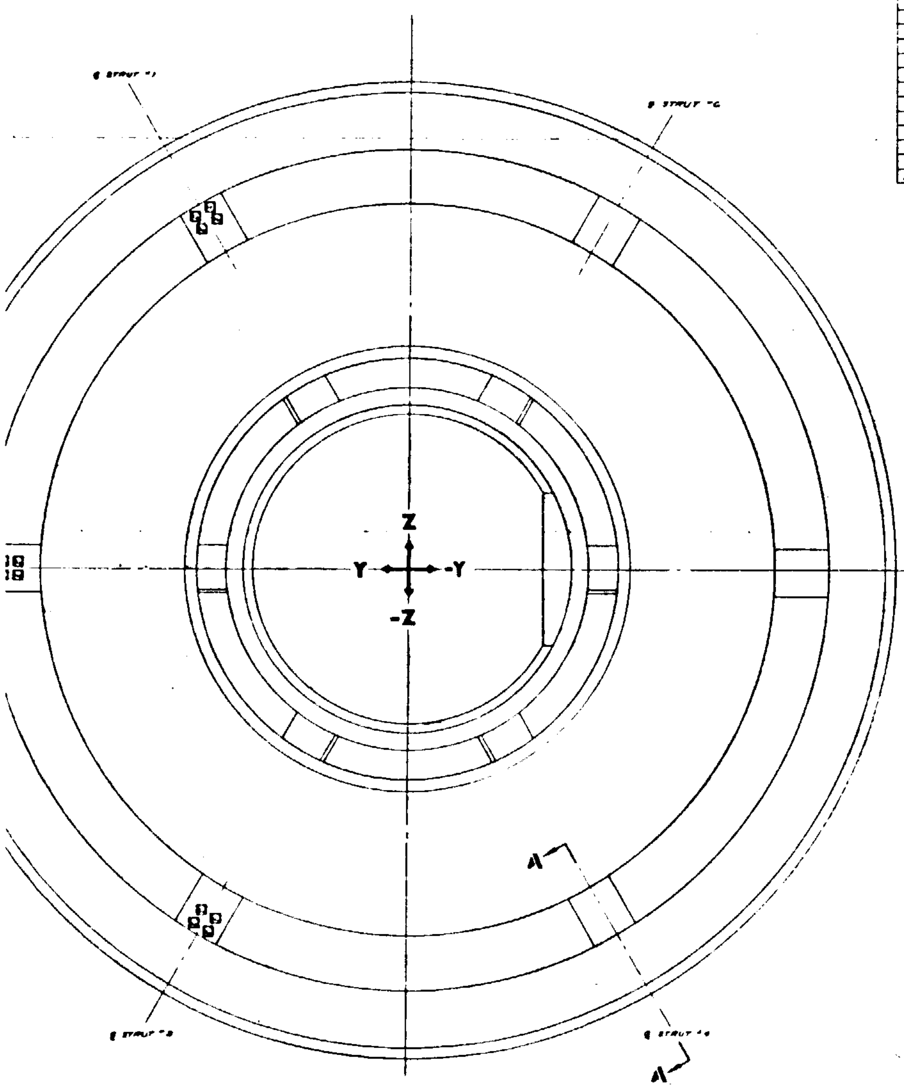

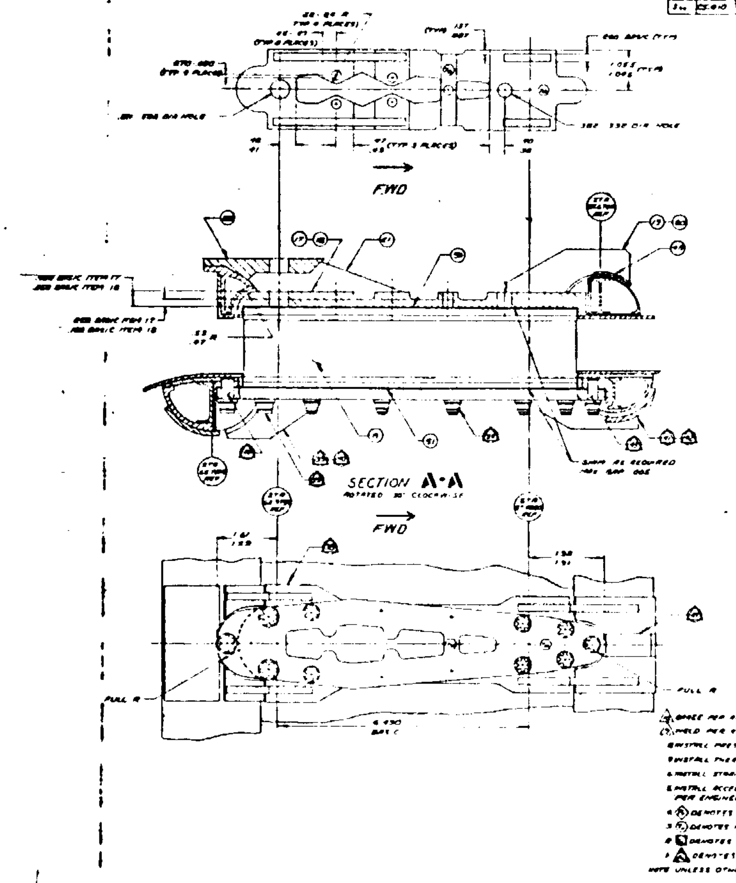

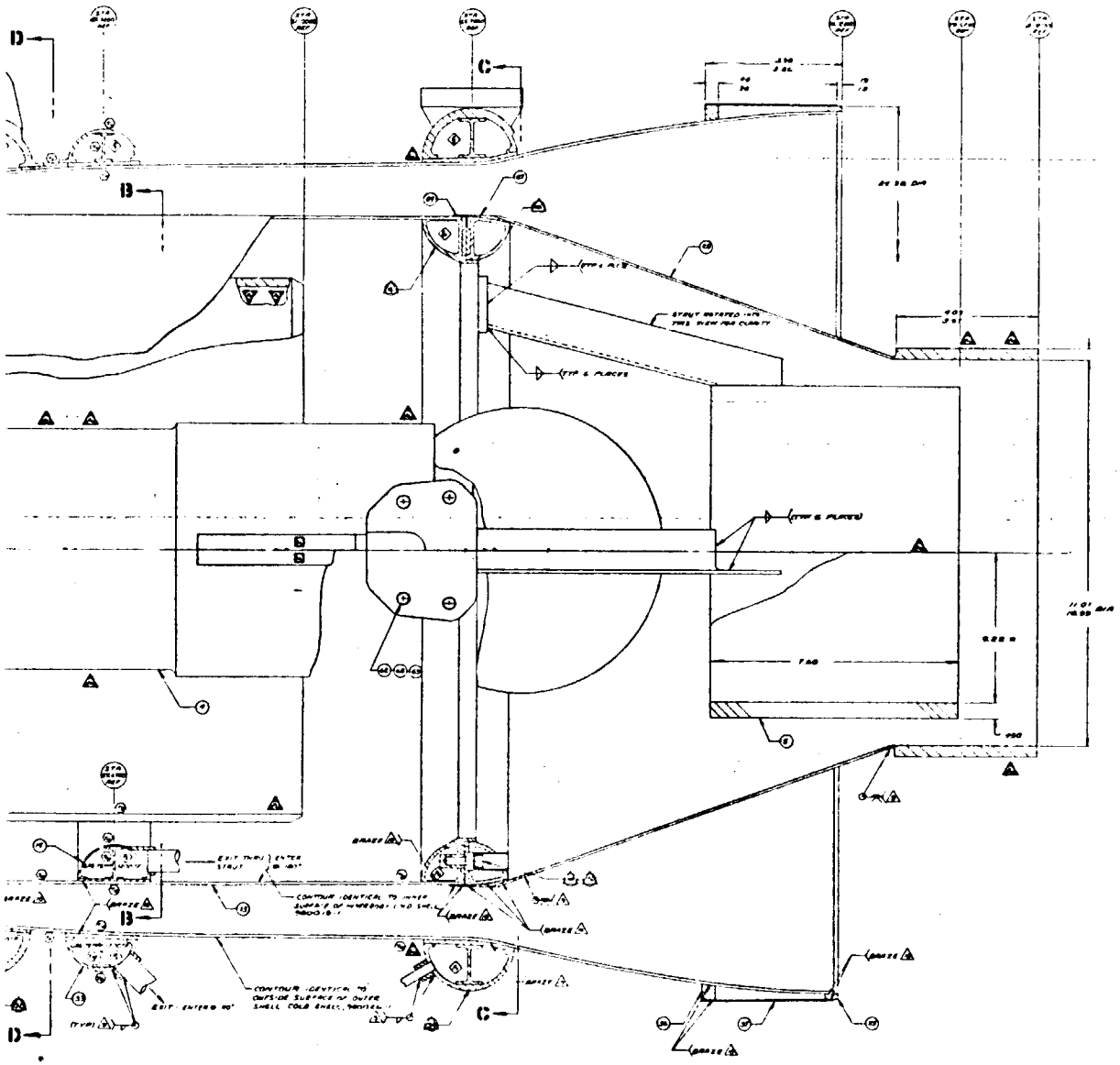

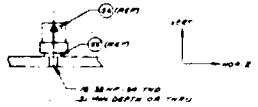

TYPICAL ACCELEROMETER INSTALLATION
(UNIAXIAL ONLY - NOTE ORIENTATION)
SCALE: NONE

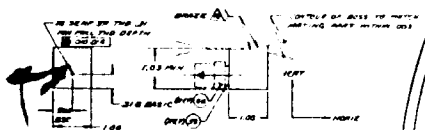

TYPICAL ACCELEROMETER INSTALLATION
(UNIAXIAL ONLY - NOTE ORIENTATION)
SCALE: NONE

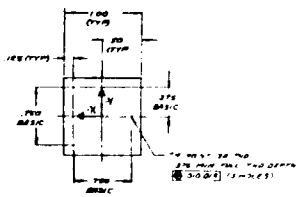

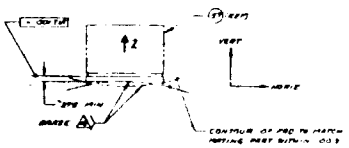

TYPICAL ACCELEROMETER INSTALLATION
(TRIAXIAL ONLY - NOTE ORIENTATION)
SCALE: NONE

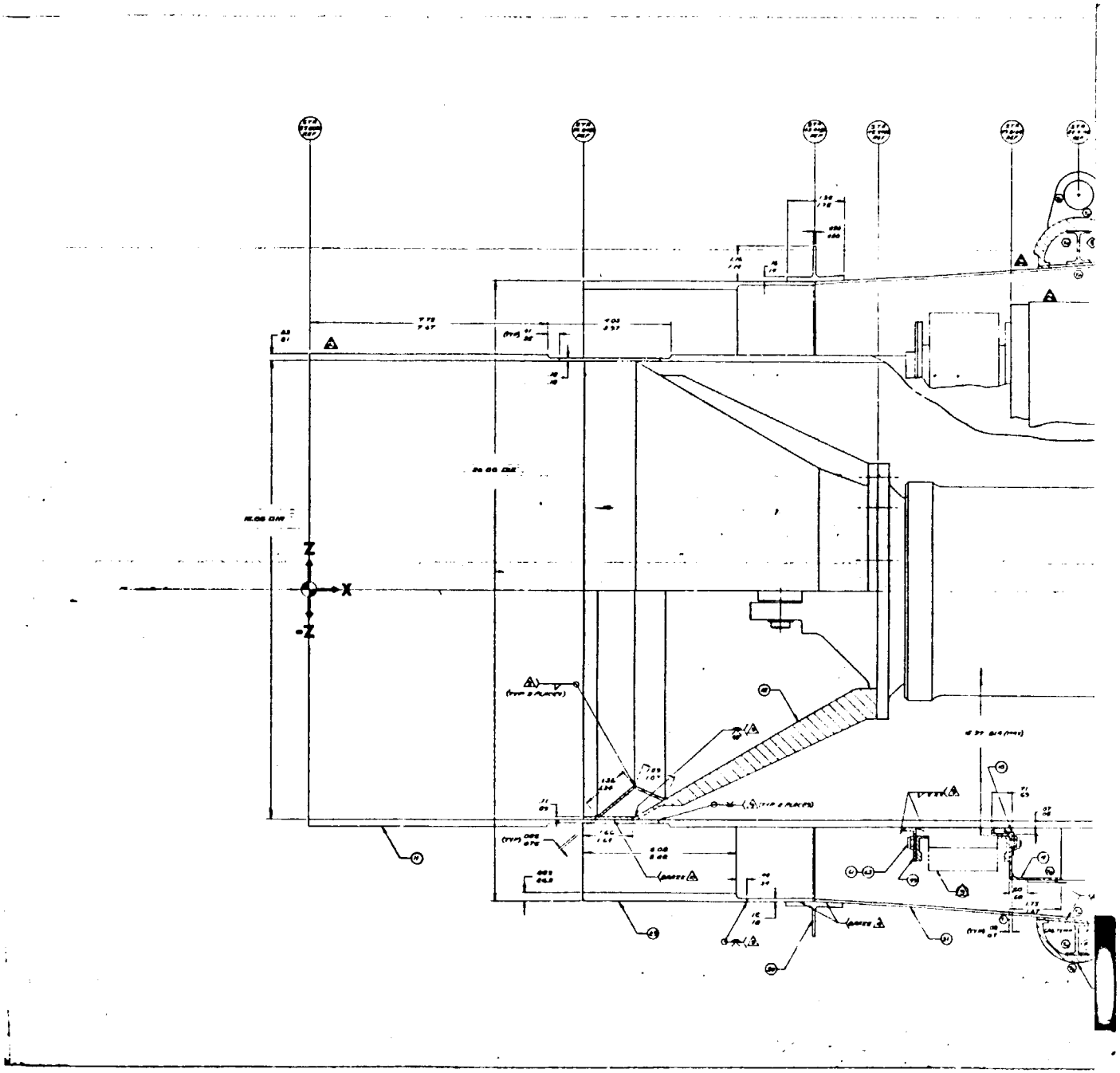
Z
X
-Z

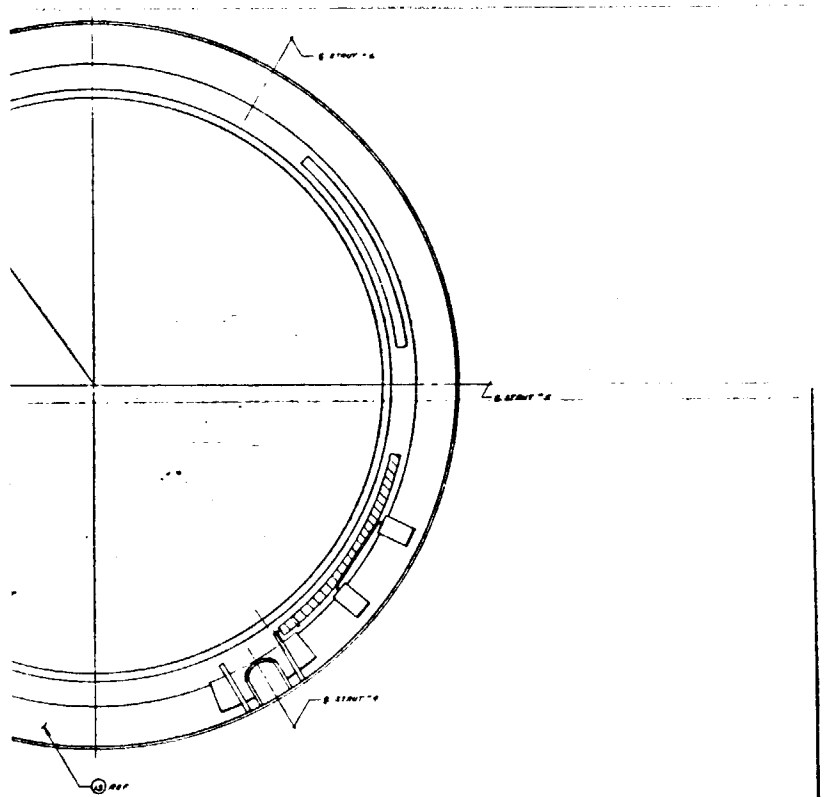

SECTION B - B

STRUTS REMOVED FOR CLARITY

LAYOUT - VIBRATION MODEL
H R E

J 70210 L 980619

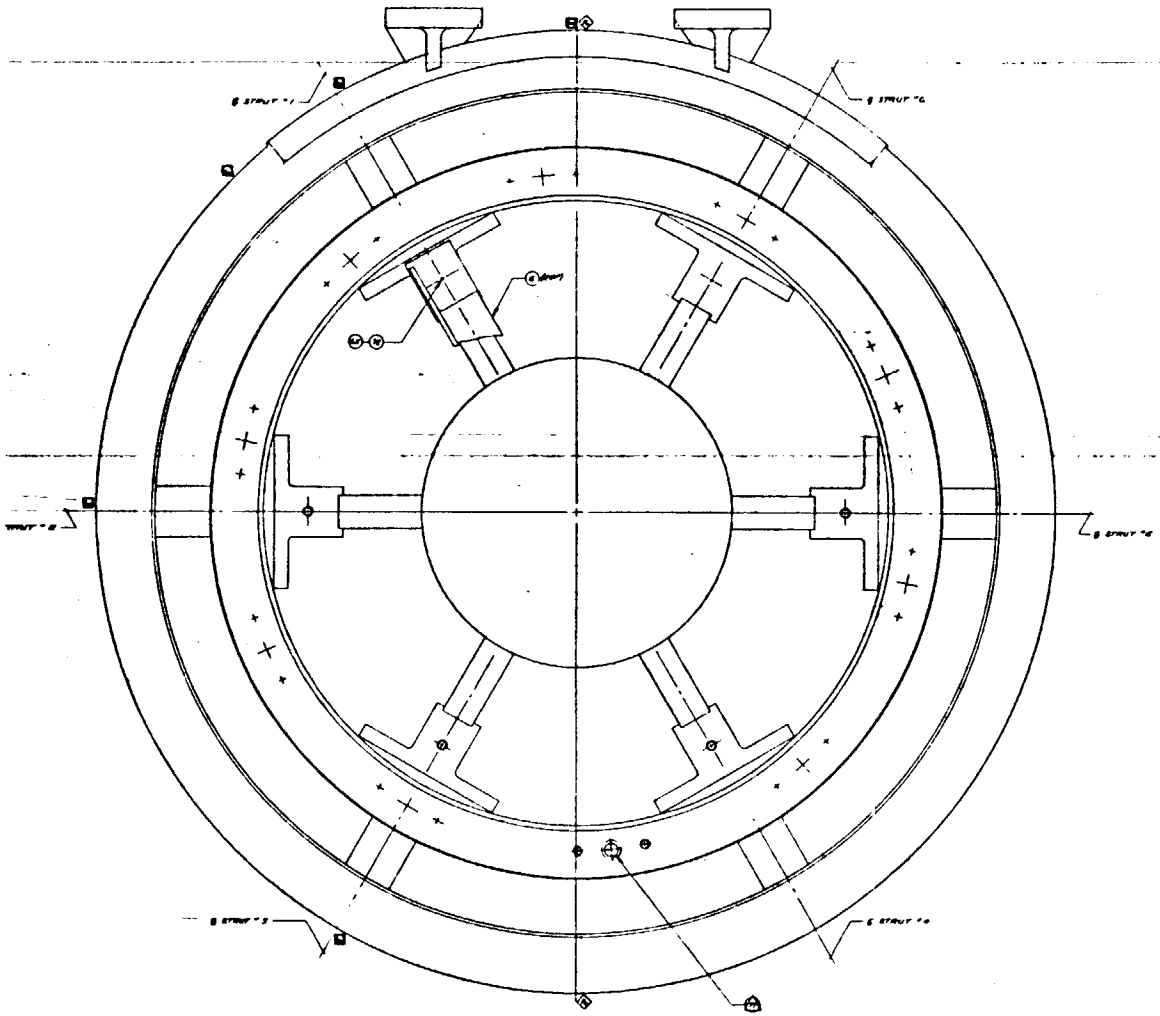

SECTION C-C

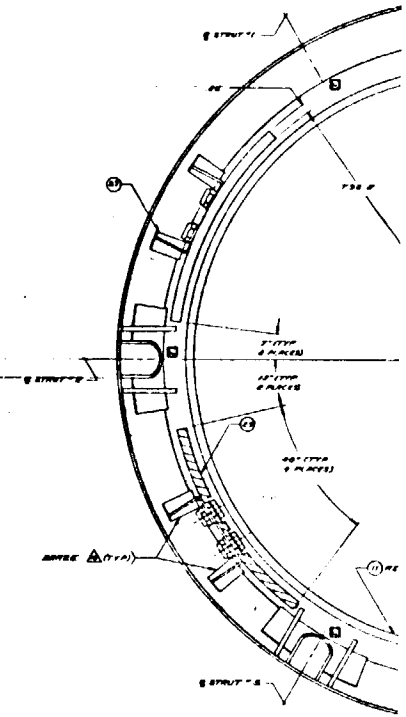

TABLE III - THERMOCOUPLE LOCATIONS

SYM	X	Y	Z	ITEM ON WHICH MOUNTED	
T_1	28.870	0.000	10.990	OUTER SHELL - OUTER SURFACE	COLD WALL
T_2	26.760	0.000	10.990	OUTER SHELL - OUTER SURFACE	
T_3	24.760	0.000	10.990	OUTER SHELL - OUTER SURFACE	
T_4	28.010	0.000	-8.080	ITEM 32 MANIFOLD ASSY	
T_5	25.010	-0.080	0.000		
T_6	25.010	0.000	8.080		
T_7	28.010	8.080	0.000	ITEM 32 MANIFOLD ASSY	
T_8	28.320	0.000	-11.990	ITEM 33 MANIFOLD ASSY	
T_9	28.320	11.990	0.000		
T_{10}	28.320	0.000	11.990		
T_{11}	28.320	11.990	0.000	ITEM 33 MANIFOLD ASSY	
T_{12}	28.010	0.000	-11.850	INSIDE ITEM 32 MANIFOLD	INTERNAL GAS TEMP
T_{13}	25.010	0.000	11.850	INSIDE ITEM 32 MANIFOLD	
T_{14}	28.320	0.000	-11.315	INSIDE ITEM 33 MANIFOLD	
T_{15}	28.320	0.000	11.315	INSIDE ITEM 33 MANIFOLD	
T_{16}	28.010	0.000	-8.600	OUTER SHELL - INNER SURFACE	COLD WALL
T_{17}	25.010	0.000	-10.600	OUTER SHELL - INNER SURFACE	
T_{18}	28.320	0.000	-10.600	OUTER SHELL - INNER SURFACE	
T_{19}	28.320	0.000	10.600	OUTER SHELL - INNER SURFACE	
T_{20}	24.120	0.000	9.990	INNER SURFACE OF ITEM 16	
T_{21}	24.620	0.000	9.990	INNER SHELL - INNER SURFACE	
T_{22}	28.670	0.000	-8.990	ITEM 5 MANIFOLD ASSY	
T_{23}	28.670	8.990	0.000		
T_{24}	28.670	0.000	8.990		
T_{25}	28.670	8.990	0.000	ITEM 5 MANIFOLD ASSY	
T_{26}	28.670	0.000	-8.990	INSIDE ITEM 15 MANIFOLD	INTERNAL GAS TEMP
T_{27}	28.670	0.000	8.990	INSIDE ITEM 5 MANIFOLD	
T_{28}	24.670	0.000	9.990	INNER SHELL - OUTER SURFACE	COLD WALL
T_{29}	28.670	0.000	9.990	INNER SHELL - OUTER SURFACE	
T_{30}	28.670	0.000	7.990	INNER SHELL - INNER SURFACE	
T_{31}	24.888	0.158	13.000	ENGINE ATTACH LUG	
T_{32}	30.488	8.800	0.000	ITEM 18 STRUT MOUNTING (TYP)	
T_{33}	32.888	8.800	0.000	ITEM 18 STRUT MOUNTING (TYP)	
T_{34}	30.488	-11.600	0.000	ITEM 38 STRUT MOUNTING (TYP)	
T_{35}	32.488	-11.600	0.000	ITEM 38 STRUT MOUNTING (TYP)	
T_{36}	—	—	—	DEFLECTION BLOCK	
T_{37}	—	—	—	DEFLECTION BLOCK	
T_{38}	—	—	—	DEFLECTION BLOCK	
T_{39}	36.796	0.000	9.990	INNERSHELL - INNER SURFACE	
T_{40}	28.796	0.000	11.990	OUTER SHELL - OUTER SURFACE	

TABLE IV - PRESSURE TAP LOCATIONS

SYM	X	Y	Z	ITEM ON WHICH MOUNTED
P_1	28.010	0.000	-11.740	INSIDE ITEM 32 MANIFOLD
P_2	25.010	0.000	11.740	INSIDE ITEM 32 MANIFOLD
P_3	28.320	0.000	-11.615	INSIDE ITEM 33 MANIFOLD
P_4	28.320	0.000	11.615	INSIDE ITEM 33 MANIFOLD
P_5	28.670	0.000	-8.490	INSIDE ITEM 15 MANIFOLD
P_6	28.670	0.000	8.490	INSIDE ITEM 15 MANIFOLD
P_7	28.720	0.000	-12.150	INSIDE ITEM 39 MANIFOLD
P_8	28.720	0.000	12.150	INSIDE ITEM 39 MANIFOLD
P_9	38.000	0.000	-8.990	INSIDE ITEM 16 MANIFOLD
P_{10}	28.000	0.000	8.990	INSIDE ITEM 16 MANIFOLD

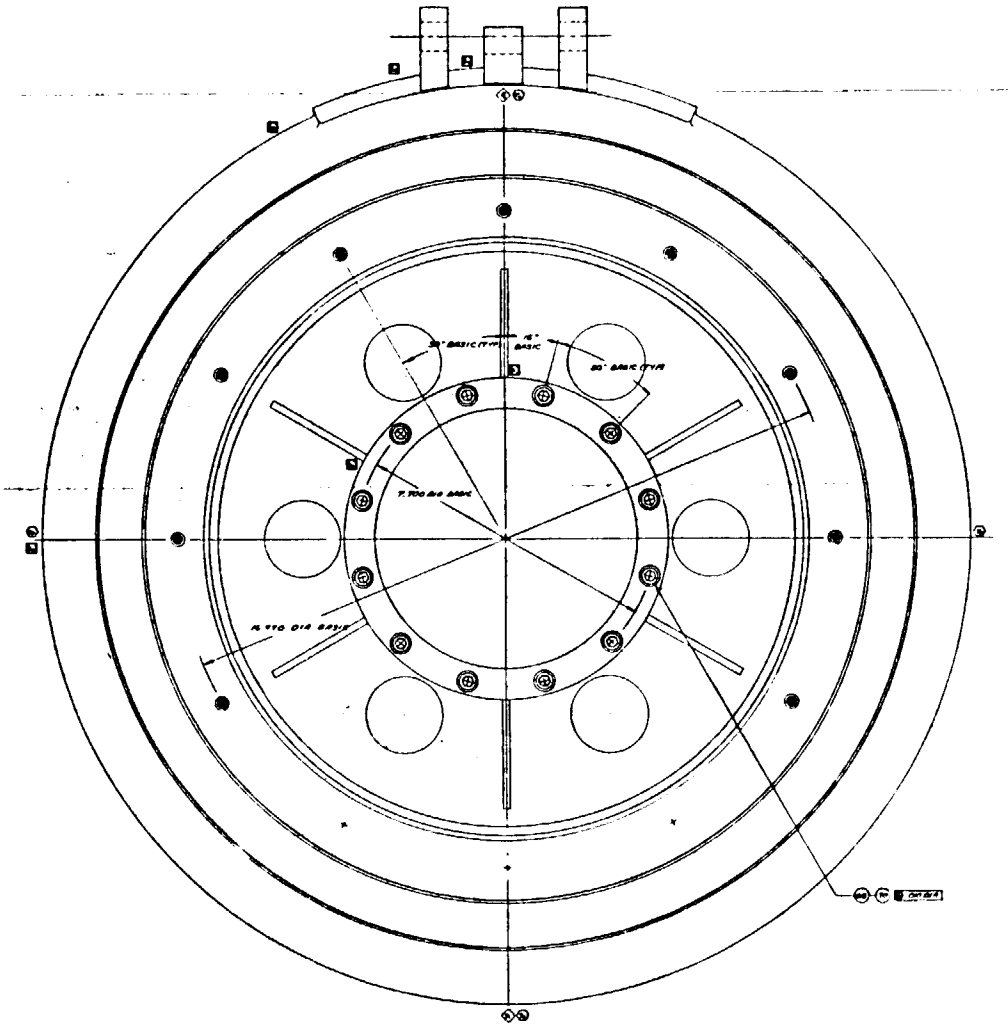

SECTION D-D
ACTUATOR REMOVED FOR CLARITY

UNCLASSIFIED

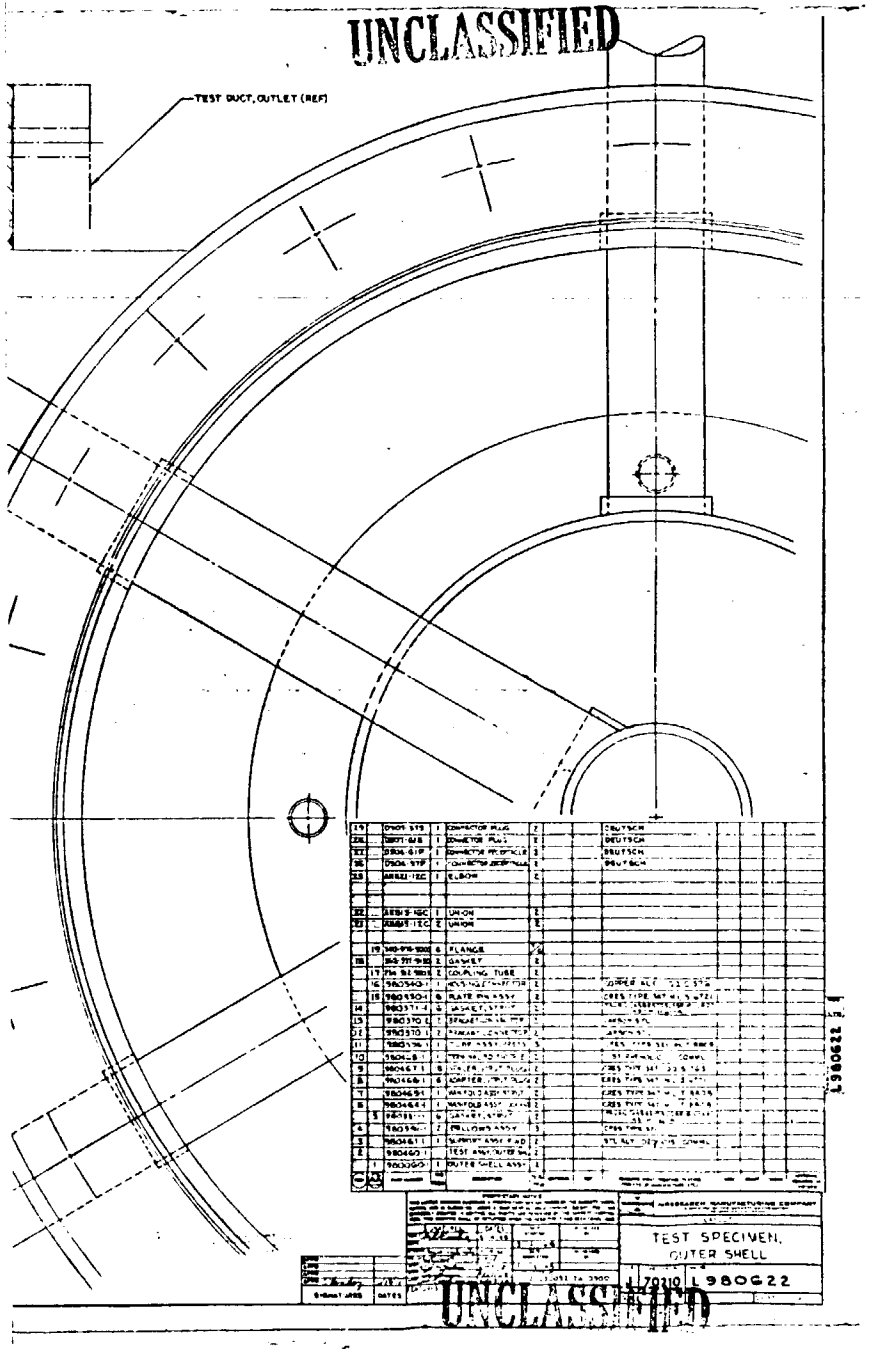

UNCLASSIFIED

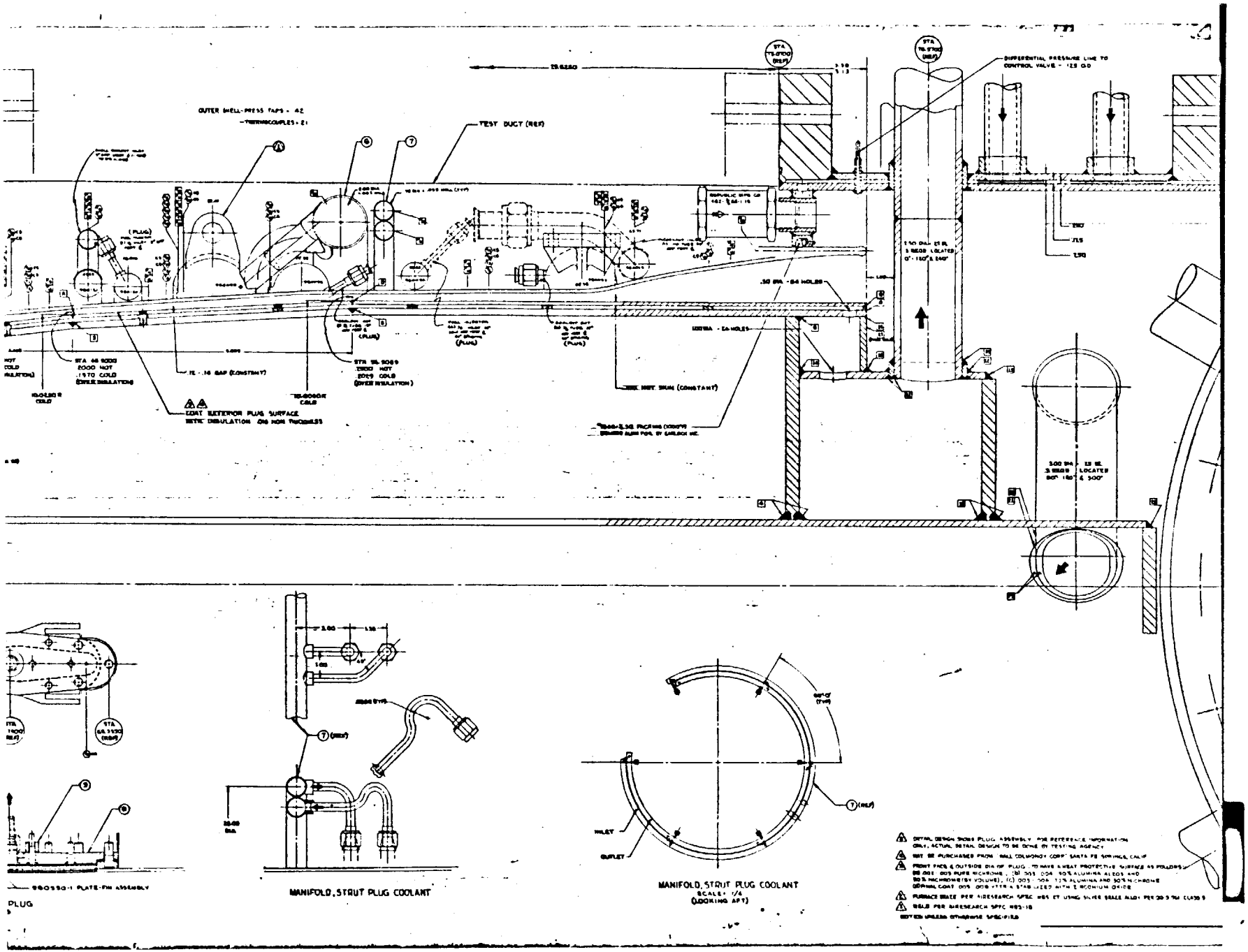
OUTER SHELL-PRESS TAPS - 42
TEST DUCT (REF)
DIFFERENTIAL PRESSURE LINE TO CONTROL VALVE - 125 O.D.
COAT EXTERIOR PLUG SURFACE
MANIFOLD, STRUT PLUG COOLANT
MANIFOLD, STRUT PLUG COOLANT
SCALE: 1/4
(LOOKING AFT)
INLET
OUTLET
PLUG

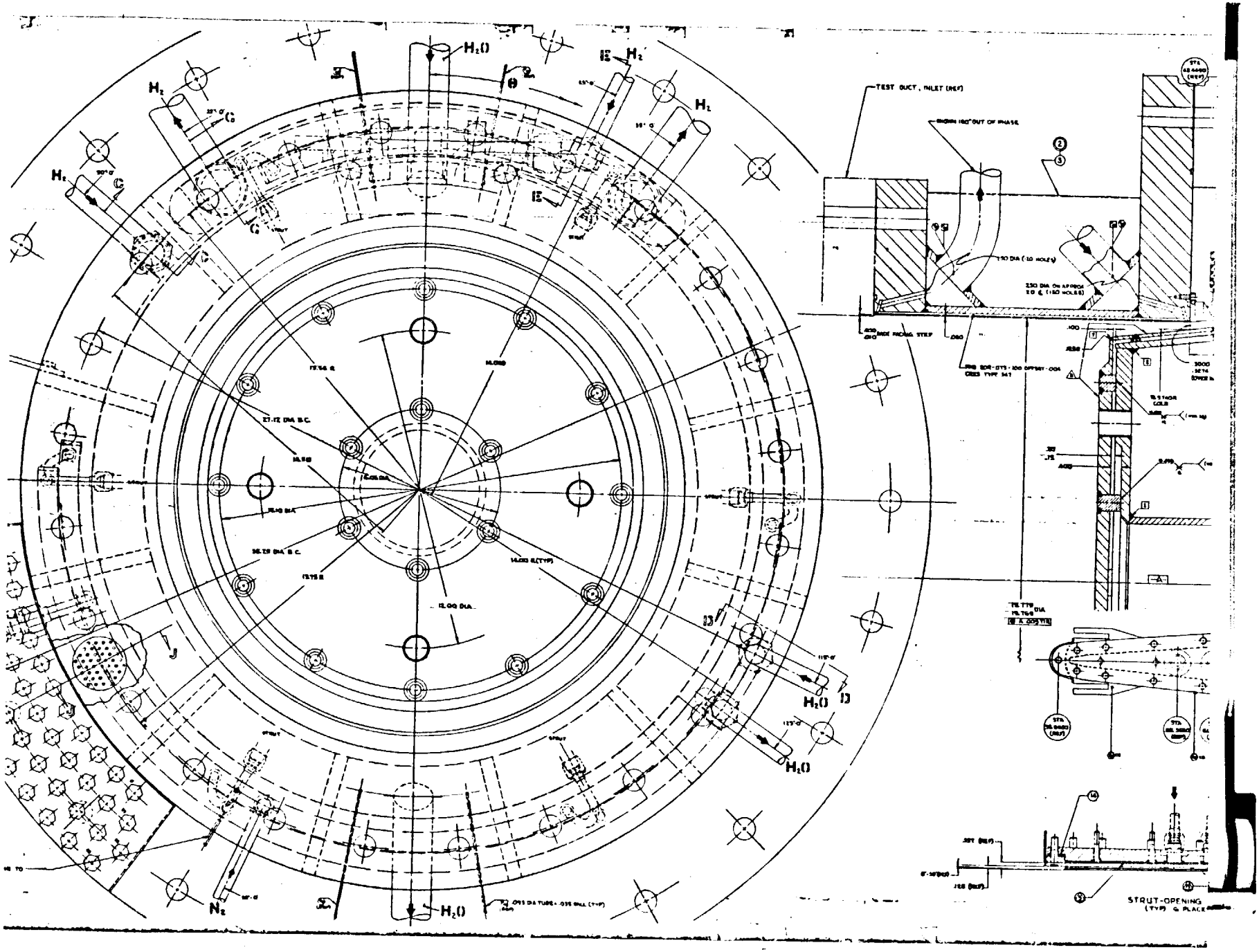
TEST DUCT, INLET (REF)
SHOWN 180° OUT OF PHASE
STRUT-OPENING
(TYP) @ PLACE

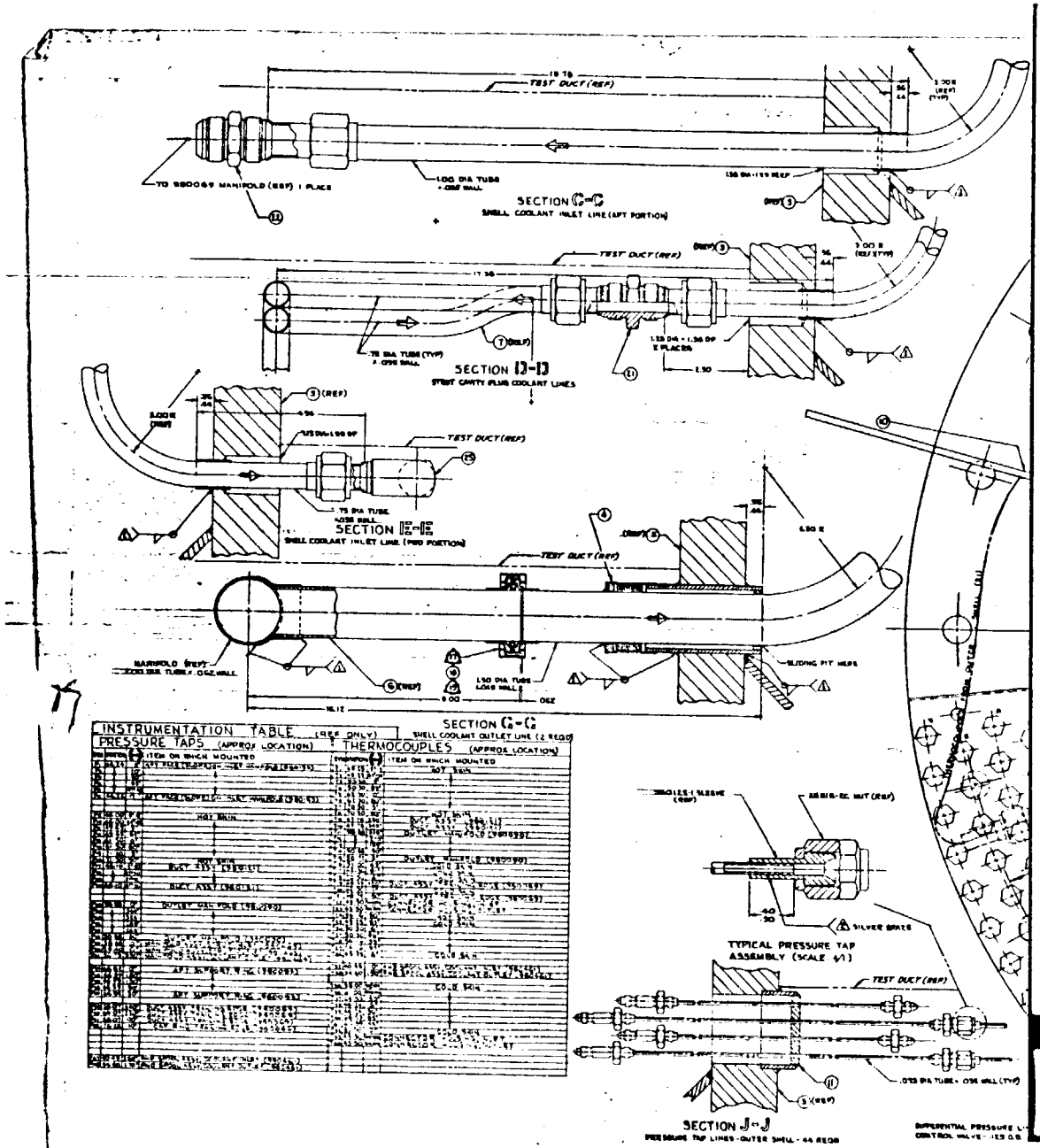

TEST DUCT (REF)
SECTION C-C
SHELL COOLANT INLET LINE (AFT PORTION)
SECTION D-D
STRUT CAVITY PLUG COOLANT LINES
SECTION E-E
SHELL COOLANT INLET LINE (FWD PORTION)
SECTION G-G
SHELL COOLANT OUTLET LINE (2 REQD)
INSTRUMENTATION TABLE (REF ONLY)
PRESSURE TAPS (APPROX LOCATION)
THERMOCOUPLES (APPROX LOCATION)
ITEM ON WHICH MOUNTED
TYPICAL PRESSURE TAP ASSEMBLY (SCALE 4/1)
SILVER BRAZE
SECTION J-J
PRESSURE TAP LINES - OUTER SHELL - 44 REQD

UNCLASSIFIED

CONNECTION	FUNCTION	TUBE/PIPE SIZE AND MATERIAL
1	WATER IN (3 PLACES)	8.00 O.D. MAX
2	WATER OUT (3 PLACES)	2.50 O.D. MAX
3	WATER IN PRESSURE	.093 DIA × .035 WALL CRES 347
4	WATER OUT PRESSURE	.093 DIA × .035 WALL CRES 347
5	WATER IN	1¼" SCH 40 STL PIPE
6	WATER OUT	1¼" SCH 40 STL PIPE
7	WATER IN	.75 DIA × .035 WALL CRES 347
8	WATER OUT	.75 DIA × .035 WALL CRES 347
9	HYDROGEN IN	.75 DIA × .035 WALL CRES 347
10	HYDROGEN IN	1.00 DIA × .035 WALL CRES 347
11	HYDROGEN OUT (2 PLACES)	.50 DIA × .049 WALL CRES 347
12	NITROGEN IN	.50 DIA × .035 WALL CRES 347
13	NITROGEN PRESSURE (1 PLC)	.125 DIA × .039 WALL CRES 347

UNCLASSIFIED

RE 125,000 PSI MIN YIELD BOLTS,
OF RATED YIELD STRENGTH
TLY SUPPORTED AT LOCATIONS NOTED
SURED OVER INSULATION

NSULATED (.016 ROCKIDE 2)
EL ONLY
ERIAL WILL REQUIRE
IONS
RWISE SPECIFIED

SIGNATURES | DATES

L980622

TEST SPECIMEN.
OUTER SHELL

J | 70210 | L980622

SCALE | SHEET 2 OF 2

L980622

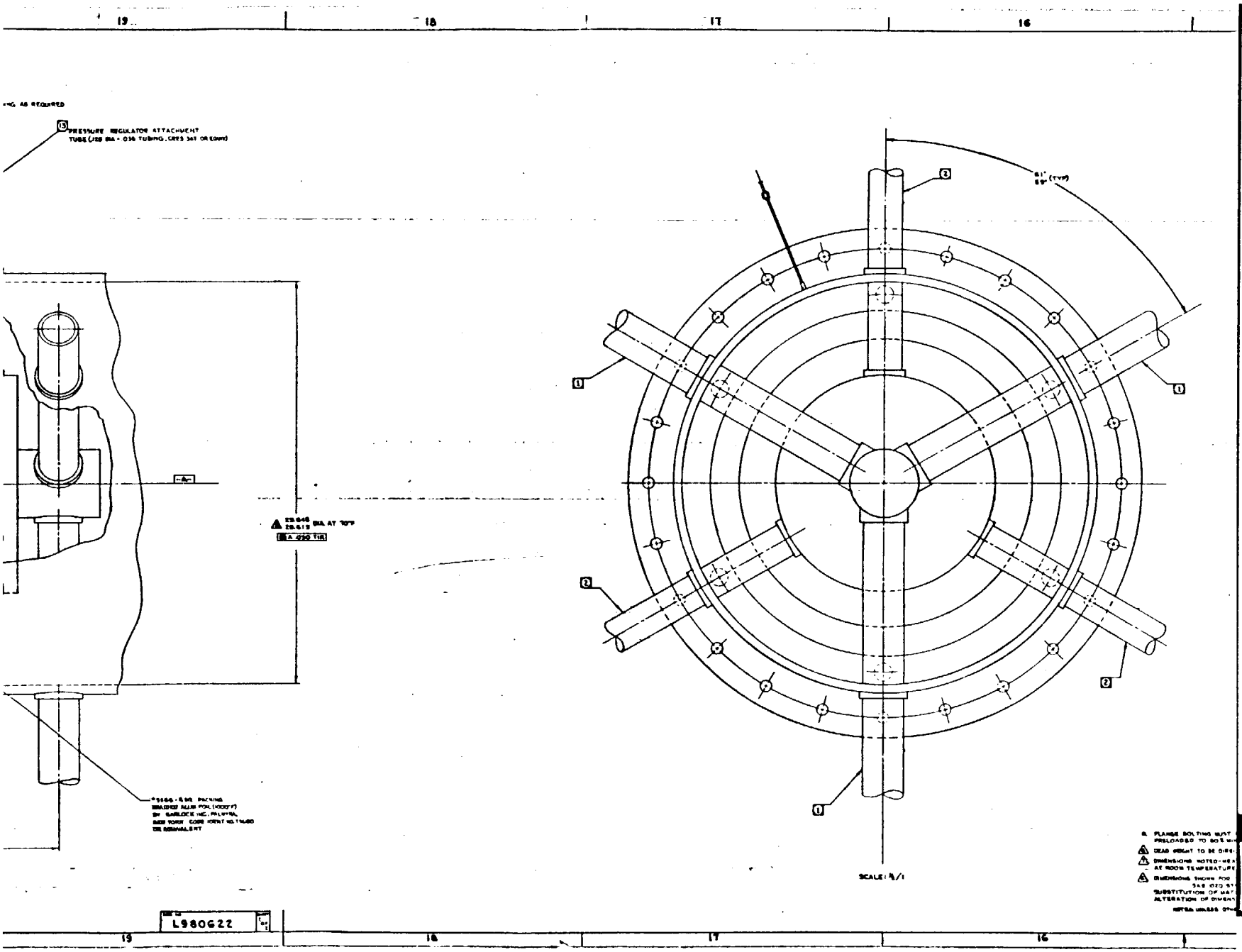
19
18
17
16
PRESSURE REGULATOR ATTACHMENT
SCALE: 3/1
L980622

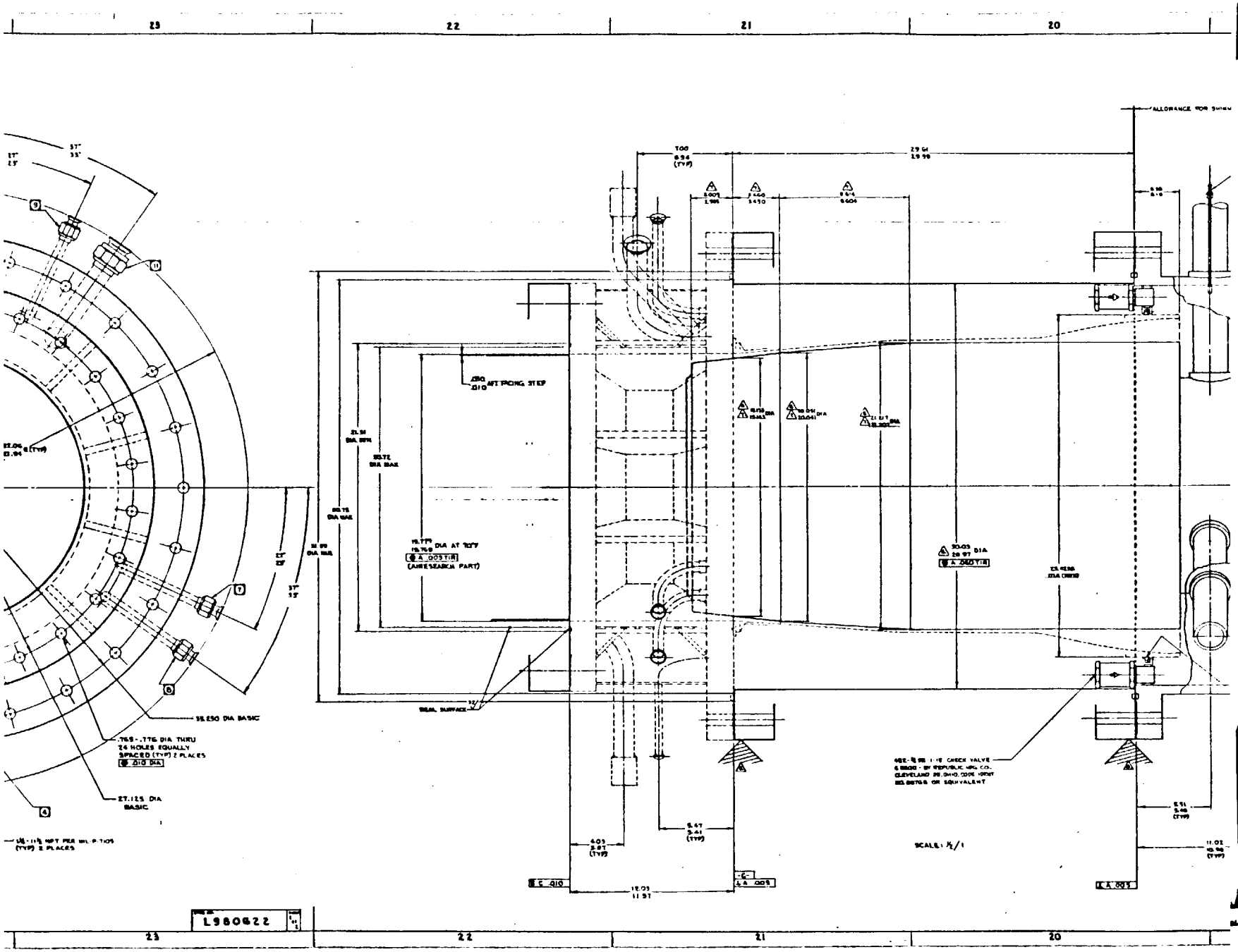

23
22
21
20
ALLOWANCE FOR SHIMMING
AFT FACING STEP
SEAL SURFACE
35.250 DIA BASIC
.765-.776 DIA THRU
24 HOLES EQUALLY
SPACED (TYP) 2 PLACES
27.125 DIA
BASIC
SCALE: 1/2/1
L980622

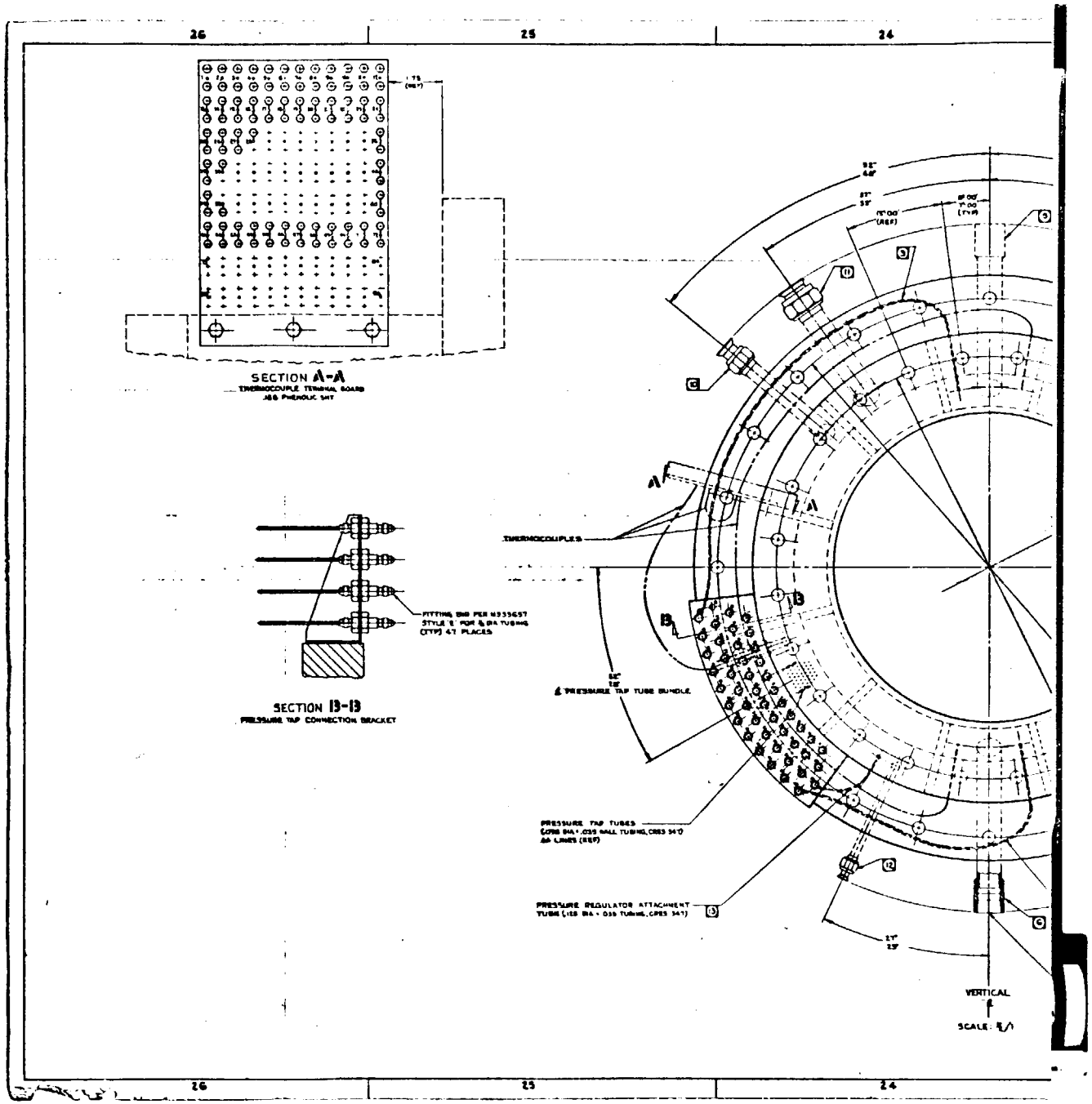
26
25
24
SECTION A-A
THERMOCOUPLE TERMINAL BOARD
.188 PHENOLIC SHT
SECTION B-B
PRESSURE TAP CONNECTION BRACKET
THERMOCOUPLES
PRESSURE TAP TUBE BUNDLE
PRESSURE TAP TUBES
PRESSURE REGULATOR ATTACHMENT
VERTICAL
SCALE: 1/1

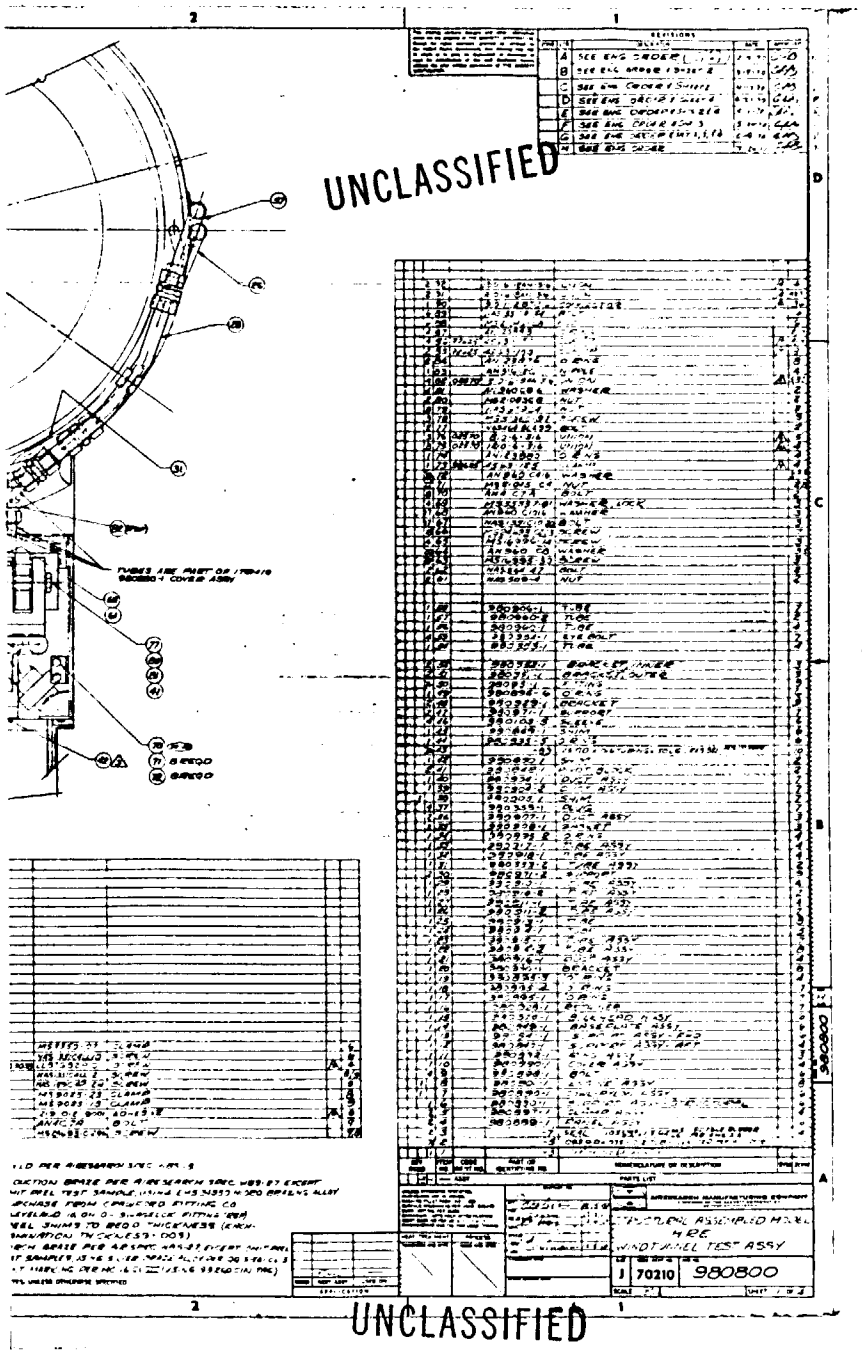
UNCLASSIFIED
REVISIONS
TUBES ARE PART OF ITEM 10 980800-4 COVER ASSY
BREQD
BREQD
PARTS LIST
AIRESEARCH MANUFACTURING COMPANY
STRUCTURAL ASSEMBLED MODEL
HRE
WINDTUNNEL TEST ASSY
J
70210
980800
980800
UNCLASSIFIED

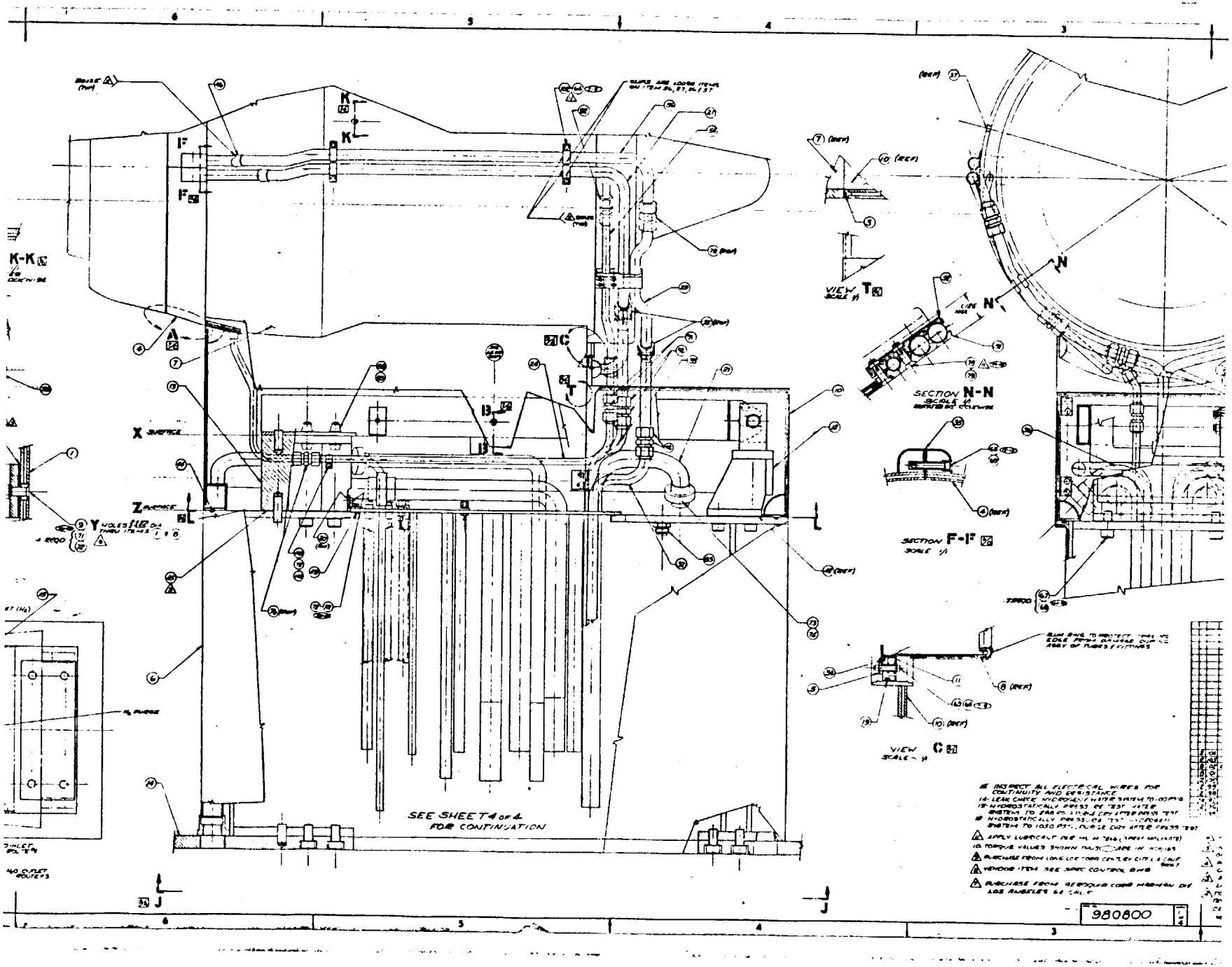
K-K
SEE SHEET 4 of 4
FOR CONTINUATION
SECTION N-N
SCALE 1/1
SECTION F-F
SCALE 1/1
VIEW T
VIEW C
SCALE 1/1
980800

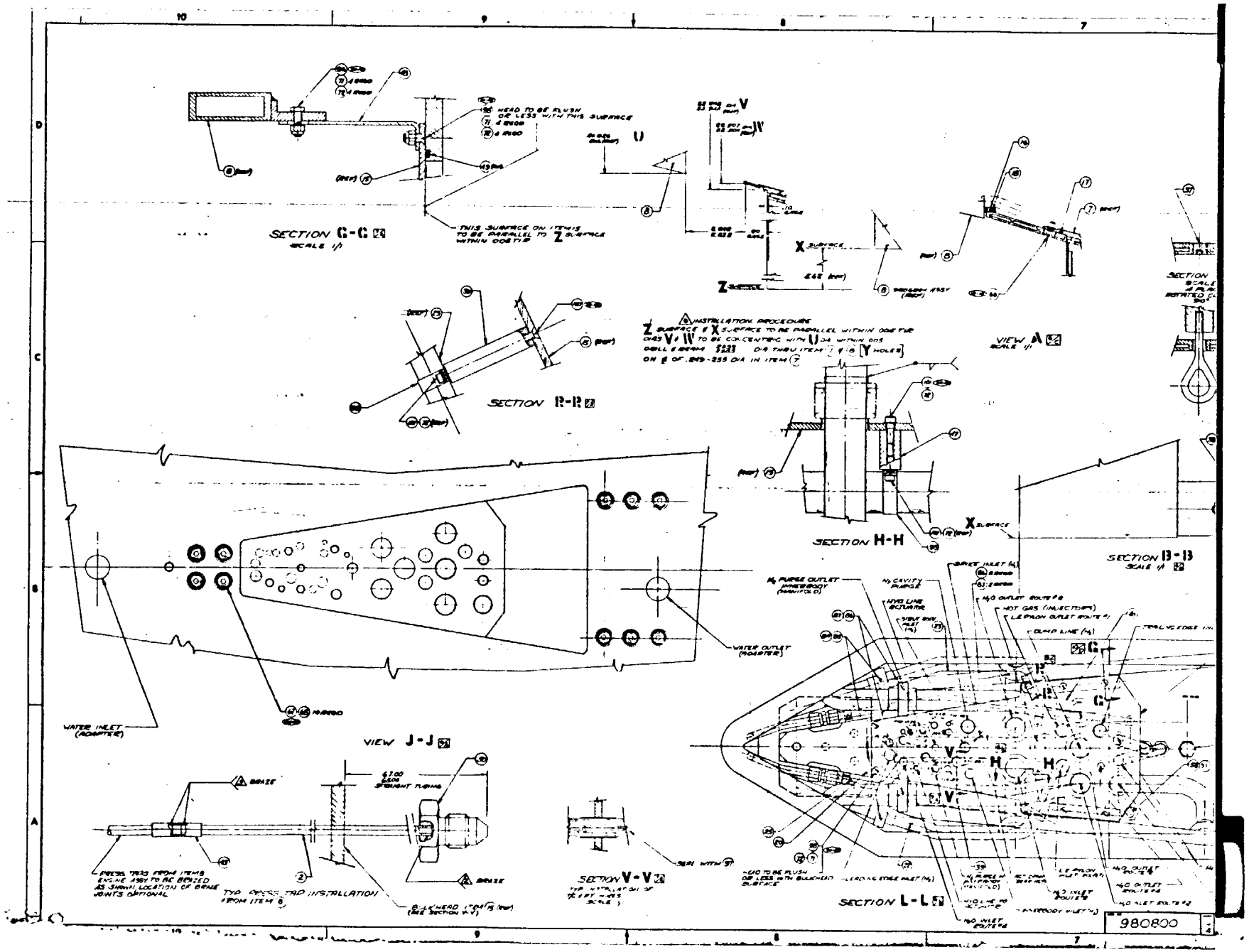
SECTION G-G
SCALE 1/1
SECTION R-R
VIEW A
SCALE 1/1
SECTION H-H
SECTION B-B
SCALE 1/1
VIEW J-J
SECTION V-V
SECTION L-L
WATER INLET (ADAPTER)
WATER OUTLET (ADAPTER)
TYP PRESS TAP INSTALLATION FROM ITEM 8
980800

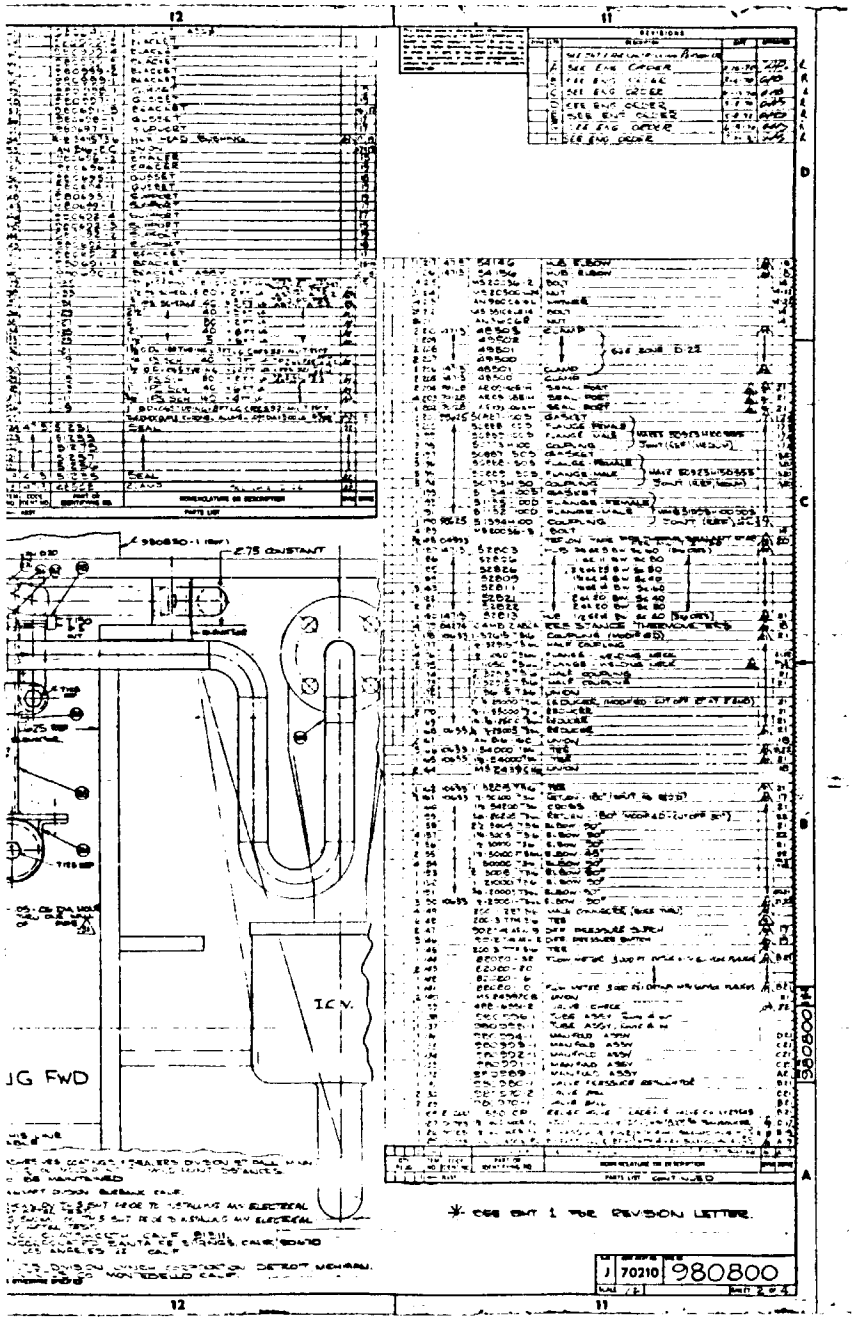

12
11
REVISIONS
PARTS LIST
NOMENCLATURE OR DESCRIPTION
2.75 CONSTANT
I.C.V.
JG FWD
PARTS LIST CONTINUED
* SEE SHT 1 FOR REVISION LETTER.
J
70210
980800
SHEET 2 OF 4
980800

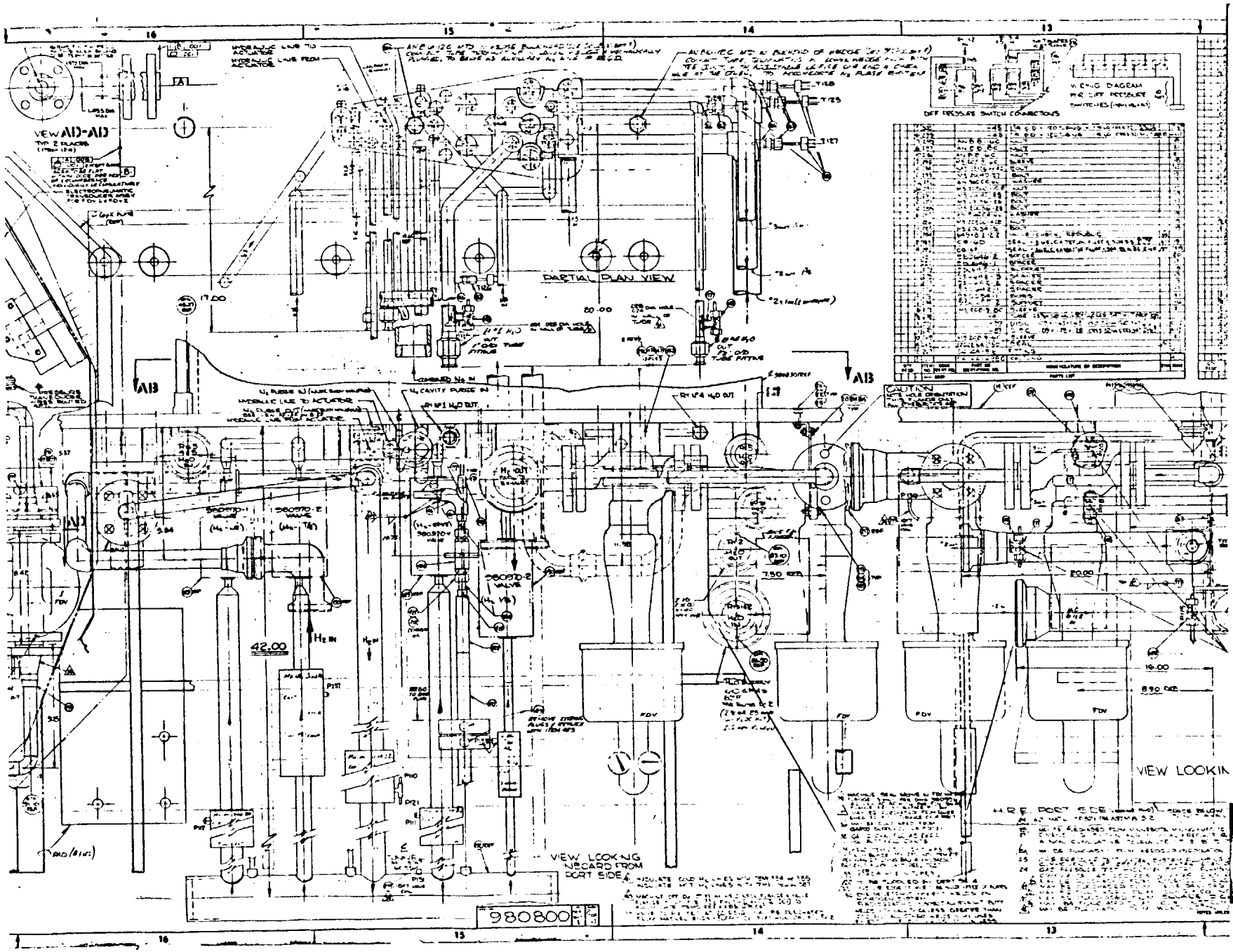

VIEW AD-AD
PARTIAL PLAN VIEW
DIFF PRESSURE SWITCH CONNECTIONS
WIRING DIAGRAM
FOR DIFF PRESSURE SWITCHES
AB
CAUTION
42.00
VIEW LOOKING INBOARD FROM PORT SIDE
VIEW LOOKIN
980800

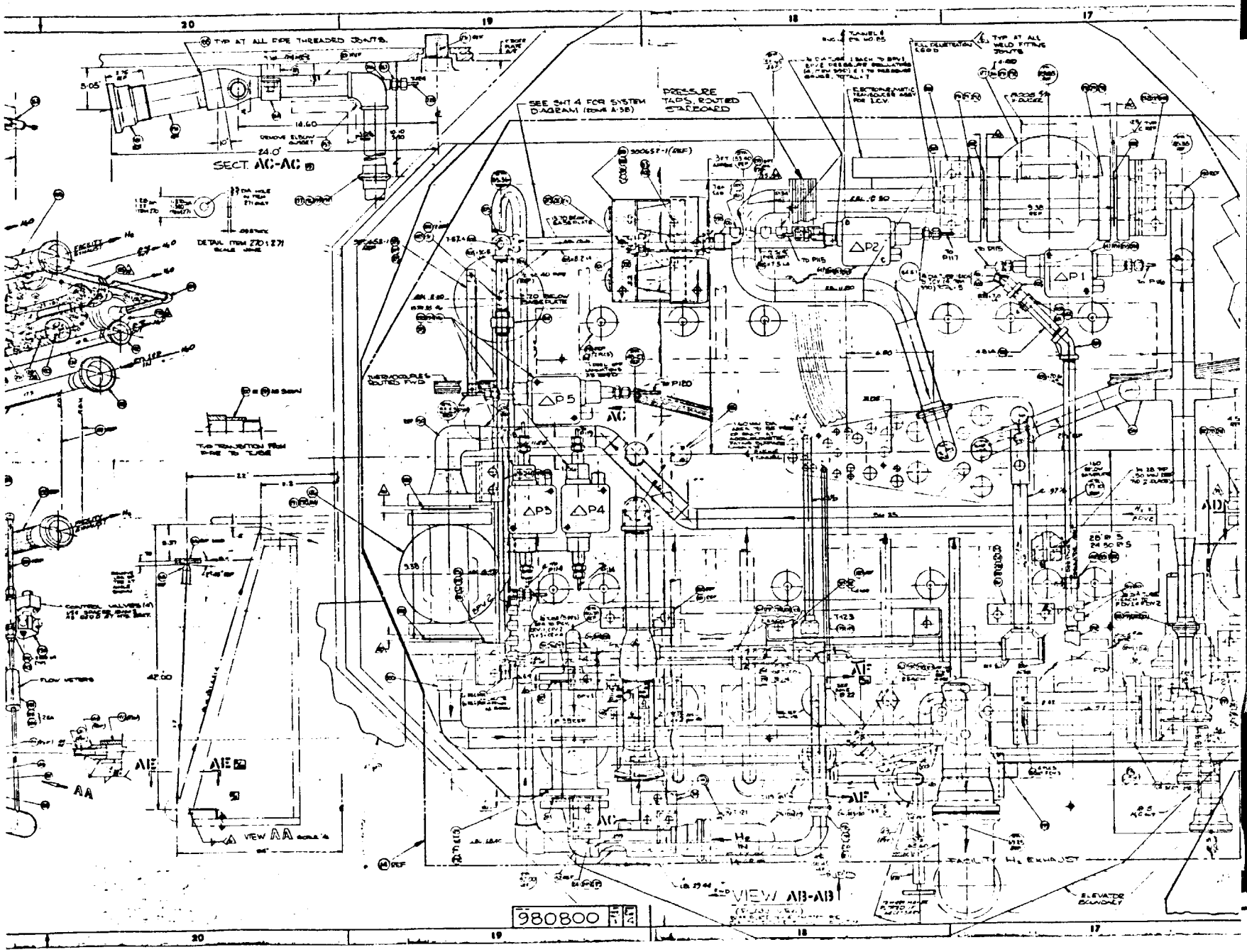
SECT. AC-AC
DETAIL ITEM 270 (27)
SEE SHT 4 FOR SYSTEM DIAGRAM
PRESSURE TAPS, ROUTED STARBOARD
VIEW AA
VIEW AB-AB
FACILITY H2 EXHAUST
980800

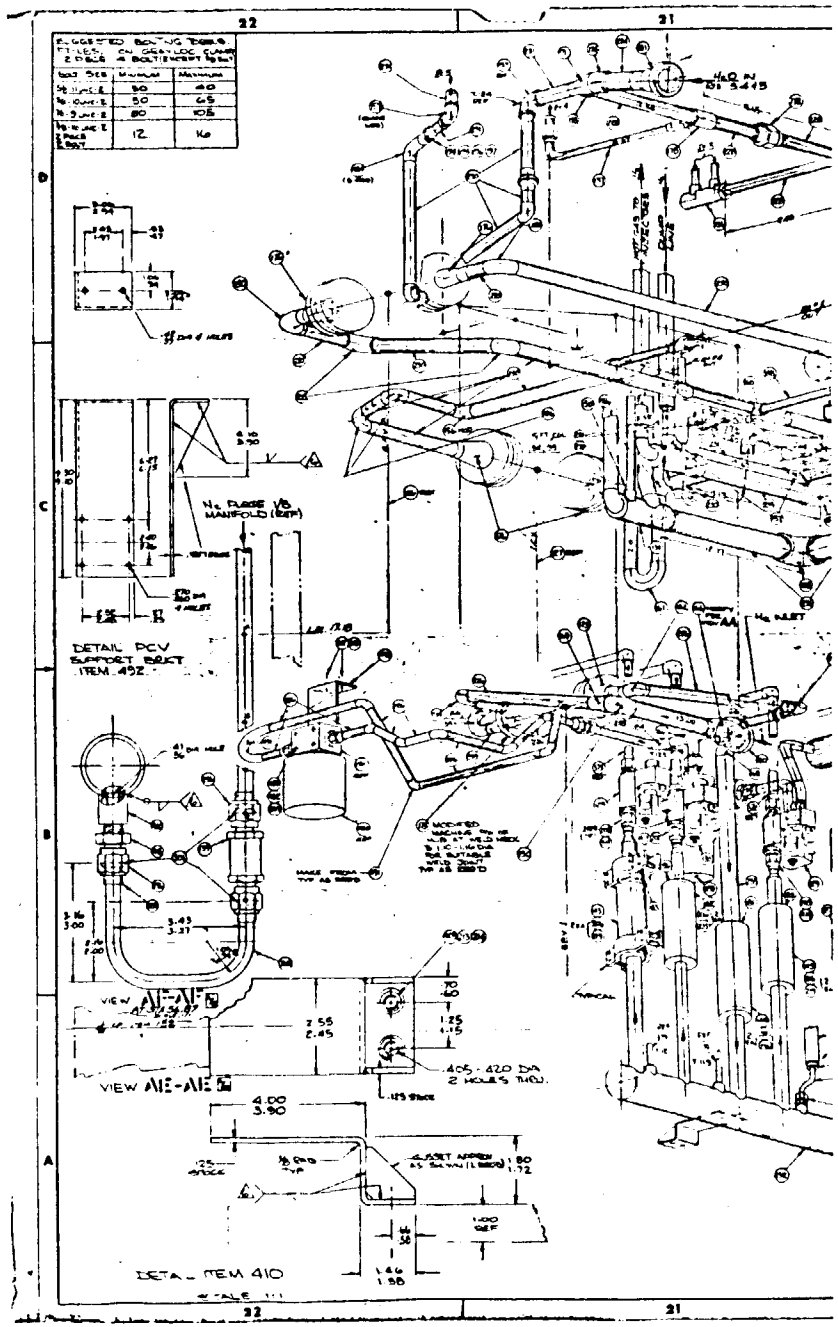
DETAIL PCV SUPPORT BRACKET ITEM 492
VIEW AE-AE
VIEW AE-AE
DETAIL ITEM 410

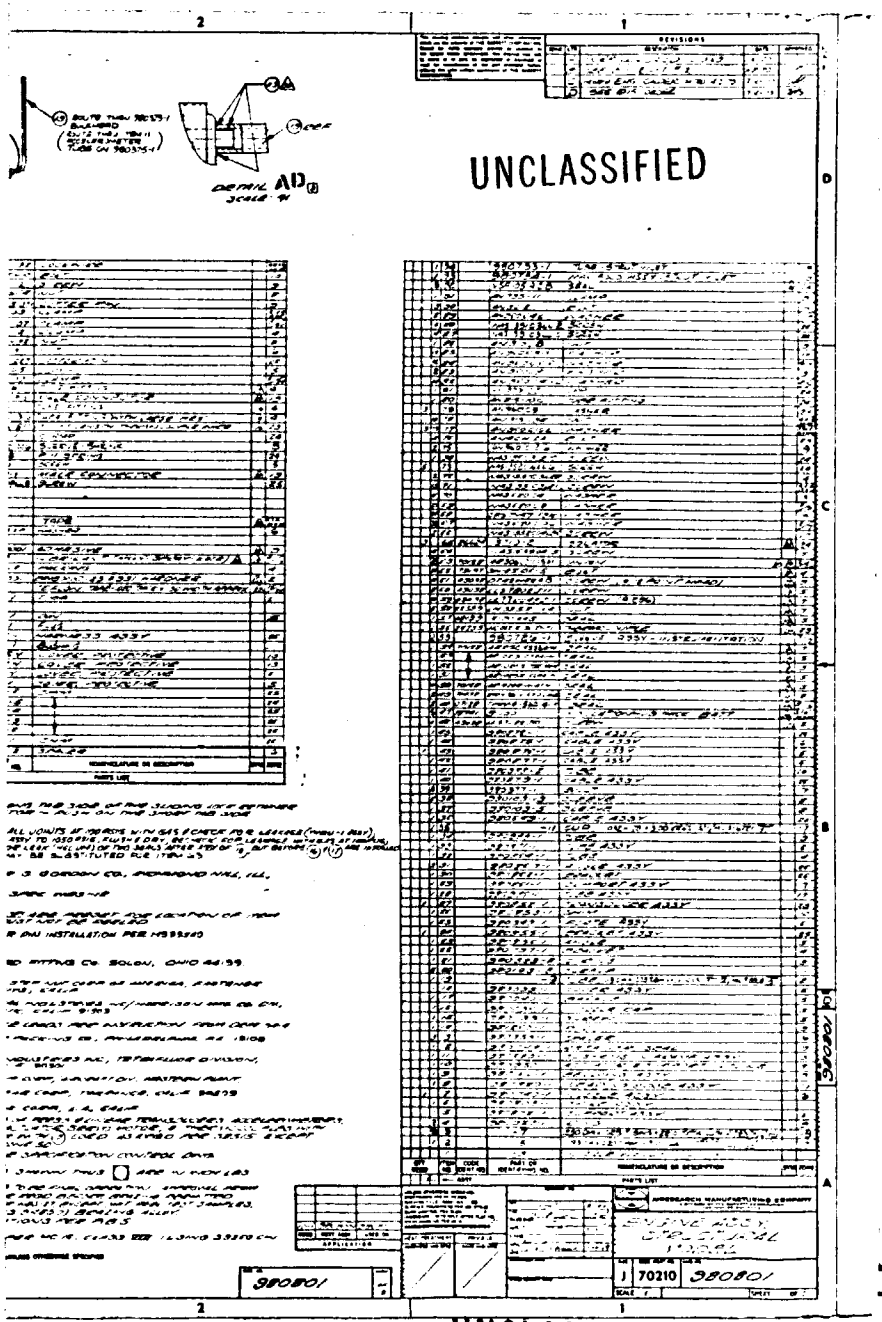

UNCLASSIFIED

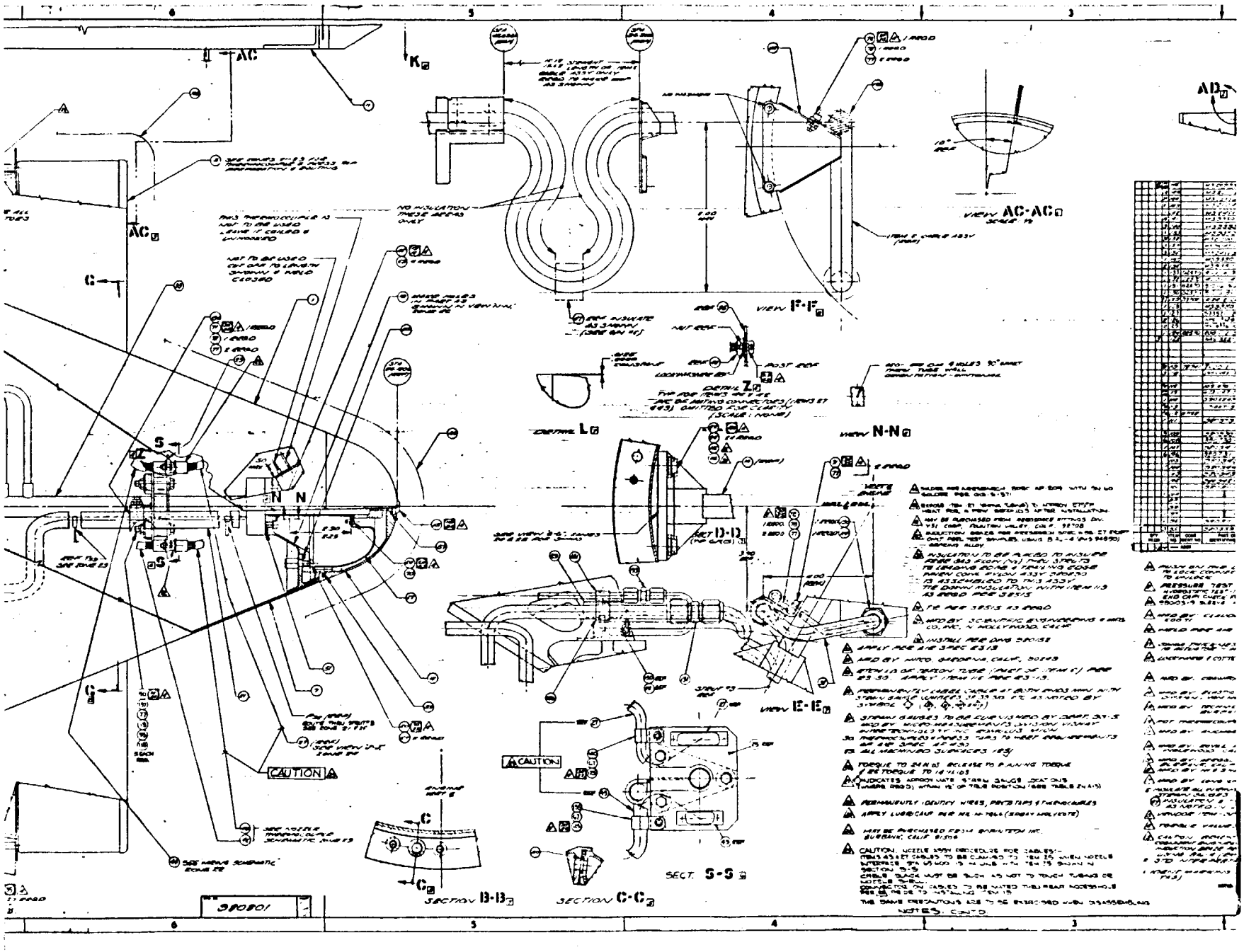
VIEW AC-AC
VIEW F-F
DETAIL Z
DETAIL L
VIEW N-N
SECT. D-D
VIEW E-E
SECT. S-S
SECTION B-B
SECTION C-C
CAUTION
NOTES: CONTD

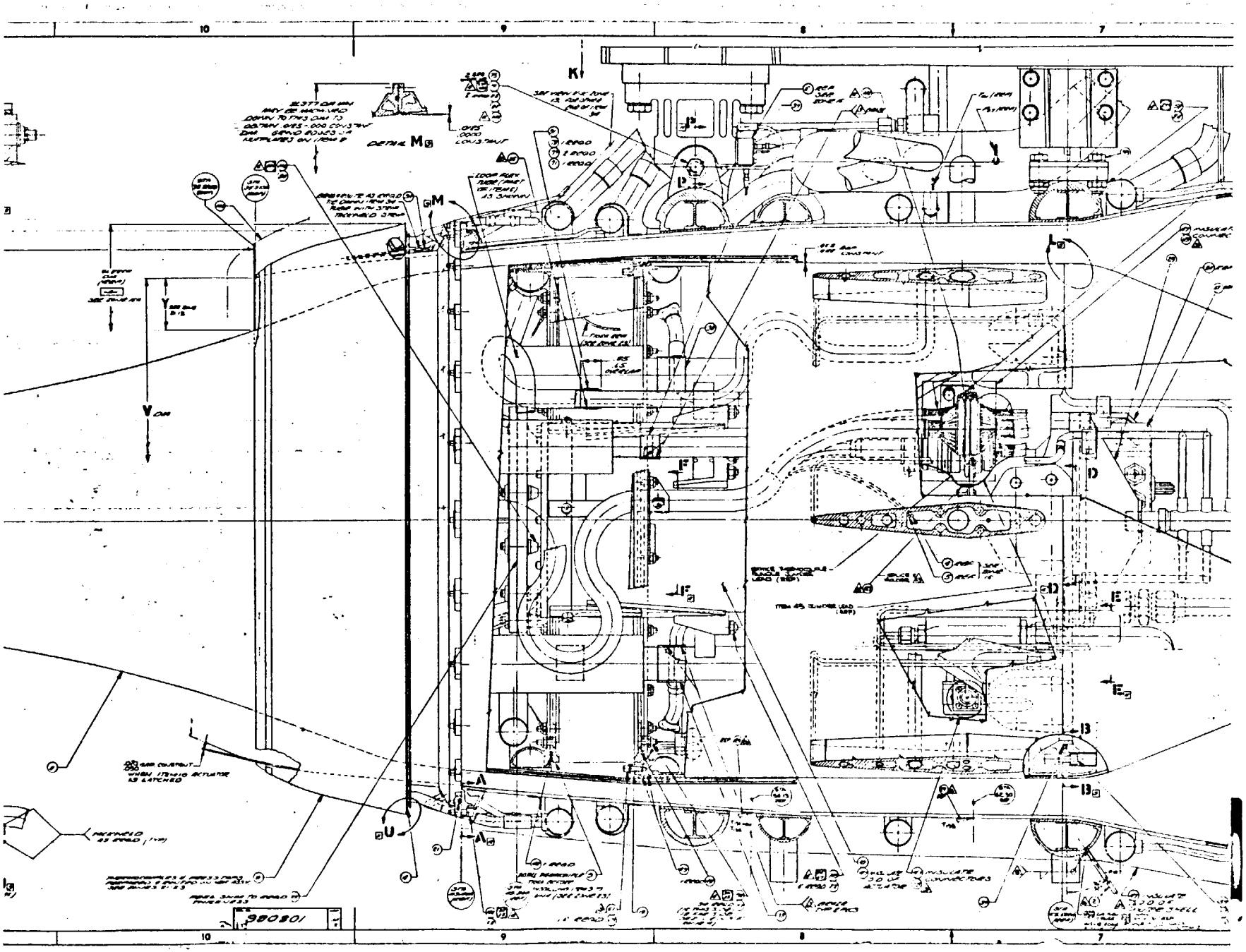

10
9
8
7
K
DETAIL M
M
Y
V
U
A
B
D
E
F
L
980801

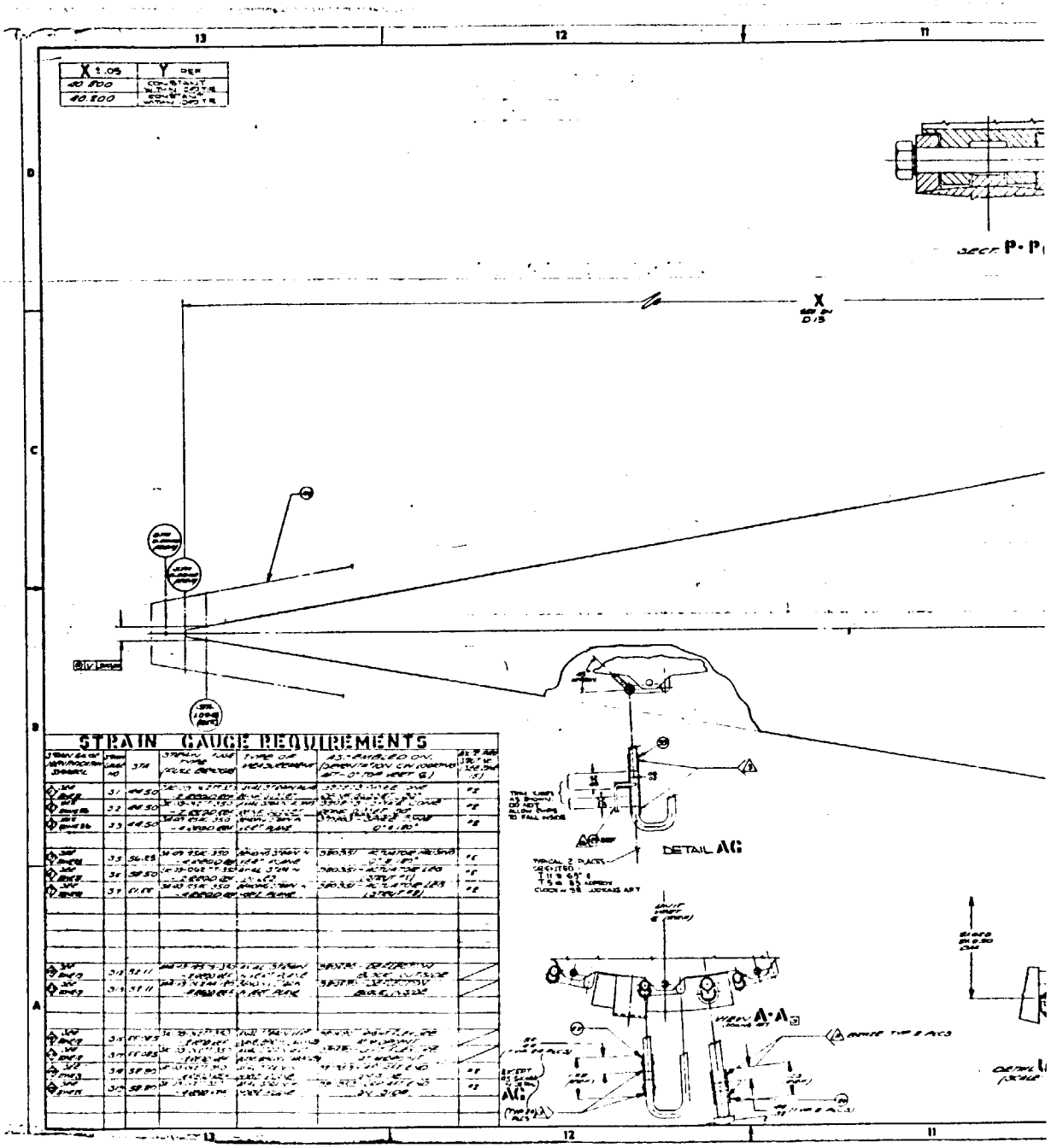
STRAIN GAUGE REQUIREMENTS
DETAIL AG
SECT. A-A
SECT. P-P

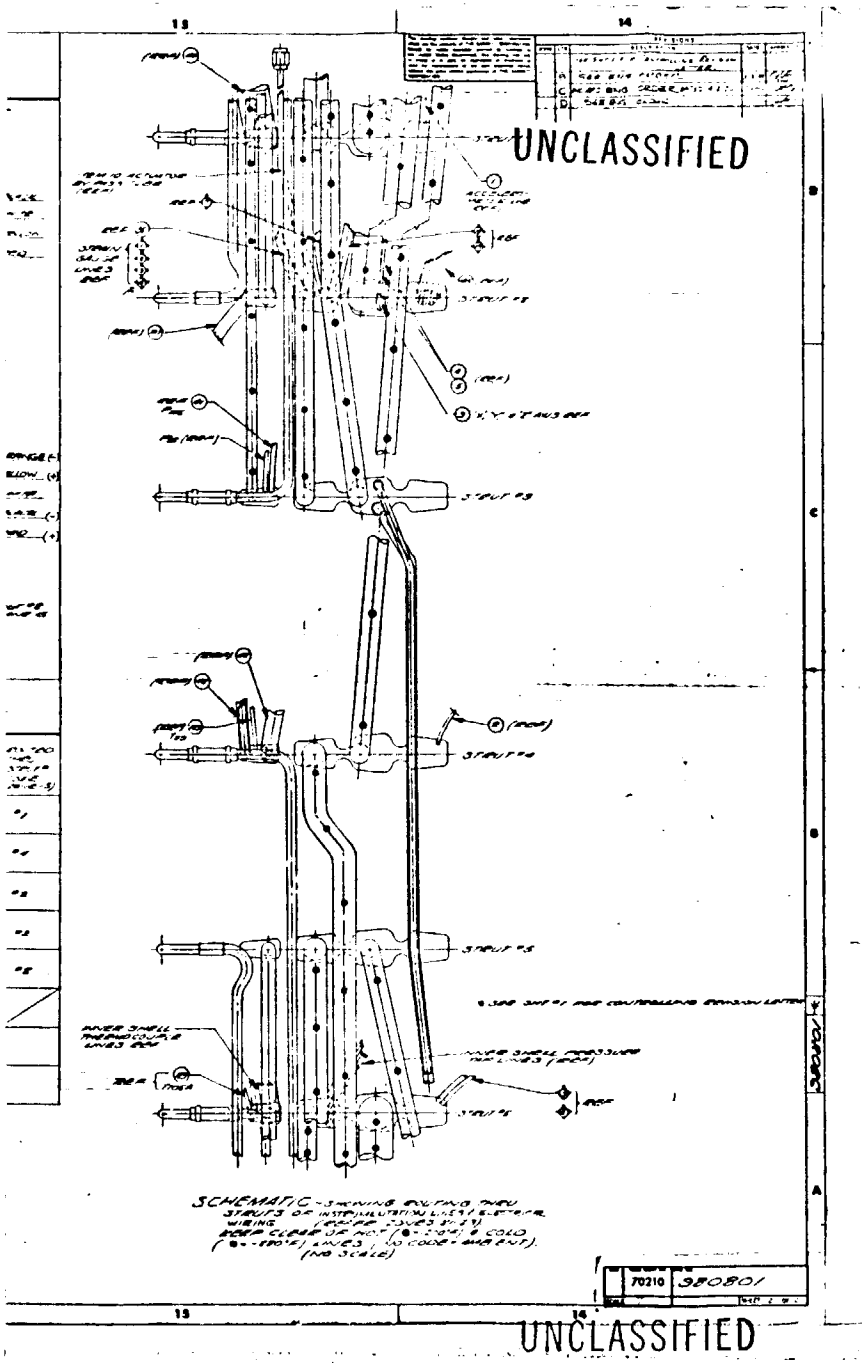
UNCLASSIFIED
SCHEMATIC
70210
380801
UNCLASSIFIED

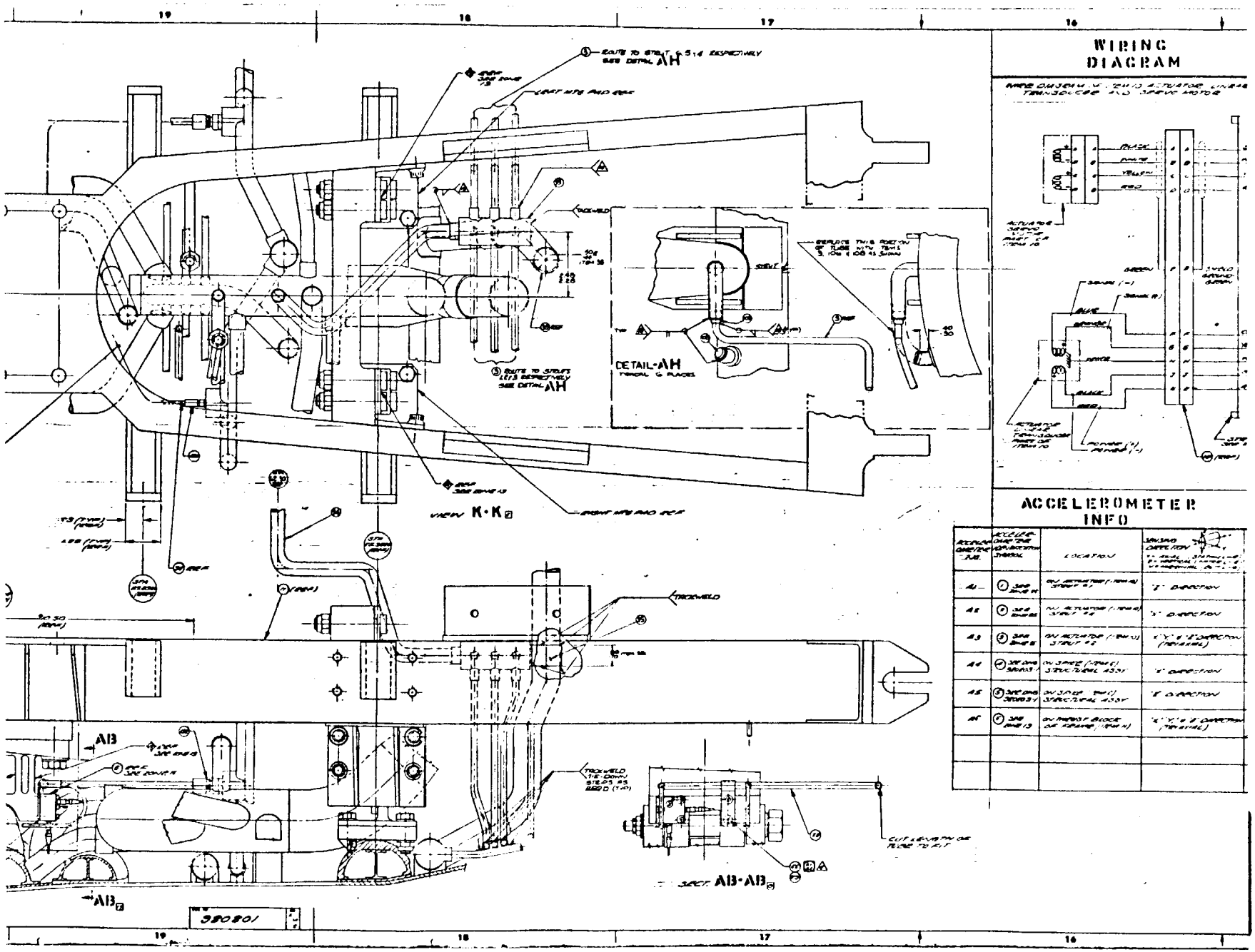
WIRING DIAGRAM
ACCELEROMETER INFO
DETAIL-AH
VIEW K-K
SECT AB-AB
380801

THERMOCOUPLE SCHEDULE & SCHEMATIC

I - LEADING EDGE (ITEM 8)
a) THERMOCOUPLE SCHEMATIC (T_1-T_{16})

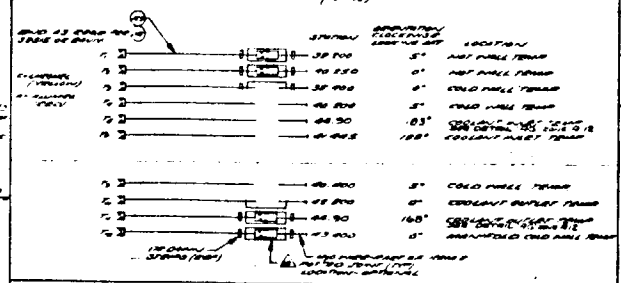

II - SPIKE (ITEM 6)
a) THERMOCOUPLE SCHEMATIC (T_{17}, T_{18}, T_{19}-T_{96})

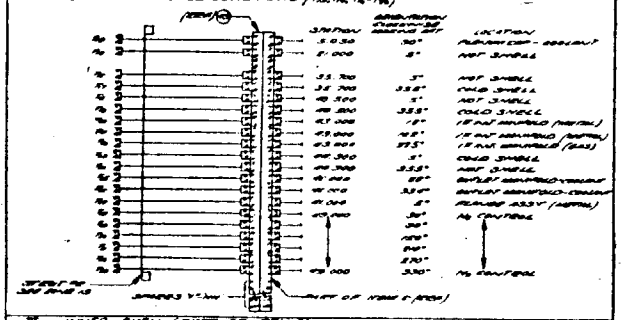

III - INNER SHELL (PART OF ITEM 5)
a) T_{97}-T_{144}, T_{145}-T_{192}, T_{193}-T_{194}, T_{195}-T_{198} INSTRUMENTED ON THE SPLIT'S ON PREVIOUS ASSY
b) THERMOCOUPLE SCHEMATIC T_{99} (PART OF ITEM 33)

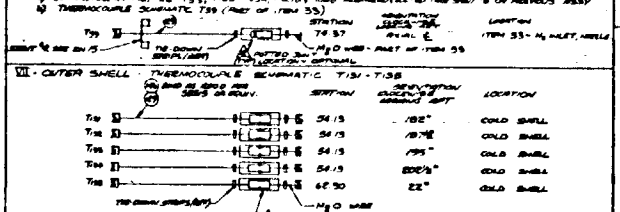

VII - OUTER SHELL THERMOCOUPLE SCHEMATIC T_{131}-T_{138}

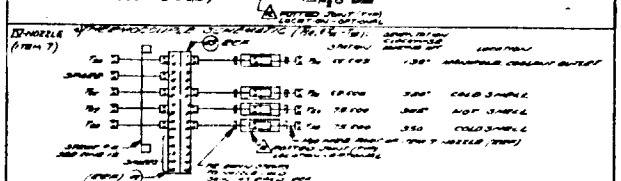

IX - NOZZLE (ITEM 7)
a) THERMOCOUPLE SCHEMATIC (T_{199}-T_{211})

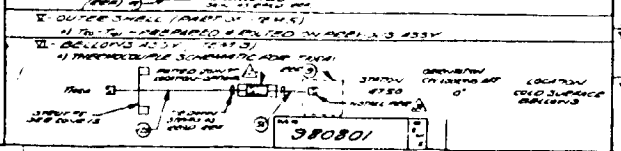

V - OUTER SHELL (PART OF ITEM 5)
a) T_{213}-T_{216} - PREPARED & ROUTED ON PREV. ASSY

VI - BELLOWS ASSY. (ITEM 3)
a) THERMOCOUPLE SCHEMATIC (DWG. 7[illegible])

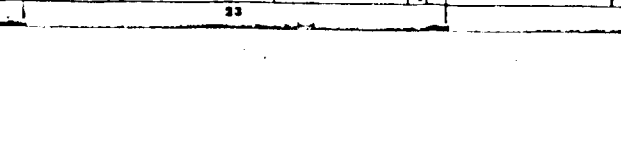

PRESS TAP SCHEDULE & SCHEMATIC

I - LEADING EDGE (ITEM 8)
a) P_1-P_8, P_{10}-P_{15} PREPARED & ROUTED ON NEXT ASSY

II - OUTER SHELL (PART OF ITEM 5)
a) P_{16}-P_{21}, P_{23}-P_{31} PREPARED & ROUTED ON NEXT ASSY

III - INNER SHELL (PART OF ITEM 5)
a) P_{32}-P_{34}, P_{36}-P_{41}, P_{44}-P_{50} OUT THRU STRUT #5, SEE LINE 16, ON PREVIOUS ASSY. TO BE PREPARED & PLENUM ROUTED ON NEXT ASSY

IV - SPIKE (ITEM 6)
a) PRESS TAP SCHEMATIC (P_{51}-P_{78})

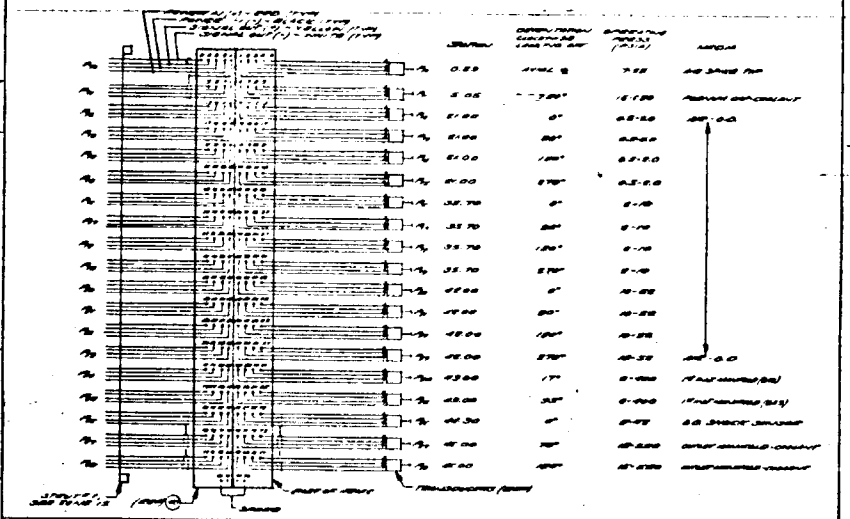

V - NOZZLE (ITEM 7)
a) PRESS TAP SCHEMATIC (P_{79}-P_{96}, & P_{100})

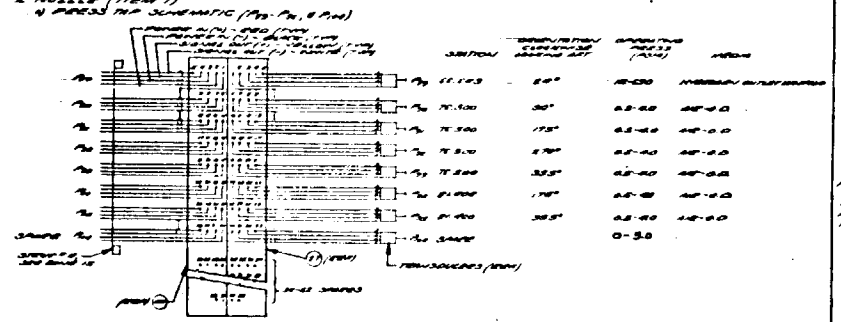

VII - OUTER SHELL - RET SUPPORT (ITEM 5) DOT

VI - INNER SHELL CAVITY PRESSURE LINE PAD

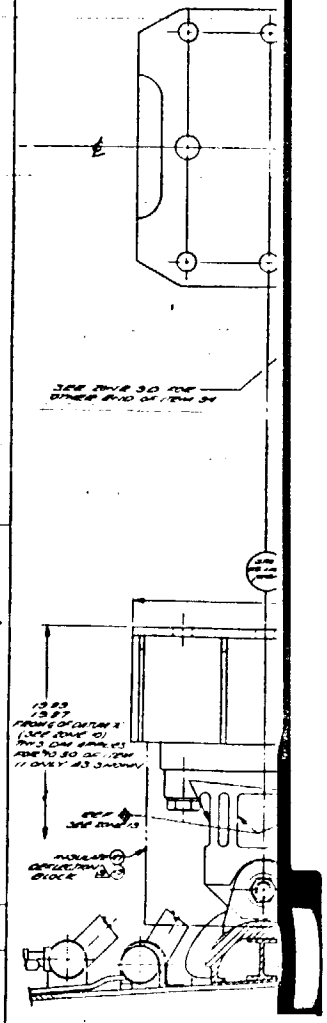

980801

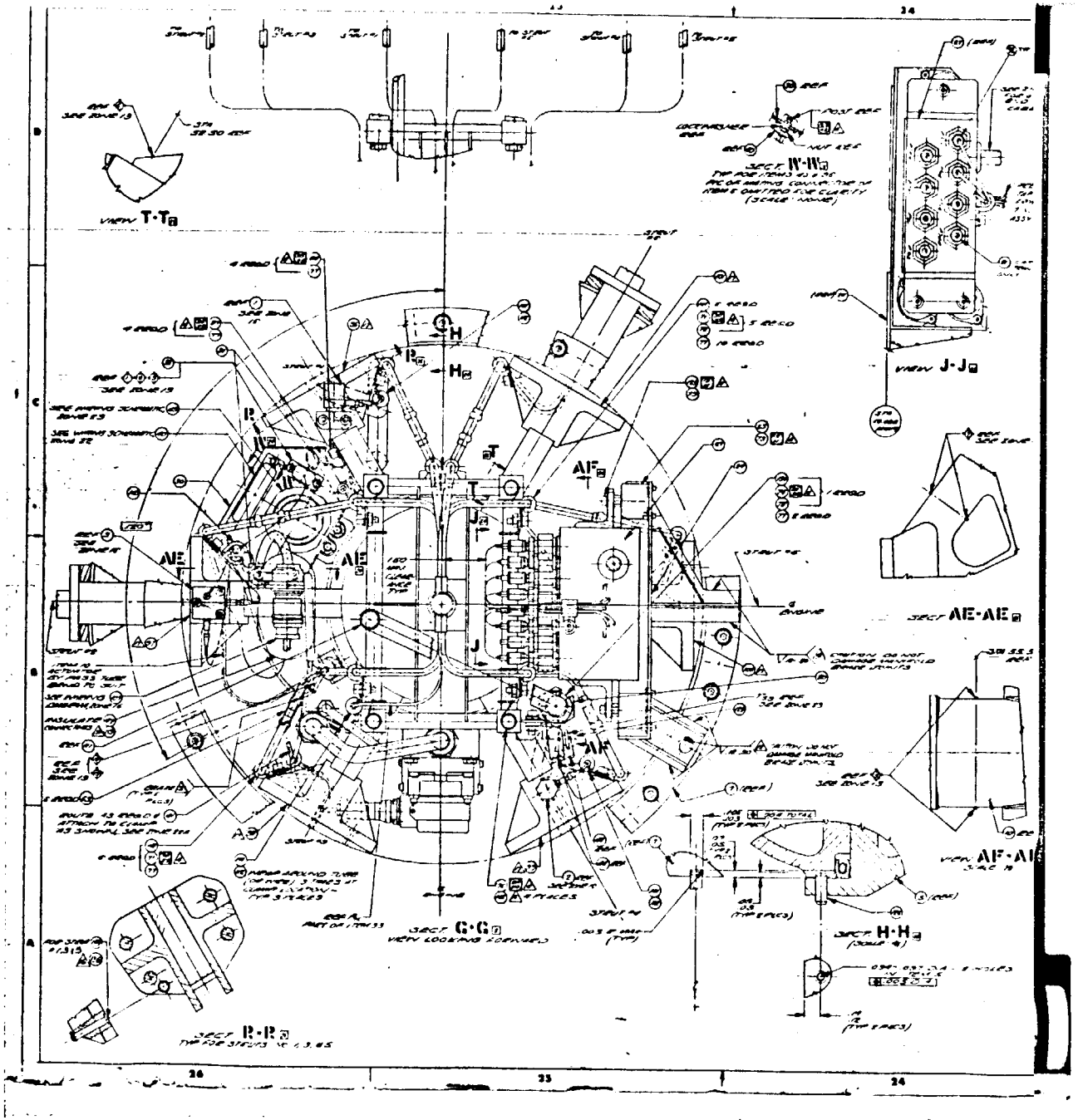
VIEW T-T
SECT W-W
VIEW J-J
SECT AE-AE
VIEW AF-AF
SECT G-G
VIEW LOOKING FORWARD
SECT H-H
SECT R-R

UNCLASSIFIED

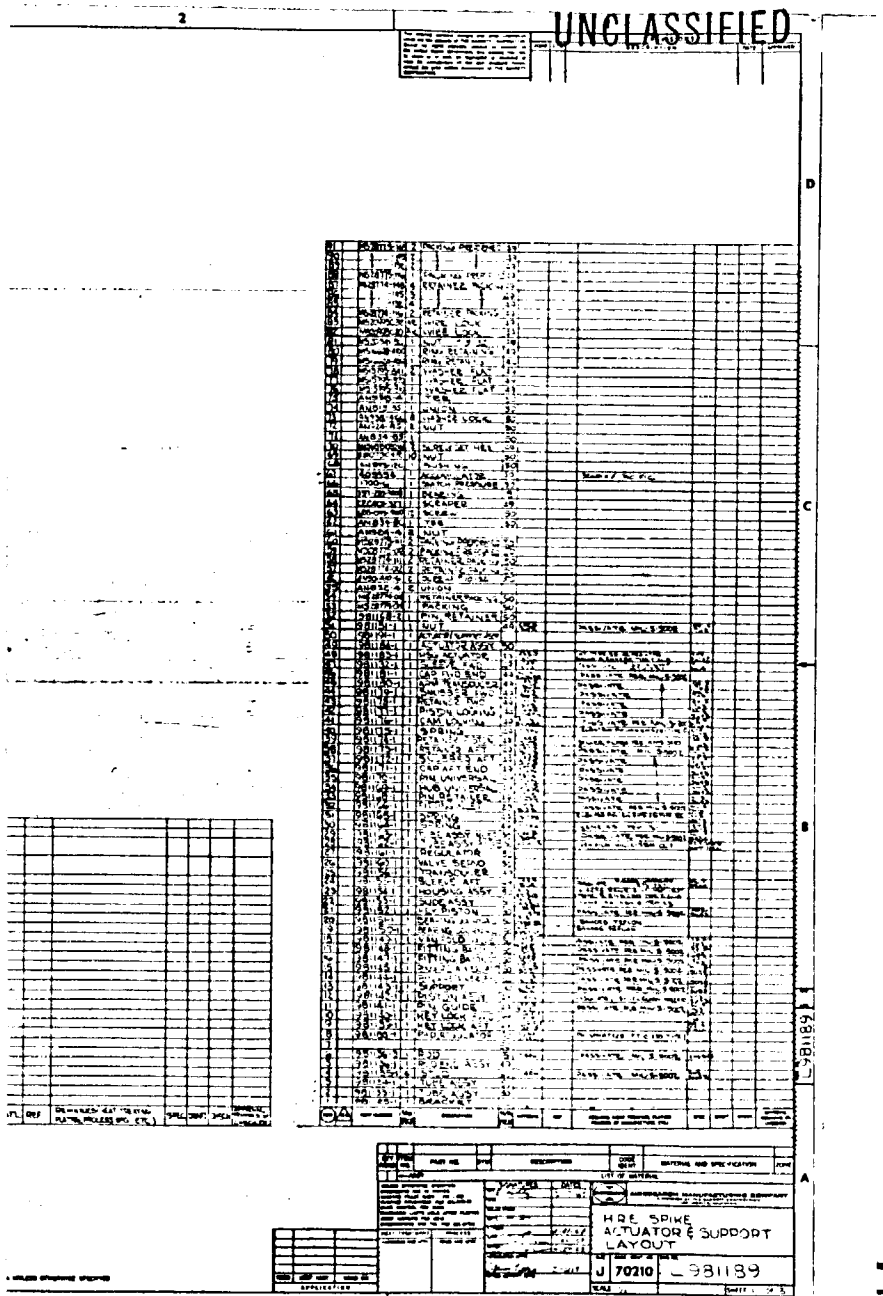

UNCLASSIFIED

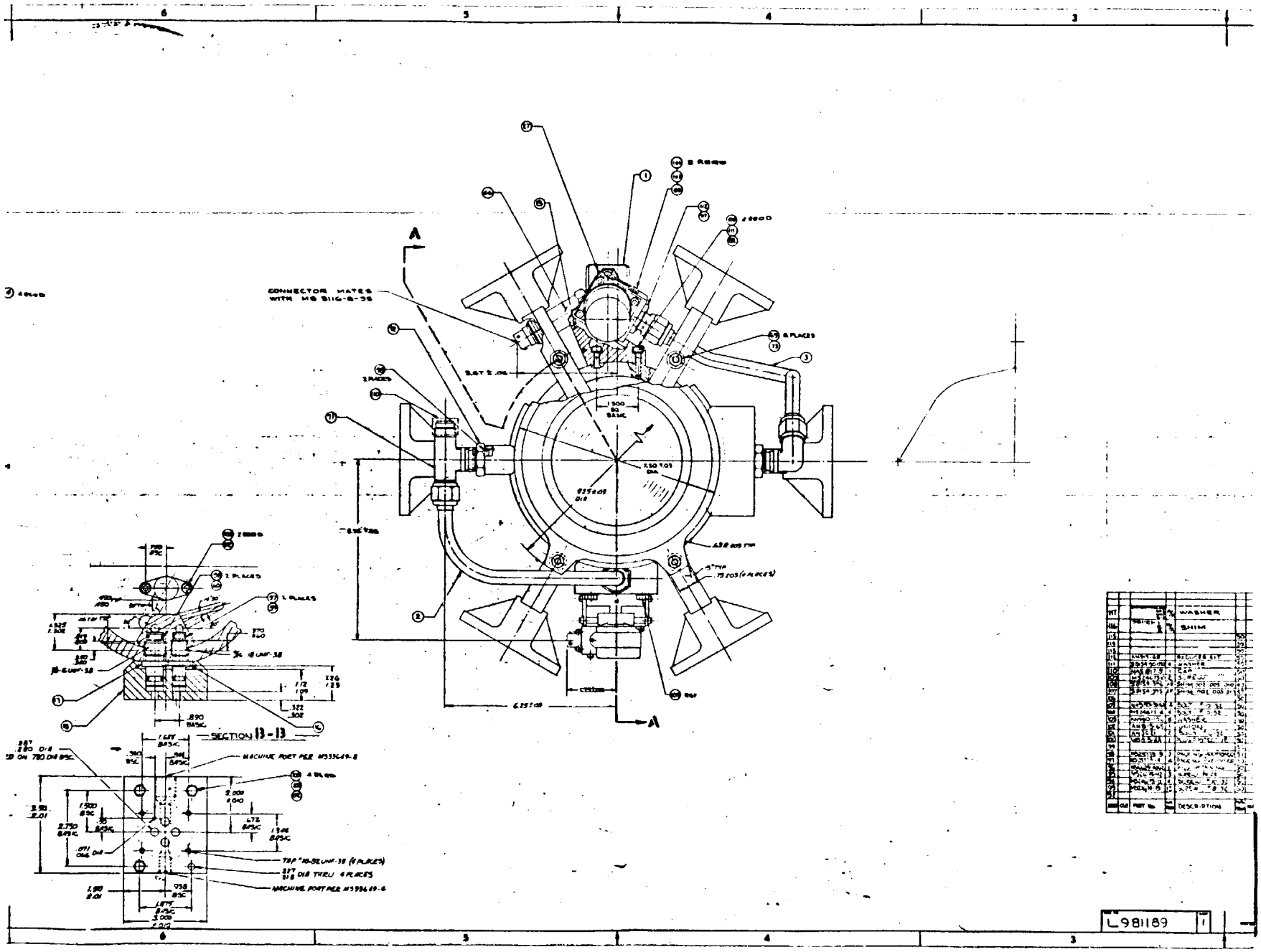
CONNECTOR MATES WITH MS 3116-8-35
SECTION B-B
MACHINE PORT PER M539649-8
MACHINE PORT PER M539649-6
WASHER
SHIM
DESCRIPTION
L981189

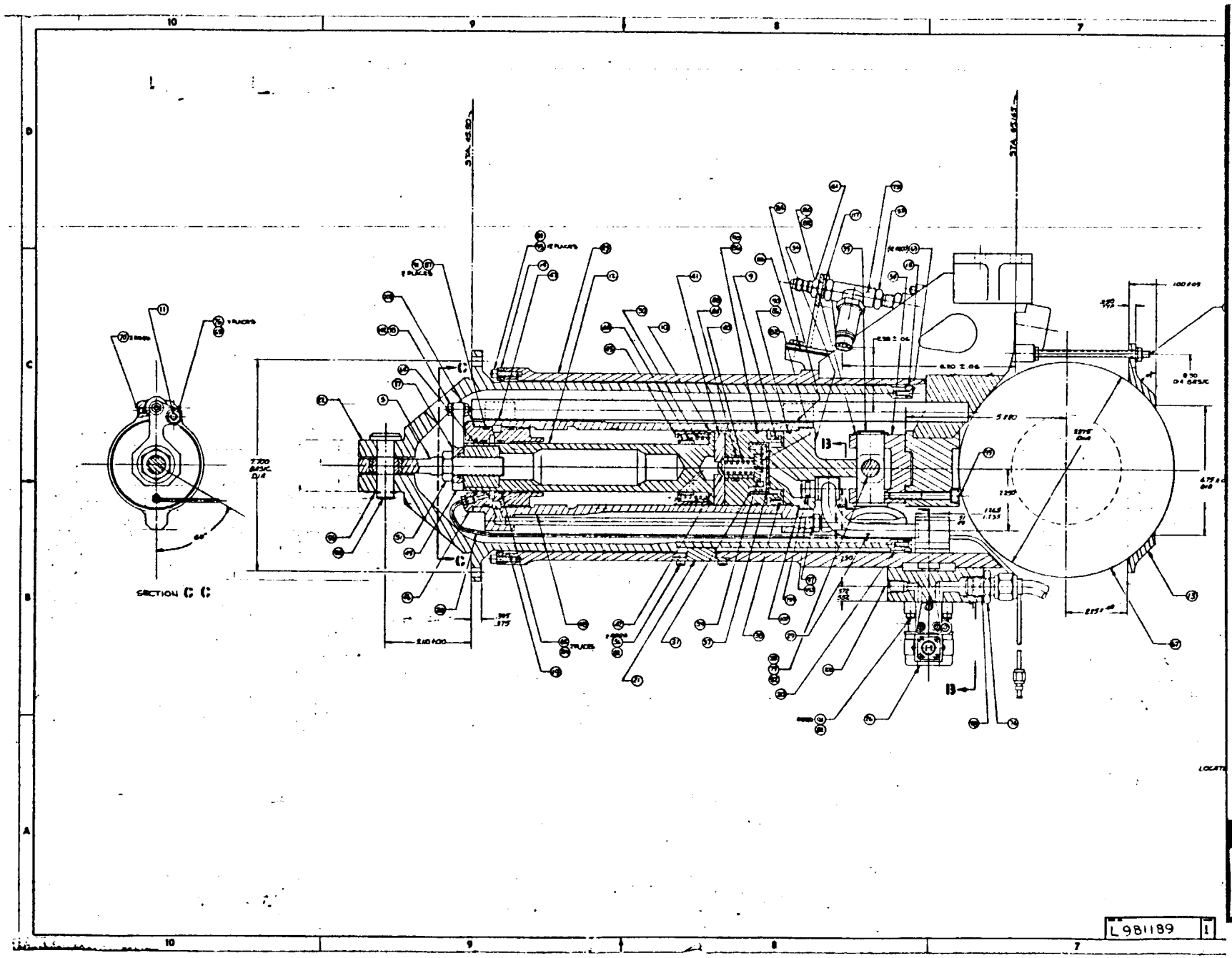
SECTION C C
L981189
1

UNCLASSIFIED

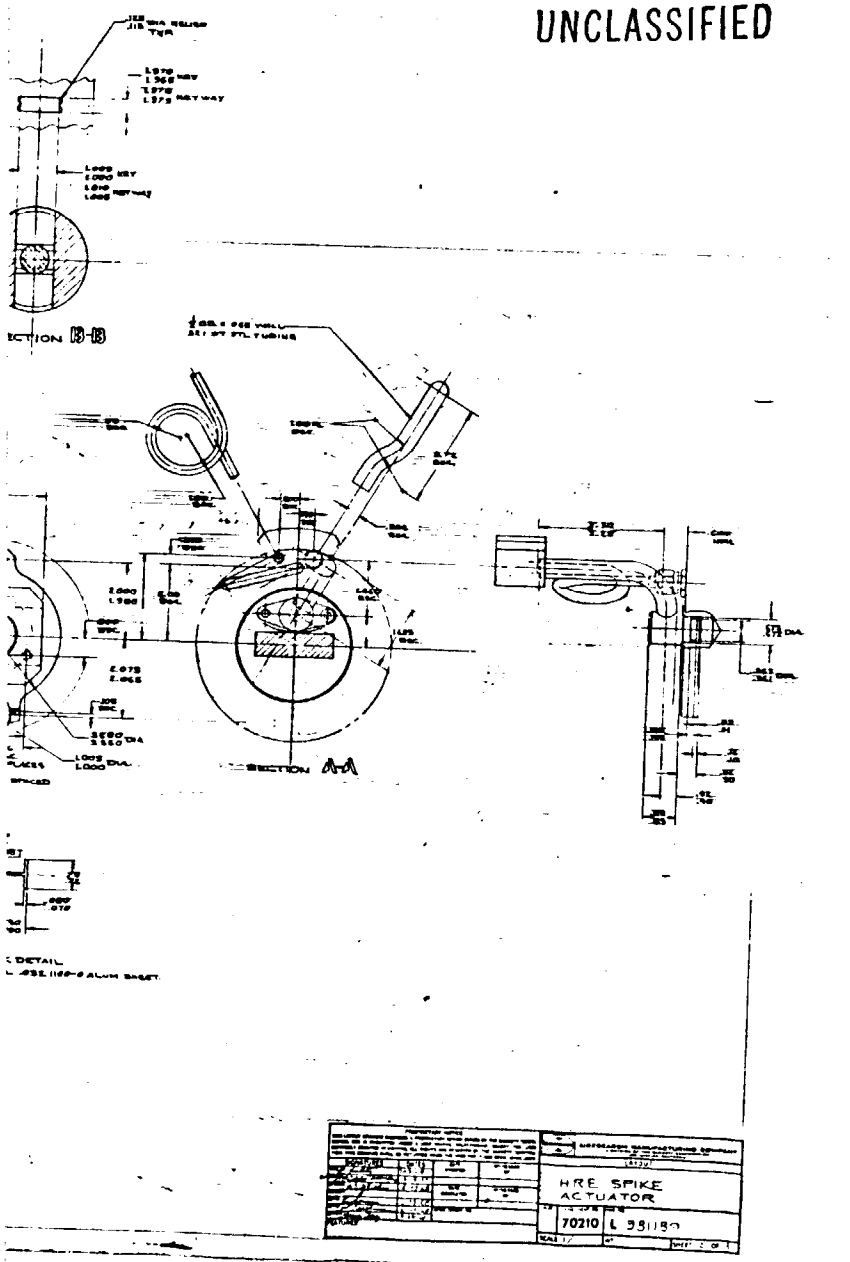

UNCLASSIFIED

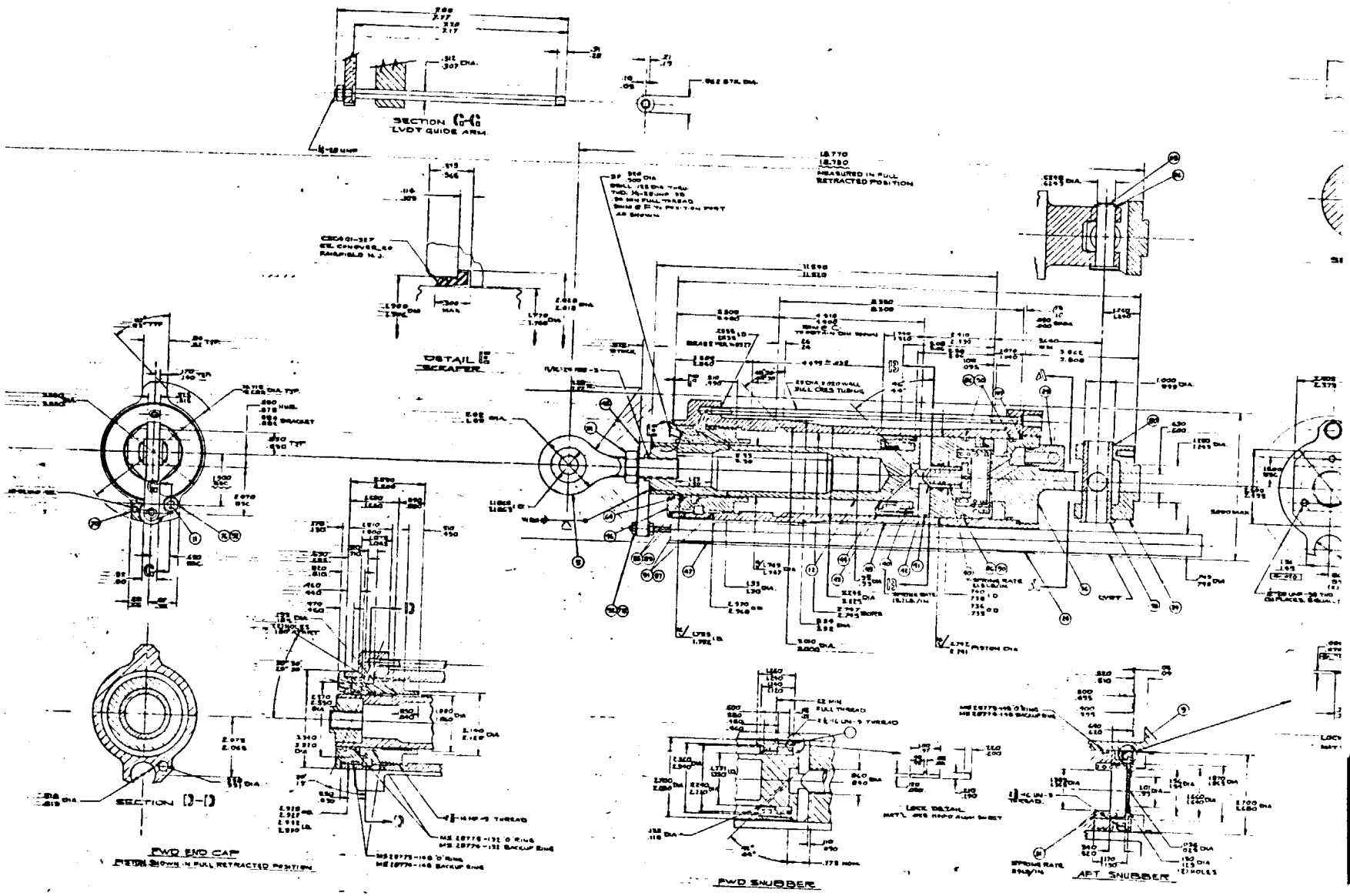
SECTION C-C
LVDT GUIDE ARM
MEASURED IN FULL RETRACTED POSITION
DETAIL
SCRAPER
SECTION D-D
FWD END CAP
PISTON SHOWN IN FULL RETRACTED POSITION
FWD SNUBBER
AFT SNUBBER
LVDT

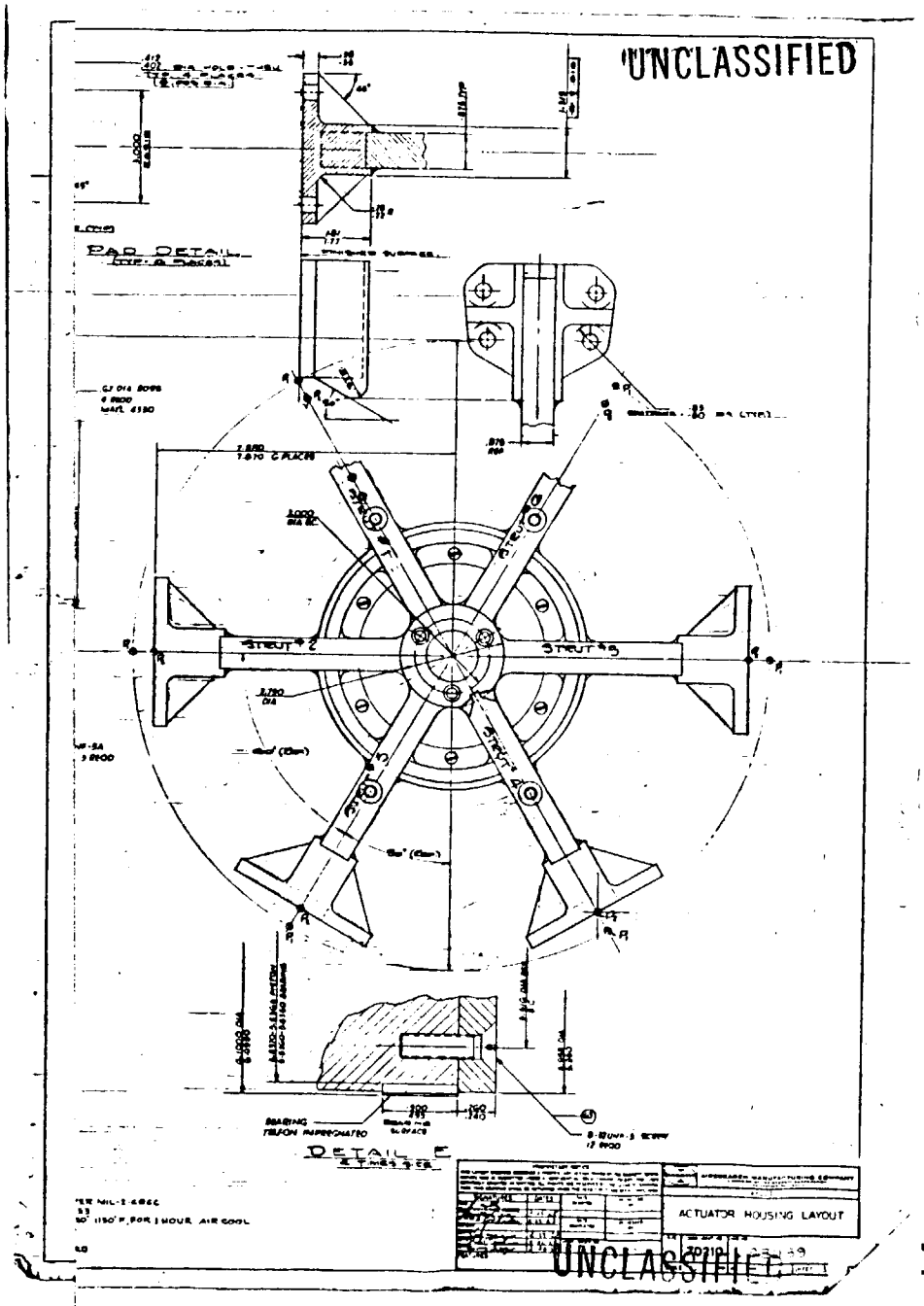
UNCLASSIFIED
PAD DETAIL
STRUT #1
STRUT #2
STRUT #3
STRUT #4
STRUT #5
DETAIL E
ACTUATOR HOUSING LAYOUT
UNCLASSIFIED

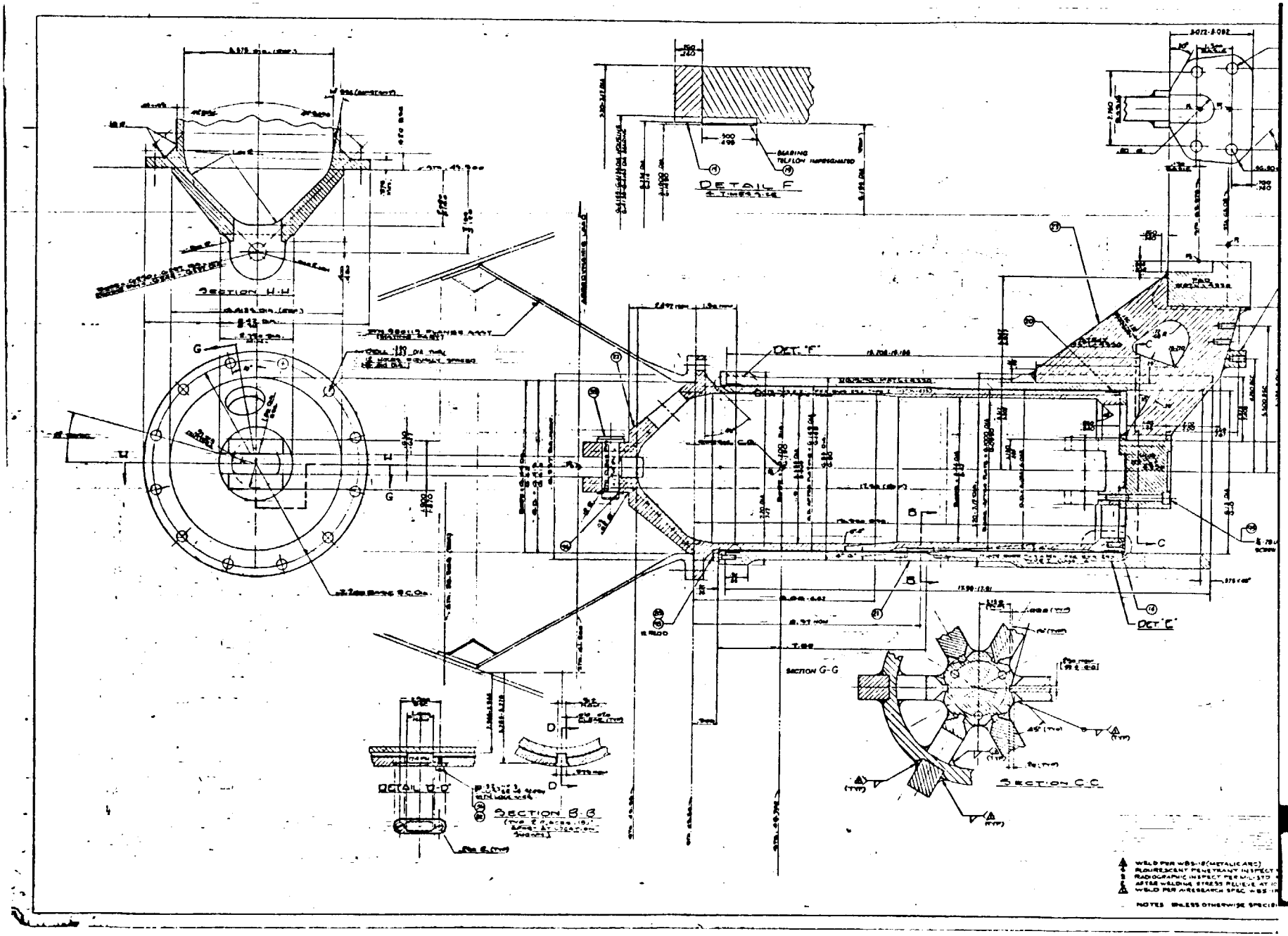
SECTION H-H
DETAIL F
BEARING TEFLON IMPREGNATED
DET. "F"
DET. "E"
SECTION G-G
SECTION C-C
SECTION B-B
DETAIL D-D
NOTES UNLESS OTHERWISE SPECIFIED